EXPERIMENTAL STUDIES AND CFD SIMULATIONS OF CONICAL SPOUTED BED HYDRODYNAMICS

by

ZHIGUO WANG

B.ASc, Tsinghua University, 1992
M.ASc, Tsinghua University, 1997

A THESIS SUBMITTED IN PARTIAL FULFILMENT OF THE REQUIREMENTS FOR THE DEGREE OF

DOCTOR OF PHILOSOPHY

IN

THE FACULTY OF GRADUATE STUDIES

(Chemical and Biological Engineering)

THE UNIVERSITY OF BRITISH COLUMBIA

July 2006

ABSTRACT

Conical spouted beds have been commonly used for drying suspensions, solutions and pasty materials. They can also be utilized in many other processes, such as catalytic partial oxidation of methane to synthesis gas, coating of tablets, coal gasification and liquefaction, pyrolysis of sawdust or mixtures of wood residues.

Literature review shows that there is still considerable uncertainty in hydrodynamics as compared to cylindrical spouted beds. No CFD simulation model has been developed to predict static pressure profiles, and there is a lack of experimental data on such characteristics as the evolution of the internal spout, particle velocity distribution, voidage distribution and gas mixing. Moreover, most empirical equations for the minimum spouting velocity and the pressure drop at stable spouting do not agree well with each other.

The main objectives of this work include both the experimental research and mathematical modeling of the conical spouted bed hydrodynamics.

Pressure transducers and static pressure probes were applied to investigate the evolution of the internal spout and the local static pressure distribution. Optical fibre probes were utilized to measure axial particle velocity profiles and voidage profiles. The step tracer technique using helium as the tracer and thermal conductivity cells as detectors was used to investigate the gas mixing behaviour inside a conical spouted bed. Many factors that might affect the calibration of the effective distance of an optical fibre probe were investigated. A new calibration setup was designed and assembled, and a comprehensive sensitivity analysis was conducted. The analysis included the effect of the glass window, the design of the rotating plate, the distance between the

rotating plate (or rotating packed bed) and the probe tip, the particle type, as well as the particle size.

A stream-tube model based on the bed structure inside a conical spouted bed was proposed to simulate partial spouting states. The proposed stream-tube model with a single adjustable parameter is capable of predicting the total pressure drop ΔP_t under different operating conditions, and estimating the distribution of the axial superficial gas velocity and the gauge pressure, especially for the descending process as well as in the region above the internal spout.

A mathematical model based on characteristics of conical spouted beds and the commercial software FLUENT was also developed and evaluated using measured experimental data. The proposed new CFD model can simulate both stable spouting and partial spouting states, with an adjustable solids source term. At stable spouting states, simulation results agree very well with almost all experimental data, such as static pressure profiles, axial particle velocity profiles, voidage profiles etc. A comprehensive sensitivity analysis was also conducted to investigate the effect of all possible factors on simulation results, including the fluid inlet profile, solid bulk viscosity, frictional viscosity, restitution coefficient, exchange coefficient, and solid phase source term.

The proposed new CFD model was also used successfully to simulate gas-mixing behaviour inside a conical spouted bed.

TABLE OF CONTENTS

LIST OF TABLES

LIST OF FIGURES

ACKNOWLEDGEMENT

I would like to express my sincere gratitude to all of those who gave their support and encouragement for the completion of this thesis.

First and foremost, I would like to thank my supervisors, Professors Xiaotao Bi and C. Jim Lim, for their invaluable and patient guidance as well as their continued support and encouragement throughout my studies.

I am especially indebted to Dr. Norman Epstein for providing me translated materials of early papers published in Russian.

Thanks to Dr. Fariborz Taghipour and Dr. Shahab Sokhansanj for their invaluable advice and assistance and for being my committee members. Thanks to other faculty members of Chemical and Biological Engineering for their comments and interests.

Thanks to all kinds of supports provided by the staff of the department. Peter Roberts, Graham Liebelt, Charles Cheung and Doug Yuen for their professional work in the experimental units. Horace Lam and Qi Chen for assisting with the procurement of experimental materials. Alex Thng for helping set up the instrumentation units of this project. Helsa Leong, Amber Lee and Lori Tanaka for their proficiency in keeping me on track. Darcy Westfall for his computer technical support.

Financial support from the NSERC and University Graduate Fellowship (UGF) is also gratefully acknowledged.

I extend my gratitude to Xuqi Song, Heping Cui, Zhiwei Chen, Aihua Chen, Tianxue Yang, Zhiming Fan, Hong E, Jianjun Dai, Ping Sun, Weisheng Wei, Qunyi Zhu, Min Xu, Jianghong Peng, Naoko Ellis, Arturo Macchi, Feridoun Fahiminia, Liangshou Zhou, Lei Wei, David Zhou and all other friends from the Great Wall Club for sharing their experience and expertise, and having made my stay at UBC a truly enjoyable one.

Most important of all, I would like to express my gratitude to my family for their love and dedication to my education. I thank my dear wife and son for their understanding, assistance and inspiration. I am sure they are too, looking forward to getting back to a normal family life.

CHAPTER 1

INTRODUCTION

1.1 Introduction

Conical spouted beds were first studied by Russian researchers in the 1960s as shown in Table A-1 (in Appendix A), with investigations mainly focused on the determination of the minimum spouting velocity, the maximum pressure drop and the pressure drop at stable spouting. Very little attention was given to the bed voidage and particle velocity distribution. According to their studies, there exist several specific transition velocities with increasing superficial gas velocity. As shown in Table A-1 (in Appendix A), they were the gas velocities for the formation of the internal spout, the formation of the outer spouting, and the carry-off of particles from the bed. The second period of research started in the late 1980s. As listed in Tables A-2, A-3, A-4 and A-5 (in Appendix A), investigations on conical spouted beds in this period covered almost all topics from hydrodynamics to modeling to applications, including the determination of minimum spouting velocity, voidage distribution, and measurement of particle velocities.

Figure 1-1 illustrates a conical spouted bed schematically, while Figure 1-2 shows a photograph of a semi-circular column at stable spouting. The bed is made up of three distinct regions: a dilute core called the spout, a surrounding annular dense region called the annulus, and a dilute fountain region above the bed surface. Solid particles are carried up rapidly with the fluid (usually gases) in the spout to the fountain and fall down onto the surface of the annulus by gravity where particles move slowly downward and, to some extent, inward as a loosely packed bed. Fluid from the spout leaks outwards into the annulus and percolates through the moving packed solids there. These solids are reentrained into the spout over its entire height. The overall system thereby consists of a centrally located dilute phase cocurrent-upward transport region surrounded by a dense-phase moving packed bed with countercurrent percolation of fluid and particle exchange.

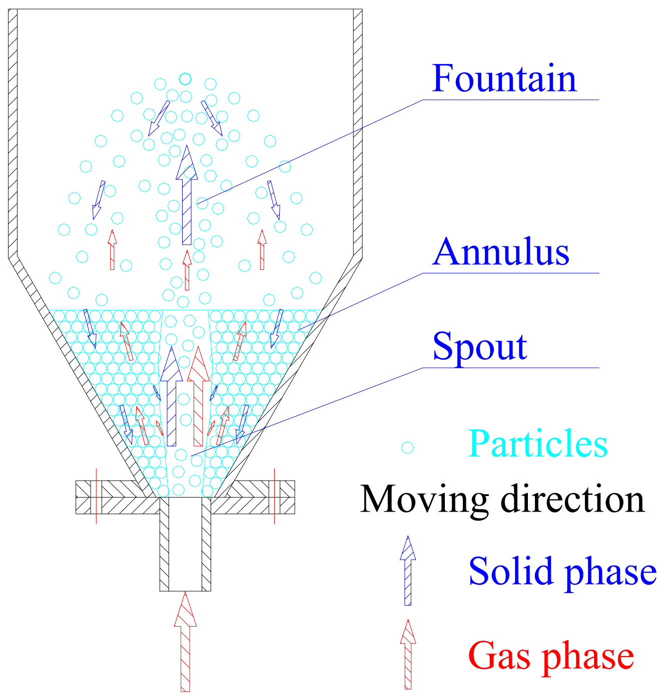

Fig. 1-1. Schematic diagram of a conical spouted bed.

Due to the vigorous systematic cyclic movement of solids and effective gas-solids contact, conical spouted beds have been commonly used for drying suspensions, solutions and pasty materials (Pham, 1983; Markowski, 1992; Passos et al., 1997, 1998; Reyes et al., 1998). Conical spouted beds can also be utilized in many other processes, such as catalytic partial oxidation of methane to synthesis gas (Marnasidou et al., 1999), coating of tablets (Kucharski and Kmiec, 1983), coal gasification and liquefaction (Uemaki and Tsuji, 1986), pyrolysis of sawdust or mixtures of wood residues (Aguado et al., 2000a, 2000b; Olazar et al., 2000a, 2000b, 2001a), although most of these are still under research and development. (See Table A-2 in Appendix A for a summary of conical spouted bed applications.)

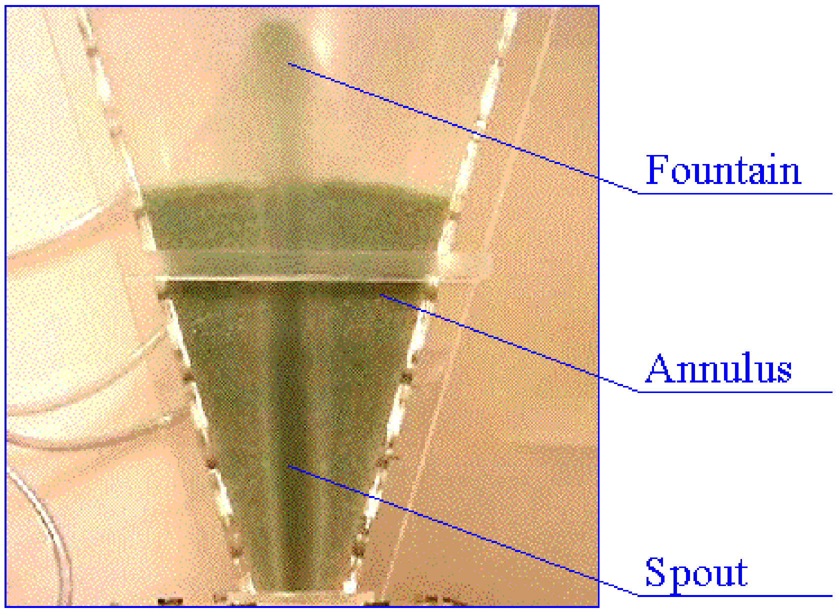

Fig. 1-2. Photograph of a semi-conical spouted bed. (γ=30º, D_i=0.0381m, D_0=0.0127m, H_0=0.23m, d_s=1.16mm, ρ_s=2,500kg/m^3, U_i=$(U_i)_{ms,d}$=6.6m/s)

Generally, to describe a conical spouted bed accurately or to design a proper conical spouted bed, one needs to know such hydrodynamic properties as follows: minimum spouting velocity, U_{ms}; maximum pressure drop, ΔP_{max}; operating pressure drop, $(\Delta P_s)_{sp}$; the diameter of the spout, D_s; the height of the fountain, H_f; the solids fraction in the fountain; gas-solids contact efficiency as well as heat transfer coefficient, gas dispersion coefficient, etc.

Although many equations are available for predicting U_{ms}, ΔP_{max} and $(\Delta P_s)_{sp}$ of conical spouted beds (Nikolaev et al., 1964; Gorshtein and Mukhlenov, 1964; Mukhlenov and Gorshtein, 1965; Tsvik et al., 1966, 1967; Wan-Fyong et al., 1969; Kmiec, 1983; Markowski et al., 1983; Olazar et al., 1992; Bi et al., 1997; Jing et al., 2000) (See Table A-5 in Appendix A for the summary of U_{ms} correlations.), there is still considerable uncertainty compared to cylindrical spouted beds. Moreover, most existing equations do not agree well with each other; there is a lack of experimental data on such hydrodynamic properties as the evolution of the internal spout, particle velocity profiles, voidage profiles, gas flow in the annulus etc. Knowledge of these properties is of fundamental importance for scale-up, modeling and design of conical spouted beds.

1.2 Flow regimes of conical spouted beds

According to San Jose et al. (1993), a typical diagram of the total pressure drop of a conical spouted bed with increasing and then decreasing superficial gas velocity is shown in Figure 1-3. In this diagram, four operating regimes can be recognized. As described by San Jose et al. (1993), these are the fixed bed regime, the stable spouting regime, the transition regime, and the jet-spouting regime, respectively. Figure 1-4 shows different states of the expansion of a conical spouted bed. After stable spouting (Figure 1-4a), on increasing the velocity, both annular and spout zones become progressively diffused and the particle movement outlined in Figure 1-4b is obtained. The transition evolves until the spout and annular zones are no longer distinguishable and the bed voidage becomes almost uniform, leading to a new state called jet spouting (Figure 1-4c). This regime stays stable with further increase in velocity, with a constant value of pressure drop.

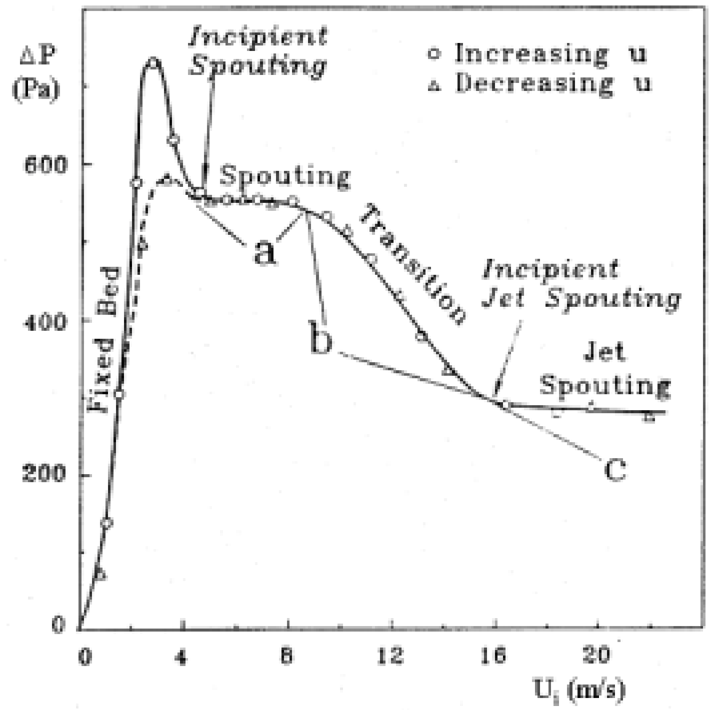

Fig. 1-3. The general pressure drop evolution curve at different flow regimes in a conical spouted bed. (San Jose et al., 1993)

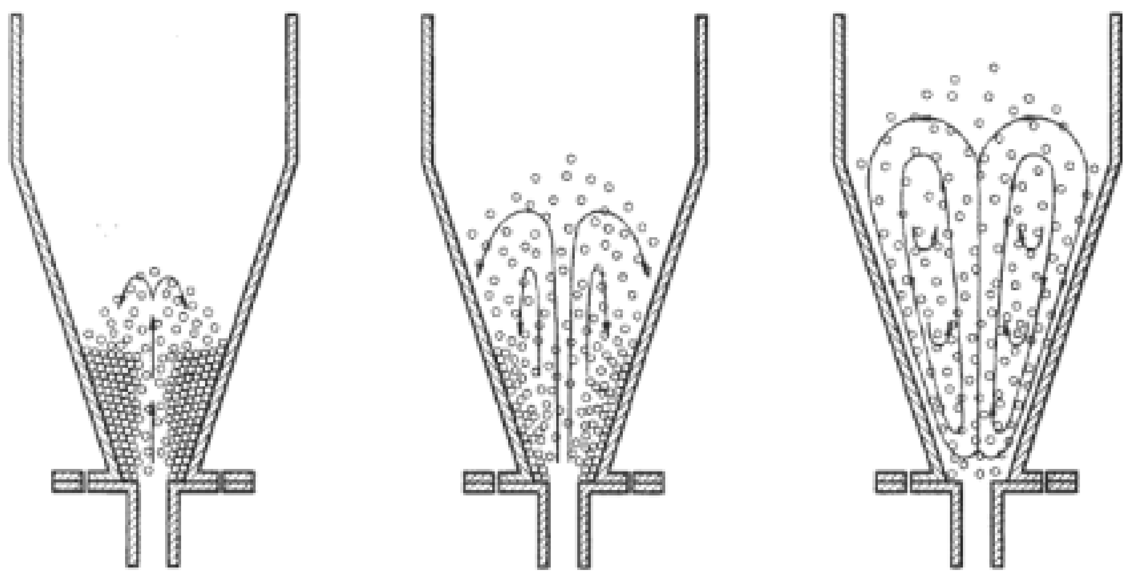

(a) Stable spouting (b) Transition (c) Jet spouting

Fig. 1-4. Different bed structures at different regimes in a conical spouted bed. (San Jose et al., 1993)

In this study, most investigations were focused on stable spouting, and partial spouting (With an internal spout or a cavity in the central region of packed particles, and his definition is more accurate than the definition of fixed bed by San Jose et al., 1993) was also investigated to some extent.

1.3 Similarity among conical spouted beds, cylindrical spouted beds and tapered fluidized beds

As shown in Figure 1-5, when $H_{01} \leq H_{c1}$, a cone-based cylindrical spouted bed becomes a conical spouted bed; a conical spouted bed can thus be treated as a cone-based spouted bed with the static bed height being equal to or lower than the height of the cone. Therefore, theoretically all equations for cylindrical spouted beds with H_0 being equal to or lower than H_c can be extrapolated to conical spouted beds, and all methods and techniques used in the research of cylindrical spouted beds can be adopted in the investigation of conical spouted beds with little modification.

Because of the similarity between conical and cylindrical spouted beds, the following reviews will include some literatures on cone-based shallow cylindrical spouted beds as shown in Table A-6 (in Appendix A).

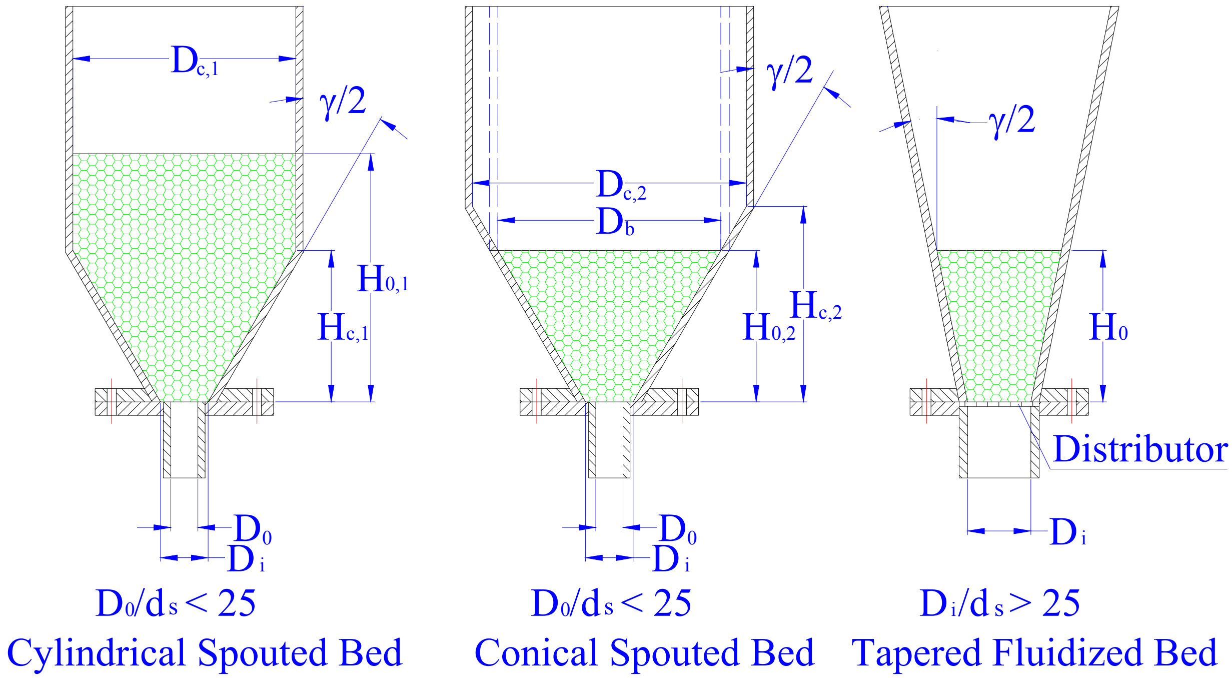

Fig. 1-5. Similarity of the bed structure between conical spouted beds, cone-based cylindrical spouted beds and tapered fluidized beds. (D_b=$D_{c,1}$, dashed lines are imaginary cylindrical wall.)

Compared with conical spouted beds, tapered fluidized beds have a distributor; the ratio of D_i to d_s (the diameter of particles) is always larger than 25. The tapered angle is typically small (<20º) and there is no stable centralized jet in tapered fluidized beds.

1.4 Hydrodynamics of conical spouted beds

1.4.1 Minimum spouting velocity

Table A-5 (in Appendix A) lists some correlations on minimum spouting velocity U_{ms}. Although quite a few investigations have been done on the minimum spouting velocity in conical spouted beds under different bed geometry and operating conditions, correlations developed by different researchers do not agree well with each other, as shown in Figure 1-6. Besides, in most studies, static bed height was lower than 0.3m, with the diameter of the gas inlet orifice being large and equal to the diameter of the bed bottom. Some U_{ms} correlations developed from the experimental data contain the diameter of the cylindrical section, which should not be included.

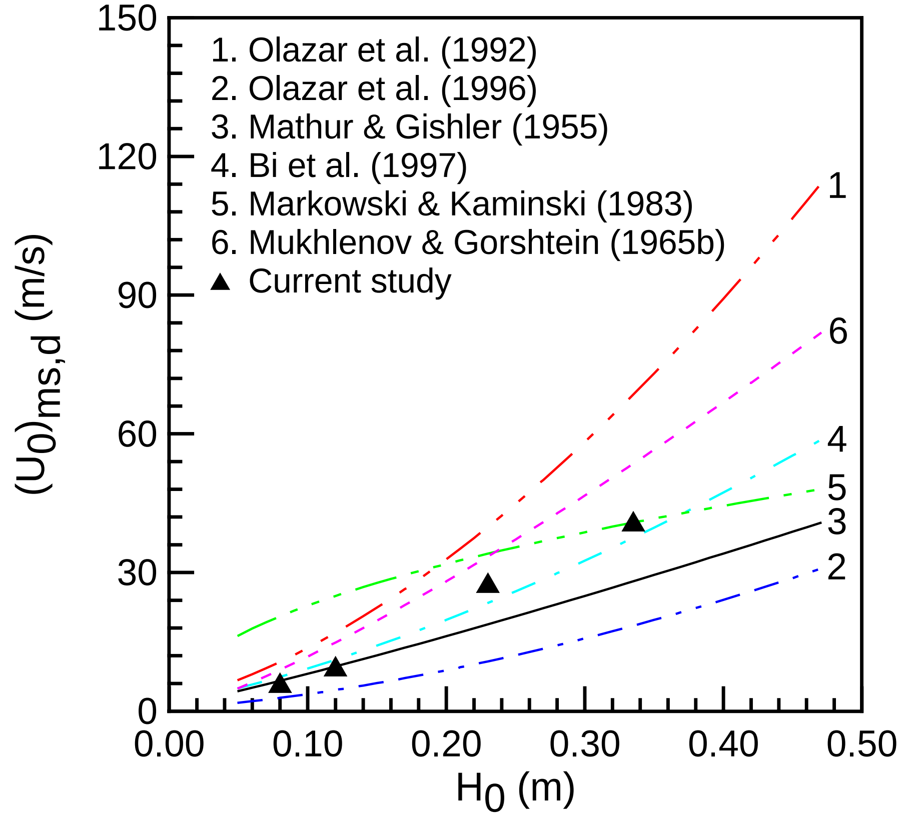

Fig. 1-6. Comparison between several correlations for the minimum spouting velocity. (γ=45º, D_i=0.0381m, D_0=0.0254m, d_s=1.16mm, ρ_s=2500kg/m^3, D_c=0.45m)

1.4.2 Maximum pressure drop and pressure drop under stable spouting

As listed in Table A-3 (in Appendix A), many studies have been done on the maximum pressure drop and the pressure drop under stable spouting in conical spouted beds. By using different geometries of conical spouted beds (different angles and gas inlet diameters) with solids of different sizes, densities and shape factors, Olazar et al. (1993c, 1994b, 1996c) proposed some correlations for calculating the maximum pressure drop and the pressure drop under stable operating conditions. Peng and Fan (1997) and Jing et al. (2000) extended the Ergun equation for the calculation of the maximum pressure drop and the pressure drop under stable operation. However, as mentioned in their papers, those models are limited to tapered fluidized beds with small cone angles.

1.4.3 Particle velocity and bed voidage

Using the piezoelectric method, Gorshtein and Mukhlenov (1967) first measured vertical solids velocity profiles in the spout of a conical spouted bed. Boulos and Waldie (1986) measured particle velocities in a half column using Laser-Doppler Anemometry. Based on their description, the column was a half conical spouted bed. Furthermore, absolute values of particle velocities were hard to read from their paper. Waldie and Wilkinson (1986) measured average particle velocity at different heights in the spout by measuring the change of inductance of a search coil using a marker particle with high electromagnetic permeability.

Using optical fibre probes, Olazar's group studied particle velocity distribution (Olazar et al., 1998, 1995b; San Jose et al., 1998a), solids cross-flow (Olazar et al., 2001b), local voidage distribution and the geometry of the spout (San Jose et al., 1998b; Olazar et al., 1995b), as listed in Table A-3 (in Appendix A). Olazar et al. (1998) determined the vertical components of particle velocities in the spout and annular regions of conical spouted beds of different bed geometries (cone angle and gas inlet diameter) under different operating conditions (particle diameter, stagnant bed height, gas velocity). San Jose et al. (1998a) determined the solids vertical velocity component and the horizontal velocity component by solving the mass conservation equations for the solids in both spout and annular zones. The experimental measurements of particle flow rate along the spout as well as the solids cross-flow rate from the annulus into the spout were also determined.

San Jose et al. (1998b) studied the local voidage, and developed a correlation relating the local voidage to the voidage at the spout axis and at the wall. By means of a probe composed of three bundles of optical fibres placed in parallel, Olazar et al. (1995b) investigated the geometry of the spout, the local voidage, and velocities and trajectories of particles.

As summarized in Table A-3 (in Appendix A), all experimental investigations on hydrodynamic behaviour of conical spouted beds have some limitations, such as the cone angle being between 28º and 60º and the static bed height being lower than 0.3 m. Most studies have been focused on minimum spouting velocity and pressure drops, few studies have been done on local flow structure, gas and solids mixing, and modeling of reactor performance.

1.5 Mathematical models for conical spouted beds

1.5.1 Mathematical models for transition velocities and pressure drops

Some hydrodynamic models used for conical spouted beds are summarized in Table A-4 (in Appendix A).

Kmiec (1983) developed a model for predicting the minimum spouting velocity and pressure drop in conical spouted beds, and found that this model agreed quite well with their experimental data. This model made the following assumptions:

- Local fluid velocities and pressures have constant values on surfaces of spherical caps;
- Pressure drop can be described by the Ergun equation;

- At the point of the minimum spouting velocity, the pressure drop not only counteracts the gravity force of the bed but also causes breaking of the bed, and a "breaking force coefficient K_B" was introduced, and estimated from an analysis of the force balance.

Hadzismajlovic et al. (1986) developed a model for calculating the minimum fluid flow rate and pressure drop in conical spouted beds. The model was based on the concept of dividing the bed into a large number of equal cylindrical segments, each of which, except that at the spout inlet, is treated as a spout-fluid bed. It also assumed that superficial gas velocity at the top of the spout equals the minimum fluidizing velocity and the spout diameter equals the spout diameter of the spout-fluid bed at the top of the bed or the last segment. This model can predict both the minimum spouting flow rate and the bed pressure drop well, and the deviations between predictions and their experimental data are 8.4% and 13.1%, respectively. Povrenovic et al. (1992) compared this model with their experimental data, and found that measured and predicted values of the minimum spouting flowrate and pressure drop differed by 10.3% and 20.0%, respectively.

In liquid-solid two-dimensional tapered fluidized beds (γ=5º, 10º, 20º, 30º), Peng and Fan (1997) applied the Ergun equation to predict pressure drop and transition velocities by incorporating force balances at the transition point. Jing et al. (2000) applied these equations to gas-solid tapered fluidized beds (γ=20º, 40º, 60º) and found that those equations gave good agreement with data in a column of small included angle (γ=20º). To bring the Ergun equation closer to the U_{ms} data in conical spouted beds, a correction factor was introduced by Bi et al. (1997).

1.5.2 Mathematical models for gas flow

Rovero et al. (1983) proposed two models, the cone-modified Mamuro-Hattori model and the vector Ergun equation model for shallow beds of cylindrical geometry with a conical base, to predict the variation of annulus gas velocities. The cone-modified Mamuro-Hattori model used Darcy's law to describe the relationship between the axial pressure drop and the annular fluid velocity, and assumed that the diameter of the spout is constant and the annular velocity at the maximum spoutable height equals the minimum fluidization velocity. The vector Ergun equation model used the vector form of the Ergun equation to describe the flow field in the annulus; at the spout-annulus interface; the pressure distribution was assumed to be governed by the relationship derived by Epstein and Levine (1978). Both models predicted well the trends of the annulus gas velocity variations with the bed height, but there existed obvious quantitative differences between the measured and predicted annulus velocities. The authors thought that these might result from the assumption of constant spout diameter, neglect of solids motion, and inadequate knowledge of behaviour at the inlet.

Olazar et al. (1995a) proposed a model for calculating the local gas velocity and estimating the gas dispersion coefficient. This model and its assumptions were mainly based on the model of Lim and Mathur (1976) for cylindrical spouted beds. Because of the different structure of the conical spouted bed, they made some modifications. The origin of the coordinates of the system is taken as the apex of the imaginary cone traced from the upper limit of the bed to the inside comer of the gas inlet, the streamlines are assumed to be straight lines and the upper surface of the bed in the annular zone is a spherical cap, instead of a flat surface. On the basis of the experimental study of gas velocity profiles measured by Pitot tubes, and hydrogen tracer concentrations measured by thermal conductivity detectors at the inlet and exit, they calculated the local gas velocity and the gas dispersion coefficient D, as shown in Figures 1-7 and 1-8, where F(t) is the cumulative distribution function. San Jose et al. (1995) further verified the hypotheses that the gas flow rate is conserved along each stream tube and that the gas is in plug flow in the spout zone. They also developed a correlation for the local gas velocity and a correlation for the gas dispersion coefficient.

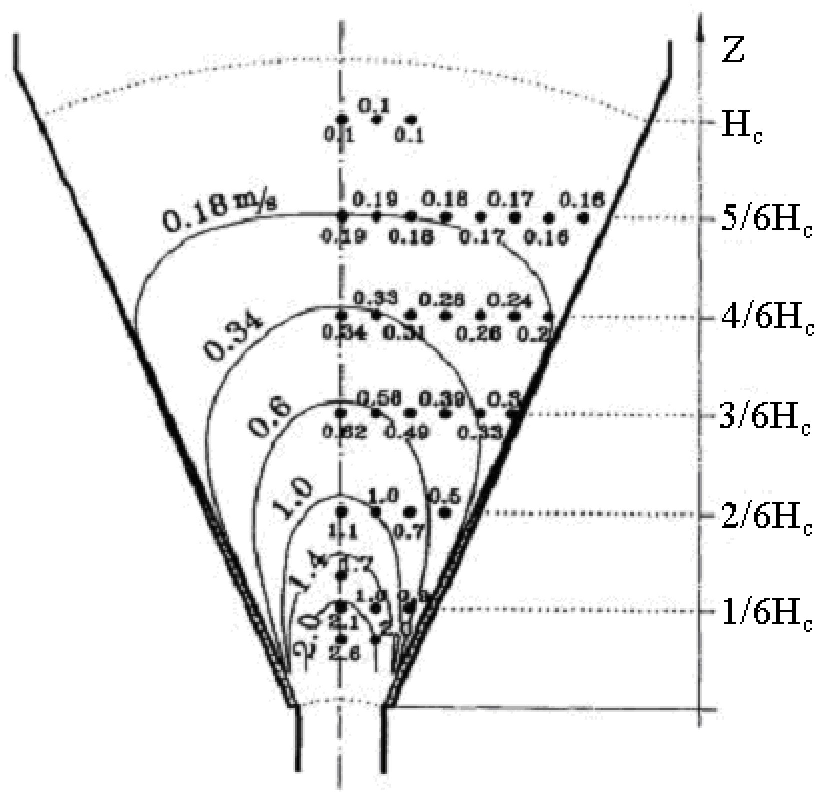

Fig. 1-7. Comparison between predicted and measured interstitial gas velocity profiles under stable spouting. (Olazar et al., 1995a, lines are predicted isokinetic curves, symbols are experimental data.) (γ=45º; D_i=0.06m; D_0=0.05m; ρ_s=14kg/m^3; H_0=0.28m; H_c=0.36m; d_s=3.5mm; U_i=2.2m/s).

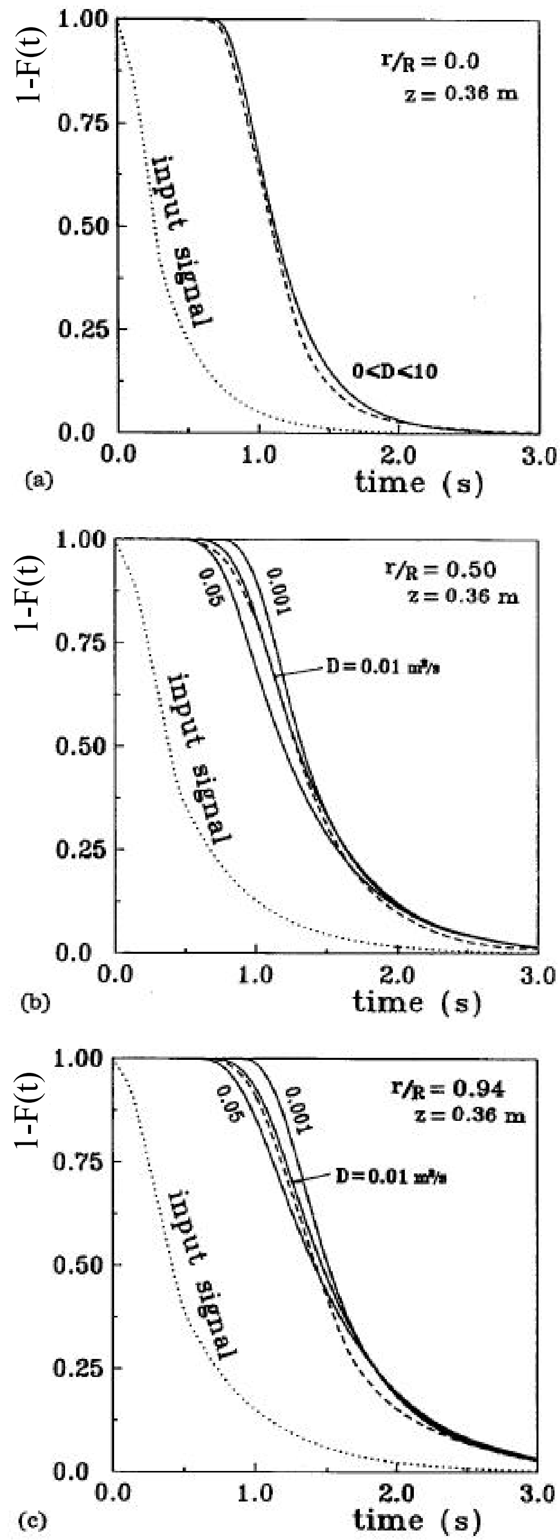

Fig. 1-8. Tracer response at the exit of a conical spouted bed in three radial positions. Solid line: Values calculated; Dashed line: Experimental response (Olazar et al., 1995a) (γ=45º; D_i=0.06m; D_0=0.05m; ρ_s=14kg/m^3; H_0=0.28m; H_c=0.36m; d_s=3.5mm; U_i=2.2m/s).

1.5.3 Computational Fluid Dynamics (CFD) simulation of spouted beds

Generally, there are two approaches that can be used to simulate multiphase systems, the Discrete Element Method (DEM) and the Two-Fluid Model (TFM).

In the DEM approach, the fluid phase is treated as a continuum by solving the time-averaged Navier-Stokes equations, and the dispersed phase is solved by tracking a large number of particles (or bubbles, droplets) through the calculated flow field, with the two phases being coupled through interphase forces.

In the TFM approach, different phases are treated mathematically as interpenetrating continua. Since the volume of a phase cannot be occupied by the other phases, the concept of phasic volume fraction is introduced. Conservation equations for each phase are derived to obtain a set of equations, which have a similar structure for all phases.

There have been only a few CFD simulations on spouted beds, fewer on conical spouted beds. Moreover, there were only a few experimental data that could be used to evaluate the CFD models. Thus, CFD simulations on both cylindrical spouted beds and conical spouted beds will be reviewed in this part, as summarized in Table A-7 (in Appendix A).

It can be seen from Table A-7 (in Appendix A) that, both approaches have been adopted in simulations of spouted beds, and experimental data that can be used to evaluate CFD simulations were mainly limited to axial solids velocity profiles and voidage profiles from few sources. In almost all simulations using the TFM approach, the gas inlet velocity was assumed to have a uniform or a parabolic profile, and the diameter of the bed bottom was assumed to be the same as the diameter of the gas inlet, obviously different from experimental conditions. Moreover, in all simulations, particles were assumed to be completely suspended; this assumption is valid in the spout and fountain, but is questionable in the annulus.

1.6 Research objectives and principal tasks

From the above review, we can make the following observations:

- Compared to cylindrical spouted beds, conical spouted beds have their unique characteristics, such as having no maximum spoutable height in the typical range of cone angle (e.g. 20º~90º) and lower pressure drops, while, the similarity is obvious.
- There are still some limitations of experimental studies. For example, in most cases, the static bed height used in previous studies was smaller than 0.3 m.
- Most experimental works on conical spouted beds have been focused on the minimum spouting velocity and the total bed pressure drop, with few studies focused on the local hydrodynamic behaviour (such as the local static pressure, local solids velocity and local voidage) and gas mixing. As a result, few experimental data can be used to evaluate the modeling of the reactor performance.
- Assumptions adopted in mathematical models were not evaluated. For example, the diameter of the spout is constant (Rovero et al., 1983; Olazar et al., 1995a; San Jose et al., 1995), all particles in partially fluidized states and spouting states were considered to be completely suspended in the fluid (Peng and Fan, 1997; Jing et al., 2000; Kawaguchi et al., 2000; Huilin et al., 2001; Lu et al., 2004; He et al., 2004; Takeuchi et al., 2004, 2005; Duarte et al., 2005; Du et al., 2006). As a result, no model can predict transition velocities and pressure drops well, and no CFD simulation can predict static pressure profiles well.

Issues outlined above suggest a need for one or several versatile and integrated conical spouted bed models. Such models should capture and describe adequately hydrodynamic behaviour within the bed, such as minimum spouting velocity, maximum pressure drop, operating pressure drop at stable spouting, the structure of the bed, the evolution of the internal spout, gas velocity distribution, solids motion, and solids cross-flow from the annulus into the spout. The main objectives of this work are therefore:

- To develop a mathematical model based on the flow structure of conical spouted beds with an internal spout ($U_0<(U_0)_{ms}$), to predict total pressure drops at different operating velocities as well as the distribution of the local static pressure and the axial superficial gas velocity, and to have the model evaluated using experimental data obtained over a wide range of operating conditions and column geometries.
- To develop a mathematical model to predict local gas and solids flow structures in a conical spouted bed under stable spouting conditions and have the model evaluated using particle velocity profiles, static pressure profiles, solids fraction profiles and gas tracer experimental data collected over a wide range of operating conditions.

Based on the above objectives, several semi-circular and circular conical spouted beds with different geometries (cone angle, gas inlet diameter) have been constructed. Several kinds of experimental techniques or probes, such as the optical fibre probe, the static pressure probe and the gas tracer technique, will be adopted to investigate solids velocity profiles, voidage profiles, static pressure profiles and gas mixing behaviour.

Experimental work will include:

- Measurement of the total pressure drop and the height of the internal spout using static pressure probes or visual observation in semicircular columns during the process of increasing and then decreasing superficial gas velocity;
- Measurement of the static pressure distribution in the bed using static pressure probes;
- Measurement of solids velocity profiles and local bed voidages using the optical fibre probe;

- Measurement of the gas mixing behaviour using helium as the tracer and the thermal conductivity cell as the detector.

1.7 Arrangement of the thesis

Chapter 1 presents a detailed literature review for conical spouted beds, and an introduction to the current work.

Chapter 2 summarizes detailed designs of conical spouted beds used in this work, together with particulate materials used.

Chapter 3 presents hydrodynamic behaviour in conical spouted beds, including determination of minimum spouting velocity and pressure drop under stable spouting, as well as axial and radial distributions of static gauge pressures. A stream-tube model is presented for predicting the overall pressure drops of conical spouted beds as well as local static pressures and axial superficial gas velocities.

Chapter 4 presents studies of local flow structure in a conical spouted bed, and mainly focuses on distributions of solids hold-up and axial solids velocity.

Chapter 5 focuses on CFD simulations for a conical spouted bed as per measurements in Chapter 4.

Chapter 6 presents the results on gas mixing behaviour in a conical spouted bed obtained both experimentally and by CFD simulations. Also, the gas tracer technique and the calibration of sampling probes are presented.

Chapter 7 is a summary of the current work, together with some recommendations for future studies.

Appendix A lists all tables cited in Chapter 1.

Appendix B presents the calibration of the orifice meter.

Appendix C lists all pressure transducers used in current study and their calibrations.

Appendix D presents the calibration of the optical fibre probe for both particle velocity and solids fraction measurements.

Appendix E presents the selection of some simulation parameters, such as the grid partition, the time step size, the convergence criterion and the discretization scheme (i.e. 1st or 2nd order).

Appendix F shows the evaluation of the proposed CFD model using experimental data measured from a packed bed and a fluidized bed.

Appendix G shows the evaluation of the proposed CFD model using experimental data from the literature.

Appendix H lists Matlab programs for the stream-tube model.

Appendix I lists Matlab programs for the cross-correlation analysis.

Appendix J lists Matlab programs for the estimation of mean residence time and variance.

Appendix K lists programs (C language) for all user-defined functions used in CFD simulations.

CHAPTER 2

EXPERIMENTAL SET-UP

2.1 Conical spouted beds

A schematic conical spouted bed is given in Figure 2-1, with all geometric factors shown and documented in Table 2-1. In the current study, four kinds of columns made of plexiglass were used, with the cone angle γ of 30º, 45º, or 60º. The diameter of the gas inlet orifice D_0 is 0.0127 m, 0.01905 m, or 0.0254 m respectively, with the diameter of the bed bottom D_i fixed at 0.0381 m and the height of the cone section H_c fixed at 0.5 m. In order to investigate the difference between the half column and the full column, a full column with the cone angle γ of 45º was also used. For each column, a series of ports were set along the wall of the column, as shown in Figure 2-2. In the cone section ($Z<H_c$), the distance between two adjacent ports is 50.8 mm, except the distance between Port 1 and Port 2, which is 38.1 mm. For half columns, the ports are located on the opposite side of the front panel. All kinds of probes, such as static pressure probes, optical fibre probes and gas sampling probes, can be installed in these ports and move conveniently along the radial direction.

A schematic diagram of an experimental unit is shown in Figure 2-2. During experiments, the gas flow rate was determined by an orifice flow meter, and two pressure transducers were used to measure the operating pressure before the orifice and the pressure drop across the orifice.

The bypass “Vent” line shown in Figure 2-2 was used to stabilize the operating pressure (eliminate the fluctuations of the operating pressure) by keeping the total flow rate almost constant and adjusting the openings of two valves to achieve different operating velocities.

Advantages of using such an arrangement are clearly shown in Figure 2-3. Thus, the bypass was used throughout the current study.

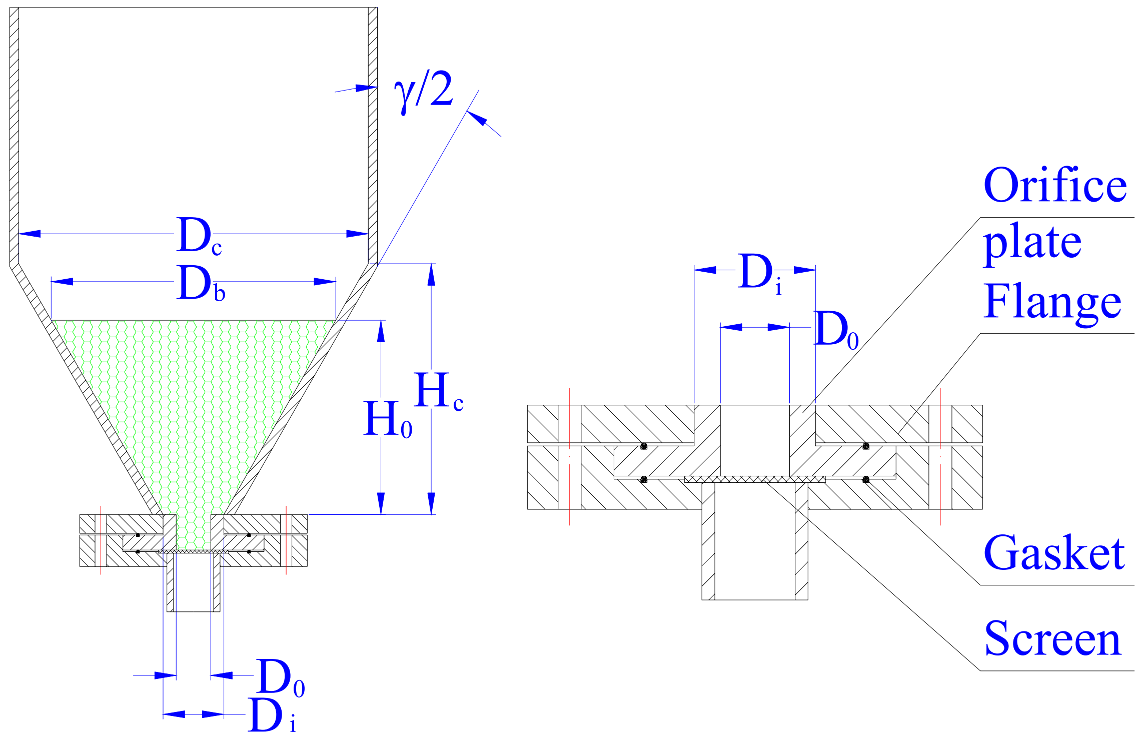

Fig. 2-1. Schematic diagram of a conical spouted bed and its main geometrical dimensions.

Table 2-1. Parameters of experimental facilities used in the current study.

γ	D_i (m)	H_c (m)	D_0 (m)
30° H			0.0127
45°H	0.0381	0.5	0.01905
45°F			0.0254
60° H			

Note: H------for the half column

F------for the full column

Except parameters listed in Table 2-1, other parameters such as D_b and D_c, can be calculated based on following equations.

$$D_b = D_i + 2H_0 \cdot \tan(\frac{\gamma}{2}) \tag{2-1}$$

$$D_c = D_i + 2H_c \cdot \tan(\frac{\gamma}{2}) \tag{2-2}$$

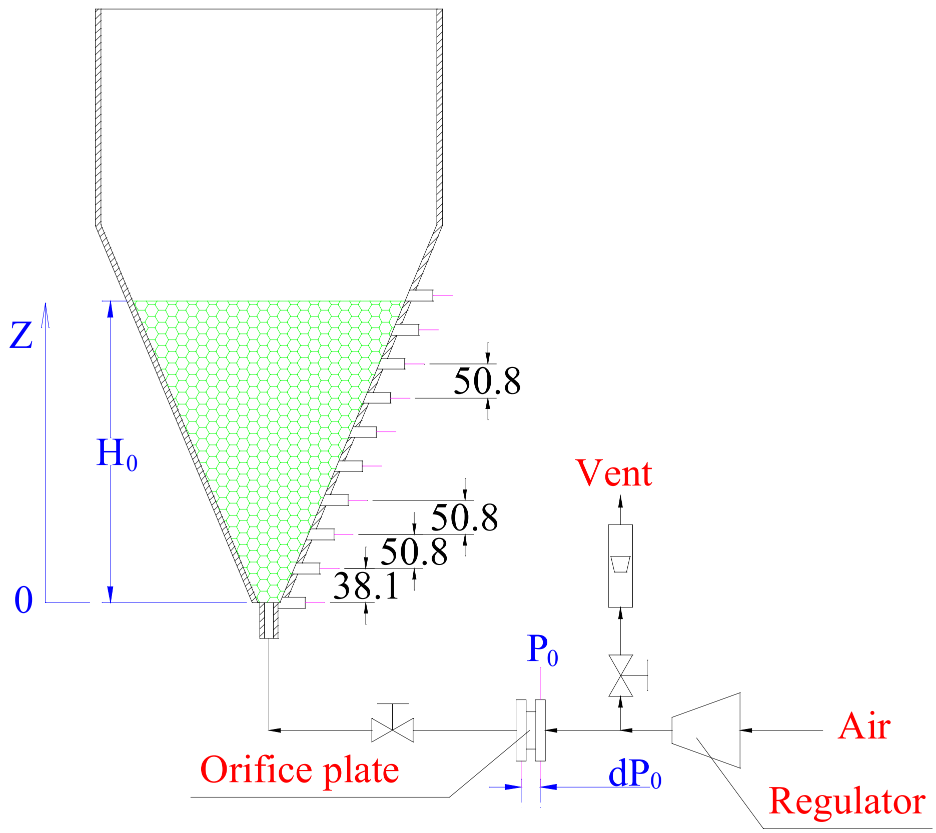

Fig. 2-2. A schematic diagram of an experimental unit (Numbers are in millimeters.).

In order to eliminate the influence of the uncontrolled initial packing state, prior to each experimental run, the conical spouted bed was pretreated by increasing superficial gas velocity to obtain full external spouting and then decreasing superficial gas velocity gradually to return to a reproducible initial fixed bed condition. Meanwhile, to obtain representative pressure drop evolution loops, gas velocity was increased all the way up until stable spouting states were obtained, and then gas velocity was decreased all the way down until the initial fixed bed was achieved.

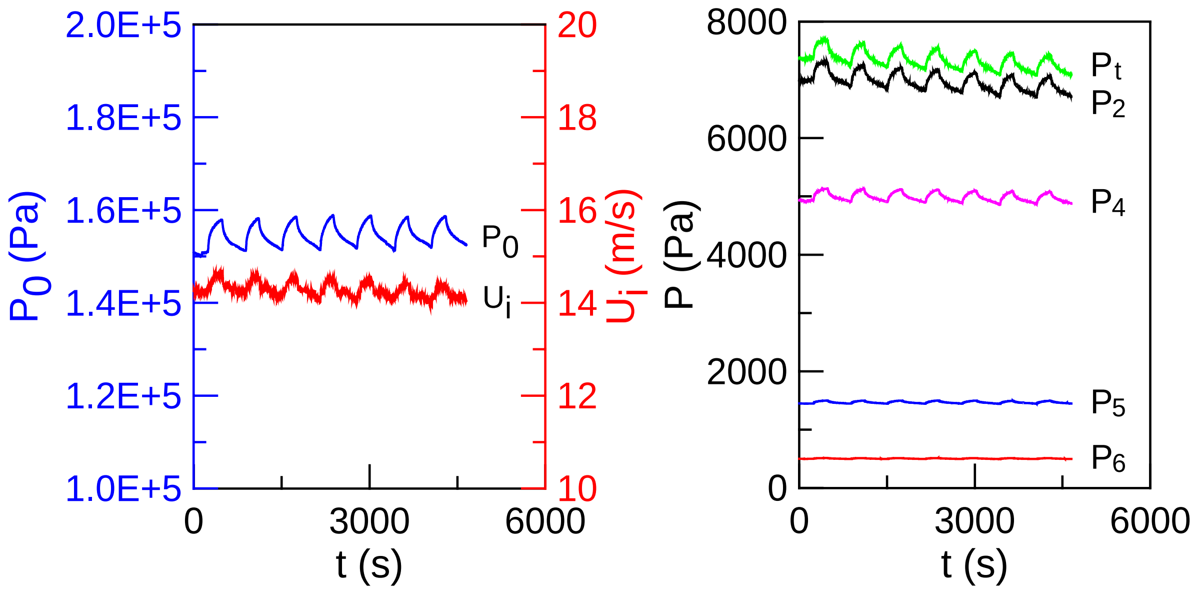

(Without bypass)

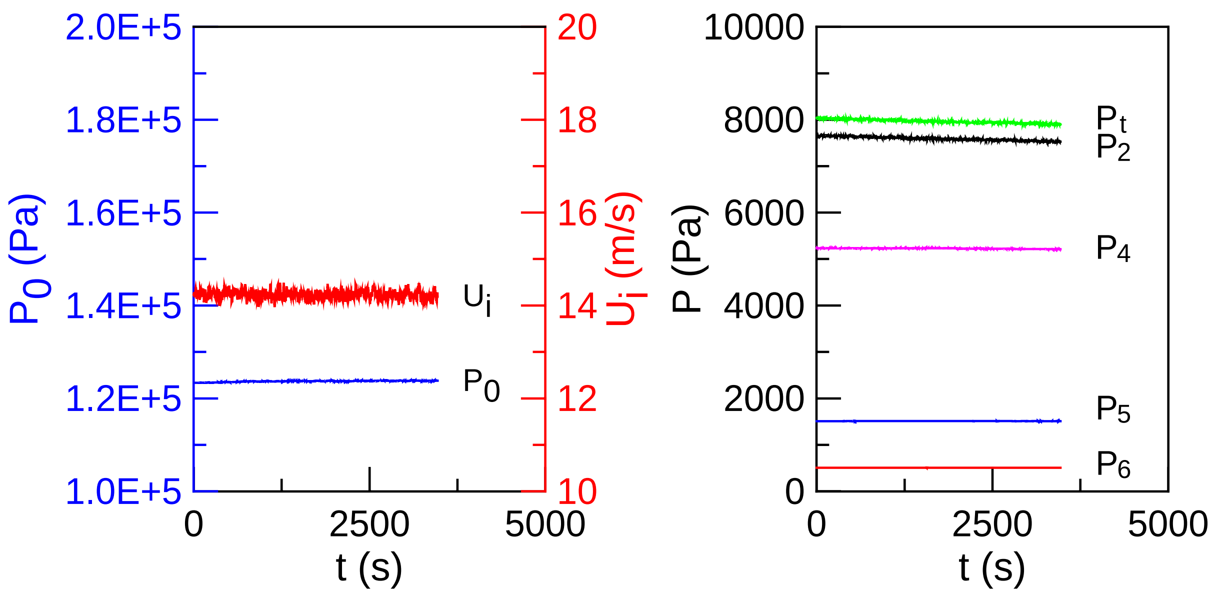

(With bypass)

Fig. 2-3. Comparison between operations with bypass and without bypass. (P is the gauge pressure, U_i is superficial gas velocity at the bottom of a conical spouted bed.)

Except for the above general considerations, detailed experimental procedures and experimental techniques for different experiments are given in corresponding sections. For example, the calibration of the pressure transducers is given in Appendix C, the calibration of the optical fibre probe is shown in Appendix D, and the calibration of thermal conductivity cells is described in Chapter 6.

2.2 Particles and the measurement of the density and voidage

Particles for the current study were glass beads of 1.16 mm in mean diameter with particle size distribution (PSD) shown in Figure 2-4. Air from the compressor was used as the spouting gas. Glass beads of 2.4 mm in diameter were also used in some cases.

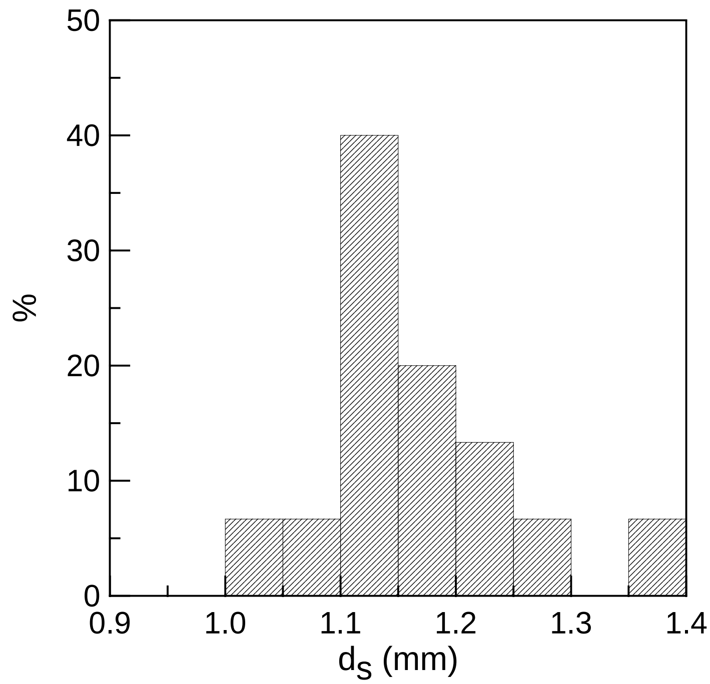

Fig. 2-4. Particle size distribution for glass beads with 1.16 mm in mean diameter.

The particle density and the packing voidage were measured using the water displacement method. First, particles (either loosely packed or tightly packed) were poured into a 500 ml volumetric flask of known weight. After measuring the total weight, the weight of particles was then calculated. Next, water was added slowly into the flask until the particles were just submerged with no bubble inside the flask. The volume of water added was recorded during this process or calculated by weighing the total assemblage (including particles, the flask and water). By subtracting the volume of water from the total volume, the volume of particles was obtained, and the density of particles could thus be calculated. The volume of water divided by the total volume gives the packing voidage. During experiments, a loosely packed state was achieved by slowly pouring particles into the flask. By intentionally compressing particles inside the flask, a tightly packed state could be achieved, although this kind of packing state will never occur in the spouted bed under stable spouting.

As shown in Table 2-2, measured maximum solids fraction was 0.63 for both kinds of glass beads, and measured loosely packed solids fraction was 0.6. Measured particle density was 2486 kg/m^3, very close to the value provided by the manufacturer, 2500 kg/m^3.

Table 2-2. Properties of glass beads used in the current study.

Material	d_s (mm)	ρ_s (kg/m^3)	Sphericity φ_s	Loosely packed solids fraction $\varepsilon_{s,0}$	Compacted solids fraction $\varepsilon_{s,\max}$
Glass beads	1.16	2487	1	0.60	0.63
Glass beads	2.40	2485	1	0.60	0.63

Because glass beads of 1.16 mm in diameter were generally used in this research, the voidage with this kind of particle was further investigated by measuring the pressure drop across a packed bed column, with an inside diameter of 101.6 mm, at different superficial gas velocities. By curve-fitting using the Ergun equation with the voidage as the unknown, the loosely packed solids fraction was found to be 0.61, as shown in Figure 2-5, consistent with Table 2-2.

In summary, because measured particle density is very close to the value provided by the manufacturer, 2500 kg/m^3, the value from the manufacturer was used in CFD simulations. In addition, using different methods, measured values of the loosely packed solids fraction were almost identical, the more accurate value measured from packed bed pressure drop measurements was selected for use in CFD simulations.

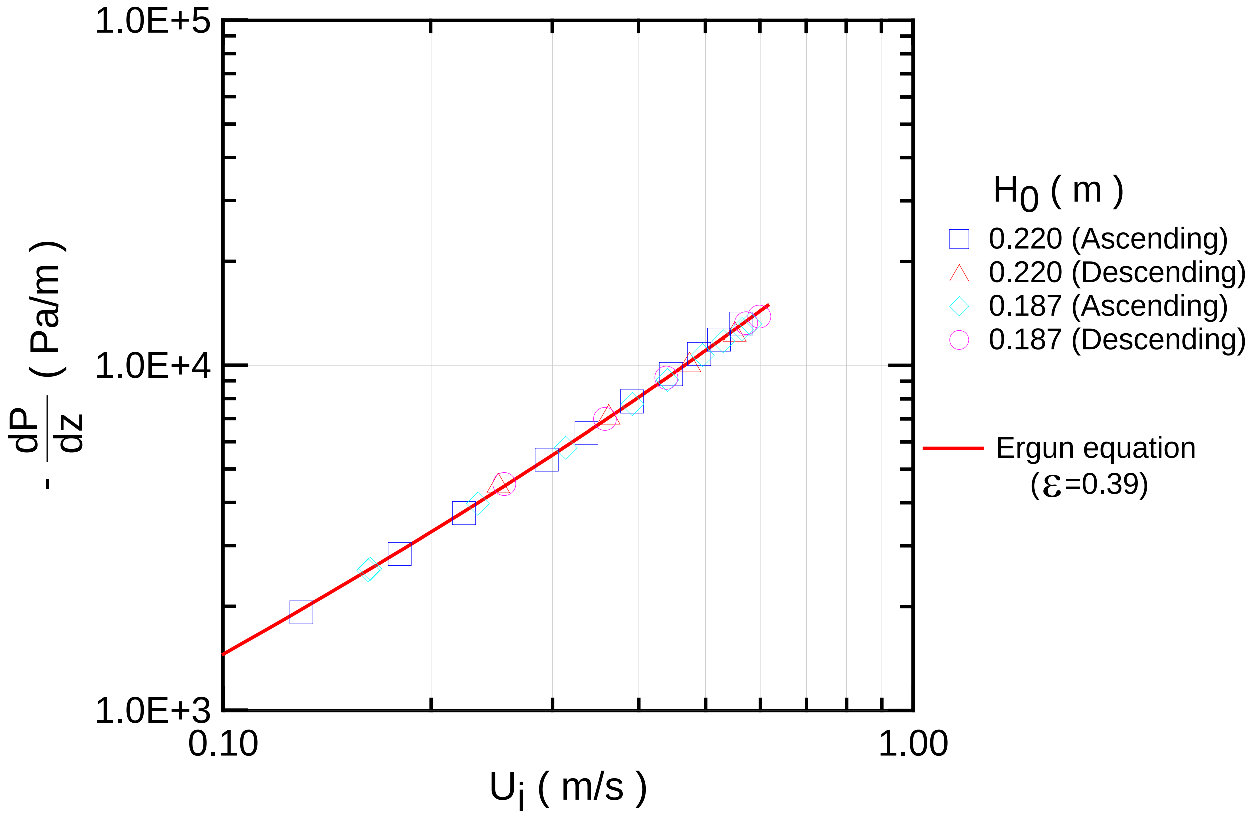

Fig. 2-5. Comparison between experimental data and predicted results using the Ergun equation. (Symbols are experimental data, the line is predicted results using the Ergun equation with ε=0.39.)

CHAPTER 3

HYDRODYNAMIC BEHAVIOUR IN CONICAL SPOUTED BEDS

The total pressure drop of a conical spouted bed under stable spouting and at the minimum spouting velocity are important operating parameters for a conical spouted bed. Although many studies have been reported on this area, as mentioned in chapter 1, there are still many uncertainties. For example, the static bed height investigated was very low, the radial distribution of the pressure was seldom reported, and the evolution of the internal spout was never investigated.

3.1 Static pressure measurement system

A schematic of the conical spouted bed is shown in Figure 3-1, with all geometric factors shown and documented in Table 3-1 for four Plexiglas columns. Particles used in the current study are glass beads of 1.16 mm and 2.4 mm in diameter, with a density of 2500 kg/m^3 and a sphericity of 1.0. Air from the compressor was used as the spouting gas.

In order to investigate the local characteristics of pressure drop, six static pressure probes were installed in six pressure ports along the wall of the conical bed, with all static pressure probes being freely movable laterally. By connecting with six differential pressure transducers, the local pressure can be measured. All signals from pressure transducers were collected and saved into a computer via a Das08 data acquisition card from Computer Board Inc.

Table 3-1. Parameters of experimental facilities and operating conditions.

<table>
<tr><th>γ</th><th>D_i
(m)</th><th>H_c
(m)</th><th>D_0
(m)</th><th>H_0
(m)</th><th>d_s
(mm)</th></tr>
<tr><td rowspan="2">30^o</td><td rowspan="11">0.0381</td><td rowspan="11">0.5</td><td>0.0127</td><td rowspan="2">0.08, 0.12, 0.23, 0.335</td><td rowspan="10">1.16</td></tr>
<tr><td>0.01905</td></tr>
<tr><td rowspan="3">45^{oH}</td><td>0.0127</td><td rowspan="2">0.08, 0.12, 0.23, 0.335</td></tr>
<tr><td>0.0254</td></tr>
<tr><td>0.01905</td><td>0.08, 0.12, 0.23, 0.335, 0.16, 0.383, 0.396, 0.468</td></tr>
<tr><td rowspan="3">45^{oF}</td><td>0.0127</td><td rowspan="2">0.08, 0.12, 0.23, 0.335</td></tr>
<tr><td>0.0254</td></tr>
<tr><td>0.01905</td><td>0.08, 0.12, 0.23, 0.335, 0.16, 0.383, 0.396</td></tr>
<tr><td rowspan="2">60^o</td><td>0.0127</td><td rowspan="2">0.08, 0.12, 0.23, 0.335</td></tr>
<tr><td>0.01905</td></tr>
<tr><td>45^{oF}</td><td>0.01905</td><td>0.12, 0.197, 0.272, 0.348</td><td>2.4</td></tr>
</table>

Note: H------for the half column

F------for the full column

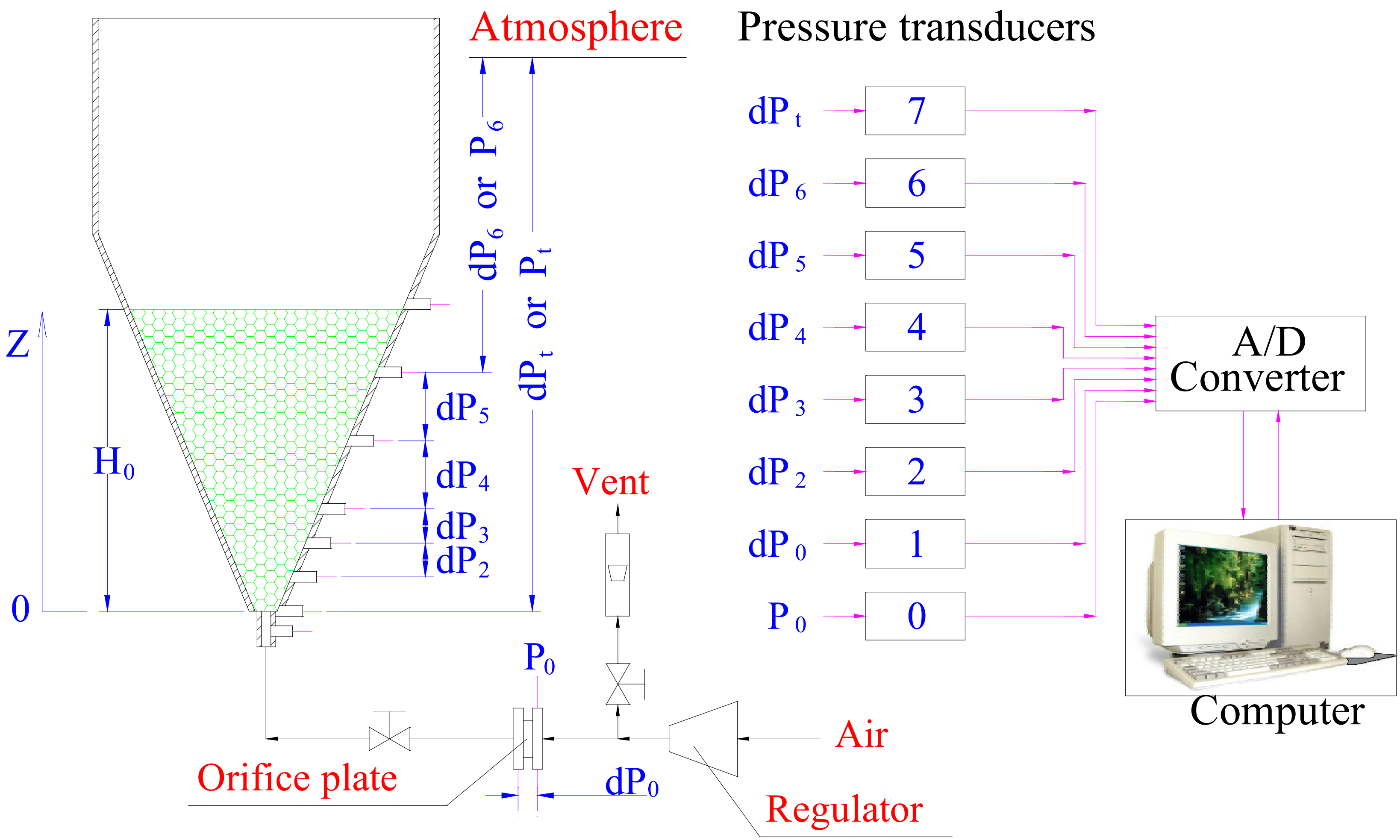

Fig. 3-1. Local pressure measurement system. (dP_i is the pressure drop, i=0,2,3,4,5,6,t, P_0 is the operating gauge pressure.)

3.2 Experimental results and discussion

3.2.1 Reproducibility of pressure measurements

To check the reproducibility of the measurements, pressure drops with increasing and then decreasing superficial gas velocity under identical conditions were measured following a controlled time interval, with results shown in Figure 3-2 (Z_s is the height of the internal spout.). Furthermore, experimental results from the full column under the same operating conditions are also shown in Figure 3-2. Before the first run (Run 01), the conical bed of particles was tightly packed by tapping the pipe connected to the bottom of the bed. As a result, the pressure drop over the bed increased quickly with increasing gas velocity, following a trend different from other runs under loosely packed conditions. Also, internal spouting was not observed in the first run. After full spouting was reached, gas velocity was reduced, with much lower pressure drops obtained in the descending process than the ascending process. It takes about one and half hours for a complete run. After the spouting gas was turned off for a certain time period, the second run was started. The time between the end of the first run and the start of the second run is one hour; and it is ten minutes between the second and the third runs as well as between the third and the fourth runs; and it is three hours between the fourth and the fifth runs. It is seen from the figure that except for the first run which has an initial tightly packed state, the evolution of the total pressure drop and the internal spout is quite reproducible for all runs with a similar initial loosely packed status. The initial packing state thus has a significant impact on the evolution curve, and there is little difference between the half column and the full column.

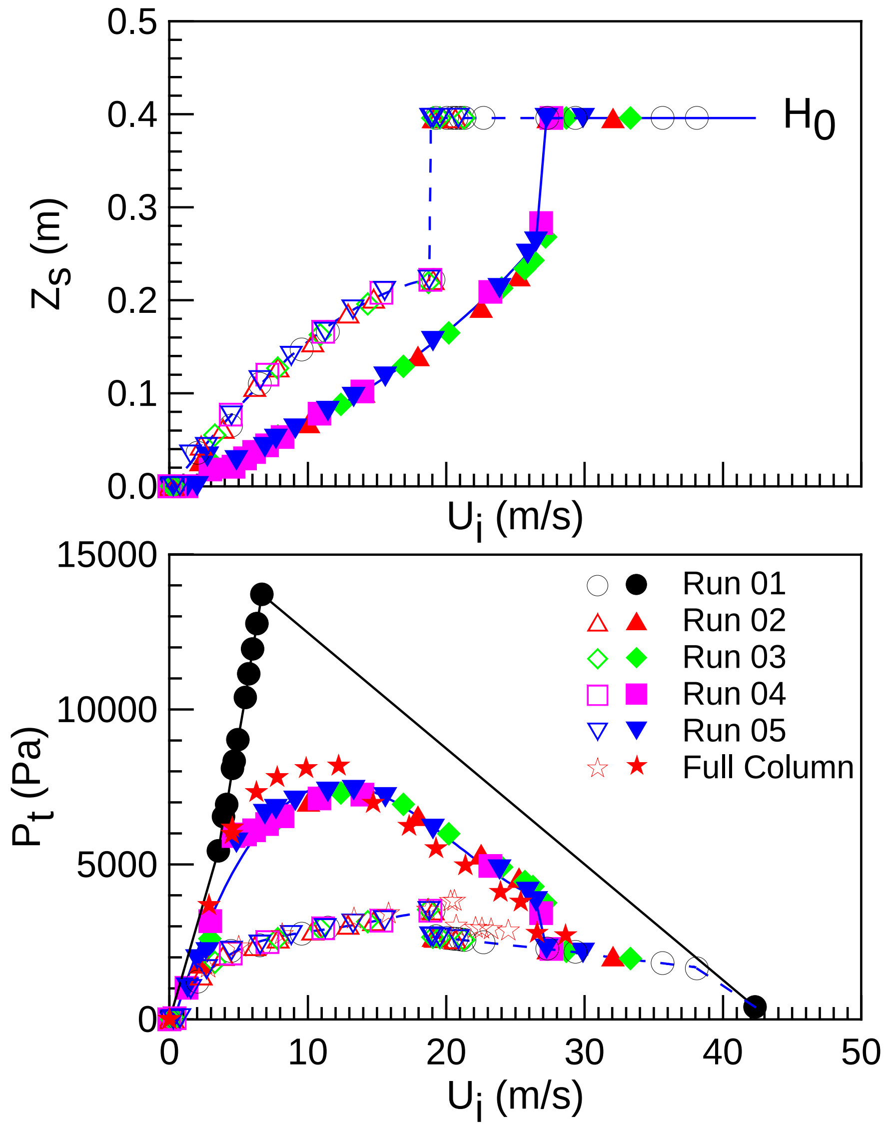

Fig. 3-2. Reproducibility of internal spout and pressure measurements. Solid lines and solid symbols are for increasing U_i, dashed lines and open symbols are for decreasing U_i. (D_0=0.019m, H_0=0.396m, γ=45°, Run 01 to Run 05 were in the half column.)

3.2.2 Evolution of the pressure drop and the internal spout

Figure 3-2 also clearly shows the existence of pressure drop – flow rate hysteresis, with both the peak pressure drop and the minimum spouting velocity from increasing gas flow rate being higher than that from decreasing gas flow rate. There is also a sudden drop in the pressure drop around the minimum spouting velocity in the velocity ascending process.

Figure 3-3 shows similar experimental phenomena at different operating conditions. The variation of gauge pressures at different positions along the bed height with increasing and then decreasing superficial gas velocity are also given. It is seen that the pressure drop curves at lower parts of the bed show significant hysteresis, and the degree of the hysteresis reduces as the elevation of the measurement location is increased. At the upper part of the bed (see P5), the pressures on increasing and decreasing gas flow rate are almost coincident at gas velocities below the minimum spouting velocity, suggesting that the upper bed region remains in the same state no matter whether gas velocity is increased or decreased. This observation, in conjunction with the observation that the height of the internal spout is systematically different for increasing and decreasing gas velocity, suggests that the hysteresis phenomenon in conical spouted beds is related to the formation of the internal spout in the entrance region.

As shown in Figure 3-3, the minimum spouting velocity obtained from increasing U_i is designated as $(U_i)_{ms,a}$, and the one from decreasing U_i is called $(U_i)_{ms,d}$. It is seen that the height of the internal spout increases steadily with increasing gas velocity. The maximum gauge pressure in the velocity ascending curve does not necessarily correspond to the onset of internal spouting, as suggested in early studies (Nikolaev et al, 1964; Tsvik et al., 1966, 1967; Wan-Fyong et al., 1969). The minimum spouting velocity, $(U_i)_{ms,a}$, from the velocity ascending process is seen to correspond to the onset of external spouting, while $(U_i)_{ms,d}$ from the velocity descending process corresponds to the collapse of external spouting. Step changes in both the gauge pressure and the height of the internal spout around the minimum spouting velocity are also observed.

Based on Figure 3-3, the height of the internal spout at the point "sp" just before the onset of minimum spouting is defined as Z_{sp}, which corresponds to the maximum height of the internal spout with increasing superficial gas velocity before full external spouting commences. The height of the internal spout at point "sm", denoted as Z_{sm}, corresponds to the maximum height of the internal spout right after the stable external spouting collapses on decreasing superficial gas velocity. The relationship between these two kinds of maximum heights is shown in Figure 3-4. It is seen that they almost remain the same within a wide range of operating conditions and column configurations.

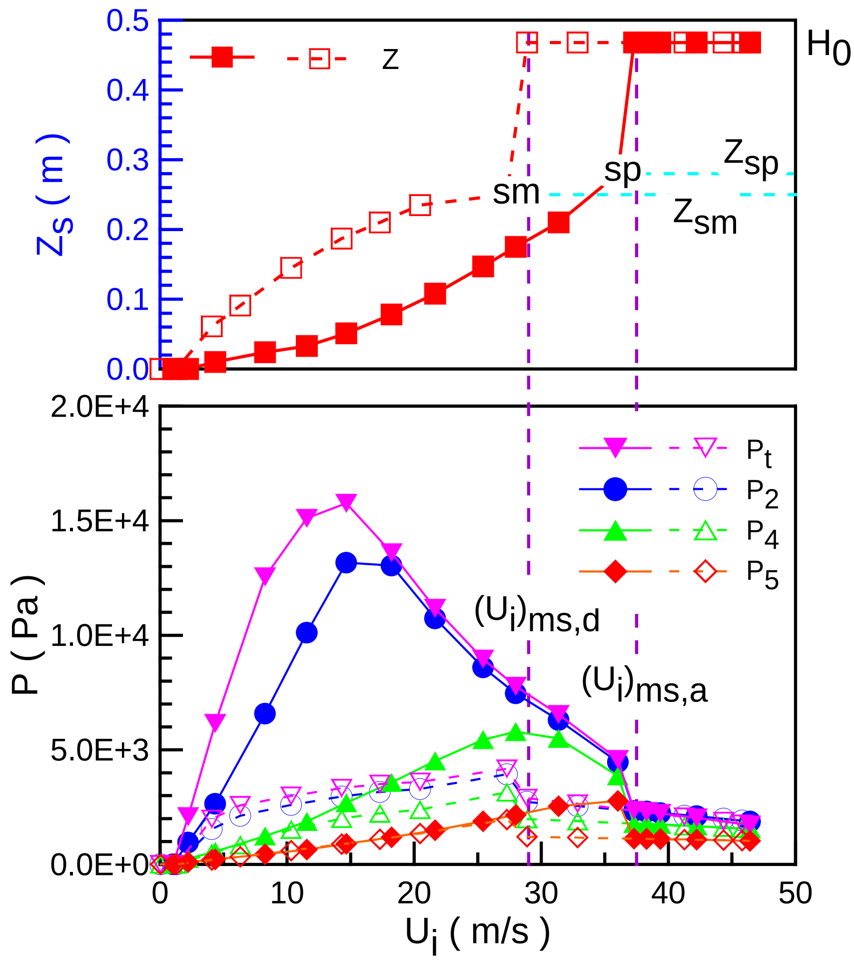

Fig. 3-3. Variations of pressure and internal spout with increasing and decreasing gas flow rate. Solid lines and closed symbols for increasing U_i, dashed lines and open symbols for decreasing U_i. (Half column, D_0=0.019m, H_0=0.468m, γ=45°)

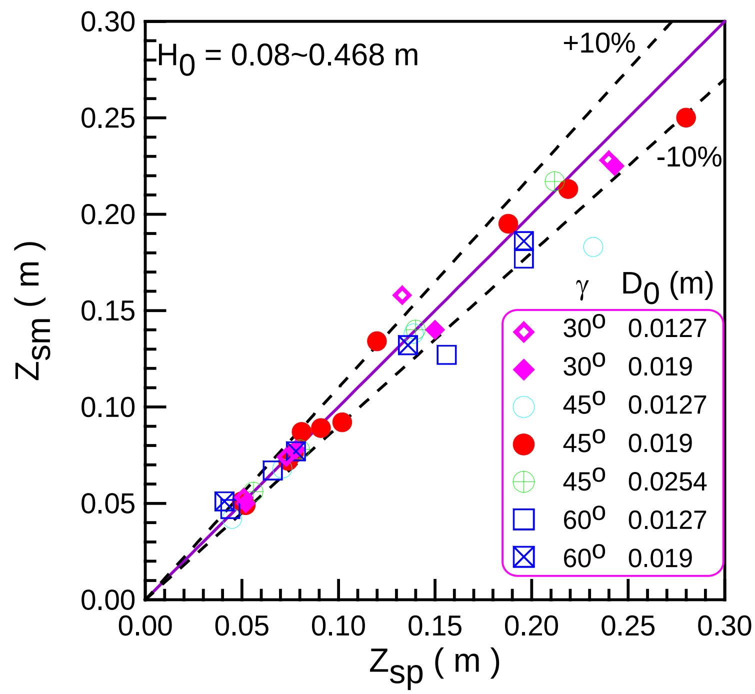

Fig. 3-4. Comparison of two kinds of maximum heights of the internal spout from increasing and decreasing superficial gas velocity. (Half column, d_s=1.16mm)

Figures 3-5 and 3-6 show the variation of the ratio of the maximum height of internal spout to the static bed height, Z_{sp}/H_0 and Z_{sm}/H_0, as a function of the static bed height, H_0. It is seen that both Z_{sp}/H_0 and Z_{sm}/H_0 are 0.62 and are insensitive to H_0.

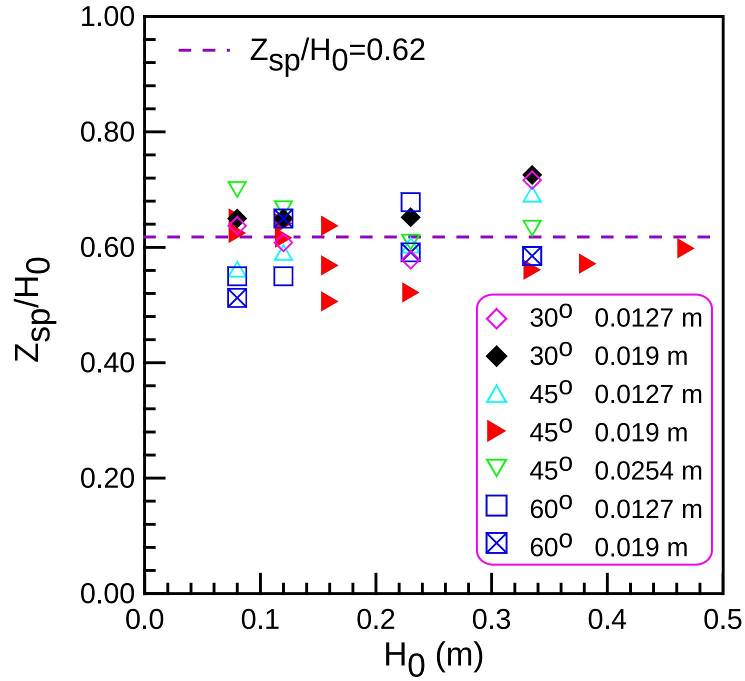

Fig. 3-5. Relationship between the maximum internal spout height Z_{sp} and the static bed height.

(Half column, H_0=0.08~0.468m, d_s=1.16mm)

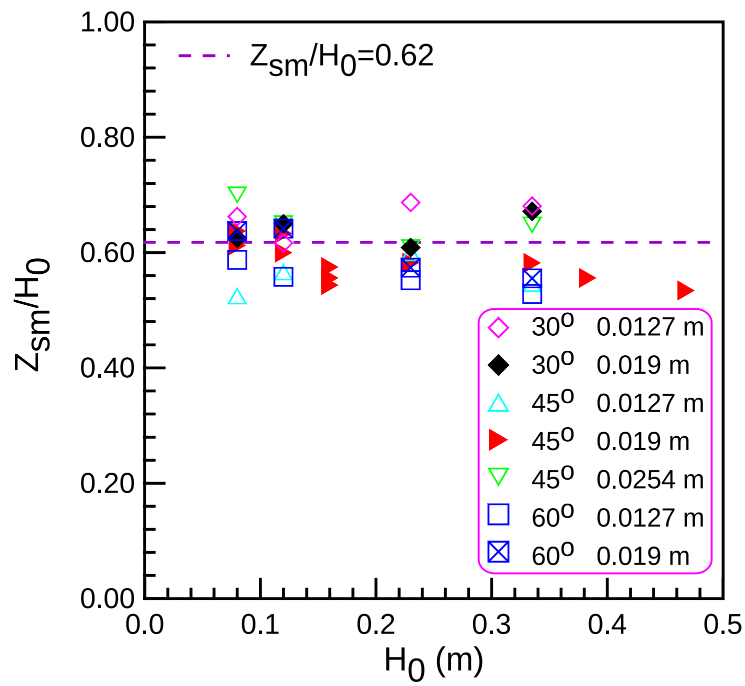

Fig. 3-6. Relationship between the maximum internal spout height Z_{sm} and the static bed height.

(Half column, H_0=0.08~0.468m, d_s=1.16mm)

As shown in Figures 3-2 and 3-3, there exists a pressure – flow rate hysteresis in conical spouted beds. Correspondingly, two kinds of minimum spouting velocity, $(U_i)_{ms,a}$ and $(U_i)_{ms,d}$, can be identified by increasing and decreasing superficial gas velocity, respectively. Based on Figures 3-2 and 3-3, the degree of hysteresis in the pressure vs. velocity curve can be reasonably represented by the ratio of $(U_i)_{ms,a}/(U_i)_{ms,d}$ and/or the ratio of peak pressures, $(dP_t)_{max,a}/(dP_t)_{max,d}$, and the more the ratios exceed unity, the more significant the hysteresis is. It is noted that in some cases, the $(U_i)_{ms,a}/(U_i)_{ms,d}$ ratio can equal 1 even when there is a persistent pressure – flow rate hysteresis, i.e. $(dP_t)_{max,a}/(dP_t)_{max,d} >1$.

As shown in Figures 3-7 and 3-8, both the ratios of $(U_i)_{ms,a}/(U_i)_{ms,d}$ and $(dP_t)_{max,a}/(dP_t)_{max,d}$ are related with the geometrical structure and the static bed height of a conical spouted bed. For a given gas inlet diameter, D_0, these ratios increase with increasing static bed height, indicating that hysteresis is more significant in deep beds than in shallow beds. At a given static bed height, H_0, the smaller the gas inlet diameter and/or the larger the included cone angle, the larger the ratio of $(U_i)_{ms,a}/(U_i)_{ms,d}$. However, the effect of D_0 and γ on the ratio of $(dP_t)_{max,a}/(dP_t)_{max,d}$ is not clear.

Under certain operating conditions, such as low static bed height with large gas inlet orifice diameter and/or small included cone angle, it is also observed in this study that there exists some kind of discontinuous spouting (spouting and partial spouting coexist intermittently) as shown in Figure 3-9, with no obvious step changes in pressure drops around the onset and collapse of the external spouting. As a result, $(U_i)_{ms,a}$ and $(U_i)_{ms,d}$ are very close.

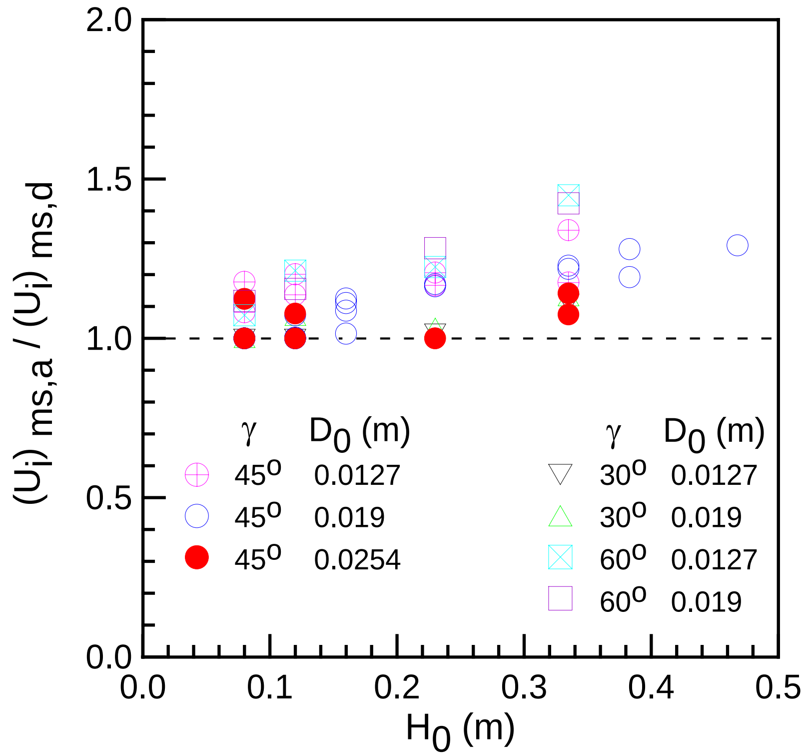

Fig. 3-7. $(U_i)_{ms,a}/(U_i)_{ms,d}$ as a function of the static bed height. (Both half and full columns)

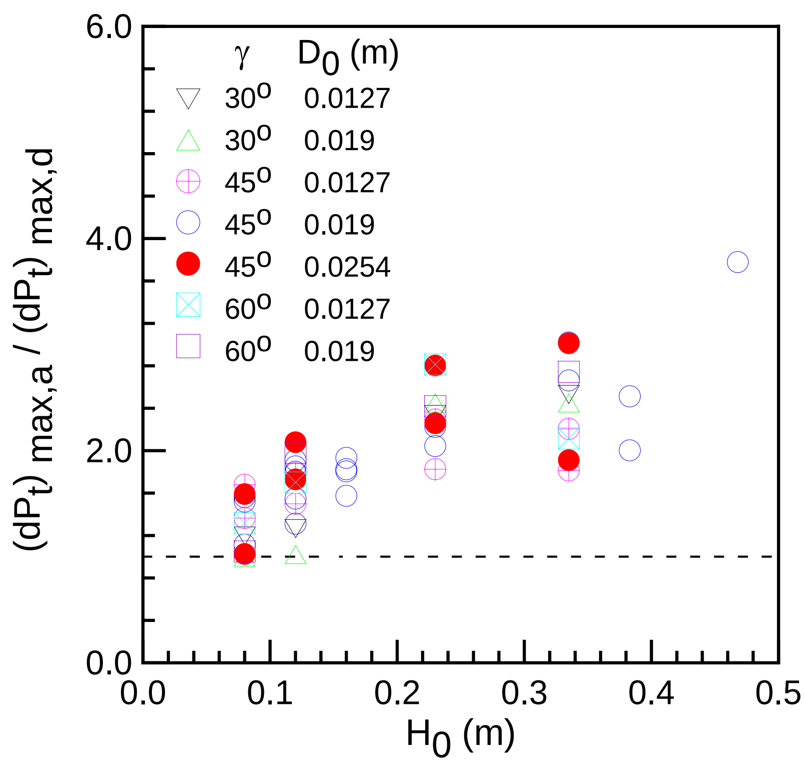

Fig. 3-8. $(dP_t)_{max,a}/(dP_t)_{max,d}$ as a function of the static bed height. (Both half and full columns)

t (s) Internal spouting

t+2.4 (s) External spouting

t+10.6 (s) Internal spouting

t+14.1 (s) External spouting

t+25.2 (s) Internal spouting

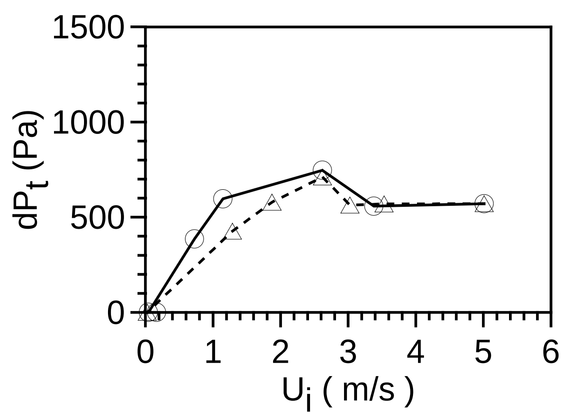

Fig. 3-9. Discontinuous spouting (spouting and partial spouting coexist intermittently) just before the collapse of external spouting at different times as well as overall pressure drops as a function of superficial gas velocity. (Half column, γ=60°, D_0 =0.019m, H_0 =0.080m, $U_i \approx (U_i)_{ms,d}$=3.03m/s). (Solid line for increasing U_i, dashed line for decreasing U_i).

In summary, the hysteresis of the pressure evolution and the step change of the pressure drop around the minimum spouting velocity tend to be more pronounced in deep beds with large included cone angles and small inlet orifice diameters. This probably explains why the "hysteresis" phenomenon of minimum spouting velocity was not reported in most previous studies using conical spouted beds of short static bed heights and large inlet orifice diameters.

3.2.3 Comparison between the full column and half column

Figure 3-10 shows the evolution of local and total pressure drops at the same position in the half and full column with the same static bed height H_0, inlet diameter D_0, included cone angle γ and particles. Similar results are also shown in Figure 3-2 on total pressure drops at different superficial gas velocities. Based on these two figures, it can be seen that there is only a small difference between pressure drops of the half and full column on increasing superficial gas velocity, and results for the evolution of the pressure drop overlap on decreasing superficial gas velocity. Corresponding minimum spouting velocities determined by evolution curves of the pressure drop in both half and full columns are almost identical whether superficial gas velocity is increased or decreased, as shown in Figure 3-111 where $(U_i)_{ms}$ between the half and full columns are compared. Therefore, $(U_i)_{ms}$ obtained from the semi-circular conical spouted beds in the current study can represent the full circular conical spouted beds with the same values of D_0, H_0, γ.

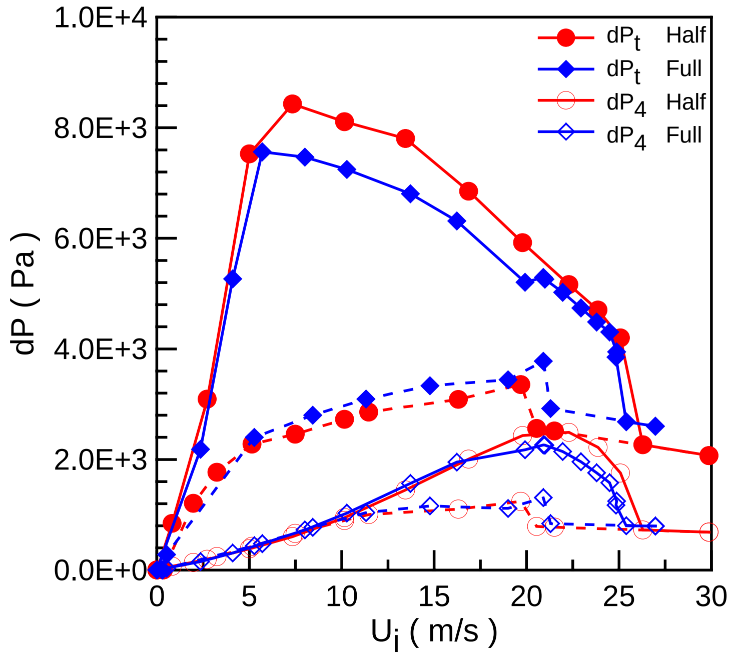

Fig. 3-10. Comparison of pressure drops between the half and full column under identical operating conditions. D_0=0.019m, H_0=0.383m, γ=45º (Solid lines for increasing U_i, dashed lines for decreasing U_i).

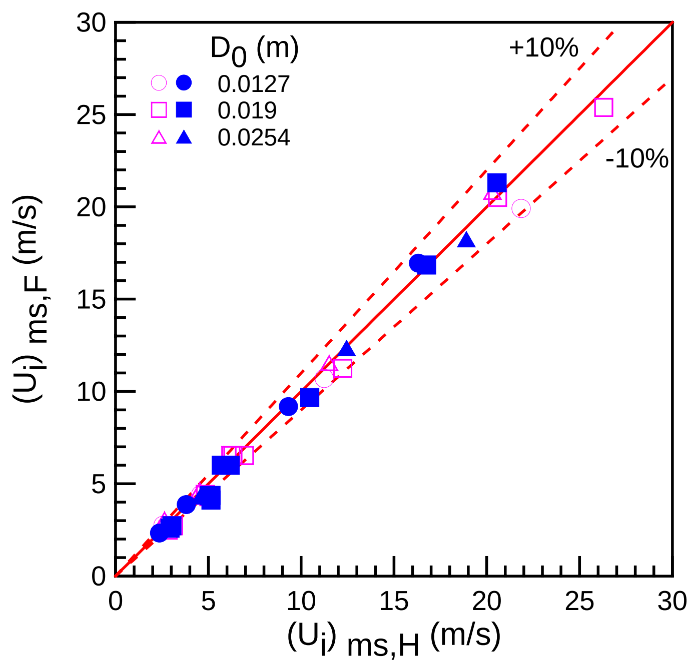

Fig. 3-11. Comparison of $(U_i)_{ms}$ between the half and full column. (γ=45º, H_0=0.08~0.383m, open symbols for increasing U_i, and closed symbols for decreasing U_i).

3.2.4 Effects of the cone angle, static bed height, inlet diameter and particle size on the minimum spouting velocity

Figures 3-12 and 3-13 show the influence of the cone angle, gas inlet diameter, static bed height and particle size on minimum spouting velocities $(U_i)_{ms,a}$ and $(U_i)_{ms,d}$ based on the bottom diameter of the conical bed.

At the same cone angle, with increase in the static bed height, more gas will leak into the annulus region or spread out laterally. As a result, more fluid is required to fluidize the top central region of the bed, leading to an increase in the minimum spouting velocity based on the bed bottom cross section. Figures 3-12 and 3-13 show that $(U_i)_{ms,a}$ and $(U_i)_{ms,d}$ increase almost linearly with increasing static bed height, in agreement with data reported in the literature (e.g. Kmiec, 1983; Olazar et al., 1992).

Under the same static bed height, as the cone angle increases, the cross-sectional area of the top bed surface will be larger for the column with a larger cone angle. As a result, more fluid is required to fluidize particles at the central top surface region, leading to an increase of the minimum spouting velocity based on the bed bottom cross section. Such a trend is in agreement with the results shown in Figures 3-12 and 3-13. However, when H_0 is smaller than 0.1m, the cone angle seems to have less effect on $(U_i)_{ms,a}$ and $(U_i)_{ms,d}$, possibly because of the low lateral spreading of gas in the inlet region when gas jet enters the column with a high vertical momentum. Most importantly, the cone angle seems to only have effect on the slope of the linear relationship between the minimum spouting velocity and the static bed height.

The gas inlet orifice diameter only affects the region close to the gas inlet. As shown in Figures 3-12 and 3-13, the influence of the gas inlet orifice diameter, D_0, is small, with $(U_i)_{ms,a}$ and $(U_i)_{ms,d}$ being slightly higher for a larger D_0. The gas inlet diameter seems to slightly affect both the intercept and the slope of the linear relationship between the minimum spouting velocity and the static bed height.

As in fluidized beds where the minimum fluidization velocity increases with increasing particle diameter, the minimum spouting velocities, $(U_i)_{ms,a}$ and $(U_i)_{ms,d}$, become higher as the diameter of particles increases.

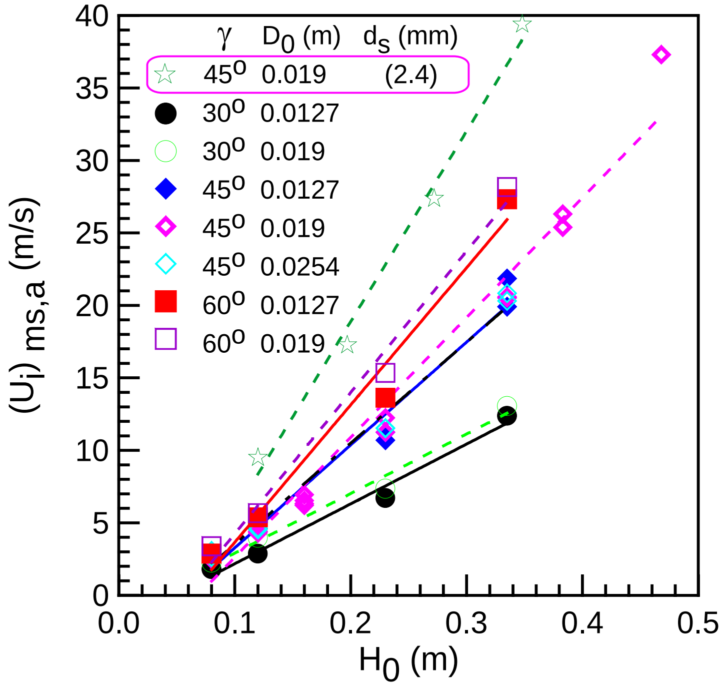

Fig. 3-12. Effects of the cone angle, gas inlet diameter, static bed height and particle size on $(U_i)_{ms,a}$. (Both half and full columns; except where indicated, all results are for d_s=1.16mm glass beads.)

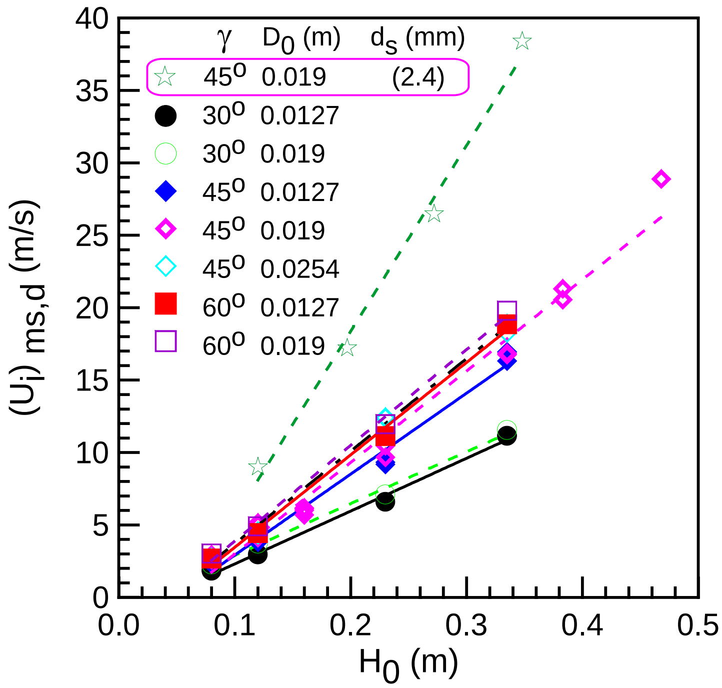

Fig. 3-13. Effects of the cone angle, gas inlet diameter, static bed height and particle size on $(U_i)_{ms,d}$. (Both half and full columns; except where indicated, all results are for d_s=1.16mm glass beads.)

3.2.5 Comparison with correlations from the literature

Correlations for the minimum spouting velocity:

Since most early correlations have been shown not to be able to predict literature data well (Bi et al., 1997). Two most recent correlations from literature were selected for comparison with our experimental data.

Figure 3-14 shows a comparison between current experimental data and the correlation of Olazar et al. (1992),

$$(\mathrm{Re}_0)_{ms,d} = 0.126 Ar^{0.5} (D_b / D_0)^{1.68} (\tan\frac{\gamma}{2})^{-0.57} \tag{3-1}$$

where $(\mathrm{Re}_0)_{ms,d} = \dfrac{\rho_g (U_0)_{ms,d} d_s}{\mu_g}$, $(U_0)_{ms,d}$ is the minimum spouting velocity based on D_0

and determined from the descending process.

It is seen that the Olazar et al. (1992) correlation, which was developed from data obtained from columns of low H_0 (lower than 0.22 m), small cone angle γ (between 28° and 45°) and large gas inlet diameter D_0 (between 0.03 m and 0.06 m), consistently over-predicts our experimental data for small glass beads (d_s=1.16 mm). However, there is a good agreement for big glass beads (d_s=2.4 mm).

The comparison with the most recent correlation of Bi et al. (1997),

$$(\mathrm{Re}_0)_{ms,d} = 0.3Ar^{0.5}[1-0.9/(D_b/D_0)^2]\sqrt{(D_b/D_0)[(D_b/D_0)^2+(D_b/D_0)+1]/3} \qquad (3\text{-}2)$$

is shown in Figure 3-15. It is seen that the Bi et al. (1997) correlation under-predicts our $(U_i)_{ms,d}$ data obtained from columns with small cone angle γ (30 degrees), or high static bed height H_0, or big particles, and over-predicts our $(U_i)_{ms,d}$ data obtained from columns with large cone angle γ (60 degrees) and low static bed height H_0. Equation (3-2) gives a much better prediction than Equation (3-1).

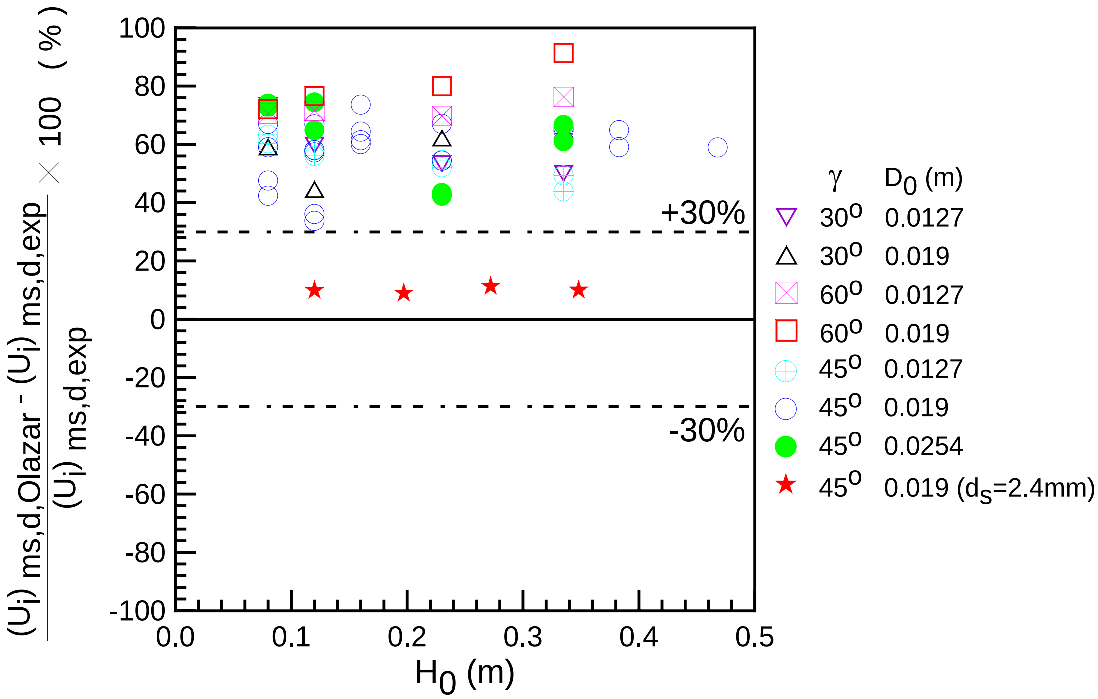

Fig. 3-14. Comparison of experimental data with the correlation of Olazar et al. (1992). (Both half and full columns; except where indicated, all results are for 1.16mm glass beads.)

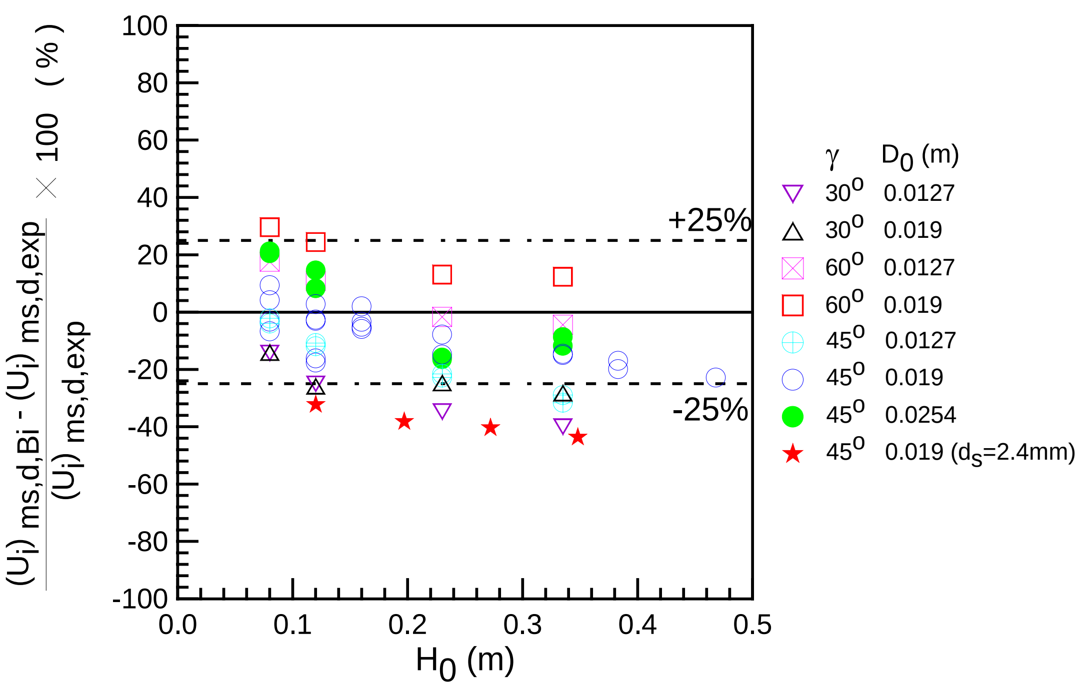

Fig. 3-15. Comparison of experimental data with the correlation of Bi et al. (1997). (Both half and full columns; except where indicated, all results are for 1.16mm glass beads.)

Correlations for the total pressure drop at stable spouting:

For conical spouted beds, two correlations have been reported for estimating the ratio of the total pressure drop at stable spouting to the pressure drop of a fluidized bed of the same static bed height. The most recent one is Equation (3-3) from Olazar et al. (1993c), and the other one is Equation (3-4) from Mukhlenov and Gorshtein (1964, 1965).

$$\frac{(\Delta P_s)_{ms,d}}{\varepsilon_{s,0}\rho_s g H_0} = 1.20\left(\tan\frac{\gamma}{2}\right)^{-0.11}(\mathrm{Re}_0)_{ms,d}^{-0.06}\left(\frac{H_0}{D_0}\right)^{0.08} \tag{3-3}$$

$$\frac{(\Delta P_s)_{ms,d}}{\varepsilon_{s,0}\rho_s g H_0} = 7.68\left(\tan\frac{\gamma}{2}\right)^{0.2}(\mathrm{Re}_0)_{ms,d}^{-0.2}\left(\frac{H_0}{D_0}\right)^{-0.33} \tag{3-4}$$

For convenience, $\frac{(\Delta P_s)_{ms,d}}{\varepsilon_{s,0}\rho_s g H_0}$ is defined as $(k_{oa})_{ms,d}$.

Equation (3-3), which was developed from the data obtained from columns of low H_0 (lower than 0.12 m), small cone angle γ (between 28˚ and 45˚) and large gas inlet diameter D_0 (between 0.03 m and 0.05 m), consistently over-predicts our experimental data.

As for Equation (3-4), except for low H_0 (lower than 0.12 m) or large cone angle γ (60˚), estimated values of $(k_{oa})_{ms,d}$ agree reasonably well with current experimental data.

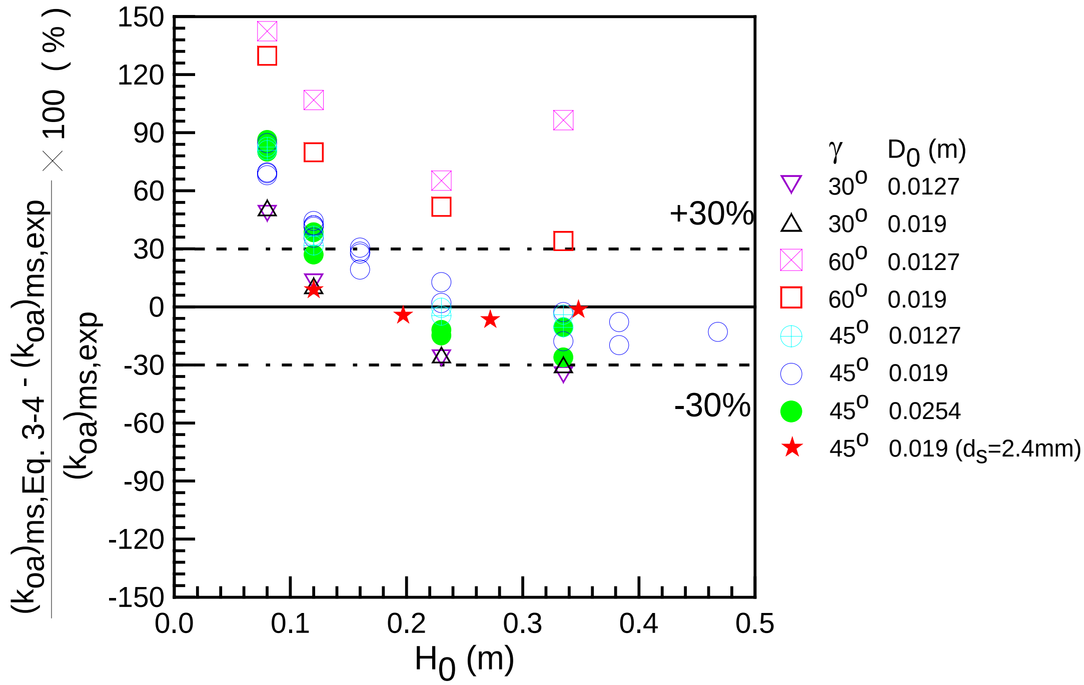

Fig. 3-16. Comparison of experimental data with the correlation of Mukhlenov and Gorshtein (1964, 1965). (Both half and full columns; except where indicated, all data are for 1.16mm glass beads.)

3.2.6 Empirical correlations for the total pressure drop at stable spouting, the evolution of the internal spout and the minimum spouting velocity

Based on correlations of the minimum spouting velocity in the literature, the minimum spouting velocity was generally correlated with the Reynolds number as a function of Archimedes number, cone angle, and diameter ratios. Based on correlations from the literature (Gorshtein and Mukhlenov, 1964; Olazar et al., 1992, 1996c; Bi et al., 1997; Jing et al., 2000), $\left(\dfrac{D_b}{D_0}\right)$ is selected to reflect the static height effect, besides, $\left(\dfrac{D_0}{D_i}\right)$ is added to reflect the inlet orifice diameter effect. By least-square curve fitting using all experimental data shown in Table 3-1 (D_0=0.0127~0.0254 m, H_0=0.08~0.468 m, γ=30°~60°, d_s=1.16 and 2.40 mm, D_i=0.0381 m), the following empirical correlations are obtained for minimum spouting velocity, internal spout height and the pressure drop at stable spouting.

The comparison between experimental data and calculated results from those correlations are shown in Figures 3-17 to 3-23.

$$(\mathrm{Re}_0)_{ms,d} = 0.00671 Ar^{0.6802}\left(\frac{D_b}{D_0}\right)^{1.685}\left(\tan\frac{\gamma}{2}\right)^{-0.808}\left(\frac{D_0}{D_i}\right)^{-0.106} \tag{3-5}$$

$$(\mathrm{Re}_0)_{ms,a} = 0.0160 Ar^{0.6080}\left(\frac{D_b}{D_0}\right)^{1.818}\left(\tan\frac{\gamma}{2}\right)^{-0.6305}\left(\frac{D_0}{D_i}\right)^{-0.0605} \tag{3-6}$$

$$\frac{(\Delta P_s)_{ms,d}}{\varepsilon_{s,0}\rho_s g H_0} = 1.924 Ar^{-0.0797}\left(\frac{D_b}{D_0}\right)^{-0.1310}\left(\tan\frac{\gamma}{2}\right)^{-0.5176}\left(\frac{D_0}{D_i}\right)^{0.6790} \tag{3-7}$$

$$\frac{Z_d}{H_0} = 0.281 Ar^{0.0361}\left(\tan\frac{\gamma}{2}\right)^{-0.119}+\left(\frac{D_0}{D_b}\right)^{0.0787}\left[\frac{\mathrm{U}_0}{(\mathrm{U}_0)_{\mathrm{ms,d}}}\right]-0.214\left[\frac{\mathrm{U}_0}{(\mathrm{U}_0)_{\mathrm{ms,d}}}\right]^2 \tag{3-8}$$

where

$$(\mathrm{Re}_0)_{ms,a} = \frac{\rho_g (U_0)_{ms,a} d_s}{\mu_g} \tag{3-9}$$

$$(\mathrm{Re}_0)_{ms,d} = \frac{\rho_g (U_0)_{ms,d} d_s}{\mu_g} \tag{3-10}$$

$(U_0)_{ms,a}$ is the minimum spouting velocity based on D_0 determined from the ascending process; $(U_0)_{ms,d}$ is the minimum spouting velocity based on D_0 determined from the descending process;

Ar is the Archimedes number, and equals $\dfrac{g d_s^3 \rho_g(\rho_s-\rho_g)}{\mu_g^2}$; D_b is the diameter of the bed surface; D_i is the diameter of the bed bottom; D_0 is the gas inlet orifice diameter; γ is the included cone angle; H_0 is the static bed height; ρ_g is the fluid density; ρ_s is the particle density; μ_g is the fluid viscosity; d_s is the particle diameter; g is the acceleration due to gravity; Z_a is the height of the internal spout in the ascending process; Z_d is the height of the internal spout in the descending process; U_i is superficial fluid velocity based on D_i; $(\Delta P_s)_{ms,d}$ is the total pressure drop at minimum spouting; $\varepsilon_{s,0}$ is the initial packed bed solids fraction.

Figures 3-17 to 3-20 show that Equations (3-5) and (3-6) agree well with experimental data from this study, and in most cases, the maximum error in the minimum spouting velocity is lower than 10%.

For other parameters, such as the total pressure drop at stable spouting, the ratio of the total pressure drop for stable spouting to that for fluidization and the height of the internal spout in the descending process, as shown in Figures 3-21 to 3-23, the proposed correlations are in reasonable agreement with the current experimental data too, with the maximum error of 20% in most cases.

As for the height of the internal spout in the ascending process, because the initial packing state of the bed can vary significantly and heights of the internal spout are small at low superficial gas velocities, errors at low superficial gas velocities are especially high. Therefore, attempts were not made to correlate experimental data. Generally, the height of the internal spout increases with increasing superficial gas velocity.

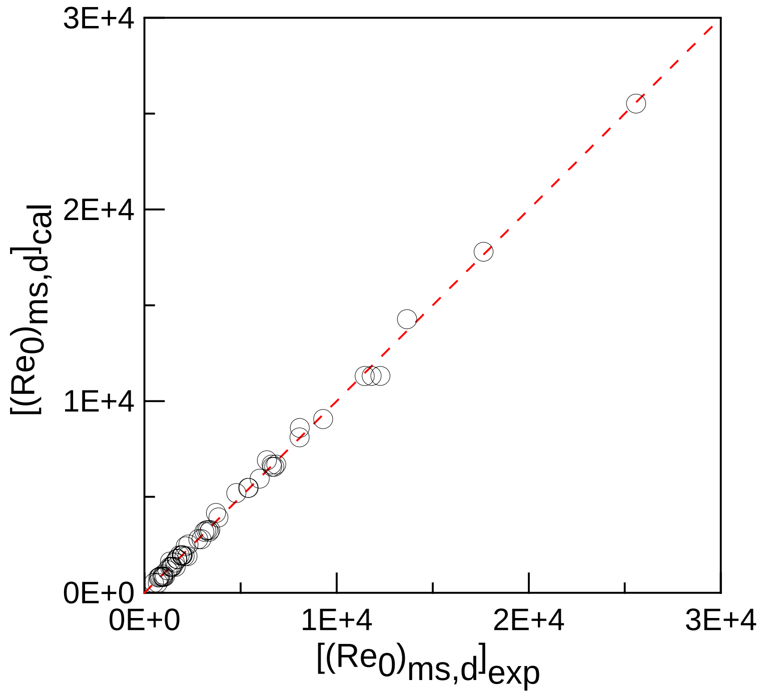

Fig. 3-17. Comparison between experimental data and calculated results by **Eq. (3-5)** on the Reynolds number. (Both half and full columns, descending process)

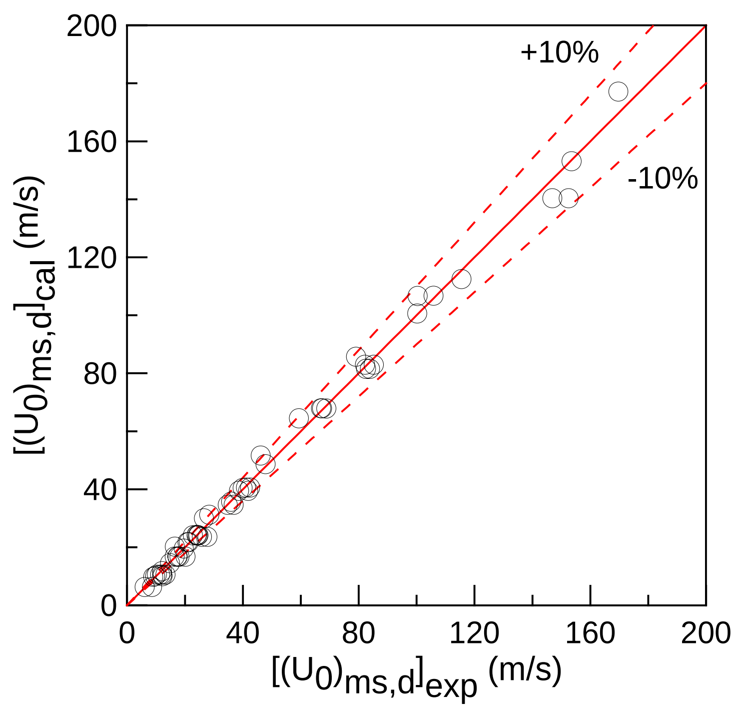

Fig. 3-18. Comparison between experimental data and calculated results by **Eq. (3-5)** on the minimum spouting velocity. (Both half and full columns, descending process)

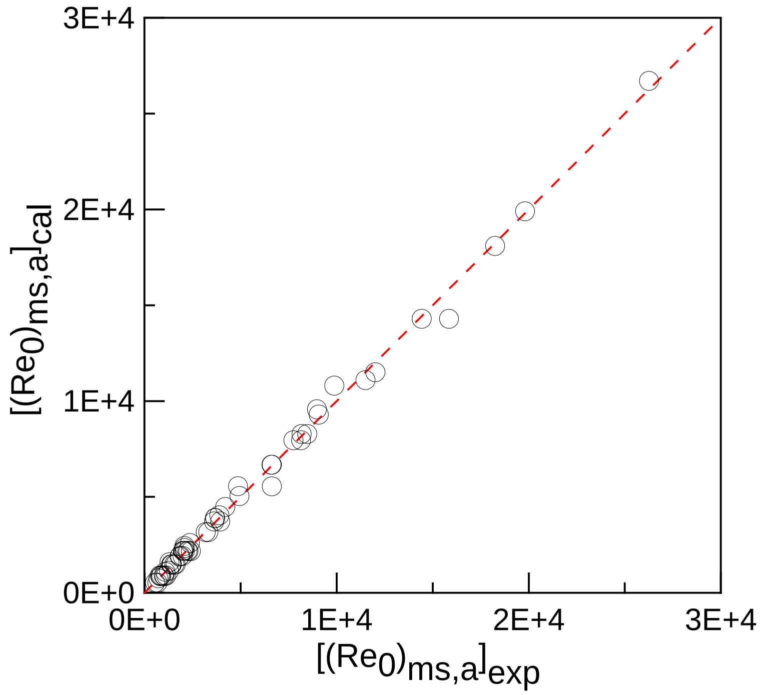

Fig. 3-19. Comparison between experimental data and calculated results by **Eq. (3-6)** on the Reynolds number. (Both half and full columns, ascending process)

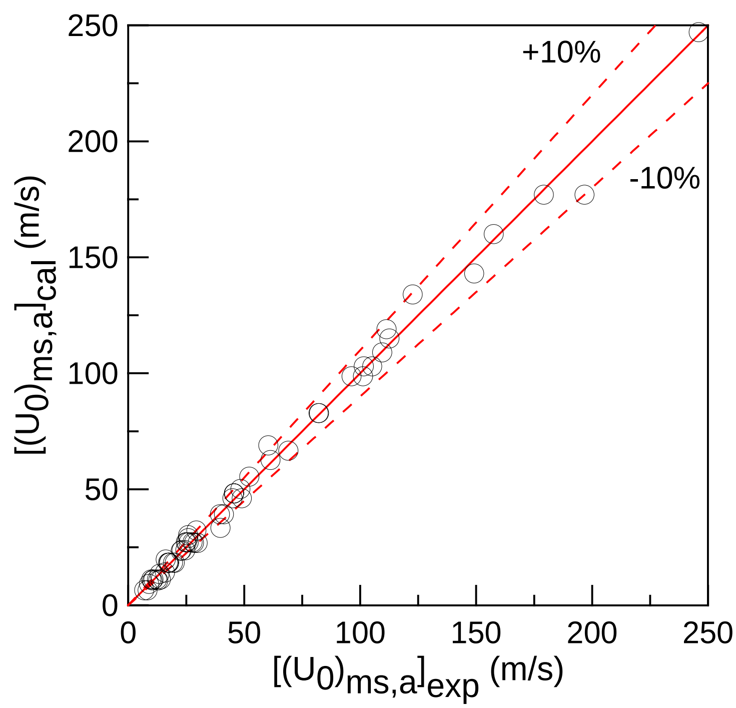

Fig. 3-20. Comparison between experimental data and calculated results by **Eq. (3-6)** on the minimum spouting velocity. (Both half and full columns, ascending process)

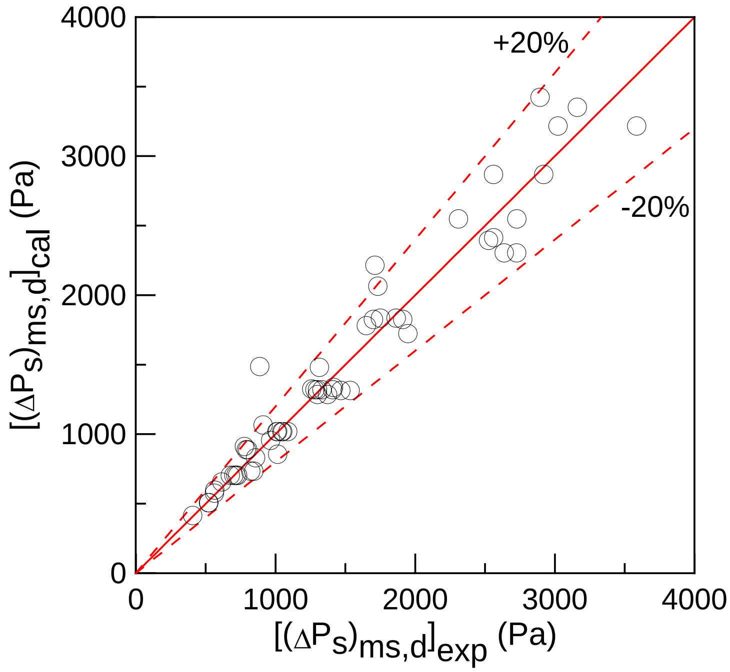

Fig. 3-21. Comparison between experimental data and calculated results by **Eq. (3-7)** on the total pressure drop at stable spouting. (Both half and full columns, $U_i=(U_i)_{ms,d}$)

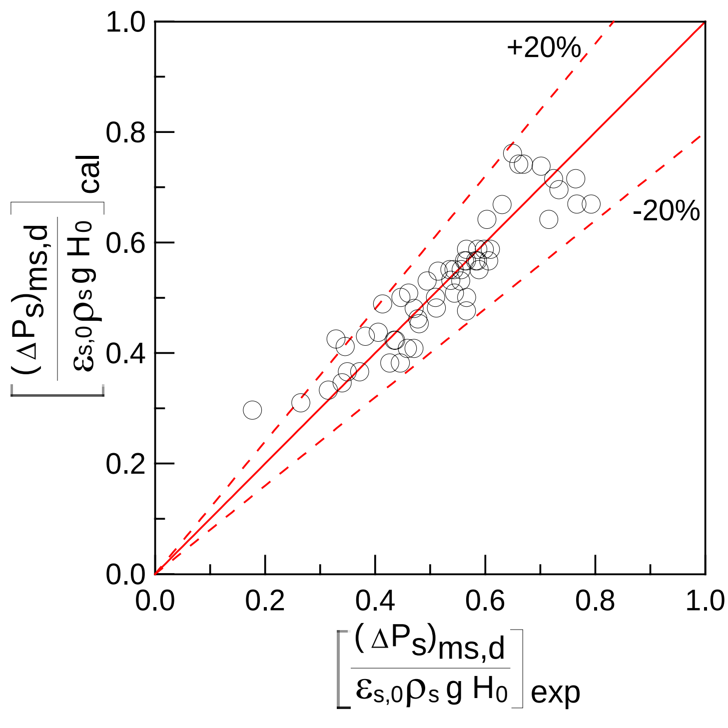

Fig. 3-22. Comparison between experimental data and calculated results by **Eq. (3-7)** on the ratio of the total pressure drop at stable spouting over a fluidized bed with the same static bed height. (Both half and full columns, $U_i=(U_i)_{ms,d}$)

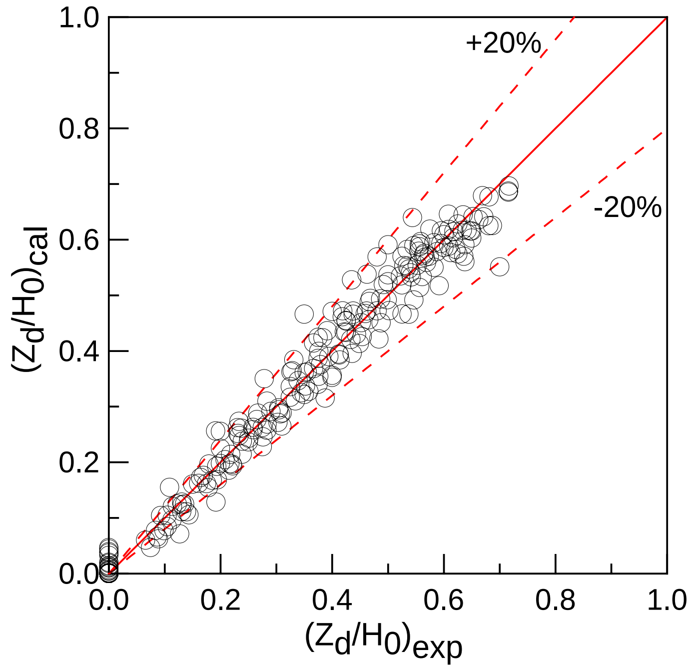

Fig. 3-23. Comparison between experimental data and calculated results by **Eq. (3-8)** on the height of the internal spout. (Half column, descending process)

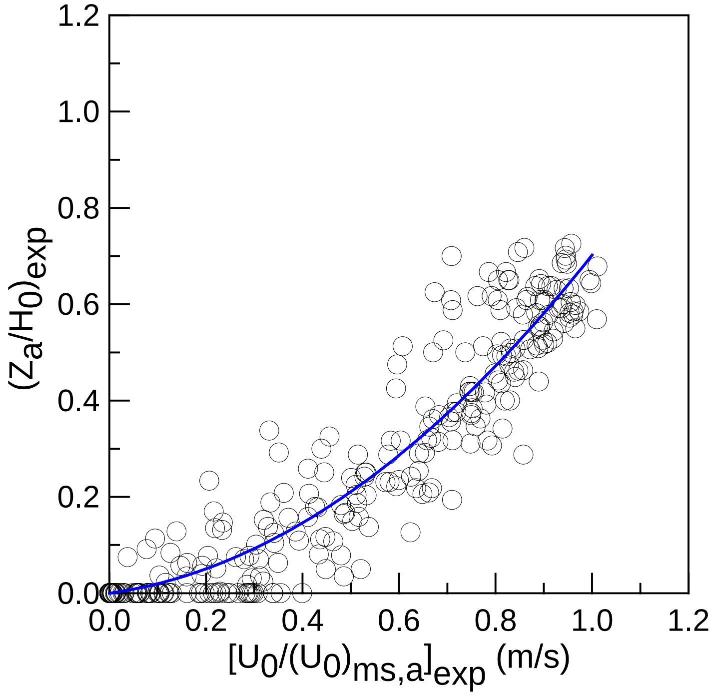

Fig. 3-24. The relationship between the height of the internal spout and superficial fluid velocity. (Half column, ascending process, symbols are experimental data, the solid line shows the trend.)

3.3 Local pressure distribution

3.3.1 Axial pressure distribution

Based on the investigation on spouting kale seeds in flat-based columns, Lefroy and Davidson (1969) noted that the longitudinal pressure distribution in cylindrical spouted beds could be described by a quarter cosine function, as shown in Equation (3-11).

$$\frac{P}{P_t} = \cos(\pi Z / 2H_0) \tag{3-11}$$

where P is the gauge pressure, P_t is the gauge pressure at the bed bottom or the total pressure drop of the bed, Z is the axial height arising from the bed bottom, H_0 is the static bed height.

Whether this function is applicable to conical spouted beds is still uncertain. To evaluate this cosine function, the axial pressure profiles near the wall region of conical spouted beds were measured and shown in Figures 3-25 to 3-27, for the ascending process, descending process and stable spouting state, respectively.

Figures 3-25 and 3-26 show that longitudinal pressure profiles at partial spouting states are not close to the quarter cosine function given by Equation (3-11). Figure 3-27 shows that longitudinal pressure profiles at stable spouting states are much closer to the quarter cosine function, and a new function, Equation (3-12b) (the combination of Equations (3-11) and (3-12a)) appears to give a better agreement. Moreover, in both velocity ascending and descending processes, the lower the operating gas velocity, the farther away experimental results deviate from the quarter cosine curve. By curve fitting, it was found that the longitudinal pressure at different operating gas velocities can be better described by Equation (3-13) with C_1, C_2, C_3 and C_4 as fitted parameters (Since the four parameters vary significantly with operating conditions, values for these parameters are not shown here).

$$\frac{P}{P_t} = 1 - Z / H_0 \tag{3-12a}$$

$$\frac{P}{P_t} = 0.5\cos(\pi Z / 2H_0) + 0.5(1 - Z / H_0) \tag{3-12b}$$

$$\frac{P}{P_t} = \frac{\left|C_1 + C_2(1 - Z / H_0)\right|}{\left[1 + C_3(1 - Z / H_0) + C_4(1 - Z / H_0)^2\right]} \tag{3-13}$$

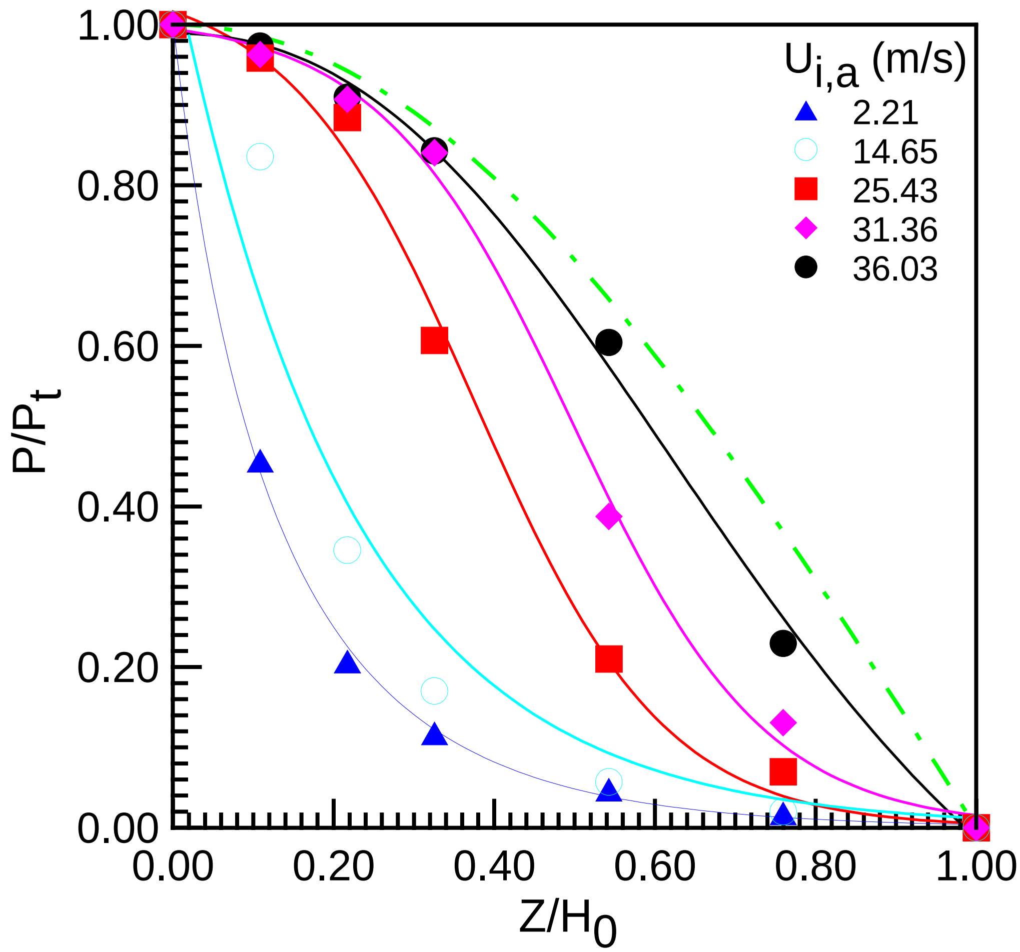

Fig. 3-25. Axial pressure distribution in **ascending process**. (Symbols are experimental data, the dotted dash line corresponds to the quarter cosine function, and other lines are fitted results.) (Half column, D_0=0.019m, H_0=0.468m, γ=45°, d_s=1.16mm, $(U_i)_{ms,a}$=37.3m/s, $(U_i)_{ms,d}$ =28.88m/s)

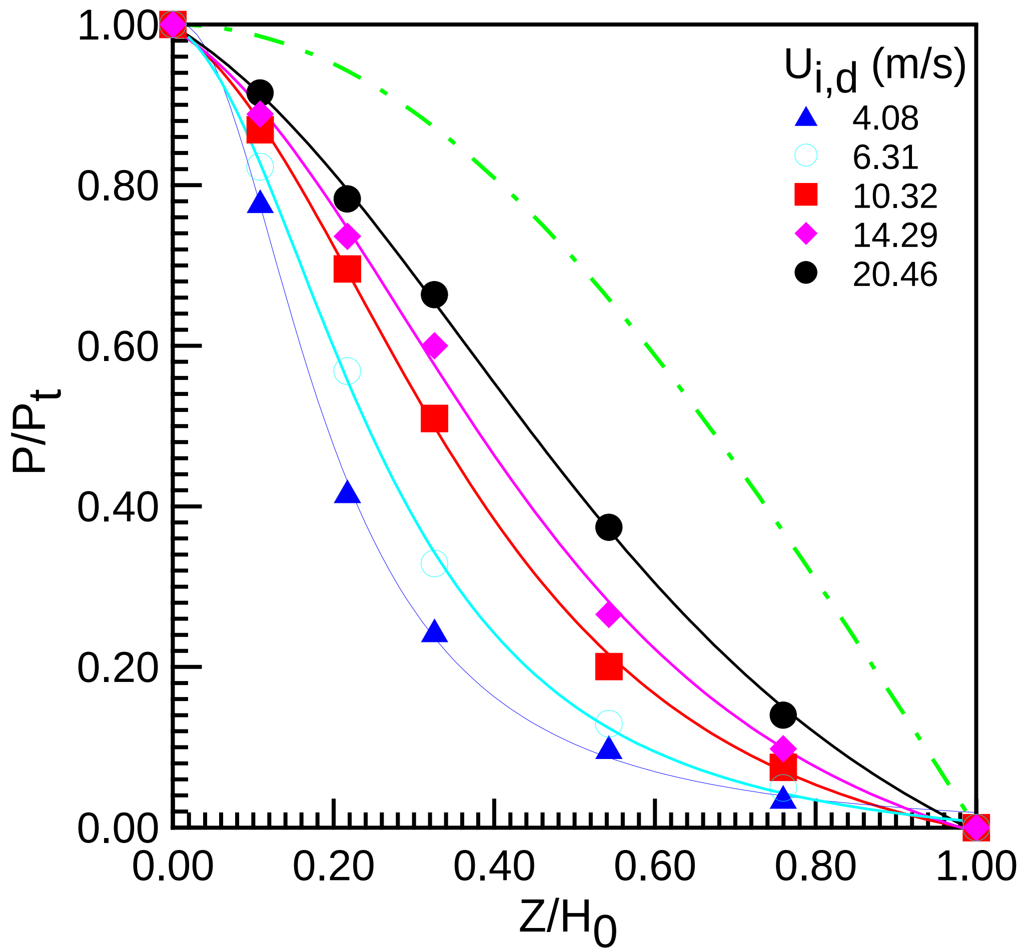

Fig. 3-26. Axial pressure distribution in **descending process**. (Symbols are experimental data, the dotted dash line corresponds to the quarter cosine function, and other lines are fitted results.) (Half column, D_0=0.019m, H_0=0.468m, γ=45º, d_s=1.16mm, $(U_i)_{ms,a}$=37.3m/s, $(U_i)_{ms,d}$ =28.88m/s)

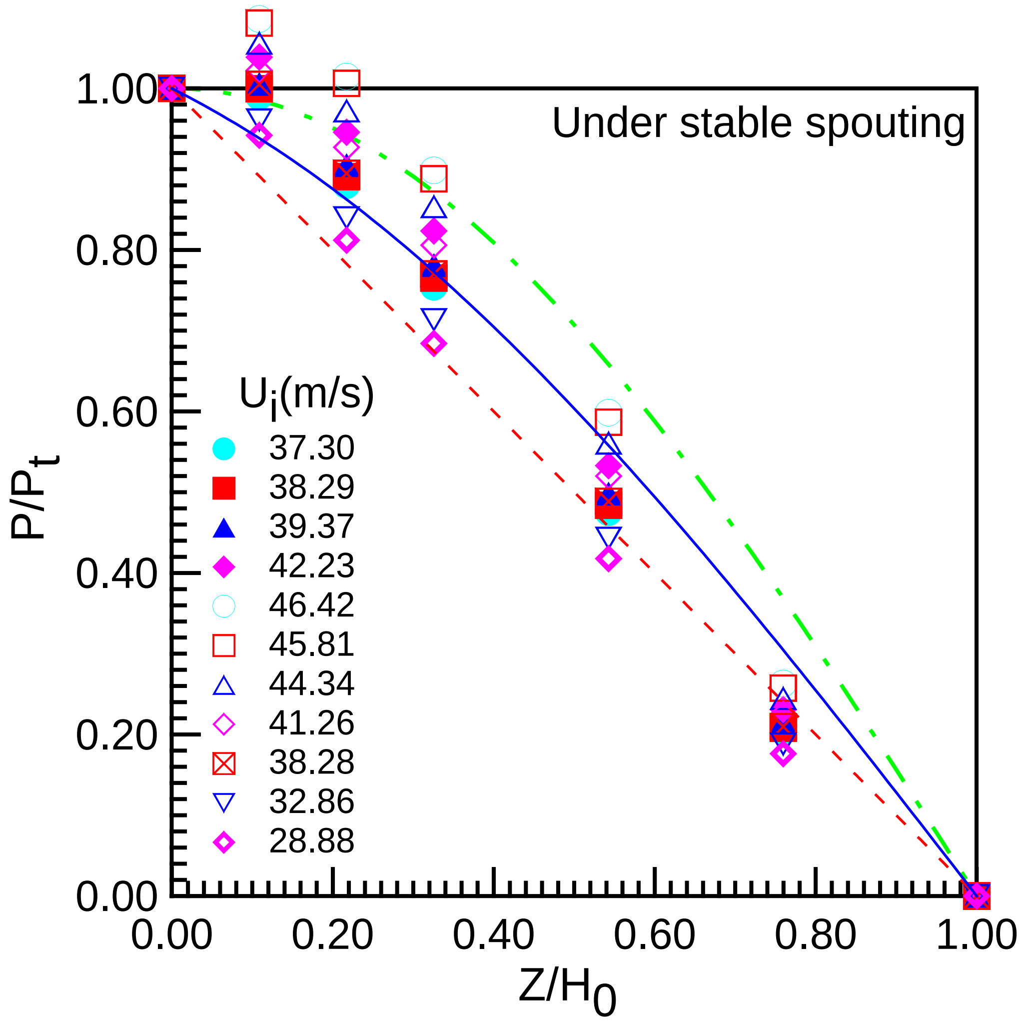

Fig. 3-27. Axial pressure distribution under **stable spouting**. (Symbols are experimental data, the solid line corresponds to Equation (3-12b), the dotted dash line corresponds to the quarter cosine function, and dashed line corresponds to Equation (3-12a).) (Half column, D_0=0.019m, H_0=0.468m, γ=45°, d_s=1.16mm, $(U_i)_{ms,a}$=37.3m/s, $(U_i)_{ms,d}$ =28.88m/s)

3.3.2 Radial pressure distribution

Figures 3-28 to 3-33 show some experimental results on the radial pressure distribution at different operating conditions, including different static bed heights (H_0=0.468 m and H_0=0.396 m) and different bed structures (stable spouting state, partial spouting state in the velocity ascending process and partial spouting state in the descending process). For convenience, the height of the internal spout is also indicated for the partial spouting state. It can be seen that experimental phenomena under different operating conditions are quite similar although operating conditions are quite different: the gauge pressure in the annulus at a certain height decreases with increasing radial distance from the centre of the column. Furthermore, the distribution of the gauge pressure in the spout is quite complex, especially near the bed bottom because of the jet penetration and the jet development.

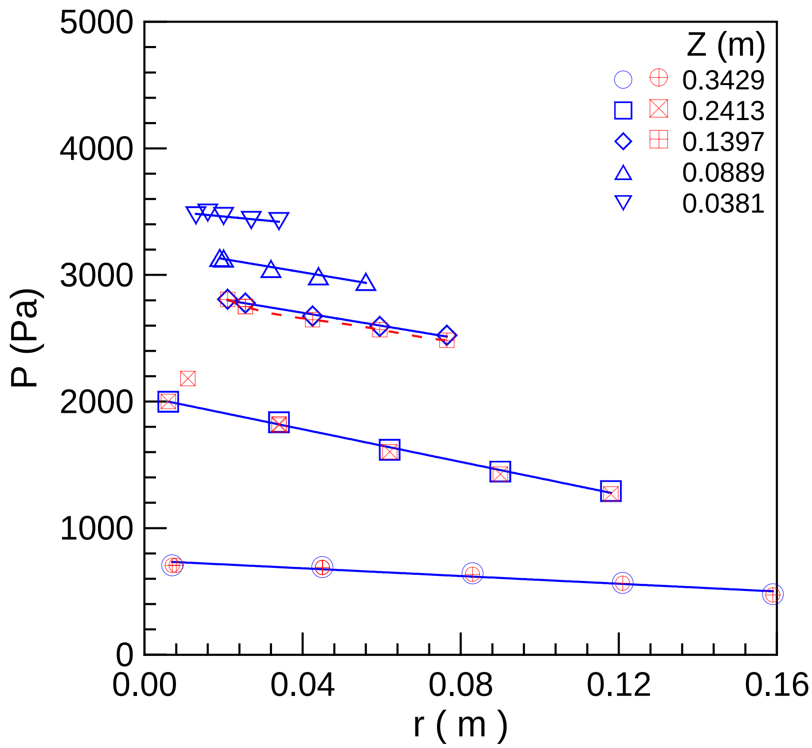

Fig. 3-28. Radial distribution of the gauge pressure in the annulus in the **descending process**.

(Half column, D_0=0.019m, H_0=0.468m, γ=45º, d_s=1.16mm, U_i=19.58m/s, Z_d=0.226m)

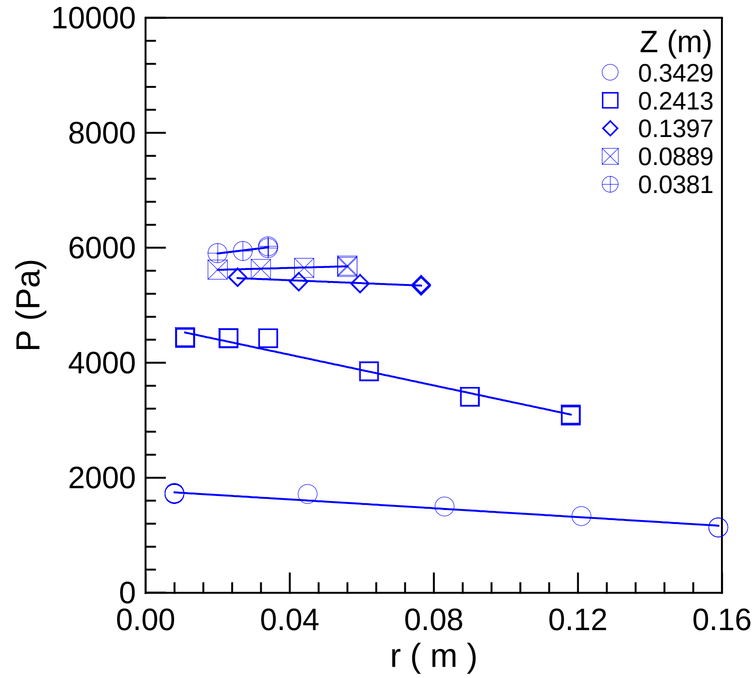

Fig. 3-29. Radial distribution of the gauge pressure in the annulus in the **ascending process**.

(Half column, D_0=0.019m, H_0=0.468m, γ=45º, d_s=1.16mm, U_i=33.86m/s, Z_a=0.251m)

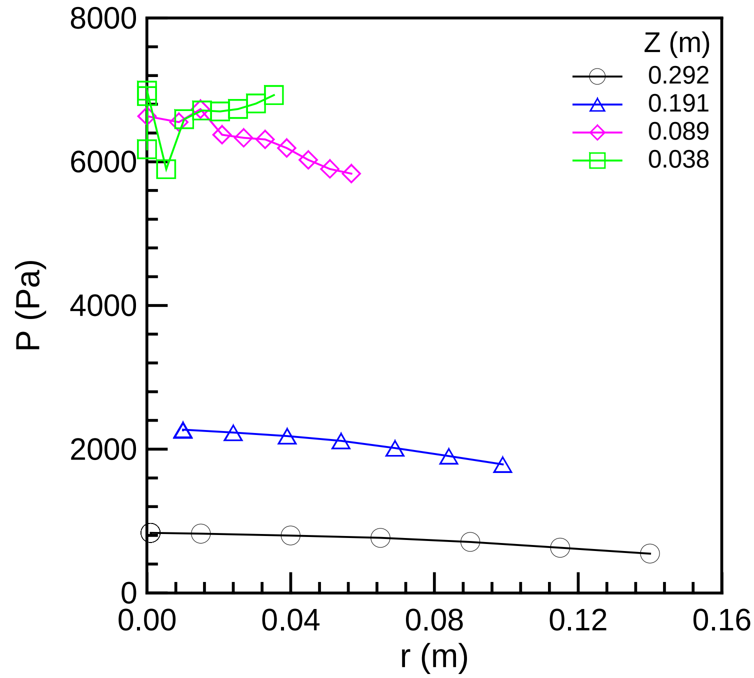

Fig. 3-30. Radial distribution of the gauge pressure in the **ascending process**. (Half column, D_0=0.019m, H_0=0.396m, γ=45º, d_s=1.16mm, U_i=17.39m/s, Z_a=0.136m)

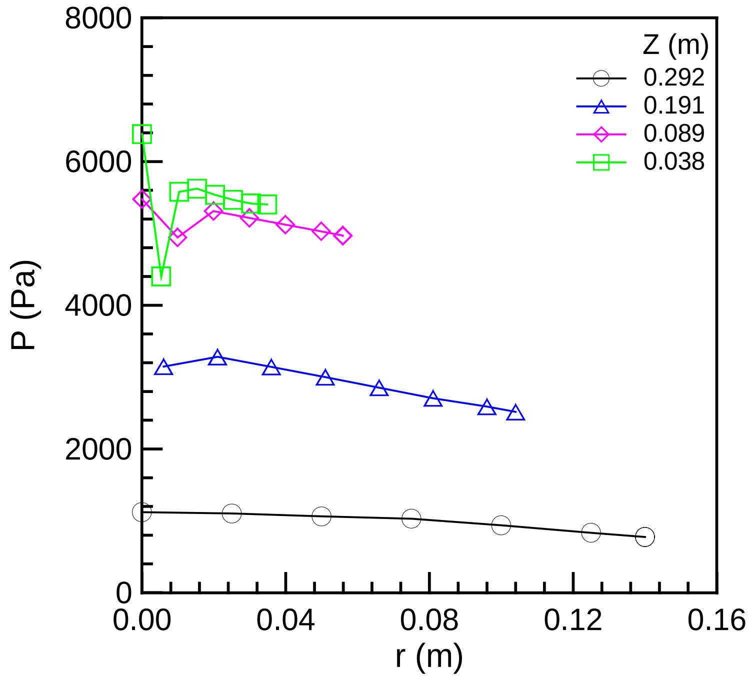

Fig. 3-31. Radial distribution of the gauge pressure in the **ascending process**. (Half column, D_0=0.019m, H_0=0.396m, γ=45º, d_s=1.16mm, U_i=21.58m/s, Z_a=0.186m)

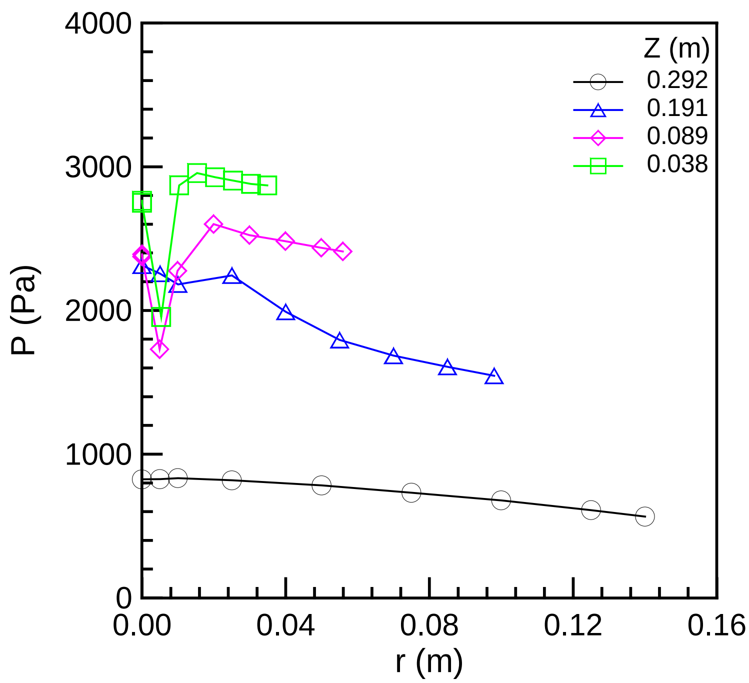

Fig. 3-32. Radial distribution of the gauge pressure in the **descending process**. (Half column, D_0=0.019m, H_0=0.396m, γ=45º, d_s=1.16mm, U_i=16.98m/s, Z_d=0.220m)

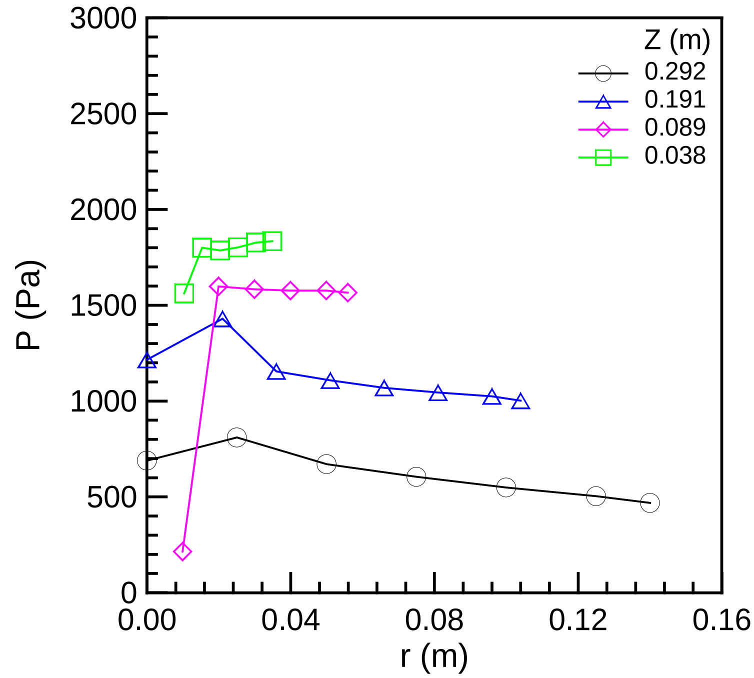

Fig. 3-33. Radial distribution of the gauge pressure under **stable spouting**. (Half column, D_0=0.019m, H_0=0.396m, γ=45º, d_s=1.16mm, U_i=33.42m/s)

3.4 Prediction of pressure and axial superficial gas velocity profiles at partial spouting

3.4.1 Stream-tube model

According to experimental observations, before the onset of the external spouting as well as after the collapse of the external spouting, there exists an internal spout. A simple mechanistic model was developed to analyze the pressure evolution in conical beds. As shown in Figure 3-34, the whole bed is divided into N straight stream tubes. The origin of the coordinates of the system, O is defined as the imaginary intersection between lines ABO and A'B'O traced from the upper limit of the bed to the inside corner of the gas inlet. The angle between lines ABO and A'B'O is divided into 2N equal intervals forming N stream tubes. Near the wall, there exists a narrow dead zone, which tapers towards the upper level, and the dead zone is a function of the gas inlet and the geometrical structure of the bed.

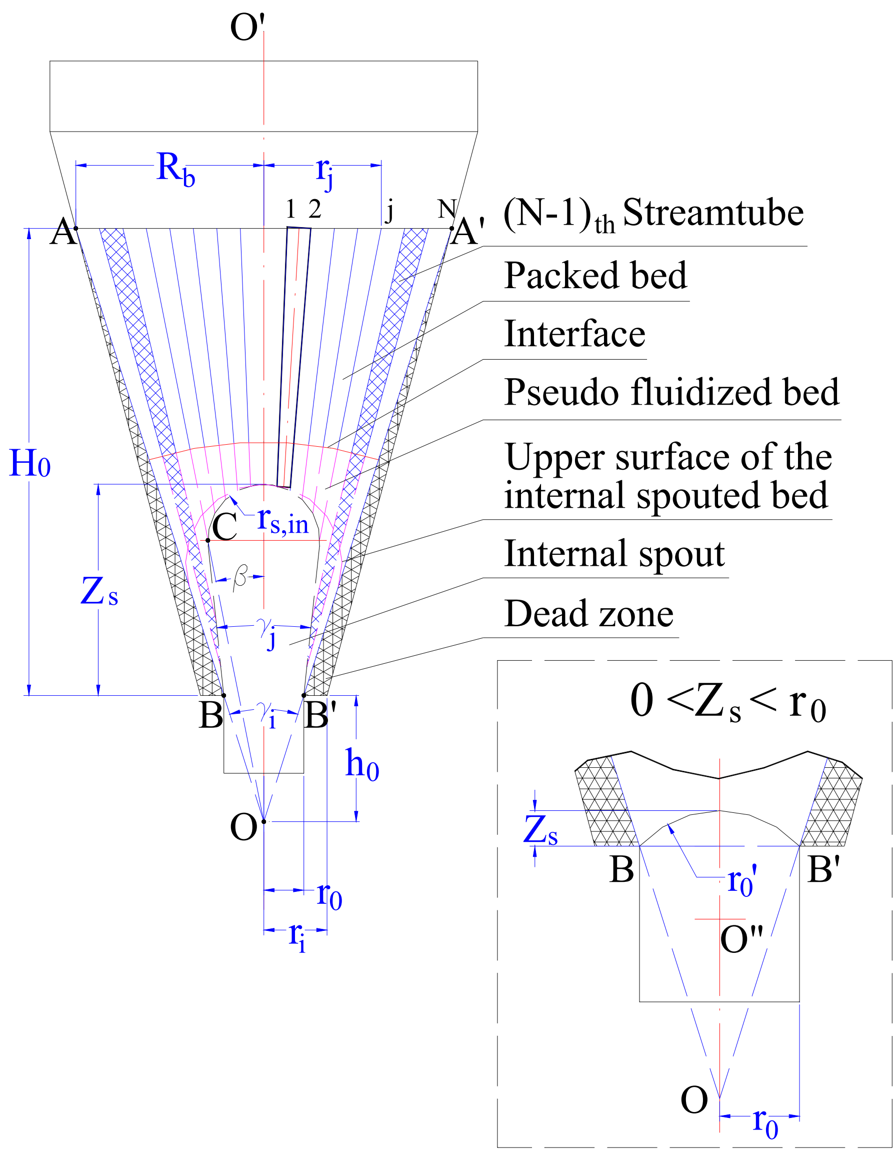

Fig. 3-34. Illustration of the stream-tube mechanistic model.

Assumptions:

1) The top of the internal spout is shaped like a half sphere with a radius of $r_{s,in}$ above a cone with the bottom radius of r_0 and a cone angle of γ_j. Values of γ_j typically range from 10 to 25 degrees as reported in the literature for gas jets in gas-solids fluidized beds. A constant value of $\gamma_j = 20^{\circ}$ is thus first used in this section.

2) The whole bed can be divided into three regions depending on the local gas velocity: the

lower fluidized region (internal spouting), the middle pseudo fluidized bed region where the local superficial gas velocity is larger than the minimum fluidization velocity (i.e. $U_{g,z} \geq U_{mf}$), and the upper packed bed region with $U_{g,z} < U_{mf}$. The total pressure drop of the conical spouted bed is therefore equal to the sum of pressure drops over the three regions.

3) The interface between the lower fluidized region (internal spouting) and the middle pseudo fluidized bed region is defined as the interface of the internal spout.

4) Along stream tube i, the gas flow rate Q_i (i=1, ……, N) keeps constant with no dispersion or mixing in the direction normal to the streamline, i.e. plug flow in each stream tube which is valid mostly when the bed is operated under fixed bed or incipiently fluidized bed conditions with no significant solids circulation.

5) Based on visual observation, the voidage in the pseudo fluidized bed region and the fixed bed region remains uniform. The pressure drop over stream tubes in the upper packed bed region can be calculated by the Ergun equation.

6) In the middle pseudo fluidized bed region, for convenience, a weight factor ω_{fb} is introduced. If ω_{fb} equals 1, the pseudo fluidized bed region is treated as a fluidized bed with a pressure drop ΔP_{fb} being equal to the weight of particles per unit area. If ω_{fb} equals 0, the pseudo fluidized bed region is treated as a packed bed with the pressure drop ΔP_{pb} being calculated by the Ergun equation. Usually, $0 < \omega_{fb} < 1$, and the pressure drop for the pseudo fluidized bed region ΔP_{pfb} is thus calculated by,

$$\Delta P_{pfb} = (1-\omega_{fb})\Delta P_{pb} + \omega_{fb}\Delta P_{fb} \tag{3-14}$$

7) Pressure gradient (dP/dL) in the lower fluidized region (internal spouting) is the same as at stable external spouting, therefore, the pressure drop over the internal spout region can

be estimated by using the pressure drop gradient measured under stable spouting.

The pressure drop for each stream tube in the packed bed region is estimated by the Ergun equation,

$$-\frac{dP}{dL}=150\frac{(1-\varepsilon_g)^2\mu_g}{\varepsilon_g^3(\varphi_s d_s)^2}U_g+1.75\frac{(1-\varepsilon_g)\rho_g}{\varepsilon_g^3\varphi_s d_s}U_g^2 \qquad (3\text{-}15)$$

or

$$-\Delta P_{pb}=\int_0^L(AU_g+BU_g^2)\cdot dL \qquad (3\text{-}16)$$

where

$$A=150\frac{(1-\varepsilon_g)^2\mu_g}{\varepsilon_g^3(\varphi_s d_s)^2} \qquad (3\text{-}17)$$

$$B=1.75\frac{(1-\varepsilon_g)\rho_g}{\varepsilon_g^3\varphi_s d_s} \qquad (3\text{-}18)$$

Geometrical parameters of the model:

Based on the geometrical structure of the bed and streamlines defined before, we can derive all corresponding parameters as follows:

The radius of the bed surface,

$$R_b=r_i+H_0\cdot\tan(\frac{\gamma}{2}) \qquad (3\text{-}19)$$

where r_i is the radius of the bed bottom, H_0 is the static bed height and γ is the cone angle.

The distance from the apex of the cone to the bottom of the bed is given by:

$$h_0=\frac{r_0\cdot H_0}{R_b-r_0} \qquad (3\text{-}20)$$

where r_0 is the radius of the gas inlet.

The angle of the imaginary cone that does not include the dead zone near the wall:

$$\gamma_i = 2\tan^{-1}\left(\frac{R_b - r_0}{H_0}\right) \tag{3-21}$$

Radial distance for each partition on the bed surface is:

$$r_j = (H_0 + h_0)\cdot\tan\left(\frac{\gamma_i \cdot j}{2N}\right) \quad , \quad j = 1,2,...,N \tag{3-22}$$

Angle between every two adjacent streamlines:

$$\alpha_1 = \tan^{-1}\left(\frac{r_1}{H_0 + h_0}\right) \tag{3-23}$$

$$\alpha_i = \tan^{-1}\left(\frac{r_i}{H_0 + h_0}\right) - \sum_{j=1}^{i-1}\alpha_j \quad , \quad i = 2,3,...,N \tag{3-24}$$

Note: For the current definition of streamlines (equal angle between every two streamlines), $\alpha_i = \frac{\gamma_i}{2N} \quad , \quad i = 1,2,...,N$. Equations (3-23) and (3-24) were developed originally for other possible definitions of streamlines, i.e., equal radial distance at the bed surface between every two streamlines, while, the same results can be obtained using Equations (3-23) and (3-24) for the current definition. Moreover, because of the axisymmetric characteristics of conical spouted beds, the central stream-tube is defined to be axisymmetric with a cone angle of $2\alpha_1$; as a result, $\delta_1 = 0$.

Angle between the centre of each stream tube and the central axis of the bed:

$$\delta_1 = 0 \tag{3-25}$$

$$\delta_i = \sum_{j=1}^{i-1}\alpha_j + \frac{\alpha_i}{2} \quad , \quad i = 2,3,...,N \tag{3-26}$$

The length for each streamline:

When Z_s=0:

$$l_i = \frac{H_0}{\cos(\sum_{j=1}^{i} \alpha_j)} \quad , \quad i = 1,2,...,N \tag{3-27}$$

When $0<Z_s<r_0$:

$$(r'_0 - Z_s)^2 + (r_0)^2 = (r'_0)^2$$

$$r'_0 = \frac{Z_s}{2} + \frac{(r_0)^2}{2Z_s} \tag{3-28}$$

$$l_i = \frac{H_0 + h_0}{\cos(\sum_{j=1}^{i} \alpha_j)} - \frac{r'_0 \cdot \sin\{180 - \sum_{j=1}^{i} \alpha_j - \sin^{-1}[\frac{h_0 + Z_s - r'_0}{r'_0} \cdot \sin(\sum_{j=1}^{i} \alpha_j)]\}}{\sin(\sum_{j=1}^{i} \alpha_j)} \quad , \quad i = 1,2,...,N \tag{3-29}$$

When $r_0<Z_s<H_0$

$$\beta = \tan^{-1}(\frac{r_{s,in}}{h_0 + Z_s - r_{s,in}}) \tag{3-30}$$

where β is defined as the angle between lines CO and OO'; C is the intersection between the half sphere above and the cone below which together consist of the internal spout; r_0' is the radius of the top spherical cap of the internal spout when $0<Z_s<r_0$; Z_s is the height of the internal spout.

If $\sum_{j=1}^{i}\alpha_j < \beta$

$$l_i = \frac{H_0 + h_0}{\cos(\sum_{j=1}^{i}\alpha_j)} - \frac{r_{s,in}\cdot\sin\{180 - \sum_{j=1}^{i}\alpha_j - \sin^{-1}[\frac{h_0 + Z_s - r_{s,in}}{r_{s,in}}\cdot\sin(\sum_{j=1}^{i}\alpha_j)]\}}{\sin(\sum_{j=1}^{i}\alpha_j)}, \quad i = 1,2,\ldots,N \tag{3-31}$$

If $\sum_{j=1}^{i}\alpha_j > \beta$

$$l_i = \frac{H_0 + h_0}{\cos(\sum_{j=1}^{i}\alpha_j)} - \frac{\dfrac{r_0\cdot\tan(\sum_{j=1}^{i}\alpha_j) - h_0\cdot\tan(\sum_{j=1}^{i}\alpha_j)\cdot\tan(\frac{\gamma_j}{2})}{\tan(\sum_{j=1}^{i}\alpha_j) - \tan(\frac{\gamma_j}{2})}}{\sin(\sum_{j=1}^{i}\alpha_j)}, \quad i = 1,2,\ldots,N \tag{3-32}$$

The average length for each stream tube:

$$L_{1,1} = \frac{[(H_0 - Z_s) + l_1]}{2} \tag{3-33}$$

$$L_{1,i} = \frac{(l_{i-1} + l_i)}{2}, \quad i = 2,3,\ldots,N \tag{3-34}$$

The length for each stream tube in the packed bed region:

$$L_{2,i} = \frac{H_0 - Z_{pf,i}}{\cos(\delta_i)}, \quad i = 1,2,\ldots,N \tag{3-35}$$

where $Z_{pf,i}$ is the vertical distance between the bed bottom and the interface between the pseudo fluidized bed region and the packed bed region for each stream tube, and can be obtained by assuming that the local vertical superficial gas velocity in each stream tube equals U_{mf} at the height of $Z_{pf,i}$. The initial value for $Z_{pf,i}$ can be assumed to be the height of the internal spout.

The cross section area at the length of L for each stream tube:

$$A_{L,1}=\pi\cdot[r_1-(L_{1,1}-L)\cdot\tan(\alpha_1)]^2 \tag{3-36}$$

$$A_{L,i}=2\pi\cdot\frac{\tan(\frac{\alpha_i}{2})}{\cos(\frac{\alpha_i}{2})}\cdot[\frac{H_0+h_0}{\cos(\delta_i)}-(L_{1,i}-L)]^2\cdot[\sin(\sum_{j=1}^{i-1}\alpha_j)+\sin(\sum_{j=1}^{i}\alpha_j)] \quad , \quad i=2,3,\ldots,N \tag{3-37}$$

Pressure drop in the upper packed bed region:

Superficial gas velocity at the length of L for each stream tube:

$$U_{L,i}=\frac{Q_i}{A_{L,i}} \quad , \quad i=1,2,\ldots,N \tag{3-38}$$

Applying the Ergun equation to each stream tube,

$$-\Delta P_{pb,i}=\int_{L_{1,i}-L_{2,i}}^{L_{1,i}}(AU_{L,i}+BU_{L,i}^2)\cdot dL \quad , \quad i=1,2,\ldots,N \tag{3-39}$$

or

$$-\Delta P_{pb,i}=A\cdot Q_i\cdot\int_{L_{1,i}-L_{2,i}}^{L_{1,i}}(\frac{1}{A_{L,i}})dL+B\cdot Q_i^2\cdot\int_{L_{1,i}-L_{2,i}}^{L_{1,i}}(\frac{1}{A_{L,i}})^2 dL \quad , \quad i=1,2,\ldots,N \tag{3-40}$$

Pressure drop in the pseudo fluidized bed region:

In the pseudo fluidized bed region, for convenience, a weight factor ω_{fb} is introduced. If ω_{fb} equals 1, it means the pseudo fluidized bed region is treated as a fluidized bed; if ω_{fb} equals 0, it means the pseudo fluidized bed region is treated as a packed bed, usually, $0< \omega_{fb} <1$.

For a fluidized bed, the pressure drop can be calculated by Equation (3-41):

$$-\Delta P_{fb,i} = \rho_s g(1-\varepsilon_g)(L_{1,i}-L_{2,i})\cos(\delta_i) \quad , \quad i=1,2,...,N \tag{3-41}$$

For a packed bed, the pressure drop can be calculated by Equation (3-42):

$$-\Delta P_{pb,i} = A\cdot Q_i \cdot \int_0^{L_{1,i}-L_{2,i}} \left(\frac{1}{A_{L,i}}\right) dL + B\cdot Q_i^2 \cdot \int_0^{L_{1,i}-L_{2,i}} \left(\frac{1}{A_{L,i}}\right)^2 dL \quad , \quad i=1,2,...,N \tag{3-42}$$

So, for a pseudo fluidized bed region, the pressure drop can be described as follows:

$$-\Delta P_{pfb,i} = (1-\omega_{fb})\cdot\left[A\cdot Q_i \cdot \int_0^{L_{1,i}-L_{2,i}} \left(\frac{1}{A_{L,i}}\right) dL + B\cdot Q_i^2 \cdot \int_0^{L_{1,i}-L_{2,i}} \left(\frac{1}{A_{L,i}}\right)^2 dL\right]$$
$$+\omega_{fb}\cdot\left\lfloor \rho_s g(1-\varepsilon_g)(L_{1,i}-L_{2,i})\cos(\delta_i)\right\rfloor \quad , \quad i=1,2,...,N \tag{3-43}$$

Pressure drop in the lower fluidized region (internal spouting):

Although this region is named as a fluidized region, it is far from a fluidized bed. Obviously, there exists a cavity in it, and it is more like a spouted bed region. So, to calculate the axial pressure distribution in this region, some characteristic parameters describing a spouted bed can be used, for example, $(\Delta P_s)_{sp}$, the pressure drop at stable spouting.

According to experimental results, at stable spouting, the total pressure drop of the bed as well as the pressure gradient remain almost constant. Most importantly, the pressure gradient in the lower fluidized region also remains constant before the onset of minimum spouting. Thus, the axial pressure drop in the lower fluidized region can be described by

$$-\Delta P_{fb,i} = \frac{H_0 - L_{1,i}\cdot\cos(\delta_i)}{H_0}(\Delta P_s)_{sp} \quad , \quad i=1,2,...,N \tag{3-44}$$

Total pressure drop:

The total pressure drop of a conical bed is equal to summation of pressure drops over the three regions (i.e. top packed bed region, middle partial fluidized bed region, and the bottom spouting region.).

$$-\Delta P_t = (-\Delta P_{fb,i}) + (-\Delta P_{pfb,i}) + (-\Delta P_{pb,i}) \quad , \quad i = 1,2,\ldots,N \tag{3-45}$$

Applying Equation (3-45) to each stream tube, N non-linear equations with the same form can be obtained.

Mass balance equation:

The spouting air can be treated as ideal gas because the operating pressure is low. Neglecting the influence of the operating temperature, the density of the spouting air is proportional to the operating pressure. Thus, the following equation can be derived.

$$\pi r_0^2 U_0 \left[\frac{P_a}{P_a + \frac{(-\Delta P_t) - (-\Delta P_{fb})}{2}} \right] = \sum_{i=1}^{N} \left[Q_i \cos(\delta_i) \right] \tag{3-46}$$

where P_a = 101325 Pa.

Equations (3-45) and (3-46) consist of N+1 non-linear equations, but there are N+3 unknowns, they are Z_s, $(\Delta P_s)_{sp}$, ΔP_t and Q_i (i=1, N). To solve this problem, we need to specify at least two of those unknown parameters. In the current calculation, the measured height of the internal spout Z_s as well as the pressure drop at stable spouting $(\Delta P_s)_{sp}$ are used as input parameters for the prediction of the total pressure drop ΔP_t under different operating conditions.

Furthermore, by solving the above proposed stream-tube model, it is also capable of estimating the distribution of the axial superficial gas velocity and the gauge pressure, as described below.

Distribution of the axial superficial gas velocity:

At any axial height Z, the corresponding length in the stream tube i, L_i, can be calculated by Equation (3-47).

$$L_i = \frac{H_0 - Z}{\cos(\delta_i)} \quad , \quad i = 1,2,\ldots,N \tag{3-47}$$

Based on Equation (3-38), after the gas flow rate in each stream tube has been obtained, the axial superficial gas velocity can be further described as

$$(U_{g,z})_{L,i} = \frac{Q_i \cos(\delta_i)}{A_{L,i}} \quad , \quad i = 1,2,\ldots,N \tag{3-48}$$

Distribution of the gauge pressure:

If $L_i < L_{2,i}$, the position is located in the upper packed bed region,

$$P = A \cdot Q_i \cdot \int_{L_{1,i} - L_i}^{L_{1,i}} \left(\frac{1}{A_{L,i}}\right) dL + B \cdot Q_i^2 \cdot \int_{L_{1,i} - L_i}^{L_{1,i}} \left(\frac{1}{A_{L,i}}\right)^2 dL \quad , \quad i = 1,2,\ldots,N \tag{3-49}$$

If $L_{1,i} > L_i > L_{2,i}$, the position is located in the pseudo fluidized bed region,

$$\begin{aligned} P = {} & A \cdot Q_i \cdot \int_{L_{1,i} - L_{2,i}}^{L_{1,i}} \left(\frac{1}{A_{L,i}}\right) dL + B \cdot Q_i^2 \cdot \int_{L_{1,i} - L_{2,i}}^{L_{1,i}} \left(\frac{1}{A_{L,i}}\right)^2 dL \\ & + (1 - \omega_{fb}) \cdot \left[A \cdot Q_i \cdot \int_{L_{1,i} - L_i}^{L_{1,i} - L_{2,i}} \left(\frac{1}{A_{L,i}}\right) dL + B \cdot Q_i^2 \cdot \int_{L_{1,i} - L_i}^{L_{1,i} - L_{2,i}} \left(\frac{1}{A_{L,i}}\right)^2 dL \right] \\ & + \omega_{fb} \cdot \left[\rho_s g (1 - \varepsilon_g)(L_i - L_{2,i}) \cos(\delta_i) \right] \quad , \quad i = 1,2,\ldots,N \end{aligned} \tag{3-50}$$

If $L_i > L_{1,i}$, the position is located in the lower fluidized region (internal spouting),

$$P = (-\Delta P_t) - \frac{H_0 - L_i \cdot \cos(\delta_i)}{H_0} (\Delta P_s)_{sp} \quad , \quad i = 1,2,\ldots,N \tag{3-51}$$

3.4.2 Results and discussions

With the height of the internal spout Z_s, pressure drop at stable spouting $(\Delta P_s)_{sp}$, and the gas flow rate measured from the experiment as input parameters, the above mechanistic model can be solved for a given value of ω_{fb} to obtain the total pressure drop over the bed (Matlab programs are listed in Appendix H.). One typical result is shown in Figure 3-35. It is seen that predicted pressure drops with the pseudo fluidized bed region considered as in fully fluidized state (i.e. ω_{fb}=1) agree quite well with experimental data for the velocity descending process, but severely underestimates the ascending process. The prediction with the pseudo fluidized bed region treated as a packed bed (i.e. ω_{fb}=0), on the other hand, overestimates measured pressure drops for the ascending process. A partially fluidized state with ω_{fb}=0.8 appears to give a reasonable agreement. The implication is not only that the internal spout height in the ascending process is generally smaller than in the descending process for a given gas velocity below the minimum spouting velocity U_{ms}, but also the particle packing structure in the region surrounding the internal spout differs in the velocity ascending and descending process with particles in the ascending process in a partially packed state and thus less mobile compared to the descending process. Figure 3-36 shows another comparison between calculated data and experimental results at different operating conditions. There is also a reasonable agreement when ω_{fb}=0.85 is chosen for the ascending process.

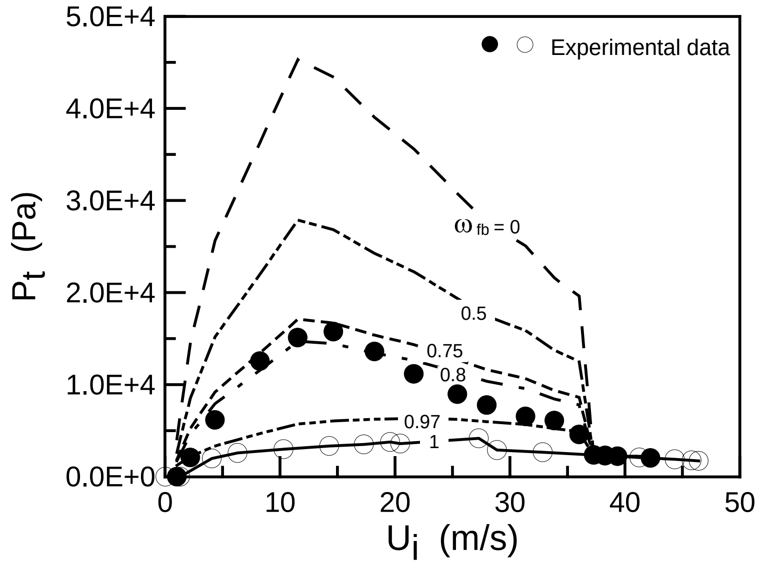

Fig. 3-35. Comparison between calculated results and experimental data. Closed symbols for experimental data in the ascending process and open symbols for the descending process. Dashed lines for simulated results in the ascending process, and the solid line for the descending process. (Half column, D_0=0.019m, H_0=0.468m, γ=45º, γ_j = 20º, constant ω_{fb} in the ascending process)

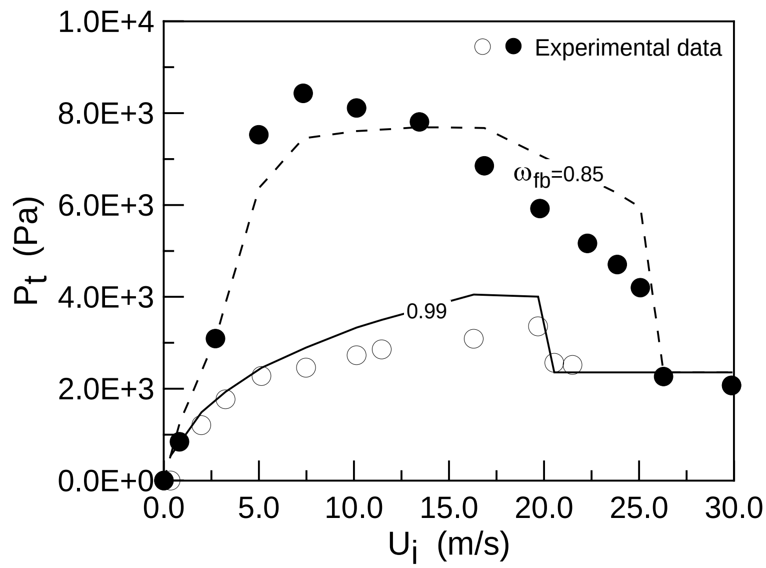

Fig. 3-36. Comparison between calculated results and experimental data. Closed symbols for experimental data in the ascending process and open symbols for the descending process. The dashed line for simulated results in the ascending process, and the solid line for the descending process. (Half column, D_0=0.019m, H_0=0.383m, γ=45º, γ_j = 20º, constant ω_{fb} in the ascending process)

From Figures 3-35 and 3-36, it is also clear that it is hard to obtain accurate fits for all operating conditions in the ascending process just using a single value of ω_{fb}. Thus, different values of ω_{fb} were obtained by fitting experimental data at different operating conditions, as shown in Table 3-2. As shown in Figures 3-37 and 3-38, better agreement is achieved using different values of ω_{fb} shown in Table 3-2.

Table 3-2. Different values of ω_{fb} used and corresponding operating conditions (γ_j = **20º**).

H_0=0.468m, γ_j = 20º		**H_0=0.383m, γ_j = 20º**	
$U_{i,a}$ (m/s)	ω_{fb}	$U_{i,a}$ (m/s)	ω_{fb}
1.0281	0.9	0.0101	0.85
2.207	0.9	0.0072	0.85
4.3453	0.9	0.8255	0.85
8.2599	0.8	2.724	0.85
11.5518	0.8	5.004	0.8
14.649	0.75	7.3381	0.8
18.22	0.8	10.1494	0.8
21.643	0.85	13.4559	0.85
25.4301	0.87	16.8698	0.9
27.9847	0.87	19.7916	0.9
31.3615	0.93	22.2902	0.93
33.8623	0.93	23.864	0.93
36.0258	0.93	25.0791	0.93
37.3017	0.93	26.2951	0.93
38.2912	0.93		
39.3683	0.93		
42.2305	0.93		

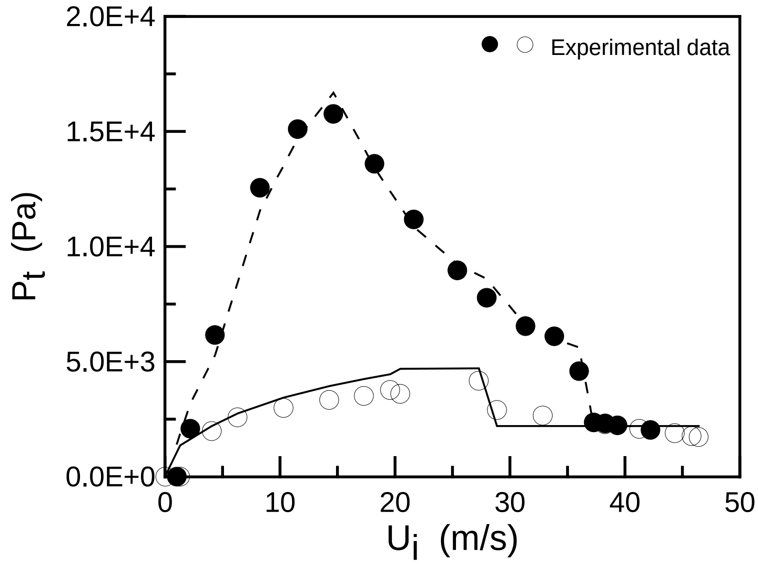

Fig. 3-37. Comparison between calculated results and experimental data. Closed symbols for experimental data in the ascending process and open symbols for the descending process. The dashed line for simulated results in the ascending process, and the solid line for the descending process. (Half column, D_0=0.019m, H_0=0.468m, γ=45º, γ_j = 20º, varied ω_{fb} in the ascending process)

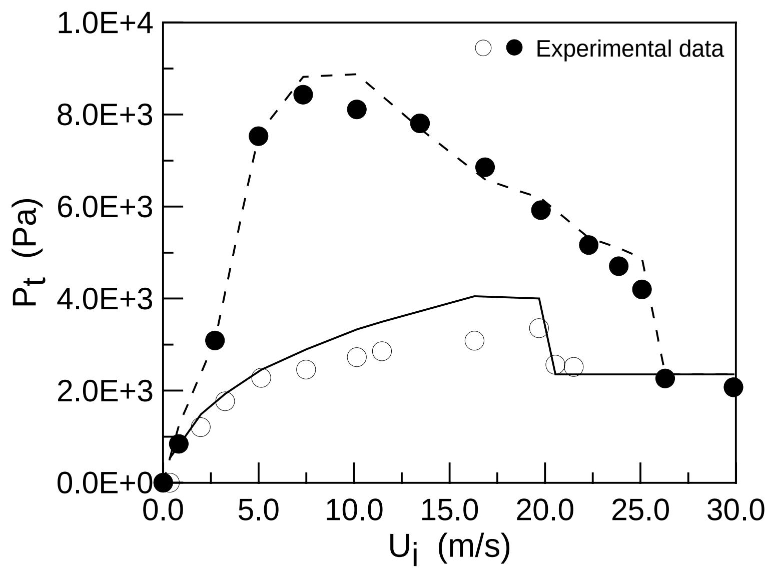

Fig. 3-38. Comparison between calculated results and experimental data. Closed symbols for experimental data in the ascending process and open symbols for the descending process. The dashed line for simulated results in the ascending process, and the solid line for the descending process. (Half column, D_0=0.019m, H_0=0.383m, γ=45º, γ_j = 20º, varied ω_{fb} in the ascending process)

It is speculated that interlocking of particles could occur in a conical spouted bed with increasing gas velocity. As gas velocity increases, an internal spout or cavity is formed, pushing aside particles originally occupying the cavity. Since the upper region of the bed remains in a packed state, interlocked immobile particles prevent the upward expansion of the bed. As a result, particles pushed out from the cavity can only move in the vicinity of the cavity, resulting in the compaction of the surrounding region. The compressed dome region will subsequently restrict the expansion of the jet. Furthermore, the dome region will become more compressed as more particles are pushed out from the growing cavity. In the velocity descending process, the shrinking cavity or spout creates space for particles. As a result, the vicinity surrounding the cavity never gets compressed. Therefore, the jet height is also expected to be much larger than in the velocity ascending process.

The above speculation is examined by reversing the gas flow rate in an ascending or descending process, with the results shown in Figures 3-39 and 3-40, respectively. The basic evolution curve of the pressure drop for ascending and descending processes corresponds to Run 02 to Run 05 in Figure 3-2. Numbers show the order of the operating sequence. When gas velocity is decreased in an ascending process, for example, from point 2 to point 3 in Figure 3-39, the pressure drop falls off from the base ascending curve to approach the base descending evolution curve, because the reduction in gas flow rate in an ascending process shrinks the cavity, relieving the compaction of the compressed pseudo fluidized region. However, when gas velocity is changed back to the original ascending path, the pressure drop will recover, and gradually approach the pressure drop in the original ascending path because the pseudo fluidized bed region is re-compressed. A similar explanation can be applied for the flow reversal in the velocity descending process in Figure 3-39. The flow reversal tests were repeated at different ranges of velocity in both the ascending and descending process, with consistent results obtained as shown in Figure 3-40.

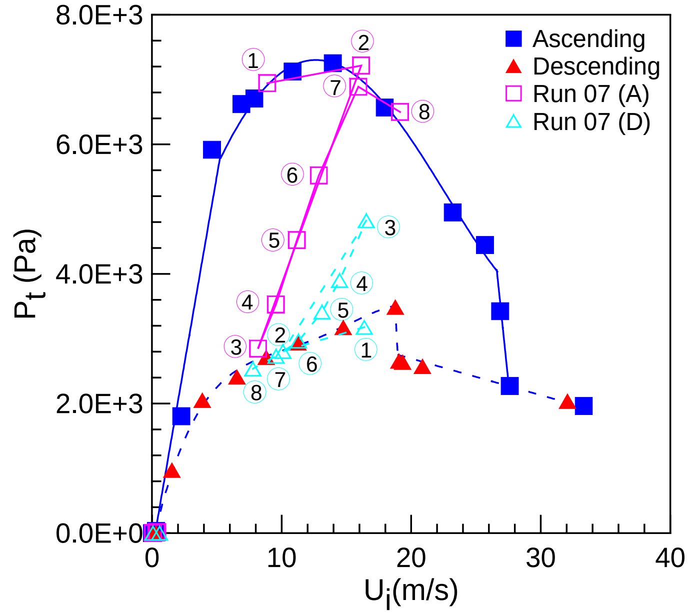

Fig. 3-39. Deviation of total pressure drops from the normal ascending or descending process.

(Half column, D_0=0.019m, H_0=0.396m, γ=45º)

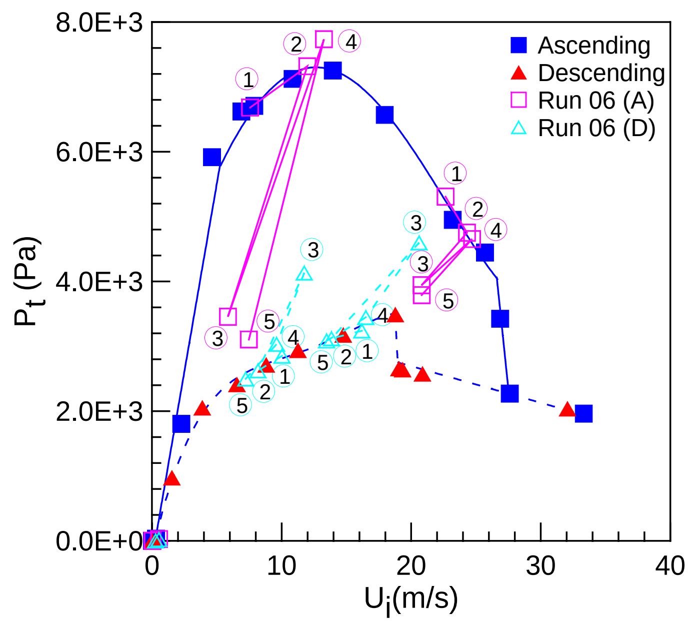

Fig. 3-40. Deviation of total pressure drops from the normal ascending or descending process.

(Half column, D_0=0.019m, H_0=0.396m, γ=45º)

3.4.3 Prediction of the local axial superficial gas velocity and gauge pressure at partial spouting

Based on Equations (3-47) to (3-51), the radial distribution of the gauge pressure and axial superficial gas velocity were calculated with the results shown in Figures 3-41 to 3-44. From Figures 3-41 and 3-42, it can be seen that predicted gauge pressures are quite different from experimental data. The predicted axial superficial gas velocity profiles are thus not reliable.

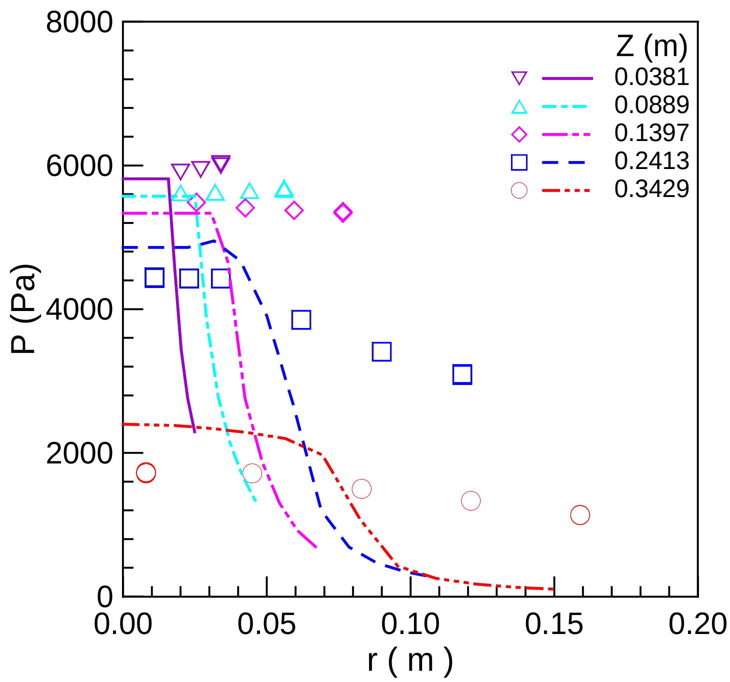

Fig. 3-41. Radial distribution of the gauge pressure in the velocity **ascending process**. Symbols are experimental data, lines are simulation results. (Half column, D_0=0.019m, H_0=0.468m, γ=45º, d_s=1.16mm, U_i=33.86m/s, Z_a=0.251m, ω_{fb}=0.93, γ_j = 20º)

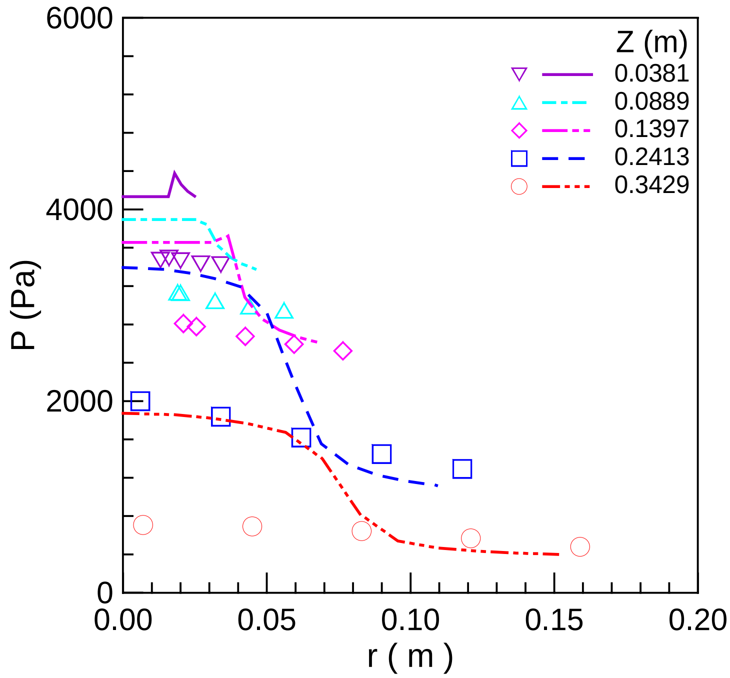

Fig. 3-42. Radial distribution of the gauge pressure in the velocity **descending process**. Symbols are experimental data, lines are simulation results. (Half column, D_0=0.019m, H_0=0.468m, γ=45º, d_s=1.16mm, U_i=19.58m/s, Z_d=0.226m, ω_{fb}=1.0, γ_j = 20º)

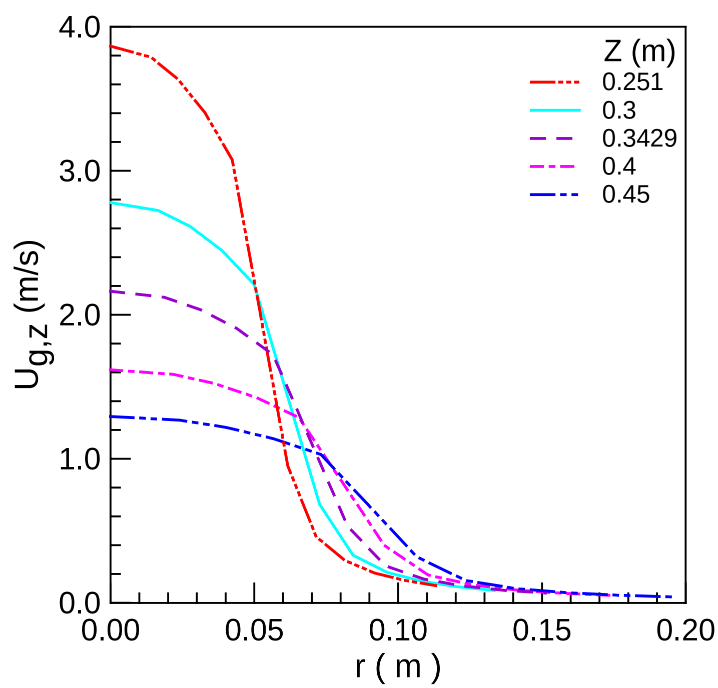

Fig. 3-43. Radial distribution of the axial superficial gas velocity in the velocity **ascending process**. (D_0=0.019m, H_0=0.468m, γ=45º, d_s=1.16mm, U_i=33.86m/s, Z_a=0.251m, ω_{fb}=0.93, γ_j = 20º)

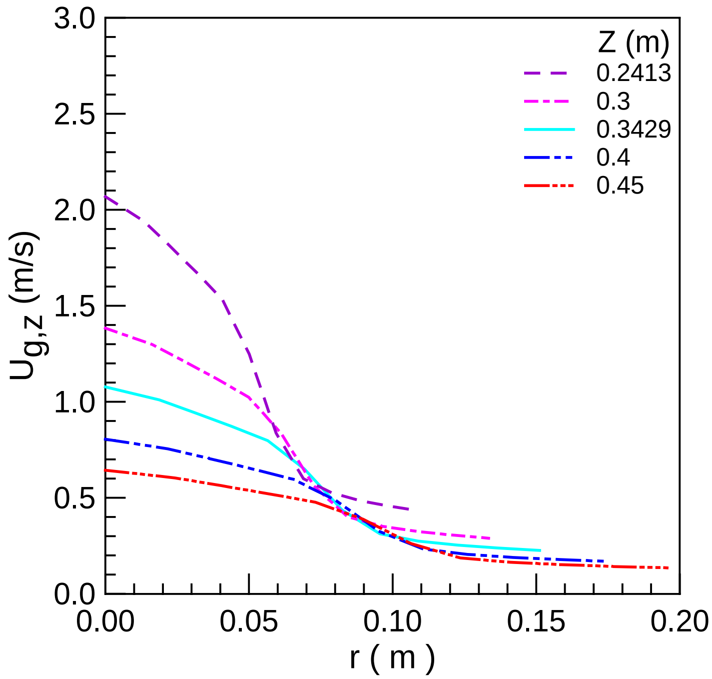

Fig. 3-44. Radial distribution of the axial superficial gas velocity in the velocity **descending process**. (D_0=0.019m, H_0=0.468m, γ=45º, d_s=1.16mm, U_i=19.58m/s, Z_d=0.226m, ω_{fb}=1.0, γ_j = 20º)

3.4.4 Improvement of the stream-tube model

Based on discussions in 3.4.3, it is clear that the above stream-tube model is not capable of simulating local gas behaviour, such as distributions of the static gauge pressure and the local gas velocity.

By trial and error, it was found that reasonable results on the gauge pressure could be achieved with the 3rd model assumption being replaced by the following assumption: the interface between the lower fluidized region (internal spouting) and the middle pseudo fluidized bed region is defined as the upper surface of an internal spouted bed, which includes both a dilute internal spout (cavity) and a dense surrounding annulus. Besides, the upper surface of the internal spouted region is defined as a half sphere. As a result, the cone angle of the internal spouted region is $2\sum_{j=1}^{N}\alpha_j \approx 47^\circ$ (Because there exists a dead zone near the wall, this angle is slightly bigger than the cone angle of the conical spouted bed, γ=45º.).

As shown in Figures 3-45 and 3-46, predicted static gauge pressures agree very well with experimental data, especially for the velocity descending process as well as in the pseudo fluidized bed and upper packed bed regions. Thus, predicted axial gas velocity profiles shown in Figures 3-47 and 3-48 are much more reliable than those in Figures 3-43 and 3-44.

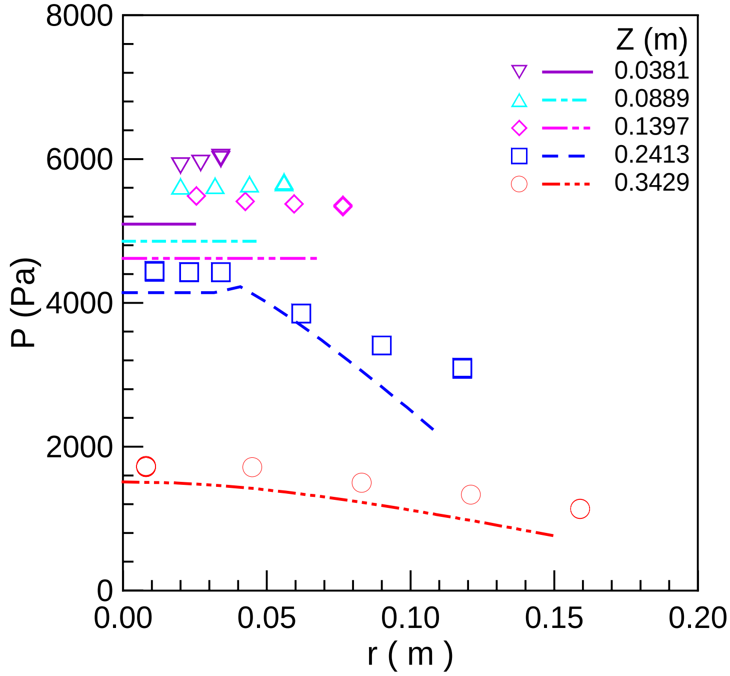

Fig. 3-45. Radial distribution of the gauge pressure in the **ascending process**. Symbols are experimental data, lines are simulation results. (Half column, D_0=0.019m, H_0=0.468m, γ=45º, d_s=1.16mm, U_i=33.86m/s, Z_a=0.251m, ω_{fb}=0.0, internal spouted bed)

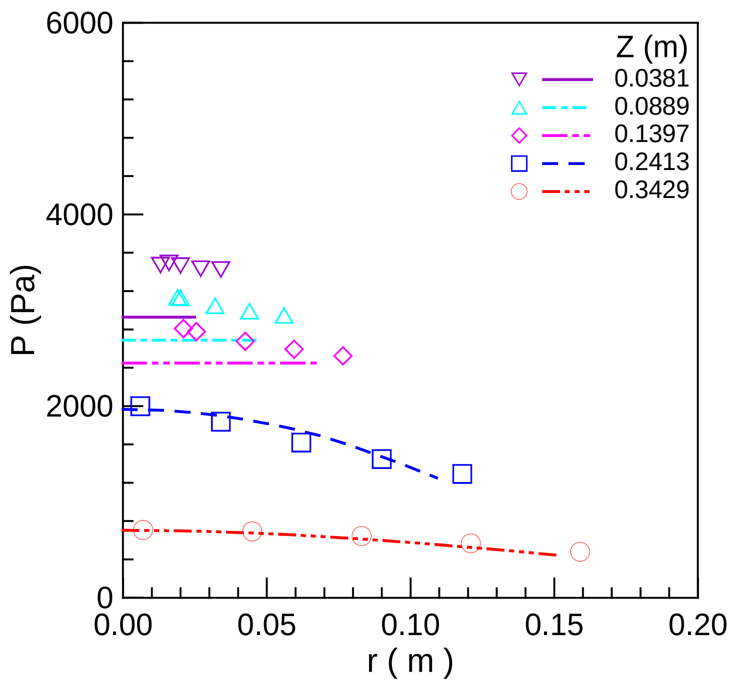

Fig. 3-46. Radial distribution of the gauge pressure in the **descending process**. Symbols are experimental data, lines are simulation results. (Half column, D_0=0.019m, H_0=0.468m, γ=45º, d_s=1.16mm, U_i=19.58m/s, Z_d=0.226m, ω_{fb}=1.0, internal spouted bed)

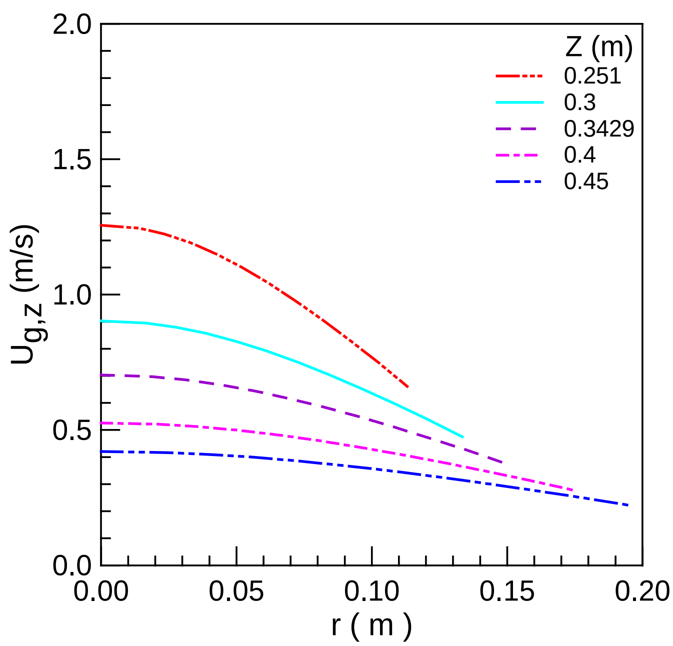

Fig. 3-47. Predicted radial distribution of the axial superficial gas velocity in the **ascending process**. (D_0=0.019m, H_0=0.468m, γ=45º, d_s=1.16mm, U_i=33.86m/s, Z_a=0.251m, ω_{fb}=0.0, internal spouted bed)

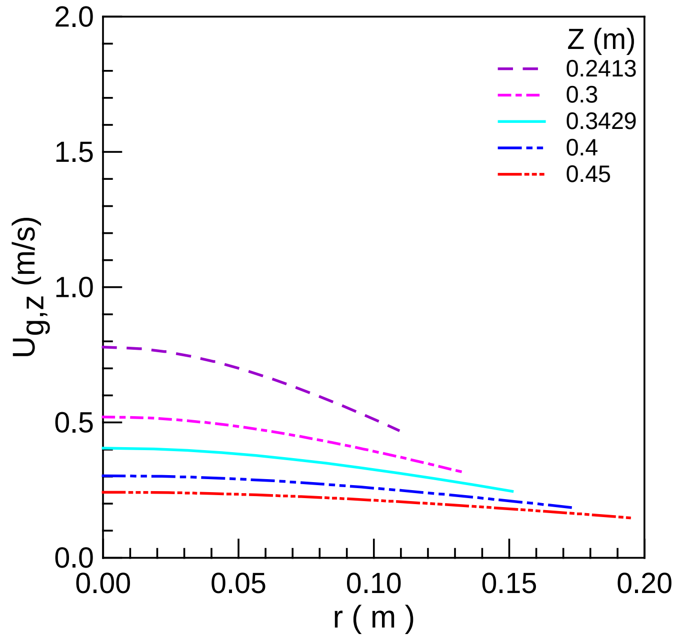

Fig. 3-48. Predicted radial distribution of the axial superficial gas velocity in the **descending process**. (D_0=0.019m, H_0=0.468m, γ=45º, d_s=1.16mm, U_i=19.58m/s, Z_d=0.226m, ω_{fb}=1.0, internal spouted bed)

Furthermore, the above new assumption was also used to simulate the pressure evolution loop as in Section 3.4.3, with results shown in Figures 3-49 and 3-50, and corresponding values of ω_{fb} given in Table 3-3. It is seen that good agreement can be achieved with ω_{fb} varied over the range of gas velocities studied.

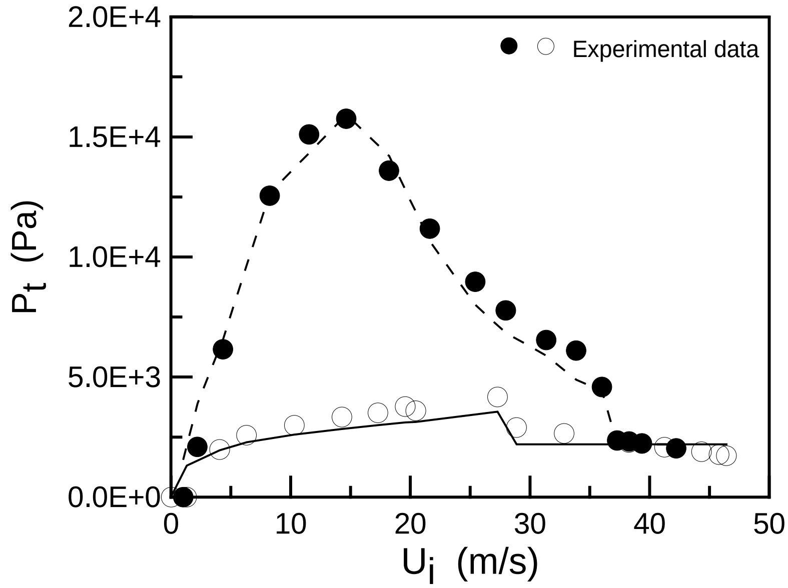

Fig. 3-49. Comparison between calculated results and experimental data. Closed symbols for experimental data in the ascending process and open symbols for the descending process. The dashed line for simulated results in the ascending process, and the solid line for the descending process. (Half column, D_0=0.019m, H_0=0.468m, γ=45º, internal spouted bed)

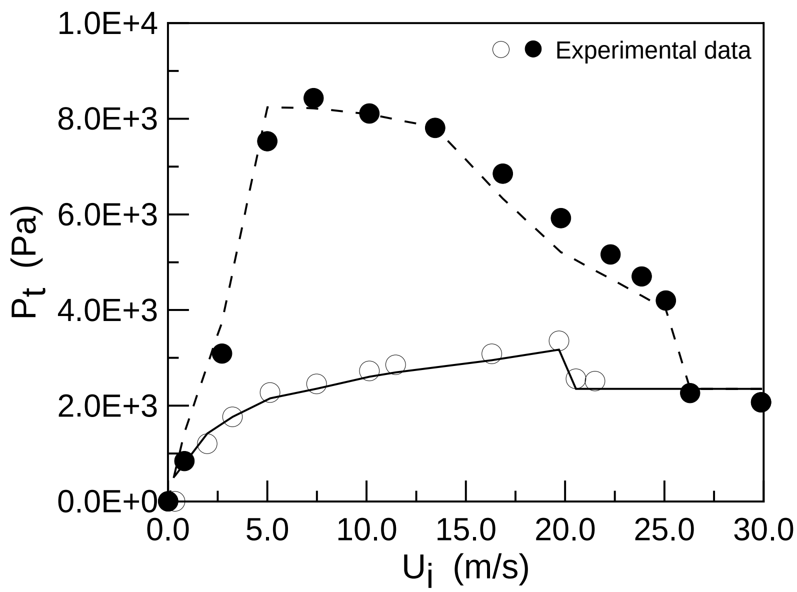

Fig. 3-50. Comparison between calculated results and experimental data. Closed symbols for experimental data in the ascending process and open symbols for the descending process. The dashed line for simulated results in the ascending process, and the solid line for the descending process. (Half column, D_0=0.019m, H_0=0.383m, γ=45º, internal spouted bed)

Table 3-3. Different values of ω_{fb} used and corresponding operating conditions (γ_i **≈47°**).

H_0=0.468m			**H_0=0.383m**	
$U_{i,a}$ (m/s)	ω_{fb}		$U_{i,a}$ (m/s)	ω_{fb}
1.0281	0.85		0.0101	0.75
2.207	0.85		0.0072	0.75
4.3453	0.85		0.8255	0.75
8.2599	0.7		2.724	0.75
11.5518	0.7		5.004	0.75
14.649	0.5		7.3381	0.75
18.22	0.3		10.1494	0.63
21.643	0.3		13.4559	0.45
25.4301	0.3		16.8698	0.45
27.9847	0.3		19.7916	0.45
31.3615	0.3		22.2902	0.45
33.8623	0		23.864	0.45
36.0258	0.3		25.0791	0.45
37.3017	0.3		26.2951	0.45
38.2912	0.3			
39.3683	0.3			
42.2305	0.3			

CHAPTER 4

LOCAL FLOW STRUCTURE IN A CONICAL SPOUTED BED

The distribution of both the local voidage (or solids fraction) and local particle velocity is of great interest in researches on multiphase systems. Among all experimental techniques reported in the literature, such as the capacitance probe (Goltsiker, 1967), the piezoelectric probe (Mikhailik and Antanishin, 1967), γ-rays technique (Waldie et al., 1986a), the optical fibre probe (Morooka et al., 1980; Matsuno et al., 1983; San Jose et al. 1998a; He, 1994b; He, 1995; Liu, 2001; Liu et al. 2003), Laser-Doppler Anemometry technique (Arastoopour and Yang 1992) etc, only the optical fibre probe can be used to measure both the local instantaneous particle velocity and solids fraction simultaneously. Therefore, optical fibre probes that were originally used to measure solids velocities in fluidized beds and spouted beds in our laboratory were applied in this study to measure both the particle velocity and solids fraction in conical spouted beds.

4.1 Optical fibre probe measurement system

The optical fibre probe measurement system used in this study, Particle Velocimeter PV-4A, was developed by the Institute of Chemical Metallurgy of the Chinese Academy of Sciences. It consists of a three-fibre optical fibre probe, a light source, two photomultipliers and a high-speed data acquisition card connected to a computer, as shown in Figure 4-1. By off-line cross-correlation of sampled signals from light receivers A and B, the time delay τ can be obtained (See Appendix D.1 for details.), and the particle velocity V_s can be calculated if one knows the effective distance D_e between two light receivers (See Appendix D.1 for details.), as shown in Equation (4-1). By off-line averaging of sampled signals from light receiver A or B, solids fraction can also be obtained based on the relationship between the solids fraction and the amplitude of the signal (See Appendix D.3 for details.).

$$V_s = \frac{D_e}{\tau} \tag{4-1}$$

where D_e is the effective distance between receivers A and B, τ is the time delay.

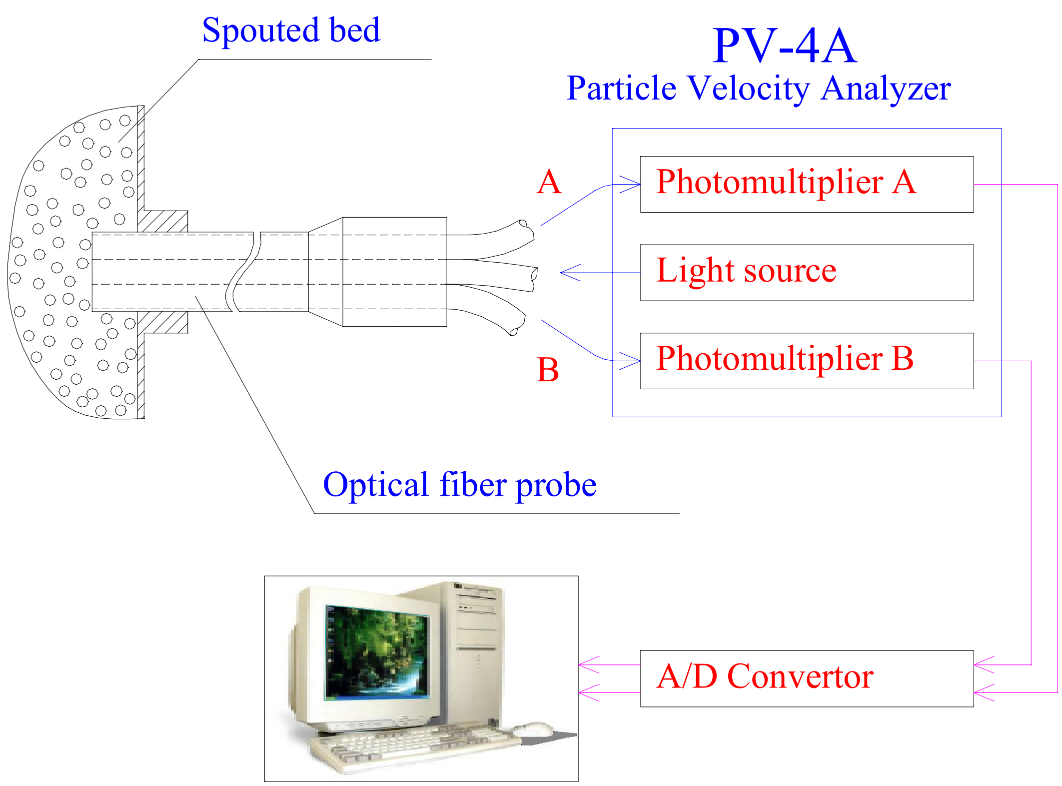

Fig. 4-1. Particle velocity measurement system.

A typical three-fibre optical fibre probe is shown in Figure 4-2; the probe consists of three aligned optical fibre groups with one in the middle as the light projector and the other two as light receivers. Each optical fibre group consists of thousands of optical fibres of 16 μm in diameter for each fibre. As shown in Figure 4-2, there are several characteristic dimensions, for example, D_{probe} is the diameter of the optical fibre probe, D_f is the diameter of each fibre group;

D_2 is the central distance between two light receivers; D_e is the effective distance calibrated through experiments; D_1 is half of D_2, and is equal to D_f if there is no gap between the light projector and each light receiver. Theoretically, D_e should be equal to D_1.

The optical fibre probe (Probe 1) used in this study was 8 mm (D_{probe}) in outside diameter, and the diameter of each optical fibre group was D_f=2.5 mm, in order to minimize the interference caused by the probe. The probe tip was a rectangle of 9 mm by 3.5 mm. To eliminate the influence of the blind zone (Liu, 2001; Liu et al. 2003), a glass window was added in front of the probe tip. Another optical fibre probe (Probe 2, as shown in Figure 4-3) of 6 mm (D_{probe}) in outside diameter was also used to investigate the effect of the glass window (quartz) on the effective distance between two light receivers, with the diameter for each optical fibre group D_f=1.5 mm and the probe tip a rectangle of 6 mm by 2 mm.

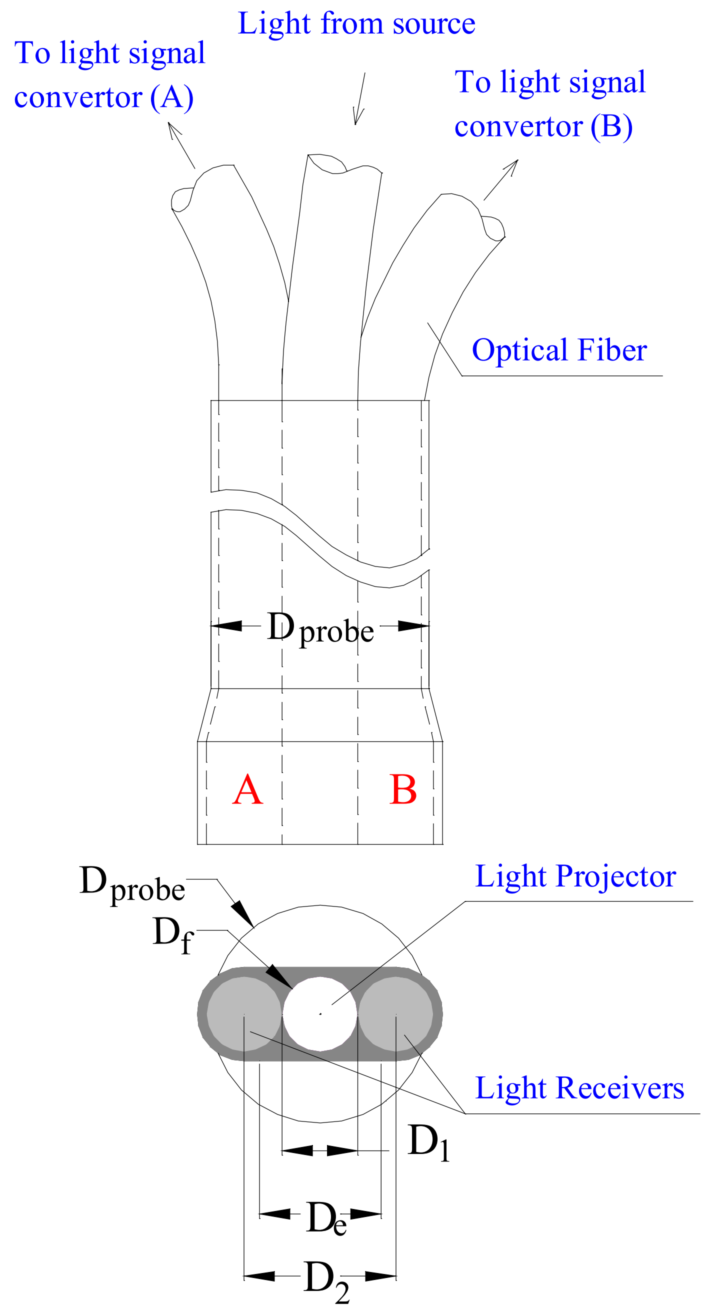

Fig. 4-2. Typical optical fibre probe for particle velocity measurement.

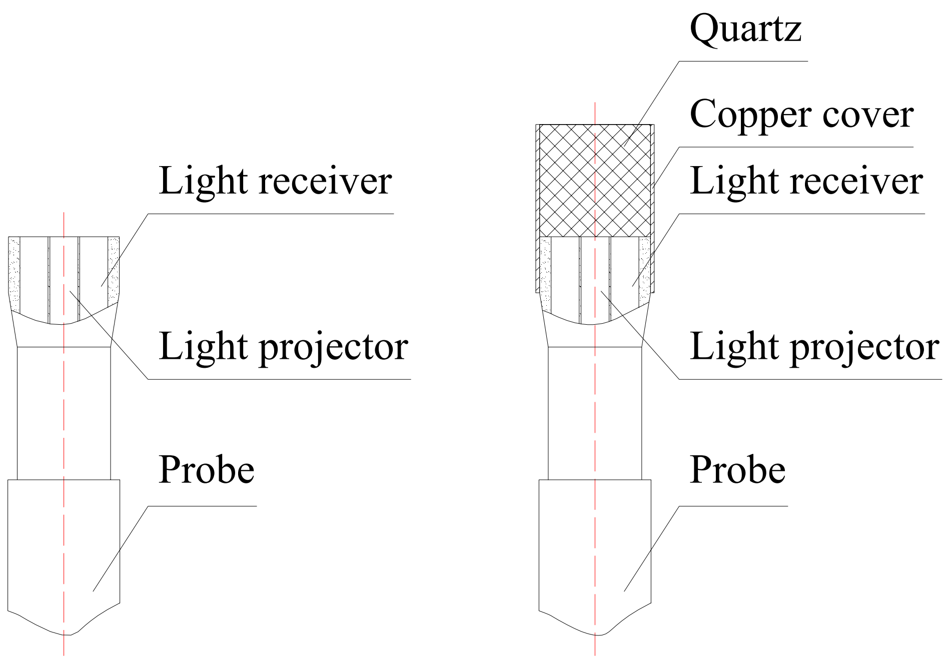

(a) (b)

Fig. 4-3. The optical fibre probe (Probe 2) (a) before and (b) after addition of the glass window.

Figure 4-4 shows the stability of the optical fibre probe measurement system at both extreme values (empty column and the packed bed state) of the solids fraction for glass beads 1.16 mm in diameter. It can be seen that the system was quite stable over a long period of operation.

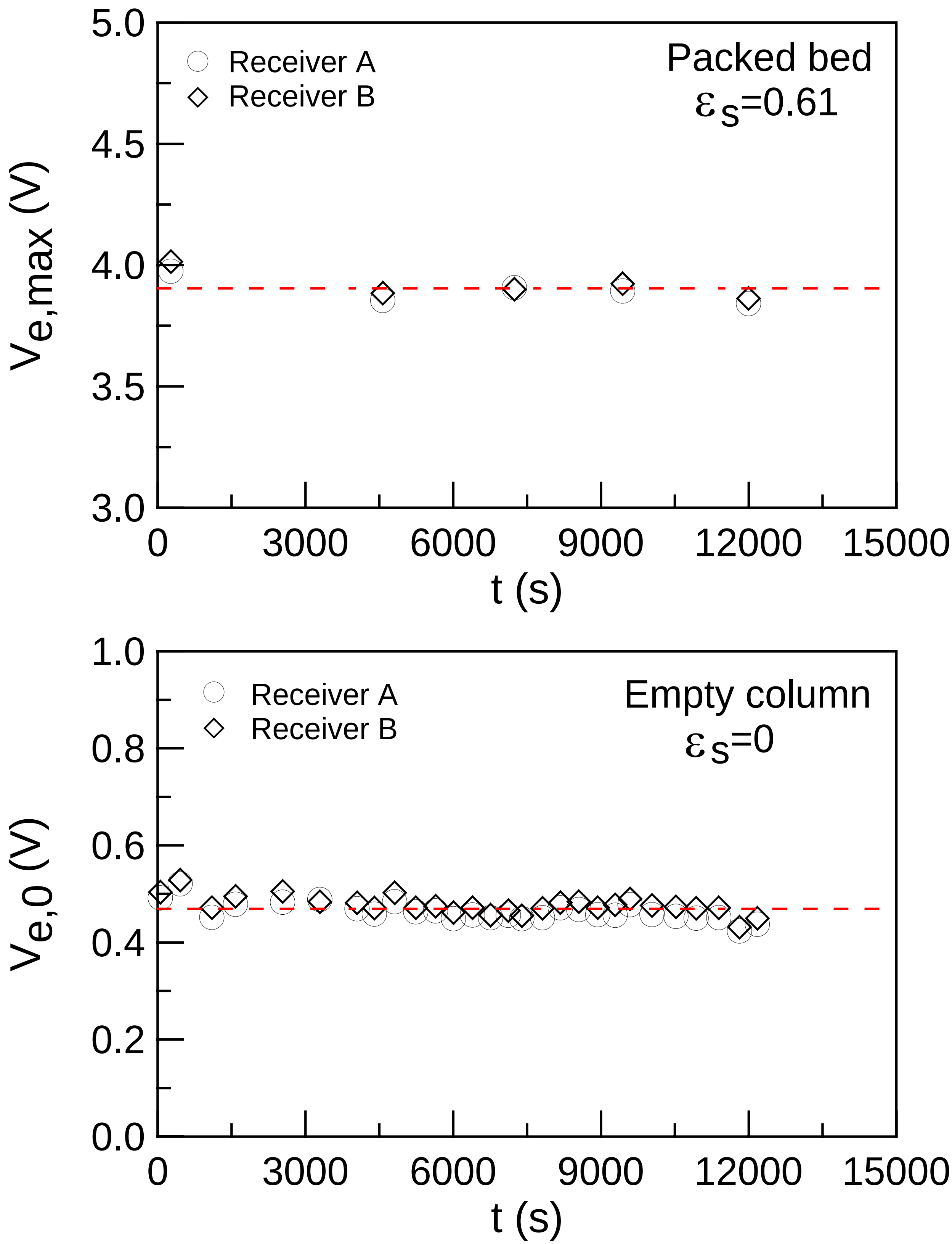

Fig. 4-4. Stability of the optical fibre probe measurement system.

4.2 Experimental setup and operating conditions

In order to investigate the effect of the bed geometry on particle velocity profiles, a full column and a half column were used, and both columns were made of Plexiglas with an included angle γ of 45^o. The diameter at the conical base D_i is 0.038 m, the diameter of the nozzle D_0 is 0.019 m, and the diameter of the upper cylindrical section D_c is 0.45 m. Used glass beads of 1.16 mm in diameter were used as the bed material, and compressed air at the ambient temperature was used as the spouting gas. Other particle properties and detailed operating conditions are shown in Table 4-1. It can be seen that similar spouting velocities were used for both columns.

Table 4-1. Particle properties and operating conditions for conical spouted beds.

Particle diameter d_s, (mm)	Particle density ρ_s, (kg/m^3)	Loose-packed voidage, $\varepsilon_{g,0}$	Geldart's classification	Static bed height H_0, (m)	Velocity U_i, (m/s)
1.16 (Used)	2500	0.39	D	0.396	24.0^H 23.5^F

Note: H: denotes the half column

F: denotes the full column

Furthermore, it was found that, for the half column, the minimum spouting velocity is 19 m/s, and the total pressure drop of the bed at stable spouting is 2.7 kPa. For the full column, the minimum spouting velocity is 20.7 m/s, and the total pressure drop of the bed at stable spouting is 3.0 kPa.

For each measurement, a total of 32768 data were taken for each channel. For particle velocity measurement, the sampling frequency was determined by Equation (4-2), implying that at least 20 data points were recorded over τ, the delay time between two signals. Typically, the sampling frequency varies from 488 Hz to 250 kHz in the current study.

$$f_s > \frac{20}{\tau} \tag{4-2}$$

For voidage measurement, sampling frequency was fixed at 1953 Hz.

4.3 Experimental results and discussion

4.3.1 Typical electrical signals and their cross-correlation analysis

Figures 4-5 to 4-12 show some actual electrical signals measured from different regions in a conical spouted bed and their cross-correlation analysis results. In the annulus (Figures 4-5 and 4-6), downward moving particles form a moving bed with the particle concentration being slightly lower than the initial solids fraction. Thus the average magnitude of the signal is the highest compared to those from the spout and fountain region. The calculated maximum correlation coefficient ranges from 0.6 to 0.8 and is distributed broadly compared to Figure D-6. Because solids in this region move very slowly, the value of the time delay is very large and the relative error among several measurements is very small. In the spout (Figures 4-7 and 4-8), because solids concentration is very low and solids move upwards quickly, particles seldom collide with each other. The distribution of the maximum correlation coefficients is very broad compared to Figure D-6, although maximum cross-correlation values are higher than in the annulus, ranging from 0.7 to 1.0. Because of the quick movement of particles, the value of the time delay is very small, resulting in a relatively large measurement error among several measurements. In the centre of the fountain region (Figures 4-9 and 4-10), as in the spout, the solids concentration is very low and solids move upwards quickly. Particles seldom collide with each other, and there is not much influence from the surroundings. Thus, the maximum correlation coefficient is very high, ranging from 0.85 to 1.0. As in the spout, because of the quick movement of particles, the value of the time delay is very small and the relative error is large too among several measurements. Outside the centre of the fountain region (Figures 4-11 and 4-12), solids move downwards. Because solids are not ejected from the same position, most importantly not from the same height, their velocities in front of the probe tip will not be the same because they have different accelerations. As a result, the maximum correlation coefficient varies significantly, ranging from 0.25 to 1.0, with very broad distribution compared to Figure D-6.

Furthermore, it appears that the optimal delay time (having minimal relative standard deviation among several measurements) obtained using the overall averaging method is slightly better than using the highest correlation coefficient method and the partial averaging method, as well as the highest appearing frequency method. However, it is still hard to determine which method is the best. Thus, the optimal delay time is determined by using the criterion of having the smallest relative standard deviation of the delay time (or the particle velocity) among several measurements (Usually, there are five to ten measurements at each position.).

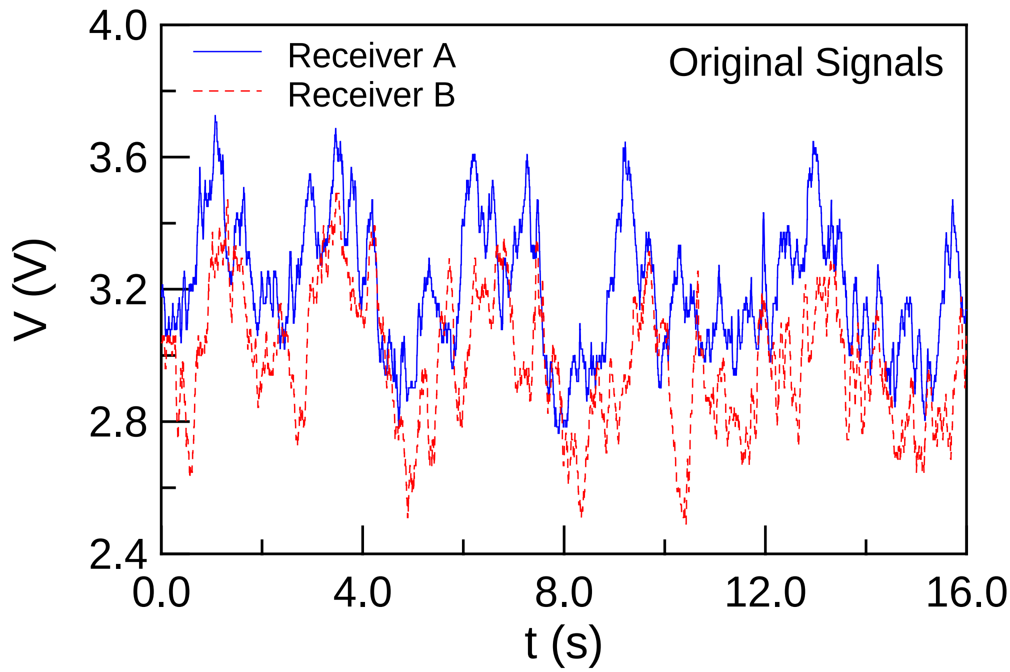

Fig. 4-5a. Typical electrical signals measured from the annulus. (Full column, Z=0.241 m, r=0.077 m)

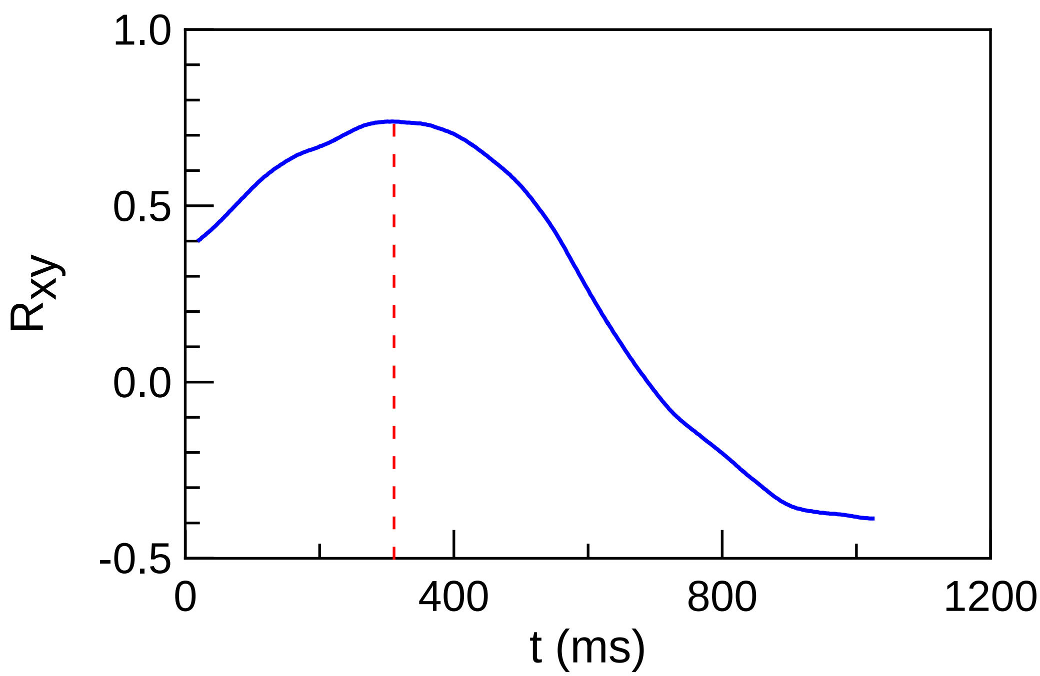

Fig. 4-5b. Typical distribution curve of the cross-correlation coefficient. (Full column, Z=0.241 m, r=0.077 m)

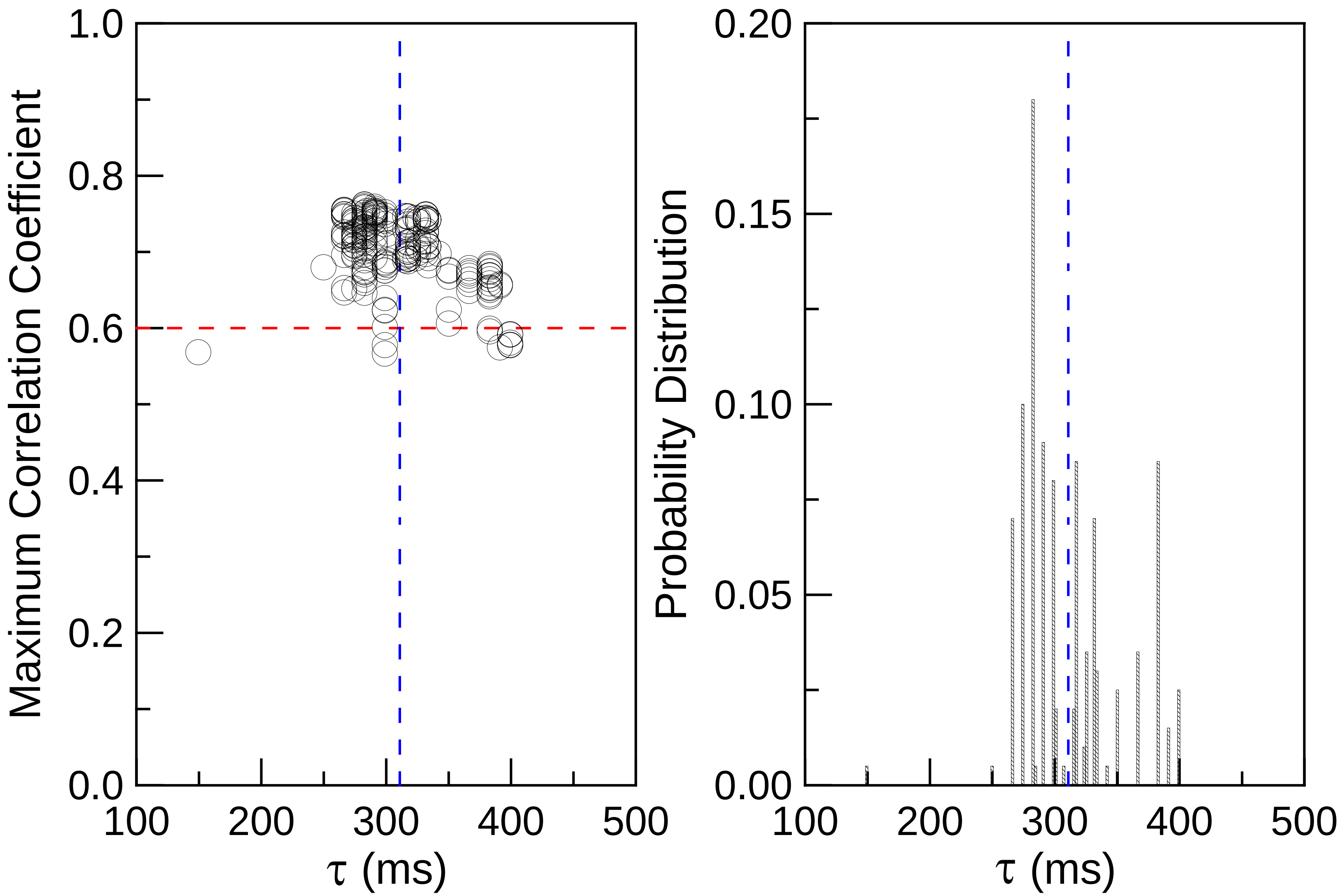

Fig. 4-6. Calculated maximum correlation coefficient and its distribution. (Full column, Z=0.241 m, r=0.077 m, in the annulus)

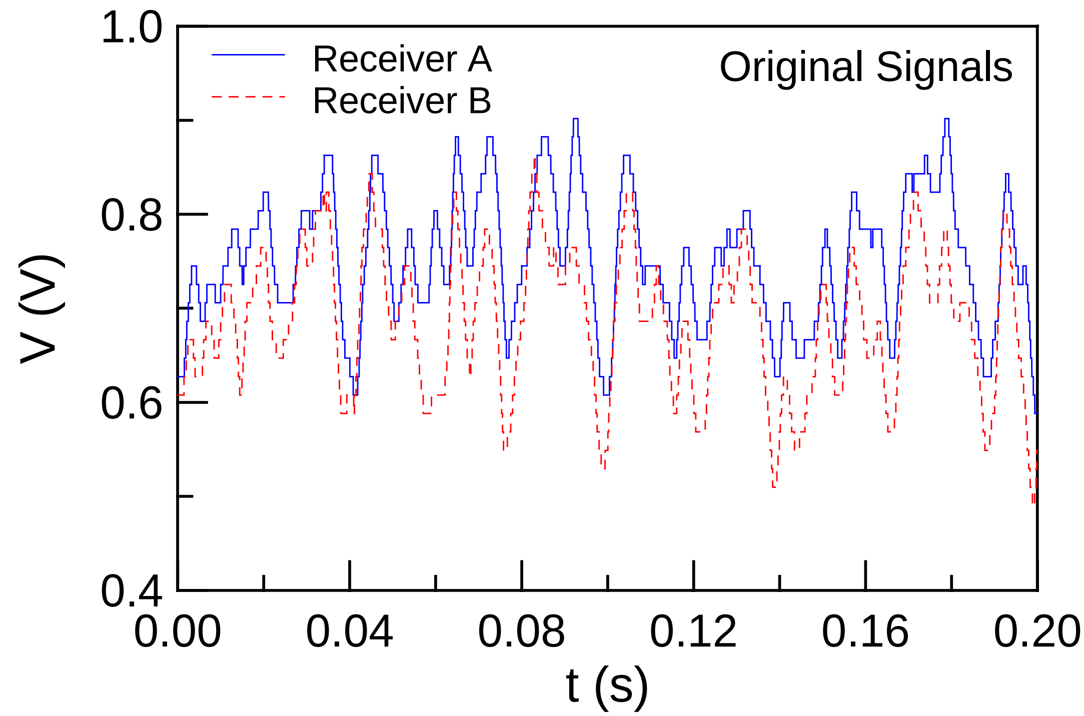

Fig. 4-7a. Typical electrical signals measured from the spout. (Full column, Z=0.241 m, r=0 m)

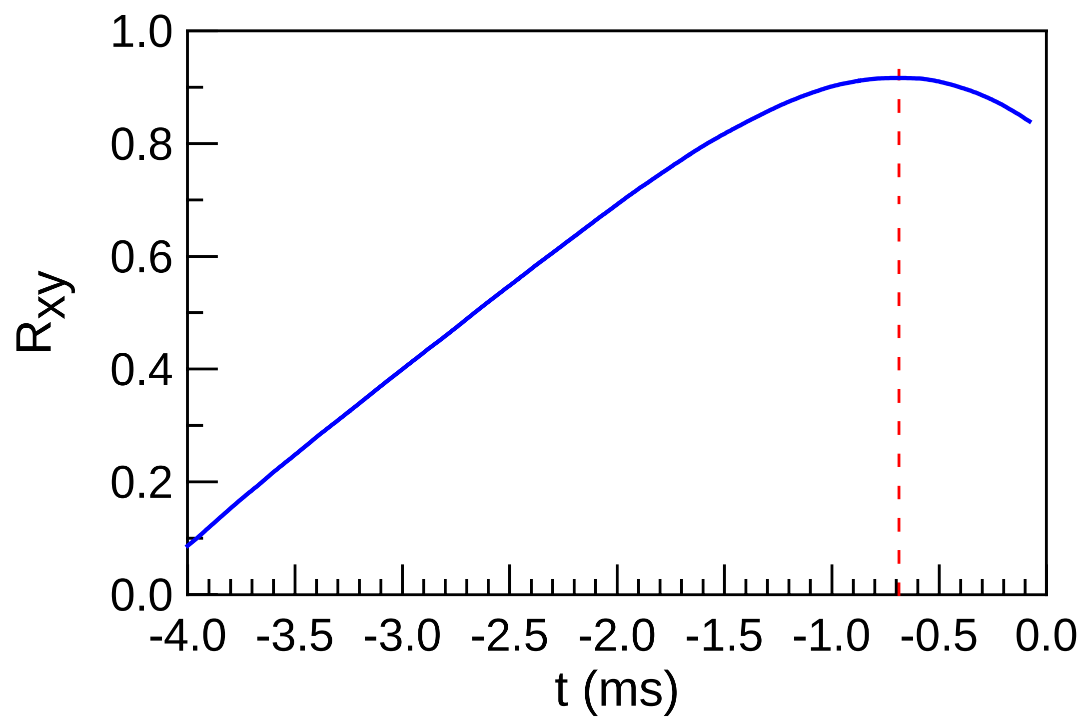

Fig. 4-7b. Typical distribution curve of the cross-correlation coefficient. (Full column, Z=0.241 m, r=0 m)

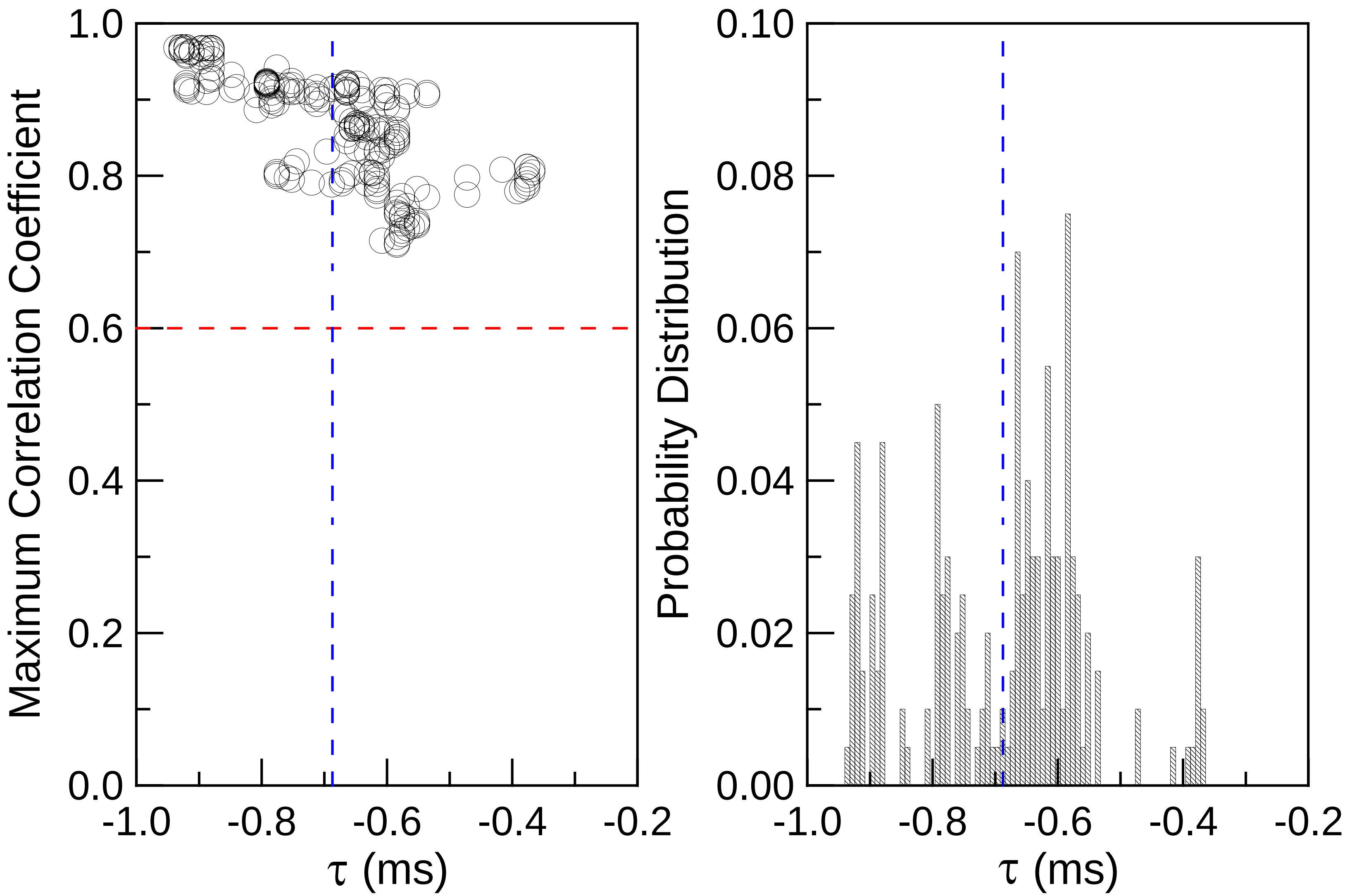

Fig. 4-8. Calculated maximum correlation coefficient and its distribution. (Full column, Z=0.241 m, r=0 m, in the spout)

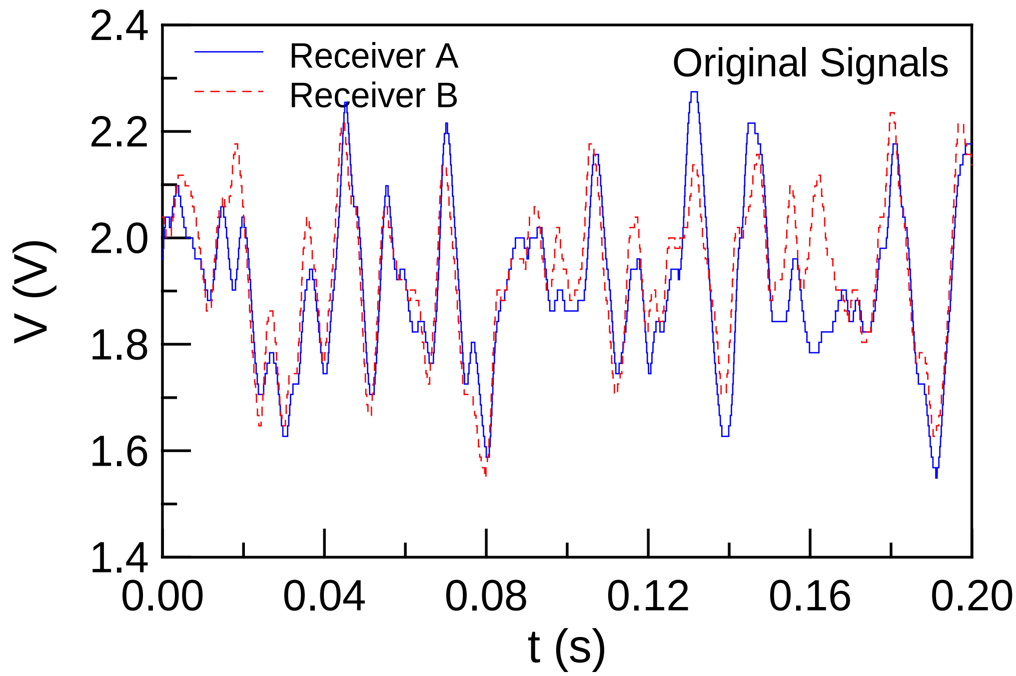

Fig. 4-9a. Typical electrical signals measured from the centre region of the fountain. (Full column, Z=0.650m, r=0.002m)

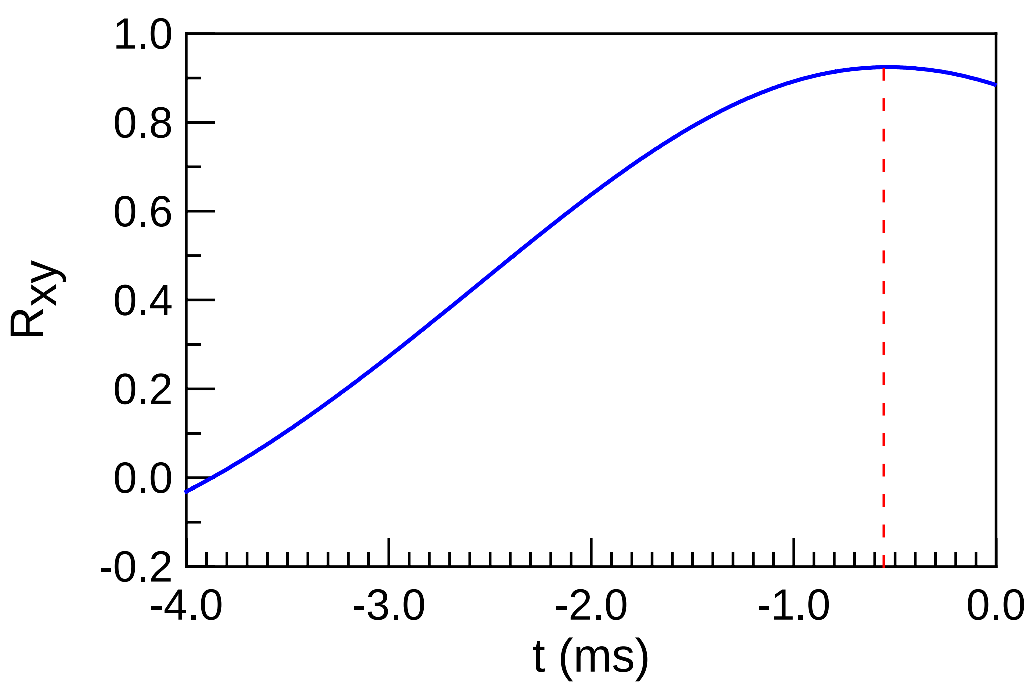

Fig. 4-9b. Typical distribution curve of the cross-correlation coefficient. (Full column, Z=0.650m, r=0.002m)

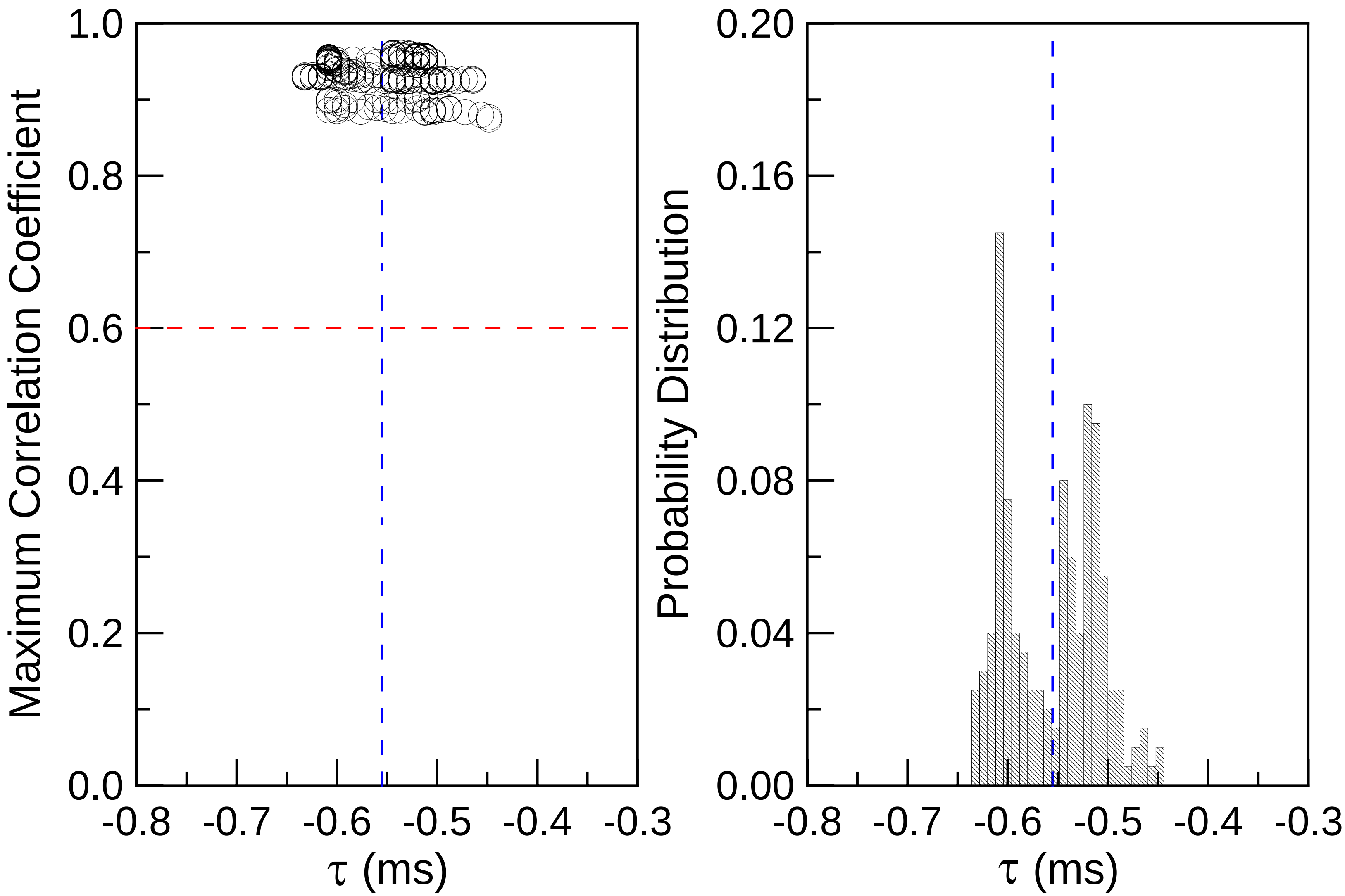

Fig. 4-10. Calculated maximum correlation coefficient and its distribution. (Full column, Z=0.650m, r=0.002m, in the central fountain)

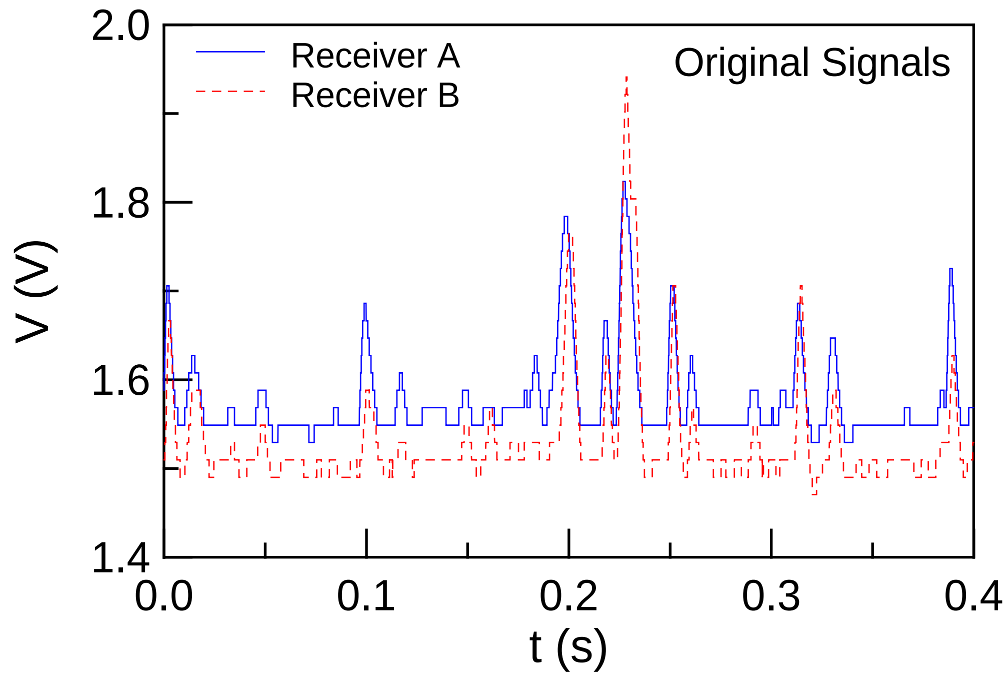

Fig. 4-11a. Typical electrical signals measured from the fountain outer region. (Full column, Z=0.650m, r=0.173m)

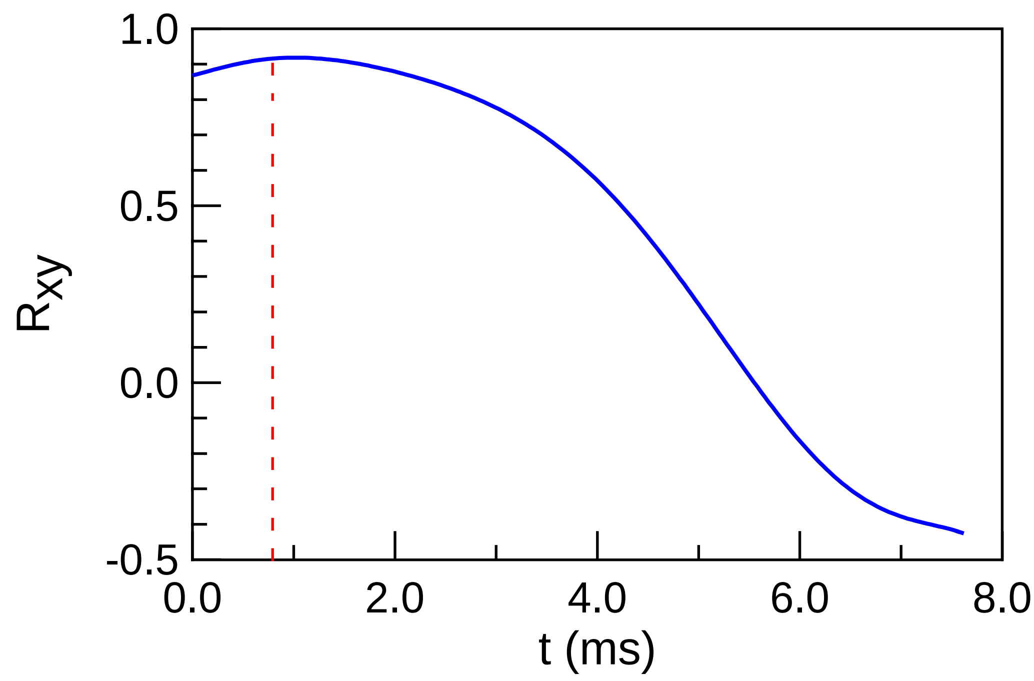

Fig. 4-11b. Typical distribution curve of the cross-correlation coefficient. (Full column, Z=0.650m, r=0.173m)

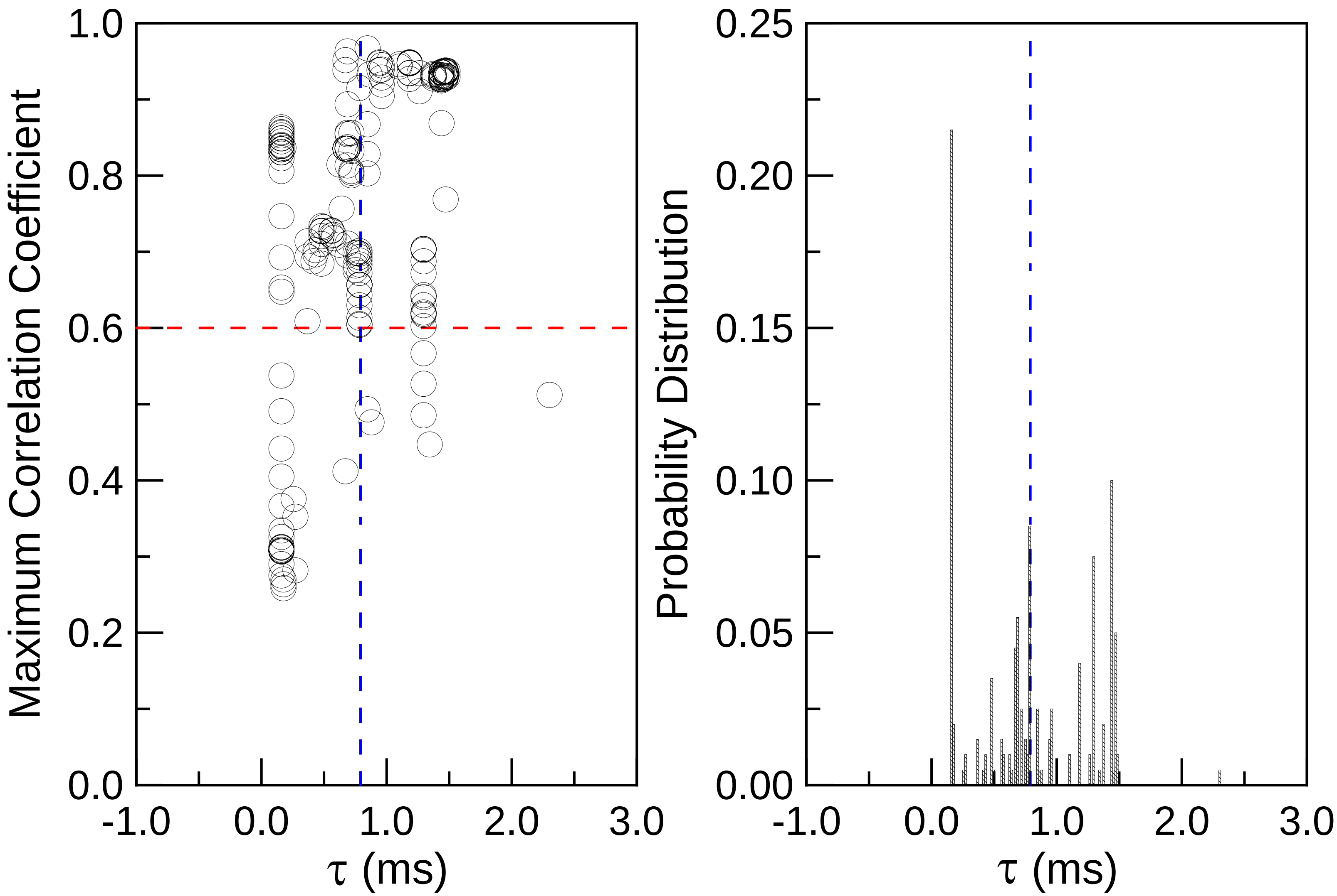

Fig. 4-12. Calculated maximum correlation coefficient and its distribution. (Full column, Z=0.650m, r=0.173m, in the outer fountain)

4.3.2 Distribution of solids hold-up and axial particle velocity

In all the experiments, probe 1 was used to measure local particle velocities and solids fractions. As shown in Appendix D, for probe 1 with 1.16 mm diameter glass beads sampled from the conical spouted bed, the effective separation distance from calibration results is D_e=2.69±0.04 mm (see Used Glass Beads in Figure D-29.).

For the voidage measurement, the optical fibre probe 1 was calibrated again before experiments using the same glass beads. Correlations between the solids fraction and the average magnitude of the sampled signal are represented by Equations (4-3) and (4-4).

For receiver A,

$$\varepsilon_s = 0.1639V \tag{4-3}$$

and for receiver B,

$$\varepsilon_s = 0.1769V \tag{4-4}$$

Figures 4-13 to 4-17 show some typical results on the distribution of the solids fraction and the axial particle velocity at different heights, with error bars (standard deviations) being provided.

In the annulus, where particles are in close contact with each other, the solids fraction is uniform and almost equal to the initial packed bed solids fraction at all levels. Particles move downwards slowly, and the lower the position, the higher the downward velocity. Because the movement of glass beads is quite steady in this region, measurement errors are very small.

In the spout, where solids concentration is relatively low, lower solids fraction and higher axial particle velocity are obtained at the lower position. Because of the interference from the surrounding annulus, as well as the higher radial gradient of the axial particle velocity, fluctuations in this region are relatively high.

In the upward flowing section of the fountain region, particles are still accelerating slightly. Compared to the spout, there is almost no interference from the surroundings. Thus, fluctuations in this region are relatively small.

In the downward flowing section of the fountain region, because of the effect of gravity, particles are always accelerating downwards. The lower the position, the higher the downward particle velocity, although the difference between Figures 4-16 and 4-17 is very small. Because particles are not accelerated/launched from the same height, fluctuations in this region are high.

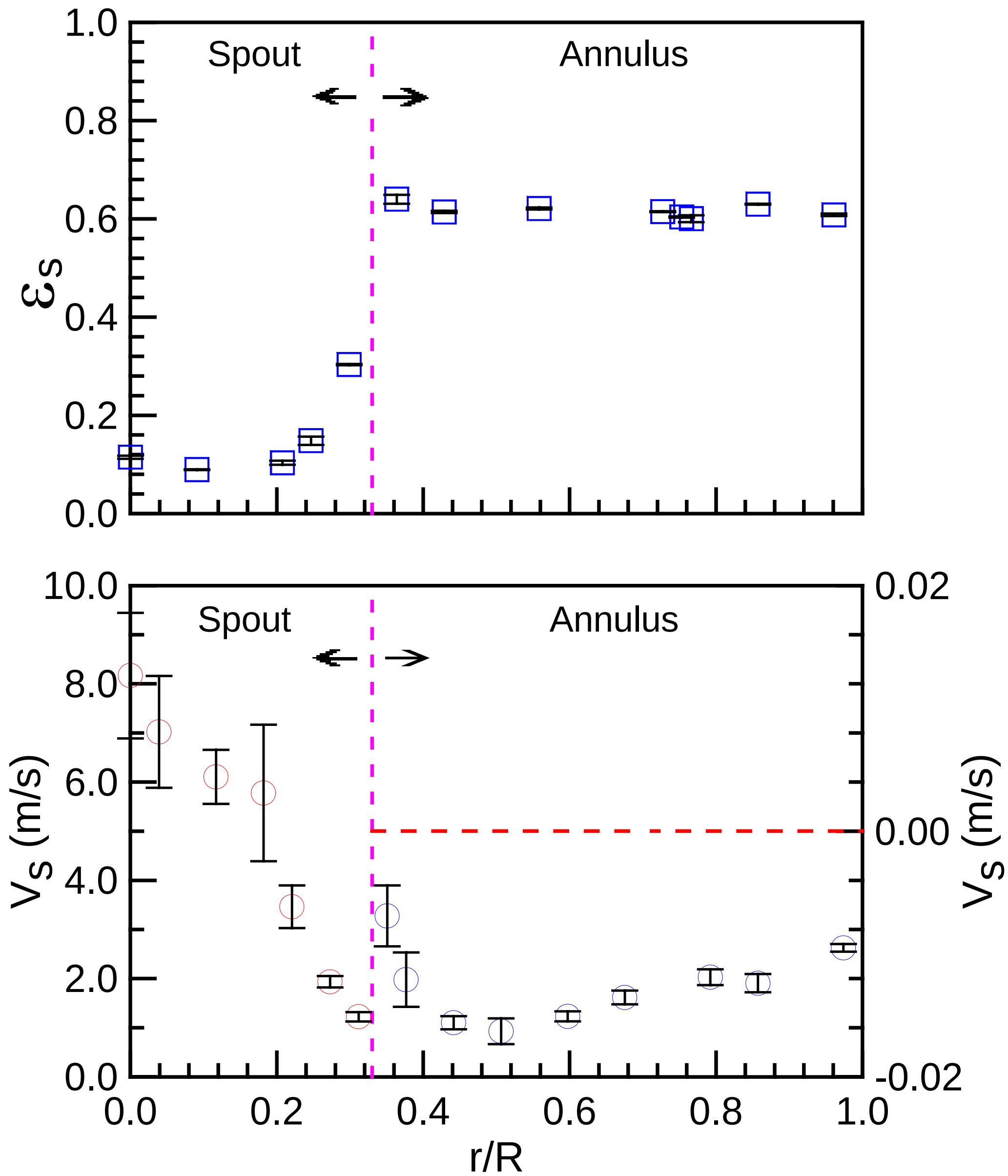

Fig. 4-13. The distribution of the solids fraction and the axial particle velocity. (Full column, Z=0.140 m, R=0.077 m)

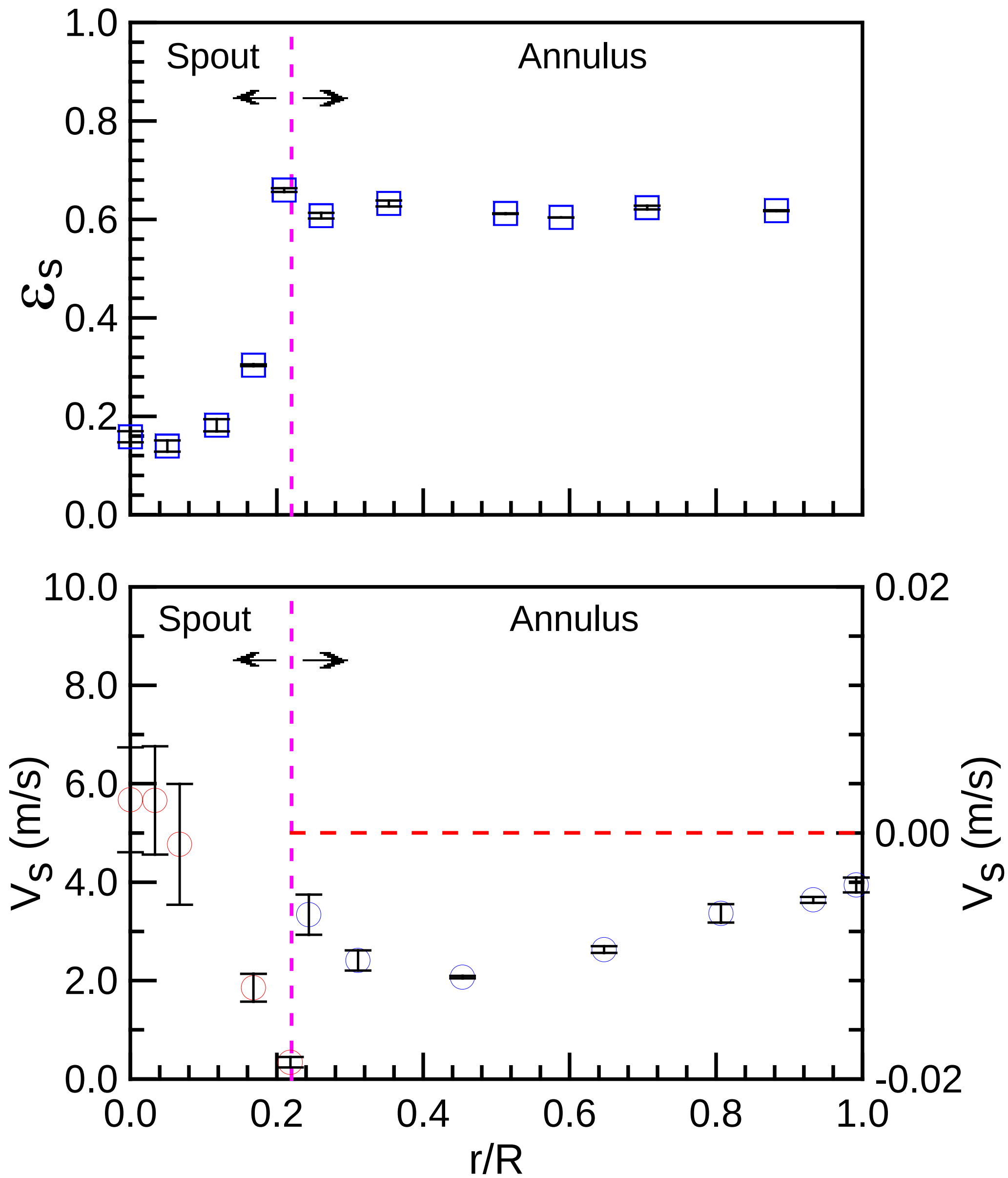

Fig. 4-14. The distribution of the solids fraction and the axial particle velocity. (Full column, Z=0.241 m, R=0.119 m)

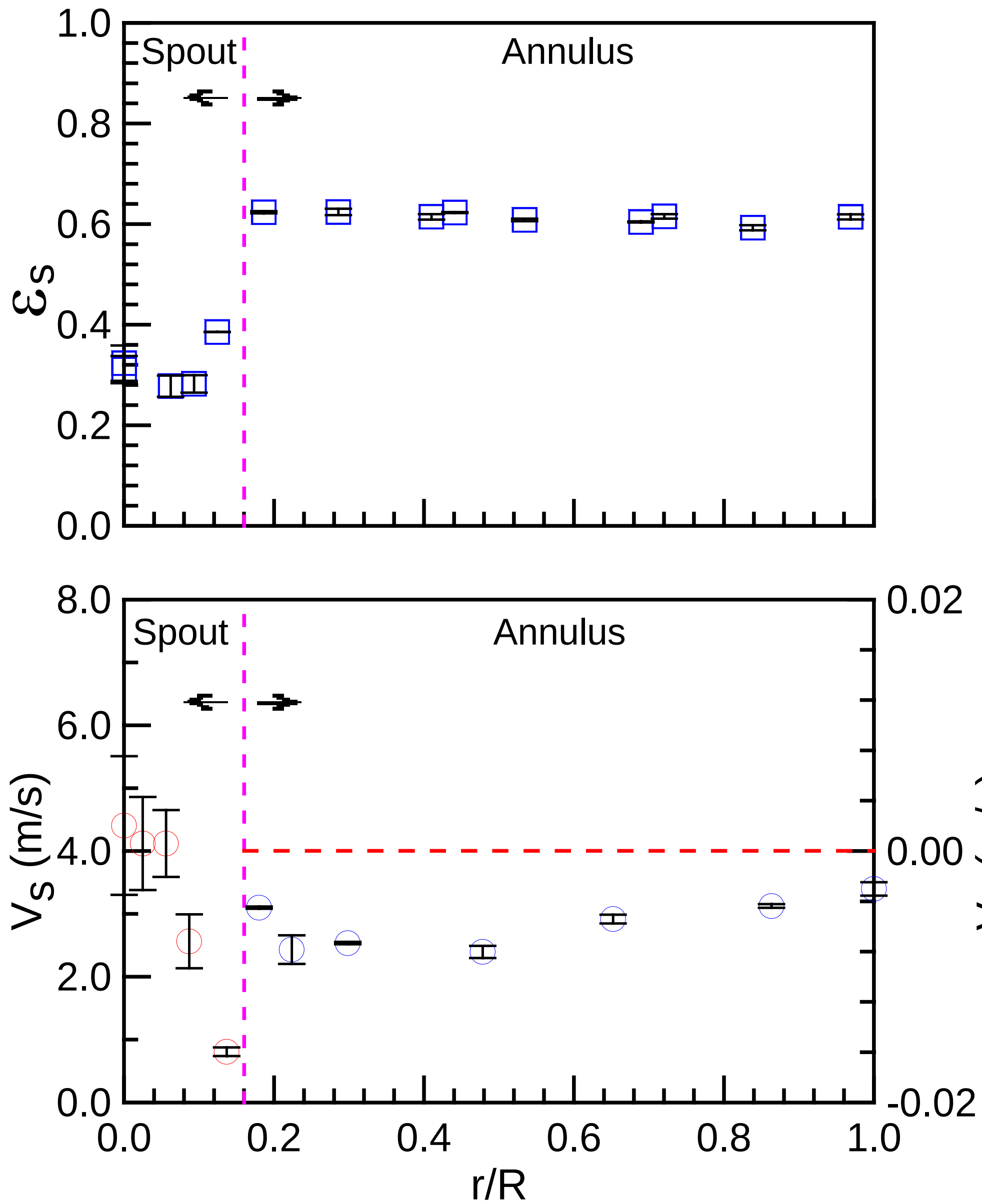

Fig. 4-15. The distribution of the solids fraction and the axial particle velocity. (Full column, Z=0.343 m, R=0.161 m)

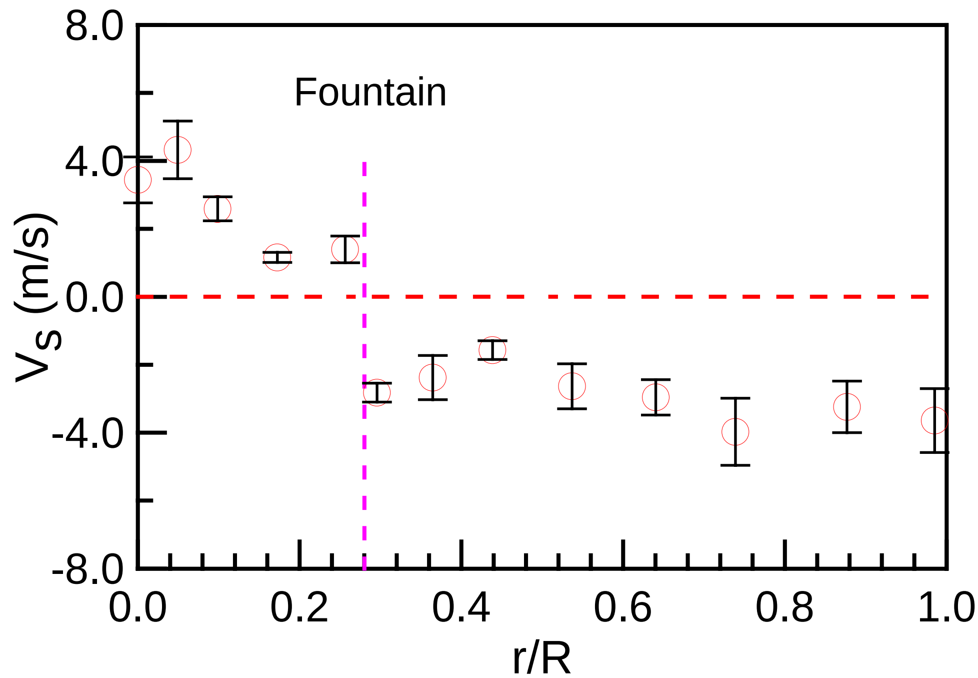

Fig. 4-16. The distribution of the axial particle velocity in the fountain. (Full column, Z=0.445 m, R=0.203 m)

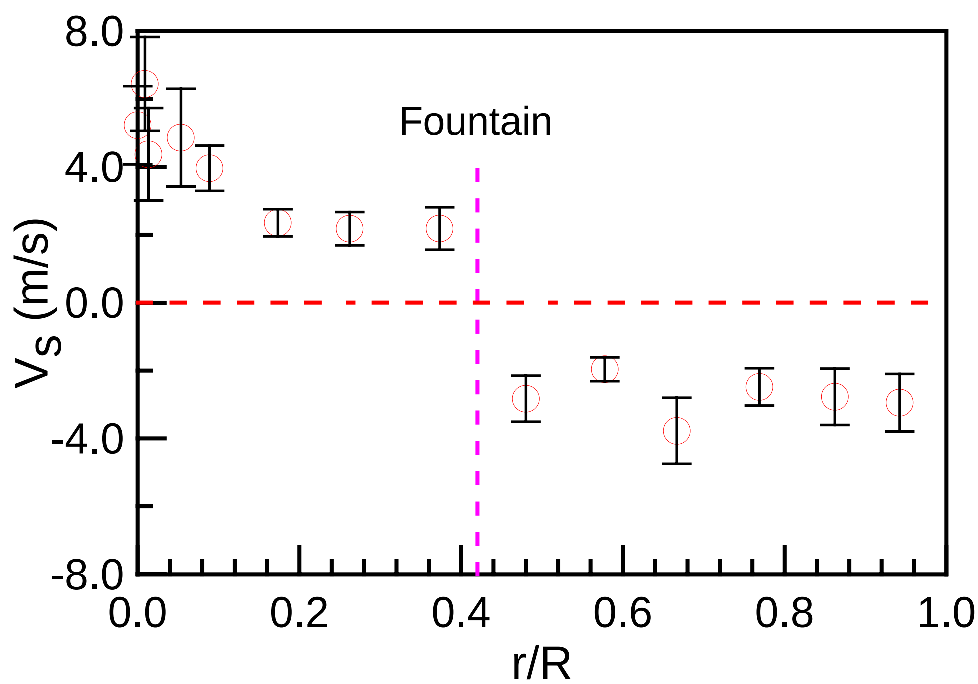

Fig. 4-17. The distribution of the axial particle velocity in the fountain. (Full column, Z=0.650 m, R=0.225 m)

Figures 4-18 to 4-21 show the comparison of the radial particle velocity distribution between the full column and the half column at different axial positions. It can be seen that overall particle velocity profiles are quite similar. Because of the existence of the flat front plate in the half column, measured solids velocities near the flat front plate are different from those in the full column, although they are still in good agreement in most cases. Furthermore, the shapes of the spout and the fountain are quite similar based on the position of the interface between the spout and the annulus and the interface between the upward moving section and the downward moving section in the fountain region.

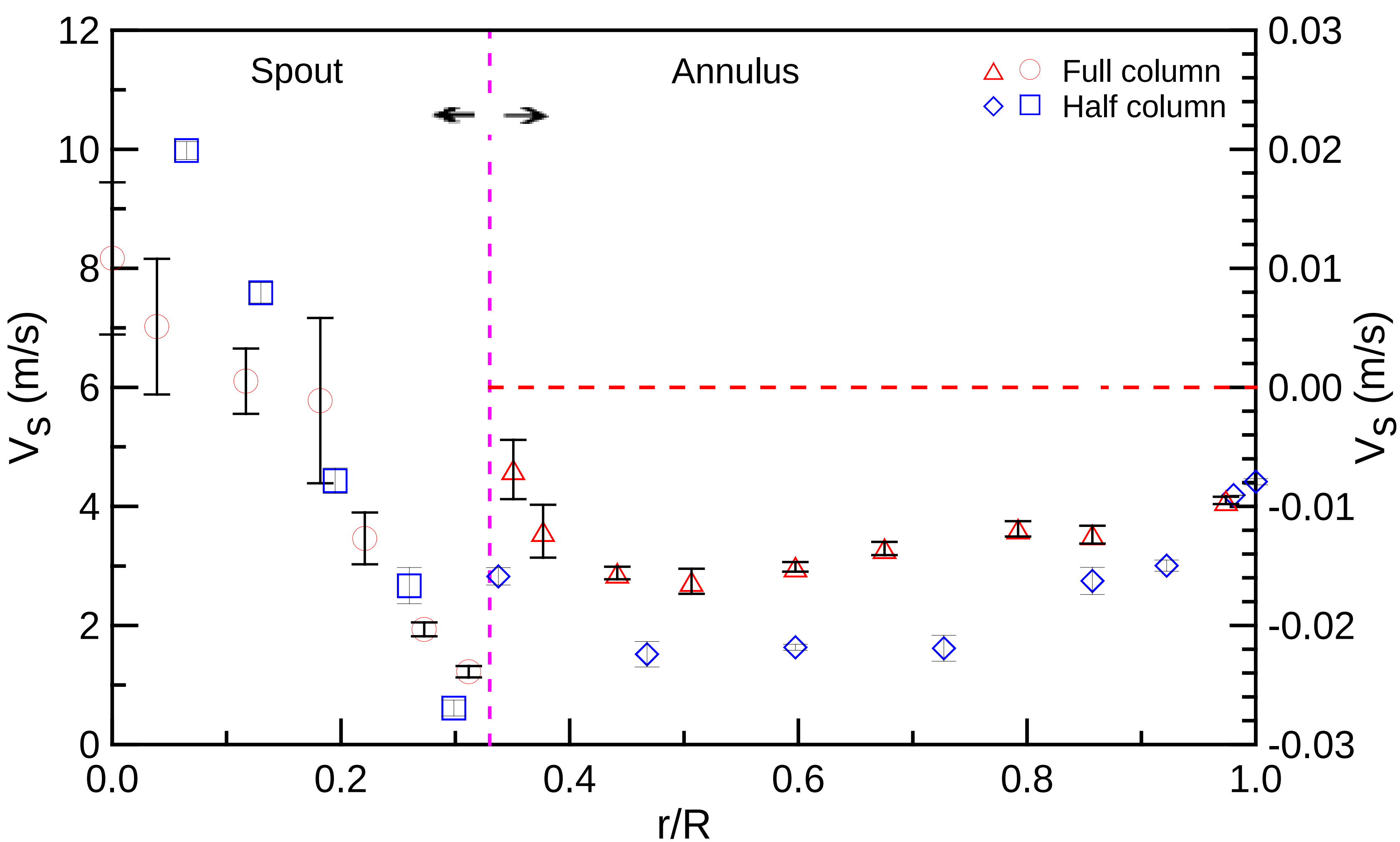

Fig. 4-18. Comparison between the half column and the full column on the distribution of the axial particle velocity. (Z=0.140m, R=0.077m)

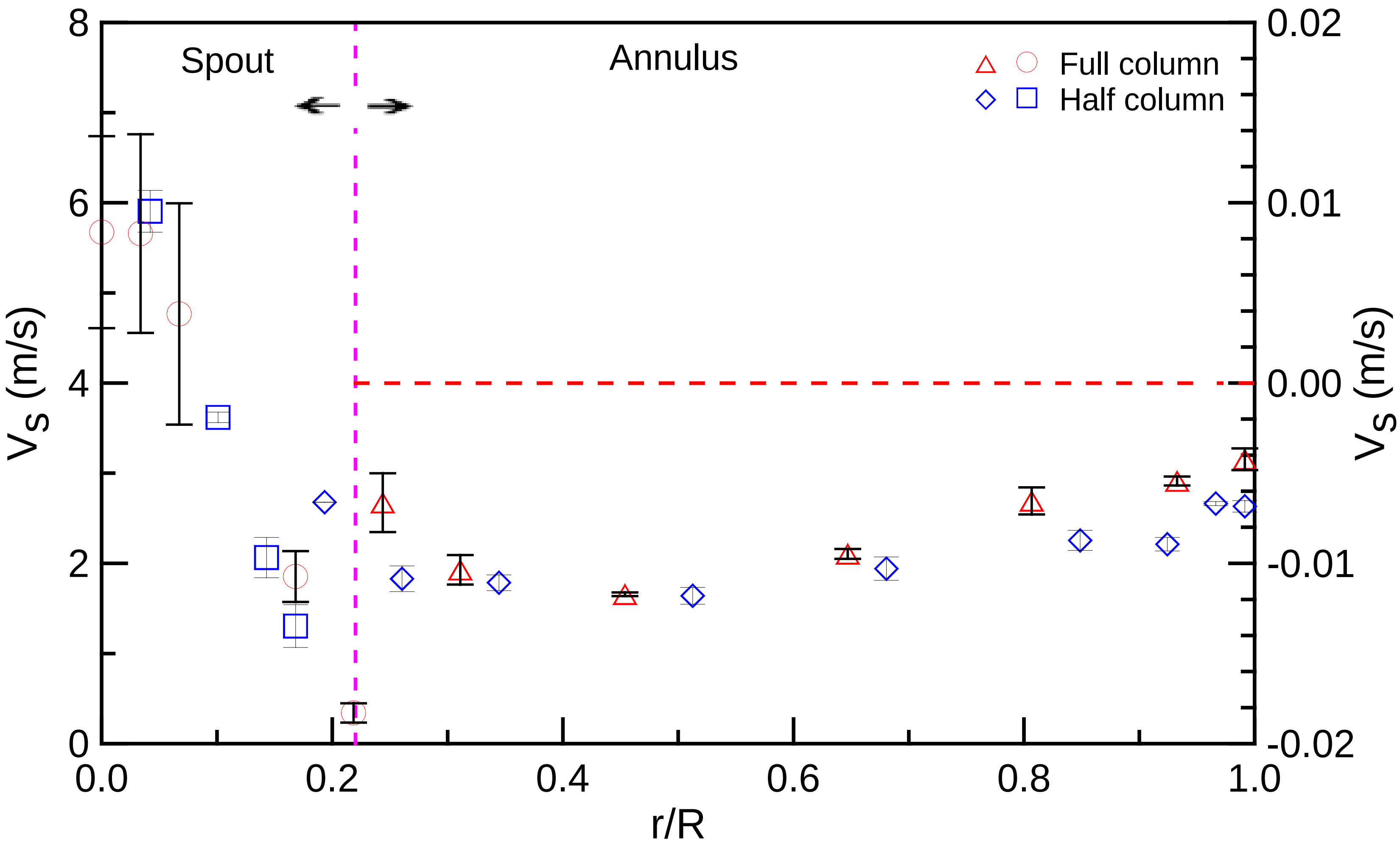

Fig. 4-19. Comparison between the half column and the full column on the distribution of the axial particle velocity. (Z=0.241m, R=0.119m)

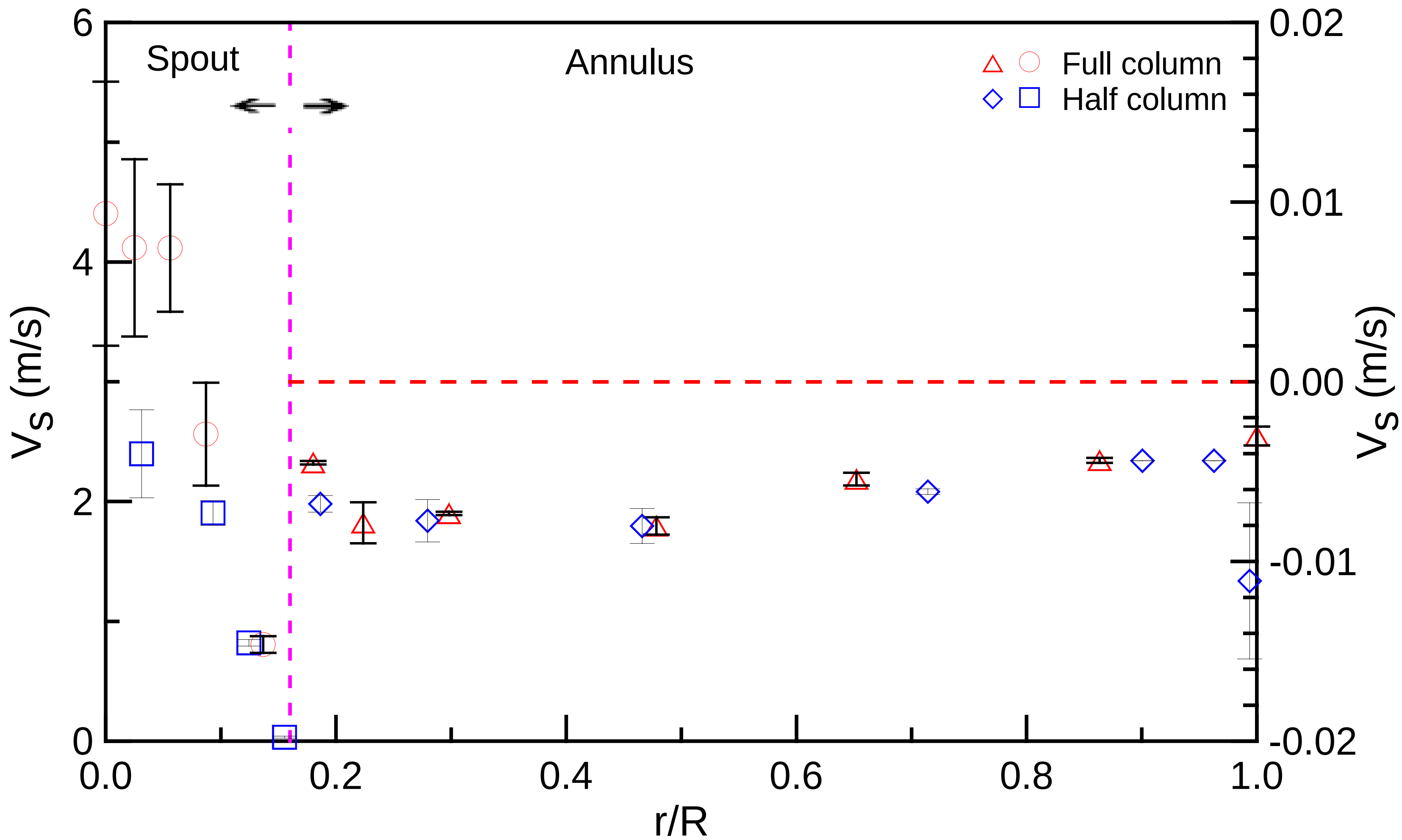

Fig. 4-20. Comparison between the half column and the full column on the distribution of the axial particle velocity. (Z=0.343 m, R=0.161 m)

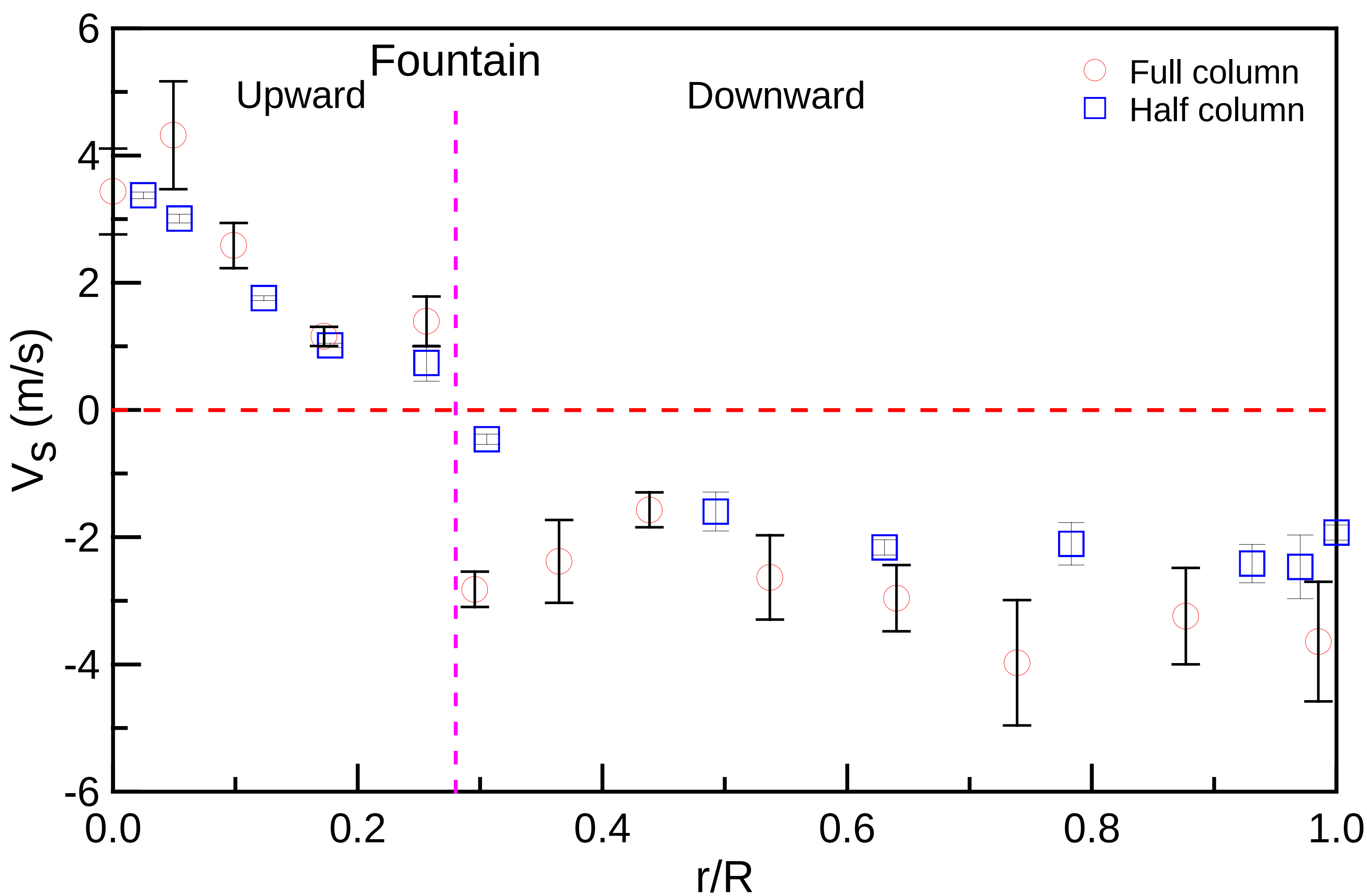

Fig. 4-21. Comparison between the half column and the full column on the distribution of the axial particle velocity. (Z=0.445m, R=0.203m)

CHAPTER 5

COMPUTIONAL FLUID DYNAMIC SIMULATIONS

Currently there are two approaches for the numerical calculation of multiphase flows: the Euler-Lagrange approach and the Euler-Euler approach.

In the Euler-Lagrange approach, the fluid phase is treated as a continuum by solving the time averaged Navier-Stokes equations, while the dispersed phase is solved by tracking a large number of particles (or bubbles, droplets) through the calculated flow field. The dispersed phase can exchange momentum, mass, and energy with the fluid phase. A fundamental assumption made in this approach is that the dispersed second phase occupies a low volume fraction.

In the Euler-Euler approach, the different phases are treated mathematically as interpenetrating continua. Since the volume of a phase cannot be occupied by the other phases, the concept of phasic volume fraction is introduced. These volume fractions are assumed to be continuous functions of space and time and their sum is equal to one.

For granular flows, such as flows in risers, fluidized beds and other suspension systems, the Eulerian multiphase model is always the first choice, and also for simulations in this research.

5.1 Primary governing equations

Assumptions:

- No mass transfer between the gas phase and the solid phase;
- External body force, lift force, as well as virtual mass force are ignored (The lift force acts on particles mainly due to velocity gradients in the primary-phase flow field, and the inclusion of the lift force is not appropriate for closely packed particles or for very small

particles; the virtual mass force is mainly due to the acceleration of the secondary phase relative to the primary phase, and it is insignificant when the secondary phase density (solid phase) is much bigger than the primary phase density (gas phase).);

- Pressure gradient at stable spouting is constant;
- Density of each phase is constant.

Based on the general description of the Eulerian multiphase model, by simplification, the following governing equations can be derived for gas-solid flow systems.

Continuity equation for phase *q* (both gas phase *g* and solid phase *s*):

$$\frac{\partial}{\partial t}(\varepsilon_q)+\nabla\cdot(\varepsilon_q \vec{v}_q)=0 \tag{5-1}$$

where $\vec{v}_q$ is the velocity vector of phase q; ε_q is the volume fraction of phase q, and the following condition holds.

$$\sum_{q=1}^{n} \varepsilon_q = 1 \tag{5-2}$$

where n is the total number of phases, and n=2 in current simulations.

Conservation equation of momentum:

For the gas phase *g*:

$$\frac{\partial}{\partial t}(\varepsilon_g \rho_g \vec{v}_g)+\nabla\cdot(\varepsilon_g \rho_g \vec{v}_g \vec{v}_g)=-\varepsilon_g \nabla P+\nabla\cdot\bar{\bar{\tau}}_g+\varepsilon_g \rho_g \vec{g}+K_{sg}(\vec{v}_s-\vec{v}_g) \tag{5-3}$$

For the solid phase *s*:

$$\frac{\partial}{\partial t}(\varepsilon_s \rho_s \vec{v}_s)+\nabla\cdot(\varepsilon_s \rho_s \vec{v}_s \vec{v}_s)=-\varepsilon_s \nabla P-\nabla P_s+\nabla\cdot\bar{\bar{\tau}}_s+\varepsilon_s \rho_s \vec{g}+K_{gs}(\vec{v}_g-\vec{v}_s)+\vec{S}_s \tag{5-4}$$

where ρ_g is the density of the gas phase, P is the static pressure (gauge pressure) shared by all phases, $\bar{\bar{\tau}}_g$ is the gas phase stress-strain tensor, $\vec{g}$ is the gravitational acceleration, K_{gs}=K_{sg} is the momentum exchange coefficient between gas phase g and solid phase s, ρ_s is the density of the particle, $\overline{\overline{\tau}}_s$ is the solid phase stress-strain tensor, P_s is the solid pressure, $\vec{S}_s$ is the solid phase source term which is introduced in this study and will be discussed later in details.

The stress-strain tensor for phase *q*:

$$\overline{\overline{\tau}}_q = \varepsilon_q \mu_q (\nabla \vec{v}_q + \nabla \vec{v}_q^T) + \varepsilon_q (\lambda_q - \frac{2}{3}\mu_q) \nabla \cdot \vec{v}_q \overline{\overline{I}} \tag{5-5}$$

where μ_q and λ_q are the shear and bulk viscosity of phase q.

For the solid phase s, the solids shear viscosity is the sum of the collisional viscosity, kinetic viscosity and the optional frictional viscosity, as shown in Equation (5-6).

$$\mu_s = \mu_{s,col} + \mu_{s,kin} + \mu_{s,fr} \tag{5-6}$$

The collision viscosity is modeled as:

$$\mu_{s,col} = \frac{4}{5} \varepsilon_s \rho_s d_s g_{0,ss} (1 + e_{ss}) (\frac{\Theta_s}{\pi})^{1/2} \tag{5-7}$$

where d_s is the diameter of the solid particles, $g_{0,ss}$ is the radial distribution function, and FLUENT (2003b) employs the following expression as Equation (5-8), e_{ss} is the coefficient of restitution, Θ_s is the granular temperature.

$$g_{0,ss} = \left[1 - \left(\frac{\varepsilon_s}{\varepsilon_{s,\max}} \right)^{1/3} \right]^{-1} \tag{5-8}$$

The following expression from Gidaspow (1994) is used to estimate the kinetic viscosity.

$$\mu_{s,kin} = \frac{10 \rho_s d_s \sqrt{\Theta_s \pi}}{96 \varepsilon_s (1 + e_{ss}) g_{0,ss}} \left[1 + \frac{4}{5} g_{0,ss} \varepsilon_s (1 + e_{ss}) \right]^2 \tag{5-9}$$

In our simulation, the solid bulk viscosity took either the following form from Lun et al. (1984) or a constant value of zero.

$$\lambda_s = \frac{4}{3}\varepsilon_s \rho_s d_s g_{0,ss}(1+e_{ss})(\frac{\Theta_s}{\pi})^{1/2} \tag{5-10}$$

The frictional viscosity was given by either Equation (5-11) from Schaeffer (1987) or a constant value of zero.

$$\mu_{s,fr} = \frac{P_s \sin(\Phi)}{2\sqrt{I_{2D}}} \tag{5-11}$$

where P_s is the solids pressure, Φ is the angle of internal friction, and I_{2D} is the second invariant of the deviatoric stress tensor.

Fluid-solid exchange coefficients:

The fluid-solid exchange coefficient K_{sg} can be written in the following general form:

$$K_{sg} = \frac{\varepsilon_s \rho_s f}{\tau_p} \tag{5-12}$$

where f is defined differently in different exchange coefficient models, and τ_p, the "particulate relaxation time", is defined as

$$\tau_p = \frac{\rho_s d_s^2}{18\mu_g} \tag{5-13}$$

In FLUENT (2003b), there are three models for the fluid-solid exchange coefficient, while the Gidaspow drag model was chosen as the base case in this work. As for the sensitivity analysis, a range between $0.8K_{sg}$ and $1.2K_{sg}$ was investigated with K_{sg} calculated based on the Gidaspow drag model.

Gidaspow drag model (1994):

The Gidaspow model is a combination of the Wen and Yu model (1966) and the Ergun equation (1952).

When $\varepsilon_g > 0.8$, the fluid-solid exchange coefficient K_{sg} is of the following form:

$$K_{sg}=\frac{3}{4}C_D\frac{\varepsilon_s\varepsilon_g\rho_g\left|\vec{v}_s-\vec{v}_g\right|}{d_s}\varepsilon_g^{-2.65} \tag{5-14}$$

where, $C_D=\frac{24}{\varepsilon_g \mathrm{Re}_s}\left[1+0.15(\varepsilon_g \mathrm{Re}_s)^{0.687}\right]$ (5-15)

$$\mathrm{Re}_s=\frac{\rho_g d_s\left|\vec{v}_s-\vec{v}_g\right|}{\mu_g} \tag{5-16}$$

When $\varepsilon_g \le 0.8$

$$K_{sg}=150\frac{\varepsilon_s(1-\varepsilon_g)\mu_g}{\varepsilon_g d_s^2}+1.75\frac{\rho_g\varepsilon_s\left|\vec{v}_s-\vec{v}_g\right|}{d_s} \tag{5-17}$$

Solids pressure:

For granular flows in the compressible regime (i.e., where the solids volume fraction is less than its maximum allowed value), a solids pressure is calculated independently and used for the pressure gradient term, ∇p_s, in the solid phase momentum equation. The solids pressure is composed of a kinetic term and a second term due to particle collisions, as shown in Equation (5-18) (Fluent Inc., 2003b).

$$P_s=\varepsilon_s\rho_s\Theta_s+2\rho_s(1+e_{ss})\varepsilon_s^2 g_{0,ss}\Theta_s \tag{5-18}$$

Granular temperature:

There is a transport equation for the calculation of the granular temperature, with several equations for different terms of the transport equation in “FLUENT 6.1 User's Guide” (2003b). FLUENT currently uses an algebraic relation for the granular temperature, and this algebraic relation has not been shown in any its publications.

The solid phase source term in conical spouted beds

For spouted beds, there exist three distinct regions: a dilute core named the spout, a dense annular region between the spout and the wall named the annulus, and a dilute fountain region above the bed surface. From the simulation point of view, the structure of spouted beds should be divided into at least two regions: a dilute fluidized region (including both the spout and the fountain) and a dense defluidized region (annulus).

It was found that the ratio of the pressure drop at stable spouting to the pressure drop at stable fluidization is usually smaller than one for both the cylindrical spouted beds and the conical spouted beds (Mathur and Epstein, 1974; Mukhlenov and Groshtein, 1964, 1965). At partial spouting state, however, the above ratio usually becomes bigger than one in the ascending process. To account for the stress exerted by the conical side wall on the gas-solids flow, as reflected by the reduced pressure gradient in a spouted bed, two solid phase source terms are introduced into the spout and annulus regions respectively, thus,

$$k_a = \frac{\nabla P_s}{\nabla P_{fb}} \tag{5-19}$$

$$k_s = f(\varepsilon_{g,0}, \rho_s, d_s, \rho_g, \mu_g, v_{g,z}) \tag{5-20}$$

where k_a and k_s are the ratios of the pressure drops of spouted beds in the corresponding dense and dilute regions to the pressure drop at stable fluidization, which are functions of operating conditions, ∇P_s is the axial pressure gradient for spouted beds which can be obtained either from experiments or empirical expressions from the literature. To simplify the problem, k_s was assumed to be one in most current simulations, and the following simple expressions were used to describe the solid phase source term.

When $\varepsilon_g \le 0.8$ and $Z \le H_0$ (in the annulus),

$$S_{s,a} = -\varepsilon_s \rho_s g + k_a(\varepsilon_s \rho_s g) = (k_a - 1)\varepsilon_s \rho_s g \quad (5\text{-}21)$$

When $\varepsilon_g > 0.8$ (in the spout and the fountain),

$$S_{s,a} = -\varepsilon_s \rho_s g + k_s(\varepsilon_s \rho_s g) = (k_s - 1)\varepsilon_s \rho_s g \quad (5\text{-}22)$$

where Z is the axial height, H_0 is the static bed height.

Based on the above description, the combination of the default gravity term and the solid phase source term in the annulus represents the Actual Pressure Gradient in a spouted bed. Different values of k_a (or different solid phase source terms) represent different values of the pressure gradient in a spouted bed.

Moreover, by adjusting k_a and k_s values, it is possible to use FLUENT to simulate a spouted bed operated at partial spouting in both the ascending and descending processes.

5.2 Simulations of conical spouted beds

5.2.1 Simulation conditions for the base case

In the simulation of the conical spouted bed, the bed geometrical structure and dimensions, the spouting gas, the bed material as well as operating conditions used were kept almost the same as in the actual experiment. The operating gas velocity used in simulations is 2% higher than in the experiment*, and the total column height is much longer than the actual experimental setup. Because of the influence of the outlet structure on flow field, comparisons between the experiment and simulation will not be considered for regions well above the bed surface. Details on simulation conditions for the base case are listed in Table 5-1, with boundary conditions given in Table 5-2.

*Note that CFD simulations were first set to simulate experimental data obtained from a half column, which was operated at 24 m/s. When the full column was utilized later, the sampling program indicated that gas velocity was 24 m/s, but the actual value was found to be 23.5 m/s.

Table 5-1. Simulation conditions for conical spouted beds for the base case.

Description	Value	Comment
Operating gas velocity, U_i	24 m/s	Based on D_i
Gas density, ρ_g	1.23 kg/m^3	Air
Gas viscosity, μ_g	1.79×10^{-5} kg/(m·s)	Air
Particle density, ρ_s	2500 kg/m^3	Spherical glass beads
Particle diameter, d_s	1.16 mm	Uniform distribution
Initial solids packing, $\varepsilon_{s,0}$	0.61	Fixed value
Packing limit, $\varepsilon_{s,max}$	0.61	Fixed value
Solid viscosity, μ_s	Gidaspow	Eq. (5-7) + Eq. (5-9)
Frictional viscosity, $\mu_{s,fr}$	0	Fixed value
Solid bulk viscosity (Base case), λ_s	0	Fixed value
Cone angle, γ	45°	Fixed value
Diameter of the upper section, D_c	0.45 m	Fixed value
Total height of the column	1.6 m	Fixed value
Gas inlet diameter, D_0	0.019 m	Fixed value
Diameter of the bed bottom, D_i	0.038 m	Fixed value
Static bed height, H_0	0.396 m	Fixed value
Solver	2 dimensional, double precision, segregated, unsteady, 1st order implicit, axisymmetric	
Multiphase Model	Eulerian Model, 2 phases	
Viscous Model	Laminar model	
Phase Interaction (Base case)	Fluid-solid exchange coefficient: Gidaspow Model Restitution coefficient: 0.9 (Du et al., 2006)	
Time steps (Final value)	10^{-5} s	Fixed value
Convergence criterion	10^{-3}	Default in FLUENT

Table 5-2. Boundary conditions for simulations of conical spouted beds.

Description	Comment
Inlet	Radial distribution based on the actual Reynolds number used for the fluid phase
	No particles enter for the solid phase
Outlet	Uniform velocity distribution for the gas phase
	No particle exits for the solid phase
Axis	Axisymmetric
Wall	Non-slip for the fluid phase
	Zero shear stress for the solid phase

Note: A uniform velocity distribution is assumed at the column outlet as the fluid phase boundary condition, with the solids velocity at the outlet set as zero. Thus, such a boundary condition serves as a screen to prevent particles being carried out of the bed under some operating conditions. Moreover, because the outlet is far from the bed surface, such a boundary condition will not affect the simulation of spouted beds well below the column outlet.

5.2.2 Sensitivity analysis

5.2.2.1 Factors investigated

At the beginning, the effects of mesh/grid partitions of the bed, time steps, convergence criterion and discretization schemes (i.e. 1^{st} or 2^{nd} order) were examined, with the simulation results shown in Appendix E and the selections of time step, discretization scheme and convergence criterion for the current study presented in Table 5-1.

In order to investigate all possible factors that may affect simulation results, parameters such as the fluid inlet velocity profile, solid bulk viscosity, frictional viscosity, restitution coefficient, exchange coefficient and the source term (or the APG term) are selected for the sensitivity analysis. All conditions investigated are summarized in Table 5-3, with C program for user-defined functions provided in Appendix K.

Table 5-3. Summary of conditions used for sensitivity analysis in a conical spouted bed.

<table>
<tr><th>Grid Partition</th><th>Fluid Inlet Radial Profile</th><th>Bulk Viscosity</th><th>Frictional Viscosity</th><th>Restitution Coefficient</th><th>Exchange Coefficient</th><th>Source Term</th></tr>
<tr><td rowspan="13">Partition 1 (10497 cells)</td><td>1/7th power law</td><td rowspan="4">0</td><td>Schaeffer</td><td rowspan="5">0.9</td><td rowspan="7">K_{sg} (Gidaspow)</td><td rowspan="9">k_a=1.0</td></tr>
<tr><td>Uniform</td><td rowspan="12">0</td></tr>
<tr><td>Parabolic</td></tr>
<tr><td rowspan="10">1/7th power law</td></tr>
<tr><td>Lun et al.</td></tr>
<tr><td rowspan="8">0</td><td>0.81</td></tr>
<tr><td>0.99</td></tr>
<tr><td rowspan="6">0.9</td><td>0.8* K_{sg}</td></tr>
<tr><td>1.2* K_{sg}</td></tr>
<tr><td rowspan="4">K_{sg} (Gidaspow)</td><td>k_a=0.7</td></tr>
<tr><td>k_a=0.5</td></tr>
<tr><td>k_a= k_s=0.5</td></tr>
<tr><td>k_a=0.41</td></tr>
</table>

Notes: a. In simulations, k_s equals 1.0 unless further indicated;

b. Conditions for the base case are as follows: partition 1; 1/7th power law fluid inlet profile; zero value of the solid bulk viscosity; zero value of the frictional viscosity; restitution coefficient equals 0.9; fluid-solid exchange coefficient estimated by the Gidaspow model; k_a=1.0.

5.2.2.2 Results and discussion

Table 5-4. Notes for Figures 5-1 to 5-6

For static pressure profiles and interstitial gas velocity profiles	For axial solids velocity profiles and solids fraction profiles
Z_1=0.038m; Z_2=0.089m; Z_3=0.191m; Z_4=0.292m	Z_1=0.140m; Z_2=0.241m; Z_3=0.343m

Effect of fluid inlet velocity profile

The influence of fluid inlet velocity profiles on the simulation result is shown in Figure 5-1. Although fluid inlet velocity profiles have little effect on the distribution of the static pressure and the solids fraction, the influence on the distribution of the axial solids velocity and the axial interstitial gas velocity is shown clearly, especially in the spout region. Simulated static pressures overestimated experimental data significantly when k_a was chosen to be equal to 1.0, although the simulated particle velocity profile is quite close to the experimental data except for the case when a parabolic inlet gas velocity profile was used. Therefore, 1/7th power law gas velocity profile for turbulent flow at the inlet was used in subsequent simulations.

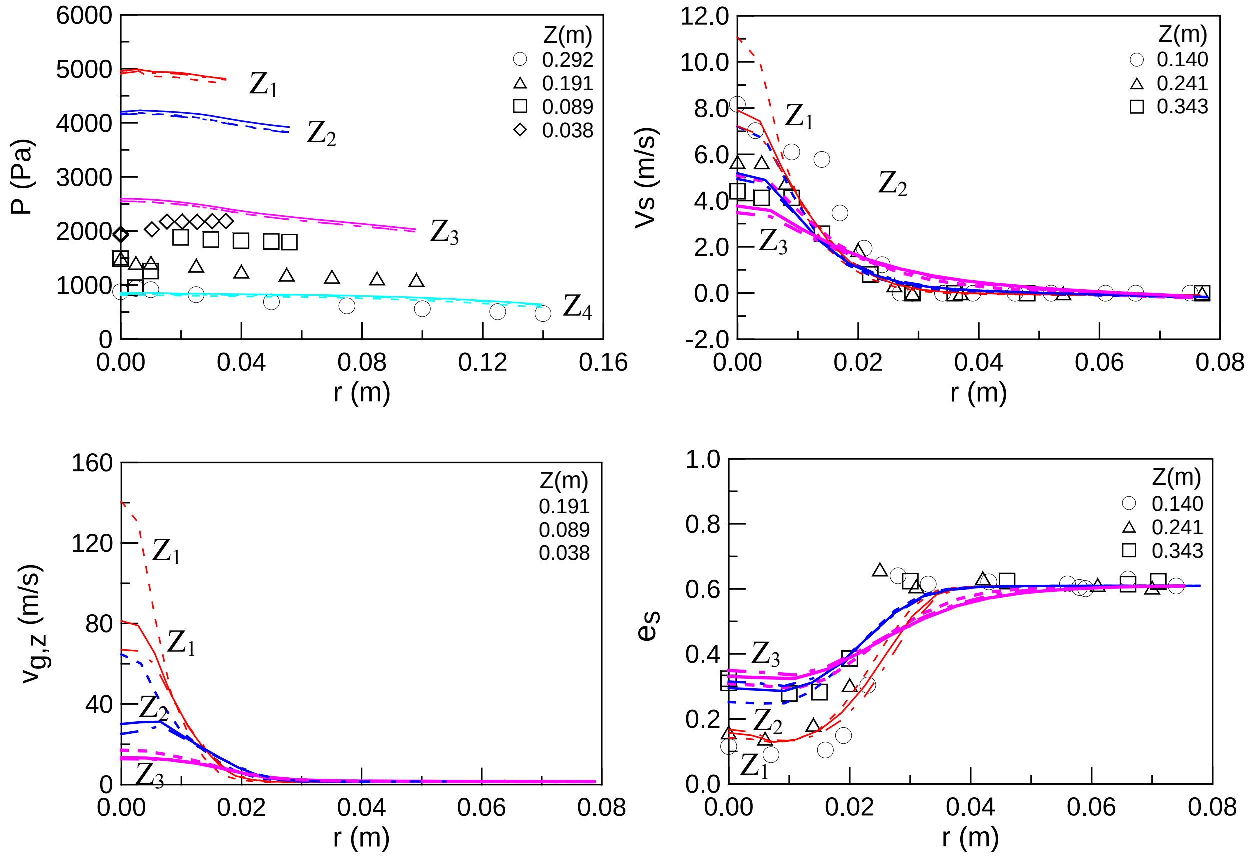

Fig. 5-1. Comparison between experimental data and simulated results with **different fluid inlet velocity profiles** at k_a=1.0 (k_s=1.0). Symbols are experimental data, and lines are simulated results. (Solid lines correspond to the 1/7th power law or turbulent flow, dashed lines correspond to the parabolic profile or laminar flow, dotted dash lines correspond to the uniform profile.)

Effect of solid bulk viscosity

Figure 5-2 shows the influence of different models for estimating the solid bulk viscosity. It is seen that, within the range of our investigations, the solid bulk viscosity has almost no effect on simulated results. Therefore, a zero value is assigned to the solid bulk viscosity in most of our subsequent simulations.

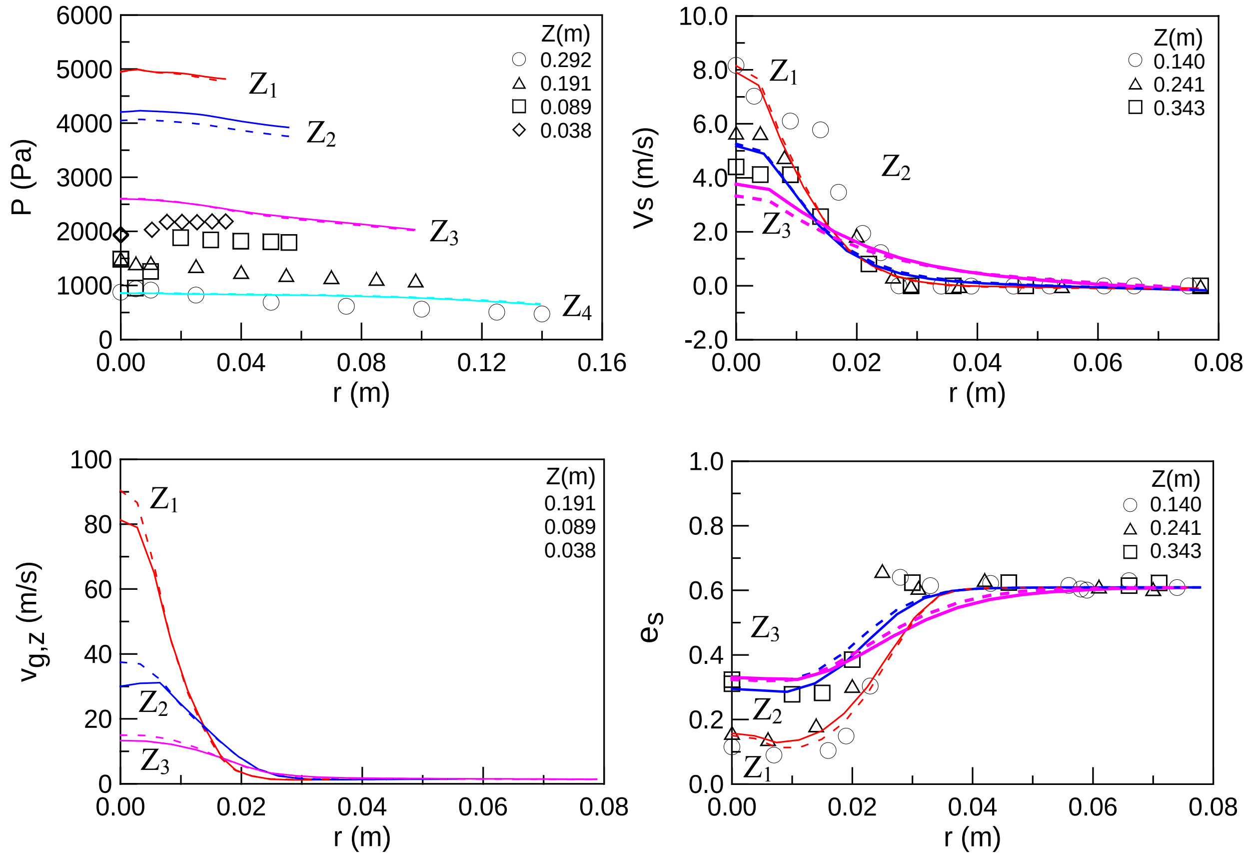

Fig. 5-2. Comparison between experimental data and simulated results with **different solid bulk viscosities** at k_a=1.0 (k_s=1.0, 1/7th power law). Symbols are experimental data, and lines are simulated results. (Solid lines correspond to zero value for the solid bulk viscosity, dashed lines correspond to the expression from Lun et al. for the solid bulk viscosity.)

Effect of frictional viscosity

Figure 5-3 shows the influence of different models for estimating the frictional viscosity. It is seen that, within the range of our investigations, the frictional viscosity has little effect on simulated results. Therefore, a zero value is assigned to the frictional viscosity in most of our subsequent simulations.

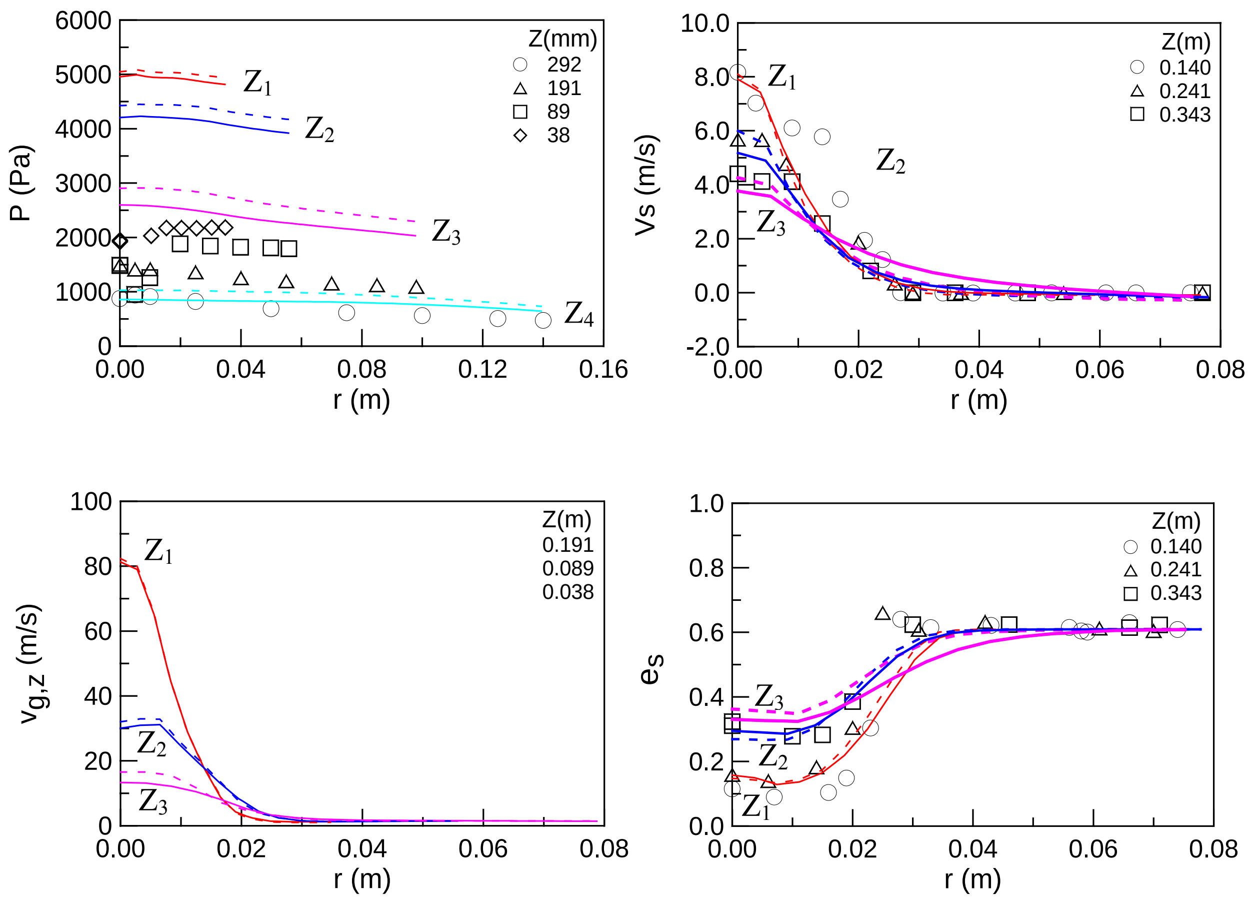

Fig. 5-3. Comparison between experimental data and simulated results with **different frictional viscosities** at k_a=1.0 (k_s=1.0, 1/7th power law). Symbols are experimental data, and lines are simulated results. (Solid lines correspond to zero value for the frictional viscosity, dashed lines correspond to the expression from Schaeffer for the frictional viscosity.)

Effect of restitution coefficient

The restitution coefficient is varied from 0.81 to 0.99 to study its effect on the simulation result (Figure 5-4). Comparing with the base case of e_{ss}=0.9, a 10% increase of the restitution coefficient affects significantly the simulated results. On the other hand, a 10% decrease of the restitution coefficient has almost no effect on the distribution of the static pressure and has a slight effect on the axial solids velocity, axial interstitial gas velocity and solids fraction. A value of 0.9, which is the typical value used in most simulations in the literature (Duarte et al., 2005;

Du et al., 2006) for glass bead particles, is thus chosen and used in the simulations throughout this work.

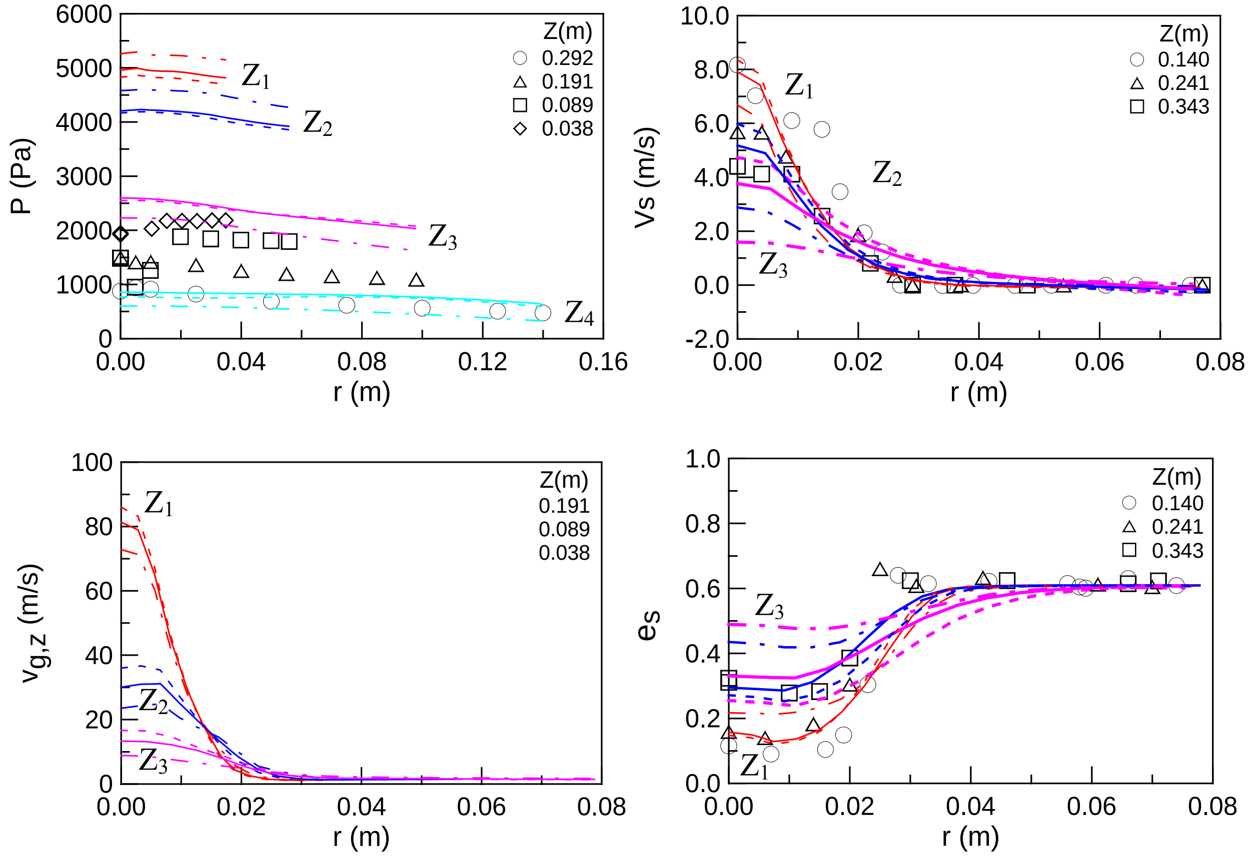

Fig. 5-4. Comparison between experimental data and simulated results with **different restitution coefficients** at k_a=1.0 (k_s=1.0, 1/7th power law). Symbols are experimental data, and lines are simulated results. (Solid lines correspond to e_{ss}=0.9, dashed lines correspond to e_{ss}=0.81, dotted dash lines correspond to e_{ss}=0.99.)

Effect of fluid-solid exchange coefficient

Figure 5-5 shows the effect of the fluid-solid exchange coefficient. Within the range of variation, there is little influence of the drag coefficient on profiles of the static pressure and the axial interstitial gas velocity, although there is a significant effect on the axial solids velocity distribution and solids fraction. As far as the axial solids velocity was concerned, the Gidaspow drag model appeared to be a good choice for estimating the fluid-solid exchange coefficient, and was used throughout this study. Furthermore, this conclusion is consistent with that from Du et al. (2006) too.

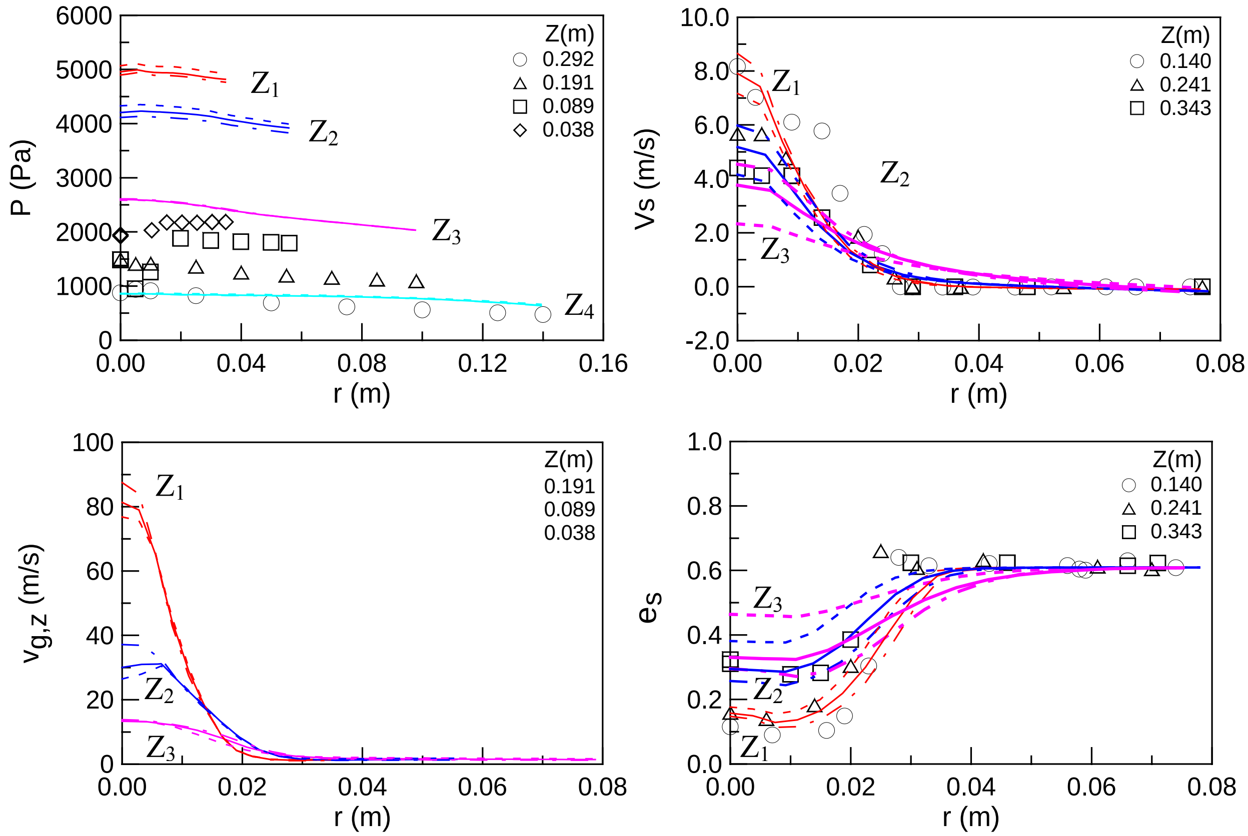

Fig. 5-5. Comparison between experimental data and simulated results with **different fluid-solid exchange coefficients** at k_a=1.0 (k_s=1.0, 1/7th power law). Symbols are experimental data, and lines are simulated results. (Solid lines correspond to the fluid-solid exchange coefficient K_{sg} from Gidaspow drag model, dashed lines correspond to 80% of K_{sg}, dotted dash lines correspond to 120% of K_{sg}.)

Effect of axial solid phase source term

It is seen from Figures 5-1 to 5-5 that the base case setting of the CFD code with proper inlet velocity profiles and parameters on the solids bulk viscosity, frictional viscosity, restitution coefficient and interphase exchange coefficient can properly capture the radial particle velocity distribution profiles in the conical spouted bed. However, variations of these key parameters failed to bring the simulation results close to the static pressure profiles. As pointed out at the beginning of this chapter, the annulus region in the spouted bed cannot be treated as a fluidized bed, and a simple source term can be used to correct the gravitational term in the vertical momentum balance equation for the particle phase. The effect of the solids source term was simulated based on Equations (5-21) and (5-22), with simulation results shown in Figure 5-6. It is seen that the axial solid phase source term has a significant impact on the static pressure profile, but has very little effect on the distribution of the axial solids velocity and the axial interstitial gas velocity and some effects on the distribution of the solids fraction. Compared to experimental data, a selection of k_a=0.7 seems to give the best agreement with the experimental data on the axial solids velocity, while a slightly smaller value of k_a gives better agreement with the static pressure data (see Figure 5-7). Therefore, a single constant value of k_a may not be sufficient for simulating conical spouted beds.

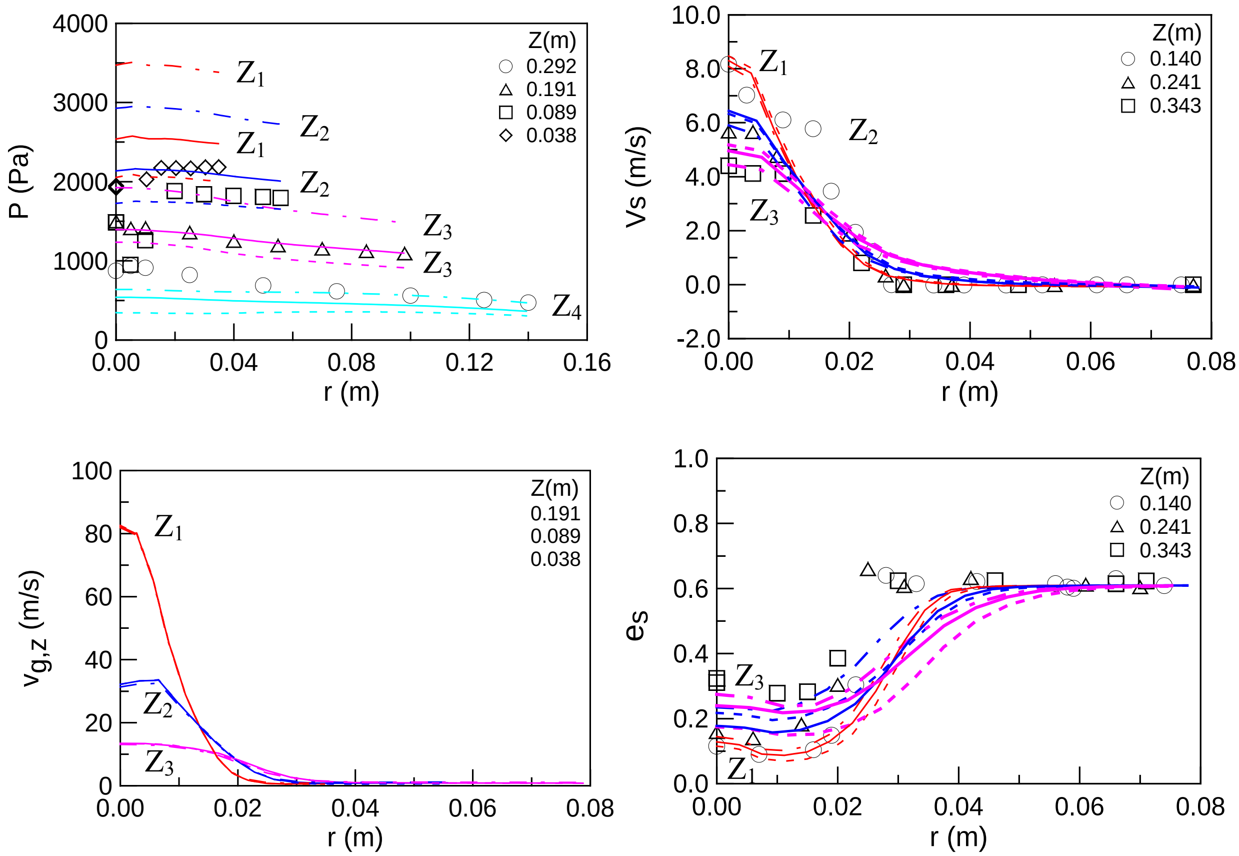

Fig. 5-6. Comparison between experimental data and simulated results with **different axial solid phase source terms** (k_s=1.0, 1/7th power law). Symbols are experimental data, and lines are simulated results. (Solid lines correspond to k_a=0.5, dashed lines correspond to k_a=0.41, dotted dash lines correspond to k_a=0.7.)

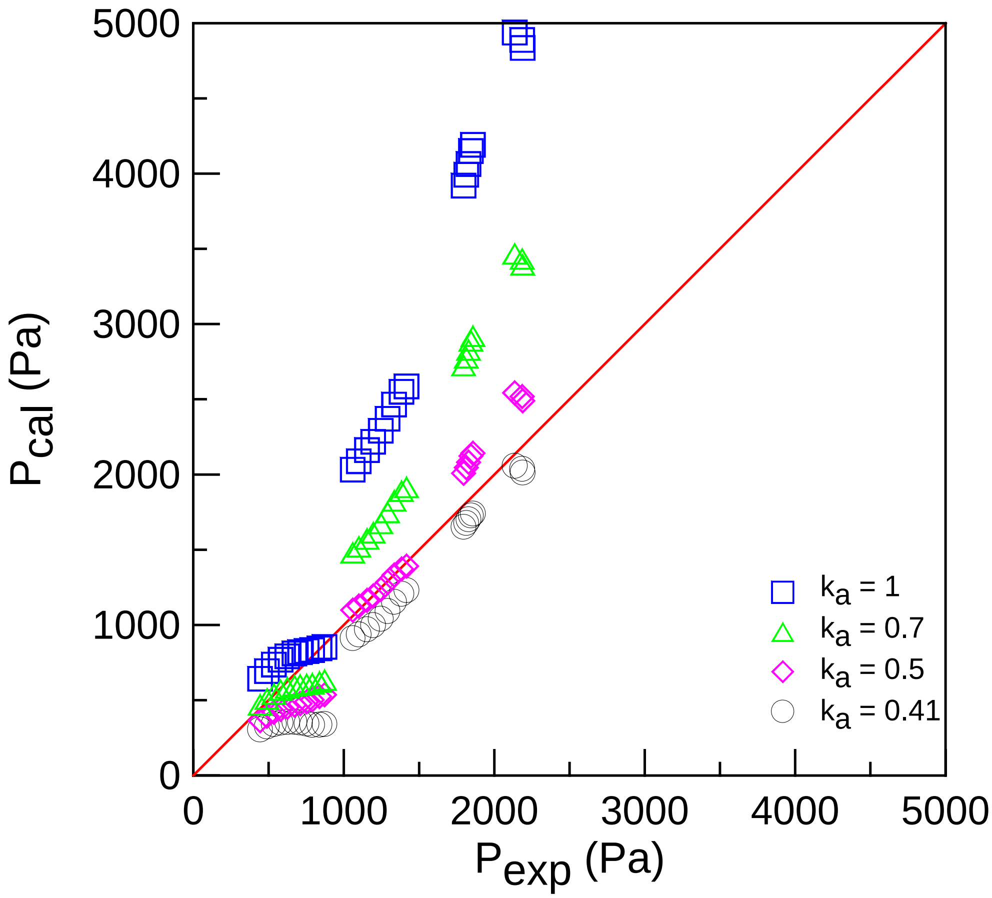

Fig. 5-7. Comparison between experimental data and simulated results on the static gauge pressure with **different axial solid phase source terms**.

Figures 5-8 and 5-9 clearly show the comparison between the CFD simulation and experiments on the axial solids velocity and the solids fraction with k_a=0.41. It is clear that, simulated axial solids velocities agree well with experimental data, but in most cases, simulated solids fraction underestimates experimental data greatly. Based on radial solids fraction profiles, this mainly results from the over-estimation of the spout diameter, and means that hydrodynamic behaviour in the spout should be considered in a different way in the future to obtain accurate results in this region.

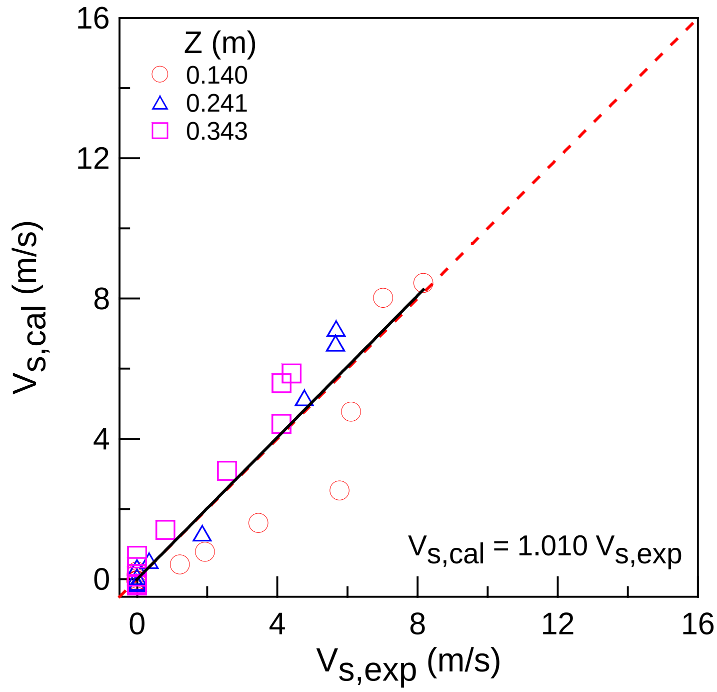

Fig. 5-8. Comparison between the simulation and experiment on the axial solids velocity.

(H_0=0.396m, D_0=0.01905m, d_s=1.16mm, γ=45º, U_i=23.50m/s, k_a=0.41)

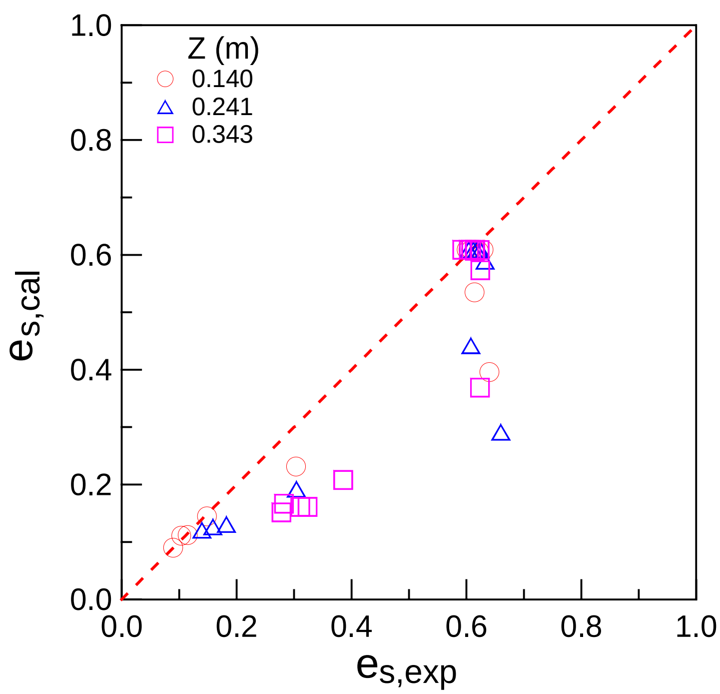

Fig. 5-9. Comparison between the simulation and experiment on the solids fraction. (H_0=0.396m, D_0=0.01905m, d_s=1.16mm, γ=45º, U_i=23.50m/s, k_a=0.41)

5.2.3 Further evaluation of the proposed approach

To further evaluate the proposed approach, conical spouted beds, with different geometrical structures (different gas inlet or cone angle) operated at different operating conditions (different static bed height or using glass beads of different diameters), were simulated. Detailed simulation information is listed in Table 5-5 with other simulation conditions listed in Table 5-6, while boundary conditions were kept the same as listed in Table 5-2.

In the simulation, k_a was first calculated by Equation (5-19) using the total pressure drop data listed in Table 5-5, and then adjusted to fit the measured total pressure drop. Axial static pressure profiles measured near the wall were then used to evaluate the proposed approach, as shown in Figure 5-10.

Figure 5-10 shows that the proposed approach, using only one empirical parameter k_a, can simulate all kinds of conical spouted beds very well, including conical spouted beds with different geometrical structures operated at different operating conditions. Because k_a was treated as a constant for each simulation condition, and k_s was set to be one, simulated results near the bed surface (gauge pressure lower than 1000 Pa) are found to be significantly lower than experimental data. It is anticipated that more accurate results can be obtained by considering the variation of k_a.

It can be seen from Table 5-5 that, for small glass beads with a diameter of 1.16 mm, fitted values of k_a are almost the same as values calculated from the total pressure drop using Equation (5-19). For big glass beads with a diameter of 2.4 mm, fitted values of k_a are much higher than calculated ones. The reason is still unclear, and needs to be further investigated.

Table 5-5. Geometrical dimensions and operating conditions used in simulations for conical spouted beds.

Particle diameter d_s (mm)	Cone angle γ (°)	Static bed height H_0 (m)	Gas inlet diameter D_0 (m)	Operating gas velocity U_i (m/s)	Total pressure drop ΔP_s (Pa)	k_a (Calculated)	k_a (Fitted)	***Note***
	30	0.335		12.04	3150	0.63	0.65	Run01
		0.230	0.01905	10.12	1910	0.55	0.56	Run02
				17.38	2690	0.54	0.54	Run03
1.16	45	0.335	0.0127	17.10	1840	0.37	0.4	Run04
			0.0254	23.04	3070	0.61	0.65	Run05
		0.396*		23.50	2400	0.414	0.414	Run06
	60	0.335		20.36	1710	0.34	0.4	Run07
		0.197	0.01905	17.45	1390	0.47	0.7	Run08
2.4	45	0.272		26.90	1600	0.39	0.6	Run09
		0.348		39.00	1600	0.31	0.55	Run10

Note: * This operating condition is further simulated using varied values of k_a.

Table 5-6. Other simulation conditions for conical spouted beds.

Description	Value	Comment
Gas density, ρ_g	1.23 kg/m^3	Air
Gas viscosity, μ_g	1.79×10^{-5} kg/(m·s)	Air
Particle density, ρ_s	2500 kg/m^3	Spherical glass beads
Initial solids packing, $\varepsilon_{s,0}$	0.61	Fixed value
Packing limit, $\varepsilon_{s,max}$	0.61	Fixed value
Solid viscosity, μ_s	Gidaspow	Eq. (5-7) + Eq. (5-9)
Frictional viscosity, $\mu_{s,fr}$	0	Fixed value
Solid bulk viscosity (Base case), λ_s	0	Fixed value
Total height of the column	1.6 m	Fixed value
Diameter of the bed bottom, D_i	0.038 m	Fixed value
Solver	2 dimensional, double precision, segregated, unsteady, 1st order implicit, axisymmetric	
Multiphase Model	Eulerian Model, 2 phases	
Viscous Model	Laminar model	
Phase Interaction (Base case)	Fluid-solid exchange coefficient: Gidaspow Model Restitution coefficient: 0.9 (Du et al., 2006)	
Time steps (Final value)	$2\sim5\times10^{-5}$ s	Fixed value
Convergence criterion	10^{-3}	Default in FLUENT

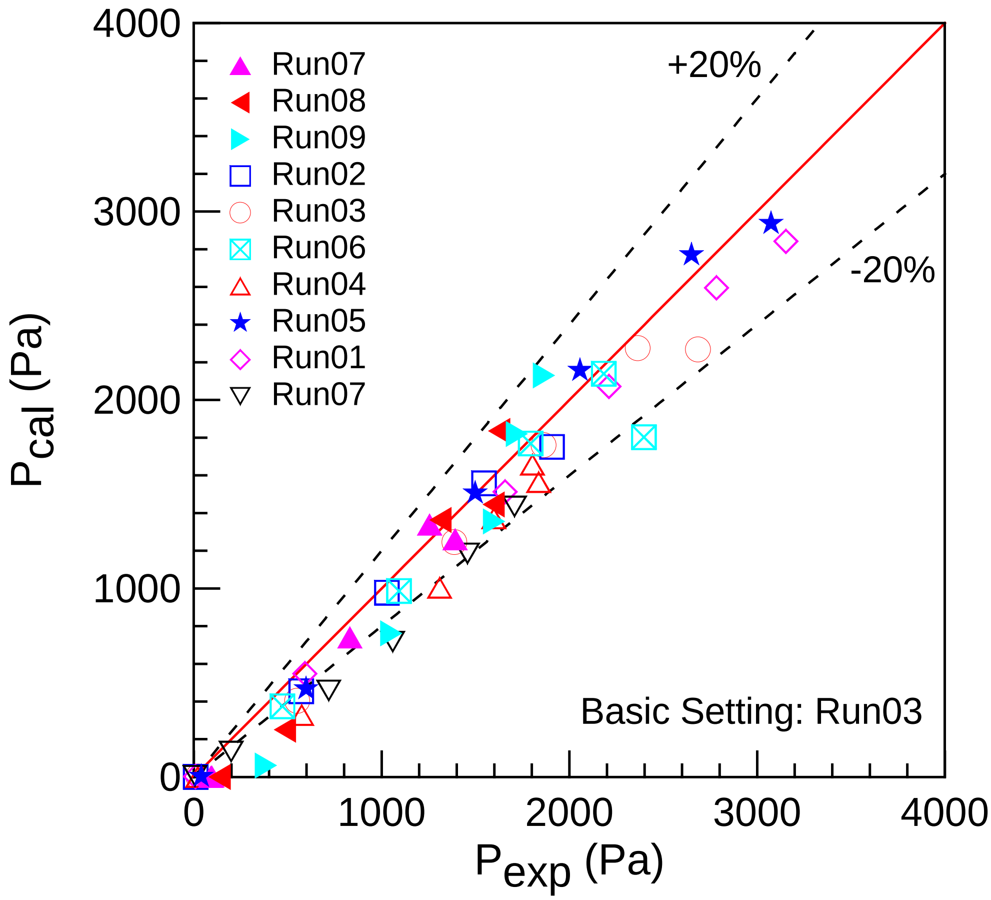

Fig. 5-10. Comparison between experimental data and simulated results on the static pressure within wide range of operating conditions as shown in Table (5-5).

5.2.4 Simulation using varied k_a values

Figure 5-11 shows the axial distribution of the static pressure measured near the wall. It can be seen that, at this specific operating condition, the axial distribution of the static pressure is quiet different from that in cylindrical spouted beds described by a quarter cosine curve (Lefroy and Davidson, 1969; Mathur and Epstein, 1974), and the axial distribution of the static pressure can be described by the following simple linear expression.

$$\frac{P_w}{\Delta P_s} = 1 - \frac{Z}{H_0} \tag{5-23}$$

where Z is the axial height, H_0 is the static bed height, P_w is the static pressure (gauge pressure) near the wall, ΔP_s is the total pressure drop.

Figure 5-12 shows the radial distribution of the static pressure at different heights. It can be seen that, if the lower section in the spout is not considered, the static pressure can be well described by

$$P = -3314.17r + C \tag{5-24}$$

where P is in pascals, r is the radial distance from the central axis in meters, C is a constant for each height. At the wall of the column,

$$P_w = -3314.17R + C \tag{5-25}$$

where R is the radius at a specific height Z, and can be calculated by

$$R = \frac{D_i}{2} + Z \cdot \tan(\frac{\gamma}{2}) \tag{5-26}$$

subtracting Equation (5-25) from Equation (5-24), the following equation is obtained:

$$P = P_w + 3314.17(R - r) \tag{5-27a}$$

which, on substituting for P_w and R by Equations (5-23) and (5-26) respectively, gives

$$P = (1 - \frac{Z}{H_0}) \cdot \Delta P_s + 3314.17\left[\frac{D_i}{2} + Z \cdot \tan(\frac{\gamma}{2}) - r\right] \tag{5-27b}$$

thus:

$$-\frac{dP}{dz} = \frac{\Delta P_s}{H_0} - 3314.17\tan(\frac{\gamma}{2}) \tag{5-28a}$$

$$-\frac{dP}{dr} = 3314.17 \tag{5-28b}$$

For fluidized beds,

$$-\frac{dP_{fb}}{dz}=-(1-\varepsilon_{g,0})\rho_s g \tag{5-29}$$

Thus,

$$k_a=\frac{(-\frac{dP}{dz})}{(-\frac{dP_{fb}}{dz})}=(\frac{\Delta P_s}{\Delta P_{fb}})\cdot\left[1.0-\frac{3314.17H_0\cdot\tan(\frac{\gamma}{2})}{\Delta P_s}\right] \tag{5-30}$$

By assuming

$$k_{a,r}=k_a\frac{P}{P_w} \tag{5-31}$$

$$k_{a,r}=(\frac{\Delta P_s}{\Delta P_{fb}})\cdot\left[1.0-\frac{3314.17H_0\cdot\tan(\frac{\gamma}{2})}{\Delta P_s}\right]\cdot\left[1+\frac{3314.17(R-r)}{(1-\frac{Z}{H_0})\cdot\Delta P_s}\right] \tag{5-32}$$

where ΔP_{fb} is the total pressure drop for a fluidized bed with the same static bed height as the conical spouted bed.

Figure 5-13 shows the comparison between experimental data and the correlation, i.e. Equation (5-27b). It is seen that the correlation can well describe the static pressure field in the conical spouted bed except for some data in the lower sections of the spout.

Figure 5-14 shows the comparison between experimental data and the CFD simulation with varied values of $k_{a,r}$ calculated by Equation (5-32). Comparing with Figure 5-7 (**k_a=0.41** or **k_a=0.5)**, it is clear that more accurate results can be obtained using varied values of $k_{a,r}$.

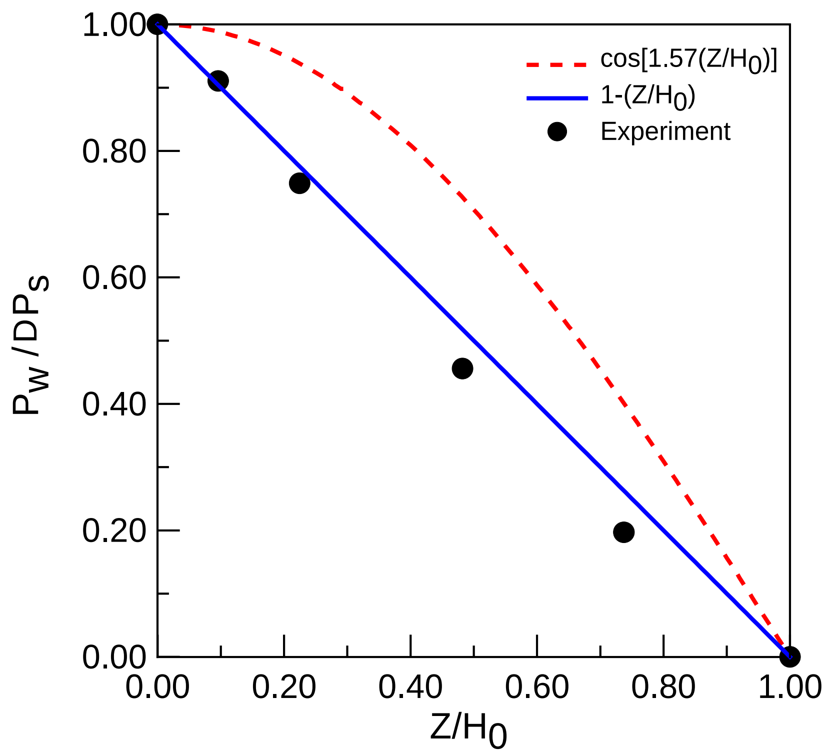

Fig. 5-11. Axial distribution of the static pressure near the wall. (H_0=0.396m, D_0=0.01905m, d_s=1.16mm, γ=45º, U_i=23.50m/s)

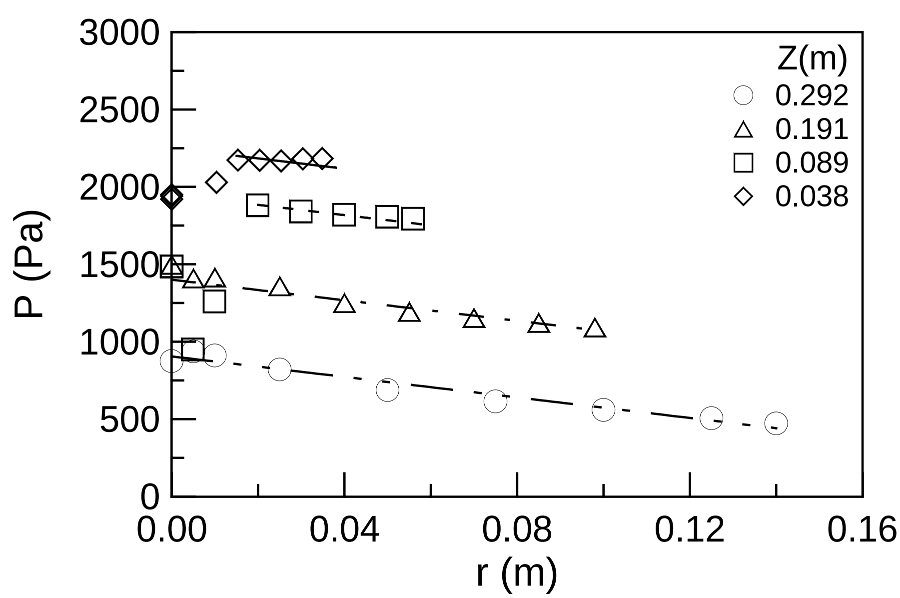

Fig. 5-12. Radial distribution of the static pressure at different heights. (H_0=0.396m, D_0=0.01905m, d_s=1.16mm, γ=45º, U_i=23.50m/s)

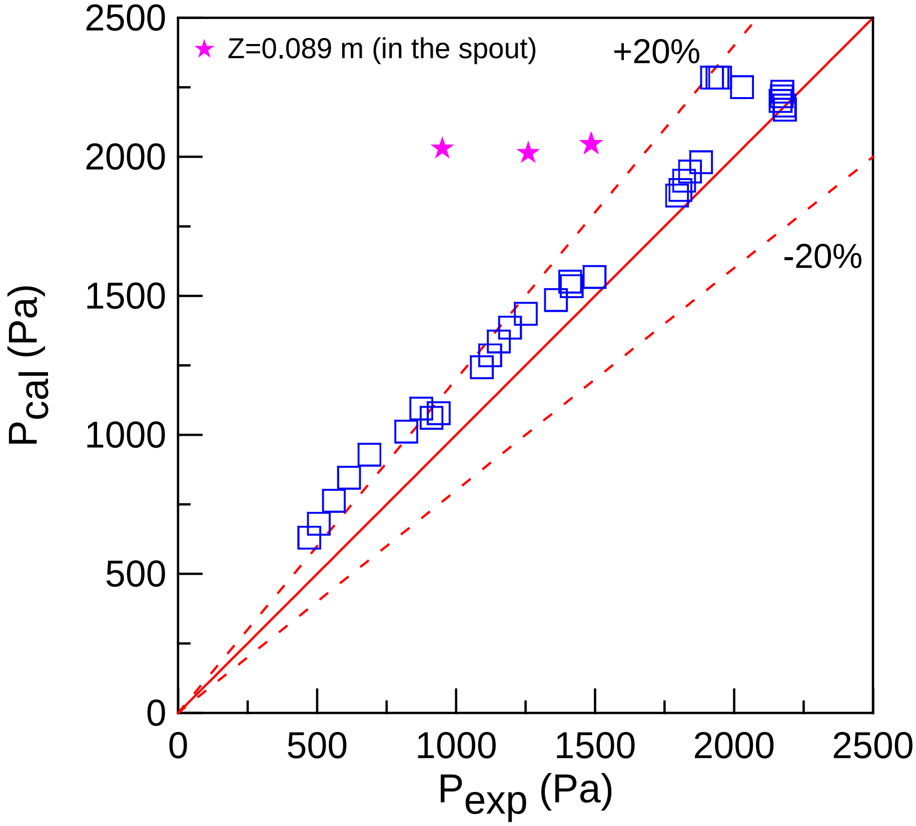

Fig. 5-13. Comparison between experimental data and Equation (5-27b) on the static pressure.

(H_0=0.396m, D_0=0.01905m, d_s=1.16mm, γ=45º, U_i=23.50m/s)

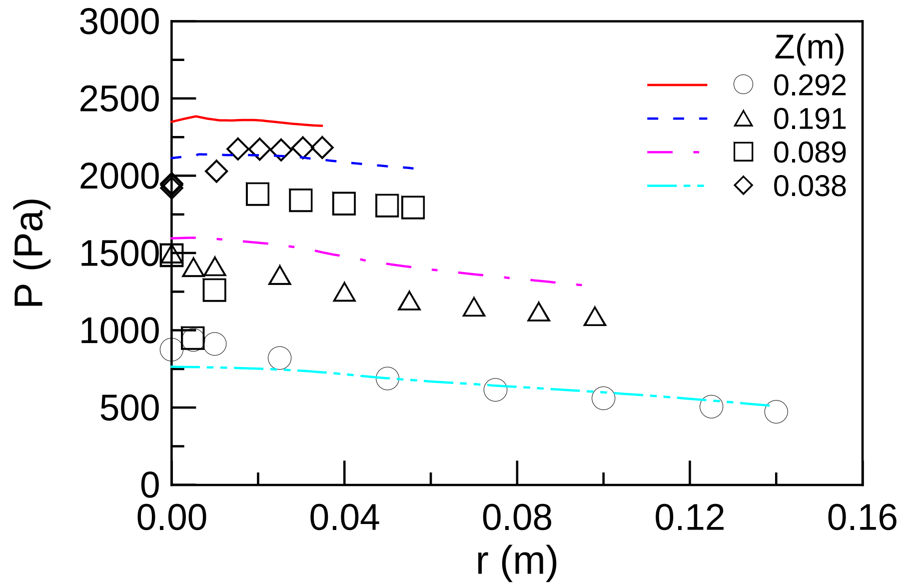

(a)

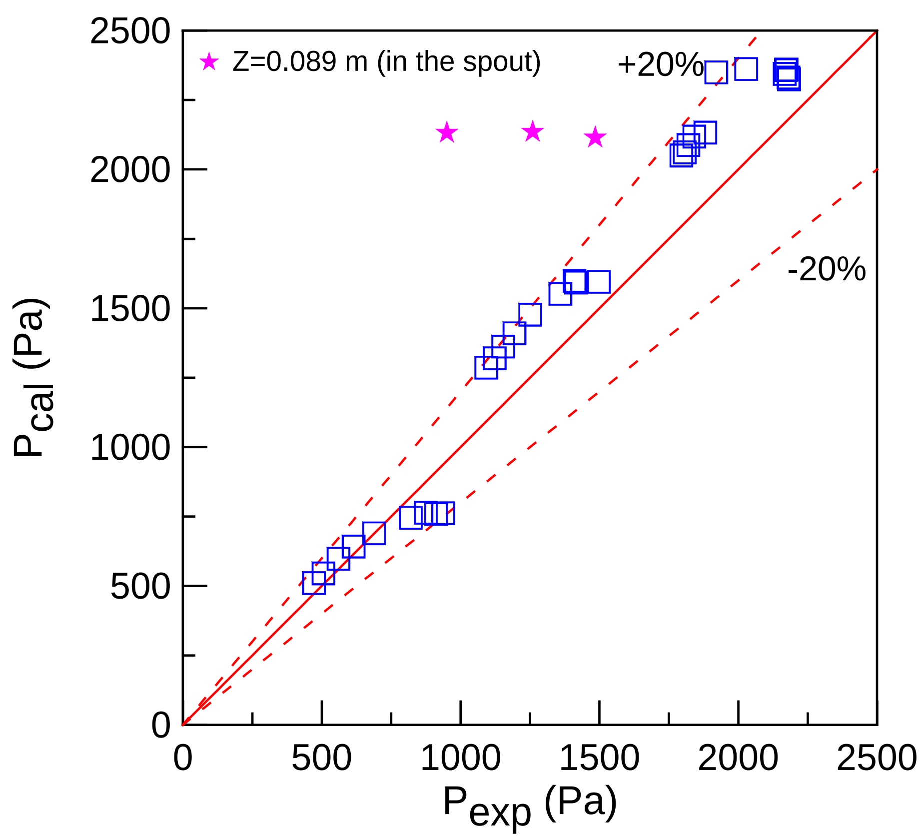

(b)

Fig. 5-14. Comparison between experimental data and the CFD simulation with varied values of $k_{a,r}$ estimated by Equation (5-32). (H_0=0.396m, D_0=0.01905m, d_s=1.16mm, γ=45º, U_i=23.50m/s)

5.2.5 Simulation of the evolution of pressure drop and internal spout

The proposed approach is applied to simulate the pressure evolution in a conical spouted bed operated at different velocities. Conditions investigated are listed in Table 5-7, with simulation conditions and boundary conditions being the same as those listed in Table 5-6 and Table 5-2.

To determine the height of the internal spout, the distribution of the average solids fraction was analyzed, as shown in Figures 5-15 and 5-16. It is obvious that the internal spout in the descending process is higher than in the ascending process at the same operating gas velocity. The average solids fraction along the central axis was plotted as a function of the axial location (as shown in Figures 5-17 and 5-18), and a half value of the solids packing limit (ε_s=0.3) was used as the criterion to determine the height of the internal spout.

Table 5-7. Conditions investigated for the evolution of the pressure drop and the internal spout in a conical spouted bed.

<table>
<tr><th>Particle diameter d_s (mm)</th><th>Cone angle γ (°)</th><th>Static bed height H_0 (m)</th><th>Gas inlet diameter D_0 (m)</th><th>Operating gas velocity U_i (m/s)</th><th>k_a (Calculated)</th><th>k_a (Fitted)</th><th>Remark</th></tr>
<tr><td rowspan="9">1.16</td><td rowspan="9">45</td><td rowspan="9">0.396</td><td rowspan="9">0.01905</td><td>5.00</td><td>0.856</td><td>0.856</td><td rowspan="4">Ascending</td></tr>
<tr><td>10.00</td><td>1.242</td><td>1.242</td></tr>
<tr><td>17.39</td><td>1.134</td><td>1.134</td></tr>
<tr><td>21.58</td><td>0.901</td><td>1.217</td></tr>
<tr><td>5.00</td><td>0.379</td><td>0.379</td><td rowspan="4">Descending</td></tr>
<tr><td>10.00</td><td>0.476</td><td>0.476</td></tr>
<tr><td>14.00</td><td>0.523</td><td>0.523</td></tr>
<tr><td>16.98</td><td>0.566</td><td>0.765</td></tr>
<tr><td>23.50</td><td>0.414</td><td>0.414</td><td>Spouting</td></tr>
</table>

Figure 5-19 shows the comparison between experimental data and CFD simulation results on the evolution of the pressure drop and the internal spout using the proposed approach. It shows that the proposed approach using a single parameter k_a can simulate conical spouted beds operated both in the ascending process and the descending process very well, including simulations on the evolution of the pressure drop and the development of the internal spout. According to Table 5-7, calculated k_a values can be used directly in most cases except when the operating gas velocity is slightly lower than or close to the corresponding minimum spouting velocity, when the fitted k_a is much higher than the calculated value. It implies that the minimum spouting velocity would be underestimated using directly calculated k_a, while the pressure drop would be overestimated using a higher k_a value.

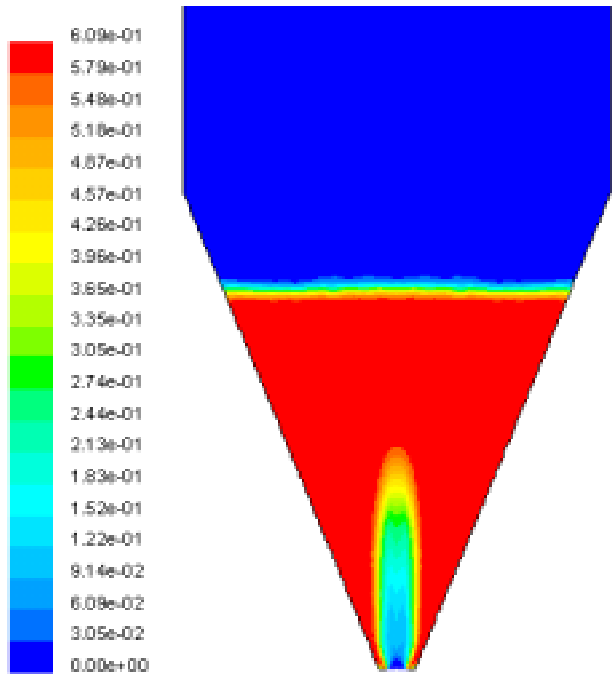

Fig. 5-15. Calculated bed structure of a conical spouted bed at partial spouting. (H_0=0.396m, D_0=0.01905m, d_s=1.16mm, γ=45º, U_i=10m/s, **descending process**)

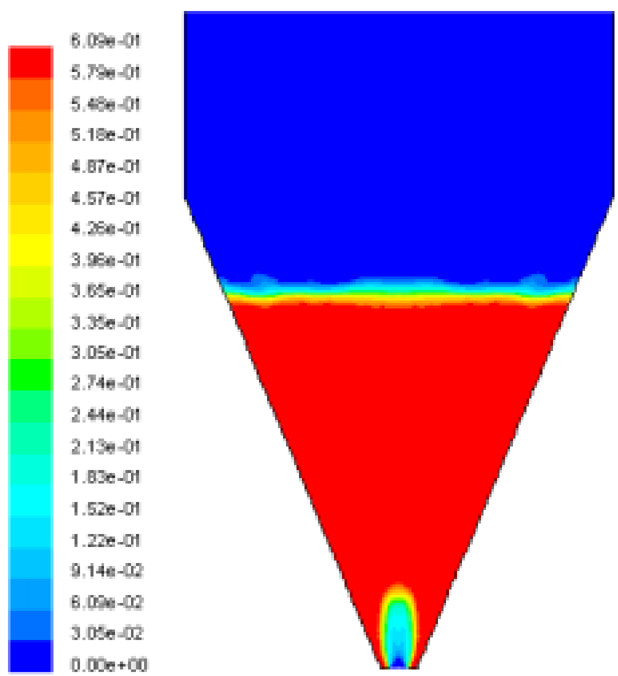

Fig. 5-16. Calculated bed structure of a conical spouted bed at partial spouting. (H_0=0.396m, D_0=0.01905m, d_s=1.16mm, γ=45º, U_i=10m/s, **ascending process**)

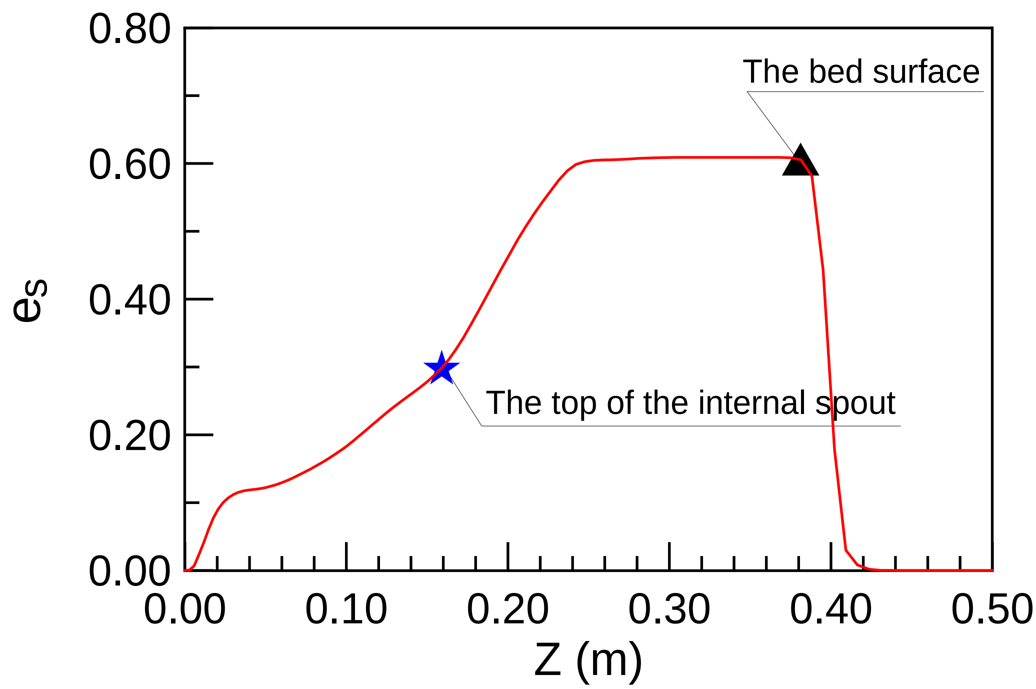

Fig. 5-17. Time average solids fraction along the axis. (H_0=0.396m, D_0=0.01905m, d_s=1.16mm, γ=45º, U_i=10m/s, **descending process**)

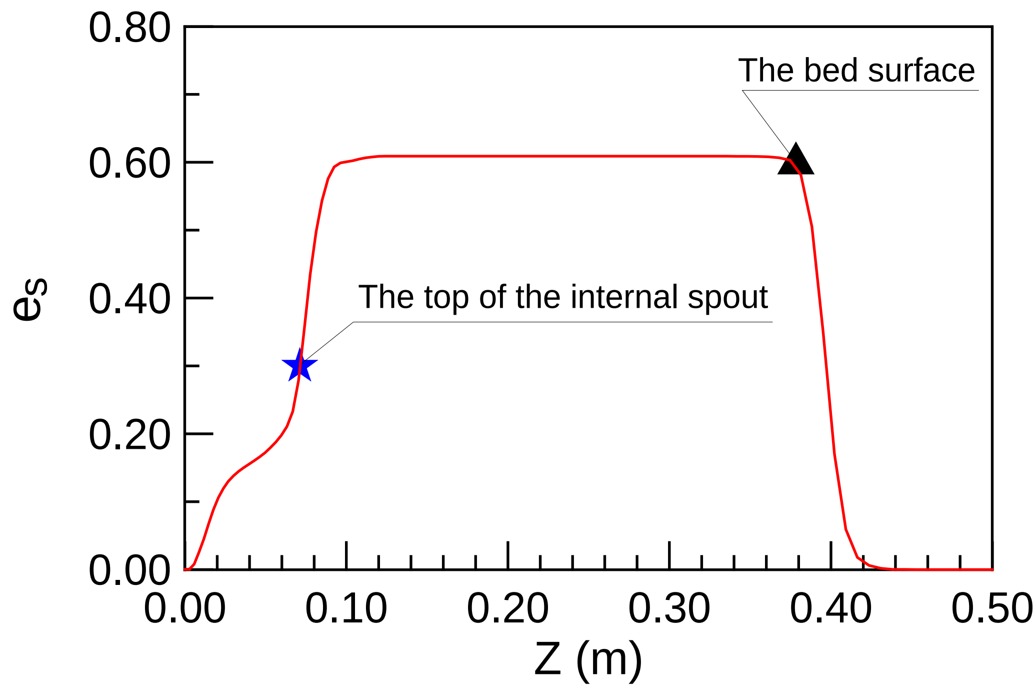

Fig. 5-18. Time average solids fraction along the axis. (H_0=0.396m, D_0=0.01905m, d_s=1.16mm, γ=45º, U_i=10m/s, **ascending process**)

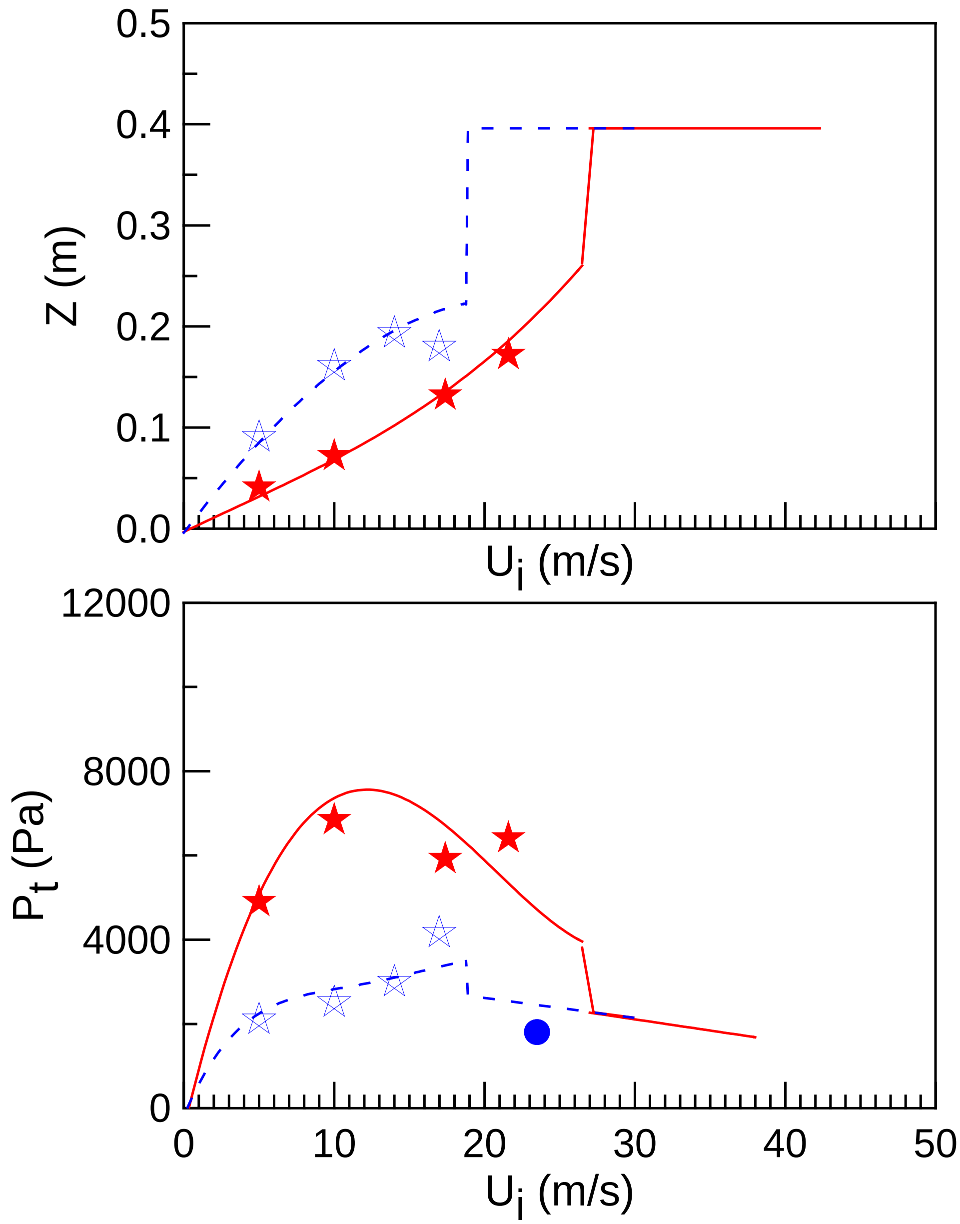

Fig. 5-19. Comparison between experimental data and CFD simulations on the evolution of pressure drop and internal spout using the proposed approach. (Symbols are simulated results, lines are fitted curves based on experimental data. Solid lines and solid stars correspond to the ascending process; dashed lines and hollow stars correspond to the descending process; the solid circle corresponds to the stable spouting state.) (H_0=0.396m, D_0=0.01905m, d_s=1.16mm, γ=45º)

CHAPTER 6

GAS MIXING BEHAVIOUR IN A CONICAL SPOUTED BED AND ITS SIMULATION

The gas residence time distribution is of considerable importance in predicting the conversion and selectivity for various catalytic reactions, and backmixing is undesirable as it leads to increased by-products.

Both vertical and horizontal mixing/dispersion can be studied using steady and unsteady state tracer techniques. In the steady state tracer experiment, a steady flow of tracer gas is introduced into the spouted bed at a certain location, and the tracer concentration is measured either downstream or upstream of the injection point. Ideally, the injection rate should be adjusted to match the local gas velocity in the bed to achieve an isokinetic injection (Bader et al., 1988). Based on the tracer concentration measured upstream of the injection point, the axial backmixing coefficient can be derived (Kunii and Levenspiel, 1991). On the other hand, the radial dispersion coefficient is obtained by analyzing radial profiles of tracer concentrations measured downstream of the injection point (Bader et al., 1988). The overall or effective axial dispersion coefficient over the entire bed could be derived using the unsteady state tracer technique.

For gas-solid multiphase systems, such as bubbling fluidized beds, circulating fluidized beds/risers and downers, there have been a large number of researches on gas backmixing and/or radial dispersion (e.g. Sotudeh-Gharebaagh and Chaouki, 2000; Sane et al., 1996; Cao and Weinstein, 2000; Bi, 2004; Bai et al., 1992; Wang and Wei, 1999), while there have been only a few studies on cylindrical spouted beds and conical spouted beds (e.g. Sun et al., 2005; Lim and Mathur, 1974, 1976; San Jose et al., 1995; Olazar et al., 1993d, 1995a), and almost no reports on the combination of residence time distribution (RTD) simulation and computational fluid dynamics (CFD) simulation on spouted beds.

6.1 Gas tracer system

Figure 6-1 presents the general set-up used for the gas tracer experiment in this study. The conical spouted bed (full column) is made of Plexiglas with an included angle γ of 45^o. The diameter at the conical base D_i is 0.038 m, the diameter of the nozzle D_0 is 0.019 m, and the diameter of the upper cylindrical section D_c is 0.45 m. Glass beads of 1.16 mm in diameter were used as the bed material; compressed air at the ambient temperature was used as the spouting gas. Other particle properties and detailed operating conditions are shown in Table 6-1.

Table 6-1. Particle properties and operating conditions for gas mixing behaviour in a conical spouted bed.

Particle diameter d_s, (mm)	Particle density ρ_s, (kg/m^3)	Loose-packed voidage, $\varepsilon_{g,0}$	Geldart's classification	Static bed height H_0, (m)	Velocity U_i, (m/s)
1.16	2500	0.39	D	0.396	23.5 16.95[a] 17.05[d]

Note: a------in the ascending process

d------ in the descending process

Helium was chosen as the tracer because it is inert and non-adsorbing on glass beads. For RTD measurements, the tracer was introduced as a step function by a solenoid valve, and the unsteady state response was measured by a TCD detection system. To enhance mixing of the helium tracer with spouting air to achieve a uniform distribution over the entire gas inlet, the tracer was injected into the spouting air far away from the bottom of the conical spouted bed.

Sampling probes were stainless steel tubes of 3 mm in outside diameter and 1 mm in inside diameter, and fine screen filters were mounted inside the tip of the probe to prevent blockage by fine particles. Two probes were connected separately to two thermal conductivity detectors (TCDs) to measure the tracer concentration, with one located just below the gas inlet and the other just above the bed surface. Output signals from TCDs were amplified and collected via a data acquisition system. Meanwhile, the probes could be radially traversed to measure the tracer concentration at different radial positions.

To obtain gas RTD curves over the reactor zone (the region between the bed bottom and the surface of the particle bed), the tracer concentration just before the gas inlet was measured and used as the input signal in the dispersion model to minimize the effect of the tracer injection system. Furthermore, to eliminate the possible effect from sampling probes, the consistency of two sampling probes was tested using the flowsheet as shown in Figure 6-2 with two sampling probes being mounted at the same position to take samples from the same gas mixture. As shown in Figure 6-3, the two sampling probes had almost the same response characteristics with a response time difference of 0.39 s, which will be corrected in the signal analysis.

During experiments, the amplification ratio was set to be 1000 with the current level at 95 mA. The sampling flow rate was 150 cc/min, and the sampling frequency was 100 Hz. By comparing the negative step injection and the positive step injection experimental data, the former method seemed to give better results. Thus, the negative step tracer technique was used throughout the experiments.

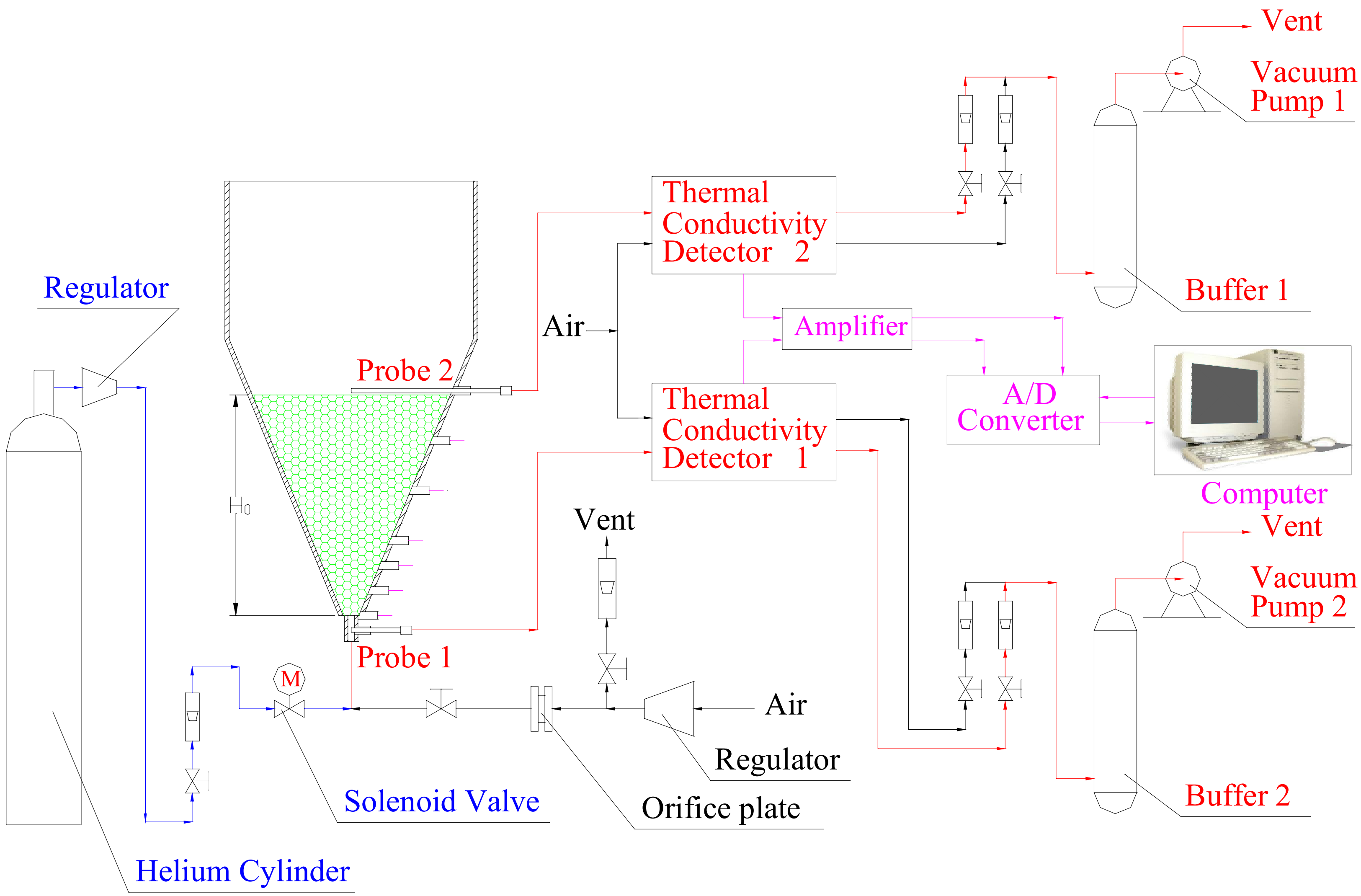

Fig. 6-1. Schematic of the gas tracer experiments.

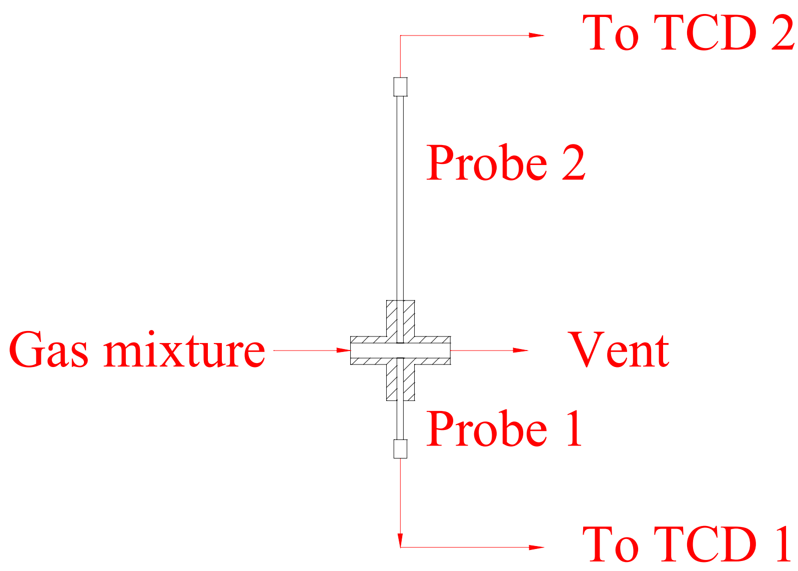

Fig. 6-2. Schematic of the gas tracer experiments for the consistency test of two sampling probes.

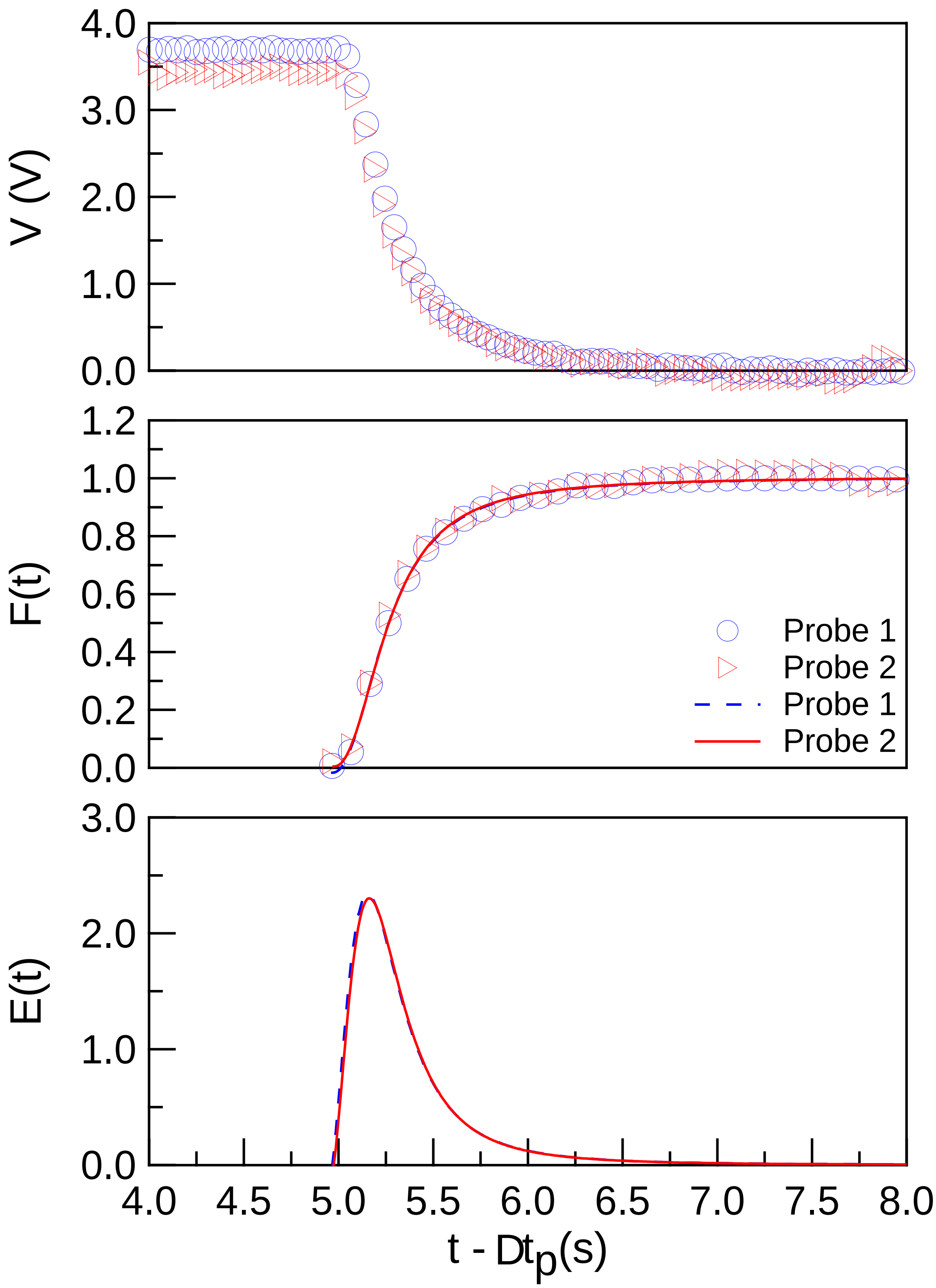

Fig. 6-3. Similarity between two sampling probes. (The response time lag Δt_p between the two probes is 0.39s, which has been corrected in this figure. Symbols correspond to experimental data; lines correspond to fitted results.)

6.2 Calibration of thermal conductivity detectors

Thermal Conductivity Detectors (TCDs) were calibrated by fixing the flow rate of the spouting gas (Air) and adjusting the flow rate of the tracer gas (Helium) to obtain a series of mixed gases with different known concentrations of helium. The flow rate of the tracer used in the experiment was usually very small, with a maximum helium volume fraction of 0.3%. Because the pressure and temperature of these mixed gases are almost constant, measured electrical signals will be directly proportional to the helium concentration. The relationship between the measured signal and the helium concentration (volume fraction) for two thermal conductivity detectors was obtained by using known-concentrations of calibration gases, with the results shown in Figure 6-4. For convenience, the measured signals have been normalized. It is seen that the normalized signals from both probes were linearly proportional to the helium concentration, where V_{min} corresponds to C_{He}=0, and V_{max} corresponds to C_{He}=0.3%.

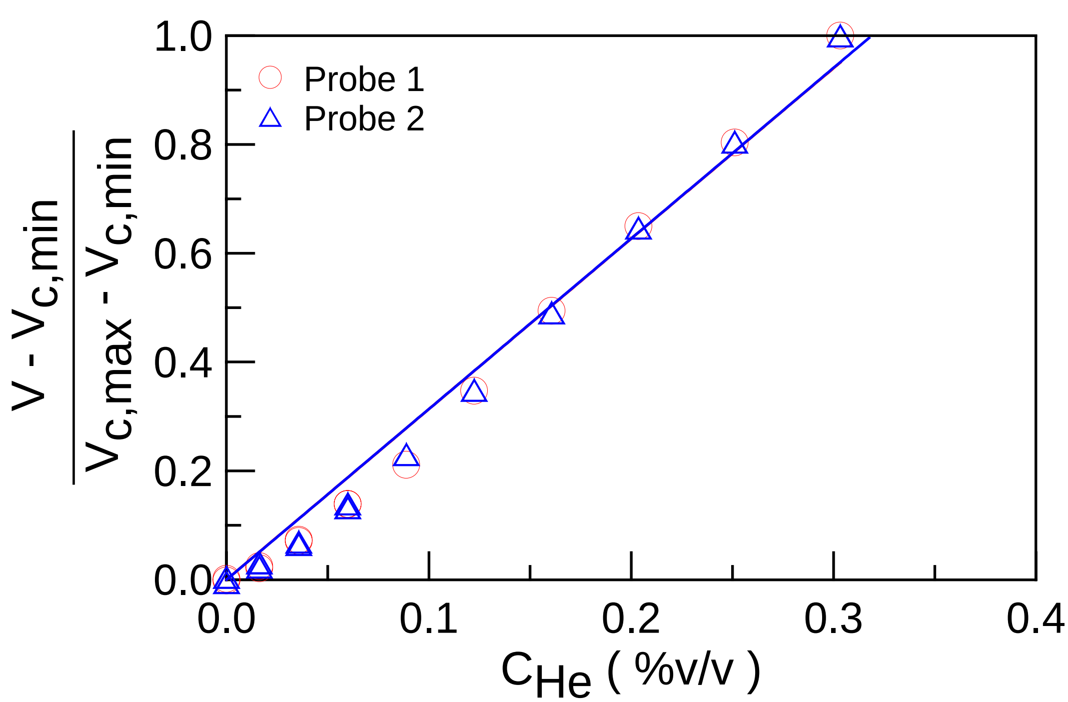

Fig. 6-4. Calibration curves for Thermal Conductivity Detectors (TCDs).

6.3 Estimation of the gas mixing behaviour

The negative step tracer input used during RTD experiments is described by

$$\begin{cases} \text{When } t<0, C_{He}=C_0 \\ \text{When } t\geq 0, C_{He}=0 \text{ at the tracer inlet} \end{cases} \tag{6-1}$$

Based on the above established calibration relationship, each response curve can be easily converted to the cumulative distribution function *F*(*t*) by

$$F(t)=1-\frac{V(t)-V_{\infty}}{V_0-V_{\infty}} \tag{6-2}$$

where V_0 is the average value corresponding to $C_{He}=C_0$, V_{∞} is the average value corresponding to $C_{He}=0$, and V(t) is the transient value.

Because the experimental data are discrete points with the same time step, the cumulative distribution function *F*(*t*) obtained from Equation (6-2) will comprise discrete points too. Thus, the accuracy on estimated results of the RTD function *E(t)* cannot be assured by using numerical differentiation directly. To solve this problem, the cumulative distribution function *F*(*t*) was fitted first using the Levenberg-Marquardt method, and the RTD function *E(t)* was further derived by differentiating the fitted *F*(*t*) curve.

$$E(t)=\frac{dF(t)}{dt} \tag{6-3}$$

The response time lag t_0 is defined as the time difference between the start of the sampling and the start of the response, and can be estimated easily from the RTD function *E(t)*. Generally, knowing the response time lag, the mean residence time $\hat{t}$ and corresponding variance σ_t^2 can be further calculated from:

$$\hat{t} = \int_0^{\infty}(t-t_0)\cdot E(t-t_0)d(t-t_0) = \frac{\sum(t-t_0)E(t-t_0)}{\sum E(t-t_0)} \tag{6-4}$$

$$\sigma_t^2 = \int_0^{\infty}(t-t_0-\hat{t})^2\cdot E(t-t_0)d(t-t_0) = \frac{\sum(t-t_0)^2 E(t-t_0)}{\sum E(t-t_0)} - \hat{t}^2 \tag{6-5}$$

By defining a dimensionless time θ in Equation (6-6), the corresponding variance σ^2 can be calculated by (6-7).

$$\theta = \frac{(t-t_0)}{\hat{t}} \tag{6-6}$$

$$\sigma^2 = \frac{\sigma_t^2}{\hat{t}^2} \tag{6-7}$$

Figure 6-5 shows the definition of the mean residence time and corresponding variance for different sections in the current experimental study. According to the experimental design, neglecting the time difference between the start of the sampling and the start of the injection, the measured electric signal from TCD 1 will include two contributions. The first is from the injection point to the tip of the probe 1 (or tip 1), and the second is from tip 1 to TCD 1. The measured electric signal from TCD 2 will include three contributions, the first is from the injection point to the tip of the probe 1 (or tip 1), the second is from tip 1 to the tip of the probe 2 (or tip 2), and the third is from tip 2 to TCD 2. Thus, estimated values of the average residence time and corresponding variance are over the whole course from the injection point to the TCD. Based on the transfer characteristics of linear systems (Levenspiel, 1999), the following equations can be derived.

$$\sigma_{t,t2}^2 = \sigma_{t,1}^2 + \Delta\sigma_t^2 + \sigma_{t,p2}^2 \tag{6-8}$$

$$\sigma_{t,t1}^2 = \sigma_{t,1}^2 + \sigma_{t,p1}^2 \tag{6-9}$$

$$\hat{t}_{t2} = \hat{t}_1 + \Delta\hat{t} + \hat{t}_{p2} \tag{6-10}$$

$$\hat{t}_{t1} = \hat{t}_1 + \hat{t}_{p1} \tag{6-11}$$

and

$$\Delta\sigma_t^2 = (\sigma_{t,t2}^2 - \sigma_{t,t1}^2) - (\sigma_{t,p2}^2 - \sigma_{t,p1}^2) \tag{6-12}$$

$$\Delta\hat{t} = (\hat{t}_{t2} - \hat{t}_{t1}) - (\hat{t}_{p2} - \hat{t}_{p1}) \tag{6-13}$$

where $\hat{t}_{t2}$ is the mean residence time for the total electric signal measured by probe 2 (from the injection point to the TCD 2), $\sigma_{t,t2}^2$ is the corresponding variance; $\hat{t}_{t1}$ is the mean residence time for the total electric signal measured by probe 1 (from the injection point to the TCD 1), $\sigma_{t,t1}^2$ is the corresponding variance; $\hat{t}_{p2}$ is the mean residence time for the probe 2 itself (from the tip of the probe 2 to the TCD 2), $\sigma_{t,p2}^2$ is the corresponding variance; $\hat{t}_{p1}$ is the mean residence time for the probe 1 itself (from the tip of the probe 1 to the TCD 1), $\sigma_{t,p1}^2$ is the corresponding variance; $\Delta\hat{t}$ is the mean residence time inside the conical spouted bed, and $\Delta\sigma_t^2$ is the corresponding variance; $\hat{t}_1$ is the mean residence time from the injection point to the tip of the probe 1, $\sigma_{t,1}^2$ is the corresponding variance.

Values of $\hat{t}_{p2}$, $\sigma_{t,p2}^2$, $\hat{t}_{p1}$ and $\sigma_{t,p1}^2$ can be estimated from data shown in Figure 6-3 (See Section 6.4 for more details).

For an open-closed system, the axial Peclet number *Pe* can be related to the variance for a flow system with small backmixing by Levenspiel (1979).

$$\sigma^2 = \frac{2}{Pe} + 3\left(\frac{1}{Pe}\right)^2 \tag{6-14}$$

If the gas backmixing is very small, the above equation can be further simplified to

$$\sigma^2 \approx \frac{2}{Pe} \tag{6-15}$$

where Pe is the Peclet number, $Pe = \frac{u_g \cdot \mathrm{L}}{\mathrm{D}}$, u_g is the interstitial gas velocity, L is the distance between two sampling points, D is the dispersion coefficient.

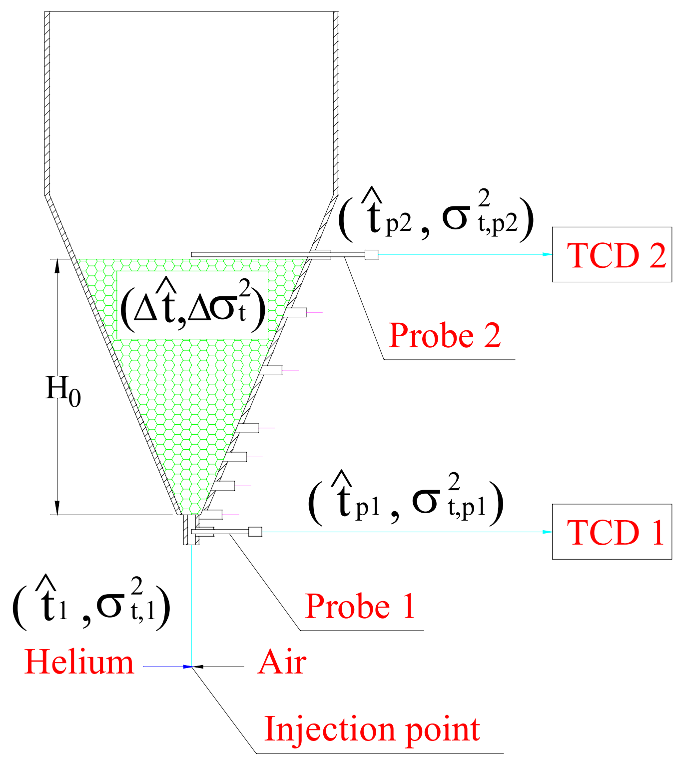

Fig. 6-5. Definition of the mean residence time and corresponding variance for different sections.

6.4 Computational procedure

Because of interference, there are some spikes or fluctuations in the sampled electrical signals. Thus, sampled electrical signals were smoothed first before Equations (6-2) to (6-5) were applied to calculate corresponding t_0, $\hat{t}$ and $\sigma_{\hat{t}}^2$ (Matlab programs are listed in Appendix J.).

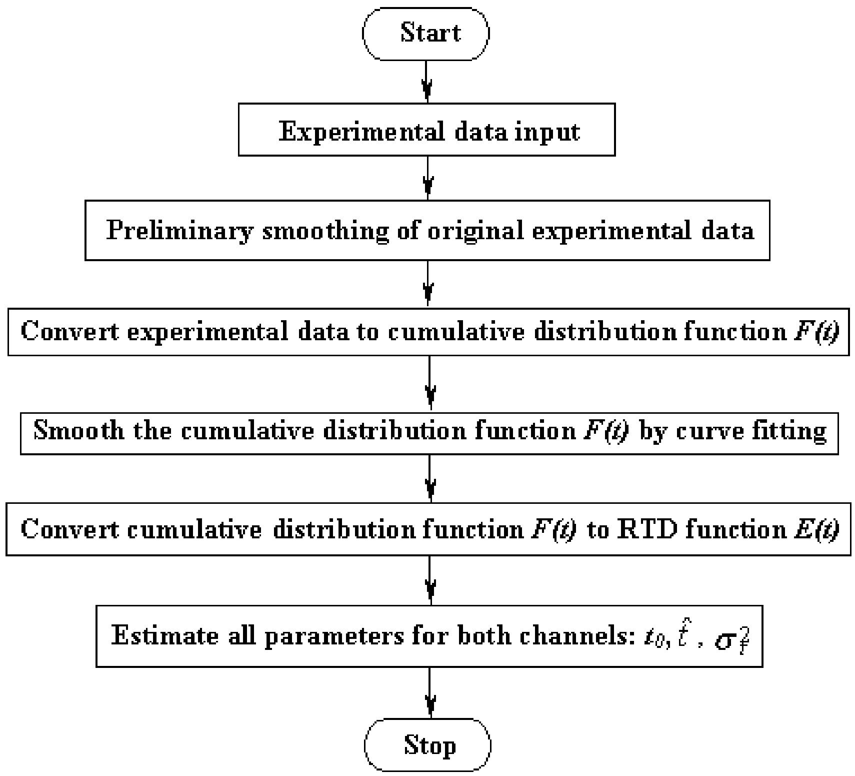

6.5 Results and discussion

Figures 6-6 to 6-8 show some original experimental signal data V, calculated F functions and E functions at the inlet as well as at the bed surface based on negative step tracer experiments with response time lags included. Discrete V values are originally measured electrical signals in volts. Based on Equation (6-2), discrete F values (symbols) are obtained. By curve fitting, smoothed F curves (lines) are then obtained. Similarly, based on Equation (6-3), discrete E values (symbols, derived from discrete F values) as well as smoothed E curves (lines, derived from smoothed F curves) can be obtained. Because of the fluctuations of measured electrical signals at the inlet, some additional small peaks still appear among discrete E values, which are not discussed in the following sections.

It can be seen from Figures 6-6 to 6-8 that the response at the gas inlet was not a perfect step function, which could mean either that there exists gas backmixing between the tracer injection point and TCD 1 or that the tracer injection was not a perfect step function.

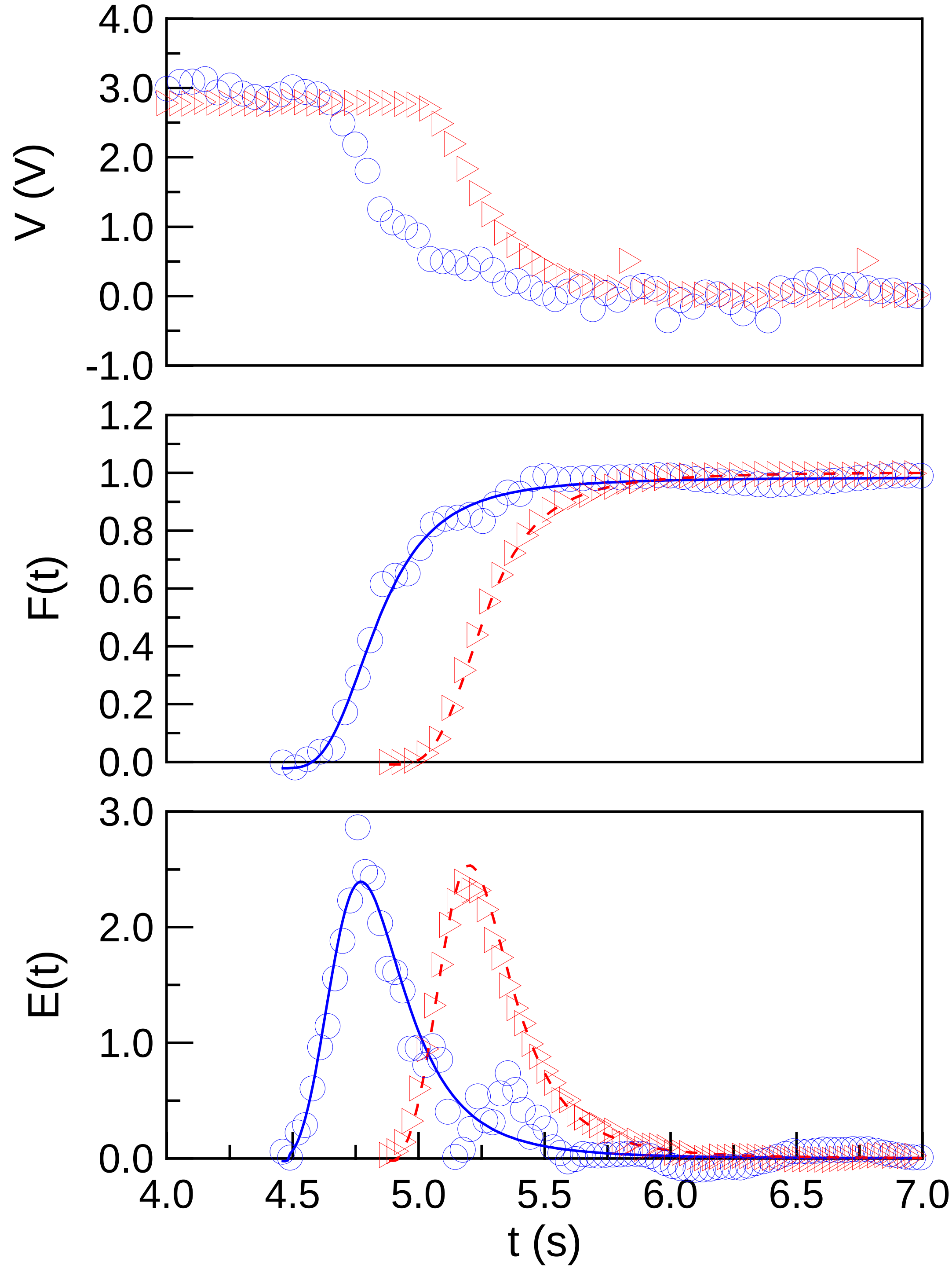

Fig. 6-6. Original experimental data V, calculated F functions and E functions at the inlet as well as at the bed surface with the probe located at the axis. (**Stable spouting**) (Circles correspond to the inlet, **r=0.0m**; triangles correspond to the bed surface, **r=0.0m**; lines are fitted curves, **full column, U_i=23.5 m/s**.)

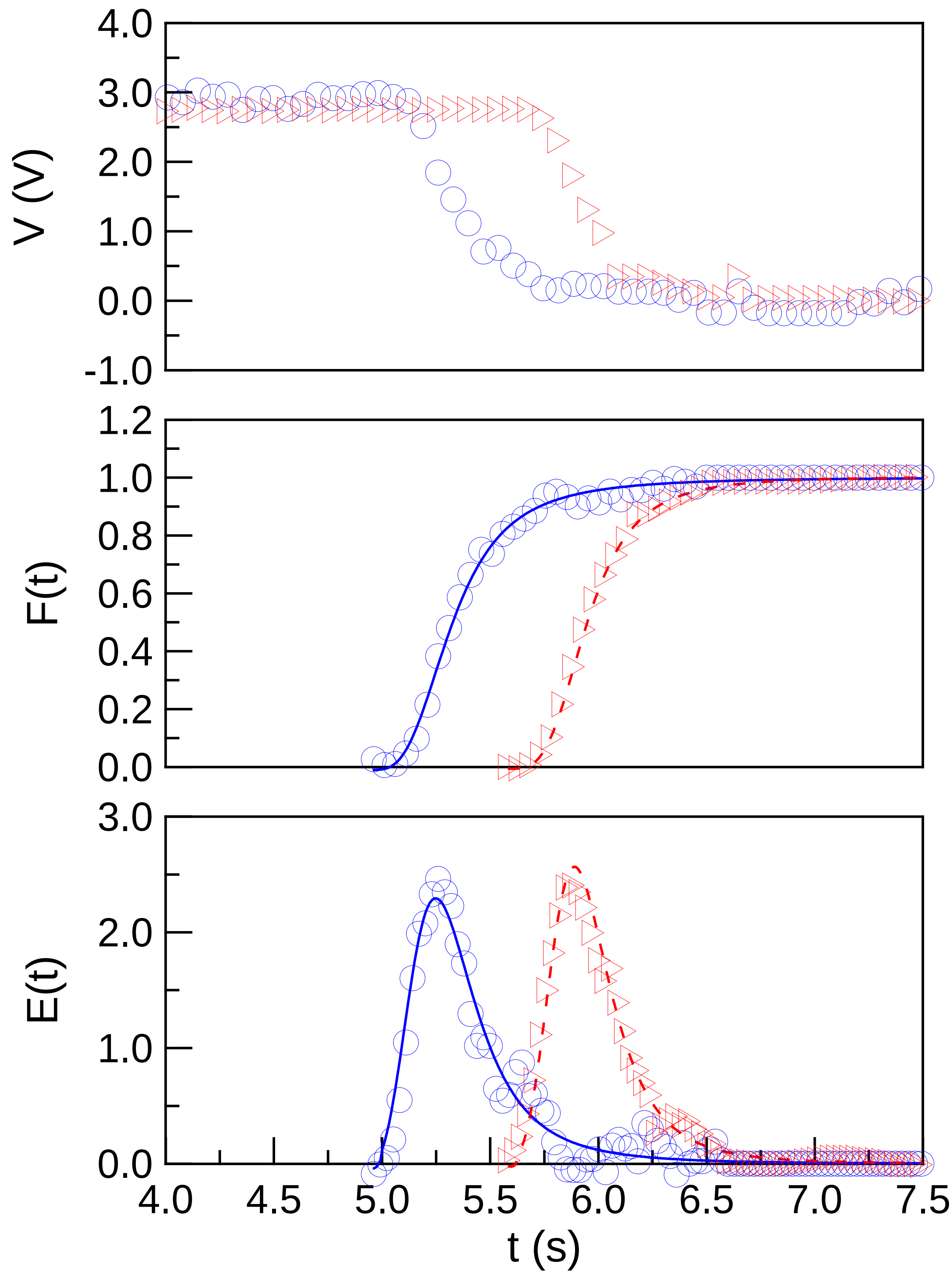

Fig. 6-7. Original experimental data V, calculated F functions and E functions at the inlet as well as at the bed surface with the probe located halfway between the axis and the wall. (**Stable spouting**) (Circles correspond to the inlet, **r=0.0m**; triangles correspond to the bed surface, **r=0.090m**; lines are fitted curves, **full column, U_i=23.5 m/s**.)

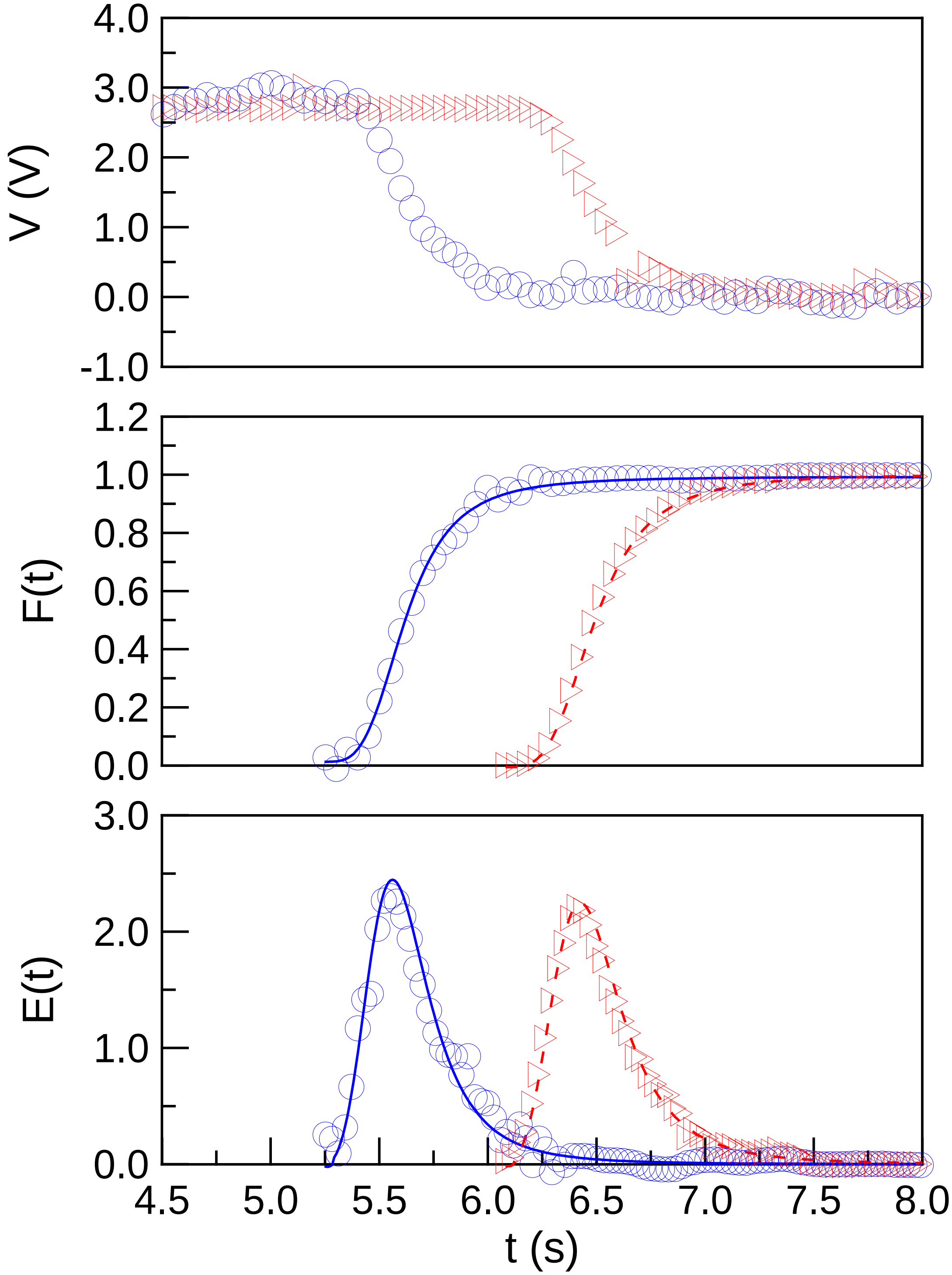

Fig. 6-8. Original experimental data V, calculated F functions and E functions at the inlet as well as at the bed surface with the probe near the wall. (**Stable spouting**) (Circles correspond to the inlet, **r=0.0m**; triangles correspond to the bed surface, **r=0.180m**; lines are fitted curves, **full column, U_i=23.5 m/s**.)

Figures 6-9 to 6-11 show calculated F values at the inlet and the bed surface at different operating velocities or states. Response time lags for the probe just below the gas inlet have been adjusted based on data at the gas inlet for the run with the probe located at the center of the bed surface, and the response time lag between two probes has also been removed. It is seen that calculated F values at the inlet are almost the same for all experiments, meaning that the tracer injection system is very stable and reproducible. Meanwhile, the injection of the tracer is far from a perfect step function. Calculated F values at the bed surface clearly show that the mean residence time is quite different at different positions of the bed surface, which means that gas velocity inside the conical spouted bed has a radial distribution, higher in the center and lower near the wall.

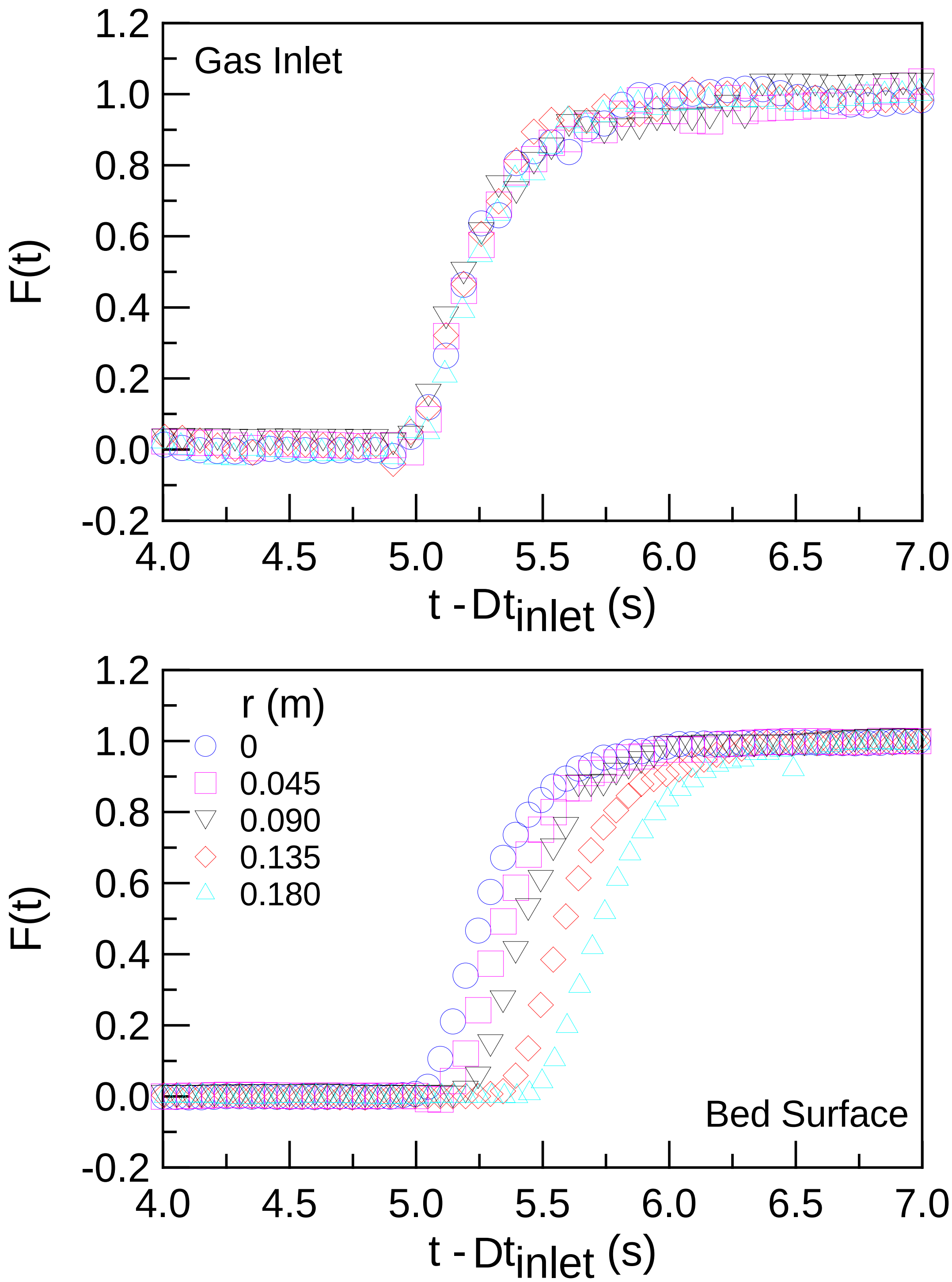

Fig. 6-9. Calculated F values at the inlet and the bed surface under stable spouting conditions. (Response time lags at the gas inlet for all runs have been adjusted based on data at the gas inlet during the run at the centre of the bed surface, and the response time lag between two probes has also been removed, **full column, U_i=23.5 m/s**.)

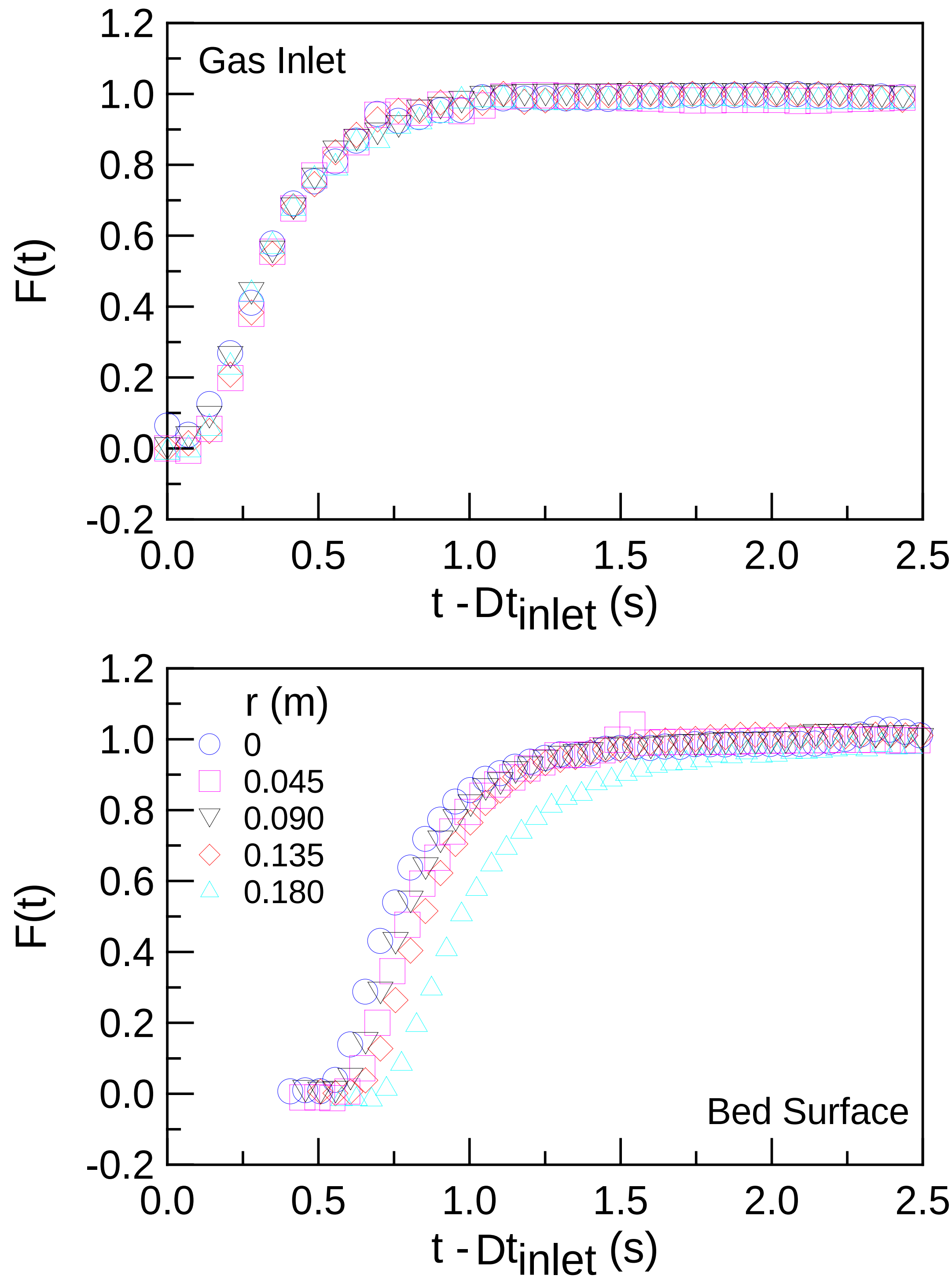

Fig. 6-10. Calculated F values at the inlet and at the bed surface at partial spouting for the velocity **ascending process**. (Response time lags at the gas inlet for all runs have been adjusted based on data at the gas inlet during the run at the centre of the bed surface, and the response time lag between two probes has also been removed, **full column, $U_{i,a}$=16.95 m/s, Z_a=0.131m**.)

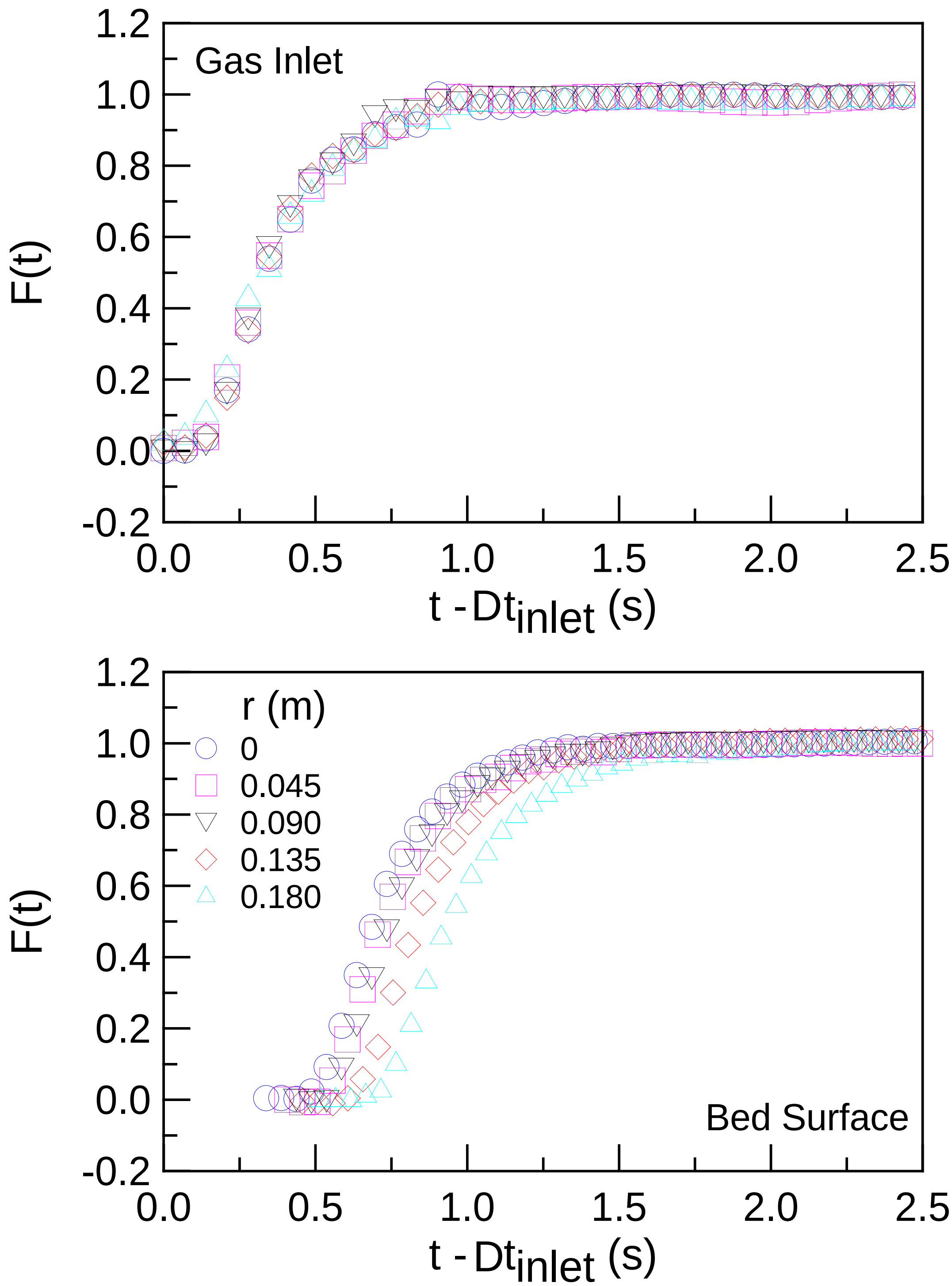

Fig. 6-11. Calculated F values at the inlet and at the bed surface at partial spouting for the velocity **descending process**. (Response time lags at the gas inlet for all runs have been adjusted based on data at the gas inlet during the run at the centre of the bed surface, and the response time lag between two probes has also been removed, **full column, $U_{i,d}$=17.05 m/s, Z_d=0.216m**.)

Figures 6-12 to 6-15 show the radial distribution of the mean residence time and the Peclet number at different operating velocities or states, such as the stable spouting state, the partial spouting state in the ascending process and the partial spouting state in the descending process. Figure 6-12 shows that the mean residence time increases with increasing radial distance from the centre of the column, meaning that gas velocity inside the conical spouted bed has a radial distribution, higher in the centre and lower near the wall. Figure 6-13 shows that the radial distribution of the Peclet number is quite complex, with a maximum value at r=0.135m (**Further analysis will be shown in section 6.6.2.**). This trend is commonly observed at different operating velocities or states as shown in Figures 6-14 and 6-15. Meanwhile, the radial distribution of gas velocity in the ascending process is different from that in the descending process, so is the gas mixing behaviour, even though operating velocities are almost the same.

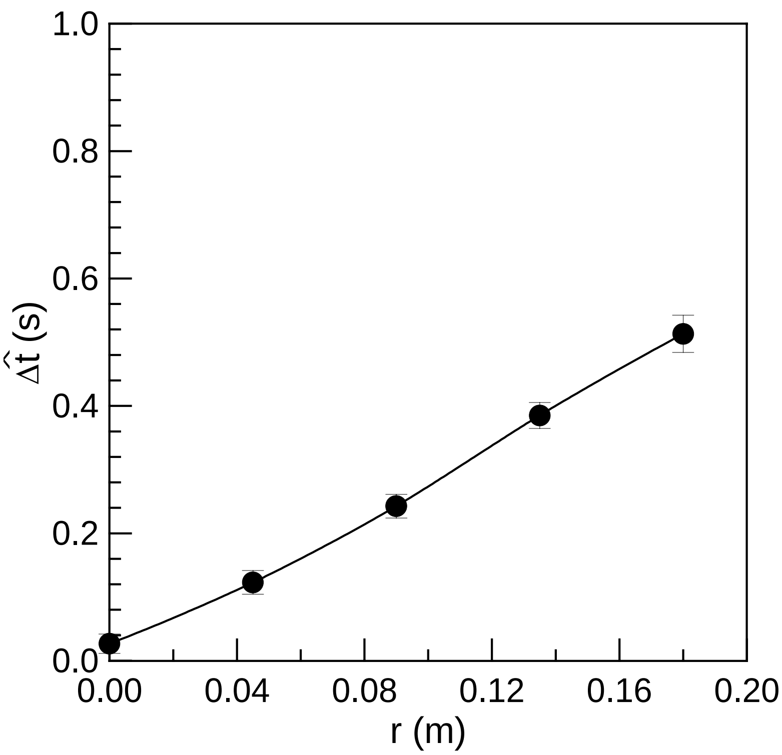

Fig. 6-12. Radial distribution of the mean residence time. **(Full column, stable spouting, U_i=23.5 m/s)**

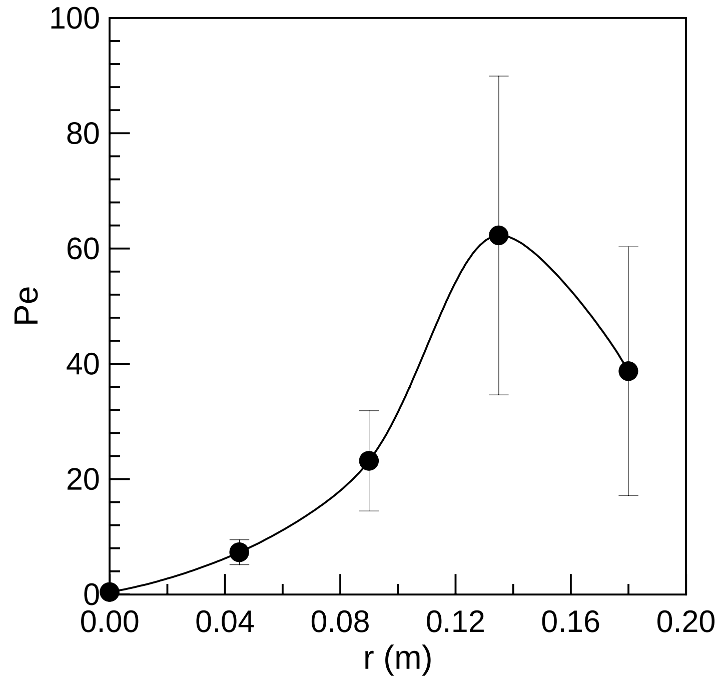

Fig. 6-13. Radial distribution of the Peclet number. **(Full column, stable spouting, U_i=23.5 m/s)**

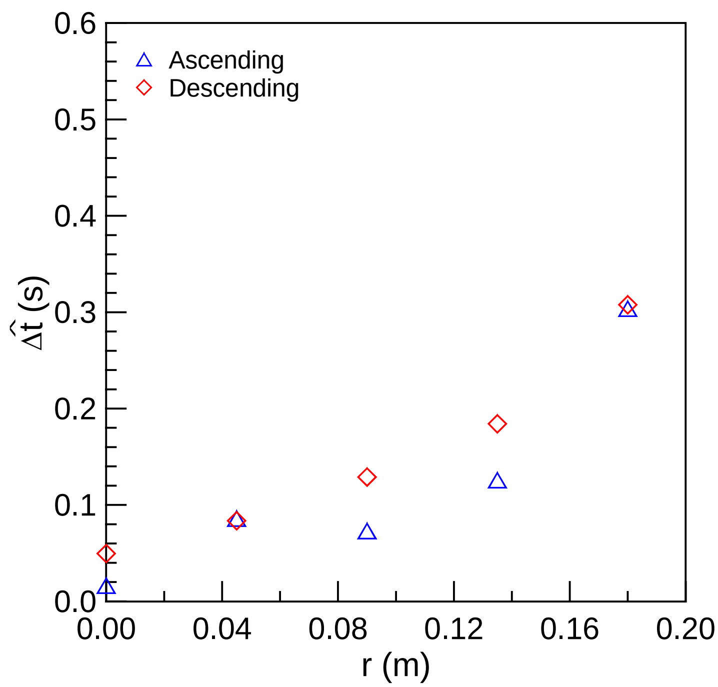

Fig. 6-14. Radial distribution of the mean residence time. **(Full column, partial spouting, $U_{i,d}$=17.05 m/s, Z_d=0.216m or $U_{i,a}$=16.95 m/s, Z_a=0.131m)**

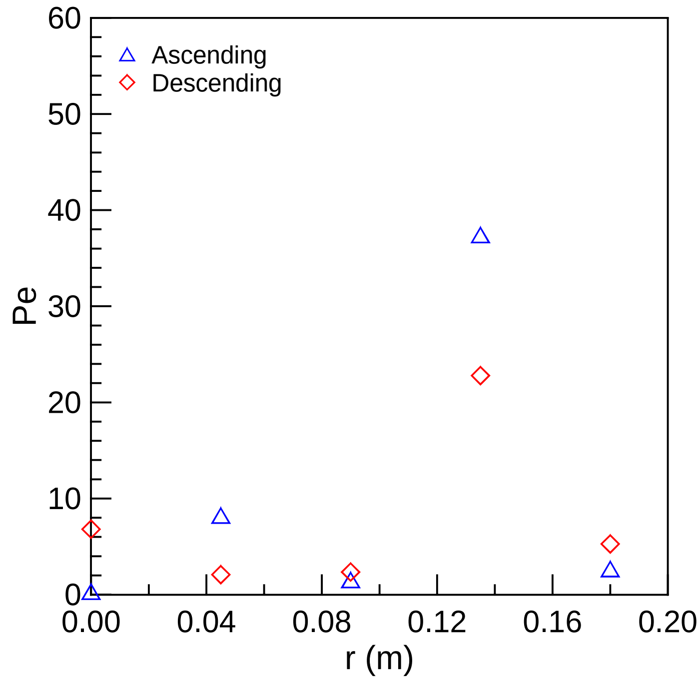

Fig. 6-15. Radial distribution of the Peclet number. **(Full column, partial spouting, $U_{i,d}$=17.05 m/s, Z_d=0.216m or $U_{i,a}$=16.95 m/s, Z_a=0.131m)**

6.6 Simulation of gas mixing in a conical spouted bed

6.6.1 General gas mixing model

For a small three-dimensional control volume as shown in Figure 6-16, the analysis of the control volume in the vertical direction is shown in Figure 6-17, and the following expressions can be derived with the following assumptions:

- The dispersion coefficient is constant within the bed;
- Gas density is constant within the bed.

Tracer In:

Carry in: $v_{g,z} \cdot A \cdot \varepsilon_g \cdot \rho_g \cdot X_a$

Disperse in: $D \cdot A \cdot \varepsilon_g \cdot \dfrac{d}{dz}\left[\rho_g \cdot X_a + d(\rho_g \cdot X_a)\right]$

Tracer Out:

Carry out: $v_{g,z} \cdot A \cdot \varepsilon_g \cdot \rho_g \cdot X_a + d(v_{g,z} \cdot A \cdot \varepsilon_g \cdot \rho_g \cdot X_a)$

Disperse out: $D \cdot A \cdot \varepsilon_g \cdot \dfrac{d}{dz}(\rho_g \cdot X_a)$

Tracer Accumulated: $\dfrac{d(A \cdot dz \cdot \varepsilon_g \cdot \rho_g \cdot X_a)}{dt}$

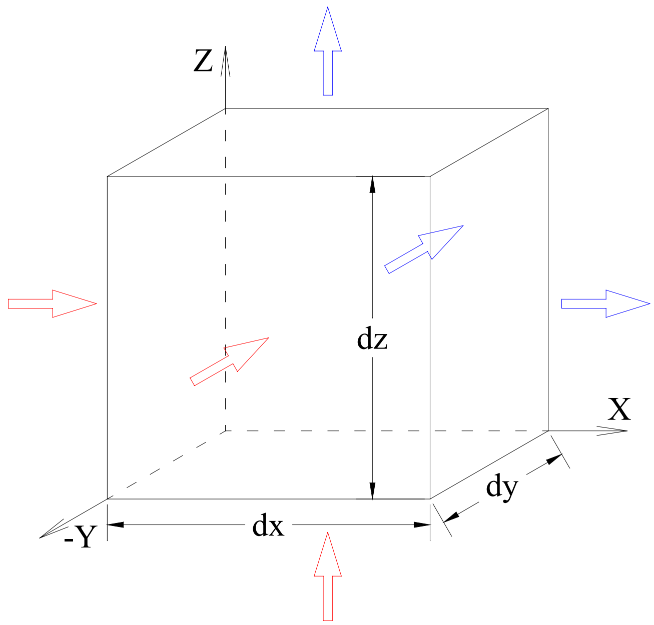

Fig. 6-16. A control volume in Cartesian coordinates.

Tracer Accumulated = Tracer In – Tracer Out

Considering that the bottom area of the control volume A and the height of the control volume dz can be defined as constants, as a result, the following general equation can be obtained:

$$\frac{d(A \cdot dz \cdot \varepsilon_g \cdot \rho_g \cdot X_a)}{dt} = -d(v_{g,z} \cdot A \cdot \varepsilon_g \cdot \rho_g \cdot X_a) + D \cdot A \cdot \varepsilon_g \cdot d\left[\frac{d(\rho_g \cdot X_a)}{dz}\right]$$

or $$\frac{d(\varepsilon_g \cdot \rho_g \cdot X_a)}{dt} + \frac{d(\varepsilon_g \cdot \rho_g \cdot v_{g,z} \cdot X_a)}{dz} - \frac{d}{dz}\left(\varepsilon_g \cdot \rho_g \cdot D \cdot \frac{d X_a}{dz}\right) = 0 \qquad (6\text{-}16)$$

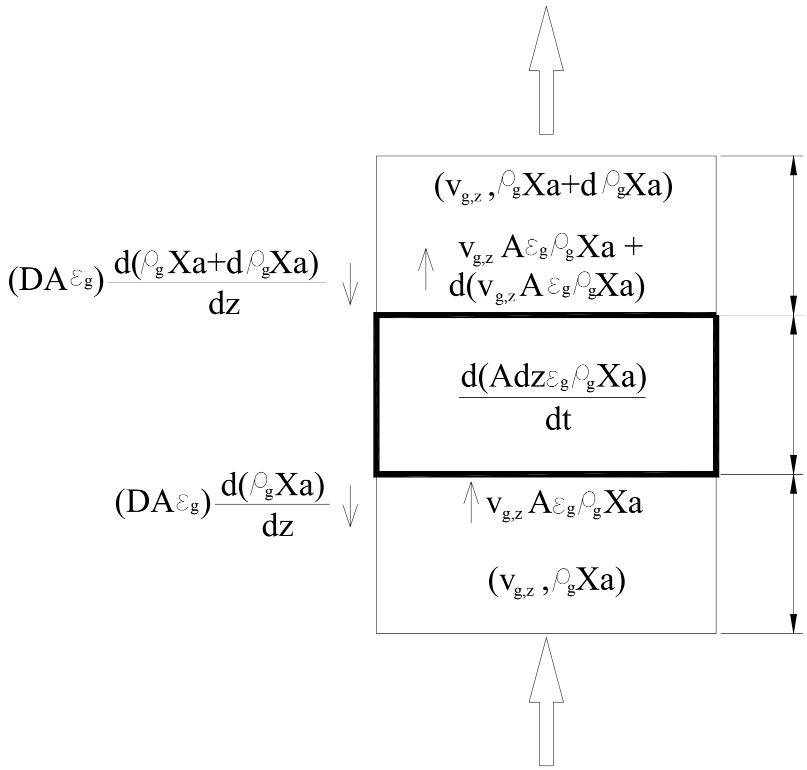

Fig. 6-17. Analysis of a control volume in the vertical direction.

A: Cross-section area, m^2

dz: Height of the control volume, m

D: Dispersion coefficient, m^2/s

$v_{g,z}$: Interstitial gas velocity, m/s

X_a: Mass fraction of the tracer gas

ε_g: Voidage

ρ_g: Gas density, kg/m^3

In X and Y directions, similar expressions can be obtained, and the general three-dimensional equation in Cartesian coordinates can be written as

$$\frac{\partial(\varepsilon_g \cdot \rho_g \cdot X_a)}{\partial t} + \nabla \cdot (\varepsilon_g \cdot \rho_g \cdot \overrightarrow{v_g} \cdot X_a) - \nabla \cdot [\varepsilon_g \cdot (\rho_g \cdot D) \cdot \nabla \cdot (X_a)] = 0 \tag{6-17}$$

Because the flow rate of the tracer is very small with a maximum helium volume fraction of 0.3% during experiments, the volume fraction of the helium is proportional to the mass fraction of the helium (During current experiments, molecular weights (or densities) of mixed gases at different compositions are constant.) as shown in Equation (6-18).

$$X_a = C_{He} \cdot \frac{\rho_{He}}{\rho_g} \tag{6-18}$$

where C_{He} is the volume fraction of helium, ρ_{He} is the density of helium.

As discussed before, using the negative step tracer input, the cumulative distribution function *F(t)* can be written as Equation (6-2). Considering the linear characteristics of Equations (6-2) and (6-18), as well as the assumed linear characteristics of the sampling probes, for convenience, the following pseudo positive step function curve (as shown in Figure 6-18) derived from experiments was used as the tracer input in the current simulation.

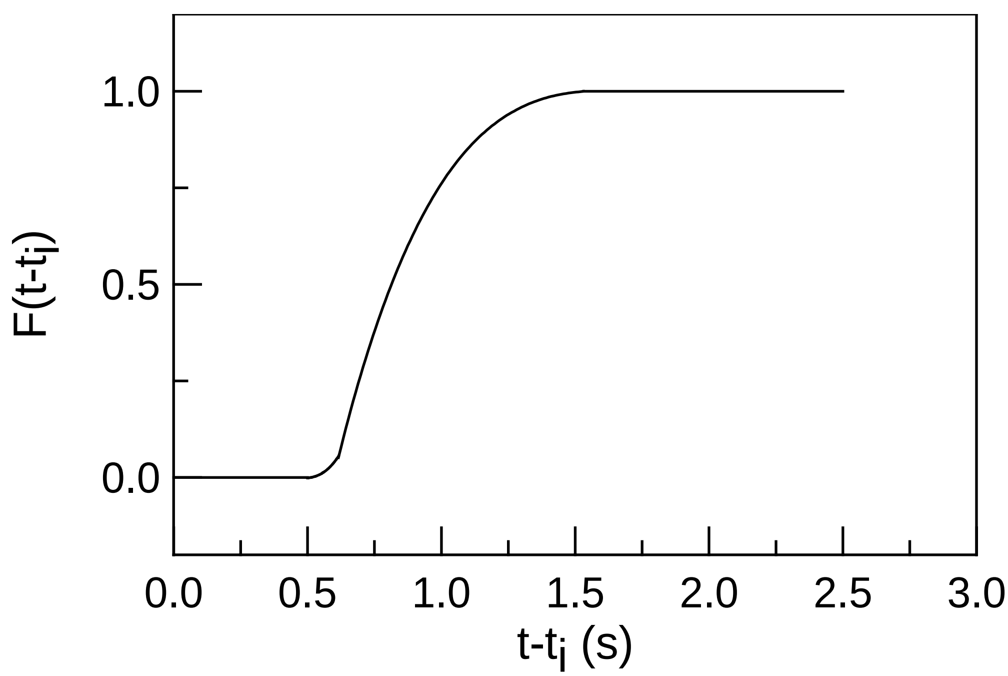

Fig. 6-18. The pseudo positive step input function. (t_i is the time when the tracer gas injection starts.)

Boundary conditions:

When $t-t_i<0$

$X_a=0$

When $t-t_i \geq 0$

$X_a=F(t-t_i)$ at the tracer inlet (Pseudo positive step function)

$\frac{\partial X_a}{\partial z}=0$ at the outlet

$\frac{\partial X_a}{\partial r}=0$ at the wall

Comparison with FLUENT:

In FLUENT, for an arbitrary scalar ϕ in the gas phase, the general User-Defined Scalar (UDS) transport equation has the following form:

$$\frac{\partial(\varepsilon_g \cdot \rho_g \cdot \phi)}{\partial t}+\nabla \cdot (\varepsilon_g \cdot \rho_g \cdot \overrightarrow{v_g} \cdot \phi)-\nabla \cdot [\varepsilon_g \cdot \Gamma \cdot \nabla \cdot (\phi)]=S_\phi \tag{6-20}$$

Comparing Equation (6-20) with Equation (6-17), the following relationships can be obtained:

$\phi=X_a$

$S_\phi=0$

$$\Gamma=\rho_g \cdot D \tag{6-21}$$

6.6.2 Simulation of gas mixing in a conical spouted bed

In order to simulate gas-mixing behaviour in a conical spouted bed, gas velocity field as well as the distribution of the voidage need to be calculated first. Thus, a conical spouted bed with the same geometrical dimensions and operating conditions as those in the experiments was simulated first. Simulation conditions are listed in Table 6-2 with boundary conditions given in Table 6-3.

Table 6-2. Simulation conditions for the conical spouted bed used in gas mixing experiment.

Description	**Value**	**Comment**
Operating gas velocity, U_i	23.5 m/s	Based on D_i
Gas density, ρ_g	1.23 kg/m^3	Air
Gas viscosity, μ_g	1.79×10^{-5} kg/(m·s)	Air
Particle density, ρ_s	2500 kg/m^3	Spherical glass beads
Particle diameter, d_s	1.16 mm	Uniform distribution
Initial solids packing, $\varepsilon_{s,0}$	0.61	Fixed value
Packing limit, $\varepsilon_{s,max}$	0.61	Fixed value
Solid viscosity, μ_s	Gidaspow	Eq. (5-7) + Eq. (5-9)
Frictional viscosity, $\mu_{s,fr}$	Schaeffer	Eq. (5-11)
Angle of internal friction, Φ	28°	Fixed value
Solid bulk viscosity (Base case), λ_s	0	Fixed value
Cone angle, γ	45°	Fixed value
Diameter of the upper section, D_c	0.45 m	Fixed value
Total height of the column	1.6 m	Fixed value
Gas inlet diameter, D_0	0.019 m	Fixed value
Diameter of the bed bottom, D_i	0.038 m	Fixed value
Static bed height, H_0	0.396 m	Fixed value
Solver	2 dimensional, double precision, segregated, unsteady, 1st order implicit, axisymmetric	
Multiphase Model	Eulerian Model, 2 phases	
Viscous Model	Laminar model	
Phase Interaction (Base case)	Fluid-solid exchange coefficient: Gidaspow Model Restitution coefficient: 0.9 (Du et al., 2006)	
Time steps (Final value)	2×10^{-5} s	Fixed value
Convergence criterion	10^{-3}	Default in FLUENT

Table 6-3. Boundary conditions for the conical spouted bed used in gas mixing experiment.

Description	**Comment**
Inlet	Radial distribution based on the actual Reynolds number used for the fluid phase
	No particles enter for the solid phase
Outlet	Uniform velocity distribution for the gas phase
	No particle exits for the solid phase
Axis	Axisymmetric
Wall	Non-slip for the fluid phase
	Zero shear stress for the solid phase

In the simulation, once stable spouting has been reached and the average gas velocity field and voidage distribution were calculated, a DEFINE_ON_DEMAND function named "average_field" was activated to pass the averaged gas velocity field and the voidage distribution to three User Defined Memories (UDMs) for further simulation of gas mixing behaviour. At the same time, the current time t_i was obtained. After changing t_i to the exact value just obtained, the User Defined Function was activated again. To achieve the negative step injection, the whole column should be patched with 1.0 (for the positive step injection, patched with 0.) for the User Defined Scalar (UDS) ϕ after it had been defined (including defining UDS and the corresponding dispersion coefficient), and corresponding boundary conditions should be defined too. To simulate gas mixing behaviour at the stable spouting state and save computation time, all equations were turned off except the newly defined UDS equation.

Figures 6-19 to 6-22 show the comparison between experimental and CFD simulation results on the mean residence time and Peclet number. It can be seen that the dispersion coefficient affects simulation results significantly, with better agreement between experimental and simulation results at D=0.0002m^2/s for the central spout region. Near the wall, simulation results underestimate the Peclet number greatly and overestimate the mean residence time significantly for all values of the dispersion coefficient investigated. With a small dispersion coefficient, CFD simulation gives a similar radial distribution curve on the Peclet number as that from the experiment. Figures 6-21 and 6-22 suggest that the difference between the CFD simulation and the experiment still cannot be resolved even using different values of the dispersion coefficient for the spout and the annulus. Moreover, neglecting the dispersion (D=0.0), the difference between the CFD simulation and the experiment near the wall (r=0.180m) still exists, suggesting that gas convection is the dominant factor near the wall, and that the simulated gas velocity is lower near the wall (or higher in the spout) than in the experiment.

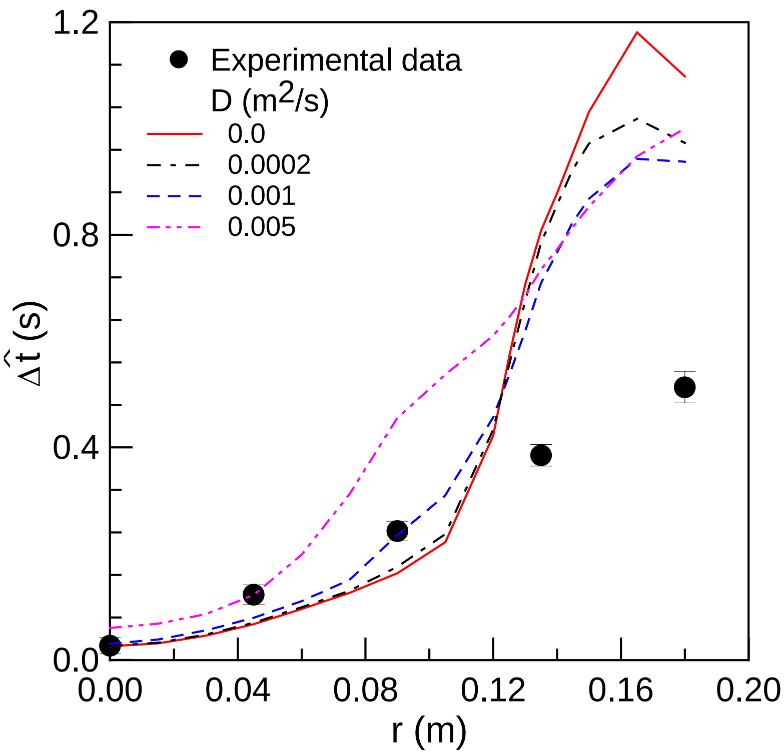

Fig. 6-19. Comparison between the experiment and simulation on the mean residence time. (Symbols are experimental data, lines are simulation results, **full column, stable spouting**, U_i=23.5 m/s.)

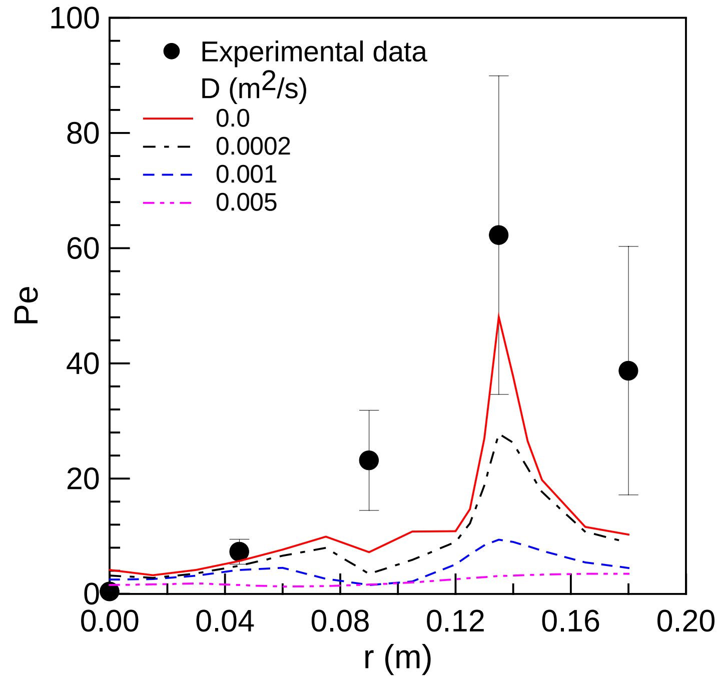

Fig. 6-20. Comparison between the experiment and simulation on the Peclet number. (Symbols are experimental data, lines are simulation results, **full column, stable spouting**, U_i=23.5 m/s.)

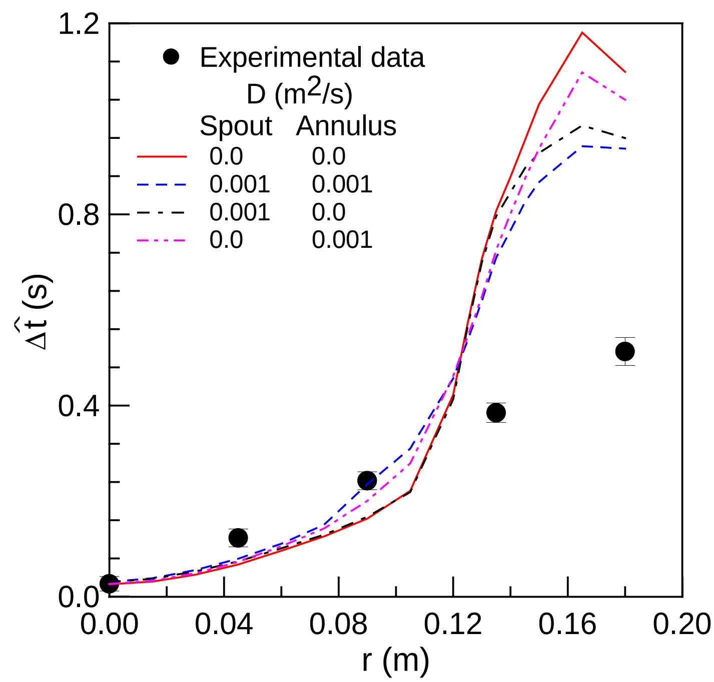

Fig. 6-21. Comparison between the experiment and simulation on the mean residence time. (Symbols are experimental data, lines are simulation results, **full column, stable spouting**, U_i=23.5 m/s.)

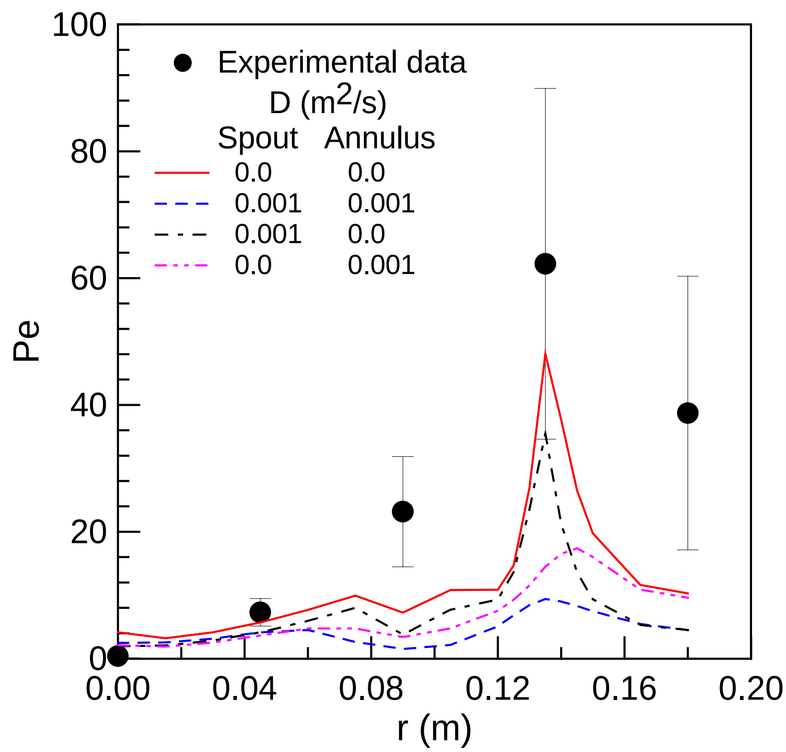

Fig. 6-22. Comparison between the experiment and simulation on the Peclet number. (Symbols are experimental data, lines are simulation results, **full column, stable spouting**, U_i=23.5 m/s.)

Since both simulated mean residence time and Peclet number did not match experimental data, it is important to evaluate the effect of the radial distribution of axial gas velocities.

Figure 6-23 shows some axial superficial gas velocity profiles obtained from the CFD simulation and modified with increased flow rate in the annulus region in order to shorten the residence time. To maintain the overall mass flow balance, gas velocities are reduced in the spout region in order to compensate the increase in the annulus region.

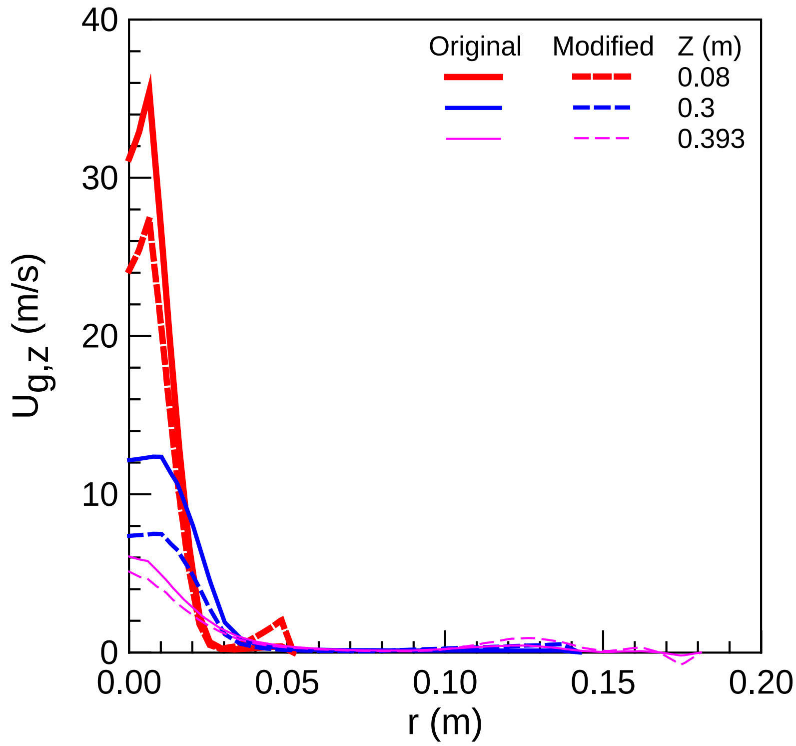

Fig. 6-23. Comparison of axial superficial gas velocity profiles before and after the modification. (Solid lines correspond to the original profiles from the CFD simulation, dashed lines correspond to the modified profiles, **full column, stable spouting**, U_i=23.5 m/s)

Figures 6-24 and 6-25 show the effect of gas velocity field on the CFD simulated mean residence time and Peclet number. It can be seen that, after the modification on the axial superficial gas velocity profile, the radial distribution of the mean residence time becomes much closer to experimental data, implying that gas velocity field is the main factor that affects simulation results on the gas mixing behaviour, although the agreement with the radial distribution of the Peclet number improves very little.

Analysis of distribution curve of the Peclet number:

As shown in Figures 6-13, 6-20, 6-22 and 6-25, the Peclet number has a maximum value near r=0.135m. By checking gas velocity profiles shown in Figure 6-23, it is found that, in the annulus region, there exists a maximum gas velocity near r=0.135m. Based on the definition of the Peclet number, the Peclet number is proportional to gas velocity and the stream tube length. With increase in radial distance from the center, the stream tube length tends to increase but the velocity decrease. Therefore, for a constant dispersion coefficient, the Peclet number may reach a maximum if there is a maximum velocity in the annulus region. Further analysis is needed in the future to investigate the variation of dispersion coefficient at different radial positions.

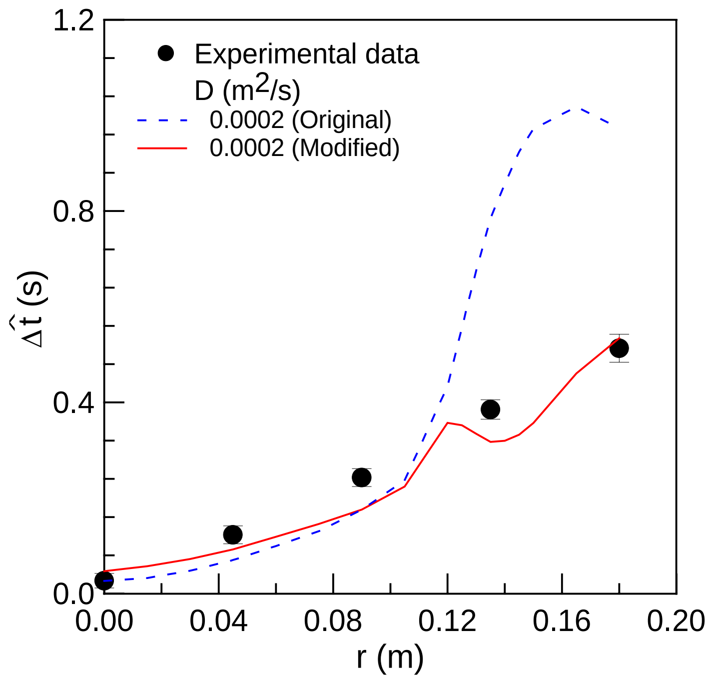

Fig. 6-24. Comparison between the experiment and simulation on the mean residence time. Symbols are experimental data, lines are simulation results, **full column, stable spouting**, U_i=23.5 m/s.)

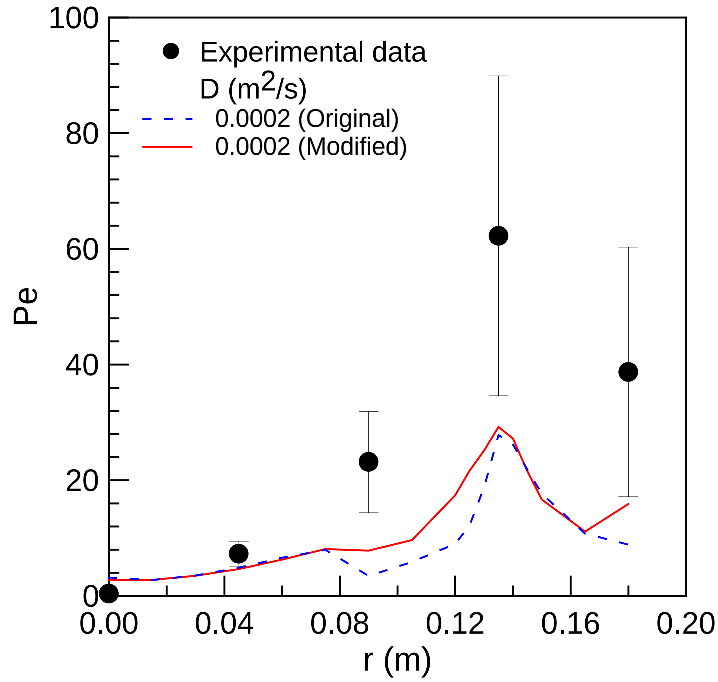

Fig. 6-25. Comparison between the experiment and simulation on the Peclet number. (Symbols are experimental data, lines are simulation results, **full column, stable spouting**, U_i=23.5 m/s.)

CHAPTER 7

CONCLUSIONS AND RECOMMENDATIONS

7.1 Conclusions

A comprehensive hydrodynamic study has been successfully carried out on conical spouted beds. Two mathematical models were developed to predict the evolution of the overall gauge pressure and internal spout, as well as local flow structures in conical spouted beds under both partial spouting and stable spouting states. The models were evaluated using experimental data. Experimental measurements on the evolution of the internal spout, gauge pressure distribution, particle velocity distribution, voidage distribution and gas mixing were conducted. The following conclusions can be drawn from this study.

- The hysteresis of the pressure evolution and the step change of the pressure drop around the minimum spouting velocity tend to be more pronounced in deep beds with large included cone angles and small inlet orifice diameters. This conclusion explains why the “hysteresis” phenomenon of the minimum spouting velocity was not reported in most previous studies using conical spouted beds with short static bed heights and large inlet orifice diameters.
- There is only a small difference between the half column and the full column on measured pressure drops with increasing superficial gas velocity and decreasing superficial gas velocity. Minimum spouting velocities determined by evolution curves of the pressure drop in both half and full columns are almost identical whether superficial gas velocity is increased or decreased. Therefore, the minimum spouting velocity obtained from a semi-circular conical spouted bed can represent the full circular conical spouted bed with the same

values of D_0, H_0, γ.

- Empirical correlations were developed for the minimum spouting velocity, the total pressure drop at stable spouting and the height of the internal spout with decreasing superficial gas velocity. The error between predictions and experimental data for the minimum spouting velocity is lower than 10%, and for the total pressure drop and the height of the internal spout is around 20%.
- For conical spouted beds, the longitudinal pressure profiles at stable spouting states are close to the quarter cosine function as in cylindrical spouted beds. However, the longitudinal pressure profiles deviate from the quarter cosine function considerably under partial spouting states.
- The gauge pressure at each height in the annulus decreases almost linearly with increasing radial distance from the centre of the column.
- The proposed stream-tube model is capable of predicting the total pressure drop ΔP_t under different operating conditions, and estimating the distribution of the axial superficial gas velocity and the gauge pressure, especially for the descending process as well as in the pseudo fluidized bed and upper packed bed regions.
- There are many factors that might affect calibration of the effective distance of optical fibre probes. **Firstly**, the glass window has a most significant impact on the probe design. **Secondly**, there are a lot of uncertainties using a rotating plate without particles glued. When the rotating plate with particles glued is used, calibrated effective distance appears to be reasonable, although the effect of the background may need to be considered. The use of a rotating packed bed seems to be the best way to calibrate the probe. **Thirdly**, to obtain a reliable effective distance, it is best to use the same particles as will be used in actual

experiments to calibrate the optical fibre probe. **Finally**, an optical fibre probe may not be suitable for all kinds of particles, and a comprehensive sensitivity analysis on calibration results should be carried out for individual particles before the probe is applied.

- Comparing the half column and the full column, overall particle velocity profiles are quite similar. Because of the existence of the front flat plate in the half column, measured solids velocities near the front flat plate are somehow lower than those in the full column. Furthermore, the shapes of the spout and the fountain are quite similar based on the position of the interface between the spout and the annulus as well as the interface between the upward moving section and the downward moving section in the fountain region.
- The proposed CFD model can simulate both packed beds and fluidized beds very well in one code package, and give much accurate results on the minimum fluidization velocity, as well as the whole pressure evolution loop (both ascending and descending process).
- Referring to the literature about CFD simulations on spouted beds, this is the first time that the radial distribution of the static pressure was used to evaluate CFD simulations. Among all factors investigated, the actual pressure gradient in conical spouted beds (the **APG** term, **presented as the sum of the axial solid phase source term and the default gravity term**) has the most significant influence on static pressure profiles.
- For complex systems such as conical spouted beds, the proposed CFD model shows a great potential to improve the CFD simulation. The proposed CFD model may be applied to other systems with the actual pressure gradient different from either fluidized beds or packed beds.
- Helium tracer experiments clearly show that there are radial distributions of gas velocity inside a conical spouted bed with a higher velocity in the centre and lower near the wall. There exists a maximum value of Peclet number at r=0.135m. Meanwhile, the gas mixing in

the ascending process is different from that in the descending process, implying that the radial distribution of gas velocity is different too, even though operating velocities are almost identical.

- The gas mixing was also simulated using the proposed CFD model. It was found that, with smaller dispersion coefficient, CFD simulation gives a similar radial distribution curve on the Peclet number as that from the experiment. The difference between the CFD simulation and the experiment cannot be eliminated using different values of the dispersion coefficient for the spout and the annulus. By adjusting the calculated gas velocity field, the radial distribution of the mean residence time becomes much closer to experimental results, proving that gas velocity field is the main factor that affects simulation results on gas mixing behaviour, although the radial distribution of the Peclet number improves only a little.

7.2 Recommendations for future work

- The direct measurement of gas velocity field is needed. Up to now, the axial superficial gas velocity field inside a spouted bed was estimated mainly based on all kinds of assumptions, such as the Ergun equation applied by He (1995) to calculate the axial superficial gas velocity in the annulus. Based on the current study, the annulus and the region above the internal spout are far from packed beds. Furthermore, as shown in Chapter 3, using different assumptions, calculated results on the gauge pressure and the axial superficial gas velocity are quite different. It is also found from Chapter 6 that, using the CFD simulation, calculated mean residence time near the wall overestimates experimental results significantly, implying that the calculated gas velocity field near the wall underestimates that of the actual experiment greatly.

- Measurements of the axial particle velocity inside cylindrical spouted beds are needed, because most literature data were measured using optical fibre probes without a glass window attached to the probe tip, which has been shown to be a main factor causing measurement errors.
- To minimize the effect of the optical fibre probe on the local velocity field for both solid and fluid phases, smaller optical fibre probes should be used in future studies to investigate the effect of the probe size.
- In **the spout region** and the **fountain region**, the movement of particles is quite complex. Particles are first **accelerated** near the inlet region, and then **decelerated** in the fountain region. Currently both the spout and the fountain regions are simulated using the default fluidized bed code (k_s=1); thus, some considerations are needed to account for the acceleration and deceleration effects using improved drag models.
- The further evaluation of current CFD simulations for conical spouted beds is needed using directly measured axial gas velocity data.
- The evaluation of the proposed CFD model for cylindrical spouted beds is still needed using newly measured axial particle velocity data in cylindrical spouted beds.
- The proposed CFD model can be extended to simulate the performance of conical spouted bed reactors or dryers with the incorporation of reaction kinetics or drying kinetics.

NOMENCLATURE

a	Constant, theoretically, a=1.0, (V)
A	$A = 150 \frac{(1-\varepsilon_g)^2}{\varepsilon_g^3} \frac{\mu_g}{(\varphi_s d_s)^2}$, parameter in the Ergun equation
A_0	Cross-section area of the fluidized bed, (m^2)
A_j	Electrical signal series from light receiver A, j=1, 2, ……, M_e, (V)
$A_{L,i}$	Cross section area at the length of L for stream tube i, i=1,……,N, (m^2)
A_o	$A_o = d_o(830 - 5000\beta_o + 9000\beta_o^2 - 4200\beta_o^3 + B_o)$, (inch)
Ar	Archimedes number, $Ar = \frac{g d_s^3(\rho_s - \rho_g)\rho_g}{\mu_g^2}$, (-)
b_o	$b_o = 0.5993 + \frac{0.007}{d_{tube}}$, (-)
B	$B = 1.75\left(\frac{1-\varepsilon_g}{\varepsilon_g^3}\right)\frac{\rho_g}{\varphi_s d_s}$, parameter in the Ergun equation
B_j	Electrical signal series from light receiver B, j=1, 2, ……, M_e, (V)
B_o	$B_o = \frac{530}{\sqrt{d_{tube}}}$, (-)

C_0	Initial volume fraction of helium in air, (%v/v)
C_D	Drag coefficient, (-)
C_{He}	Volume fraction of helium in air, (%v/v)
d	Distance between the probe tip and the surface of the rotated plate or rotated packed bed, (mm)
d_o	Throat diameter or the orifice diameter, (inch)
dP	Pressure drops, (Pa)
dP_0	Pressure drop over the orifice plate, (Pa)
$dP_{0,s}$	Pressure drop over the standard orifice plate, (Pa)
dP_i	Pressure drop at different locations (i=2, 3, 4, 5, 6, and t) along the bed, (Pa)
$(dP_t)_{max,a}$	Maximum value among total pressure drops during ascending U_i, (Pa)
$(dP_t)_{max,d}$	Maximum value among total pressure drops during descending U_i, (Pa)
d_s	Particle diameter, (m or mm)
d_{spot}	Diameter of white spots on rotated plates, (mm)
d_{tube}	Diameter of the tube/pipe connected to the orifice meter, (inch)
D	Dispersion coefficient, (m^2/s)
D_0	Gas inlet diameter, (m)

D_1	Geometric distance between two central points formed by the light projector and each light receiver, (mm)
D_2	Geometric central distance between two light receivers, D_2=2D_1, (mm)
D_b	Diameter at the static bed height, (m)
D_c	Diameter of the cylindrical section, (m)
D_e	Effective distance calibrated through experiments, (mm)
D_f	Diameter of each fibre group, (mm)
D_i	Diameter of the bed bottom, (m)
D_{probe}	Diameter of the optical fibre probe, (mm)
D_s	Diameter of the spout, (m)
e_{ss}	Restitution coefficient, (-)
E(t)	RTD function
f	Drag force, (N)
f_s	Sampling frequency, (1/s)
F_g	Gas mass flow rate, kg/h
F(t)	Cumulative distribution function
g	Gravitational acceleration in axial direction, g=9.81, (m/s^2)

$\vec{g}$ — Vector of the gravitational acceleration, in axial direction, the value is -9.81 m/s^2; in radial direction, the value is zero, (m/s^2)

$g_{0,ss}$ — Radial distribution function

h_0 — Distance from the apex of the cone to the bottom of the bed (Figure 3-26), (m)

H_0 — Static bed height, (m)

$H_{0,1}$ — Static bed height, (m)

$H_{0,2}$ — Static bed height, (m)

H_c — Height of the cone section, (m)

$H_{c,1}$ — Height of the cone section, (m)

$H_{c,2}$ — Height of the cone section, (m)

H_f — Height of the fountain, (m)

I_{2D} — Second invariant of the deviatoric stress tensor

k — Ratio of the pressure drop for any columns over a fluidized bed with the same static bed height, $k = \dfrac{\nabla P}{\nabla P_{fb}}$, (-)

k_a — Value of the factor *k* in the annulus, (-)

$k_{a,r}$ — Local values of the factor *k* in the annulus, (-)

k_{fb} Ratio for fluidized beds, $k_{fb} = \frac{\nabla P_{fb}}{\nabla P_{fb}}$, theoretically, $k_{fb} = 1.0$, (-)

k_{oa} Overall average value of the factor k, the ratio of the total pressure drop of the spouted bed to the pressure drop of a fluidized bed with the same static bed height, $k_{oa} = \frac{\Delta P_s}{\Delta P_{fb}}$, (-)

$(k_{oa})_{ms,d}$ Ratio of the total pressure drop at minimum spouting over the total pressure drop of a fluidized bed with the same static bed height, (-)

k_p Constant, different from pressure transducers in different scales, (Pa/V)

k_{pb} Pressure drop ratio for packed beds, $k_{pb} = \frac{\nabla P_{pb}}{\nabla P_{fb}}$, (-)

k_s Value of the factor k in the spout and fountain region, (-)

K Parameter used in equation 3-48, (-)

K_e Orifice discharge coefficient when $Re=(Re)_e$, (-)

$K_{gs}=K_{sg}$ Momentum exchange coefficient between gas phase g and solid phase s

K_o Orifice discharge coefficient, (-)

K' $K' = K_o(\pi d_o^2)\sqrt{\frac{2R_0}{M_g}}$

l_i Length of streamline i, i=1,……,N, (m)

L	Length at the stream tube, (m)
$L_{1,i}$	Length of stream tube i, i=1, 2,……,N, (m)
$L_{2,i}$	Length of stream tube i in packed bed region, i=1, 2,……,N, (m)
L_{gap}	Gap between every two white spots on the same ring on rotating plates, (mm)
L_i	Length at the stream tube i, (m)
L_m	$\tau = \frac{L_m}{f_s}$, corresponding to the maximum correlation coefficient and the minimum time delay, (-)
m_g	Mass of gas, (kg)
M_e	Length of series A_j and B_j, (-)
Mg	Molecular weight of the gas, (kg/mol)
n	Total number of phases, and n=2 in current simulations, (-)
n_o	$n_o = 0.364 + \frac{0.076}{\sqrt{d_{tube}}}$, (-)
N	Number of stream tubes, (-)
N_e	Length of series x_i and y_i, (-)
n_g	Number of moles, (mol)
P	Static gauge pressure, (Pa)

P_0	Pressure just before the orifice plate, (Pa)
$P_{0,s}$	Pressure just before the standard orifice plate, (Pa)
P_i	Static gauge pressure at different locations (i=2, 3, 4, 5, 6, and t) along the bed, (Pa)
P_a	Atmospheric pressure, P_a=101325, (Pa)
P_{cal}	Simulation results on the static gauge pressure, (Pa)
P_{exp}	Experimental data on the static gauge pressure, (Pa)
Pe	Peclet number, $Pe=\frac{u_g \cdot \mathrm{L}}{\mathrm{D}}$, (-)
P_g	Operating pressure or gas pressure, (Pa)
P_s	Solid pressure, (Pa)
P_w	Static gauge pressure near the wall, (Pa)
Q	Volumetric flow rate, (m^3/s)
$Q_{i,}$	Volumetric flowrate of gas in stream tube i, i=1,……,N, (m^3/s)
r	Radial coordinate, (m)
r_0	Radius of the gas inlet, (m)
$r_0^{'}$	Radius of the top spherical cap of the internal spout when $0<Z_s<r_0$, (m)

r_i Radius of the bed bottom, (m)

r_j Radial distance from partition point j to the centre of the bed on the bed surface, j=1,……,N, (m)

r_p Radial distance between the centre of the optical fibre probe and the centre of the rotating plate or rotating packed bed, (mm)

$r_{s,in}$ Radius of the top half sphere in an internal spout, (m)

R Radius at height Z, (m)

R_0 Gas constant, R_0=8.3145, (J/(mol·K))

R_b Radius of the bed surface, (m)

Re Reynolds number based on the diameter of the orifice, $\mathrm{Re} = \frac{\rho_g U_o d_o}{\mu_g}$, (-)

$(\mathrm{Re})_e$ $(\mathrm{Re})_e = \frac{10^6 d_o}{15}$, (-)

$(\mathrm{Re}_0)_1$ Particle Reynolds number based on $U_{0,1}$, $(\mathrm{Re}_0)_1 = \frac{\rho_g U_{0,1} d_s}{\mu_g}$, (-)

$(\mathrm{Re}_0)_{ms,a}$ Particle Reynolds number based on $(U_0)_{ms,a}$, $(\mathrm{Re}_0)_{ms,a} = \frac{\rho_g (U_0)_{ms,a} d_s}{\mu_g}$, (-)

$(\mathrm{Re}_0)_{ms,d}$ Particle Reynolds number based on $(U_0)_{ms,d}$, $(\mathrm{Re}_0)_{ms,d} = \frac{\rho_g (U_0)_{ms,d} d_s}{\mu_g}$, (-)

$(Re_b)_{ms,a}$ Particle Reynolds number based on $(U_b)_{ms,a}$, $(\mathrm{Re}_b)_{ms,a} = \frac{\rho_g (U_b)_{ms,a} d_s}{\mu_g}$, (-)

Re_s Relative particle Reynolds number, $\mathrm{Re}_s = \frac{\rho_g d_s |\vec{v}_s - \vec{v}_l|}{\mu_g}$, (-)

Re_t Particle Reynolds number based on U_t, $\mathrm{Re}_t = \frac{\rho_g U_t d_s}{\mu_g}$, (-)

R_{xy} Correlation coefficient, (-)

$S_{s,z}$ Axial solid phase source term in the axial solid phase moment equation, (N/m^3)

$\vec{S}_s$ Vector of the solid phase source term in solid phase moment equations, (N/m^3)

Sx Standard deviation of x_i, $S_x = \sqrt{\frac{1}{N_e - 1} \sum_{i=1}^{N_e} (x_i - \overline{x})^2}$, (V)

S_y Standard deviation of y_i, $S_y = \sqrt{\frac{1}{N_e - 1} \sum_{i=1}^{N_e} (y_i - \overline{y})^2}$, (V)

S_ϕ Source term in the User-Defined Scalar (UDS) transport equation, ($kg/(m^3 \cdot s)$)

t Time, (s, ms)

t_0 Time difference between the start of sampling and the start of response, (s)

$t_{0,1}$ Time difference between the start of sampling and the start of response for probe 1, (s)

$t_{0,2}$	Time difference between the start of sampling and the start of response for probe 2, (s)
t_i	Time starting the injection of tracer gas, (s)
$\hat{t}$	Mean residence time, (s)
$\hat{t}_{p1}$	Mean residence time for the electric signal from probe 1 itself, (s)
$\hat{t}_{p2}$	Mean residence time for the electric signal from probe 2 itself, (s)
$\hat{t}_{t1}$	Mean residence time for the total electric signal from probe 1 at the gas inlet, (s)
$\hat{t}_{t2}$	Mean residence time for the total electric signal from probe 2 at the bed surface, (s)
T	Absolute temperature, (K)
u_g	Interstitial gas velocities, (m/s)
U_0	Superficial gas velocity based on D_0 at standard conditions, (m/s)
$U_{0,1}$	Superficial gas velocity based on D_0, which corresponds to the velocity of the formation of internal spout, (m/s)
$U_{0,2}$	Superficial gas velocity based on D_0, which corresponds to the velocity of the carry off of particles out of the bed, (m/s)
$(U_0)_{ms}$	U_{ms} based on D_0, (m/s)

$(U_0)_{ms,a}$	U_{ms} based on D_0 with ascending superficial gas velocity, (m/s)
$(U_0)_{ms,d}$	U_{ms} based on D_0 with descending superficial gas velocity, (m/s)
$(U_b)_{ms,a}$	U_{ms} based on D_b with ascending superficial gas velocity, (m/s)
U_c	Superficial gas velocity based on D_c, (m/s)
U_g	Superficial gas velocities, (m/s)
$U_{g,z}$	Local axial superficial gas velocities, (m/s)
U_i	Superficial gas velocity based on D_i, (m/s)
$U_{i,a}$	Superficial gas velocity based on D_i during ascending process, (m/s)
$U_{i,d}$	Superficial gas velocity based on D_i during descending process, (m/s)
$(U_i)_{ms,a}$	U_{ms} based on D_i , determined from ascending U_i, (m/s)
$(U_i)_{ms,d}$	U_{ms} based on D_i, determined from descending U_i, (m/s)
$(U_i)_{ms,F}$	U_{ms} in circular columns based on D_i, (m/s)
$(U_i)_{ms,H}$	U_{ms} in semi-circular columns based on D_i, (m/s)
$U_{L,i}$	Superficial gas velocity at the length L of stream tube i, i=1,……,N, (m/s)
U_{mf}	Minimum fluidization velocity, (m/s)
U_{ms}	Minimum spouting velocity, (m/s)
U_o	Gas velocity through the orifice, (m/s)

U_t	Terminal settling velocity, (m/s)
$v_{g,z}$	Local axial interstitial gas velocity, (m/s)
V	Magnitude of the measured electrical signal, (V)
V_0	Average magnitude of the electrical signal corresponding to C_{He}=C_0, (V)
V_∞	Average magnitude of the electrical signal corresponding to C_{He}=0, (V)
V_b	Voltage corresponding to original clear glass beads at the loosely packed state $\varepsilon_{s,0}$, (V)
V_c	Voltage corresponding to colored glass beads at the loosely packed state, theoretically, for black glass beads, or fluid such as air, $V_c = 0$, (V)
$V_{c,max}$	Voltage corresponding to C_{He}=0.3%, (V)
$V_{c,min}$	Voltage corresponding to C_{He}=0, (V)
$V_{e,0}$	Magnitude of the measured electrical signal corresponding to the minimum solids fraction ($\varepsilon_s = 0$),(V)
$V_{e,max}$	Magnitude of the measured electrical signal corresponding to the maximum solids fraction ($\varepsilon_{s,0}$),(V)
V_g	Gas volume, (m^3)
$\vec{v}_q$	Vector of the velocity of phase *q*, *q* could be gas phase *g* and solid phase *s*, (m/s)

V_s Axial particle velocity, (m/s)

$V_{s,cal}$ Simulation results on the axial solids velocity, (m/s)

$V_{s,exp}$ Experimental data on the axial solids velocity, (m/s)

W Weight of glass beads, (kg)

$\overline{x}$ Average value of x_i, $\overline{x} = \frac{1}{N_e} \cdot \sum_{i=1}^{N_e} x_i$, (V)

x_i Electrical signal series 1 derived from A_j, $x_i = A_{K_e+i}$, i=1, 2, ……, N_e, (V)

X_a Mass fraction of the tracer gas, (-)

X_b Volume fraction for original clear glass beads, (-)

X_c Volume fraction for colored glass beads, (-)

$\overline{y}$ Average value of y_i, $\overline{y} = \frac{1}{N_e} \cdot \sum_{i=1}^{N_e} y_i$, (V)

y_i Electrical signal series 1 derived from B_j, $y_i = B_{K_e+L_e+i}$, i=1, 2, ……, N_e, (V)

Y Mass fraction for original clear glass beads, (-)

Z Axial coordinate, (m)

Z_a Height of the internal spout in the ascending process, (m)

Z_d Height of the internal spout in the descending process, (m)

$Z_{pf,i}$	Vertical distance between the bed bottom and the interface of the pseudo fluidized bed region and the packed bed region in stream tube i, i=1,……,N, (m)
Z_s	Height of the internal spout, (m)
Z_{sm}	Maximum height of the internal spout determined from descending U_i, (m)
Z_{sp}	Maximum height of the internal spout determined from ascending U_i, (m)

Greek letters

α_1	Angle between the central axis and the first streamline, (º)
α_i	Angle between every two adjacent streamlines, i=2,……,N, (º)
β	Angle between lines CO and OO' in Figure 3-34, $\beta = a\tan(\frac{r_{s,in}}{h_0 + Z_s - r_{s,in}})$, (º)
β_o	Diameter ratio, (-)
$\theta = \frac{(t-t_0)}{\hat{t}}$	Dimensionless time, (-)
Θ_s	Granular temperature, (m^2/s^2)
δ_i	Angle between the centre of each stream tube and the central axis of the bed, i=1,……,N, (º)
ΔP	Pressure drop, (Pa)
ΔP_{fb}	pressure drop for fluidized bed region, (Pa)

$\Delta P_{fb,i}$	Pressure drop for fluidized bed region in stream tube i, i=1,……,N, (Pa)
ΔP_{max}	Maximum pressure drop, (Pa)
ΔP_{pb}	Pressure drop for packed bed region, (Pa)
$\Delta P_{pb,i}$	Pressure drop for packed bed region in stream tube i, i=1,……,N, (Pa)
ΔP_{pfb}	Pressure drop for pseudo fluidized bed region, (Pa)
$\Delta P_{pfb,i}$	Pressure drop for pseudo fluidized bed region in stream tube i, i=1,……,N, (Pa)
ΔP_s	Pressure drop of a spouted bed, (Pa)
$(\Delta P_s)_{ms,d}$	Pressure drop at minimum spouting, determined from descending U_i, (Pa)
$(\Delta P_s)_{sp}$	Pressure drop at stable spouting, (Pa)
ΔP_t	Total pressure drop, (Pa)
Δt	Time lag, (s)
$\Delta\hat{t}$	Mean residence time inside the conical spouted bed, (s)
Δt_{inlet}	Time lag at the gas inlet, (s)
Δt_p	Time lag between two probes, (s)
$\Delta\sigma_t^2$	Variance corresponds to $\Delta\hat{t}$, (s^2)
ε_g	Voidage, (-)

$\varepsilon_{g,0}$	Loosely packed voidage, (-)
ε_q	Volume fraction of phase *q*, *q* could be gas phase *g* and solid phase *s*, (-)
ε_s	Solids fraction, (-)
$\varepsilon_{s,0}$	Loosely packed solids fraction, (-)
$\varepsilon_{s,cal}$	Simulation results on the solids fraction, (-)
$\varepsilon_{s,exp}$	Experimental data on the solids fraction, (-)
$\varepsilon_{s,\max}$	Maximum solids fraction or packing limit, (-)
ε_{ms}	Voidage of the bed at minimum spouting, (-)
ϕ	Arbitrary scalar in the gas phase, (-)
Φ	Angle of internal friction, (º)
φ_s	Particel sphericity, (-)
γ	Cone angle, (º)
γ_i	Angle between lines ABO and A'B'O which does not include the dead zone in Figure 3-34, (º)
γ_j	Angle of the internal spout as shown in Figure 3-34, (º)
λ_q	Bulk viscosity of phase *q*, *q* can be gas phase *g* or solid phase *s*, (kg/(m·s))

Γ	Diffusion coefficient, $\Gamma = \rho_g \cdot D$, (kg/(m·s))
μ_g	Gas viscosity, (Pa · s)
μ_q	Viscosity of phase *q*, *q* can be gas phase *g* or solid phase *s*, (kg/(m·s))
$\mu_{s,col}$	Solid collisional viscosity, (kg/(m·s))
$\mu_{s,fr}$	Solid frictional viscosity, (kg/(m·s))
$\mu_{s,kin}$	Solid kinetic viscosity, (kg/(m·s))
$\rho_{g,st}$	Density of air at standard conditions, (kg/m^3)
ρ_{He}	Density of helium, (kg/m^3)
ρ_g	Density of the gas phase, (kg/m^3)
ρ_s	Density of particles, (kg/m^3)
$\sigma^2 = \frac{\sigma_t^2}{\hat{t}^2}$	Variance corresponding to $\theta = \frac{(t - t_0)}{\hat{t}}$, (-)
σ_t^2	Variance corresponding to $\hat{t}$, (s^2)
$\sigma_{t,p1}^2$	Variance corresponding to $\hat{t}_{p1}$, (s^2)
$\sigma_{t,p2}^2$	Variance corresponding to $\hat{t}_{p2}$, (s^2)
$\sigma_{t,t1}^2$	Variance corresponding to $\hat{t}_{t1}$, (s^2)

$\sigma^2_{t,t2}$ Variance corresponding to $\hat{t}_{t2}$, (s^2)

τ Time delay between two signals from two light receivers, (ms)

$\overline{\overline{\tau}}_g$ Gas phase stress-strain tensor, (Pa)

τ_p Particulate relaxation time, (s)

$\overline{\overline{\tau}}_s$ Solid phase stress-strain tensor, (Pa)

ω_{fb} Weighting factor that shows the similarity to a fluidized bed, ω_{fb}=1 means the operating state can be treated as a fluidized bed; ω_{fb}=0 means a packed bed, usually, 0<ω_{fb}<1, (-)

∇P Axial pressure gradient, (Pa/m)

∇P_{fb} Axial pressure gradient at fluidization state, (Pa/m)

∇P_{pb} Axial pressure gradient at packed bed state, (Pa/m)

∇P_s Solids pressure gradient, (Pa/m)

Subscripts:

cal Calculated results or simulation results

exp Experimental results

fb Fluidized bed

fit Fitted results

max	Maximum value
min	Minimum value
ms	Minimum spouting
pb	Packed bed
pfb	Partial fluidized bed

REFERENCES

Aguado, R.; Prieto, R.; San Jose, M. J.; Alvarez, S.; Olazar, M.; Bilbao, J., "Defluidization modelling of pyrolysis of plastics in a conical spouted bed reactor", Chemical Engineering and Processing, 44(2), 231-235 (2005).

Aguado, R.; Olazar, M.; Gaisan, B.; Prieto, R.; Bilbao, J., "Kinetics of polystyrene pyrolysis in a conical spouted bed reactor", Chemical Engineering Journal (Amsterdam, Netherlands), 92(1-3), 91-99 (2003).

Aguado, R.; Olazar, M.; San Jose, M. J.; Gaisan, B.; Bilbao, J., "Wax Formation in the Pyrolysis of Polyolefins in a Conical Spouted Bed Reactor", Energy & Fuels, 16(6), 1429-1437 (2002a).

Aguado, R.; Olazar, M.; Gaisan, B.; Prieto, R.; Bilbao, J., "Kinetic Study of Polyolefin Pyrolysis in a Conical Spouted Bed Reactor", Industrial & Engineering Chemistry Research, 41(18), 4559-4566 (2002b).

Aguado, R.; Olazar, M.; San Jose, M. J.; Aguirre, G.; Bilbao, J., "Pyrolysis of sawdust in a conical spouted-bed reactor. Yields and product composition", Ind. Eng. Chem. Res., 39(6), 1925-1933 (2000a).

Aguado, R.; Olazar, M.; Barona, A.; Bilbao, J., "Char-formation kinetics in the pyrolysis of sawdust in a conical spouted bed reactor", J. Chem. Technol. Biotechnol., 75(7), 583-588 (2000b).

Al-Jabari, M.; Weber, M. E.; van de Ven, T. G. M., "Particle elutriation from a spouted bed of recycled pulp fibers", J. Pulp Pap. Sci., 22(7), J231-J236 (1996).

Arastoopour, H. and Yang, Y., "Experimental studies on dilute gas and cohesive particles flow behaviour using laser Doppler anemometer", in "Fluidization VII: Proceedings of the Seventh Engineering Foundation Conference on Fluidization", Engineering Foundation, New York, 723-730 (1992).

Atutxa, A.; Aguado, R.; Gayubo, A. G.; Olazar, M.; Bilbao, J., “Kinetic Description of the Catalytic Pyrolysis of Biomass in a Conical Spouted Bed Reactor”, Energy & Fuels, 19(3), 765-774 (2005).

Bacelos, M. S. and Freire, J. T., “Stability of Spouting Regimes in Conical Spouted Beds with Inert Particle Mixtures”, Industrial & Engineering Chemistry Research, 45(2), 808-817 (2006).

Bacelos, M. S.; Spitzner Neto, P. I.; Silveira, A. M.; Freire, J. T., “Analysis of fluid dynamics behavior of conical spouted bed in presence of pastes”, Drying Technology, 23(3), 427-453 (2005).

Bader R.; Findlay J.; Knowlton T. M., “Gas/Solids Flow Patterns in a 30.5-cm-Diameter Circulating Fluidized Bed”, in “Circulating Fluidized Bed Technology II: Proceedings of the 2nd International Conference on Circulating Fluidized Beds”, Basu, P. and Large, J. F., Pergamon Press, Oxford, 123-137 (1988).

Bai, D.; Yi, J.; Jin, Y.; Yu, Z., “Residence time distributions of gas and solids in a circulating fluidized bed”, in “Fluidization VII: Proceedings of the Seventh Engineering Foundation Conference on Fluidization”, Engineering Foundation, New York, 195-202 (1992).

Baskakov, A. P. and Pomortseva, A. A., “Hydrodynamics and heat transfer of a spouting layer in conical apparatus”, Khim. Prom., 46(11), 860-863 (1970).

Benkrid, A. and Caram, H. S., “Solid flow in the annular region of a spouted bed”, AIChE J., 35(8), 1328-1336 (1989).

Bi, H. T.; Macchi, A.; Chaouki, J.; Legros, R., “Minimum spouting velocity of conical spouted beds”, Can. J. Chem. Eng., 75(2), 460-465 (1997).

Bi, X. T., “Gas and solid mixing in high-density CFB risers”, International Journal of Chemical Reactor Engineering, 2, Article A12 (2004).

Bischoff, K. B. and Levenspiel, O., “Fluid dispersion-generalization and comparison of mathematical models. I. Generalization of models”, Chemical Engineering Science, 17, 245-55 (1962).

Bischoff, K. B. and Levenspiel, O., “Fluid dispersion-generalization and comparison of mathematical models. II. Comparison of models”, Chemical Engineering Science, 17, 257-64 (1962).

Cao, C.-S. and Weinstein, H., “Gas dispersion in downflowing high velocity fluidized beds”, AIChE Journal, 46(3), 523-528 (2000).

Charbel, A. L. T.; Massarani, G.; Passos, M. L., “Analysis of effective solid stresses in a conical spouted bed”, Brazilian Journal of Chemical Engineering, 16(4), 433-449 (1999).

Choi, M. and Meisen, A., “Hydrodynamics of shallow, conical spouted beds”, Can. J. Chem. Eng., 70(5), 916-924 (1992).

Di Felice, R., “The voidage function for fluid-particle interaction systems”, International Journal of Multiphase Flow, 20(1), 153-159 (1994).

Dolidovich, A. F. and Efremtsev, V. S., “Hydrodynamics and heat transfer of spouted beds with a two-component (gas-solid) dispersing medium”, Can. J. Chem. Eng., 61(3), 398-405 (1983a).

Dolidovich, A. F. and Efremtsev, V. S., “Studies of spouted beds with small outlet-inlet cross-section ratios”, Can. J. Chem. Eng., 61(3), 382-389 (1983b).

Du, W.; Bao, X.-J.; Xu, J.; Wei, W.-S., “Computational fluid dynamics (CFD) modeling of spouted bed: Assessment of drag coefficient correlations”, Chemical Engineering Science, 61(5), 1401-1420 (2006).

Duarte, C. R.; Murata, V. V.; Barrozo, M. A. S., “A study of the fluid dynamics of the spouted bed using CFD”, Brazilian Journal of Chemical Engineering, 22(2), 263-270 (2005).

Dudas, J.; Seitz, O.; Jelemensky, L., “Chemical reaction in spouted beds”, Chem. Eng. Sci., 48(17), 3104-3107 (1993).

Ergun, S., “Fluid Flow through Packed Columns”, Chem. Eng. Prog., 48(2), 89-94 (1952).

Fluent Inc., “FLUENT 6.1 UDF Manual” (2003a).

Fluent Inc., “FLUENT 6.1 User's Guide” (2003b).

Freitas, L. A. P. and Freire, J. T., “Heat transfer in spouted beds”, Drying Technol., 11(2), 303-317 (1993).

Geldart, D., “Types of gas fluidization”, Powder Technology, 7(5), 285-292 (1973).

Gidaspow, D., “Multiphase flow and fluidization: Continuum and kinetic theory descriptions”, Academic Press, London (1994).

Glicksman, L. R., “Scaling relationships for fluidized beds”, Chem. Eng. Sci., 43(6), 1419-1421 (1988).

Glicksman, L. R., “Scaling relationships for fluidized beds”, Chem. Eng. Sci., 39(9), 1373-1379 (1984).

Goldschmidt, M. J. V.; Kuipers, J. A. M.; Van Swaaij, W. P. M., “Hydrodynamic modelling of dense gas-fluidized beds using the kinetic theory of granular flow: effect of coefficient of restitution on bed dynamics”, Chem. Eng. Sci., 56(2), 571-578 (2001).

Goltsiker, A. D., Doctoral dissertation, Lensovet Technol. Inst., Leningrad (1967). Quoted by Mathur and Epstein (1974).

Goltsiker, A. D.; Bashkovskaya, N. B.; Romankov, P. G., “Hydraulics of a fluidized bed in a cyclone. I. Mechanism of the begining of fluidization in a cyclone”, Zh. Prikl. Khim., 37(5), 1030-1035 (1964).

Golubkovich, A. V.; Kondukov, N. B.; Vorob'ev, Kh. S., “Some hydrodynamic features of a spouting-pulsing process for fluidizing granular substances in conical apparatus”, Khim. Prom-st., 43(7), 526-530 (1967).

Gorkem, K., “Solid motion and mixing in high-density circulating fluidized beds”, Ph.D. Thesis, University of British Columbia, Vancouver, Canada (2004).

Gorshtein, A. E. and Mukhlenov, I. P., "Hydraulic resistance of a fiuidized bed in a cyclone without a grate. II. Critical gas rate corresponding to the beginning of jet formation", Zh. Prikl. Khim., 37(9), 1887-1893 (1964).

Gorshtein, A. E. and Mukhlenov, I. P., "Movement of solid material in a spouting layer", Zh. Prikl. Khim., 40(11), 2469-2474 (1967).

Grace, J. R.; Mathur, K. B., "Height and structure of the fountain region above spouted beds", Can. J. Chem. Eng., 56(5), 533-537 (1978).

Hadzismajlovic, D. E.; Grbavcic, B.; Vukovic, D. V.; Povrenovic, D. S.; Littman, H., "A model for calculating the minimum fluid flowrate and pressure drop in a conical spouted bed", in "Fluidization ∏ ", Editor(s): Oestergaard, Knud; Soerensen, Ansgar, Publisher: Eng. Found., New York, 241-248 (1986).

He, Y.-L., "Hydrodynamic and scale-up studies of spouted beds", doctorial thesis, (1995).

He, Y.-L.; Qin, S.-Z.; Lim, C. J.; Grace, J. R., "Particle velocity profiles and solid flow patterns in spouted beds", Can. J. Chem. Eng., 72(4), 561-568 (1994a).

He, Y. L.; Lim, C. J.; Grace, J. R.; Zhu, J. X., "Measurements of voidage profiles in spouted beds", Journal of Chemical Engineering, 72(2), 229-234 (1994b).

He, Y.-R., Zhao, G.-B., Bouillard, J., Lu, H.-L., "Numerical simulations of the effect of conical dimension on the hydrodynamic behaviour in spouted beds", Can. J. Chem. Eng., 82(1), 20-29 (2004).

Hong, R.-Y.; Li, H.-Zh.; Cheng, M.-Y.; Zhang, J.-Y., "Numerical simulation and verification of a gas-solid jet fluidized bed", Powder Technology, 87(1), 73-81 (1996).

Hu, Q.-Y.; Jing, S.; Wang, J.-F.; Jin, Y., "Fluidization of coarse powder in tapered beds", Gaoxiao Huaxue Gongcheng Xuebao, 14(1), 12-18 (2000).

Huilin, L.; Yongli, S.; Yang, L.; Yurong, H.; Bouillard, J., "Numerical simulations of hydrodynamic behaviour in spouted beds", Chemical Engineering Research and Design, 79(A5), 593-599 (2001).

Jing, S.; Cai, G.-B.; Fan, M.; Yu, B.; Wang, J.-F.; Jin, Y., "Fluidization of fine particles in conical beds", Powder Technology, 118(3), 271-274 (2001).

Jing, S.; Hu, Q.-Y.; Wang, J.-F.; Jin, Y., "Fluidization of coarse particles in gas-solid conical beds", Chem. Eng. Process, 39(4), 379-387 (2000).

Kawaguchi, T.; Sakamoto, M.; Tanaka, T.; Tsuji, Y., "Quasi-three-dimensional numerical simulation of spouted beds in cylinder", Powder Technology, 109(1-3), 3-12 (2000).

Kmiec, A., "The minimum spouting velocity in conical beds", Can. J. Chem. Eng., 61(3), 274-280 (1983).

Kucharski, J. and Kmiec, A., "Hydrodynamics, heat and mass transfer during coating of tablets in a spouted bed", Can. J. Chem. Eng., 61(3), 435-439 (1983).

Kunii D. and Levenspiel O., "Fluidization Engineering", 2nd edition, Butterworth-Heinemann, Boston (1991).

Lefroy, G. A. and Davidson, J. F., "The mechanics of spouted beds", Trans. Instn. Chem. Engrs., 47, T120-T128 (1969).

Levenspiel, Octave, "The chemical reactor omnibook", Publisher: Corvallis, OR (1979)

Levenspiel, Octave, "Chemical reaction engineering", Publisher: John Wiley & Sons, New York (1999).

Lim, C. J. and Mathur, K. B., "Residence time distribution of gas in spouted beds", Can. J. Chem. Eng., 52(Set 2), 150-155 (1974).

Lim, C. J. and Mathur, K. B., "A flow model for gas movement in spouted beds", AIChE J., 22(4), 674-680 (1976).

Limtrakul, S.; Boonsrirat, A.; Vatanatham, T., “DEM modeling and simulation of a catalytic gas-solid fluidized bed reactor: a spouted bed as a case study”, Chemical Engineering Science, 59(22-23), 5225-5231 (2004).

Liu, J.-Z.; Grace, J. R.; Bi, X.-T., “Novel multifunctional optical-fiber probe: I. Development and validation”, AIChE Journal, 49(6), 1405-1420 (2003).

Liu J.-Z., “Particle and gas dynamics of high density circulating fluidized beds”, Ph.D. Thesis, University of British Columbia, Vancouver, Canada (2001).

Liu, J.-Z.; Grace, J. R.; Bi, H. T.; Morikawa, H.; Zhu, J.-X., “Gas dispersion in fast fluidization and dense suspension upflow”, Chemical Engineering Science, 54(22), 5441-5449 (1999).

Lu, H.-L.; He, Y.-R.; Liu, W.-T.; Ding, J.-M.; Gidaspow, D.; Bouillard, J., “Computer simulations of gas-solid flow in spouted beds using kinetic-frictional stress model of granular flow”, Chem. Eng. Sci., 59(4), 865-878 (2004).

Lun, C. K. K.; Savage, S. B.; Jeffrey, D. J.; Chepurniy, N., “Kinetic theories for granular flow: Inelastic particles in Couette flow and slightly inelastic particles in a general flow field”, J. Fluid Mech., 140, 223-256 (1984).

Markowski, A. S., “Drying characteristics in a jet-spouted bed dryer”, Can. J. Chem. Eng., 70(5), 938-944 (1992).

Markowski, A. and Kaminski, W., “Hydrodynamic characteristics of jet-spouted beds”, Can. J. Chem. Eng., 61(3), 377-381 (1983).

Marnasidou, K. G.; Voutetakis, S. S.; Tjatjopoulos, G. J.; Vasalos, I. A., “Catalytic partial oxidation of methane to synthesis gas in a pilot-plant-scale spouted-bed reactor”, Chem. Eng. Sci., 54(15-16), 3691-3699 (1999).

Mathur, K. B. and Epstein N., “Spouted beds”, Academic Press, New York (1974).

Mathur, K. B. and Gishler P. E., “A technique for contacting gases with coarse solid particles”, AIChE J., 1, 157-164 (1955).

Matsuno, Y.; Yamaguchi, H.; Oka, T.; Kage, H.; Higashitani, K., "The use of optic fiber probes for the measurement of dilute particle concentrations: calibration and application to gas-fluidized bed carryover", Powder Technology, 36(2), 215-221 (1983).

McKeen, T. and Pugsley, T., "Simulation and experimental validation of a freely bubbling bed of FCC catalyst", Powder Technology, 129(1-3), 139-152 (2003).

Mikhailik, V. D. and Antanishyn, M. V., "Particle velocity and porosity in the center of a spouting bed", Vestsi Akademii Navuk BSSR, Seryya Fizika-Tekhnichnykh Navuk, (3), 81-86(1967). Quoted by Mathur and Epstein (1974).

Morooka, S.; Kawazuishi, K.; Kato, Y., "Holdup and flow pattern of solid particles in freeboard of gas-solid fluidized bed with fine particles", Powder Technology, 26(1), 75-82 (1980).

Mukhlenov, I. P. and Gorshtein, A. E., "Spouting beds", Khim. Prom., 41(6), 443-446 (1965a).

Mukhlenov, I. P. and Gorshtein, A. E., "Hydrodynamics of reactors with a spouting bed of granular material", Vses. Konf. Khim. Reactrom Novosibirsk, (3) 553-562 (1965b).

Mukhlenov, I. P. and Gorshtein, A. E., "Hydraulic resistance of a fluidized layer in a cyclone without a grate", Zh. Prikl. Khim., 37(3), 609-615 (1964).

Nikolaev, A. M.; Golubev, L. G.; Kirov, S. M., "Basic hydrodynamic characteristics of a spouting bed", Khim. i Khim. Tekhnol., 7(5), 855-857 (1964).

Oki, K.; Walawender, W. P.; Fan, L. T., "The measurement of local velocity of solid particles", Powder Technology, 18, 171-178 (1977).

Oki, K. and Shirai, T., "Particle velocity in fluidized bed", in "Fluidization Technology", Vol.1, Editer(s): Keairns, D. L.; Hemisphere, Washington, D. C., 95-110 (1976).

Olazar, M.; Aguado, R.; Velez, D.; Arabiourrutia, M.; Bilbao, J., "Kinetics of Scrap Tire Pyrolysis in a Conical Spouted Bed Reactor", Industrial & Engineering Chemistry Research, 44(11), 3918-3924 (2005).

Olazar, M.; San Jose, M. J.; Alvarez, S.; Morales, A.; Bilbao, J., “Design of Conical Spouted Beds for the Handling of Low-Density Solids”, Industrial & Engineering Chemistry Research, 43(2), 655-661 (2004).

Olazar, M.; Alvarez, S.; Aguado, R.; San Jose, M. J., “Spouted bed reactors”, Chemical Engineering & Technology, 26(8), 845-852 (2003).

Olazar, M.; Aguado, R.; San Jose, M. J.; Bilbao, J., “Kinetic study of fast pyrolysis of sawdust in a conical spouted bed reactor in the range 400-500°C”, Journal of Chemical Technology & Biotechnology, 76(5), 469-476 (2001a).

Olazar, M.; San Jose, M. J.; Izquierdo, M. A.; Ortiz de Salazar, A.; Bilbao, J., “Effect of operating conditions on solid velocity in the spout, annulus and fountain of spouted beds”, Chem. Eng. Sci., 56(11), 3585-3594 (2001b).

Olazar, M.; Aguado, R.; San Jose, M. J.; Bilbao, J., “Performance of a conical spouted bed in biomass catalytic pyrolysis”, Recents Progres en Genie des Procedes, 14(76), 499-506 (2000a).

Olazar, M.; Aguado, R.; Bilbao, J.; Barona, A., “Pyrolysis of sawdust in a conical spouted-bed reactor with a HZSM-5 catalyst”, AIChE J., 46(5), 1025-1033 (2000b).

Olazar, M., “Spouted bed technology: state of the art and applications”, Recents Progres en Genie des Procedes, 14(76), 403-418 (2000c).

Olazar, M.; Jose, M. J. San; Aguado, R.; Gaisan, B.; Bilbao, J. , “Bed Voidage in Conical Sawdust Beds in the Transition Regime between Spouting and Jet Spouting”, Ind. Eng. Chem. Res., 38(10), 4120-4122 (1999).

Olazar, M.; San Jose, M. J.; Alvarez, S.; Morales, A.; Bilbao, J., “Measurement of Particle Velocities in Conical Spouted Beds Using an Optical Fiber Probe”, Ind. Eng. Chem. Res., 37(11), 4520-4527 (1998).

Olazar, M.; Jose, M. J. San; Arandes, J. M.; Bilbao, J., “A model for gas flow in jet-spouted beds”, in “Mixed-Flow Hydrodyn.”, Editor(s): Cheremisinoff, Nicholas P., Publisher: Gulf Publishing, Houston, 759-784 (1996a).

Olazar, M.; San Jose, M. J.; Aguado, R.; Bilbao, J., "Solid Flow in Jet Spouted Beds", Ind. Eng. Chem. Res., 35(8), 2716-2724 (1996b).

Olazar, M.; San Jose, M. J.; Cepeda, E.; Oritz de Latierro, R.; Bilbao, J., "Hydrodynamics of fine solids on conical spouted beds", in "Fluid. VIII, Proc. Eng. Found. Conf. Fluid., 8th", Editor(s): Large, Jean-Francois; Laguerie, Claude, Publisher: Engineering Foundation, New York, 197-205 (1996c).

Olazar, M.; Jose, M. J. San; Bilbao, J., "Hydrodynamics and applications of conical spouted beds", Trends Chem. Eng., 3, 219-233 (1996d).

Olazar, M.; San Jose, M. J.; Penas, F. J.; Aguayo, A. T.; Arandes, J. M.; Bilbao, J., "A simplified model for gas flow in conical spouted beds", Chem. Eng. J. (Lausanne), 56(2), 19-26 (1995a).

Olazar, M.; San Jose, M. J.; LLamosas, R.; Alvarez, S.; Bilbao, J., "Study of Local Properties in Conical Spouted Beds Using an Optical Fiber Probe", Ind. Eng. Chem. Res., 34(11), 4033-4039 (1995b).

Olazar, M.; San Jose, M. J.; Zabala, G.; Bilbao, J., "New reactor in jet spouted bed regime for catalytic polymerizations", Chem. Eng. Sci., 49(24A), 4579-4588 (1994a).

Olazar, M.; San Jose, M. J.; Llamosas, R.; Bilbao, J., "Hydrodynamics of Sawdust and Mixtures of Wood Residues in Conical Spouted Beds", Ind. Eng. Chem. Res., 33(4), 993-1000 (1994b).

Olazar, M.; San Jose, M. J.; Penas, F. J.; Aguayo, A. T.; Bilbao, J., "Stability and hydrodynamics of conical spouted beds with binary mixtures", Ind. Eng. Chem. Res., 32(11), 2826-2834 (1993a).

Olazar, M.; San Jose, M. J.; Aguayo, A. T.; Arandes, J. M.; Bilbao, J., "Design factors of conical spouted beds and jet spouted beds", Ind. Eng. Chem. Res., 32(6), 1245-1250 (1993b).

Olazar, M.; San Jose, M. J.; Aguayo, A. T.; Arandes, J. M.; Bilbao, J., "Pressure drop in conical spouted beds", Chem. Eng. J. (Lausanne), 51(1), 53-60 (1993c).

Olazar, M.; San Jose, M. J.; Penas, F. J.; Aguayo, A. T.; Arandes, J. M.; Bilbao, J., "A model for gas flow in jet spouted beds", Can. J. Chem. Eng., 71(2), 189-194 (1993d).

Olazar, M.; San Jose, M. J.; Aguayo, A. T.; Arandes, J. M.; Bilbao, J., "Stable operation conditions for gas-solid contact regimes in conical spouted beds", Ind. Eng. Chem. Res., 31(7), 1784-1792 (1992).

Oliveira, I. M.; Passos, M. L., "Simulation of drying suspensions in a conical spouted bed", in "Drying '96, [Proc. Int. Drying Symp.], 10^{th}", Editor(s): Strumillo, Czeslaw; Pakowski, Zdzislaw, Publisher: Lodz Technical University, 307-314 (1996).

Oliveira, W. P.; Freire, J. T., "Analysis of evaporation rate in the spouted bed zones during drying of liquid materials using a three region model", in "Drying '96, [Proc. Int. Drying Symp.], 10^{th}", Editor(s): Strumillo, Czeslaw; Pakowski, Zdzislaw, Publisher: Lodz Technical University, 504-512 (1996).

Passos, M. L.; Oliveira, L. S.; Franca, A. S.; Massarani, G., "Bixin powder production in conical spouted bed units", Drying Technol., 16(9 & 10), 1855-1879 (1998).

Passos, M. L.; Massarani, G.; Freire, J. T.; Mujumdar, A. S., "Drying of pastes in spouted beds of inert particles: design criteria and modeling", Drying Technol., 15(2), 605-624 (1997).

Patrose, B. and Caram, H. S., "Optical fiber probe transit anemometer for particle velocity measurements in fluidized beds", AIChE J., 28(4), 604-609 (1982).

Peng, Y.-M. and Fan L. T., "Hydrodynamic characteristics of fluidization in liquid-solid tapered beds", Chem. Eng. Sci., 52(14), 2277-2290 (1997).

Peng, Y.-M. and Fan L. T., "Hysteresis in liquid-solid tapered beds", Chem. Eng. Sci., 50(16), 2669-2671 (1995).

Pham, Q. T., "Behavior of a conical spouted-bed dryer for animal blood", Can. J. Chem. Eng., 61(3), 426-434 (1983).

Povrenovic, D. S.; Hadzismajlovic, Dz. E.; Grbavcic, Z. B.; Vukovic, D. V.; Littman, H., “Minimum fluid flowrate, pressure drop and stability of a conical spouted bed”, Can. J. Chem. Eng., 70(2), 216-222 (1992).

Reyes, A.; Diaz, G.; Blasco, R., “Slurry drying in gas-particle contactors: fluid-dynamics and capacity analysis”, Drying Technol., 16(1 & 2), 217-233 (1998).

Reyes, A.; Diaz, G.; Blasco, R., “Experimental study of slurries drying on inert particles in spouted bed and fluidized bed dryers”, in “Drying '96, [Proc. Int. Drying Symp.], 10th”, Editor(s): Strumillo, Czeslaw; Pakowski, Zdzislaw, Publisher: Lodz Technical University, 605-612 (1996).

Richardson, J. F. and Zaki, W. N., “Sedimentation and fluidisation: Part I”, Trans. Instn. Chem. Engrs., 32, 35-53 (1954).

Romankov, P. G. and Rashkovskaya, N. B., “Drying in a suspended state”, 2nd ed., Chem. Publ. House, Leningrad Branch (1968).

Romankov, P. G. and Rashkovskaya, N. B.; Gol'tsiker, A. D.; Seballo, V. A., “Structural study of spouting beds”, Khim. Prom., 46(5), 372-375 (1970).

Rovero, G.; Brereton, C. M. H.; Epstein, N.; Grace, J. R.; Casalegno, L.; Piccinini, N., “Gas flow distribution in conical-base spouted beds”, Can. J. Chem. Eng., 61(3), 289-296 (1983).

Rowe, P. N., “A convenient empirical equation for estimation of the Richardson-Zaki exponent”, Chemical Engineering Science, 42(11), 2795-2796 (1987).

San Jose, M. J.; Olazar, M.; Alvarez, S.; Morales, A.; Bilbao, J., “Local porosity in conical spouted beds consisting of solids of varying density”, Chemical Engineering Science, 60(7), 2017-2025 (2005a).

San Jose, M. J.; Olazar, M.; Alvarez, S.; Morales, A.; Bilbao, J., “Spout and Fountain Geometry in Conical Spouted Beds Consisting of Solids of Varying Density”, Industrial & Engineering Chemistry Research, 44(1), 193-200 (2005b).

San Jose, M. J.; Olazar, Martin; Alvarez, Sonia; Izquierdo, Miguel A.; Bilbao, Javier, "Solid cross-flow into the spout and particle trajectories in conical spouted beds", Chem. Eng. Sci., 53(20), 3561-3570 (1998a).

San Jose, M. J.; Olazar, Martin; Alvarez, Sonia; Bilbao, Javier, "Local Bed Voidage in Conical Spouted Beds", Ind. Eng. Chem. Res., 37(6), 2553-2558 (1998b).

San Jose, M. J.; Olazar, M.; Llamosas, R.; Izquierdo, M. A.; Bilbao, J., "Study of dead zone and spout diameter in shallow spouted beds of cylindrical geometry", Chem. Eng. J. (Lausanne), 64(3), 353-359 (1996a).

San Jose, M. J.; Olazar, M.; Aguado, R.; Bilbao, J., "Influence of the conical section geometry on the hydrodynamics of shallow spouted beds", Chem. Eng. J. (Lausanne), 62(2), 113-120 (1996b).

San Jose, M. J.; Olazar, M.; Penas, F. J.; Arandes, J. M.; Bilbao, J., "Correlation for calculation of the gas dispersion coefficient in conical spouted beds", Chem. Eng. Sci., 50(13), 2161-2172 (1995).

San Jose, M. J.; Olazar, Martin; Penas, Francisco J.; Bilbao, Javier, "Segregation in Conical Spouted Beds with Binary and Ternary Mixtures of Equidensity Spherical Particles", Ind. Eng. Chem. Res., 33(7), 1838-1844 (1994).

San Jose, M. J.; Olazar, M.; Aguayo, A. T.; Arandes, J. M.; Bilbao, J, "Expansion of spouted beds in conical contactors", Chem. Eng. J. (Lausanne), 51(1), 45-52 (1993).

San Jose, M. J.; Olazar, M J.; Aguayo, M.; Arandes, A. T.; Bilbao, J., "Hydrodynamic correlations of conical jet spouted beds", in "Fluid. VII, Proc. Eng. Found. Conf. Fluid. 7th", Editor(s): Potter, Owen E.; Nicklin, D. J., Publisher: Eng. Found., New York, 381-388 (1992).

San Jose, M. J.; Olazar, M.; Aguyo, A. T.; Arandes, J. M.; Bilbao, J, "Design and hydrodynamics of conical jet spouted beds", Recents Prog. Genie Procedes, 5(11, Fluidisation), 146-153 (1991).

Sane, S. U.; Haynes, H. W. J.; Agarwal, P. K., "An experimental and modeling investigation of gas mixing in bubbling fluidized beds", Chemical Engineering Science, 51(7), 1133-1147 (1996).

Schaeffer, D. G., "Instability in the evolution equations describing incompressible granular flow", J. Diff. Eq., 66, 19-50 (1987).

Sotudeh-Gharebaagh, R. and Chaouki, J., "Gas mixing in a turbulent fluidized bed reactor", Canadian Journal of Chemical Engineering, 78(1), 65-74 (2000).

Spitzner Neto, P. I.; Cunha, F. O.; Freire, J. T., "Effect of the presence of paste in a conical spouted bed dryer with continuous feeding", Drying Technology, 20(4 & 5), 789-811 (2002).

Spitzner Neto, P. I.; Cunha, F. O.; Freire, J. T., "The influence of paste feed on the minimum spouting velocity", Brazilian Journal of Chemical Engineering, 18(3), 243-251 (2001).

Stearns, R. F.; Johnson, R. R.; Jackson, R. M.; Larson, C. A., "Flow measurement with orifice meters", Published by D. Van Nostrand Company, Inc., Toronto (1951).

Sun, S.-L.; Bao, X.-J.; Wei, W.-S., "Gas residence time distributions in a spouted bed", Chinese Journal of Chemical Engineering, 13(3), 291-296 (2005).

Szafran, R. G. and Kmiec, A., "CFD Modeling of Heat and Mass Transfer in a Spouted Bed Dryer", Industrial & Engineering Chemistry Research, 43(4), 1113-1124 (2004).

Takeuchi, S.; Wang, S.; Rhodes, M., "Discrete element simulation of a flat-bottomed spouted bed in the 3-D cylindrical coordinate system", Chemical Engineering Science, 59(17), 3495-3504 (2004).

Takeuchi, S.; Wang, X.-S.; Rhodes, M. J., "Discrete element study of particle circulation in a 3-D spouted bed", Chemical Engineering Science, 60(5), 1267-1276 (2005).

Tsvik, M. Z.; Nabiev, M. N.; Rizaev, N. U.; Merenkov, K. V., "Angular value of a spouting center", Uzb. Khim. Zh., 11(4), 64-65 (1967a).

Tsvik, M. Z.; Nabiev, M. N.; Rizaev, N. U.; Merenkov, K. V.; Vyzgo, V. S., "External flow rates in composite production of granulated fertilizers", Uzb. Khim. Zh., 11(2), 50-51 (1967b).

Tsvik, M. Z.; Nabiev, M. N.; Rizaev, N. U.; Merenkov, K. V.; Vyzgo, V. S., "Minimal rate of internal gushing during composite production of granulated fertilizers", Uzb. Khim. Zh., 10(6), 3-6 (1966).

Uemaki, O. and Tsuji, T., "Gasification of a sub-bituminous coal in a two-stage, jet-spouted bed reactor", in "Fluidization V: Proceedings of the Fifth Engineering Foundation Conference on Fluidization", Engineering Foundation, New York, 497-504 (1986).

Waldie, B.; Wilkinson, D.; McHugh, T. G. P., "Measurement of voidage in the fountain of a spouted bed", Can. J. Chem. Eng., 64(6), 950-953 (1986a).

Waldie, B. and Wilkinson, D., "Measurement of particle movement in a spouted bed using a new microprocessor based technique", Canadian Journal of Chemical Engineering, 64(6), 944-949 (1986b).

Wan-Fyong, F.; Romankov, P. G.; Rashkovskaya, N. B., "Hydrodynamics of spouting bed", Zh. Prikl. Khim. (Leningrad), 42(3), 609-617 (1969).

Wang, Z.-G. and Wei, F., "Study on gas mixing in turbulent fluidized bed", Engineering Chemistry & Metallurgy, 20(Supplement), 80-86 (1999).

Wen, C. Y.; Yu, Y. H., "Mechanics of fluidization", Chemical Engineering Progress, Symposium Series, 62(62), 100-111 (1966).

Yang, N.; Wang, W.; Ge, W.; Li, J.-H., "CFD simulation of concurrent-up gas-solid flow in circulating fluidized beds with structure-dependent drag coefficient", Chemical Engineering Journal (Amsterdam, Netherlands), 96(1-3), 71-80 (2003).

Zhang, K.; Zhang, H.; Lovick, J.; Zhang, J.-Y.; Zhang, B.-J., "Numerical Computation and Experimental Verification of the Jet Region in a Fluidized Bed", Industrial & Engineering Chemistry Research, 41(15), 3696-3704 (2002).

Zhang, Y.-H.; Reese, J. M., “The drag force in two-fluid models of gas-solid flows”, Chemical Engineering Science, 58(8), 1641-1644 (2003).

Zhu J.-X. and Hong J., “spouted beds”, in “Fluidization Engineering Principles”, Jin Y.; Zhu J.-X.; Wang Z.-W.; Yu Z.-Q., Eds., Tsinghua University Press, Beijing, 360-396 (2001).

APPENDIX A

TABLES CITED IN CHAPTER 1

Table A-1. Some definitions of transition velocities in conical spouted beds.

<table>
<tr><th>Author</th><th>Experimental conditions and remarks</th><th>Experimental observations</th></tr>
<tr><td>Nikolaev and Golubev (1964)</td><td>1. $D_0=D_i=0.02\sim0.05$m, $H_0=0.09\sim0.15$m;
2. Based on increasing superficial gas velocity, $(U_0)_{ms,a}$ corresponds to the start of spouting.</td><td>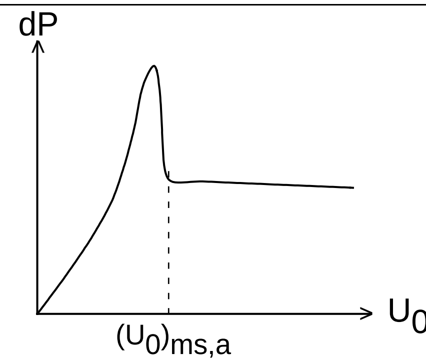

There was no step change of pressure drops when full spouting starts.</td></tr>
<tr><td>Mukhlenov and Gorshtein (1965a,1965b)</td><td>1. $D_0=D_i$, $H_0/D_0=1.3\sim8.5$;
2. Based on increasing superficial gas velocity, $U_{0,1}$ corresponds to the minimum gas velocity for spouting (i.e. for formation of the internal spout).</td><td rowspan="2">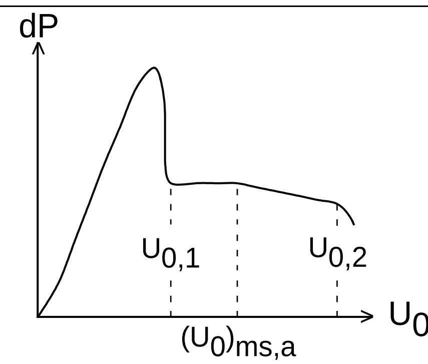

There was no step change of pressure drops when full spouting starts.
Based on increasing superficial gas velocity, $U_{0,2}$ corresponds to the speed of carry off of the particles out of the bed.</td></tr>
<tr><td>Gorshtein and Mukhlenov (1964)</td><td>1. $D_0=D_i$, $H_0=0.03\sim0.15$m, $H_0/D_0=1.6\sim5.0$;
2. Based on increasing superficial gas velocity, $(U_0)_{ms,a}$ corresponds to the formation of the outer spouting.</td></tr>
</table>

Table A-1. Continued.

Author	Experimental conditions and remarks	Experimental observations
Tsvik et al. (1966)	1. $D_0=D_i$, H_0 =0.1~0.5m; 2. Based on increasing superficial gas velocity, $U_{0,1}$ corresponds to the gas velocity for internal spouting and the maximal resistance of the bed.	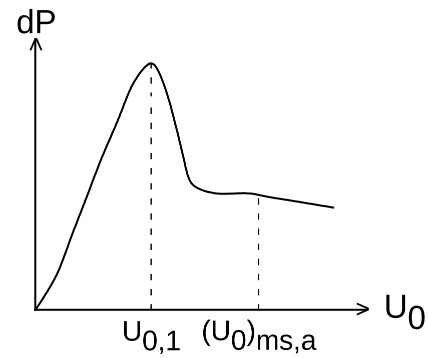
Tsvik et al. (1967b)	1. $D_0=D_i$, H_0/D_0=1.6~8.7; 2. Based on increasing superficial gas velocity, $(U_0)_{ms,a}$ corresponds to the onset of external spouting; 3. $(U_0)_{ms,a}/U_{0,1}$ = 1.6~3.1.	
Wan-Fyong et al. (1969)	1. $D_0=D_i$, D_0=0.026~0.076m, H_0=0.07~0.3m. 2. Based on increasing superficial gas velocity, $U_{0,1}$ corresponds to the velocity at the beginning of spouting; $(U_0)_{ms,a}$ corresponds to the velocity at the beginning of steady spouting and good mixing of the bed; $U_{0,2}$ corresponds to the velocity at the end of steady spouting; 3. $(U_0)_{ms,a}/U_{0,1}$ = 1.94~2.	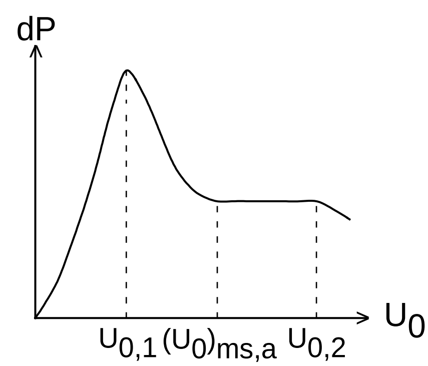 There was no step change of pressure drops when full spouting starts.
Kmiec (1983)	1. $D_0=D_i$; 2. D_c is included in correlation.	

Table A-1. Continued.

Author	Experimental conditions and remarks	Experimental observations
Markowski et al. (1983)	1. $D_0=D_i$, $H_0/D_i=0.6\sim2.3$; 2. D_c is included in correlation; 3. $\gamma=37^o$.	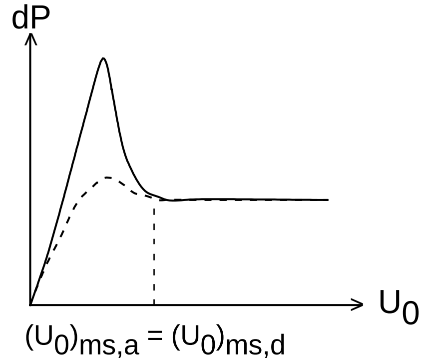 There were no step changes of pressure drop when spouting starts and finishes.
Olazar et al. (1992)	1. $D_i=0.06$m, $D_0/D_i=1/2 \sim 5/6$; 2. $H_0<0.23$m; 3. $\gamma=28^o\sim 45^o$.	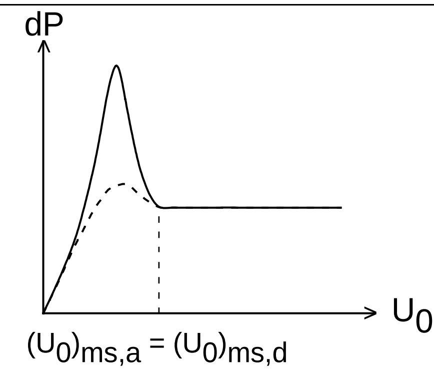 There were no step changes of pressure drop when spouting starts or finishes.
Jing et al. (2000)	1. $D_0=D_i=0.05$m, $H_0=0.165\sim0.3$m; 2. A perforated plate was used as gas distributor; 3. U_{ms} was defined based on the increasing process of superficial gas velocity.	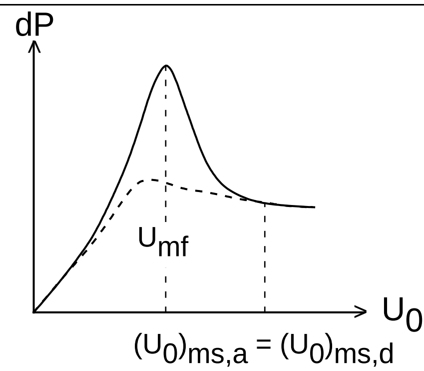 There were no step changes of pressure drop when spouting starts or finishes.

Table A-2. Summary of application studies on conical spouted beds.

Authors	Experimental conditions	Applications
Kucharski and Kmiec (1983)	γ=34º; D_i=0.082m; D_0=0.0334m; D_c=0.3m; ρ_s=1476kg/m^3; 0.004×0.007m and 0.0043×0.009m tablets; H_0<0.17m; T=363K.	Coating of tablets
Pham (1983)	γ=60º; D_i=D_0=0.24m; D_c=1.044m; H_0=0.342~0.729m; d_s=4mm; T=493K; ρ_s=900kg/m^3.	Drying of animal blood
Uemaki and Tsuji (1986)	γ=40º; D_i=D_0=0.015m; D_c=0.21m; d_s=1.27, 1.95mm; ρ_s=1290kg/m^3; T=1000~1300K; atmospheric pressure.	Gasification of coal
Markowski (1992)	γ=38º; D_i=D_0=0.082m; ρ_s=2178kg/m^3; d_s=4.95mm; T=423~453K.	Drying
Dudas et al. (1993)	γ=30º; D_i=D_0=0.002m; D_c=0.05m; d_s=1.41mm; ρ_s=740.4kg/m^3; H_0=0.12m; T=673K; P=201kPa.	Propylene disproportionation
Olazar et al. (1994a)	γ=28º; D_i=0.02m; D_0=0.004~0.01m; D_c=0.12m; d_s=0.08~0.1mm; ρ_s=2100kg/m^3; T=523~583K.	Catalytic polymerization
Passos et al. (1997, 1998)	γ=60º; D_i=D_0=0.0524m; D_c=0.06m; d_s=3.4mm; ρ_s=1277~1426kg/m^3; T=323~373K.	Drying and particle attrition
Reyes et al. (1998)	D_i=D_0=0.05m; D_c=0.6m; Polypropylene chips; ρ_s=940kg/m^3; T=353~383K.	Slurry drying
Marnasidou et al. (1999)	γ=40º; D_i=D_0=0.0016m; D_c=0.05m; d_s=0.15~0.2mm, 0.6mm; Al_2O_3; T=1173~1323K; P=1~10bar.	Catalytic partial oxidation of methane to syngas
Aguado et al. (2000a, 2000b)	γ=28º; D_i=0.02m; D_0=0.01m; D_c=0.123m; T=623~973K.	Pyrolysis of sawdust

Table A-2. Continued.

Authors	Experimental conditions	Applications
Olazar et al. (2000a, 2000b, 2001a)	Same as Aguado et al. (2000a, 2000b) $T=673\sim773K$	Catalytic pyrolysis of sawdust
Spitzner Neto et al. (2002)	$\gamma=60^o$; $D_i=0.06m$; $D_0=0.05m$; $D_c=0.3m$; $d_s=2.6mm$; $\rho_s=2490kg/m^3$, glass beads as inert particles; $T=333K$.	Drying of pasty materials (egg paste, bovine blood)
Aguado et al. (2002a, 2002b)	Same as Aguado et al. (2000a, 2000b) $T=723\sim873K$	Pyrolysis of polyolefins (LDPE, HDPE, PP)
Aguado et al. (2003)	Same as Aguado et al. (2000a, 2000b) $T=723\sim823K$	Pyrolysis of polystyrene
Aguado et al. (2005)	Same as Aguado et al. (2000a, 2000b) $T=723\sim873K$	Defluidization modeling of pyrolysis of plastics
Olazar et al. (2005)	Same as Aguado et al. (2000a, 2000b) $T=723\sim873K$	Pyrolysis of scrap tire
Atutxa et al. (2005)	Same as Aguado et al. (2000a, 2000b) $T=673K$	Catalytic pyrolysis of sawdust

Table A-3. Summary of hydrodynamic and heat transfer studies on conical spouted beds.

Authors	**Experimental conditions**	**Studies**
Goltsiker et al. (1964)	γ=30, 40, 50, 60º; D_0=D_i=0.025, 0.05, 0.075, 0.1m; D_c=0.3m; H_0=0.05~0.3m; d_s=3.2mm.	Correlations for maximum pressure drop
Gorshtein and Mukhlenov (1964)	γ=20~65º; H_0/D_0=1.3~8.5; Ar=1.1×10^4~8.06×10^5; H_0=0.03~0.15m.	Correlations for specific velocity
Mukhlenov and Gorshtein (1964)	γ=12, 30, 45, 60º; D_i=D_0=0.0103, 0.0125, 0.012, 0.0129m; D_c=0.0615, 0.06, 0.0573, 0.0575m; ρ_s=700~1630kg/m^3; d_s=0.5~2.5mm.	Correlations for pressure drop
Nikolaev and Golubev (1964)	D_0=D_i=0.02, 0.03, 0.04, 0.05m; D_c=0.12m; H_0=0.09~0.15m; d_s=1.75~5.6mm.	Correlations for maximum pressure drop and corresponding velocity
Mukhlenov and Gorshtein (1965a)	γ=20~65º; Ar=1.1×10^4~8.06×10^5; H_0/D_0=0.6~10.	Correlations for transition velocities, maximum pressure drop, and voidage
Mukhlenov and Gorshtein (1965b)	Review	Correlations for the transition velocities, pressure drop, and voidage
Tsvik et al. (1966)	γ=20, 30, 40, 50º; D_i=D_0=0.02~0.042m.	Correlation for internal spouting velocity
Golubkovich et al. (1967)	γ=30, 45, 60º; D_0=D_i=0.051, 0.06, 0.075m; D_c=0.25~0.36m; ρ_s=670~2350kg/m^3; d_s=0.21~4mm.	Correlations for transition velocities and pressure drop
Gorshtein and Mukhlenov (1967)		Correlation for local particle velocity

Table A-3. Continued.

Authors	Experimental conditions	Studies
Tsvik et al. (1967a)	Same as Tsvik et al. (1966).	Measurement of the initial angle of a spouting bed core
Tsvik et al. (1967b)	γ=20, 30, 40, 50º; d_s=1.5~4mm; H_0/D_0=2.9~12.	Correlation for external spouting velocity
Romankov and Rashkovskaya (1968)	Review	Review of works on conical spouted bed in Russia
Wan-Fyong et al. (1969)	γ=10~70º; D_0=D_i=0.026~0.076m; D_c=0.112~0.22m; H_0=0.07~0.3m; d_s=0.35~4mm; ρ_s=453~1393kg/m^3.	Correlations for several specific velocities and pressure drop
Baskakov and Pomortseva (1970)	γ=30, 60º; D_0=D_i=0.02, 0.03, 0.04, 0.045, 0.06m; D_c=0.18, 0.3m; H_0=0.095~0.22m; d_s=0.06~0.32mm.	Flow characteristics and heat-transfer
Romankov et al. (1970)	γ=30, 40, 50, 60º; D_0=D_i=0.025, 0.05, 0.075, 0.1m; D_c=0.3m; H_0=0.05~0.3m; d_s=0.2~0.25mm.	Flow structure
Dolidovich and Efremtsev (1983a)	γ=20, 30, 40º; D_0=D_i=0.012~0.016m; D_c=0.048~0.072m; H_0=0.05~0.2m; d_s=1~4mm; ρ_s=880~11400kg/m^3.	Pressure drop and heat transfer
Dolidovich and Efremtsev (1983b)	γ=30, 45, 60º; D_0=D_i=0.033, 0.05, 0.066m; D_c=0.1m; H_0=0.033~0.132m; d_s=0.055~3.5mm; ρ_s=2650~4000kg/m^3.	Hydrodynamics and heat transfer
Kmiec (1983)	γ=24, 34, 53, 60º; D_i=D_0=0.015, 0.035, 0.05, 0.071, 0.082, 0.15m; ρ_s=845~2986kg/m^3; d_s=0.875~6.17mm; D_c=0.088, 0.18, 0.308, 0.9m; H_0=0.05~0.51m.	Minimum spouting velocity

Table A-3. Continued.

Authors	Experimental conditions	Studies
Markowski and Kaminski (1983)	γ=37º; D_i=D_0=0.018, 0.029, 0.056, 0.2, 0.3m; ρ_s=1120~2384kg/m^3; d_s=3.41~10.35mm; D_c=0.11, 0.14, 0.30, 0.48, 1.1m; H_0<0.4m.	Minimum spouting velocity, bed voidage and pressure drop
Waldie et al. (1986a)	γ=60º; D_i=D_0=0.012m; D_c=0.16m; H_0=0.11m.	Voidage in the fountain
Boulos and Waldie (1986)	γ=35º; D_i=D_0=0.006m; D_c=0.145m; d_s=0.595~0.71mm; H_0=0.195m. Half column	Particle velocity by Laser-Doppler Anemometry
Waldie and Wilkinson (1986b)	γ=35º; D_i=D_0=0.013m or 0.019m; D_c=0.145m; H_0=0.195m or 0.23m.	Average particle velocity at different height in the spout by measuring the change of inductance of a search coil using a marker particle.
San Jose et al. (1991)	γ=28, 33, 36, 39, 45º; D_i=0.06m; d_s=1~8mm; ρ_s=2420kg/m^3; H_0<0.2m; D_0=0.03, 0.04, 0.05, 0.06m.	Minimum jet spouting velocity
Choi and Meisen (1992)	γ=60º; D_i=D_0=0.038m; d_s=2.16~2.8mm; ρ_s=927~1490kg/m^3; D_c=0.24m. **Particular column structure**	Minimum spouting velocity
Olazar et al. (1992)	γ=28~ 45º; D_i=0.06m; D_0=0.03, 0.04, 0.05, 0.06m; ρ_s=240~3520kg/m^3; d_s=1~25mm; H_0<0.18m.	Minimum spouting velocity
San Jose et al. (1992)	γ=28~45º; D_i=0.06m; ρ_s=2420kg/m^3; d_s=1~8mm; D_c=0.36m; D_0=0.03~0.06m.	Minimum jet spouting velocity; pressure drop and voidage
Freitas and Freire (1993)	D_i=D_0=0.05m; d_s=0.9~3.1mm; H_0=0.17~0.26m; Glass bead.	Heat transfer

Table A-3. Continued

Authors	Experimental conditions	Studies
Olazar et al. (1993a)	γ=28~ 45º; D_i=0.06m; D_0=0.03, 0.04, 0.05m; d_s=1~8mm; ρ_s=2420kg/m^3; D_c=0.36m; H_0<0.55m.	Hydrodynamics with binary mixture
Olazar et al. (1993b)	γ=28~45º; D_i=0.06m; D_0=0.03, 0.04, 0.05, 0.06m; d_s=1~9.6mm; D_c=0.36m; H_0<0.3m; ρ_s=14~2800kg/m^3.	Minimum spoutable bed height and jet spouting
Olazar et al. (1993c)	γ=28~ 45º; D_i=0.06m; D_0=0.03, 0.04, 0.05, 0.06m; ρ_s=240~3520kg/m^3; d_s=1~25mm; H_0<0.11m.	Pressure drops
San Jose et al. (1993)	γ=28~ 45º; D_i=0.06m; D_0=0.03, 0.04, 0.05, 0.06m; ρ_s=960~3520kg/m^3; d_s=1~9.6mm; H_0<0.12m.	Global voidage
Olazar et al. (1994b)	γ=28~ 45º; D_i=0.06m; D_0=0.03, 0.04, 0.05, 0.06m; d_s=0.95, 1.5, 4.2, 25mm; H_0<0.2m; ρ_s=242kg/m^3; D_c=0.36m.	Hydrodynamics of sawdust and wood residues
San Jose et al. (1994)	γ=36º; D_i=0.06m; D_0=0.03, 0.04, 0.05m; d_s=1~8mm; D_c=0.36m; H_0=0.05~0.4m; ρ_s=2420kg/m^3.	Segregation of binary and ternary mixtures of equidensity spherical particles
Olazar et al. (1995b)	γ=28~ 45º; D_i=0.06m; D_0=0.03, 0.04, 0.05m; ρ_s=2420kg/m^3; d_s=1, 2, 3, 4, 6, 8mm; H_0=0.1~0.3m.	Local bed voidage and trajectories of particles
Peng and Fan (1995)	γ=5~ 30º; H_0=0.1~0.2m; d_s=1.19mm. Two-dimensional tapered fluidized beds for liquid-solid system	Transition velocities and pressure drop
San Jose et al. (1995)	γ=28~ 45º; D_i=0.06m; d_s=1~8mm; H_0=0.1~0.34m; ρ_s=960~2420kg/m^3; D_0=0.03, 0.04, 0.05m.	Gas dispersion/mixing

Table A-3. Continued

Authors	Experimental conditions	Studies
Al-Jabari et al. (1996)	γ=31º; D_i=D_0=0.0085m	Liquid-solid system Particle elutriation
Olazar et al. (1996b)	Similar to Olazar et al. (1992)	Particle trajectories; spout geometry and local bed voidage of jet spouted beds
Olazar et al. (1996c)	γ=15, 20, 25, 30, 40, 45, 50º; D_i=0.012m; D_0=0.003, 0.004, 0.005, 0.006, 0.008, 0.01, 0.012m; D_c=0.2m; d_s=0.4~1.15mm; ρ_s=910~2420kg/m^3; H_0=0.05~0.4m.	Hydrodynamics of fine particles
Olazar et al. (1996d)	"Hydrodynamics and applications of conical spouted beds", Trends Chem. Eng., 3, 219-233	Review on conical spouted beds.
Olazar et al. (1998)	γ=33, 36, 45º; D_i=0.06m; D_0=0.03, 0.04, 0.05m; d_s=3, 4, 5mm; D_c=0.36m; H_0=0.05~0.3m; ρ_s=2420kg/m^3.	Particle velocity profile measurement using optical fibre probes
San Jose et al. (1998a)	Same as Olazar et al. (1998)	Solid cross-flow and particle trajectories
San Jose et al. (1998b)	Same as Olazar et al. (1998)	Local bed voidage
Olazar et al. (1999)	Same as Olazar et al. (1992) Sawdust	Bed voidage in different regimes
Hu et al. (2000) Jing et al. (2000, 2001)	γ=20, 40, 60º; H_0≤0.3m; D_0=0.05m; d_s=0.077mm, 1.81mm; ρ_s=1398kg/m^3, 1650kg/m^3. Tapered fluidized beds	Pressure drop and transition velocities
Spitzner Neto et al. (2001)	γ=60º; D_i=0.06m; D_0=0.05m; D_c=0.3m; d_s=2.6mm; ρ_s=2490kg/m^3, glass beads as inert particles.	Influence of paste feed on minimum spouting velocity

Table A-3. Continued

Authors	Experimental conditions	Studies
Olazar et al. (2003)	"Spouted bed reactors", Chemical Eng. Technol., 26, 845-852	Review on conical spouted beds.
Olazar et al. (2004)	γ=28, 33, 36, 39, 45º; D_i=0.06m; D_0=0.03, 0.04, 0.05m; d_s=1, 2, 3.5mm; D_c=0.36m; H_0=0.05~0.35m; ρ_s=65~1030kg/m^3.	Pressure drops, minimum spouting velocity and voidage using low-density particles
Bacelos et al. (2005)	γ=60º; D_i=0.06m; D_0=0.05m; D_c=0.3m; d_s=2.6mm; ρ_s=2490kg/m^3, glass beads as inert particles.	Fluid dynamic behaviour in the presence of pastes (egg paste, glycerol)
San Jose et al. (2005a)	γ=33, 36, 45º; D_i=0.06m; D_0=0.03, 0.04, 0.05m; d_s=3.5mm; D_c=0.36m; H_0=0.05~0.3m; ρ_s=65~2420kg/m^3.	Local voidage in conical spouted beds with identical or mixed particles (same size and different density)
San Jose et al. (2005b)	γ=28, 33, 36, 39, 45º; D_i=0.06m; D_0=0.03, 0.04, 0.05m; d_s=1, 2, 3.5mm; D_c=0.36m; H_0=0.05~0.35m; ρ_s=65~1030kg/m^3.	Geometry of the spout and fountain in conical spouted beds with identical or mixed particles
Bacelos and Freire (2006)	γ=60º; D_i=0.06m; D_0=0.05m; d_s=0.79~4.38mm; D_c=0.30m; H_0=0.105, 0.195m; ρ_s=2490kg/m^3.	The stability of spouting in conical spouted beds with uniform particles or particle mixtures

Table A-4. Summary of hydrodynamic models for conical spouted beds.

Authors	Bed geometry and experimental conditions	Models
Kmiec (1983)	γ=24, 34, 53, 60º; D_i=D_0=0.015, 0.035, 0.05, 0.071, 0.082, 0.15m; ρ_s=845~2986kg/m^3; d_s=0.875~6.17mm; D_c=0.088, 0.18, 0.308, 0.9m; H_0=0.05~0.51m.	Model for minimum spouting velocity (Using radial non-uniform gas distribution)
Rovero et al. (1983)	γ=40º; D_c=0.08 and 0.14m; D_i=0.02 and 0.025m; D_0=0.006 and 0.009m. Conical-base spouted bed	Model for gas flow distribution
Hadzismajlovic et al. (1986)	γ=30, 60º; D_i=0.025, 0.05, 0.1m; D_0=0.025, 0.05, 0.06, 0.1m; ρ_s=1275kg/m^3; d_s=5mm; H_0<0.3m, Half column	Model for minimum spouting velocity and pressure drop
Povrenovic et al. (1992)	γ=20(full-column), 30, 60º(half-columns); H_0=0.1~0.5m; D_0=0.025~0.1m; d_s=2.4~10mm; D_i=0.025~0.1m.	Model for minimum spouting velocity and pressure drop
Olazar et al. (1993d, 1995a, 1996a, 2000c)	γ=45º; D_i=0.06m; D_0=0.05m; d_s=1, 3.5mm; D_c=0.36m; H_0=0.015m, 0.28m; ρ_s=14kg/m^3, 2420kg/m^3.	Model for gas flow distribution
Peng and Fan (1997)	γ=5, 10, 20, 30º; H_0=0.10~0.20m; d_s=1.19mm. Two-dimensional tapered columns for liquid-solid system, Perforated distributor	Model for pressure drop and all transition velocities
Charbel et al. (1999)	γ=60º; H_0=0.237, 0.337, 0.377m; D_0=0.05m; D_i=0.065m; d_s=2.96mm; ρ_s=960kg/m^3.	Model for effective solid stresses in the annulus
Hu et al. (2000) Jing et al. (2000, 2001)	γ=20, 40, 60º; H_0=<0.3m; D_0=0.05m; d_s=0.077mm, ρ_s=1398kg/m^3, d_s=1.81mm, 1650kg/m^3.	Same Model as Peng and Fan (1997) for pressure drop and transition velocities

Table A-5. Summary of correlations for the minimum spouting velocity in conical spouted beds.

Author	**Correlation**
Nikolaev and Golubev (1964)	$\left(\mathrm{Re}_b\right)_{ms,a} = 0.051\, Ar^{0.59} \left(\frac{H_0}{D_b}\right)^{0.25} \left(\frac{D_0}{D_b}\right)^{0.1}$
Gorshtein and Mukhlenov (1964)	$\left(\mathrm{Re}_0\right)_{ms,a} = 0.174\, Ar^{0.5} \left[1 + \frac{2\tan\left(\frac{\gamma}{2}\right) H_0}{D_0}\right]^{0.85} \left(\tan\left(\frac{\gamma}{2}\right)\right)^{-1.25}$
Mukhlenov and Gorshtein (1965a)	$\left(\mathrm{Re}_0\right)_1 = 3.32\, Ar^{0.33} \left(\frac{H_0}{D_0}\right) \left(\tan\left(\frac{\gamma}{2}\right)\right)^{0.55}$
Mukhlenov and Gorshtein (1965b)	$\left(\mathrm{Re}_0\right)_{ms,a} = 1.35\, Ar^{0.45} \left(\frac{H_0}{D_0}\right)^{1.25} \left(\tan\left(\frac{\gamma}{2}\right)\right)^{0.58}$
Tsvik et al. (1966)	$\left(\mathrm{Re}_0\right)_1 = 1.81\, Ar^{0.37} \left(\frac{H_0}{D_0}\right) \left(\tan\left(\frac{\gamma}{2}\right)\right)^{0.45}$
Tsvik et al. (1967b)	$\left(\mathrm{Re}_0\right)_{ms,a} = 0.4\, Ar^{0.52} \left(\frac{H_0}{D_0}\right)^{1.24} \left(\tan\left(\frac{\gamma}{2}\right)\right)^{0.42}$

Table A-5. Continued.

Author	Correlation
Wan-Fyong et al. (1969)	The beginning of spouting: $(\mathrm{Re}_0)_1 = 0.64\,\mathrm{Re}_t\left(\frac{H_0}{D_0}\right)^{0.82}\left(\tan\left(\frac{\gamma}{2}\right)\right)^{0.92}$, 16º≤γ≤70º $(\mathrm{Re}_0)_1 = 0.24\,\mathrm{Re}_t\left(\frac{H_0}{D_0}\right)^{0.82}\left(\tan\left(\frac{\gamma}{2}\right)\right)^{0.49}$, 10º<γ<16º The beginning of stable spouting: $(\mathrm{Re}_0)_{ms,a} = 1.24\,\mathrm{Re}_t\left(\frac{H_0}{D_0}\right)^{0.82}\left(\tan\left(\frac{\gamma}{2}\right)\right)^{0.92}$, 16º≤γ≤70º $(\mathrm{Re}_0)_{ms,a} = 0.465\,\mathrm{Re}_t\left(\frac{H_0}{D_0}\right)^{0.82}\left(\tan\left(\frac{\gamma}{2}\right)\right)^{0.49}$, 10º≤γ<16º
Markowski and Kaminski (1983)	$(\mathrm{Re}_0)_{ms,d} = 0.028\,Ar^{0.57}\left(\frac{H_0}{D_0}\right)^{0.48}\left(\frac{D_c}{D_0}\right)^{1.27}$
Kmiec (1983)	$(\mathrm{Re}_0)^2_{ms,a}\left[1.75 + \frac{150(1-\varepsilon_{ms})}{(\mathrm{Re}_0)_{ms,a}}\right] = 31.31 Ar \bullet \left(\frac{H_0}{D_0}\right)^{1.757}\left(\frac{D_0}{D_c}\right)^{0.029}\left(\tan\left(\frac{\gamma}{2}\right)\right)^{2.073}\varepsilon^3_{ms}$
Olazar et al. (1992)	$(\mathrm{Re}_0)_{ms,d} = 0.126\,Ar^{0.5}\left[\frac{D_b}{D_0}\right]^{1.68}\left(\tan\left(\frac{\gamma}{2}\right)\right)^{-0.57}$

Table A-5. Continued.

Author	Correlation
Olazar et al. (1996c)	$(\mathrm{Re}_0)_{ms,d} = 0.126\, Ar^{0.39}\left[\frac{D_b}{D_0}\right]^{1.68}\left(\tan\left(\frac{\gamma}{2}\right)\right)^{-0.57}$ **For fine particles**
Bi et al. (1997)	$(\mathrm{Re}_0)_{ms,d} = \left[0.30 - 0.27\Big/\left(\frac{D_b}{D_0}\right)^2\right]\bullet\sqrt{Ar\left(\frac{D_b}{D_0}\right)\left[\left(\frac{D_b}{D_0}\right)^2+\left(\frac{D_b}{D_0}\right)+1\right]\Big/3}$ **For** $\frac{D_b}{D_0} > 1.66$ $(\mathrm{Re}_0)_{ms,d} = 0.202\sqrt{Ar\left(\frac{D_b}{D_0}\right)\left[\left(\frac{D_b}{D_0}\right)^2+\left(\frac{D_b}{D_0}\right)+1\right]\Big/3}$ **For** $\frac{D_b}{D_0} < 1.66$
Jing et al. (2000)	$A\left(\frac{D_0}{D_b}\right)^2 (U_0)_{ms,a} + B\left(\frac{D_0}{D_b}\right)^4 (U_0)^2_{ms,a} - (1-\varepsilon_g)(\rho_s-\rho_g)g = 0$ $A = 150\frac{(1-\varepsilon_g)^2}{\varepsilon_g^3}\frac{\mu_g}{(\varphi_s d_s)^2}$; $B = 1.75\left(\frac{1-\varepsilon_g}{\varepsilon_g^3}\right)\frac{\rho_g}{\varphi_s d_s}$

238

Table A-6. Summary of hydrodynamic studies on shallow cone-based spouted beds.

Authors	Experimental conditions	Studies
San Jose et al. (1996a)	D_c=0.15m; D_0=0.03, 0.04, 0.05m; d_s=1~8mm; ρ_s=2420kg/m^3; $H_0\leq$0.3m.	Cylindrical geometry Dead zone and spout diameter
San Jose et al. (1996b)	γ=30, 50, 60, 90, 120, 150º; D_i=0.06m; D_0=0.02, 0.03, 0.04, 0.05, 0.06m; D_c=0.15m; d_s=1~8mm; ρ_s=2420kg/m^3; H_0<0.35m.	Influence of the conical section
Olazar et al. (2001b)	γ=30, 45, 60, 120, 180º; D_i=0.063m (D_i= D_c, for γ=180º); D_0=0.003, 0.004, 0.005m; D_c=0.152m; d_s=2, 3, 4, 5mm; H_0=0.05~0.35m; ρ_s=2420kg/m^3.	Effect of operating conditions on solids velocity

Table A-7. Summary of CFD simulations on spouted beds.

Authors	Experimental data used for evaluation	Remarks
Kawaguchi et al. (2000)	Vertical solids velocity profiles and the shape of the spout from He et al. (1994b), and the shape of the spout from Roy et al. (1994)	**DEM approach, quasi-three-dimensional (two dimensional for fluid motion, three dimensional for particle motion)** **Gas inlet velocity profile was assumed to be uniform;** **Particles were assumed to be completely suspended;** **The diameter of the bed bottom was assumed to be the same as the diameter of the gas inlet;** Calculated spout diameter agreed quantitatively well with experimental data; Calculated velocity profiles agreed qualitatively well with experimental results.
Huilin et al. (2001)	Voidage profiles from He et al. (1994a), vertical solids velocity profiles from He et al. (1994b) and solids velocity profiles from San Jose et al. (1998a)	**TFM approach (Using K-FIX code), two dimensional, Δt=1e-4~1e-5 s** **Gas inlet velocity profile was assumed to be uniform;** **Particles were assumed to be completely suspended;** **The diameter of the bed bottom was assumed to be the same as the diameter of the gas inlet;** **Superficial gas velocity at the inlet and the initial solids fraction were smaller than the experiments;** Empirical correlations were used to estimate solids viscosity and solids elasticity modulus.

Table A-7. Continued.

Authors	Experimental data used for evaluation	Remarks
Lu et al. (2004)	Voidage profiles from He et al. (1994a), vertical solids velocity profiles from He et al. (1994b) and solids velocity profiles from San Jose et al. (1998a)	**TFM approach (Using K-FIX code), two dimensional, e_{ss}=0.9, 0.99** **Gas inlet velocity profile was assumed to be uniform;** **Particles were assumed to be completely suspended;** **The diameter of the bed bottom was assumed to be the same as the diameter of the gas inlet;** **Superficial gas velocity at the inlet and the initial solids fraction were smaller than the experiments;** Kinetic theory was used to estimate solids viscosity and solids pressure; Friction was considered.
He et al. (2004)	Solids velocity profiles and the shape of the spout from Roy et al. (1994), voidage profiles from He et al. (1994a), and vertical solids velocity profiles and the shape of the spout from He et al. (1994b)	**TFM approach (Using K-FIX code), two dimensional** **Gas inlet velocity profile was assumed to be uniform;** **Particles were assumed to be completely suspended;** **The diameter of the bed bottom was assumed to be the same as the diameter of the gas inlet;** Empirical correlations were used to estimate solids viscosity and solids elasticity modulus.

Table A-7. Continued.

Authors	Experimental data used for evaluation	Remarks
Limtrakul et al. (2004)	The unconverted ozone fraction from Rovero et al. (1983) (D_c=0.152m, D_0=0.019m, γ=60°, d_s=4.4mm, ρ_s=2200kg/m^3)	**DEM approach, two dimensional for fluid motion, three dimensional for particle motion, Δt=2e-4 s, e_{ss}=0.9** A spouted bed reactor for the decomposition of ozone on oxide catalyst was simulated, and simulation results agreed well with experimental data.
Szafran and Kmiec (2004)	Drying of microspherical particles from Kmiec and Szafran (2000) (D_c=0.17m, D_0=0.03m, γ=50°, H_0=0.1m, d_s=0.22mm, ρ_s=630kg/m^3, with draft tube)	**TFM approach (FLUENT), two dimensional, Δt=1e-4~3e-4 s, second order upwind scheme, convergence criterion was 1e-3 except continuity (1e-4) and energy (1e-6)** Heat and mass transfer in a spouted bed dryer with the draft tube installed were simulated, and CFD simulations predicted very well the mass transfer rate while underestimated the heat transfer rate.
Takeuchi et al. (2004, 2005)	Vertical solids velocity profiles in the annulus from Tsuji et al. (1997) (In experiments, D_c=0.14m, D_0=0.02m, **d_s=1.71mm**, flat-bottomed column)	**DEM approach, three dimensional, second order scheme, e_{ss}=0.9** **A top-hat shape of velocity profile was adopted;** Particle motion and circulation were investigated, particles were found to feed from annulus to spout along the entire spout; particle velocity profiles show good agreement with experimental data, although simulated spouted bed was quite different from the experimental setup. (In simulation, D_c=0.15m, D_0=0.02m, H_0=0.2m, **d_s=2.4mm**, ρ_s=2650kg/m^{3,} flat-bottomed column)

Table A-7. Continued.

Authors	Experimental data used for evaluation	Remarks
Duarte et al. (2005)	Voidage profiles from He et al. (1994a) and vertical solids velocity profiles and the shape of the spout from He et al. (1994b)	**TFM approach (Using FLUENT code), two dimensional, Δt=1e-6~1e-3 s, second order upwind scheme, convergence criterion was 1e-3, e_{ss}=0.9** **Gas inlet velocity profile was assumed to be parabolic;** **Particles were assumed to be completely suspended;** **The diameter of the bed bottom was assumed to be the same as the diameter of the gas inlet;** Kinetic theory was used to estimate solids viscosity and solid pressure; **The average gas inlet velocity was higher than the experimental value.**
Du et al. (2006)	Voidage profiles from He et al. (1994a) and vertical solids velocity profiles from He et al. (1994b)	**TFM approach (Using FLUENT code), two dimensional, Δt=1e-3~2e-3 s, e_{ss}=0.9** **Gas inlet velocity profile was assumed to be uniform;** **Particles were assumed to be completely suspended;** **The diameter of the bed bottom was assumed to be the same as the diameter of the gas inlet;** Kinetic theory was used to estimate solids viscosity and solid pressure; Different correlations for the exchange coefficient were investigated, and the Gidaspow (1994) drag model seemed to be the best; Simulated solids velocity profiles were lower than experimental data.

APPENDIX B

CALIBRATION OF THE ORIFICE METER

In the current study, pressure taps of an orifice meter were located on flanges, the discharge coefficient of the orifice meter can be calculated based on the throat diameter of the orifice plate, and the diameter of the tube connected to the orifice meter using following equations (Stearns et al., 1951).

$$\beta_o = \frac{d_o}{d_{tube}} \tag{B-1}$$

$$B_o = \frac{530}{\sqrt{d_{tube}}} \tag{B-2}$$

$$A_o = d_o(830 - 5000\beta_o + 9000\beta_o^2 - 4200\beta_o^3 + B_o) \tag{B-3}$$

$$b_o = 0.5993 + \frac{0.007}{d_{tube}} \tag{B-4}$$

$$n_o = 0.364 + \frac{0.076}{\sqrt{d_{tube}}} \tag{B-5}$$

$$K_e \approx b_o + n_o \beta_o^4 \tag{B-6}$$

$$(\mathrm{Re})_e = \frac{10^6 d_o}{15} \tag{B-7}$$

$$K_o = K_e \frac{1 + A_o/\mathrm{Re}}{1 + A_o/(\mathrm{Re})_e} \tag{B-8}$$

$$\mathrm{Re} = \frac{\rho_g U_o d_o}{\mu_g} \tag{B-9}$$

where d_o (inch) is the throat diameter or the orifice diameter, d_{tube} (inch) is the diameter of the tube/pipe connected to the orifice meter, β_o is the diameter ratio, Re is Reynolds number based on the diameter of the orifice, K_o is the orifice discharge coefficient, K_e is the orifice discharge coefficient when $Re=(Re)_e$, U_o (m/s) is gas velocity through the orifice, μ_g (Pa·s) is the gas viscosity, ρ_g (kg/m^3) is the gas density. While, A_o, B_o, b_o, n_o and $(Re)_e$ are intermediate parameters which are functions of d_o and/or d_{tube}. For the standard orifice meter (d_{tube}=3 inch, d_o=0.75 inch) and the orifice meter (d_{tube}=1.5 inch, d_o=0.6 inch) used in this study, some parameters are listed in Table B-1.

Based on Equation (B-8), K_o is a function of the operating velocity, and K_o will equal K_e when Re is big enough.

For any orifice meter, the volume flow rate can be written as

$$Q = K_o(\pi d_o^2)\sqrt{\frac{2\Delta P}{\rho_g}} \tag{B-10}$$

Table B-1. Parameters for the standard orifice meter and the orifice meter used in this study.

d_{tube} (inch)	d_o (inch)	β_o	$(Re)_e$	B_o	A_o	b_o	n_o	K_e
3[s]	0.75[s]	0.25[s]	50000[s]	305.996[s]	287.153[s]	0.6016[s]	0.4079[s]	0.6032[s]
1.5[a]	0.6[a]	0.4[a]	40000[a]	432.743[a]	260.366[a]	0.6037[a]	0.4261[a]	0.6149[a]

Note: s------for the standard orifice meter

a------for the orifice meter used in this study

Under present experimental conditions, the ideal gas law can be applied for estimating gas density,

$$P_g V_g = n_g R_0 \cdot T = \frac{m_g}{M_g} R_0 \cdot T \tag{B-11}$$

$$\rho_g = \frac{m_g}{V_g} = \frac{P_g M_g}{R_0 \cdot T} \tag{B-12}$$

Substituting Equation (B-12) into Equation (B-10), one obtains,

$$Q = K_o(\pi d_o^2)\sqrt{\frac{2\Delta P(R_0 \cdot T)}{P_g M_g}} = \left[K_o(\pi d_o^2)\sqrt{\frac{2R_0}{M_g}}\right] \cdot \sqrt{\frac{\Delta P \cdot T}{P_g}} = K^{'} \cdot \sqrt{\frac{\Delta P \cdot T}{P_g}} \tag{B-13}$$

$$K^{'} = K_o(\pi d_o^2)\sqrt{\frac{2R_0}{M_g}} \tag{B-14}$$

where Q (m^3/s) is the volume flow rate, ΔP (Pa) is the pressure drop of a orifice meter, P_g (Pa) is the operation pressure or gas pressure, V_g (m^3) is the gas volume, n_g (mol) is the number of moles, R_0=8.3145 J/(mol·K) is the universal gas constant, m_g (kg) is the weight of gas, Mg (kg/mol) is the molar weight of the gas (for air, M_g=0.029 kg/mol), T (K) is the absolute temperature.

Note: From Equations (B-1) to (B-9), d_o was used in inch; from Equations (B-10) to (B-14), d_o was used in meter.

In the current study, the operating gas velocity is usually big enough, thus, K_o=K_e, and by substituting other parameters into Equation (B-14), K' can be obtained. For the orifice meter used in the current study, K'=0.002686.

The orifice meter used in this study was also calibrated using a standard orifice meter as shown in Figure B-1. Orifice discharge coefficients for the standard orifice meter were calculated from Equation (B-8). Considering that the two orifice meters were installed in series, and the operating temperature was almost constant, orifice discharge coefficients for the orifice meter used in this study can then be calculated.

Figure B-2 shows the comparison of orifice discharge coefficients calculated by Equation (B-8) and obtained using the calibration method. It can be seen that, within the mass flow rate investigated, orifice discharge coefficients are almost a constant. Moreover, orifice discharge coefficients calculated from Equation (B-8) are close to those obtained from calibration experiments using the standard orifice meter with a mean relative deviation less than 3%. Thus, the mean value on calculated orifice discharge coefficients was applied throughout this study, i.e., K_o=0.61546, and K'=0.002688.

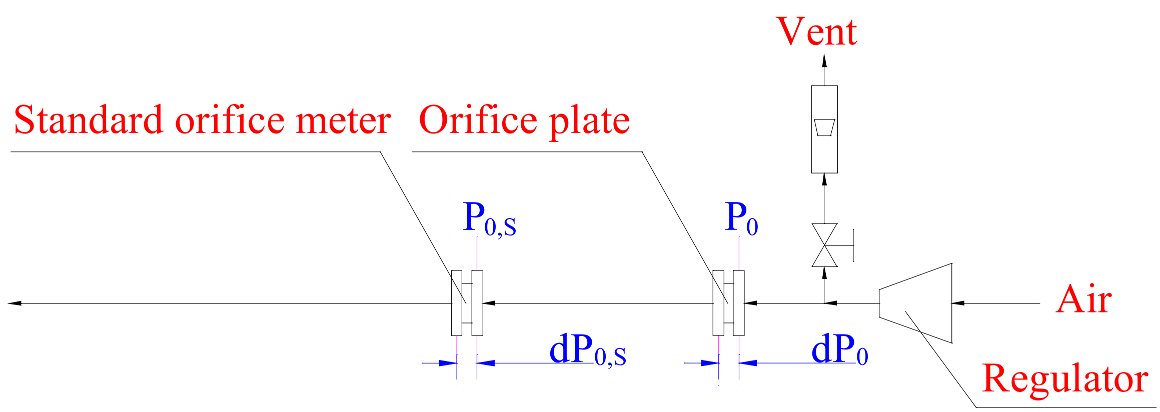

Fig. B-1. Calibration of the orifice plate using a standard orifice meter.

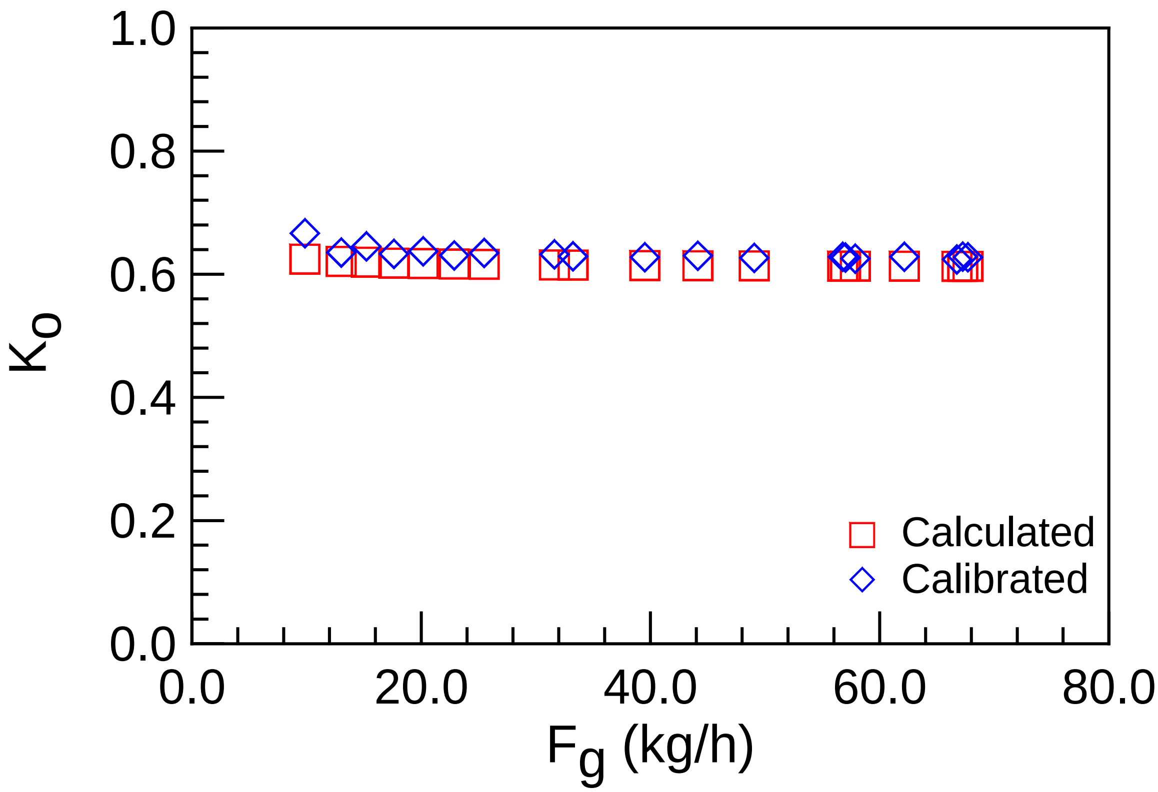

Fig. B-2. Comparison of orifice discharge coefficients for the orifice meter used in this study at different mass flow rates.

APPENDIX C

CALIBRATION OF PRESSURE TRANSDUCERS

Pressure transducers used in current study are shown in Table C-1, including model number, pressure range etc.

Table C-1. Pressure transducers used in current study.

<table>
<tr><th>Using Location</th><th>Model Number</th><th>Pressure Range</th></tr>
<tr><td>dP_0</td><td>PX142-002D5V</td><td>0~2 psi</td></tr>
<tr><td>dP_2</td><td rowspan="3">PX142-001D5V</td><td rowspan="3">0~1 psi</td></tr>
<tr><td>dP_3</td></tr>
<tr><td>dP_4</td></tr>
<tr><td>dP_5</td><td rowspan="2">PX164-010D5V</td><td rowspan="2">0~10 inch H2O</td></tr>
<tr><td>dP_6</td></tr>
<tr><td>P_0</td><td rowspan="2">PX142-030G5V</td><td rowspan="2">0~30 psi</td></tr>
<tr><td>$P_{0,n}$</td></tr>
<tr><td>dP_t</td><td>PX142-005D5V</td><td rowspan="2">0~5 psi</td></tr>
<tr><td>$dP_{t,n}$</td><td>142PC05G</td></tr>
</table>

The pressure transducer calibration system is shown in Figure C-1. By adjusting the amount of the air in the system, a series of pressures can be created. The pressure values were measured using two U-tube manometers, with water as the indicator for low-pressure measurement and mercury as the indicator for high-pressure measurement.

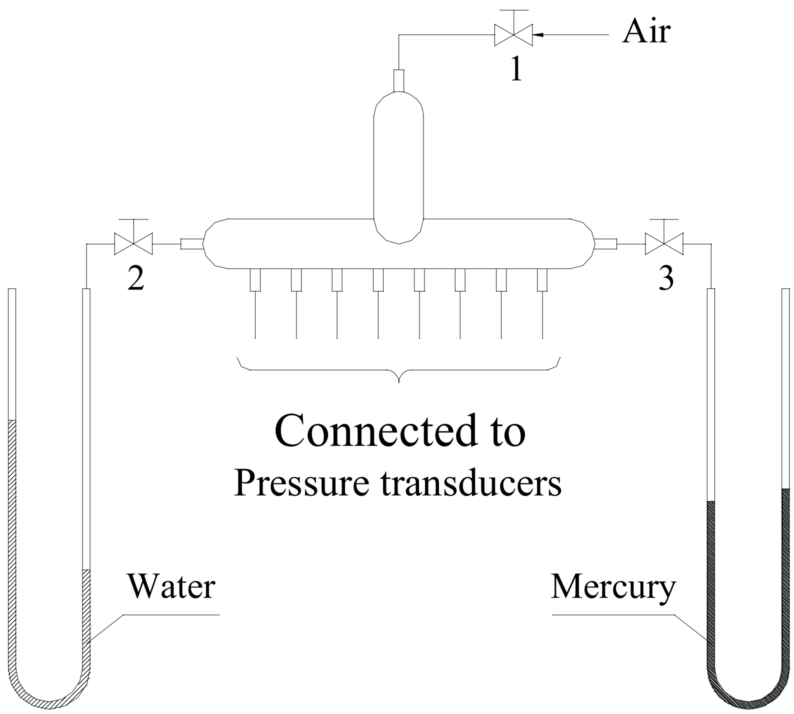

Fig. C-1. Pressure transducer calibration system.

Figures C-1 and C-3 show calibration results for all pressure transducers used in this study. It was found that the gauge pressure P is proportional to the magnitude of the measured electrical signal V, although the zero pressure value “a” is somewhat different from its default value of 1. Thus, before each experiment, the “a” value was calibrated based on the actual zero value of the gauge pressure with the assumption that the slope parameter “k_p” remains constant.

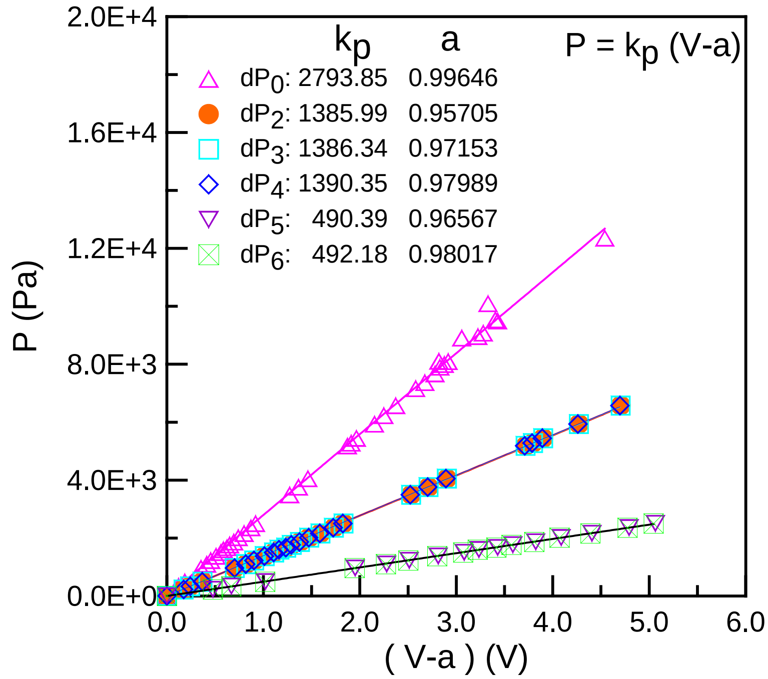

Fig. C-2. Calibration results for pressure transducers. (P is the gauge pressure, V is the magnitude of the measured electrical signal in volt.)

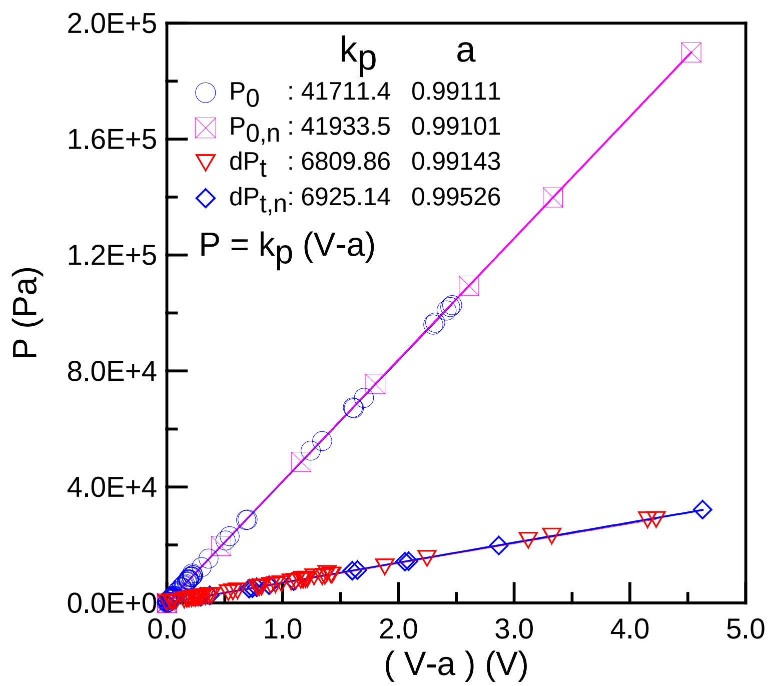

Fig. C-3. Calibration results for pressure transducers. (P is the gauge pressure, V is the magnitude of the measured electrical signal in volt.)

APPENDIX D

CALIBRATION OF THE OPTICAL FIBRE PROBE

D.1 Calibration of the optical fibre probe for the measurement of particle velocity

Calibration setup and calibration principle:

The effective distance between the light-projection and light-receiving fibres of an optical velocity probe was commonly determined using rotating disks (San Jose et al. 1998a), rotating disks (or rod) with one or more particles attached (He, 1995), or a well-mixed water-particle tank (Liu, 2001). In this research, rotating disks with different designs, rotating disks with particles glued, as well as rotating packed bed were applied to investigate the effective distance. As shown in Figure D-1, compared to an old design of the calibration setup (Liu, 2001; Gorkem, 2004) that only had a motor and the rotating disk 2, a reducing gear was added to minimize the system error and enlarge the measurement range. A rotating container was also added to construct a rotating packed bed. Furthermore, rotating disk 2 was reconstructed to improve the accuracy.

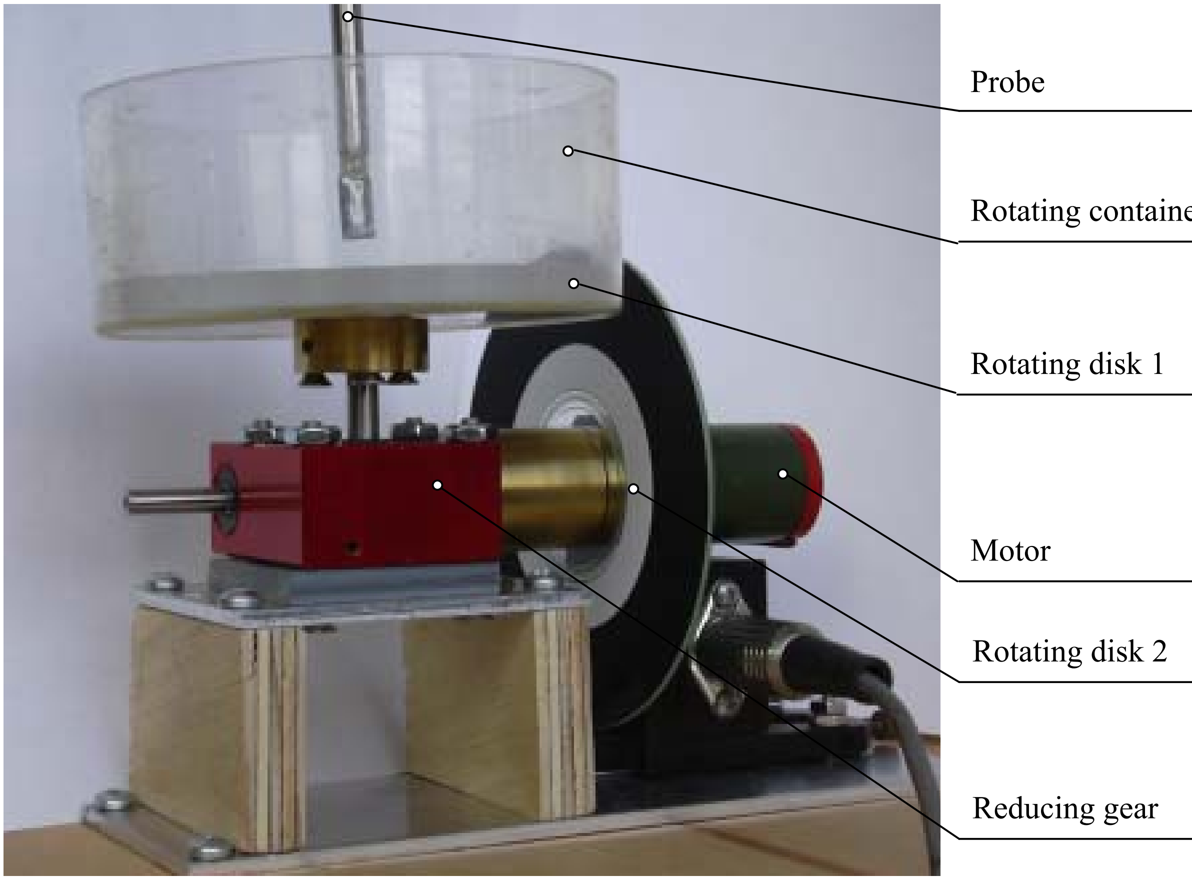

Fig. D-1. Calibration setup for the measurement of effective distances of optical velocity probes.

Assuming that particles 1 and 2 are located in front of the probe tip just before the sampling, as shown in Figure D-2. When the sampling is finished, corresponding measured signals are shown in Figure D-3 (from 0 to t). It means that particle 1 did not pass by receiver B, and the initial part in the signal from receiver A did not appear in the signal from receiver B (shown as dashed line in the initial part). Similarly, the final part in the signal from receiver B did not appear in the signal from receiver A (shown as dashed line in the final part). To avoid the missing data in cross-correlation, experimental data were selected far from the beginning and the end. For example, original signals are from 0 to t, and selected experimental data used for the cross-correlation analysis are from τ and t-τ.

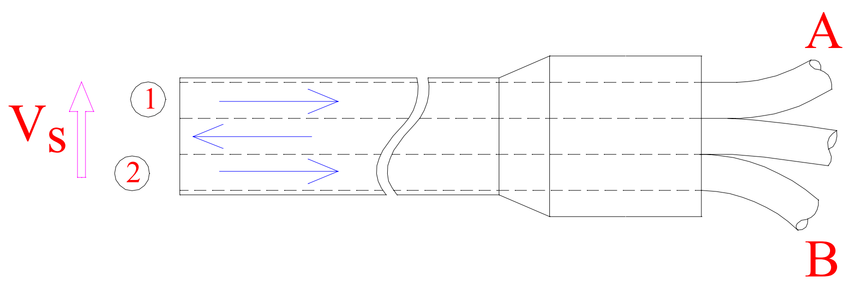

Fig. D-2. Assumed conditions at the tip of the optical fibre probe just before the sampling. (t=0)

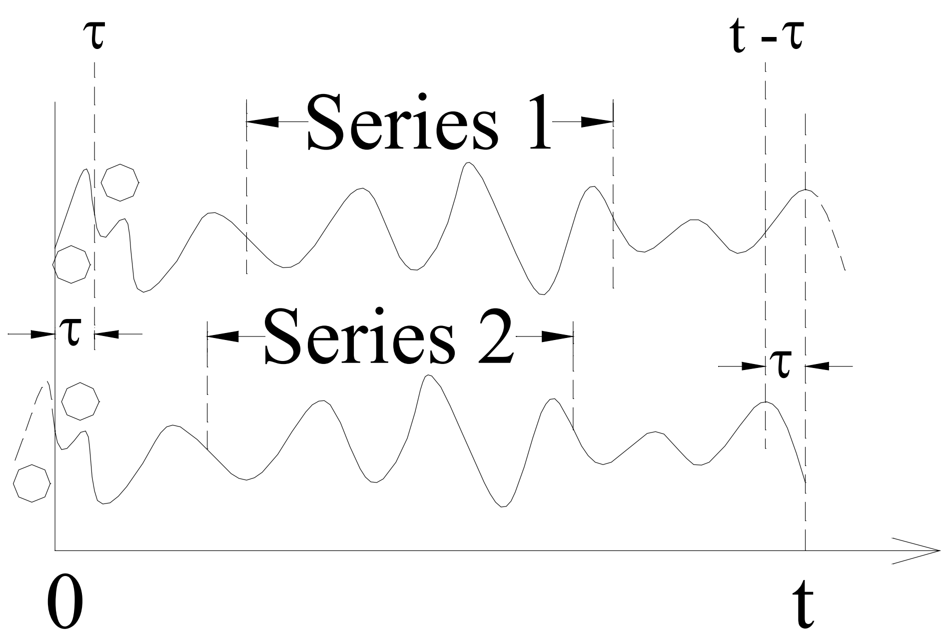

Fig. D-3. Measured signals from the optical fibre probe. ($t \geq 0$)

There are more than 32,768 data in each signal series. To better utilize sampled data, the best group number (2, 4, 8, 16, 32, 64 or128) or the best length of the signal segment/series (the total length divided by the best group number) was determined before further analysis. For example, for a single signal segment used for the cross-correlation analysis shown as “Series 1” in Figure D-3, the maximum cross-correlation coefficient and the time delay were determined from the plot of cross-correlation coefficient versus the delay time. The best length of signal segment to be used for analysis was then determined based on the criterion of having the highest maximum correlation coefficient. Sometimes, there are multiple maximum correlation coefficients in the cross-correlation coefficient vs. delay time plot. The minimum value was then selected as the right delay time.

After the selection of the optimal length of data for cross-correlation, within the data range from τ to $t-\tau$, more than 200 segments were selected for cross-correlation analysis. Further statistical analysis of the estimated maximum correlation coefficient and delay time from each segment was carried out to determine the mean time delay using four different criteria.

Figure D-4 shows the flowsheet of the cross-correlation analysis using following equations with Matlab programs listed in Appendix I.

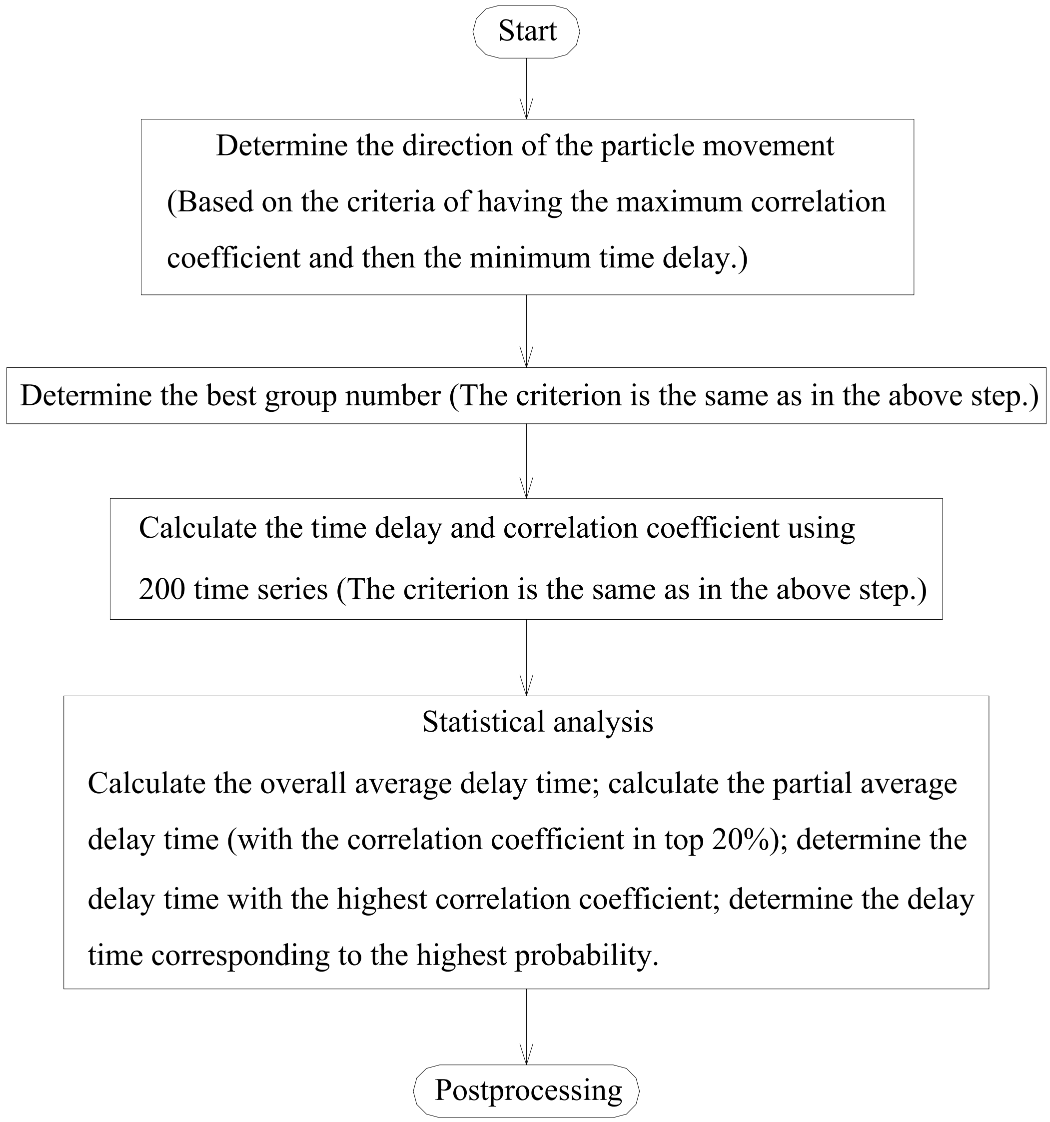

Fig. D-4. Flowsheet for the cross-correlation analysis.

Assuming that the total signal series from receiver A is A_j, and the total signal series from receiver B is B_j, j=1, 2, ……, M_e; the series 1 from receiver A is x_i, and the series 2 from receiver B is y_i, i=1, 2, ……, N_e, with N_e<<M_e; for a sampling frequency of f_s, and a time delay of τ, following relationship exists.

$$x_i = A_{K_e+1}, A_{K_e+2}, \ldots\ldots, A_{K_e+N_e}, \ \tau \cdot f_s \le K_e \le M_e - \tau \cdot f_s \qquad \text{(D-1)}$$

$$y_i = B_{K_e+L_e+1}, B_{K_e+L_e+2}, \cdots\cdots, B_{K_e+L_e+N_e} \tag{D-2}$$

L_e<0 means that particles pass by receiver B first, moving from receiver B to receiver A as shown in Figure D-3. Contrarily, L_e>0 means that the moving direction is from receiver A to receiver B. For above discrete signal series x_i and y_i, the correlation coefficient can be calculated by

$$R_{xy} = \frac{\Sigma[(x_i - \overline{x})(y_i - \overline{y})]}{(N_e - 1) S_x S_y} \tag{D-3}$$

where R_{xy} is the correlation coefficient, $\overline{x}$ and $\overline{y}$ are average values for x_i and y_i respectively, N_e is the number of points in the selected signal series, S_x and S_y are the corresponding standard deviations for x_i and y_i respectively.

$$\overline{x} = \frac{1}{N_e} \cdot \sum_{i=1}^{N_e} x_i \tag{D-4}$$

$$\overline{y} = \frac{1}{N_e} \cdot \sum_{i=1}^{N_e} y_i \tag{D-5}$$

$$S_x = \sqrt{\frac{1}{N_e - 1} \sum_{i=1}^{N_e} (x_i - \overline{x})^2} \tag{D-6}$$

$$S_y = \sqrt{\frac{1}{N_e - 1} \sum_{i=1}^{N_e} (y_i - \overline{y})^2} \tag{D-7}$$

By changing the value of L_e, a series of correlation coefficient can be calculated for each fixed value of K_e. By using the criteria of having the maximum correlation coefficient and then the minimum time delay (Sometimes, corresponding to the maximum correlation coefficient, there are several values of the time delay.), the time delay τ can be obtained by

$$\tau = \frac{L_m}{f_s} \tag{D-8}$$

where L_m is the number of data points corresponding to the time delay. $\tau < 0$ means that the moving direction is from receiver B to receiver A, and $\tau > 0$ means that the moving direction is from receiver A to receiver B.

By conducting cross-correlation for different segments (with different values of K_e), a series of time delay values were obtained and used for further statistical analysis to obtain probability distribution, the overall mean delay time, the partial average delay time (with correlation coefficient in top 20%), the delay time corresponding to the maximum correlation coefficient and the delay time having the highest probability. Finally, the optimum delay time for the calculation of a mean particle velocity was obtained based on the criterion of having the smallest relative standard deviation of the delay time (or the particle velocity) among several measurements (Usually, there are five to ten measurements in each position.).

Figure D-5 shows typical electrical signals and the distribution curve of the cross-correlation coefficient using the rotating plate with glued glass beads, and Figure D-6 shows the distribution of calculated maximum correlation coefficient. It is seen that particles pass by receiver B first with a negative estimated time delay. The calculated maximum cross-correlation coefficients are very high. When the time delay is adjusted for the receiver B, the two signal traces look very similar. The distribution of calculated maximum correlation coefficients is relatively narrow.

When the rotating packed bed was used, as shown in Figures D-7 and D-8, although the two signal traces look similar too, calculated maximum correlation coefficients are relatively small, occasionally even smaller than 0.6. At the same time, the distribution of calculated correlation coefficients is relatively broad comparing to Figure D-6.

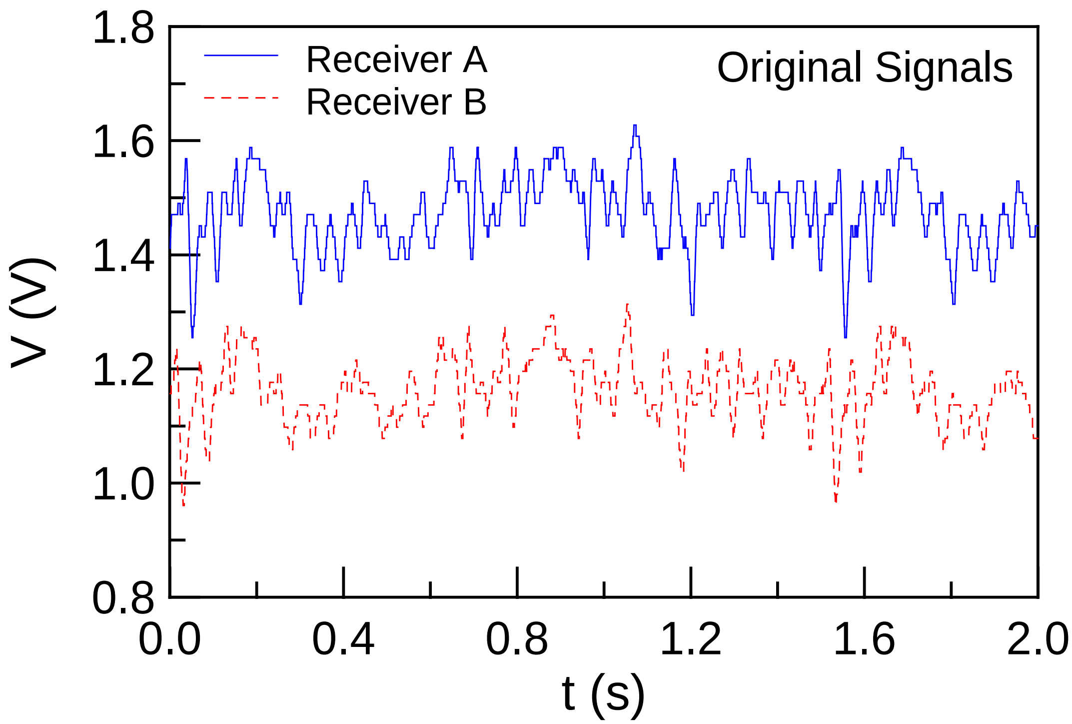

Fig. D-5a. Typical electrical signals using rotating plate with glued glass beads.

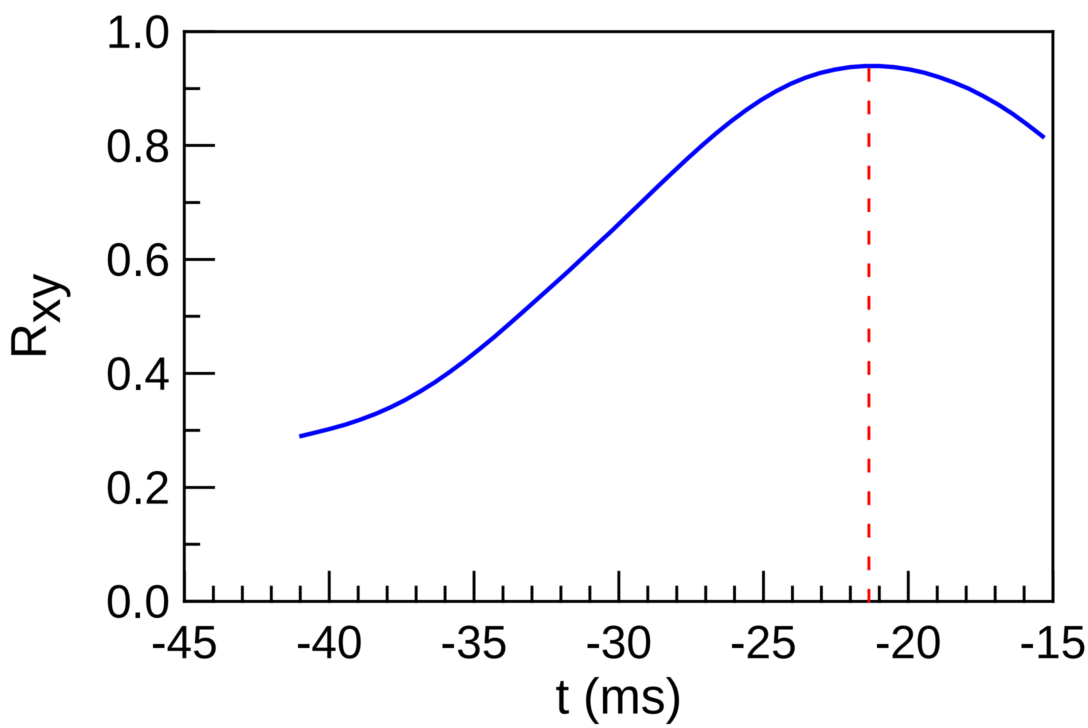

Fig. D-5b. Typical distribution curve of the cross-correlation coefficient using rotating plate with glued glass beads.

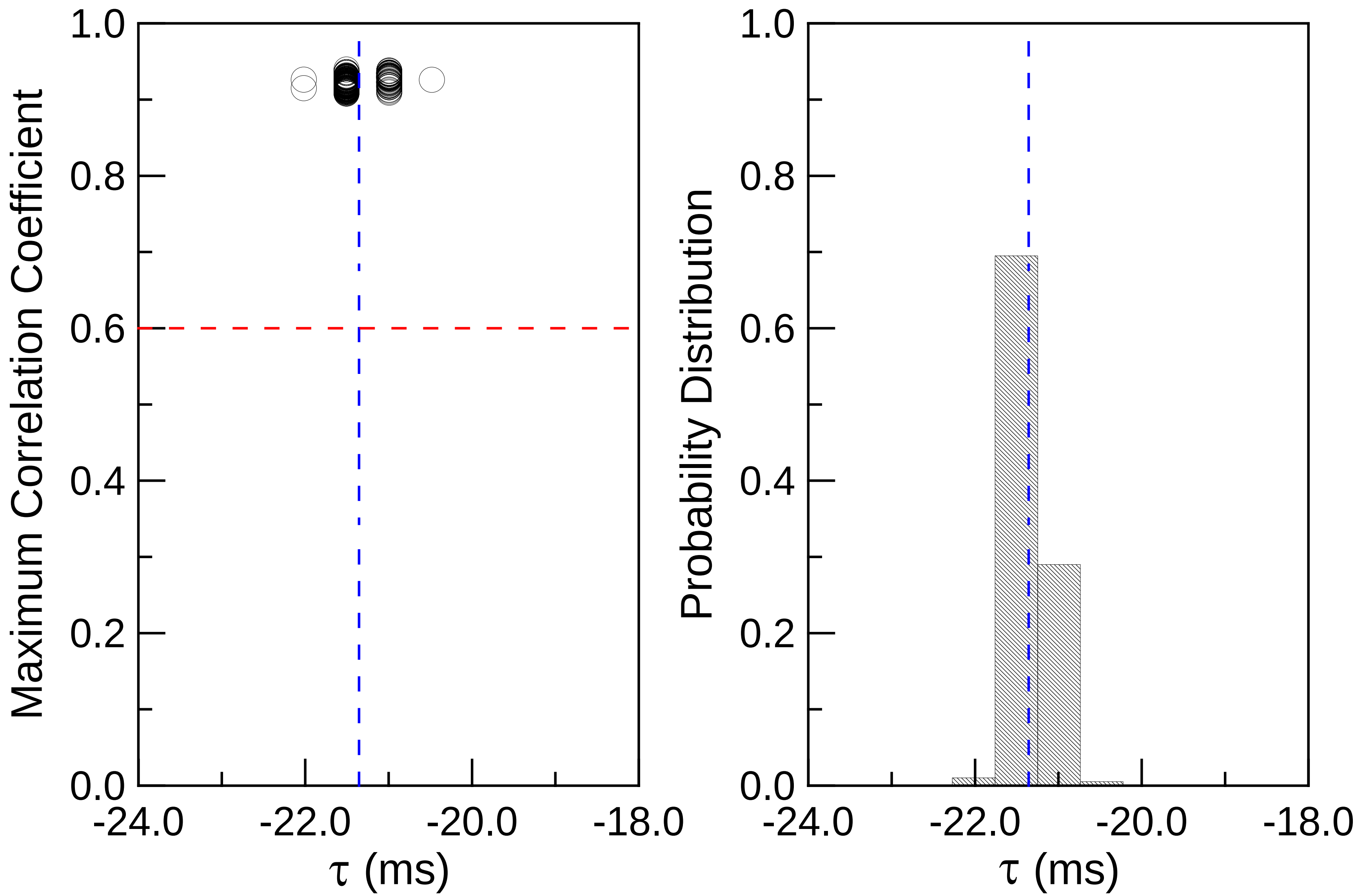

Fig. D-6. Calculated maximum correlation coefficient and its distribution. (Rotating plate with glued glass beads)

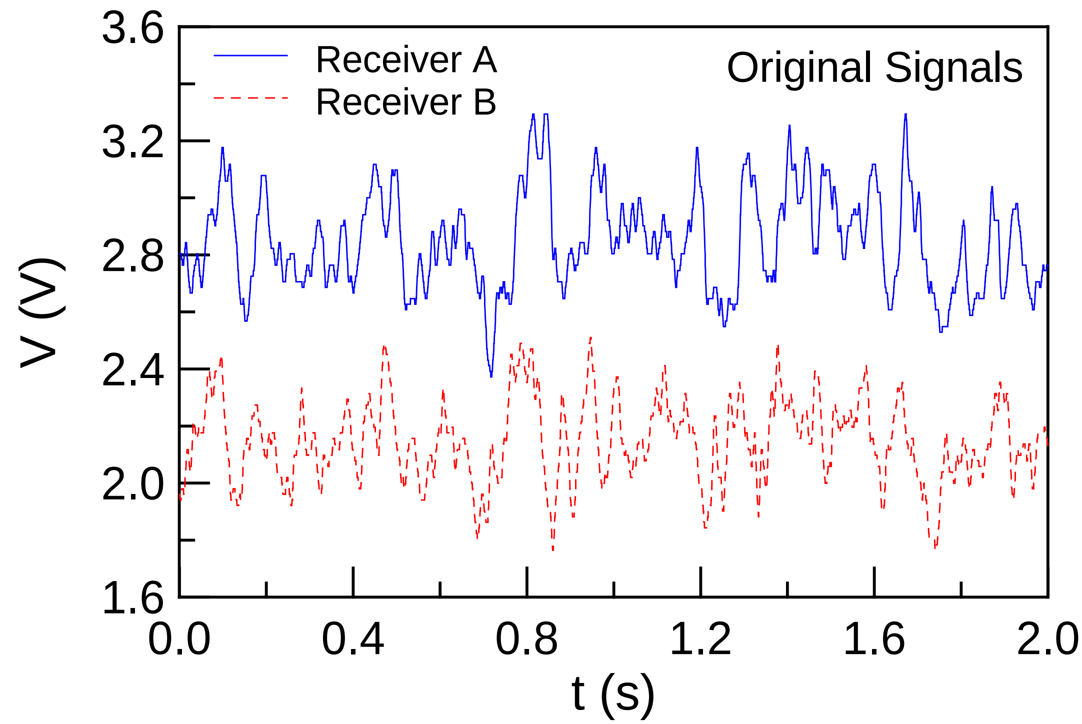

Fig. D-7a. Typical electrical signals using rotating packed bed.

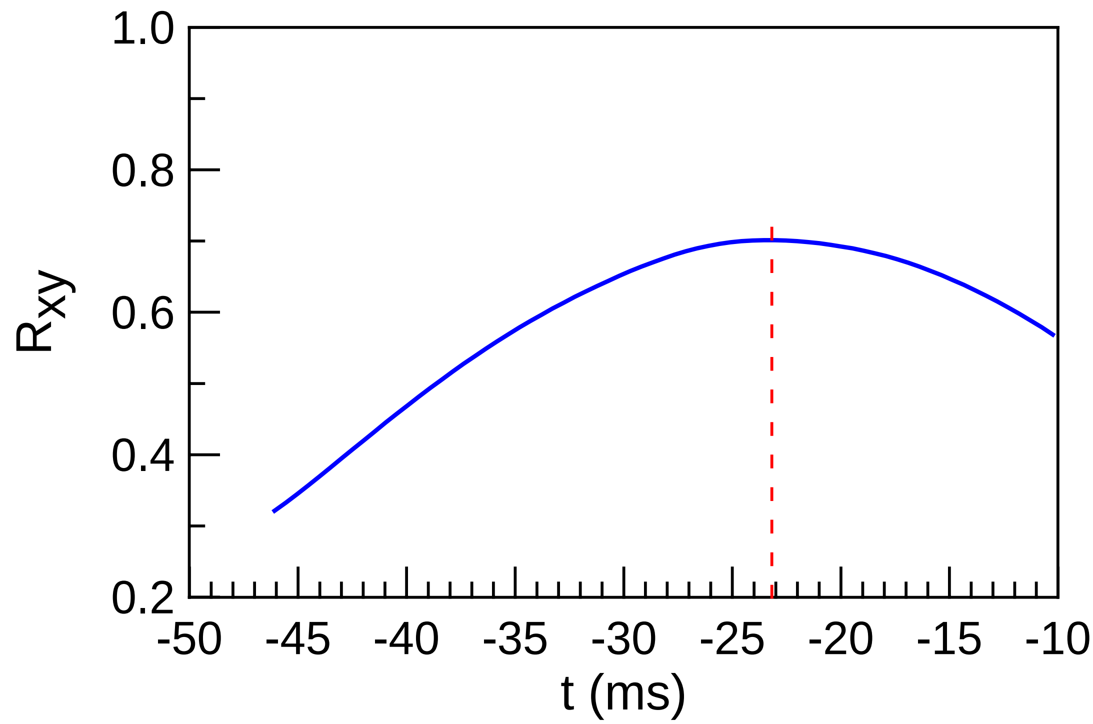

Fig. D-7b. Typical distribution curve of the cross-correlation coefficient using rotating packed bed.

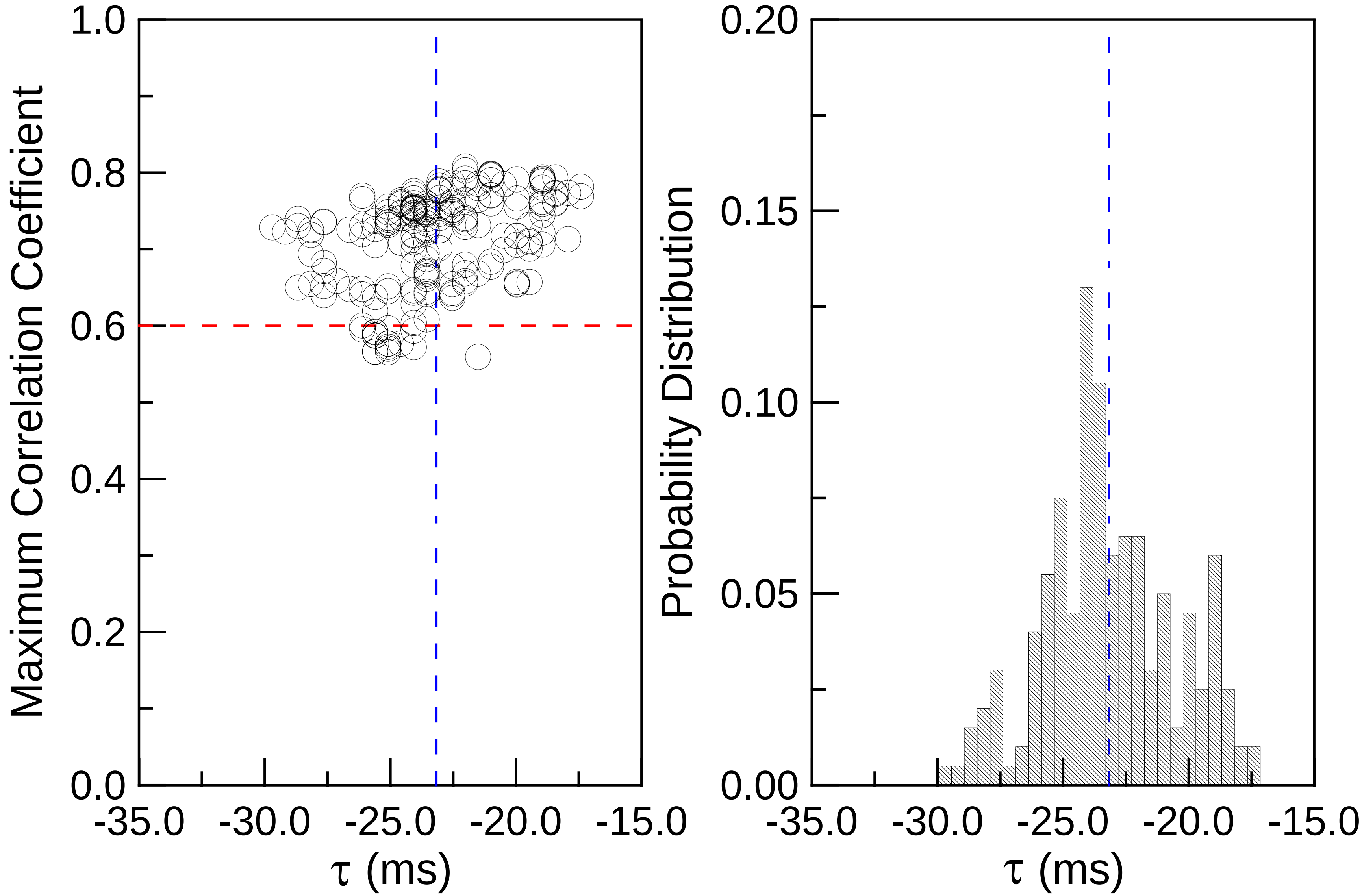

Fig. D-8. Calculated maximum correlation coefficient and its distribution. (Rotating packed bed)

Effect of the glass window:

By using the rotating packed bed filled with glass beads of 1.16 mm in diameter, or using rotating plate (Plate 1 as shown in Figure D-10), the optical fibre probe 2 with and without the glass window was calibrated. The effect of the glass window (5 mm in thickness) on the effective distance is shown in Figures D-9a and D-9b. It can be seen that the glass window does affect the effective distance. Without the glass window, the effective distance varies with the distance between the probe tip and the surface of the bed or the plate, especially significant when the probe tip is above the surface with 1 mm$<d\leq$4 mm. The effective distance obtained when the probe tip is immersed under the bed surface ($d<0$), or above the surface with $0<d\leq1$ mm, is about 2.5 times as much as the effective distance obtained when the probe tip is far away from the bed surface ($d>4$ mm). When the distance between the probe tip and the surface of the bed or the plate is around 2 mm, the measured effective distance is about the same as the geometrical distance D_1. When the glass window was added, the effective distance varies only slightly. Therefore, optical fibre probe 1 installed with a glass window (8.5 mm in thickness) was used in subsequent experiments presented below.

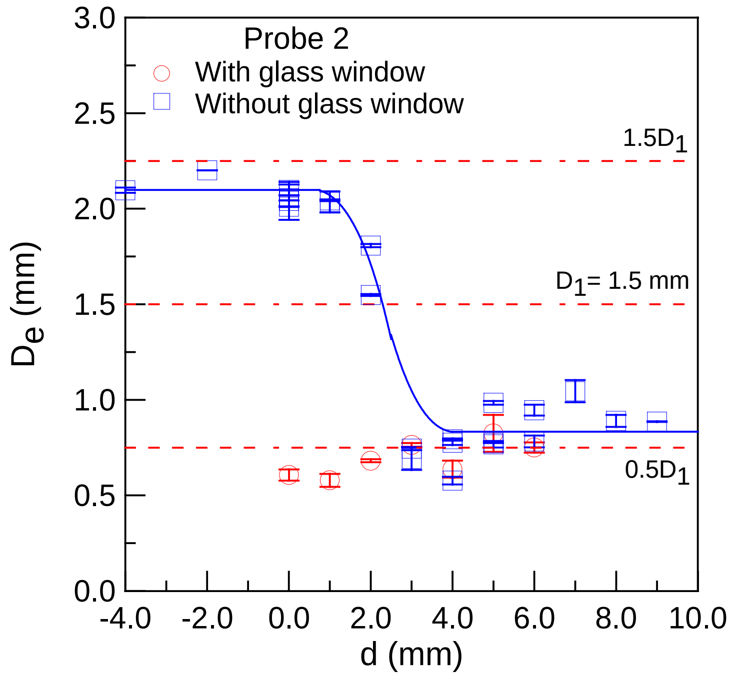

Fig. D-9a. The effect of the glass window on the effective distance. (Rotating packed bed) (Probe 2, D_f=1.5 mm, d_s=1.16mm, d is the distance between the probe tip and the bed surface.)

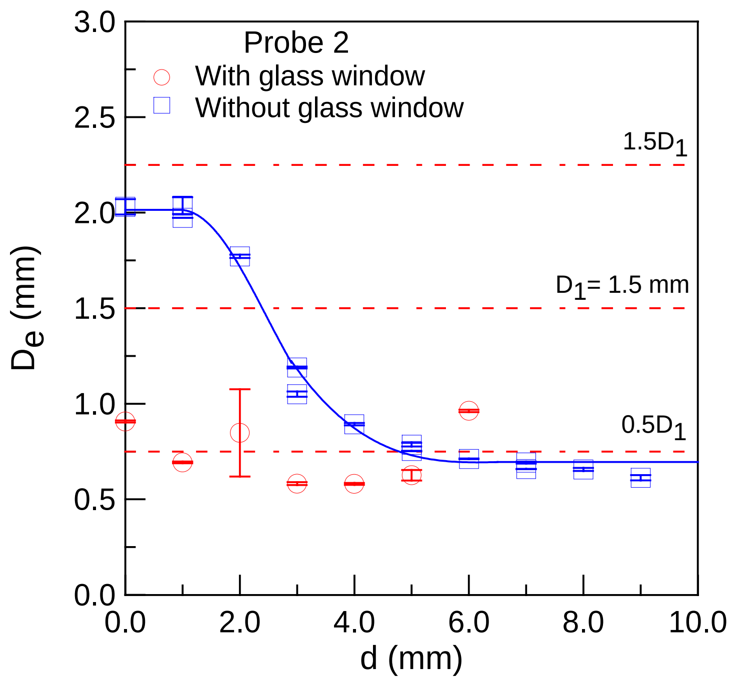

Fig. D-9b. The effect of the glass window on the effective distance. (Rotating plate) (Probe 2, D_f=1.5 mm, d is the distance between the probe tip and the plate.)

Effect of the plate design:

The original design of the rotating plate is shown in Figure D-10, and corresponding measured effective distance is shown in Figures D-11 and D-12, where, r_p is the radial distance between the centre of the optical fibre probe and the centre of the rotating plate or rotating packed bed. It can be seen that the distance between the probe tip and the plate has a significant impact on the effective distance. Furthermore, the radial position has some influence too. Considering that the width of the white slot is different at different radial position, it implies that the size of the white slot may have the same effect. Thus, a series of plates, Plate A to K as shown in Figures D-13 to D-23 respectively, were designed to investigate their influences.

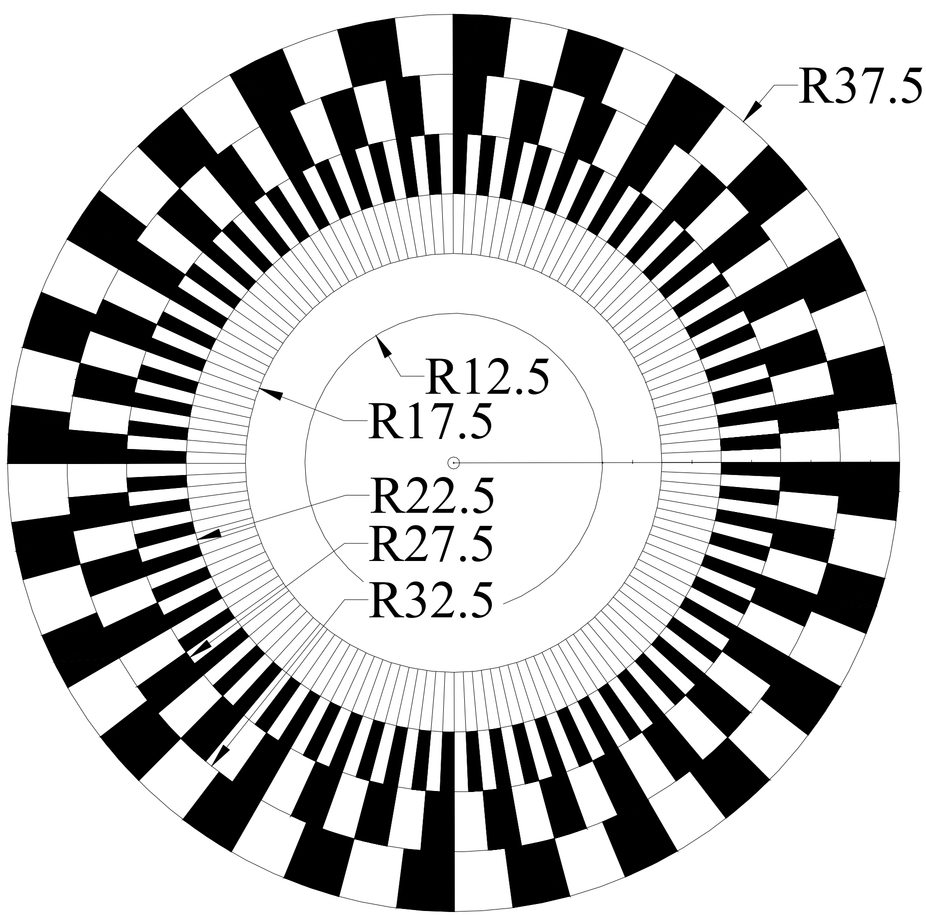

Fig. D-10. The original design of the rotating plate. (Plate 1)

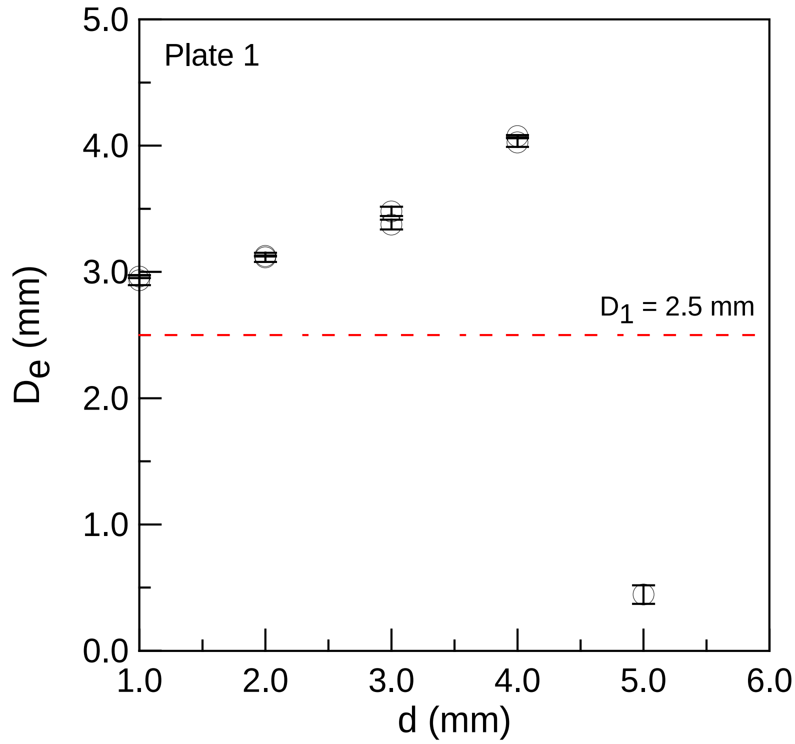

Fig. D-11. The effect of the distance between the probe tip and the plate on D_e. (r_p=25 mm)

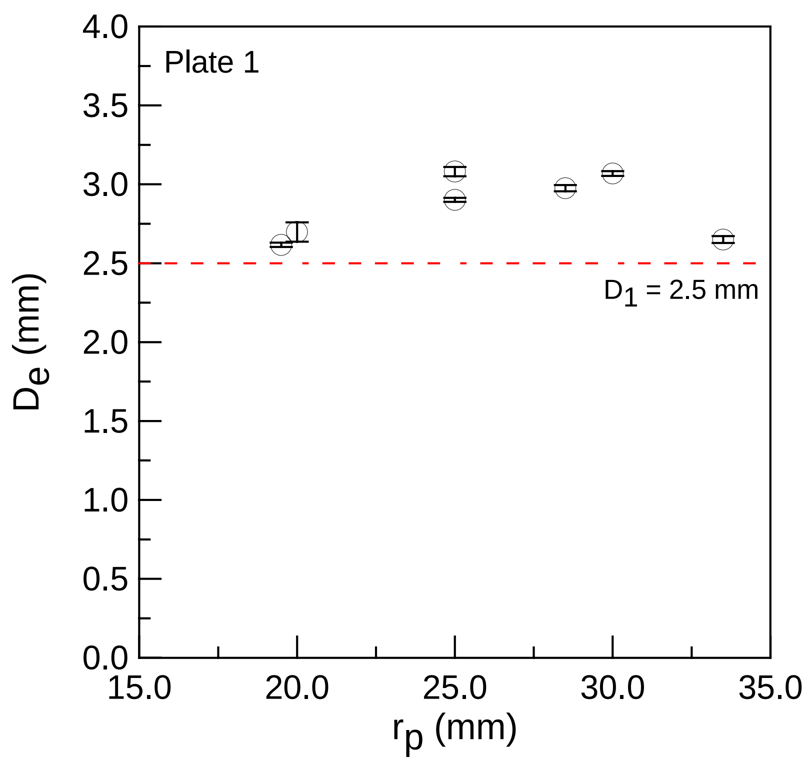

Fig. D-12. The effect of the radial position on D_e. (d=1 mm)

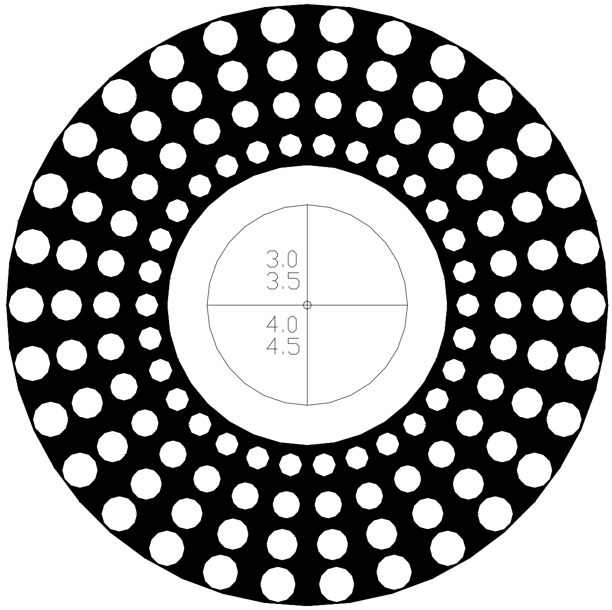

Fig. D-13. Plate A. (From inside out the diameters of white spots are 3.0, 3.5, 4.0 and 4.5 mm, respectively.)

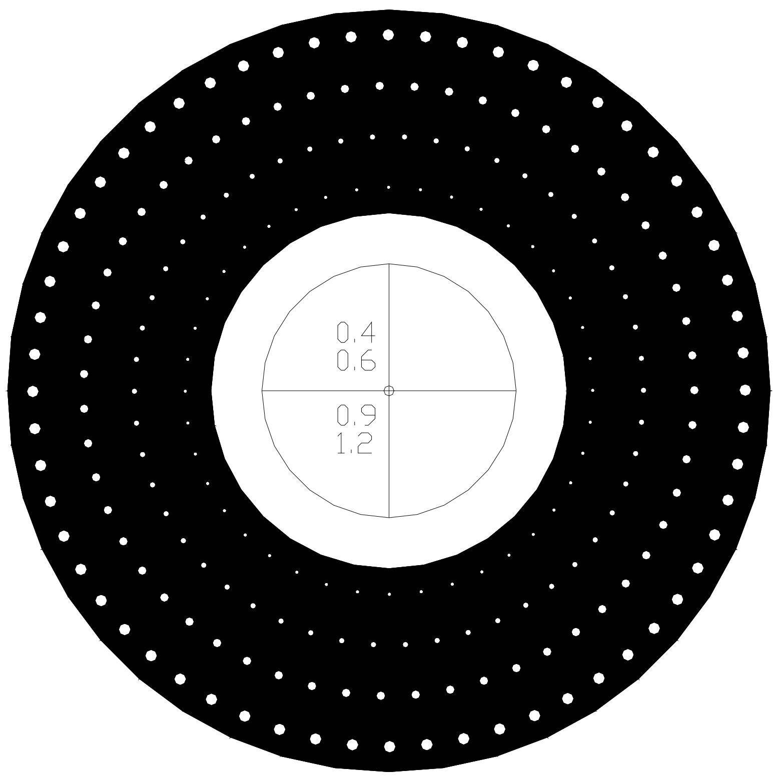

Fig. D-14. Plate B. (From inside out the diameters of white spots are 0.4, 0.6, 0.9 and 1.2 mm, respectively.)

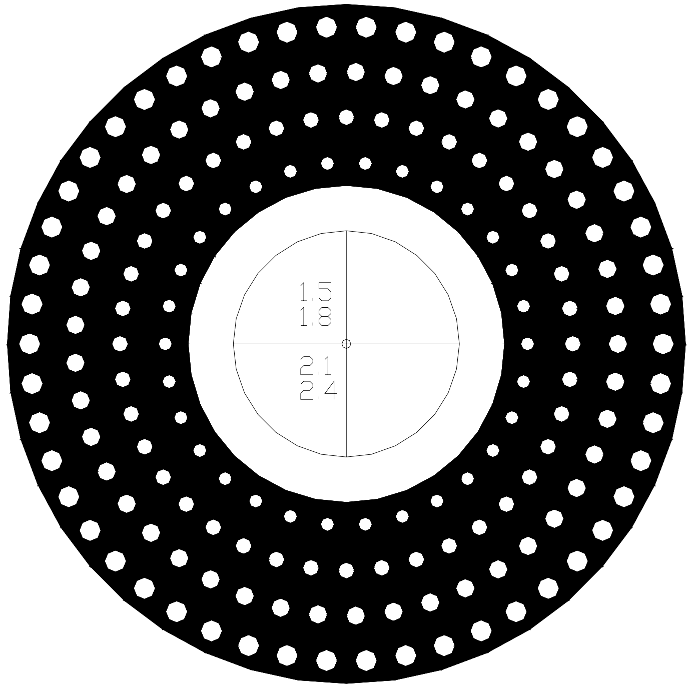

Fig. D-15. Plate C. (From inside out the diameters of white spots are 1.5, 1.8, 2.1 and 2.4 mm, respectively.)

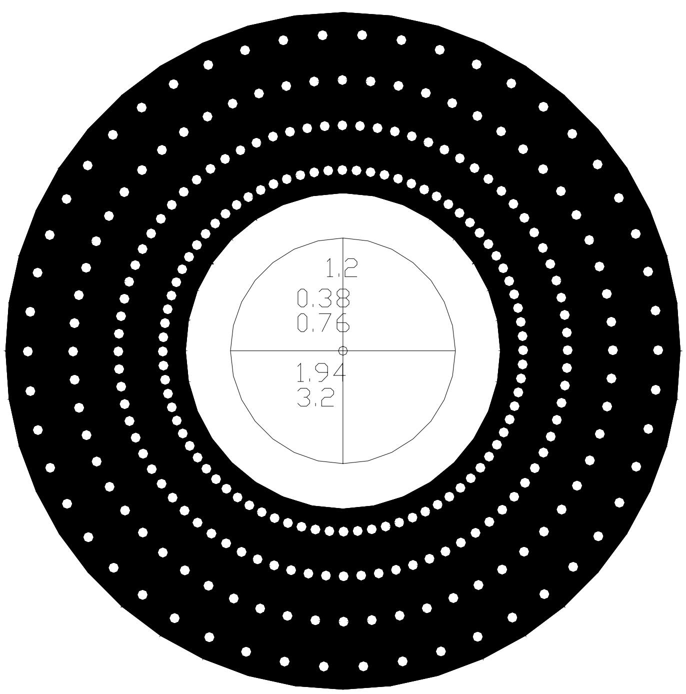

Fig. D-16. Plate D. (The size of white spots is 1.2 mm, the gaps between white spots are 0.38, 0.76, 1.94 and 3.2 mm, respectively.)

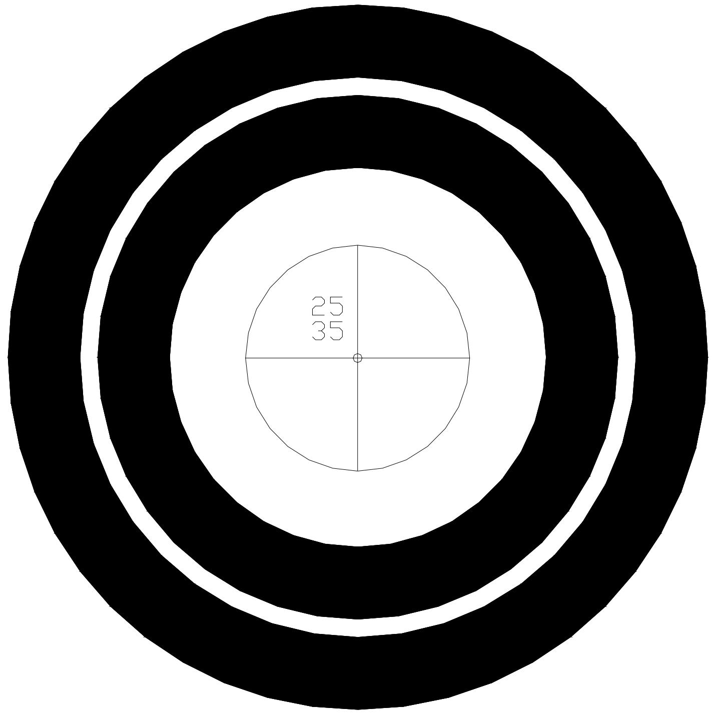

Fig. D-17. Plate E. (Glass beads with 1.16 mm in diameter glued at the outside black ring, Polyethylene with 1 mm in diameter glued at the inside black ring)

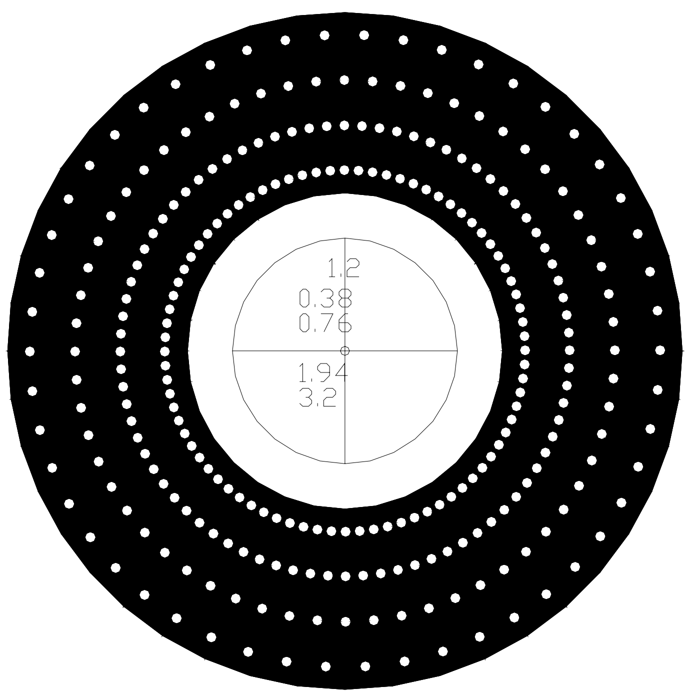

Fig. D-18. Plate F. (Glass beads with 1.16 mm in diameter glued on the white spots.)

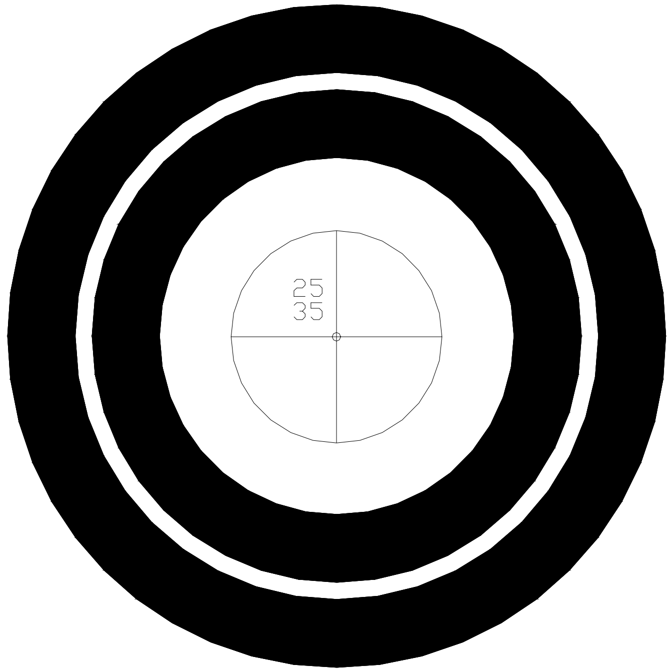

Fig. D-19. Plate G. (Glass beads with 1.16 mm in diameter glued, with smaller distance between particles at the outside black ring and bigger distance between particles at the inside black ring.)

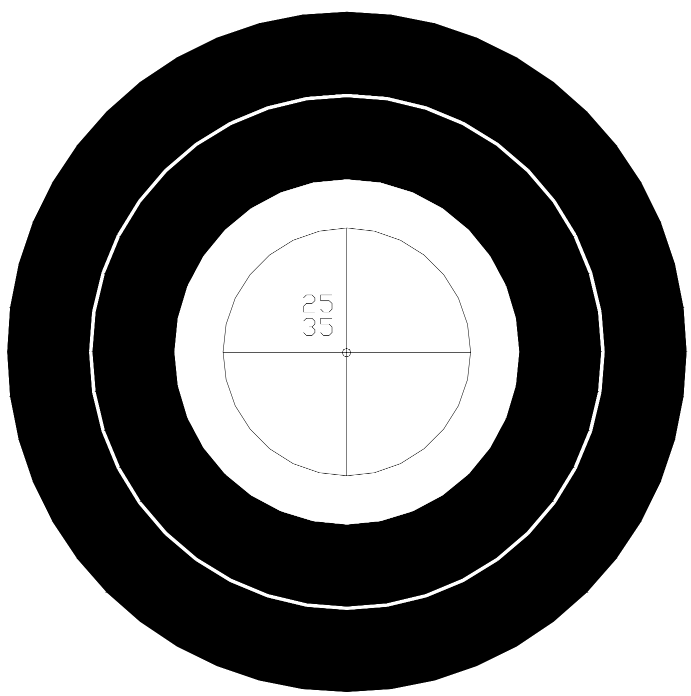

Fig. D-20. Plate H. (Glass beads with 0.85 mm at the outside black ring and 1.16 mm at the inside black ring.)

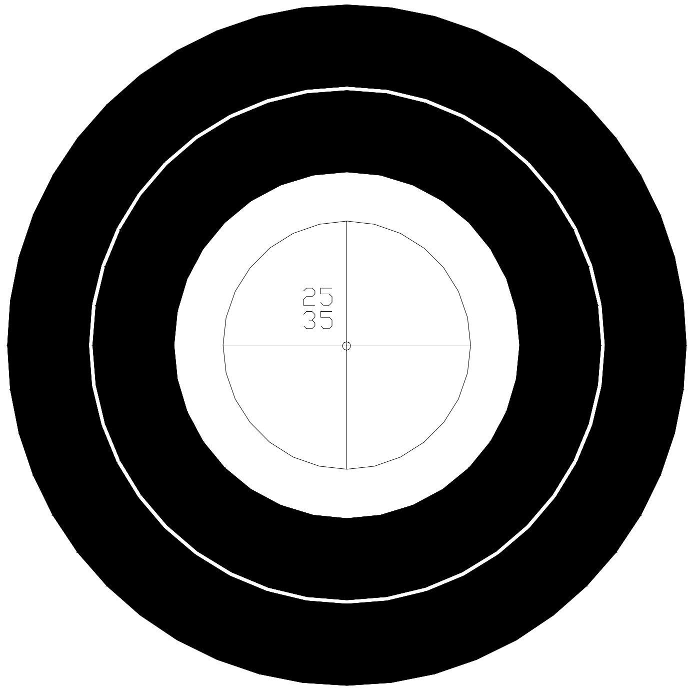

Fig. D-21. Plate I. (1.16 mm glass beads densely glued at the outside black ring and sparsely glued at the inside black ring.)

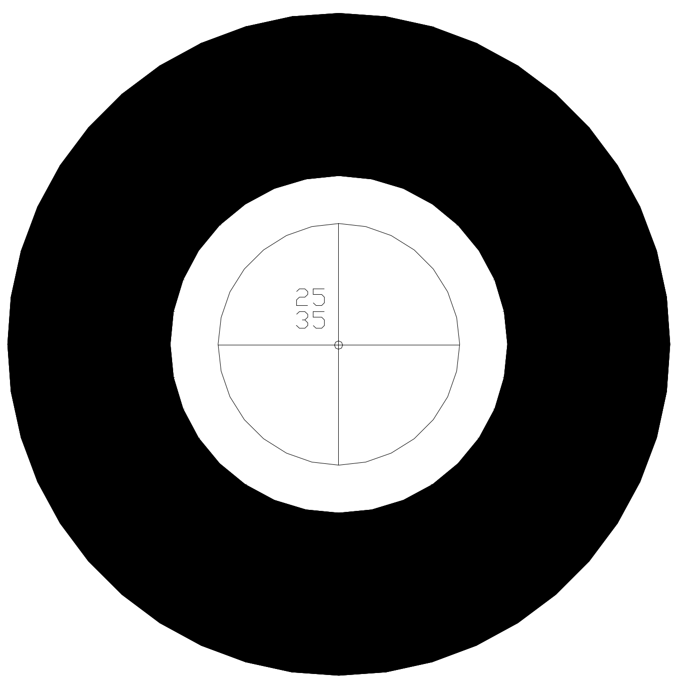

Fig. D-22. Plate J. (Sparsely glued glass beads with 1.16 mm in diameter.)

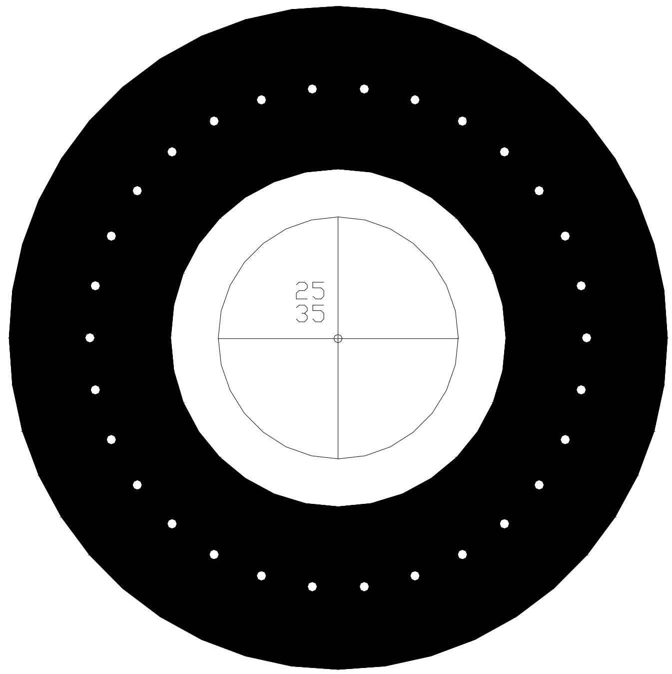

Fig. D-23. Plate K. (White spots with 1.2 mm in diameter.)

Effect of the size of white spots:

Using Plate A, Plate B and Plate C, the effect of the size of white spots was investigated. As shown in Figure D-24, the size of white spots does have certain influence on the effective distance, and its effect is quite complex.

Effect of the gap size between white spots:

Figure D-25 shows the effect of the gap size between white spots based on experiments using Plate B and Plate D. The size of the gap affects the effective distance too, and its effect is also quite complex.

Effect of the distance between the plate and the probe tip:

Plate K was used to investigate the influence of the distance between the plate and the probe tip. As shown in Figure D-26, the effective distance increases with increasing the distance between the plate and the probe tip.

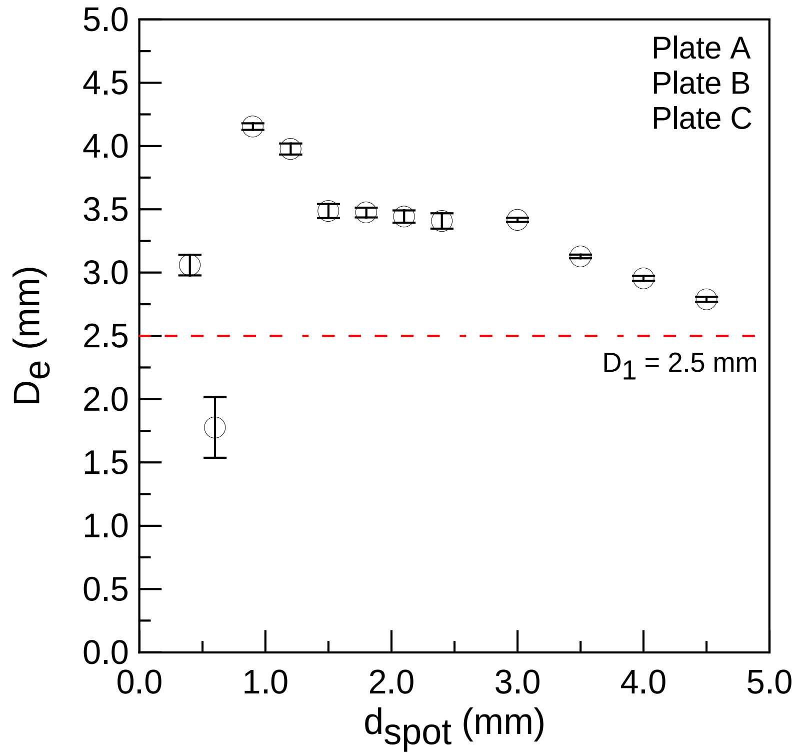

Fig. D-24. The effect of the size of white spots on D_e. (d=1 mm)

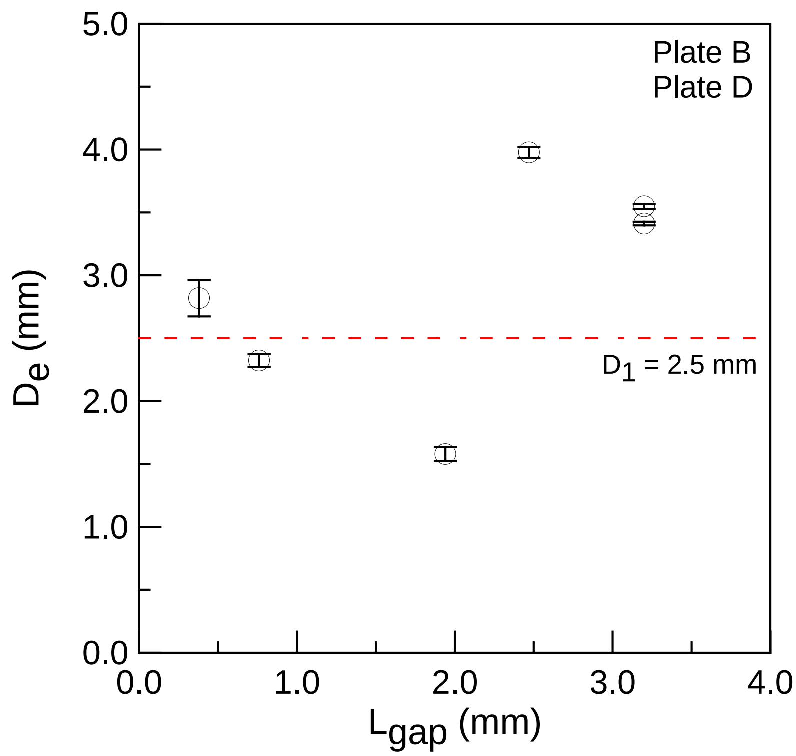

Fig. D-25. The effect of the gap size between white spots on D_e. (d=1 mm)

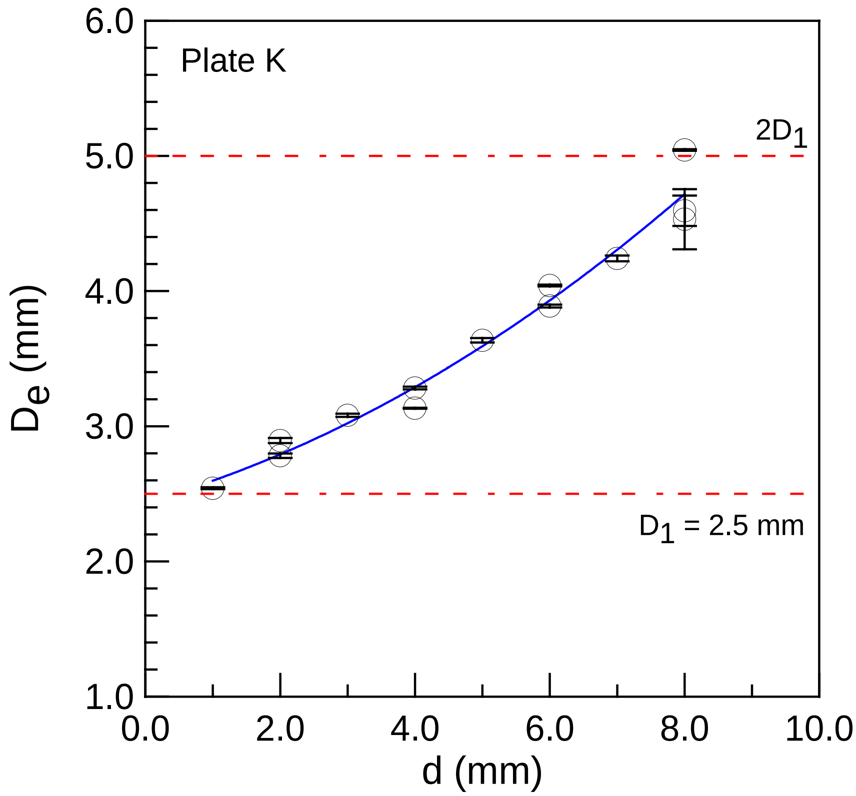

Fig. D-26. Influence of the distance between the plate and the probe tip. (Plate K)

Based on the above analysis, it is concluded that there are tremendous uncertainties on determining the effective distance just using the rotating plate, and other method should be considered.

Effect of glued glass beads:

As shown in Figure D-27, the effective distance is almost a constant within a wide range of the distance between the plate and the probe tip when plates with glued glass beads were tested. This is quite different from Figure D-26. Figure D-28 shows more experimental results using different designed plate with glued glass beads and other similar particles. For comparison, some results using rotating packed bed are also shown in this figure. Overall, it seems that the effective distance is almost a constant, and the background behind glued particles seems to have little influence. For example, the effective distance using the white background is only slightly smaller (Plate F) than using the rotating packed bed where particles underneath the first layer form a kind of background.

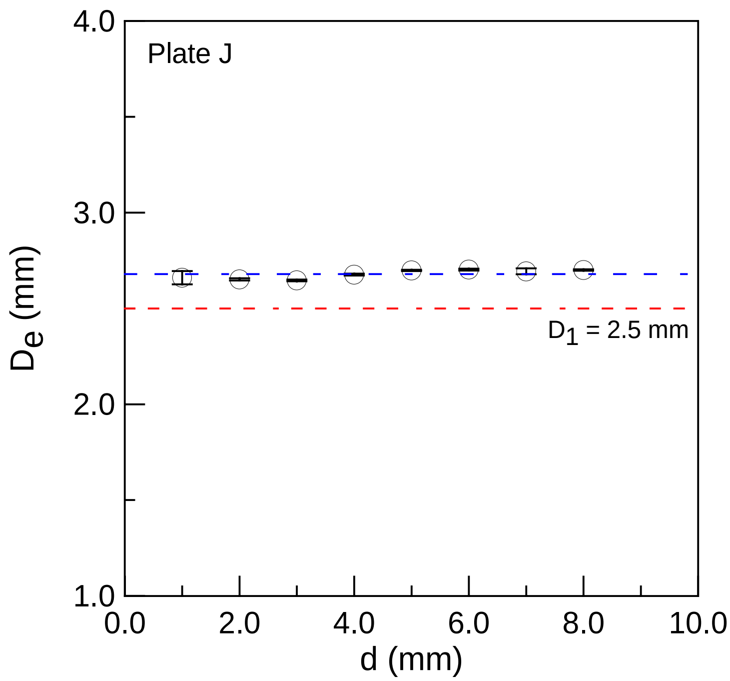

Fig. D-27. Influence of the distance between the plate and the probe tip. (Plate J)

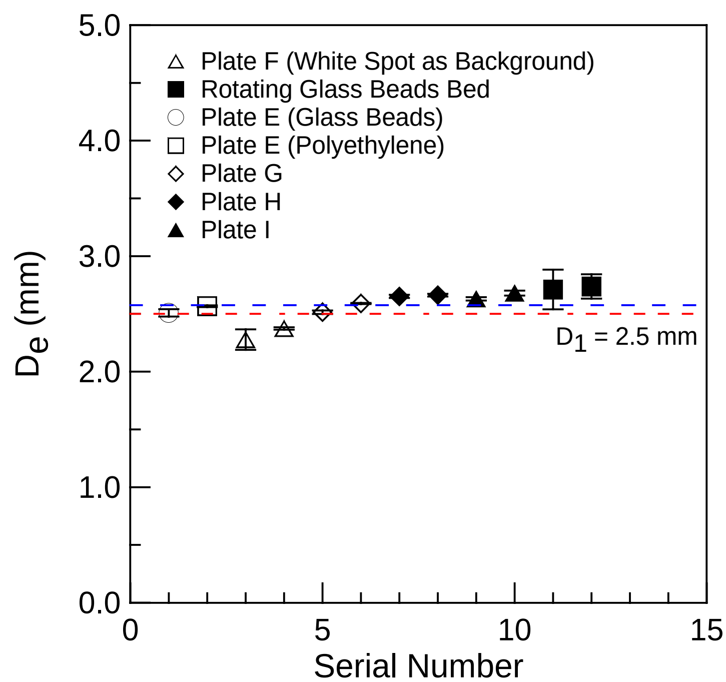

Fig. D-28. Influence of different designed plates with particles glued on D_e. (d=1 mm)

Effect of different materials:

Figures D-29 to D-33 show some experimental results on effective distance using different materials, such as new glass beads with 1.16 mm in diameter; used glass beads with 1.16 mm in diameter; used glass beads with 2.4 mm in diameter; FCC particles with mean diameter of 70 μm; small millet seeds with 1.5 mm in diameter; and big millet seeds with about 2 mm in diameter. It is seen that, for all kinds of glass beads, the distance between the probe tip and the bed surface (or the plate surface) almost does not have effect on the effective distance. However, there is a slight difference on the effective distance for different glass beads, even for glass beads of almost the same size but of different surface characteristics, i.e. fresh (new) versus spent (used). For other particles, such as FCC particles, small millet seeds and big millet seeds, the effective distance varies with the distance between the probe tip and the bed surface.

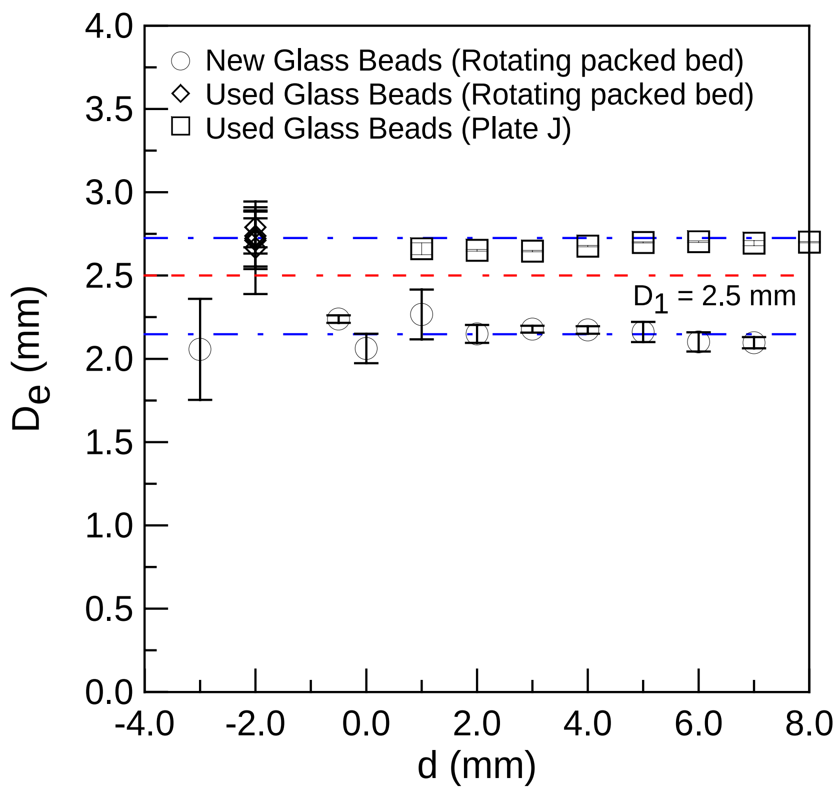

Fig. D-29. Comparison between used glass beads and new glass beads. (d_s=1.16 mm)

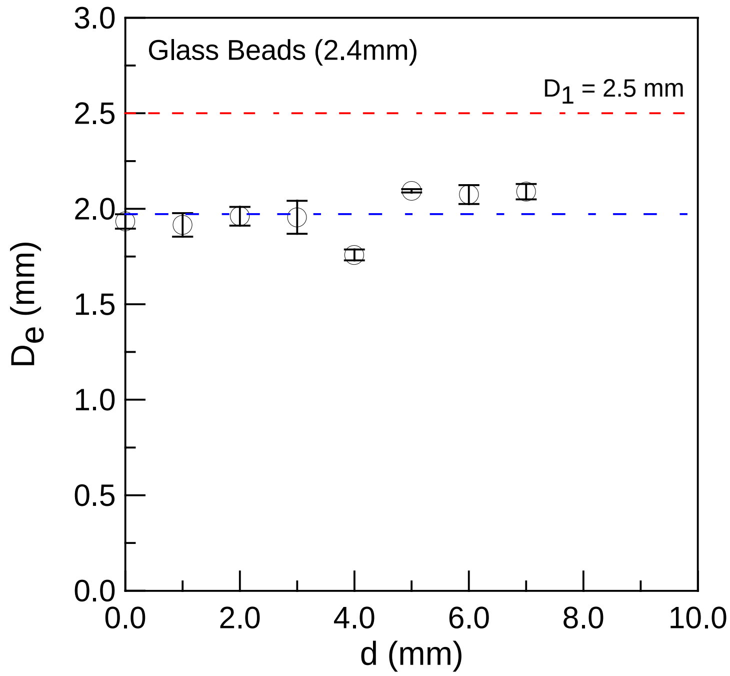

Fig. D-30. Experimental results using used glass beads with 2.4 mm in diameter. (Rotating packed bed)

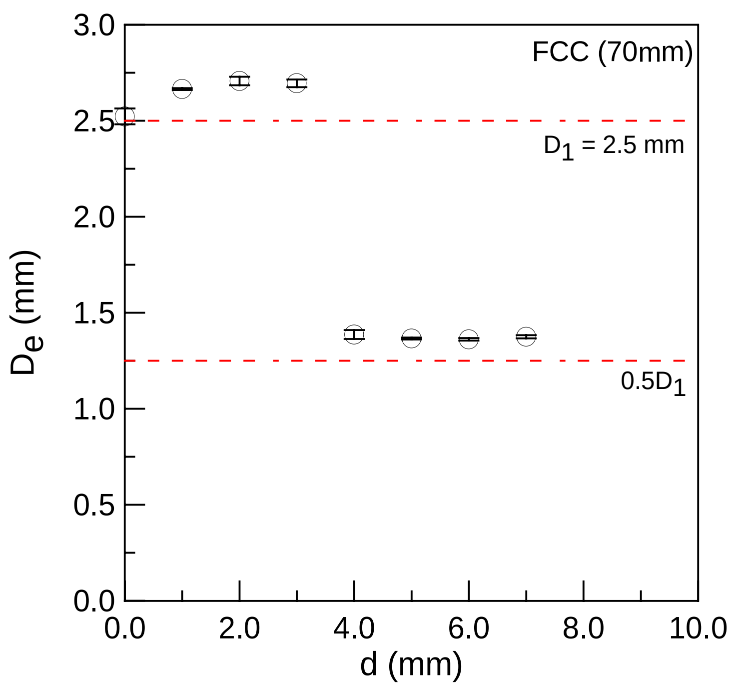

Fig. D-31. Experimental results using FCC particles. (Rotating packed bed)

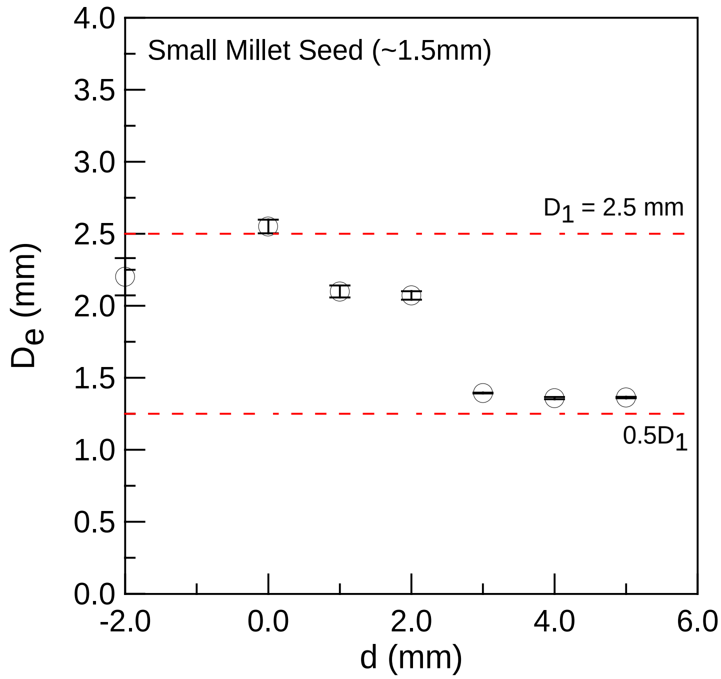

Fig. D-32. Experimental results using small millet seeds with 1.5 mm in diameter. (Rotating packed bed)

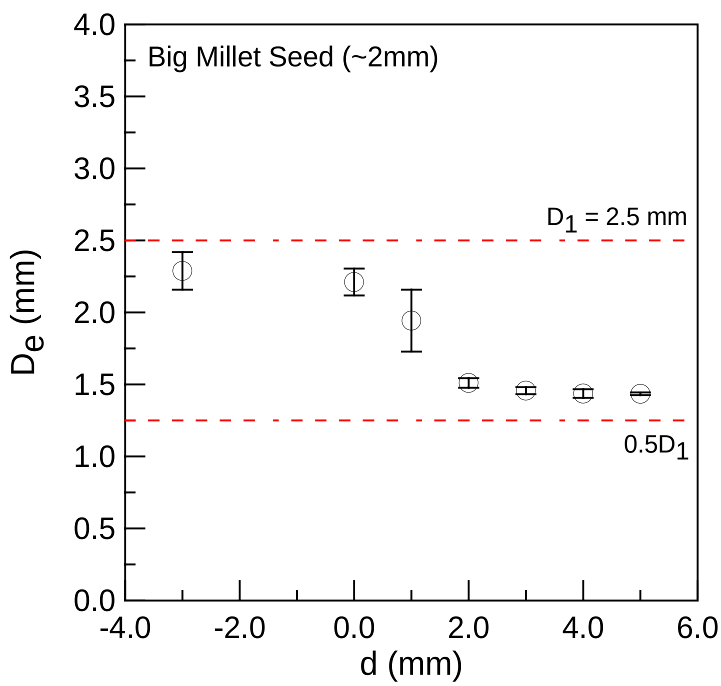

Fig. D-33. Experimental results using big millet seeds with about 2 mm in diameter. (Rotating packed bed)

Effect of the size of glass beads:

By using glass beads of different sizes, the influence of the size of glass beads was investigated, with the results shown in Figure D-34. It can be seen that, for the same optical fibre probe, the size of glass beads does affect the effective distance, and its effect is very complex. For the particles studied, the variation is within 20%, implying that a systematic error/bias of up to 20% can occur for a system with particles of a broad size distribution.

Conclusions:

Based on the above analysis, it is clear that there are many factors that may affect calibrated results on the effective distance of optical fibre probes. At first, the glass window has a most significant impact for the probe design, and should be considered in advance. Secondly, it was found that there were a lot of uncertainties associated with the use of a rotating plate without particles glued. When the rotating plate with particles glued is used, calibrated effective distance appears to be reasonable, although the effect of the background may need to be considered. The use of a rotating packed bed seems to be the best way, although it is hard to simulate the circumstance with low solids fractions. Thirdly, to obtain a reliable effective distance, it is best to use the same particles as to be used in actual experiments to calibrate the optical fibre probe. Finally, an optical fibre probe may not be suitable for all kinds of particles (For example, Probe 1 is suitable for glass beads used in this study, but it is not suitable for FCC particles, small millet seeds or big millet seed because the effective distance of Probe 1 is not a constant for these kinds of particles.), and a comprehensive sensitivity analysis on calibration results should be carried out for individual particles before the probe is applied.

Using probe 1 and 1.16 mm glass beads, calibration results show that D_e=2.69±0.04 mm (see Used Glass Beads in Figure D-29.), and this probe was used to measure local particle velocities and solids fractions in this study in conical spouted beds.

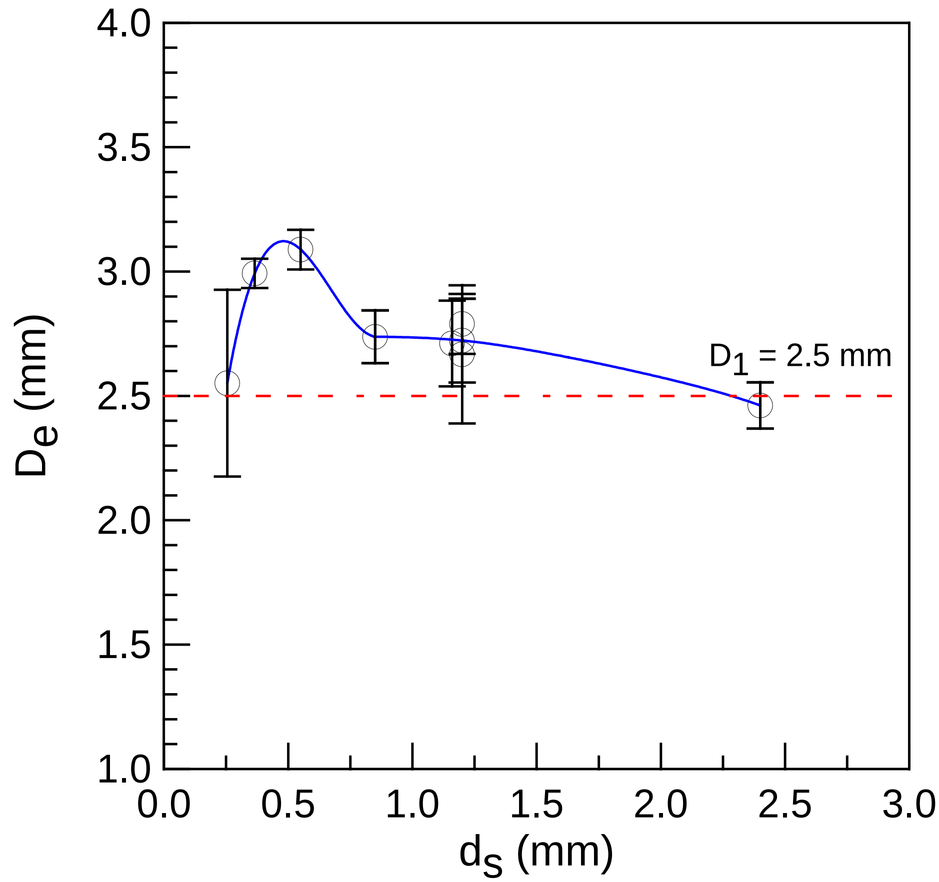

Fig. D-34. Influence of the diameter of particles on D_e. (Rotating packed bed, d≤0 mm)

D.2 Comparison with the literature

Table D-1 summarizes some optical fibre probes used in the literature as well as their calibrations and results. It is clear that researchers hardly had considered the effect of the glass window and/or the distance between the rotating plate surface and the probe tip, except Liu (2001) and Gorkem (2004). As for experimental researches on spouted beds, such as experimental work by He (1995) and San Jose et al. (1998a) that were most often cited in recent publications on CFD simulations, the glass window was not used in their researches. Therefore, systematic errors were inevitable.

Table D-1. Some optical fibre probes used in the literature and the current study as well as their calibrated effective distances.

Authors	**Geometrical dimensions and calibration method**	**Calibrated effective distance, D_e (mm)**	**D_e/D_1**
Patrose and Caram (1982)	D_f=0.125 mm, D_2=0.37 mm **without glass window** Using freefalling stream of glass beads (d_s=0.5 mm)	0.14	0.757
Benkrid and Caram (1989)	D_f=0.125 (or 0.15 mm) **without glass window** **Verified by stopwatch measurement**	0.167	<1.336 (or <1.113)
He (1995)	D_f=0.6 mm, D_2=1.06 mm **without glass window** Using a single rotating particle	0.82 (d was fixed.)	1.55
Olazar et al. (1995b) San Jose et al. (1998a)	D_f=0.7 mm, D_2=3.6 mm **without glass window** Using rotating plate	4.3 (d was fixed.)	2.39
Liu (2001)	D_f=1 mm, D_2=2 mm **without glass window** Using well-mixed water-FCC suspension	≈1.2	≈1.2
Liu (2001)	D_f=0.26 mm, D_2=0.53 mm **without glass window** Using rotating disk with FCC particles glued and well-mixed water-FCC suspension	0.31 (d was not given.)	1.17

Table D-1. Continued.

Authors	**Geometrical dimensions and calibration method**	**Calibrated effective distance, D_e (mm)**	**D_e/D_1**
Liu (2001)	D_f=0.26 mm, D_2=0.53 mm **with glass window** **(0.5 mm in thickness)** Using rotating disk with FCC particles glued	0.25 (d varied from 0.25 mm to 2.5 mm.)	**0.943**
Gorkem (2004)	D_f=0.26 mm, D_2=0.53 mm **with glass window** Using rotating disk with FCC particles glued	0.31 (d was not given.)	**1.17**
Current study	D_f=1.5 mm, D_1≈D, D_2≈2D **with glass window** **(5mm in thickness)** Using rotating packed bed (d_s=1.16 mm) or rotating plate	≈0.75 (Varied slightly with varied d.)	**0.5**
	D_f=1.5 mm, D_1≈D, D_2≈2D **without glass window** Using rotating packed bed (d_s=1.16 mm) or rotating plate	0.75~2.1 (Varied significantly with varied d.)	Varies
Current study	D_f=2.5 mm, D_1≈D, D_2≈2D **with glass window** Using rotating packed bed or rotating plate glued with particles (d_s=1.16 mm)	2.69±0.04 (Varied slightly with varied d.)	**1.08**

D.3 Calibration of the optical fibre probe for the measurement of solids concentration

Experimental study of He (1995) using relatively large particles in liquid fluidized beds and spouted beds had reported a linear relationship between the solids holdup and the voltage signals from the optical fibre probe. In the current study, the optical fibre probe was calibrated using colored particle method and the liquid-solids fluidized bed method by assuming that there exists a simple linear relationship.

Using colored glass beads:

Assumptions:

- Colored glass beads have the same density and the maximum solids fraction as original clear glass beads.
- For mixed glass beads, measured corresponding voltage is linearly proportional to the fractions of the colored particles by

$$V = X_b \cdot \frac{V_b}{\varepsilon_{s,0}} + X_c \cdot \frac{V_c}{\varepsilon_{s,0}} \tag{D-9}$$

where V is the measured voltage for mixed glass beads, X_b is the volume fraction of the original clear glass beads, $\varepsilon_{s,0}$ is the loosely packed solids fraction of original clear glass beads, V_b is the corresponding voltage; X_c is the volume fraction of colored glass beads, V_c is the voltage of colored glass beads at the loosely packed state. Theoretically, for black glass beads, or fluid such as air, $V_c = 0$.

For mixed glass beads with a mass fraction of Y for original clear glass beads, corresponding volume fraction can be derived as Equation (D-10).

$$X_b = Y \cdot \varepsilon_{s,0} \tag{D-10}$$

$$X_c = (1-Y)\cdot \varepsilon_{s,0} \tag{D-11}$$

Based on equations above, the following expression can be derived,

$$V = Y \cdot V_b + (1-Y)\cdot V_c \tag{D-12}$$

Equation (D-12) divided by V_o, the following equation can be obtained.

$$\frac{V}{V_b} = Y + (1-Y)\cdot \frac{V_c}{V_b} \tag{D-13}$$

Based on experiments on several types of colored glass beads as shown in Figure D-35, it shows that Equation (D-13) is true (as shown in Figures D-36a and D-36b). Therefore, Equation (D-9) which is based on the assumption of a linear relationship is validated, and a linear calibration relationship for the optical fibre probe and glass beads can be used in the current experiments.

For the clear glass beads and air system, the solids fraction X_b is actually the solids fraction ε_s, and $V_c = 0$, based on Equation (D-9), the following equation can be obtained.

$$\varepsilon_s = \left(\frac{\varepsilon_{s,0}}{V_b}\right)\cdot V \tag{D-14}$$

It means that the solids fraction ε_s is proportional to the voltage V, and the slope is $\frac{\varepsilon_{s,0}}{V_b}$.

Based on current experimental results, the slop is 0.175 for both fibre receivers.

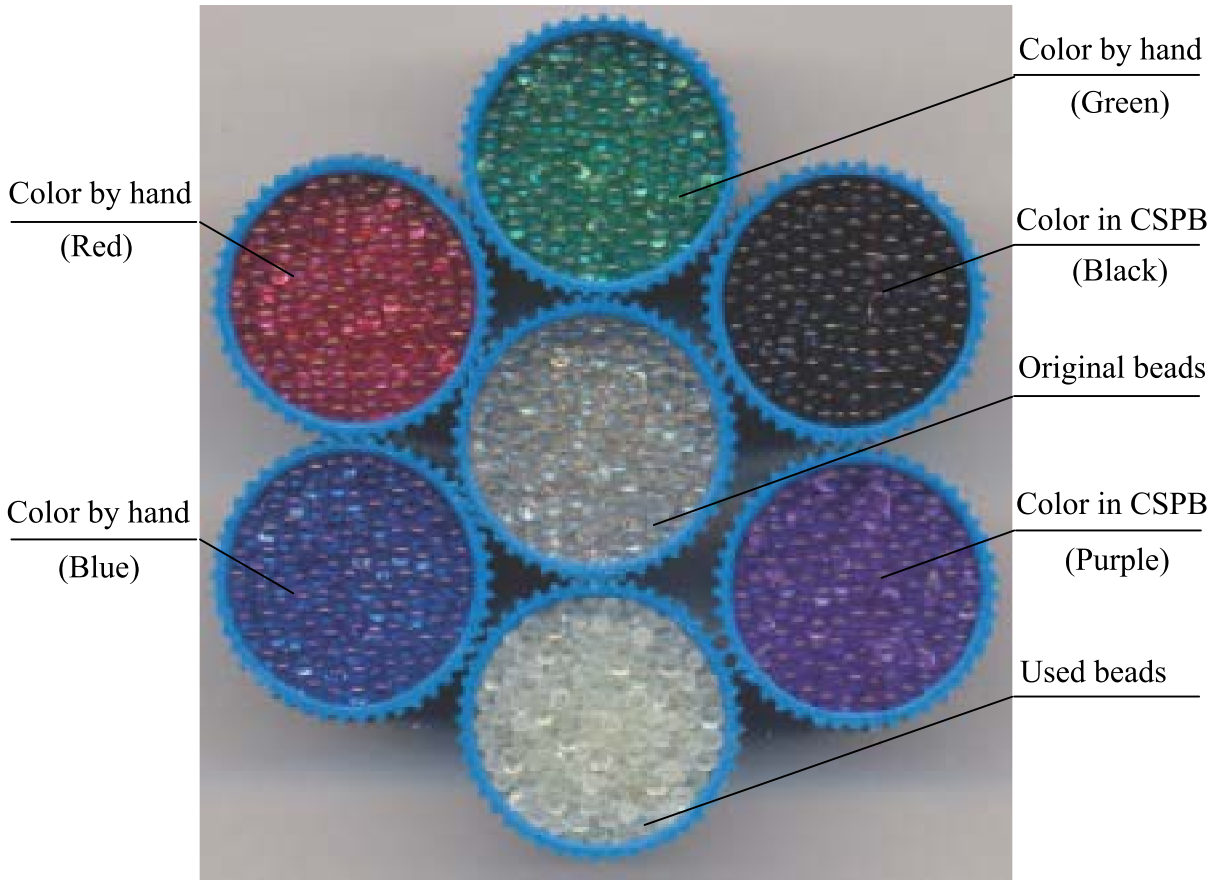

Fig. D-35. Glass beads used in current experiments.

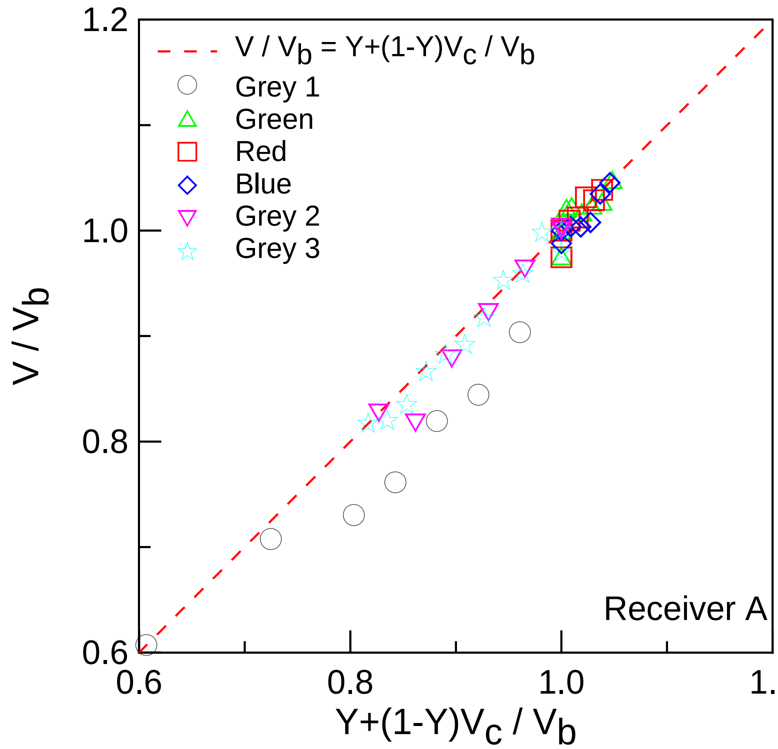

Fig. D-36a. Experimental results using different colored glass beads.

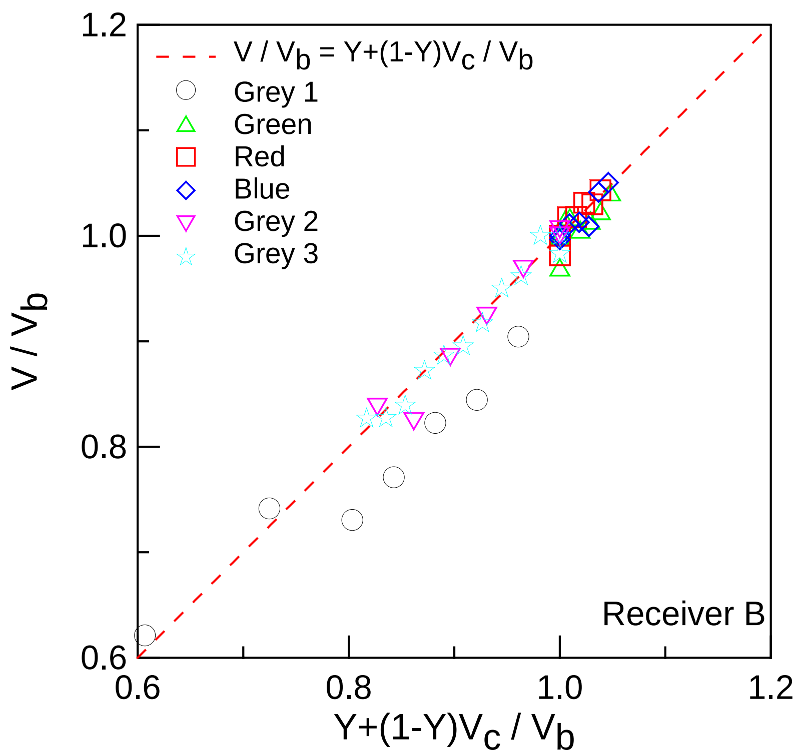

Fig. D-36b. Experimental results using different colored glass beads.

Using the liquid-solid fluidized bed:

With the assumption that solids fraction is uniform in the liquid-solid fluidized bed, the weight of glass beads W used in the fluidized bed can be written as Equations (D-15) and (D-16).

$$W = \rho_s \varepsilon_{s,0} H_0 A_0 \tag{D-15}$$

$$W = \rho_s \varepsilon_s H A_0 \tag{D-16}$$

where ρ_s is the density of glass beads, H_0 is the static bed height, $\varepsilon_{s,0}$ is the solids fraction at packed state, H is the expended height of the dense fluidized bed, ε_s is the corresponding solids fraction, A_0 is the cross section area of the fluidized bed.

Equation (D-17) can be derived by combination of Equations (D-15) and (D-16). Thus, the solids fraction can be obtained by measuring the height of the dense region at different superficial fluid velocities,

$$\varepsilon_s = (\varepsilon_{s,0} \cdot H_0) \cdot \frac{1}{H} \tag{D-17}$$

Figure D-37 shows the relationship between the solids fraction and measured voltage, it can be seen that the solids fraction ε_s is proportional to the voltage V, although the slop is slightly different from the one obtained from the colored particle method.

To eliminate all possible factors that may affect experimental results, before each experiment, the optical fibre probe was calibrated again by simply measuring two points with one at $\varepsilon_s = 0$ (zero value) and one at $\varepsilon_s = \varepsilon_{s,0}$ (full value). During experiments, particle velocity varies a lot in spouted beds, and the sampling frequency has to be varied correspondingly. As a result, the sampling time varies too. On the other hand, because the collision between particles and the probe tip is quite different in the spout and in the annulus, and the attrition of the probe tip during measurements may affect experimental results on the solids fraction. Thus, although the optical fibre probe 1 can measure the particle velocity and solids fraction simultaneously, the measurement of the particle velocity and solids fraction was conducted separately. Each measurement of the solids fraction was implemented quickly and the zero value verified frequently.

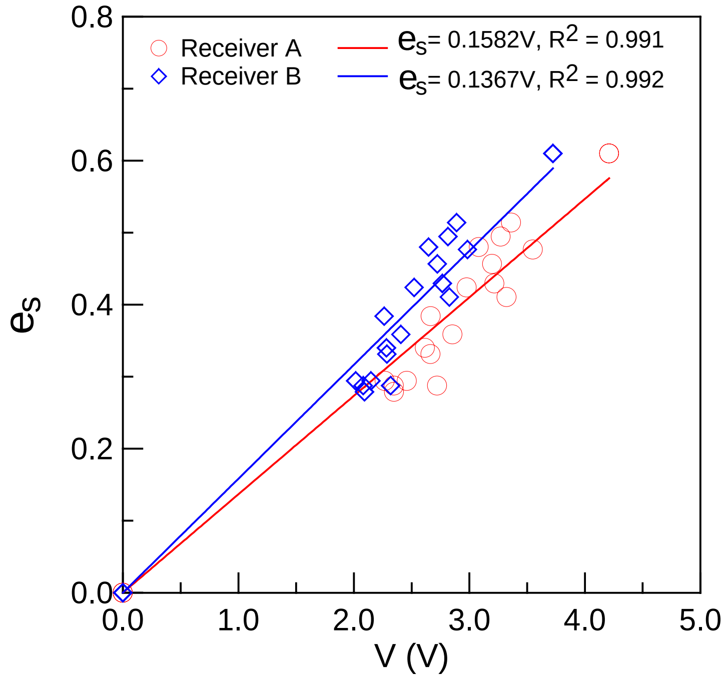

Fig. D-37. Correlation between the solids fraction and measured voltage.

APPENDIX E

SELECTION OF SIMULATION PARAMETERS

Simulation conditions and boundary conditions are shown in Table 5-1 and 5-2, other remarks are given in Table E-1.

Table E-1. Notes for Figures E-1 to E-4

For static pressure profiles and interstitial gas velocity profiles	For axial solids velocity profiles and solids fraction profiles
Z_1=0.038m; Z_2=0.089m; Z_3=0.191m; Z_4=0.292m	Z_1=0.140m; Z_2=0.241m; Z_3=0.343m

E.1 Effect of grid partition

The effect of grid size or grid partition on the simulation results is first examined by comparing the simulation results from three grid sizes (i.e., Partition 1, 10497 cells; Partition 2, 4102 cells; Partition 3, 2598 cells.). As shown in Figure E-1, the grid size within the range investigated in the current simulation has little effect on the radial distribution of the static pressure and the solids fraction, although some influence on the distribution of the axial solids velocity and the axial interstitial gas velocity is observed, especially in the spout region. Thus, the more accurate grid partition with the smallest grid size, partition 1, was selected for the current study. It is also seen from Figure E-1 that simulated results on the axial solids velocity agree very well with experimental data, but not for static pressure profiles and solids fraction profiles under the base operating conditions without the consideration of the solid phase source term.

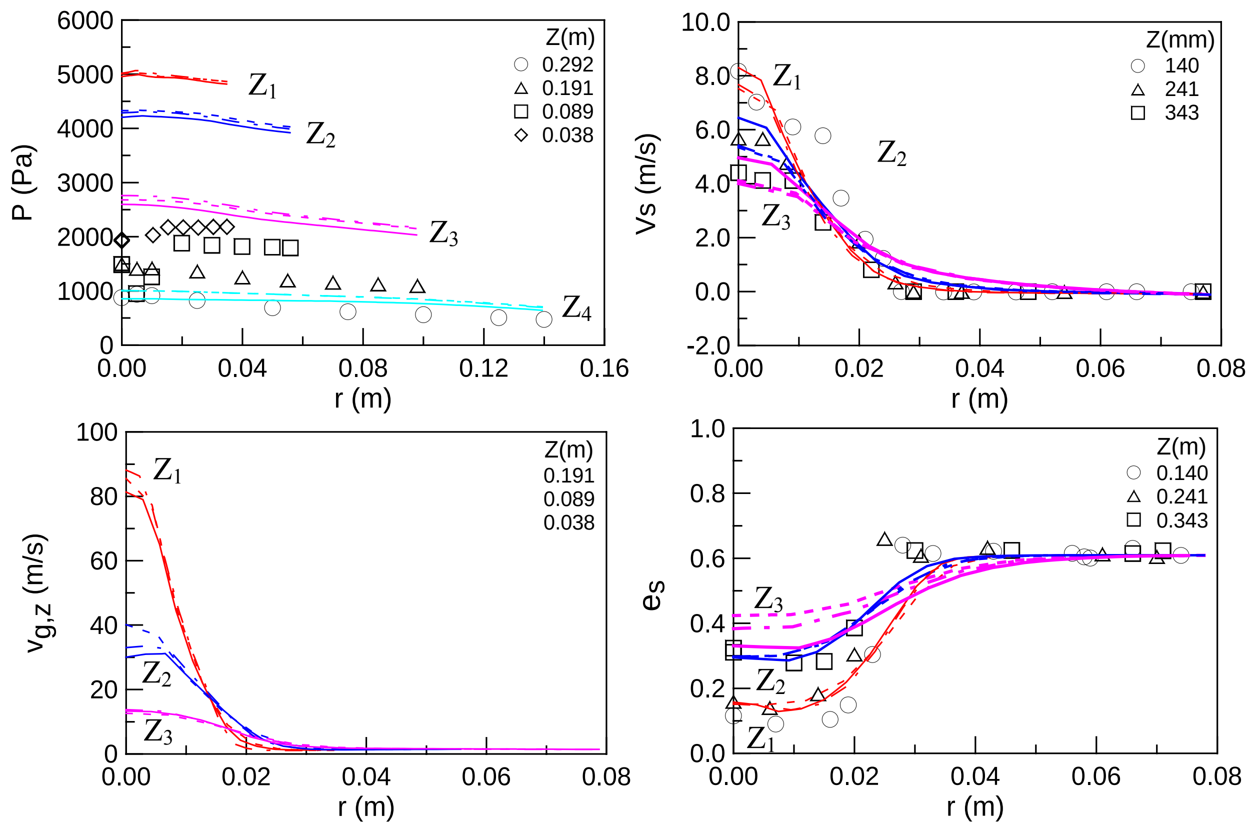

Fig. E-1. Comparison between experimental data and simulated results with **different grid partitions** at k_a=1.0 (k_s=1.0, 1/7[th] power law). Symbols are experimental data, and lines are simulated results. (Solid lines correspond to partition 1, dotted dash lines correspond to partition 2, dash lines correspond to partition 3.)

E.2 Effect of the time step size

Figure E-2 shows the influence of the simulation time step. It is seen that, within the range of our investigations (1e-6 ~ 1e-5 s), the time step size has almost no effect on simulated results except static pressures in the lower spout region. A time step size of of 1e-5 s was thus selected in our study in order to reduce the simulation time.

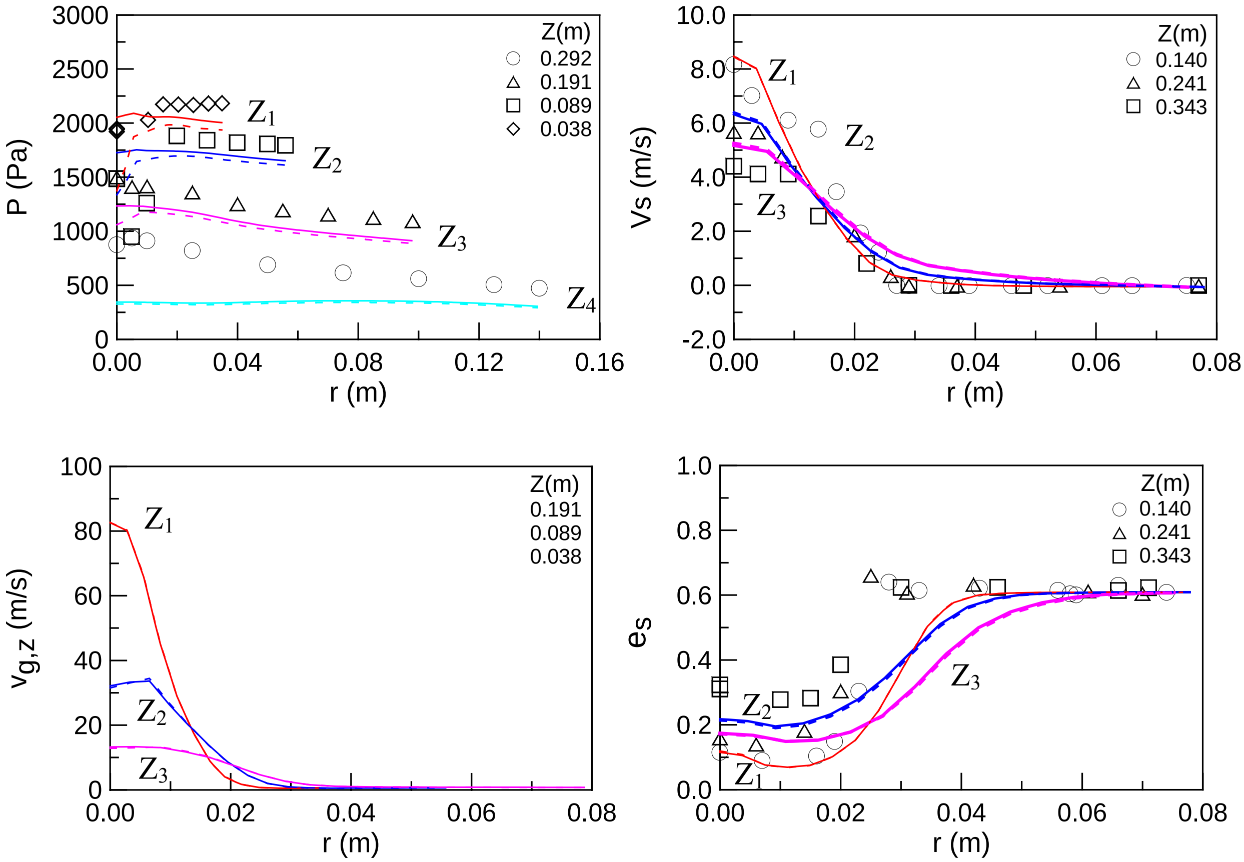

Fig. E-2. Comparison between experimental data and simulated results with **different time step sizes** at ka=0.41 (ks=1.0, 1/7th power law, ess=0.9, first order upwind scheme, convergence criterion of 1e-3). Symbols are experimental data, and lines are simulated results. (Solid lines correspond to the time step of 1e-5 s, dashed lines correspond to the time step of 1e-6 s.)

E.3 Effect of the convergence criterion

Figure E-3 shows the influence of the convergence criterion. It is seen that, within the range of our investigations (1e-5 ~ 1e-3), the convergence criterion has little effect on simulated results. In fact, when all convergence criteria were set to 1e-3 (**or 1e-5**), simulation results showed that actual residuals were far below the set value, for example smaller than 1e-4 (**or 1e-7**) for gas velocities and particle velocities, and smaller than 1e-5 for solids fractions.

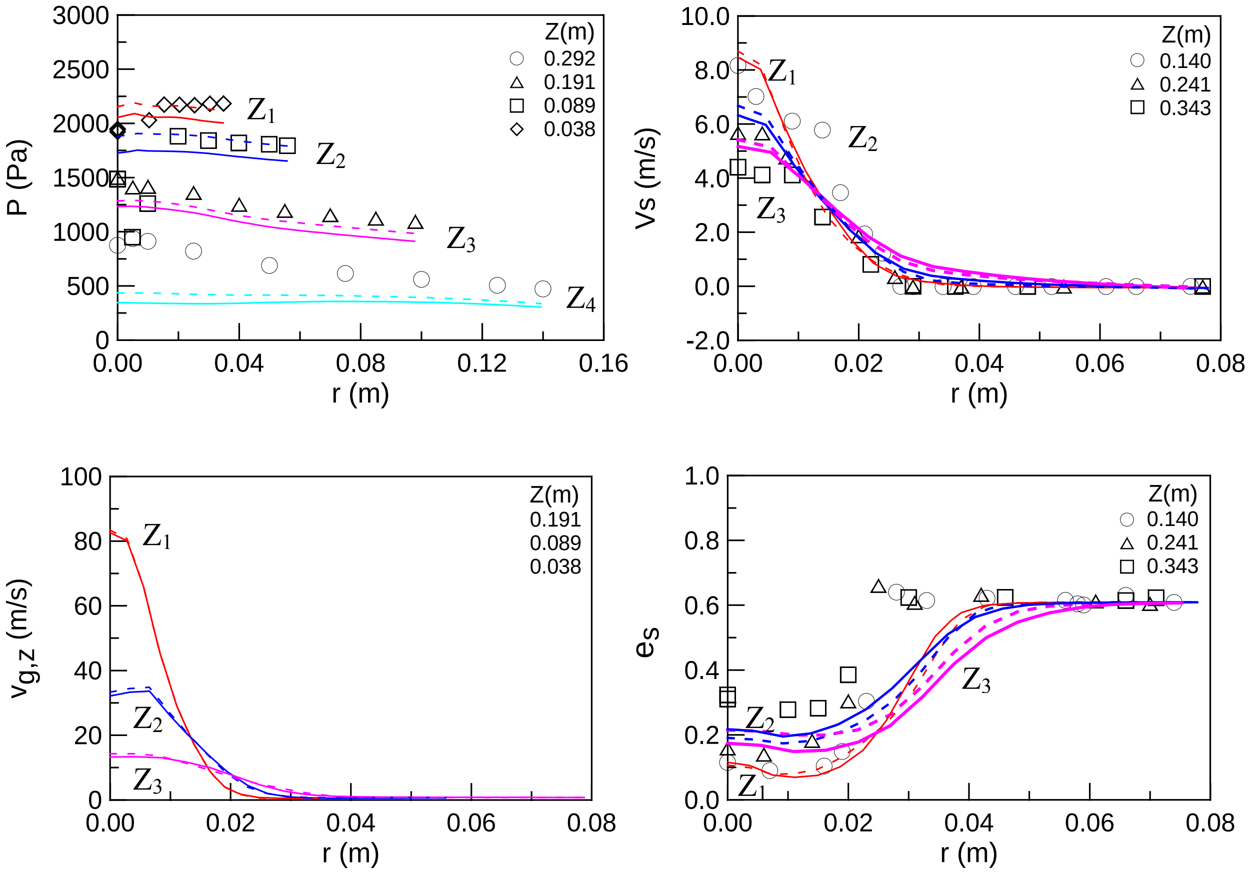

Fig. E-3. Comparison between experimental data and simulated results with **different convergence criteria** at k_a=0.41 (k_s=1.0, 1/7th power law, e_{ss}=0.9, first order upwind scheme, time step size of 1e-5 s). Symbols are experimental data, and lines are simulated results. (Solid lines correspond to the convergence criterion of 1e-3, dashed lines correspond to the convergence criterion of 1e-5.)

E.4 Comparison between First Order Upwind scheme and Second Order Upwind scheme

Figure E-4 shows the influence of different discretization schemes. It is seen that, there is almost no effect on static pressure profiles and solids fraction profiles, although simulation results using the second order scheme overestimate particle velocities and gas velocities in the spout region. Comparing with Figures 4-13 to 4-15 with experimental errors indicated, it is seen that simulation results are still in reasonable agreement using the second order scheme. To save computational time, the first order scheme was selected in this study.

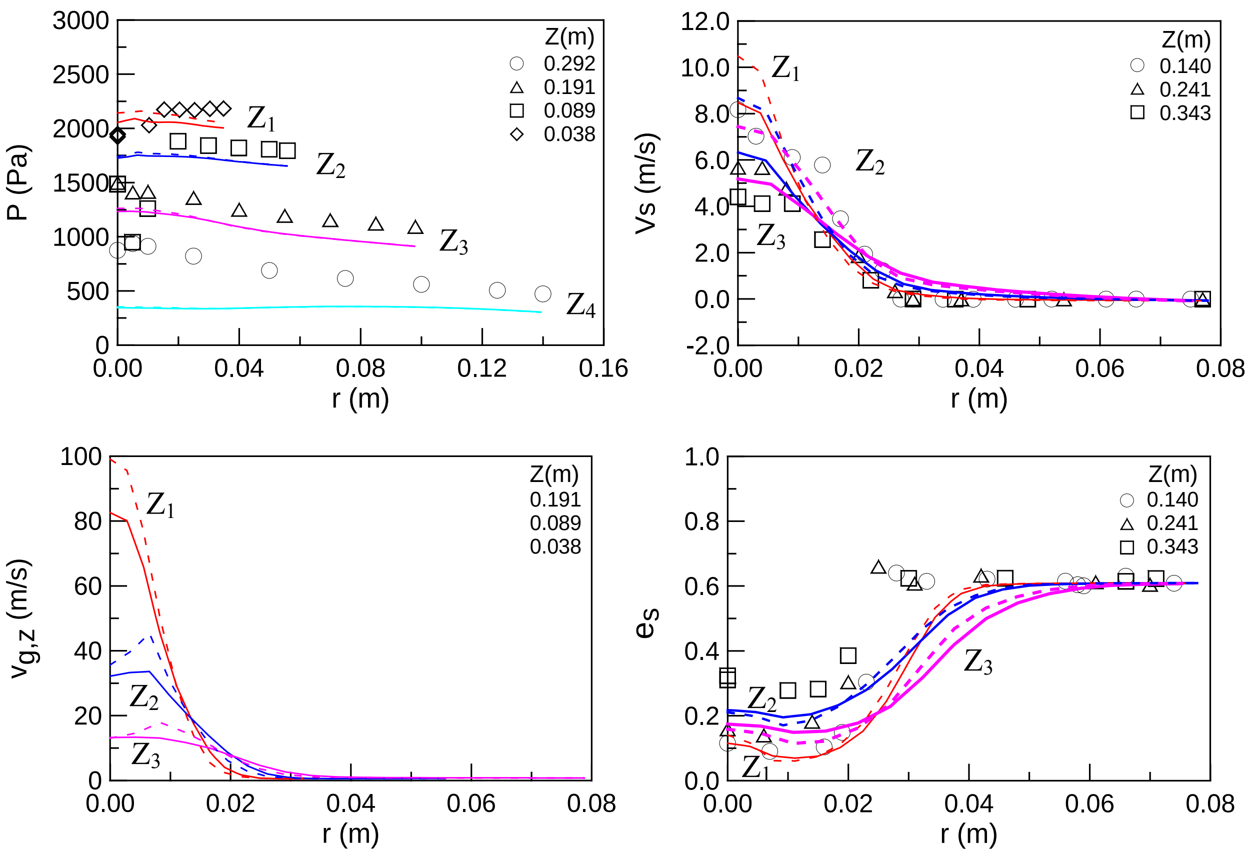

Fig. E-4. Comparison between experimental data and simulated results with **different discretization schemes** at k_a=0.41 (k_s=1.0, 1/7th power law, e_{ss}=0.9, time step size of 1e-5 s, convergence criterion of 1e-3). Symbols are experimental data, and lines are simulated results. (Solid lines correspond to the first order upwind scheme, dashed lines correspond to the second order upwind scheme.)

APPENDIX F

EVALUATION OF PROPOSED CFD MODEL USING A FLUIDIZED BED AND A PACKED BED

F.1 The solid phase source term in packed beds and fluidized beds

It is well known that particles are fully suspended and are in dynamic balance under steady fluidization state, with the pressure drop being equal to the weight of the bed, as shown in Equation (F-1). When the column is operated at packed bed state, particles remain stagnant, and the pressure drop of the packed bed can be described by the Ergun equation (1952) as shown in Equation (F-2). Usually, the pressure drop of a bed operated under packed bed state is smaller than the same bed operated under fluidization state, or, the ratio of the pressure drop for a packed bed over a fluidized bed is always smaller than one. Thus, the existence of the gravity term, or the Actual Pressure Gradient term (the APG term) for fluidized beds in the axial solid phase momentum equation for fluidized beds must be modified in order to be able to be used for the simulation of packed beds or partially fluidized beds.

Axial pressure gradient at fluidization state can be calculated by (**g=-9.81m^2/s**):

$$\nabla P_{fb} = (1-\varepsilon_{g,0})\rho_s g \tag{F-1}$$

Axial pressure gradient at packed bed state can be calculated by:

$$\nabla P_{pb} = -150\frac{(1-\varepsilon_{g,0})^2 \mu_g}{\varepsilon_{g,0}^2 d_s^2} v_{g,z} - 1.75\frac{\rho_g (1-\varepsilon_{g,0})}{\varepsilon_{g,0} d_s} v_{g,z}^2 \tag{F-2}$$

The ratio of the pressure drop for any columns over fluidized beds is defined as:

$$k = \frac{\nabla P}{\nabla P_{fb}} \tag{F-3}$$

For packed beds, $k_{pb} = \dfrac{\nabla P_{pb}}{\nabla P_{fb}}$ (F-4)

For fluidized beds, $k_{fb} = \dfrac{\nabla P_{fb}}{\nabla P_{fb}} = 1.0$ (F-5)

where g is the gravitational acceleration, ∇P is the axial pressure gradient for any columns, ∇P_{fb} is the theoretical axial pressure gradient calculated at fluidization state, ∇P_{pb} is the axial pressure gradient calculated at packed bed state, $v_{g,z}$ is the axial fluid velocity, k_{pb} is the ratio of the pressure drop for packed beds to the pressure drop at stable fluidization, k_{fb} is the ratio of the pressure drop for fluidized beds to the pressure drop at stable fluidization. Theoretically, k_{fb}=1.0, and k_{pb} is a function of operating conditions.

Based on the above analysis, an axial solid phase source term $S_{s,z}$ is introduced in this study,

$$S_{s,z} = -\varepsilon_s \rho_s g + k(\varepsilon_s \rho_s g) = (k-1)\varepsilon_s \rho_s g \tag{F-6}$$

When $\left|\nabla P_{pb}\right| < \left|\nabla P_{fb}\right|$ (at packed bed state), $k = k_{pb}$

When $\left|\nabla P_{pb}\right| \geq \left|\nabla P_{fb}\right|$ (at fluidization state), $k = k_{fb}$

It is obvious that the sum of the default gravity term in Equation (5-4) and the new solid phase source term is just equal to the Actual Pressure Gradient for packed beds or fluidized beds. Thus, by applying the above solid phase source term, it becomes possible to simulate a column operated at both packed bed state and stable fluidization state using the same fluidized bed code.

F.2 Simulating conditions

For the rectangular column, the width of the column is 0.3 m, the depth is 1.0 m (For two dimensional problems, the depth is set to be one meter in FLUENT by default.), the height is 1.0

m, and the column is partitioned into 16000 cells. For the cylindrical column, the diameter of the column is 0.3 m, the height is also 1.0 m, and the half column is partitioned into 8000 cells. Boundary conditions used are listed in Table F-1, and detailed simulation conditions are listed in Table F-2.

Table F-1. Boundary conditions for simulations of fluidized beds and packed beds.

Description	**Type**	**Comment**
Inlet	Velocity-inlet	Uniform distribution for gas phase
		No particles enter for solid phase
Outlet	Pressure-outlet	
Axis	Axis	Axisymmetric for the cylindrical column
Wall	Stationary wall: Specified shear	Zero shear stress

Table F-2. Simulation conditions for packed beds and fluidized beds.

Description	Value	Comment
Inlet gas velocity, U_i	0.1, 0.2, 0.25, 0.4, 0.57, 0.6, 0.66, 0.8 m/s	Uniform distribution
Gas density, ρ_g	1.23 kg/m^3	Air
Gas viscosity, μ_g	1.79×10^{-5} kg/(m·s)	Air
Particle density, ρ_s	2500 kg/m^3	Spherical glass beads
Particle diameter, d_s	1.16 mm	Uniform distribution
Initial solids packing, $\varepsilon_{s,0}$	0.61	Fixed value
Packing limit, $\varepsilon_{s,max}$	0.61	Fixed value
Solid viscosity, μ_s	Gidaspow	Eq. (5-7) + Eq. (5-9)
Solid bulk viscosity, λ_s	Lun et al.	
Width/depth of the rectangular column	0.3 m / 1.0 m	Fixed value
Diameter of the cylindrical column, D_c	0.3 m, 0.102 m	Fixed value
Total height of the column	1.0 m, 0.5 m	Fixed value
Static bed height, H_0	0.4 m, 0.22 m	Fixed value
Solver	double precision, segregated, unsteady, 1st order implicit; 2 dimensional axisymmetric model for the cylindrical column; 2 dimensional model for the rectangular column	
Multiphase Model	Eulerian Model, 2 phases	
Viscous Model	Laminar model	
Phase Interaction	Fluid-solid exchange coefficient: Gidaspow Model Restitution coefficient: 0.9 (Du et al., 2006)	
Time steps (Final value)	$10^{-5} \sim 2\times10^{-4}$ s	Fixed value
Convergence criterion	10^{-3}	Default in FLUENT

F.3 Experiments

A schematic diagram of the packed bed and fluidized bed is shown in Figure F-1. The column is made of Plexiglas with an inner diameter of 0.102 m. Glass beads of 1.16 mm in diameter were used as the bed material, and compressed air at ambient temperature was used as the fluidizing gas. Other particle properties and static bed heights are listed in Table F-3.

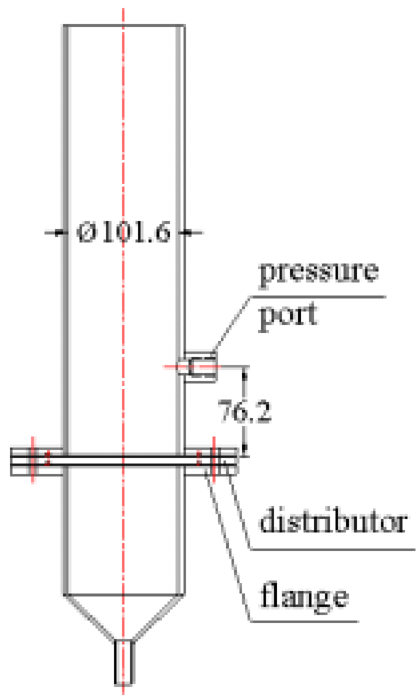

Fig. F-1. Schematic drawing of the Plexiglas fluidized bed column. (Numbers are in millimeters.)

Table F-3. Particle properties and operating conditions for packed beds and fluidized beds.

Particle diameter d_s, (mm)	Particle density ρ_s, (kg/m^3)	Loose-packed voidage, $\varepsilon_{g,0}$	Geldart classification	Static bed height H_0, (m)
1.16	2500	0.39	D	0.187 and 0.22

Considering that the axial pressure gradient is almost constant in packed beds and fluidized beds, the position of the probe does not affect the measured pressure gradient. To eliminate the possible influence arising from the gas distributor, the pressure port is located well above the distributor with a distance of 0.0762 m.

F.4 Results and discussion

Figure F-2 shows comparison between the rectangular (2D) and the cylindrical column (2DA) using the fluidized bed approach, it is seen that almost the same results can be obtained for both columns using the two-dimensional model.

Figure F-3 shows the comparison between cylindrical columns with different diameters using the new approach. It is seen that almost same results can be obtained for both columns with the pressure gradient in the small column lower than the large column but within 10%.

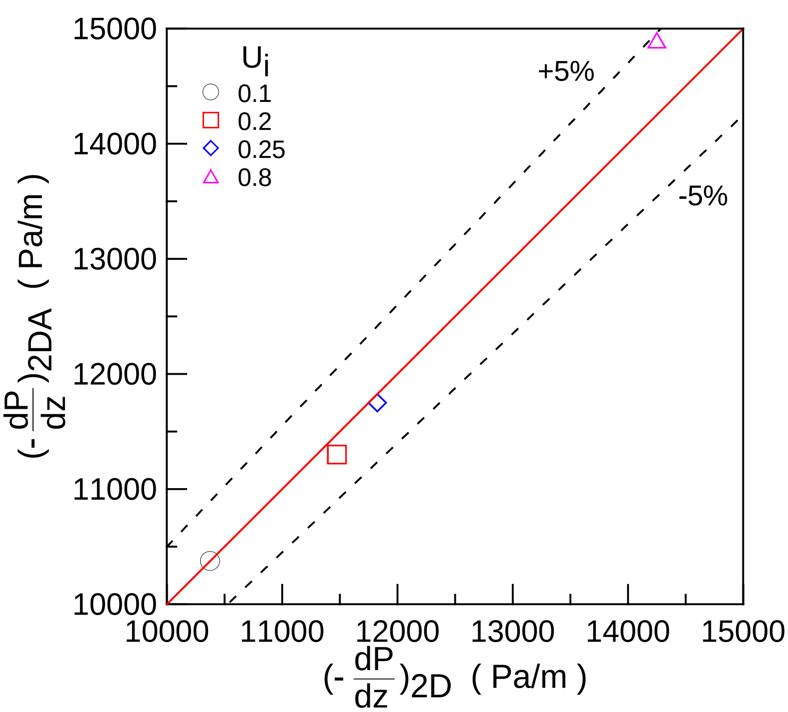

Fig. F-2. Comparison of simulated pressure drops in both fixed and fluidized bed regions between the rectangular (2D) and the cylindrical column (2DA). (Using fluidized bed approach.)

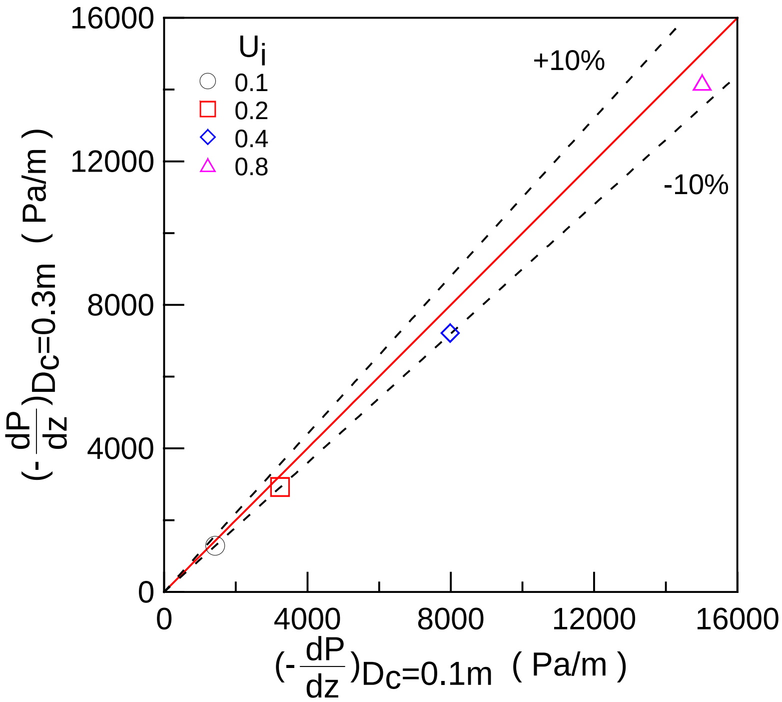

Fig. F-3. Comparison of simulated pressure drops in both packed beds and fluidized beds between cylindrical columns of different diameters. (Using the new approach.)

Figure F-4 shows the pressure gradient in both fixed bed and fluidized bed regions from experiments and calculations. It can be seen that for particles used in this work there is almost no difference on the pressure evolution curve between the ascending process and the descending process, the pressure gradient in the fixed bed region can be well described by the Ergun equation (Equation (F-2)), and the pressure gradient in the fluidized bed region can be predicted by Equation (F-1) with 8% overestimation.

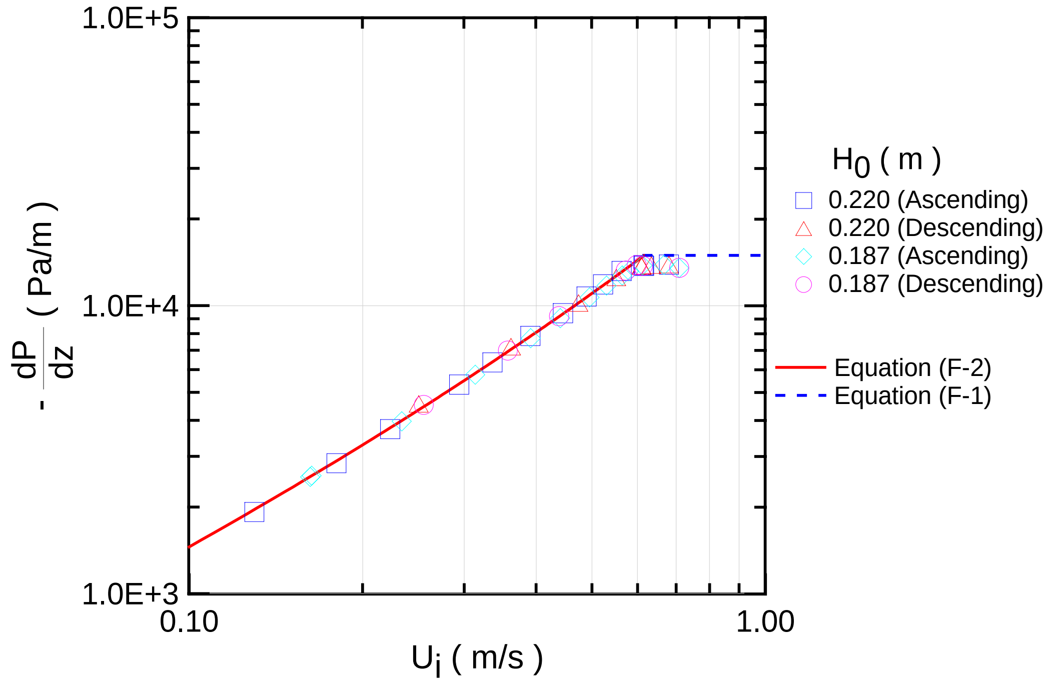

Fig. F-4. Comparison between experiments and calculations using Equations (F-1) and (F-2).

Figure F-5 shows the pressure gradient in both packed bed and fluidized bed regions from experiments and CFD simulations. When the packed bed code is used to simulate the packed bed region, the simulated pressure gradients agree very well with experimental data. However, when the fluidized bed code is used for the simulation of the packed bed region, or the packed bed code is used for the simulation of the fluidized bed region, simulated pressure gradients overestimate experimental data significantly. This is because particles are stationary in the packed bed, with particles being supported somehow by the gas distributor. Contrarily, particles are fully suspended by the upflowing gases in the fluidized bed.

When the gravity term is added in the axial solid phase momentum equation following the proposed approach, the packed bed can be simulated very well. Using the new approach, the fluidized bed (k_{fb}=1) can be simulated with the same accuracy as the fluidized bed approach, although the estimated minimum fluidization velocity is slightly higher than the experimental result. It is found that a better agreement can be achieved with a lower value of k_{fb} (k_{fb}=0.92) by assuming that particles in a fluidized bed are not completely suspended in reality due to the existence of possible dead zones in the distributor region.

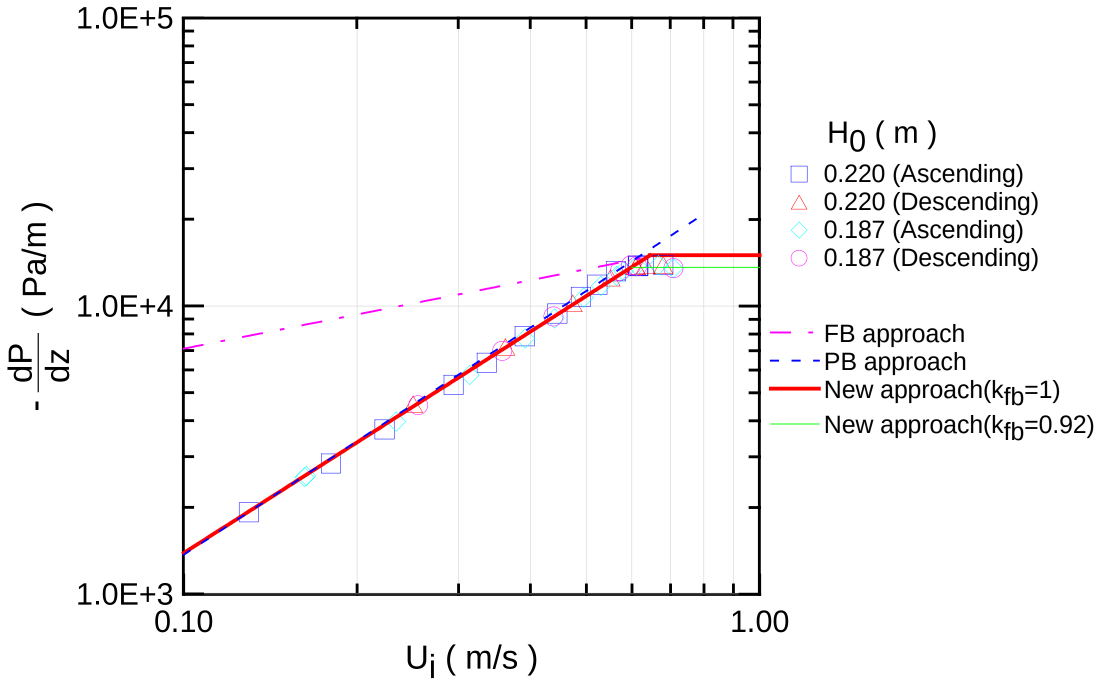

Fig. F-5. Comparison between experimental data and simulation results using different approaches.

Using the new approach, simulation results in the packed bed region show that axial solids velocities are around zero; solids fractions are around the setting value. Figure F-6 shows that the pressure gradient below the bed surface is a constant while is zero above the bed surface. All these simulation results are consistent with experimental data, confirming that the introduction of a source term into the fluidized bed code makes it capable of simulating packed beds.

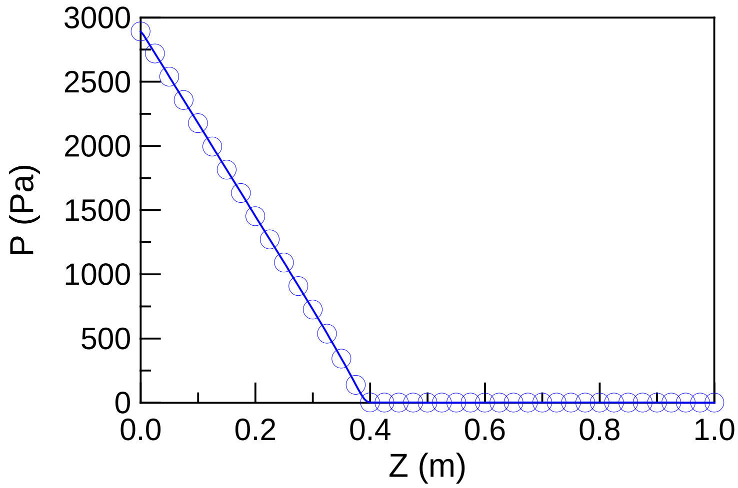

Fig. F-6. Simulated results of the axial static pressure for a packed bed using the new approach.

(U_i=0.4m/s, D_c=0.3m, H_0=0.4m)

APPENDIX G

EVALUATION OF PROPOSED CFD MODEL USING EXPERIMENTAL DATA FROM THE LITERATURE

G.1 Simulations of a cylindrical spouted bed

The proposed approach was used to simulate the cylindrical spouted bed as reported by He et al. (1994a, 1994b) and He (1995). In the simulations, all bed geometrical dimensions and operating conditions were kept the same as in He (1995), with boundary conditions listed in Table G-1 and simulation conditions listed in Table G-2. Several different settings were applied to investigate the effect of the solid bulk viscosity, the frictional viscosity and the source term. According to He (1995), the pressure drop for the full column operated at U_c=0.7m/s is 3000 Pa, thus, the corresponding k_a is 0.64. A slightly larger value of 0.7 was used in the simulation.

Table G-1. Boundary conditions for simulations of the cylindrical spouted bed by He (1995).

Description	Comment
Inlet	Radial distribution based on the actual Reynolds number used for the fluid phase
	No particles enter for the solid phase
Outlet	Pressure-outlet
Axis	Axisymmetric
Wall	Non-slip for the fluid phase
	Zero shear stress for the solid phase

Table G-2. Simulation conditions for the cylindrical spouted bed by He (1995).

Description	Value	Comment
Operating gas velocity, U_c	0.7 m/s	Based on D_c
Gas density, ρ_g	1.23 kg/m^3	Air
Gas viscosity, μ_g	1.79×10^{-5} kg/(m·s)	Air
Particle density, ρ_s	2503 kg/m^3	Spherical glass beads
Particle diameter, d_s	1.41 mm	Uniform distribution
Initial solids packing, $\varepsilon_{s,0}$	0.588	Fixed value
Packing limit, $\varepsilon_{s,max}$	0.588	Fixed value
Solid viscosity, μ_s	Gidaspow	Eq. (5-7) + Eq. (5-9)
Frictional viscosity, $\mu_{s,fr}$	0 or Schaeffer	**Different settings**
Solid bulk viscosity (Base case), λ_s	0 or Lun et al.	**Different settings**
Diameter of the upper section, D_c	0.152 m	Fixed value
Total height of the column	0.899 m	Fixed value
Gas inlet diameter, D_0	0.019 m	Fixed value
Diameter of the bed bottom, D_i	0.038 m	Fixed value
Static bed height, H_0	0.325 m	Fixed value
Solver	2 dimensional, double precision, segregated, unsteady, 1st order implicit, axisymmetric	
Multiphase Model	Eulerian Model, 2 phases	
Viscous Model	Laminar model	
Phase Interaction (Base case)	Fluid-solid exchange coefficient: Gidaspow Model Restitution coefficient: 0.9 (Du et al., 2006)	
Time steps (Final value)	10^{-5} s	Fixed value
Convergence criterion	10^{-3}	Default in FLUENT

As shown in Figures G-1 to G-3, the influence of frictional viscosity was insignificant. The solid bulk viscosity also had little effect when the Lun et al. expression was applied to estimate the solid bulk viscosity. Some kind of unstable spouting could be obtained as shown in Figure G-

3. The solid phase source term had significant impact on simulation results. Partial spouting is observed in Figure G-2 when the solid phase source term was not considered (k_a=1.0), while stable spouting could be achieved in Figure G-1 with k_a=0.7.

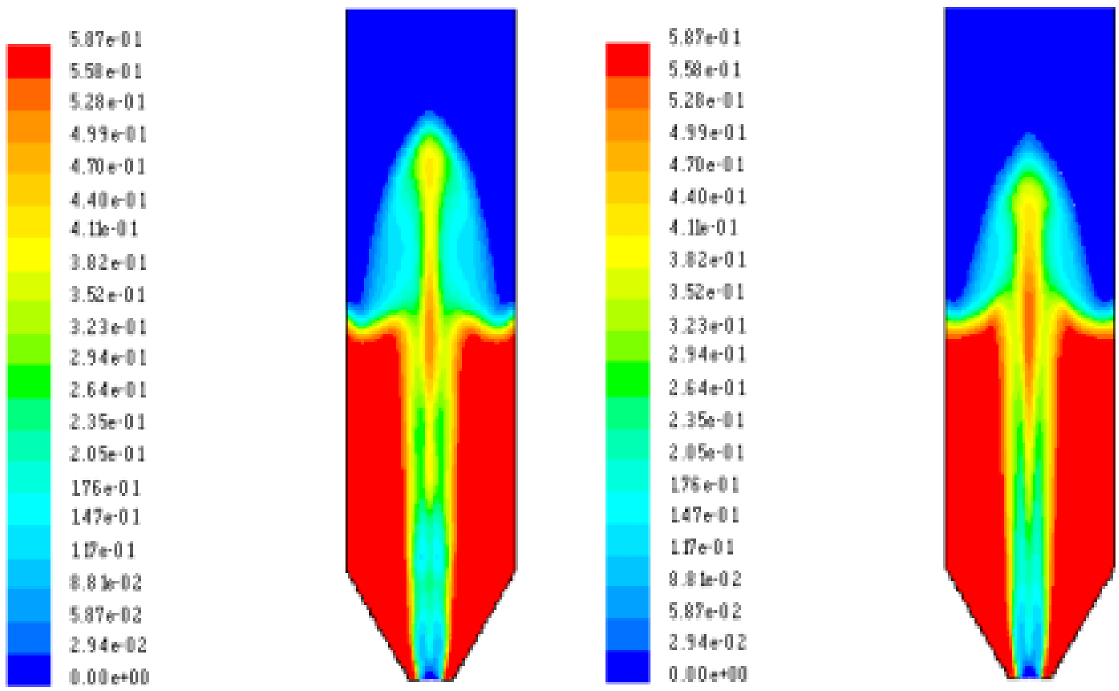

(λ_s=0, $\mu_{s,fr}$=0, k_a=0.7) (λ_s=0, $\mu_{s,fr}$ from Schaeffer' expression, k_a=0.7)

Fig. G-1. Effects of frictional viscosity on simulation results (***k*$_a$=0.7**).

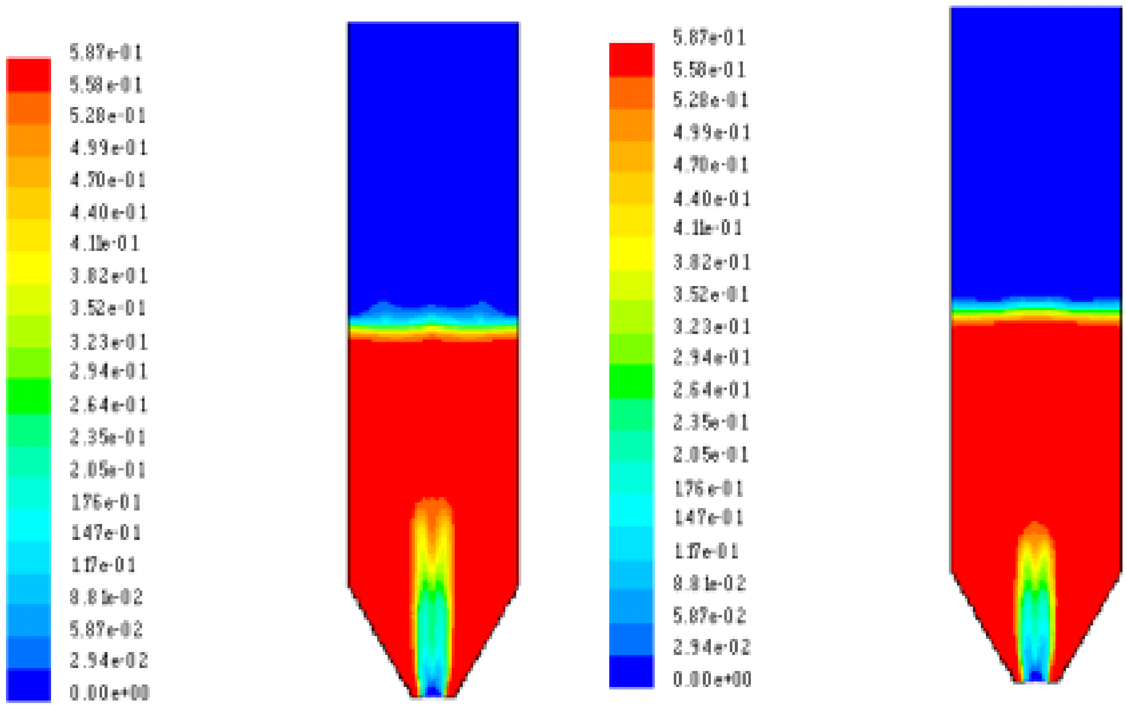

(λ_s=0, $\mu_{s,fr}$=0, k_a=1.0) (λ_s=0, $\mu_{s,fr}$ from Schaeffer' expression, k_a=1.0)

Fig. G-2. Effects of frictional viscosity on simulation results (***k_a*=1.0**).

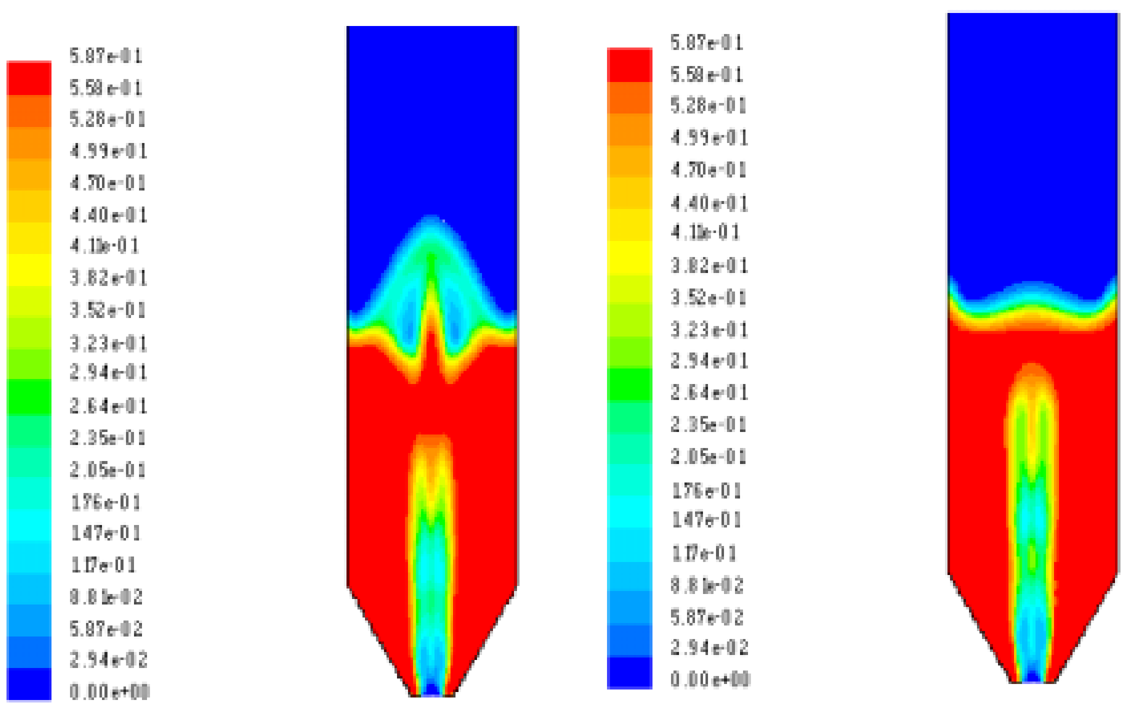

Fig. G-3. The phenomenon of unstable spouting. (λ_s from Lun et al. equation, $\mu_{s,fr}$=0, k_a=0.7)

He (1995) reported some experimental data on the static pressure, voidage and solids velocity, and these data were used to evaluate the proposed approach. According to his description, the axial distributions of the static pressure and voidage were measured along the centre of the annulus, or half-way between the column wall and the spout-annulus interface. Based on his experimental data, the diameter of the spout was about 40 mm in diameter except near the gas inlet. Simulation results used for the comparison were based on the assumption that λ_s=0, $\mu_{s,fr}$=0 and k_a=0.7.

As shown in Figure G-4, simulated static pressures in the annulus agree very well with experimental data. Figure G-5 shows that simulated voidage in the annulus is slightly smaller than experimental data, and the difference increases with increasing the axial position. Figure G-6 shows that the solids fraction in the spout was overestimated in most cases.

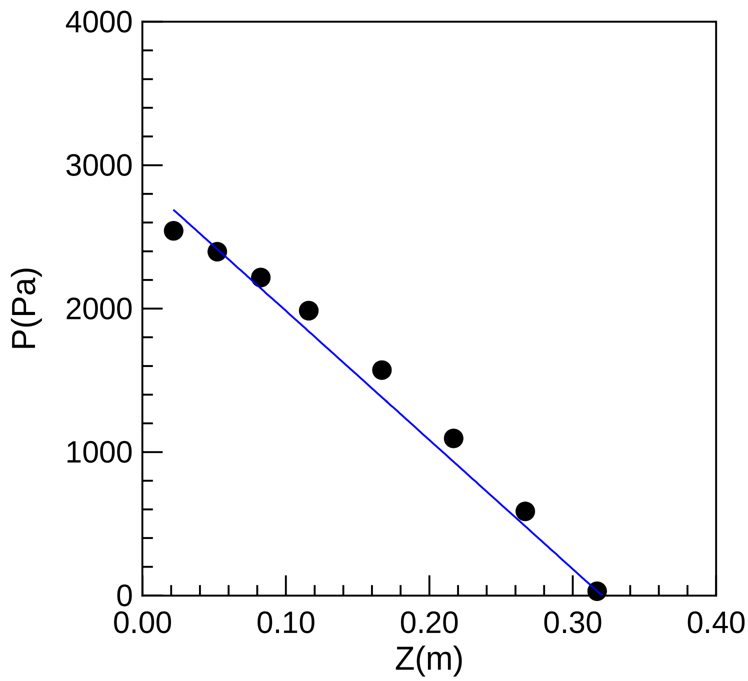

Fig. G-4. Comparison between simulation results and experimental data on the static pressure in the annulus. (Symbols are experimental data, the solid line corresponds to simulation results.)

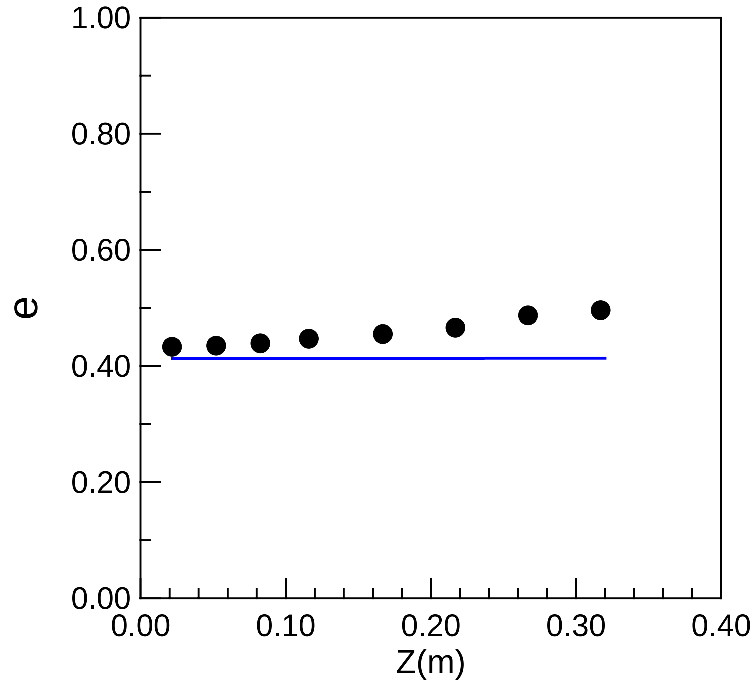

Fig. G-5. Comparison between simulation results and experimental data on the voidage in the annulus. (Symbols are experimental data, the solid line corresponds to simulation results.)

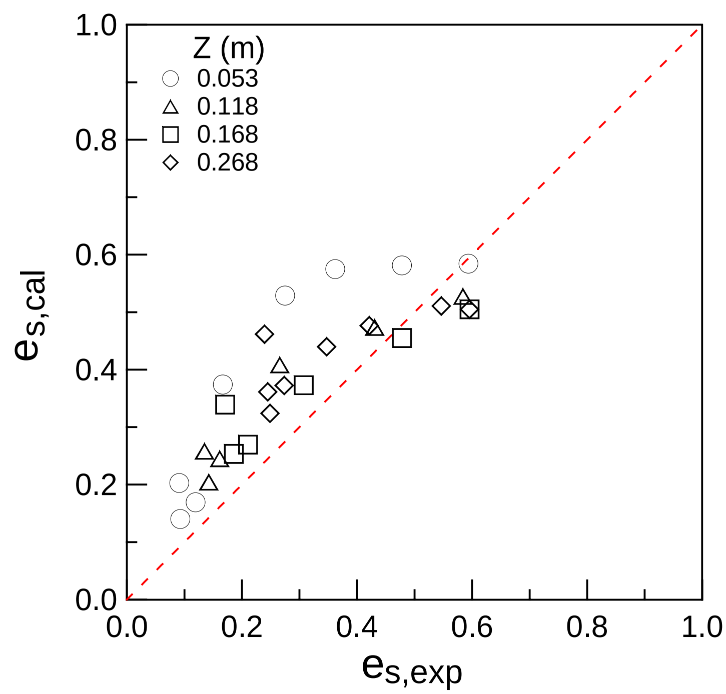

Fig. G-6. Comparison between simulation results and experimental data on the solids fraction in the spout.

Figure G-7 compares the simulated and measured axial solids velocity. It is obvious that simulation results underestimated experimental data significantly at every axial level. Figure G-8 is another kind of comparison between the simulation and experiment. Surprisingly, simulation results are proportional to experimental data, with a correlation coefficient of 0.986. This suggests that there exists some kind of systematic error either in the experiment or in the CFD simulation. Based on the analysis in Chapter 4 on the calibration of the optical fibre probe using different calibration methods (rotated plates with different designs, rotated particle bed), calibrated effective distance between receiving fibres could be different even using the same plate at different distance from the probe tip. The optical fibre probe used by He (1995) was calibrated by using a single particle fixed at the end of a rotated metal rod, with the blind zone not being considered in their study (no glass window). Calibrated effective distance was 1.55 times the geometric distance D_1, it is possible that some systematic errors could arise from their measurement using optical fibre probes.

Using the correlation obtained from Figure G-8, experimental data on the axial solids velocity were adjusted, and the comparison between simulation results and adjusted experimental data is shown in Figure G-9. It is seen that there is a good agreement.

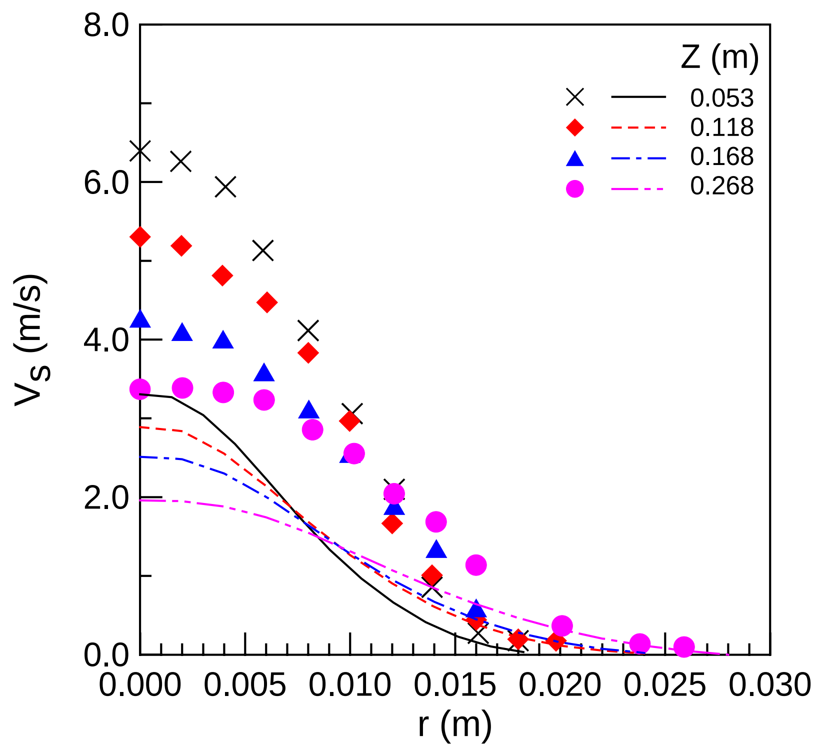

Fig. G-7. Comparison between the simulation and experiment on the axial solids velocity.

(Symbols are experimental data, lines correspond to simulation results.)

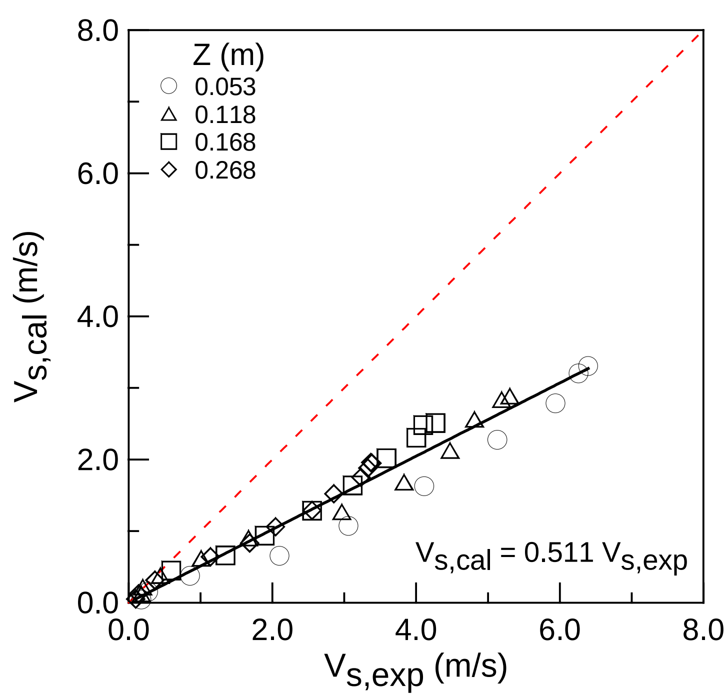

Fig. G-8. Comparison between the simulation and experiment on the axial solids velocity.

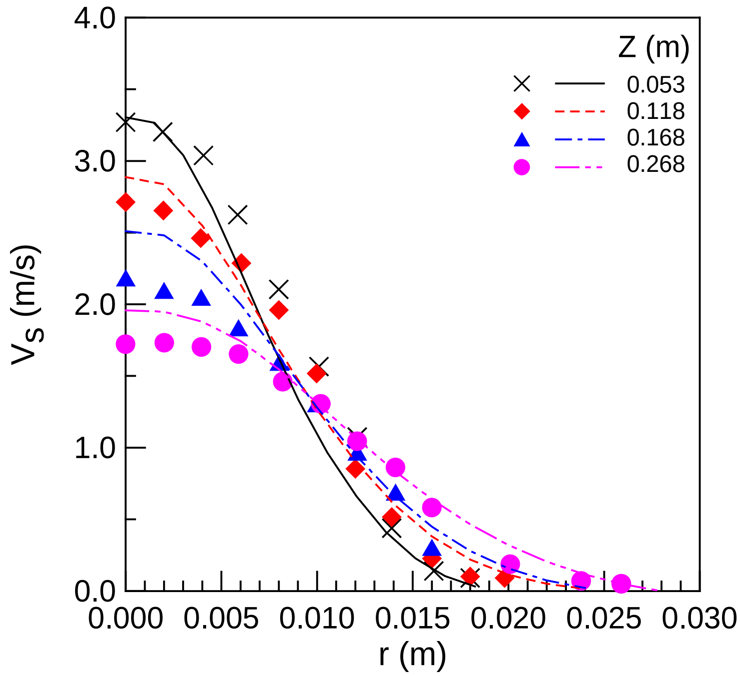

Fig. G-9. Comparison between the simulation and experiment on the axial solids velocity. (Symbols are **adjusted** experimental data, lines correspond to simulation results.)

G.2 Simulations of a conical spouted bed

The proposed approach was also evaluated using the conical spouted bed data reported by San Jose et al. (1998a). In the simulation, all bed geometrical dimensions and operating conditions were kept the same as in San Jose et al. (1998a), with simulation conditions listed in Table G-3 and boundary conditions as listed in Table 5-2. Based on previous sensitivity analysis, restitution coefficient has been found to have significant impact on axial solids velocity profiles. Thus, several different values of restitution coefficient were applied in the current study. Furthermore, based on Olazar et al. (1993c), the ratio of the pressure drop of a conical spouted bed over a fluidized bed with the same static bed height can be calculated by Equation (3-3). Under above operating conditions, the corresponding k_a is slightly smaller than 1.0. Thus, a value of 1.0 was used in the simulation.

Table G-3. Simulation conditions for the conical spouted bed by San Jose et al. (1998a).

Description	Value	Comment
Operating gas velocity, U_i	8.3 m/s	Based on D_i
Gas density, ρ_g	1.23 kg/m^3	Air
Gas viscosity, μ_g	1.79×10^{-5} kg/(m·s)	Air
Particle density, ρ_s	2420 kg/m^3	Spherical glass beads
Particle diameter, d_s	3 mm	Uniform distribution
Initial solids packing, $\varepsilon_{s,0}$	0.655	Fixed value
Packing limit, $\varepsilon_{s,max}$	0.655	Fixed value
Solid viscosity, μ_s	Gidaspow	Eq. (5-7) + Eq. (5-9)
Frictional viscosity, $\mu_{s,fr}$	0	Fixed value
Solid bulk viscosity (Base case), λ_s	0	Fixed value
Diameter of the upper section, D_c	0.36 m	Fixed value
Cone angle, γ	33°	Fixed value
Total height of the column	0.8 m	Fixed value
Gas inlet diameter, D_0	0.03 m	Fixed value
Diameter of the bed bottom, D_i	0.06 m	Fixed value
Static bed height, H_0	0.18 m	Fixed value
Solver	2 dimensional, double precision, segregated, unsteady, 1st order implicit, axisymmetric	
Multiphase Model	Eulerian Model, 2 phases	
Viscous Model	Laminar model	
Phase Interaction (Base case)	Fluid-solid exchange coefficient: Gidaspow Model Restitution coefficient: **0.81, 0.9, 0.99**	
Time steps (Final value)	5×10^{-5} s	Fixed value
Convergence criterion	10^{-3}	Default in FLUENT

As shown in Figure G-10, the effect of the restitution coefficient on axial solids velocity profiles is quite similar to previous results. Comparing with the base case with e_{ss}=0.9, a 10%

increase of the restitution coefficient affects significantly the simulated results, but a 10% decrease of the restitution coefficient has less effects. Furthermore, in most cases, simulated results underestimate experimental data significantly even using different values of restitution coefficient, as shown in Figures G-11 and G-12. The systematic error, again, could come from the particle velocity measurement system. In their experiments, instant axial solids velocity was measured using an optical fibre probe of a large separation distance between the light projector and each receiving fibre, without the installation of a glass window. As a result, there existed a blind zone in front of the probe tip. Also, a rotating disk was used in their study to calibrate the effective distance. According to the current study, both the existence of a blind zone and the rotating disk design can introduce significant errors to the particle velocity measurement.

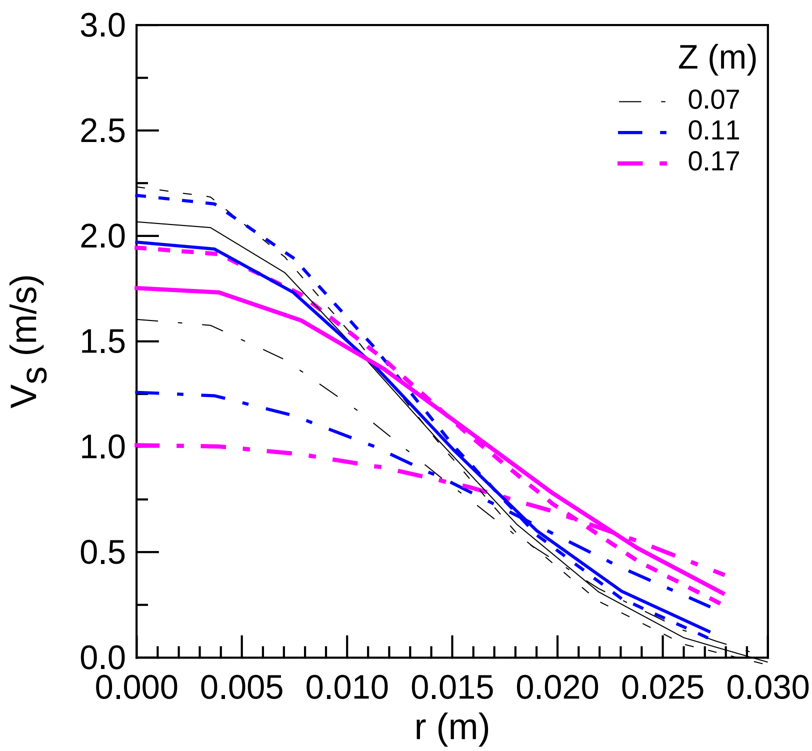

Fig. G-10. Effects of restitution coefficient on simulated axial solids velocity.(k_a=1.0, k_s=1.0, 1/7th power law, Solid lines: e_{ss}=0.9; dashed lines: e_{ss}=0.81; dotted dash lines: e_{ss}=0.99; Thin lines: Z=0.07m; Medium lines: Z=0.11m; Thick lines: Z=0.17m.)

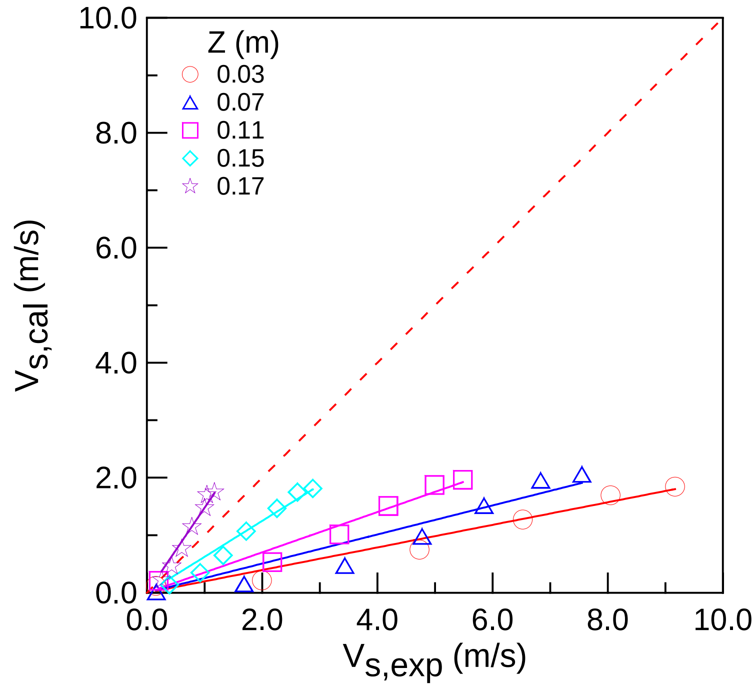

Fig. G-11. Comparison between the simulation and experiment on the axial solids velocity.

(k_a=1.0, k_s=1.0, 1/7th power law, $\boldsymbol{e_{ss}}$**=0.9**.)

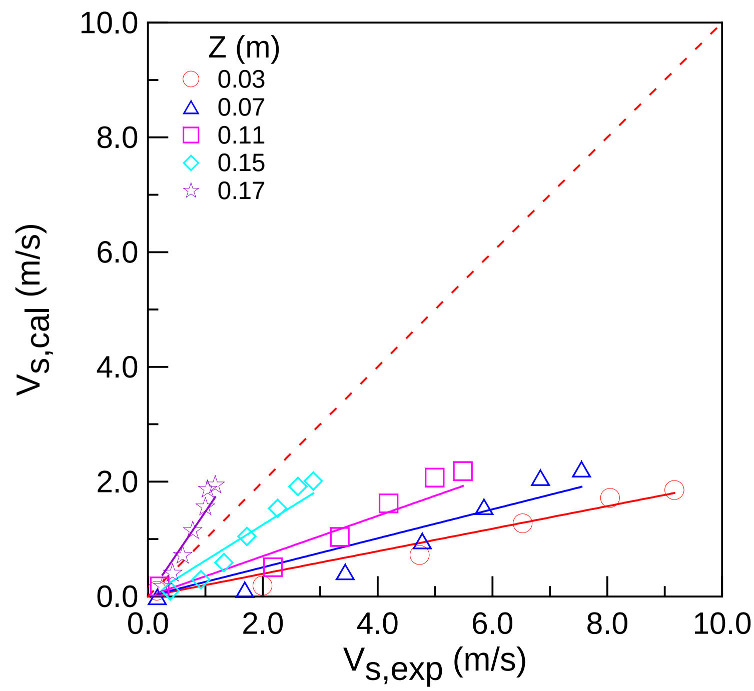

Fig. G-12. Comparison between the simulation and experiment on the axial solids velocity.

(k_a=1.0, k_s=1.0, 1/7th power law, $\boldsymbol{e_{ss}}$**=0.81**.)

APPENDIX H

PROGRAMS FOR THE STREAM-TUBE MODEL

Model1n5.m (Main Program)

```
tic
path(path,'E:\wzg')
clear
clc
global Rop EPUN r N alpha Li1 Li2 AA BB Zs DPs H0 r0 ugie kk Ai Bi ri delta
Gammaj rr Zstmp QQ h0 ratio lambda lam CHOICE
lam=[0.1 0.5 -1.5 1]';

N=12;
Di=0.0381;
dp=1.16/1000;
EPUN=0.39;
FAI=1.0;
Rog=1.25;
Miug=1.8e-5;

Rop=2500;

inputfile0='run001.dat';
inputfile='run001n.dat';
%inputfile0='run015.dat';
%inputfile='run015n.dat';
%inputfile0='run028.dat';
%inputfile='run028n.dat';
%inputfile0='run044.dat';
%inputfile='run044n.dat';
%inputfile0='run052.dat';
%inputfile='run052n.dat';
%inputfile0='RunPdist.dat';
%inputfile='RunPdistn.dat';
mb=load(inputfile0);
%GAMMA      H0    Z     Ug,I     DPt,exp     D0
%           m     m     m/s        kPa       m
Gammae=mb(:,1);
H0e=mb(:,2);
Zse=mb(:,3);
ugie=mb(:,4);
DPtexp=mb(:,5);
D0e=mb(:,6);
nn=length(D0e);
indexU=find(ugie==max(ugie));
%nj1=indexU;
%nj1=12;  % Ascending Za=251mm %
%nj2=12;  % Ascending Za=251mm %

nj1=27;  % Descending Zd=226mm %
```

```
nj2=27;  % Descending Zd=226mm %
%nj1=1;
%nj2=nn;

sume=0.0;
nk=0;
for kk=1:nn
   if H0e(kk)-Zse(kk)<0.01
      sume=sume+DPtexp(kk)*1000;
      kk1=kk;
      nk=nk+1;
   end
end
DPs=sume/nk;
kk0=kk1-nk+1;
umsa=ugie(kk0);
umsd=ugie(kk1);
for kk=1:nn-1
   if ugie(kk)<ugie(kk+1)
      Zsc(kk)=3.9071E-005*ugie(kk)^1.727*H0e(kk)^(-1.6482)*(tan(Gammae(kk)
/2/180*pi))^(-1.7769);
      if ugie(kk)>=umsa
         Zsc(kk)=H0e(kk);
      end
   else
      Zsc(kk)=0.0123004*ugie(kk)^0.7615*H0e(kk)^(-0.024)*(tan(Gammae(kk)/
2/180*pi))^(-0.726);
      if ugie(kk)>=umsd
         Zsc(kk)=H0e(kk);
      end
   end
end
Zsc(nn)=0;
C1=33.7;
C2=0.0408;
Ar=dp^3*Rog*(Rop-Rog)*9.81/Miug^2;
umf=Miug/(dp*Rog)*(sqrt(C1^2+C2*Ar)-C1);
Uta(1)=9.81*dp^2*(Rop-Rog)/(18*Miug);
Uta(2)=(2*dp^1.5*(Rop-Rog)*9.81/(15*Rog^0.5*Miug^0.5))^(2/3);
Uta(3)=sqrt(4/3*dp*(Rop-Rog)*9.81/(0.43*Rog));
Ret=mean(Uta)*dp*Rog/Miug;
if Ret<0.4
   Ut=Uta(1);
elseif Ret<500
   Ut=Uta(2);
else
   Ut=Uta(3);
end
ratio1=0;
ratio2=0;
ratio3=0;

indexP=find(DPtexp==max(DPtexp));
indexU=find(ugie==max(ugie));
% Varied weight (ratioV) %
% ************************** %
%ratioV(1:indexP-2)=0.85;                 % run015.dat
```

```
%ratioV(indexP-1:indexP+1)=0.8;           % run015.dat
%ratioV(2+indexP)=0.85;                   % run015.dat
%ratioV(3+indexP:4+indexP)=0.9;           % run015.dat
%ratioV(5+indexP:indexU-1)=0.93;          % run015.dat
%ratioV(indexU:nj2)=0.99;                 % run015.dat
% *************************** %
% *************************** %
ratioV(1:indexP-3)=0.85;                  % run001.dat
ratioV(indexP-2:indexP-1)=0.7;            % run001.dat
ratioV(indexP)=0.5;                       % run001.dat
ratioV(indexP+1:indexU-1)=0.3;            % run001.dat
ratioV(indexU:nj2)=1.00;                  % run001.dat
ratioV(12)=0.93;                          % run001.dat
ratioV(27)=1.0;                           % run001.dat
% *************************** %
Zstmp=0;
if nj1==nj2
   Zstmp=1;
end
for kk=nj1:nj2
   assumption=1;
   %assumption=3;
   kk
   % Constant weight (ratio1 or ratio2 or ratio3) %
   if kk<indexU
      if kk<indexP
         ratio1=0.75;          %%%% Assume the weight of fluidized bed
         ratio=ratio1;
      else
         ratio2=0.5;           %%%% Assume the weight of fluidized bed
         ratio=ratio2;
      end
   else
      ratio3=1.0;              %%%% Assume the weight of fluidized bed
      ratio=ratio3;
   end

   ratio=ratioV(kk);
   Gamma=0;
   H0=0;
   Zs=0;
   D0=0;
   ug0=0;
   ri=0;
   r0=0;
   AA=0;
   BB=0;
   r=0;
   h0=0;
   alpha(1:N)=0;
   delta(1:N)=0;
   rr(1:N)=0;
   Li1(1:N)=0;
   tt(1)=0;
   yy(1)=0;
   %lii(1:N)=0;
```

```
   Gamma=Gammae(kk);

   H0=H0e(kk);
   ugi=ugie(kk);
   Zs=Zse(kk);
   %Zs=Zsc(kk);
   D0=D0e(kk);
   ri=Di/2;
   r0=D0/2;
   r=ri+H0*tan(Gamma/2/180*pi);
   AA=150*(1-EPUN)^2/EPUN^3*Miug/(FAI*dp)^2;
   BB=1.75*(1-EPUN)/EPUN^3*Rog/FAI/dp;
   h0=r0*H0/(r-r0);
   GammaN=180/pi*atan((r-r0)/H0);
   QQ(1:N)=pi*ri^2*ugie(kk)/N;%%%%%%%%%%%%%%%%%%%%%%%%%%%%%%
   for j=1:N
      %rr(j)=r*sqrt(j/N);  % Cross section area of the bed surface is divided
into N equal internals.
      %rr(j)=r*(j/N);      % Radial of the bed surface is divided into N
equal intervals.
      rr(j)=(H0+h0)*tan(GammaN/N*j/180*pi);
   end
   if H0e(kk)-Zse(kk)<0.01
      DPt(kk)=DPs;
   else
      alpha(1)=180/pi*atan(rr(1)/(H0+h0));
      for ii=2:N
         sum1=0;
         for jj=1:ii-1
            sum1=sum1+alpha(jj);
         end
         alpha(ii)=180/pi*atan(rr(ii)/(H0+h0))-sum1;
      end
      delta(1)=0;
      for ii=2:N
         sum1=0;
         for jj=1:ii-1
            sum1=sum1+alpha(jj);
         end
         delta(ii)=alpha(ii)/2+sum1;
      end

      if assumption==1
         %1 The length of stream tube from the edge of the internal spout
         %Gammaj=2*sum(alpha);   % Angle of the lower conical fluidized bed
          Gammaj=20;             % Angle of the actual internal spout
          Gammaj1=Gammaj;
          rsin1=(r0+Zs*tan(Gammaj1/2/180*pi))/(1+tan(Gammaj1/2/180*pi));
          [Li10,li0]=fun_Li0(H0,Zs,alpha,r0,h0,Gammaj);
          Li1=Li10;
          li=li0;
      elseif assumption==2
          %2 The length of the stream tube from the top plane of the internal
spout
          Gammaj1=20;            % Angle of the actual internal spout
          rsin1=(r0+Zs*tan(Gammaj1/2/180*pi))/(1+tan(Gammaj1/2/180*pi));
          [Li11,li1]=fun_Li1(H0,Zs,alpha);
```

```
        Li1=Li11;
        li=li1;
    elseif assumption==3
        %3 The length of the stream tube from the top spherical surface of
the internal spout
        Gammaj1=20;            % Angle of the actual internal spout
        rsin1=(r0+Zs*tan(Gammaj1/2/180*pi))/(1+tan(Gammaj1/2/180*pi));
        [Li12,li2]=fun_Li2(H0,Zs,alpha,h0);
        Li1=Li12;
        li=li2;
    elseif assumption==4
        %4 The length of the stream tube from the top elliptical surface of
the internal spout
        Gammaj1=20;            % Angle of the actual internal spout
        rsin1=(r0+Zs*tan(Gammaj1/2/180*pi))/(1+tan(Gammaj1/2/180*pi));
        [Li13,li3]=fun_Li3(H0,Zs,alpha,GammaN,h0);
        Li1=Li13;
        li=li3;
    end

    %Pplotshape3(li,rsin1,Gammaj1,Gamma)
    %%%%%%%%%%%%%%%%%%%%%%%%%%%%%%%%%%%%%%%%%%%%
    Zpf0(1:N)=0;
    Zpf1(1:N)=Zs;
    criteria(1:N)=1;
    Ncal=1;
    while max(criteria)>1e-2
       if Ncal==1
          Li2=Li1;   % The length of the stream tube from the interface
with Uz=Umf
          %criteria(1:N)=1e-3; % Do not consider the difference in upper
packed bed
       else
          Zpf0=Zpf1;
          Q0=Q1;
          for jj=1:N
             Aumf(jj)=Q0(jj)*cos(delta(jj)/180*pi)/umf;
             if jj==1
                Lii(jj)=Li1(jj)-(rr(jj)-sqrt(Aumf(jj)/pi))/tan(alpha(jj)
/180*pi);
                Zpf1(jj)=H0-(Li1(jj)-Lii(jj))*cos(delta(jj)/180*pi);
                Zpf1(jj)=real(Zpf1(jj));
                if Zpf1(jj)-H0>1e-6
                   Zpf1(jj)=H0-1e-3;
                elseif Zpf1(jj)<0
                   Zpf1(jj)=1e-4;
                end
                Li2(jj)=(H0-Zpf1(jj))/cos(delta(jj)/180*pi);
             else
             sum2=0;
             for jjj=1:jj-1
                sum2=sum2+alpha(jjj);
             end
             Lii(jj)=Li1(jj)+sqrt(Aumf(jj)*cos(alpha(jj)/2/180*pi)
/(sin(sum2/180*pi)+sin((sum2+alpha(jj))/180*pi))/(2*pi*tan(alpha(jj)/2/180*pi
)))-(H0+h0)/cos(delta(jj)/180*pi);
             Zpf1(jj)=H0-(Li1(jj)-Lii(jj))*cos(delta(jj)/180*pi);
```

```
            Zpf1(jj)=real(Zpf1(jj));
            if Zpf1(jj)-H0>1e-6
               Zpf1(jj)=H0-1e-3;
            elseif Zpf1(jj)<0
               Zpf1(jj)=1e-4;
            end
            Li2(jj)=(H0-Zpf1(jj))/cos(delta(jj)/180*pi);
            end
         end
         for jj=1:N
            criteria(jj)=abs((Zpf1(ii)-Zpf0(ii))/Zpf1(ii));
         end
         %%Li1=Li0;%%%1111111111111111111%%%
      end

      %2 Newton Raphson method for non-linear equation
      tt0=DPtexp(kk)*1000+0.7e3;
      if assumption==3
         CHOICE=2;
         DPt(kk)=NewtonR(tt0,5e-2);
         CHOICE=3;
         DPt(kk)=NewtonR(tt0,5e-2);
      else
         CHOICE=4;
         DPt(kk)=NewtonR(tt0,5e-2);
      end
      Q1=real(QQ);
      Ncal=Ncal+1;
   end
   %Pplotshape31(Zpf1,Gamma)
   %%%%%%%%%%%%%%%%%%%%%%%%%%%%%%%%%%%%%%%%%%%%%%%%
   Pplot3(umf,Ut,Zpf1,inputfile,DPt(kk))
  end
  clear X0
end
plotDPt(assumption,inputfile0,DPtexp,nj1,nj2,DPt,ratio1,ratio2,ratio3,Gamma,D
0);
%figure
%plot(ugie(nj1:nj2),Zse(nj1:nj2),'ro')
%hold on
%plot(ugie(nj1:nj2),Zsc(nj1:nj2),'b-')
outputfile1=inputfile0;
outputfile1(8:10)='rat',
fid=fopen(outputfile1,'wt');
fprintf(fid,'%s\n','      Ug       DPt-Exp(Pa)  DPt-Cal(Pa)     ratio');
for ii=nj1:nj2
   fprintf(fid,'%10.4f %12.4f %12.4f %12.4f\n',ugie(ii),DPtexp(ii)
,DPt(ii)/1000,ratioV(ii));
end
fclose(fid);
toc
```

Pplotshape3.m

```
%path(path,'E:\wzg')
```

```
function funPlot=Pplotshape3(li,rsin1,Gammaj1,Gamma)
global Rop EPUN r N alpha Li1 Li2 AA BB Zs DPs H0 r0 ugie kk Ai Bi ri delta
Gammaj rr Zstmp QQ h0 ratio
figure
%%for Us=0
shapeX(1)=0;
shapeY(1)=Zs;
for ii=1:N
   sum1=0;
   for jj=1:ii
      sum1=sum1+alpha(jj);
   end
   shapeX(ii+1)=((H0+h0)/cos(sum1/180*pi)-li(ii))*sin(sum1/180*pi);
   shapeY(ii+1)=((H0+h0)/cos(sum1/180*pi)-li(ii))*cos(sum1/180*pi)-h0;
end
plot(shapeX,shapeY,'r--')
hold on
tmpY=0.85*max(shapeY);
tmpX=1.3*(ri+tmpY*tan(Gamma/2/180*pi));
if max(shapeY)<1e-3
   set(gcf,'DefaultTextColor','red');
   text(tmpX,tmpY,'Us=0','FontSize',14)
else
   set(gcf,'DefaultTextColor','red');
   text(tmpX,tmpY,'Us=0','FontSize',14)
end

%%assumed boundary line for dead zone
shapeBedX1=0:r/20:r;
shapeBedY1=tan((90-sum(alpha))/180*pi)*shapeBedX1-h0;
plot(shapeBedX1,shapeBedY1,'c--','LineWidth',1)
%%for bed surface
shapeBedY2(1:length(shapeBedX1))=H0;
plot(shapeBedX1,shapeBedY2,'k--','LineWidth',2)
set(gcf,'DefaultTextColor','black')
text(1.1*max(shapeBedX1),min(shapeBedY2),['H0=',num2str(H0,3),'m'],'FontSize'
,14)
%%for the outside shape of the bed
shapeBedX=0:1.2*r/20:1.2*r;
shapeBedY=tan((90-Gamma/2)/180*pi)*shapeBedX-ri/tan(Gamma/2/180*pi);
plot(shapeBedX,shapeBedY,'r-','LineWidth',2)
%%for the shape of the internal spout
if Zs>r0
   shapespoutX1=(r0:(Zs-rsin1)*tan(Gammaj1/2/180*pi)/10:r0+(Zs-
rsin1)*tan(Gammaj1/2/180*pi));
   shapespoutY1=tan((90-Gammaj1/2)/180*pi).*shapespoutX1-
r0/tan(Gammaj1/2/180*pi);
   shapespoutX2=(0:(r0+(Zs-rsin1)*tan(Gammaj1/2/180*pi))/10:r0+(Zs-
rsin1)*tan(Gammaj1/2/180*pi));
   shapespoutY2=Zs-rsin1+sqrt(abs(rsin1^2-shapespoutX2.^2));
   plot(shapespoutX1,shapespoutY1,'g--')
   plot(shapespoutX2,shapespoutY2,'g--')
end
%%for the streamline
for ii=1:N
   sum1=0;
   for jj=1:ii
```

```
      sum1=sum1+alpha(jj);
   end
   lineX0=rr(ii)-li(ii)*sin(sum1/180*pi);
   lineX1=rr(ii);
   lineX=lineX0:(lineX1-lineX0)/10:lineX1;
   lineY=H0-(lineX1-lineX)./tan(sum1/180*pi);
   plot(lineX,lineY,'m--')
end
%%the upper crosssection area for each stream tube
for ii=1:N
   coef=up_area(ii);
   x0=coef(1);
   x1=coef(2);
   lk=coef(3);
   lb=coef(4);
   linX=x0:(x1-x0)/10:x1;
   linY=lk.*linX+lb;
   plot(linX,linY,'r-')
end
%%for the figure
axis([0 (16.7/12.9)*1.2*0.5 0 1.2*0.5])
xlabel('R (m)','FontSize',14)
ylabel('Z (m)','FontSize',14)
```

Pplotshape31.m

```
%path(path,'E:\wzg')
function funPlot=Pplotshape31(Zpf1,Gamma)
global Rop EPUN r N alpha Li1 Li2 AA BB Zs DPs H0 r0 ugie kk Ai Bi ri delta
Gammaj rr Zstmp QQ h0 ratio
%%for Uz=Umf
for jj=1:N
   rumf(jj)=tan(delta(jj)/180*pi)*(Zpf1(jj)+h0);
end
plot(rumf,Zpf1,'b--')
tmpY=0.85*abs(Zpf1(1));
tmpX=1.3*(ri+tmpY*tan(Gamma/2/180*pi));
set(gcf,'DefaultTextColor','blue')
text(tmpX,tmpY,'Uz=Umf','FontSize',14)
hold off
```

NewtonR.m

```
%path(path,'E:\wzg')
function X1=NewtonR(X0,eps)
crit=1;
while crit>=eps
   tmp=DPt1n5(X0);
   df=(DPt1n5((1+eps)*X0)-tmp)/(eps*X0);
   X1=X0-tmp/df;
   crit=abs((X1-X0)/X1);
   X0=X1;
end
```

Pplot3.m

```
%path(path,'E:\wzg')
function funPlot=Pplot3(umf,Ut,Zpf1,inputfile,DPt)
global Rop EPUN r N alpha Li1 Li2 AA BB Zs DPs H0 r0 ugie kk Ai Bi ri delta
Gammaj rr Zstmp QQ h0 ratio
first=1;

if Zstmp==1
   Hprob=[38.1 88.9 139.7 241.3 342.9]'; % Same as ZZZ in Pexp5.m
   Htmp=[300 400 450]';
   j11=0;
   for j22=1:length(Hprob)
      if Hprob(j22)/1000.>=Zs
         ZsU(j11+1)=Hprob(j22)/1000.;
         j11=j11+1;
      end
   end
   ZsU(j11+1:j11+3)=Htmp/1000.;
   ZsU(j11+4)=Zs;
   ZsUP=Hprob./1000.;
else
   Hprob=[0 38.1 88.9 139.7 241.3 342.9]';
   %Hprob=226+(468-226)/5.*[0:5]';
   for ii=1:length(Hprob)
      if Hprob(ii)/1000-H0>=1e-4
         ZsU(jj+1)=H0;
         break
      else
         if Hprob(ii)/1000-Zs>1e-4
            if Hprob(ii)/1000-max(Zpf1)>1e-4
               if first==1
                  if abs(Zs-Zpf1)>1e-4
                     ZsU(jj+1)=max(Zpf1);
                     ZsU(jj+2)=Hprob(ii)/1000;
                     jj=jj+2;
                     first=2;
                  else
                     ZsU(jj+1)=Hprob(ii)/1000;
                     jj=jj+1;
                     first=2;
                  end
               else
                  ZsU(jj+1)=Hprob(ii)/1000;
                  jj=jj+1;
               end
            else
               ZsU(jj+1)=Hprob(ii)/1000;
               jj=jj+1;
            end
         else
            ZsU(1)=Zs;
            jj=1;
         end
```

```
      end
   end
   ZsUP=ZsU;
end

col='ro-cs-md-b^-gv-rp-c>-m<-';
figure
for ii1=1:length(ZsUP)
   for jj1=1:N
      Li3=(H0-ZsUP(ii1))/cos(delta(jj1)/180*pi);%%%%%%%%%%%%%
      Pz(ii1,jj1)=DPtn3(Li3,jj1,DPt);%%%%%%%%%%%%%
      rzP(ii1,jj1)=tan(delta(jj1)/180*pi)*(ZsUP(ii1)+h0);%%%%%%%%%%%%%
   end
   Ymax1(ii1)=max(Pz(ii1,:));
end

for ii=1:length(ZsU)
   for jj=1:N
      Li4=(H0-ZsU(ii))/cos(delta(jj)/180*pi);%%%%%%%%%%%%%
      Lii(jj)=Li1(jj)-Li4;
      rz(jj)=tan(delta(jj)/180*pi)*(ZsU(ii)+h0);
      rzU(ii,jj)=rz(jj);
      if jj==1
         As(jj)=pi.*(rr(jj)-(Li1(jj)-Lii(jj)).*tan(alpha(jj)/180*pi)).^2.0;
      else
         sum1=0;
         for jjj=1:jj-1
            sum1=sum1+alpha(jjj);
         end
         E1=2*pi*tan(alpha(jj)/2/180*pi)*(sin(sum1/180*pi)+sin((sum1+
alpha(jj))/180*pi))/cos(alpha(jj)/2/180*pi);
         As(jj)=E1.*((H0+h0)/cos(delta(jj)/180*pi)-(Li1(jj)-Lii(jj))).^2.0;
      end
      UUZ(jj)=QQ(jj)*cos(delta(jj)/180*pi)/As(jj);
      UZ(ii,jj)=UUZ(jj);
      UMF(jj)=umf;
      UT(jj)=Ut;
   end
   plot(rz,UUZ,col(3*ii-2:3*ii))
   hold on
   Ymax(ii)=max(UUZ);
end
if max(Ymax)>umf
   plot(0.8.*rz,UMF,'b--')
end
xlabel('R (m)','FontSize',14)
ylabel('Uz (m/s)','FontSize',14)
text(0.16,umf,'Umf','FontSize',14)
title(['Ugi=',num2str(ugie(kk),3),'(m/s)'],'FontSize',16)
for ii=1:length(ZsU)
   if abs(ZsU(ii)-Zs)<1e-5
      text(0.6*max(rz),(1-0.05*ii)*max(Ymax),['Z=',num2str(ZsU(ii)*1000,3)
,'(mm)----Zs'],'FontSize',12)
   elseif abs(ZsU(ii)-max(Zpf1))<1e-5
      text(0.6*max(rz),(1-0.05*ii)*max(Ymax),['Z=',num2str(ZsU(ii)*1000,3)
,'(mm)----Zpf,1'],'FontSize',12)
   else
```

```
      text(0.6*max(rz),(1-0.05*ii)*max(Ymax),['Z=',num2str(ZsU(ii)*1000,3)
,'(mm)'],'FontSize',12)
   end
   plot(0.5*max(rz),(1-0.05*ii)*max(Ymax),col(3*ii-2:3*ii-1))
end
text(0.6*max(rz),(1-0.05*(length(ZsU)+1))*max(Ymax),['kk=',num2str(kk,2)]
,'FontSize',14)
hold off
%%%%%
figure
for ii=1:length(ZsUP)
   plot(rzP(ii,:),Pz(ii,:)/1000,col(3*ii-2:3*ii))
   hold on
end
xlabel('R (m)','FontSize',14)
ylabel('Pz (kPa)','FontSize',14)
title(['Ugi=',num2str(ugie(kk),3),'(m/s)'],'FontSize',16)
if Zstmp==1
   fid2=fopen('UZrd.dat','wt');
   fid3=fopen('PZrd.dat','wt');
   fprintf(fid2,'%s\n','          r(m)            Z(m)          U(m/s)');
   fprintf(fid3,'%s\n','          r(m)            Z(m)          P(Pa)');
   for j1=1:length(ZsU)
      for j2=1:N
         fprintf(fid2,'%15.5f %15.5f %15.5f\n',rzU(j1,j2),ZsU(j1),UZ(j1,j2));
      end
      fprintf(fid2,'%s\n',' ');
   end

   for j1=1:length(ZsUP)
      for j2=1:N
         fprintf(fid3,'%15.5f %15.5f %15.5f\n',rzP(j1,j2),ZsUP(j1)
,Pz(j1,j2));
      end
      fprintf(fid3,'%s\n',' ');
   end

   fclose(fid2);
   fclose(fid3);
   Pzexp=Pexp5(col,Ymax1,ZsUP,Zs,kk,Zpf1,length(ZsUP));
else

Pzexp=Pexp4(ugie,kk,rzP,N,ZsUP,col,length(ZsUP),Zs,max(Ymax1),Zpf1,H0,inputfi
le);
end
hold off
%%%%%
```

Pexp5.m

```
%path(path,'E:\wzg')
function funPexp=Pexp5(col,Ymax1,ZsUP,Zs,kk,Zpf1,kn)
%col='cs-md-b^-gv-c>-m<-';

%%%%%%%%%%%%%%%%%%%%%%%%%%%%%%%%%%%%%%%%%%%%%%%%%%%%%%%%
```

```
% Data input
%datad=load('exp-data-A.dat');
%P6   P5 P4 P3 P2 P2-r  P3-r  P4-r  P5-r  P6-r
%Neff=[10 10 10 10 10];                % Numbers of actual effective data
used
%Ugba=33.86227;                        % Superficial gas velocity, m/s
%Zs=251./1000.;                        % Height of the spout, mm

datad=load('exp-data-D.dat');
%%P6  P5 P4 P3 P2 P2-r  P3-r  P4-r  P5-r  P6-r
Neff=[12 12 11 5 5];                   % Numbers of actual effective data
used
Ugbd=19.57868;                         % Superficial gas velocity, m/s
Zs=226./1000.;                         % Height of the spout, mm

Rd=[34 56 76.5 118 159];               % mm
ZZZ=[38.1 88.9 139.7 241.3 342.9];     % mm
H0=468;                                % Static bed height, mm
P0=101325;                             % Atmosphere pressure, Pa
Di=0.0381;                             % Diameter of the bed bottom, m,
Gamma=45;                              % Cone angle, degree
Mt=29;                                 % Molecular weight of air, g/mol
NN=length(Rd);
for j=1:NN
   Pp(:,NN+1-j)=datad(:,j);
   rRp(:,j)=datad(:,j+NN);
   rp(:,j)=Rd(j)*rRp(:,j)/1000;
   Zp(j)=ZZZ(j)/1000;
end
for jj=1:length(Rd)
   for ii1=1:min(Neff)
      plot(rp(ii1,jj),Pp(ii1,jj),col(3*jj-2:3*jj-1),'MarkerFaceColor','k')
      hold on
   end
end
xlim=(0.7*max(max(rp)));
ylim=max(max(max(Pp)),max(Ymax1/1000));
for ii=1:kn
  if abs(ZsUP(ii)-Zs)<1e-5
     text(xlim,(1-0.05*ii)*ylim,['Z=',num2str(ZsUP(ii)*1000,3),'(mm)----
Zs'],'FontSize',12)
  elseif abs(ZsUP(ii)-max(Zpf1))<1e-5
     text(xlim,(1-0.05*ii)*ylim,['Z=',num2str(ZsUP(ii)*1000,3),'(mm)----
Zpf,1'],'FontSize',12)
  else
     text(xlim,(1-
0.05*ii)*ylim,['Z=',num2str(ZsUP(ii)*1000,3),'(mm)'],'FontSize',12)
  end
  plot(0.9*xlim,(1-0.05*ii)*ylim,col(3*ii-2:3*ii-1))
end
text(xlim,(1-0.05*(kn+1))*ylim,['kk=',num2str(kk,2)],'FontSize',14)
text(0.5*xlim,ylim,'Solid symbols are experimental results.','FontSize',12)
fid3=fopen('PZrdexp.dat','wt');
fprintf(fid3,'%s\n','          r(m)            Z(m)          P(Pa)');
for j1=1:length(Zp)
   for j2=1:min(Neff)
      fprintf(fid3,'%15.5f %15.5f %15.5f\n',rp(j2,j1),Zp(j1),Pp(j2,j1)*1000);
```

```
   end
   fprintf(fid3,'%s\n',' ');
end
fclose(fid3);
funPexp=1;
```

Pexp4.m

```
%path(path,'E:\wzg')
function funPexp=Pexp4(ugie,kk,rzP,N,ZsU,col,kn,Zs,Ymax1,Zpf1,H0,inputfile)
Data=load(inputfile);
%[P7/DPt P6/DPt P5/DPt P4/DPt P3/DPt P2/DPt 1-H7/H0 1-H6/H0 1-H5/H0 1-H4/H0
1-H3/H0 1-H2/H0 Ug,b DPt Z]
AA(:,7)=Data(:,1);
AA(:,2)=Data(:,2);
AA(:,3)=Data(:,3);
AA(:,4)=Data(:,4);
AA(:,5)=Data(:,5);
AA(:,6)=Data(:,6);
AA(:,1)=0;
BB(:,7)=Data(:,7);
BB(:,2)=Data(:,8);
BB(:,3)=Data(:,9);
BB(:,4)=Data(:,10);
BB(:,5)=Data(:,11);
BB(:,6)=Data(:,12);
BB(:,1)=0;
CC=Data(:,13);
DD=Data(:,14);
EE=Data(:,15);
AT=AA';
BT=BB';
Ugb=CC';
DPt=DD';
HZ=EE';
tmp=AT(:,1);
P(1:length(AT(:,1)))=0;
Pprint=P;
for ii=1:length(Ugb)
   if abs(Ugb(ii)-ugie(kk))<1e-5
      KKK=ii;
      P=AT(:,KKK).*DPt(KKK);
      H=(1-BT(:,KKK)).*H0;
      for ii1=1:length(ZsU)
         for jj=1:length(H)
            if abs(H(jj)-ZsU(ii1))<1e-5
               plot(rzP(ii1,N),P(jj),col(3*ii1-2:3*ii1-1),'MarkerFaceColor'
,'k')
               Pprint(jj)=P(jj);
               hold on
            end
         end
      end
   end
end
```

```
funPexp=P;
Ymax2(1)=Ymax1;
Ymax2(2)=max(Pprint*1000);
xlim=0.7*max(max(rzP));
for ii=1:kn
  if abs(ZsU(ii)-Zs)<1e-5
     text(xlim,(1-0.05*ii)*max(Ymax2)/1000,['Z=',num2str(ZsU(ii)*1000,3)
,'(mm)----Zs'],'FontSize',12)
  elseif abs(ZsU(ii)-max(Zpf1))<1e-5
     text(xlim,(1-0.05*ii)*max(Ymax2)/1000,['Z=',num2str(ZsU(ii)*1000,3)
,'(mm)----Zpf,1'],'FontSize',12)
  else
     text(xlim,(1-0.05*ii)*max(Ymax2)/1000,['Z=',num2str(ZsU(ii)*1000,3)
,'(mm)'],'FontSize',12)
  end
  plot(0.9*xlim,(1-0.05*ii)*max(Ymax2)/1000,col(3*ii-2:3*ii-1))
end
text(xlim,(1-0.05*(kn+1))*max(Ymax2)/1000,['kk=',num2str(kk,2)],'FontSize'
,14)
text(0.5*xlim,max(Ymax2)/1000,'Solid symbols are experimental
results.','FontSize',12)
```

DPtn3.m

```
%path(path,'E:\wzg')
function funPz=DPtn3(Li3,jj,DPt)
global Rop EPUN r N alpha Li1 Li2 AA BB Zs DPs H0 r0 ugie kk Ai Bi ri delta
Gammaj rr Zstmp QQ h0 ratio
if Li3<Li1(jj)
   if Li3>Li2(jj)
      intg1=quad8('intfun1n3',Li1(jj)-Li2(jj),Li1(jj),1e-3,[],jj);
      intg2=quad8('intfun2n3',Li1(jj)-Li2(jj),Li1(jj),1e-3,[],jj);
      Ai=BB*intg2;
      Bi=AA*intg1;
      DPpb(jj)=Bi*QQ(jj)+Ai*QQ(jj)^2;

      intg1_pb=quad8('intfun1n3',Li1(jj)-Li3,Li1(jj)-Li2(jj),1e-3,[],jj);
      intg2_pb=quad8('intfun2n3',Li1(jj)-Li3,Li1(jj)-Li2(jj),1e-3,[],jj);
      Ai_pb=BB*intg2_pb;
      Bi_pb=AA*intg1_pb;
      DP_pb(jj)=Bi_pb*QQ(jj)+Ai_pb*QQ(jj)^2;
      DP_fb(jj)=Rop*9.81*(1-EPUN)*((Li1(jj)-Li2(jj))-(Li1(jj)-Li3))
*cos(delta(jj)/180*pi);
      DPpfb=(1-ratio)*DP_pb(jj)+ratio*DP_fb(jj);
      funPz=DPpfb+DPpb(jj);
   elseif Li3<1e-6
      funPz=0;
   else
      intg1=quad8('intfun1n3',Li1(jj)-Li3,Li1(jj),1e-3,[],jj);
      intg2=quad8('intfun2n3',Li1(jj)-Li3,Li1(jj),1e-3,[],jj);
      Ai=BB*intg2;
      Bi=AA*intg1;
      funPz=Bi*QQ(jj)+Ai*QQ(jj)^2;
   end
else
```

```
   funPz=DPt-(H0-Li3*cos(delta(jj)/180*pi))/H0*DPs;
end
```

intfun1n3.m

```
%path(path,'E:\wzg')
function intf1=intfun1n3(L,iii)
global Rop EPUN r N alpha Li1 Li2 AA BB Zs DPs H0 r0 ugie kk Ai Bi ri delta
Gammaj rr Zstmp QQ h0 ratio
if iii==1
   AiL=pi.*(rr(1)-(Li1(iii)-L).*tan(alpha(iii)/180*pi)).^2.0;
else
   sum1=0;
   for jjj=1:iii-1
      sum1=sum1+alpha(jjj);
   end
   EE1=(H0+h0)/cos(delta(iii)/180*pi)-(Li1(iii)-L);
   EL=2*EE1*tan(alpha(iii)/2/180*pi);
   ER=EE1*sin((sum1+alpha(iii))/180*pi)/cos(alpha(iii)/2/180*pi);
   Er=EE1*sin(sum1/180*pi)/cos(alpha(iii)/2/180*pi);
   EAiL=pi.*EL.*(ER+Er);
   E1=2*pi*tan(alpha(iii)/2/180*pi)*(sin(sum1/180*pi)+sin((sum1+alpha(iii))
/180*pi))/cos(alpha(iii)/2/180*pi);
   AiL=E1.*((H0+h0)/cos(delta(iii)/180*pi)-(Li1(iii)-L)).^2.0;
end
%K1=12.8717*(H0-(Li1(iii)-L)*cos(delta(iii)/180*pi))-2.51315;
K1=1;       %%%% Assume the difference from Ergun's equation, K1=1 means no
difference.
intf1=K1./AiL;
```

intfun2n3.m

```
%path(path,'E:\wzg')
function intf2=intfun2n3(L,iii)
global Rop EPUN r N alpha Li1 Li2 AA BB Zs DPs H0 r0 ugie kk Ai Bi ri delta
Gammaj rr Zstmp QQ h0 ratio
if iii==1
   AiL=pi.*(rr(1)-(Li1(iii)-L).*tan(alpha(iii)/180*pi)).^2.0;
else
   sum1=0;
   for jjj=1:iii-1
      sum1=sum1+alpha(jjj);
   end
   E1=2*pi*tan(alpha(iii)/2/180*pi)*(sin(sum1/180*pi)+sin((sum1+alpha(iii))
/180*pi))/cos(alpha(iii)/2/180*pi);
   AiL=E1.*((H0+h0)/cos(delta(iii)/180*pi)-(Li1(iii)-L)).^2.0;
end
%K1=12.8717*(H0-(Li1(iii)-L)*cos(delta(iii)/180*pi))-2.51315;
K1=1;       %%%% Assume the difference from Ergun's equation, K1=1 means no
difference.
intf2=K1./AiL.^2;
```

plotDPt.m

```
%path(path,'E:\wzg')
function
f=plotDPt(assumption,inputfile0,DPtexp,nj1,nj2,DPt,ratio1,ratio2,ratio3,Gamma
,D0)
global Rop EPUN r N alpha Li1 Li2 AA BB Zs DPs H0 r0 ugie kk Ai Bi ri delta
Gammaj rr Zstmp QQ h0 ratio lambda lam CHOICE
figure
plot(ugie(nj1:nj2),DPtexp(nj1:nj2)*1000,'ro')
hold on
plot(ugie(nj1:nj2),DPt(nj1:nj2),'b-')
Ymax1=max(DPtexp*1000);
Ymax2=max(DPt);
Xmax=(floor(max(ugie)/5)+1)*5;
Ymax3=(floor(1.2*max(Ymax1,Ymax2)/1000)+1)*1000;
axis([0 Xmax 0 Ymax3])
xlabel('Ugi (m/s)','FontSize',14)
ylabel('DPt (Pa)','FontSize',14)
title('Evolution of the total pressure drop','FontSize',16)
legend('Experimental results','Calculated results')
text(0.85*max(ugie),(1-
0.05*9.5)*max(Ymax3),['{\omega}_{fb,A1}{=}',num2str(ratio1,3)],'FontSize',12)
text(0.85*max(ugie),(1-
0.05*11)*max(Ymax3),['{\omega}_{fb,A2}{=}',num2str(ratio2,3)],'FontSize',12)
text(0.85*max(ugie),(1-
0.05*12.5)*max(Ymax3),['{\omega}_{fb,D}{=}',num2str(ratio3,3)],'FontSize',12)
if assumption==1
   text(0.85*max(ugie),(1-
0.05*1)*max(Ymax3),['{\gamma}_{j}{=}',num2str(Gammaj,3),'^{o}'],
'FontSize',12)
elseif assumption==2
   text(0.5*max(ugie),(1-0.05*1)*max(Ymax3),'Assumption of plane','FontSize'
,12)
elseif assumption==3
   text(0.5*max(ugie),(1-0.05*1)*max(Ymax3),'Assumption of spherical surface'
,'FontSize',12)
elseif assumption==4
   text(0.5*max(ugie),(1-0.05*1)*max(Ymax3),'Assumption of elliptical
surface','FontSize',12)
end
text(0.05*max(ugie),(1-0.05*1)*max(Ymax3),inputfile0(1:6),'FontSize',14)
text(0.8*max(ugie),(1-0.05*5)*max(Ymax3),['{\gamma}_{b}{=}',num2str(Gamma,3)
,'^{o}'],
'FontSize',12)
text(0.8*max(ugie),(1-0.05*6.5)*max(Ymax3),['{H}_{0}{=}',num2str(H0*1000,3)
,'mm'],'FontSize',12)
text(0.8*max(ugie),(1-0.05*8)*max(Ymax3),['{D}_{0}{=}',num2str(D0*1000,4)
,'mm'],'FontSize',12)

outputfile='run001Rd.dat';
fid=fopen(outputfile,'wt');
fprintf(fid,'%s\n','      Ug     DPt-Exp(Pa)  DPt-Cal(Pa)');
for ii=nj1:nj2
   fprintf(fid,'%10.4f %12.4f %12.4f\n',ugie(ii),DPtexp(ii),DPt(ii)/1000);
end
```

```
if assumption==1
   fprintf(fid,'%s %6.2f %s\n','Gammaj=',Gammaj,'(o)');
elseif assumption==2
   fprintf(fid,'%s\n','Assumption of plane');
elseif assumption==3
   fprintf(fid,'%s\n','Assumption of spherical surface');
elseif assumption==4
   fprintf(fid,'%s\n','Assumption of elliptical surface');
end
fprintf(fid,'%s %6.2f\n','ratio1=',ratio1);
fprintf(fid,'%s %6.2f\n','ratio2=',ratio2);
fprintf(fid,'%s %6.2f\n','ratio3=',ratio3);
fprintf(fid,'%s %6.2f %s\n','Gamma=',Gamma,'(o)');
fprintf(fid,'%s %6.2f %s\n','H0=',H0*1000,'(mm)');
fprintf(fid,'%s %6.2f %s\n','D0=',D0*1000,'(mm)');
fclose(fid);
```

DPt1n5.m

```
%path(path,'E:\wzg')
function funDPt=DPt1n5(DPt0)
global Rop EPUN r N alpha Li1 Li2 AA BB Zs DPs H0 r0 ugie kk Ai Bi ri delta
Gammaj rr Zstmp QQ h0 ratio CHOICE
sum1=0;
for iii=1:N
   intg1=quad8('intfun1n3',Li1(iii)-Li2(iii),Li1(iii),1e-3,[],iii);
   intg2=quad8('intfun2n3',Li1(iii)-Li2(iii),Li1(iii),1e-3,[],iii);
   Ai_fb=BB*intg2;
   Bi_fb=AA*intg1;

   PtmP=funPtmP(CHOICE,iii,DPt0);      %%%% Calculate the total pressure drop
   %PtmP=funPtmP(0);    %%%% Calculate the pressure drop of the upper packed
bed only
   if Li1(iii)>Li2(iii)
      CCi=PtmP-DPt0;
      Ci=ratio*Rop*9.81*(1-EPUN)*(Li1(iii)-Li2(iii))*cos(delta(iii)
/180*pi)+CCi;
      intg_pfb1=quad8('intfun1n3',0,Li1(iii)-Li2(iii),1e-3,[],iii);
      intg_pfb2=quad8('intfun2n3',0,Li1(iii)-Li2(iii),1e-3,[],iii);
      Ai_pfb=BB*intg_pfb2*(1-ratio);
      Bi_pfb=AA*intg_pfb1*(1-ratio);
   else
      CCi=PtmP-DPt0;
      Ci=CCi;
      Ai_pfb=0;
      Bi_pfb=0;
   end
   Ai=Ai_fb+Ai_pfb;
   Bi=Bi_fb+Bi_pfb;
   if Ai>0
      Q=(-Bi+(Bi^2-4*Ai.*Ci).^0.5)./(2*Ai);
   else
      Q=(-Bi-(Bi^2-4*Ai.*Ci).^0.5)./(2*Ai);
   end
   QQ(iii)=Q;
```

```
   sum1=sum1+Q*cos(delta(iii)/180*pi);%**********************%
end
funDPt=sum1-pi*ri^2*ugie(kk)*(101325/(101325-CCi/2));
```

fun_Li0.m

```
%path(path,'E:\wzg')
% The length of stream tube from the edge of the internal spout
function [Li0,li]=fun_Li0(H0,Zs,alpha,r0,h0,Gammaj)
N=length(alpha);
rsin=(r0+Zs*tan(Gammaj/2/180*pi))/(1+tan(Gammaj/2/180*pi));
if Zs==0
   for ii=1:N
      sum1=0;
      for jj=1:ii
         sum1=sum1+alpha(jj);
      end
      li(ii)=H0/cos(sum1/180*pi);
   end
elseif Zs<r0
   r00=Zs/2+r0^2/2/Zs;
   for ii=1:N
      sum1=0;
      for jj=1:ii
         sum1=sum1+alpha(jj);
      end
      li(ii)=(H0+h0)/cos(sum1/180*pi)-r00*sin((180-sum1-180/pi*asin((h0+Zs-
r00)*sin(sum1/180*pi)/r00))/180*pi)/sin(sum1/180*pi);
   end
else
   cita=180/pi*atan(rsin/(h0+Zs-rsin));
   for ii=1:N
      sum1=0;
      for jj=1:ii
         sum1=sum1+alpha(jj);
      end
      if sum1<cita
         li(ii)=(H0+h0)/cos(sum1/180*pi)-rsin*sin((180-sum1-180/pi*asin((h0
+Zs-rsin)*sin(sum1/180*pi)/rsin))/180*pi)/sin(sum1/180*pi);
      elseif abs(cita-sum1)<1e-6
         li(ii)=(H0+h0)/cos(sum1/180*pi)-rsin*sin((180-sum1-180/pi*asin((h0
+Zs-rsin)*sin(sum1/180*pi)/rsin))/180*pi)/sin(sum1/180*pi);
      else
         li(ii)=(H0+h0)/cos(sum1/180*pi)-(r0*tan(sum1/180*pi)-h0*tan(sum1/180
*pi)*tan(Gammaj/2/180*pi))/sin(sum1/180*pi)/(tan(sum1/180*pi)-tan(Gammaj/2
/180*pi));
      end
   end
end
Li0(1)=((H0-Zs)+li(1))/2;
for ii=2:N
   Li0(ii)=(li(ii-1)+li(ii))/2;
end
```

fun_Li1.m

```
%path(path,'E:\wzg')
% The length of the stream tube from the top plane of the internal spout
function [Li1,lin]=fun_Li1(H0,Zs,alpha)
N=length(alpha);
for ii=1:N
   sum1=0;
   for jj=1:ii
      sum1=sum1+alpha(jj);
   end
   lin(ii)=(H0-Zs)/cos(sum1/180*pi);
end
Li1(1)=((H0-Zs)+lin(1))/2;
for ii=2:N
   Li1(ii)=(lin(ii-1)+lin(ii))/2;
end
```

fun_Li2.m

```
%path(path,'E:\wzg')
% The length of the stream tube from the top spherical surface of the
internal spout
function [Li2,lin1]=fun_Li2(H0,Zs,alpha,h0)
N=length(alpha);
for ii=1:N
   sum1=0;
   for jj=1:ii
      sum1=sum1+alpha(jj);
end
if Zs==0
   lin1(ii)=(H0-Zs)/cos(sum1/180*pi);
else
   lin1(ii)=(H0+h0)/cos(sum1/180*pi)-(h0+Zs);
end
end
Li2(1)=((H0-Zs)+lin1(1))/2;
for ii=2:N
   Li2(ii)=(lin1(ii-1)+lin1(ii))/2;
end
```

fun_Li3.m

```
%path(path,'E:\wzg')
% The length of the stream tube from the top elliptical surface of the
internal spout
function [Li3,lin1]=fun_Li3(H0,Zs,alpha,GammaN,h0)
N=length(alpha);
rcb=(Zs+h0)/2;
rca=rcb*tan(GammaN/180*pi);
for ii=1:N
   sum1=0;
```

```
   for jj=1:ii
      sum1=sum1+alpha(jj);
   end
   if Zs==0
      lin1(ii)=(H0-Zs)/cos(sum1/180*pi);
   else
      ll=2*cos(sum1/180*pi)*rcb*rca^2/(rcb^2*(sin(sum1/180*pi))^2+rca^2
*(cos(sum1/180*pi)^2));
      lin1(ii)=(H0+h0)/cos(sum1/180*pi)-ll;
   end
end
Li3(1)=((H0-Zs)+lin1(1))/2;
for ii=2:N
   Li3(ii)=(lin1(ii-1)+lin1(ii))/2;
end
```

up_area.m

```
%path(path,'E:\wzg')
function coef=up_area(iii)
global Rop EPUN r N alpha Li1 Li2 AA BB Zs DPs H0 r0 ugie kk Ai Bi ri delta
Gammaj rr Zstmp QQ h0
L=Li1(iii);
if iii==1
   AiL=pi.*(rr(1)-(Li1(iii)-L).*tan(alpha(iii)/180*pi)).^2.0;
   lk=0;
   lb=H0;
   x0=0;
   x1=rr(1);
else
   sum1=0;
   for jjj=1:iii-1
      sum1=sum1+alpha(jjj);
   end
   EE1=(H0+h0)/cos(delta(iii)/180*pi)-(Li1(iii)-L);
   EL=2*EE1*tan(alpha(iii)/2/180*pi);
   ER=EE1*sin((sum1+alpha(iii))/180*pi)/cos(alpha(iii)/2/180*pi);
   Er=EE1*sin(sum1/180*pi)/cos(alpha(iii)/2/180*pi);
   xe=(H0+h0)*tan(delta(iii)/180*pi);
   ye=H0;
   x1=ER;
   y1=ER*tan((90-(sum1+alpha(iii)))/180*pi)-h0;
   ELhf=sqrt((y1-ye)^2+(x1-xe)^2);
   EL1=2*ELhf;
   lk=(y1-ye)/(x1-xe);
   lb=y1-lk*x1;
   x0=Er;
   y0=lk*x0+lb;
   AiL=pi.*EL.*(ER+Er);
end
coef(1)=x0;
coef(2)=x1;
coef(3)=lk;
coef(4)=lb;
```

funPtmP.m

```
%path(path,'E:\wzg')
function PtmP=funPtmP(tt,iii,DPt0)
global Rop EPUN r N alpha Li1 Li2 AA BB Zs DPs H0 r0 ugie kk Ai Bi ri delta
Gammaj rr Zstmp QQ h0 ratio lambda
if tt==1
   a=-0.3725;
   b=6.126;
   c=0.1456e-2;

   a1=0.13639e-1;
   b1=-0.17663e-4;

   indexu=find(ugie==max(ugie));
   if Zs==0
      PtmPs=0;
      PtmP=0;
   else
      Zsmm=Zs*1e3;
      if kk<indexu
         PtmPs=(a+Zsmm)/(b+c*Zsmm^2)*1e3;
         PtmP=PtmPs;
      else
         PtmPs=(a1*Zsmm+b1*Zsmm^2)*1e3;
         PtmP=PtmPs;
      end
   end
elseif tt==0
   PtmP=0;     %%%% Calculate the pressure drop of the upper packed bed only
elseif tt==2
   PtmP=(H0-Li1(N)*cos(delta(N)/180*pi))*DPs/H0;
elseif tt==4
   PtmP=(H0-Li1(iii)*cos(delta(iii)/180*pi))*DPs/H0;
elseif tt==3
   lambda=Pwall(DPt0);
   XX=1-(H0-Li1(N)*cos(delta(N)/180*pi))/H0;
   PtmP=(lambda(1)+lambda(2)*XX)/(1+lambda(3)*XX+lambda(4)*XX^2)*DPt0;
elseif tt==5
   PtmP=Rop*9.81*(1-EPUN)*(H0-Li1(iii)*cos(delta(iii)/180*pi));
end
```

APPENDIX I

PROGRAMS FOR CROSS CORRELATION ANALYSIS

Sol_PVA.m (Main program for calculating delay time and statistical analysis)

```
%path(path,'G:\2005solidvelocity\vsvd_bed')
%%%%%%%%%%%%%%%%%%%%%%%%%%%%%%%%%%%%%%%%%%%%%%%%%%%%%%%%%%%%%%%%%%%
%%                                                               %
%% Read the data from .pct and .pva files, which is the processed %
%% data of optical probe.                                        %
%%                                                               %
%% Namestr: Data file name                                       %
%% M      : Number of groups                                     %
%% datax  : Data series of CH1                                   %
%% datay  : Data series of CH2                                   %
%% datacnt: Data counts                                          %
%% datagap: 1/Frenquency                                         %
%%                                                               %
%%%%%%%%%%%%%%%%%%%%%%%%%%%%%%%%%%%%%%%%%%%%%%%%%%%%%%%%%%%%%%%%%%%

tic
clear
clc
Firp=1;
Nexp=7;
skip=0;
%*****************************************************%
fid1=fopen('namelist7_usedP.txt','r');
fid2=fopen('dt_results_usedP.dat','w');
fprintf(fid2,'%s\n',' File Name     Time Delay(Part)   Time Delay(All)   Time
Delay(Max. Coef.)   Time Delay(Max. Freq.)   Total Number');
for LL2=1:skip
   skip_line=fgetl(fid1);
end
for LL=Firp:Nexp
   Namestr=fgetl(fid1);
%*****************************************************%

   N0=0+50.*(1:200);
   LTN0=length(N0);
   fid=fopen(Namestr,'r');
   tmp0=fscanf(fid,'%d,%f',2);
   dxtoy=tmp0(2);
   tt1=fgets(fid);
   tmp1=fscanf(fid,'%d,%f',2);
   datacnt=tmp1(1);
   datagap=tmp1(2);
   tmp2=fscanf(fid,'%f,%f',2);
   avex=tmp2(1);
   avey=tmp2(2);
```

```
for n=1:4
   tt2=fgets(fid);
end
datax=fscanf(fid,'%d',datacnt);
tt3=fgets(fid);
tt4=fgets(fid);
datay=fscanf(fid,'%d',datacnt);
fclose(fid);
ddtt=0.001*datagap;
tt=ddtt*(1:datacnt);

MM=[8 2 4 16 32 64 128];
Mmax=128;
p1=10;
p2=500;
% Find upwind or downwind
clear pmax Rxymax
[direct,Rxymax1,pmax1]=find_direct(MM,Mmax,datacnt,datax,datay,N0);
Rxymax(1)=Rxymax1;
pmax(1)=pmax1;
p1=floor(pmax1/2);
p2=floor(1.5*pmax1);
if p1<10
   p1=10;
end
if p2>500
   p2=500;
end

if abs(direct)>1e-3
   Mmax=datacnt/(20*pmax(1));
   % Find better number of groups
   for ii=2:7
      clear Rxy xx yy
      M=MM(ii);
      if M<=Mmax
         N=floor(datacnt/M);
         for j1=p1:1:p2
            if direct>0
               xx=datax(N0(1)+1:N0(1)+N);
               yy=datay(j1+N0(1)+1:j1+N0(1)+N);
            else
               xx=datax(j1+N0(1)+1:j1+N0(1)+N);
               yy=datay(N0(1)+1:N0(1)+N);
            end
            xave=mean(xx);
            yave=mean(yy);
            stdx=std(xx,1);
            stdy=std(yy,1);
            if stdx*stdy==0
               Rxy(j1)=0;
            else
               Rxy(j1)=mean((xx-xave).*(yy-yave))/(stdx*stdy);
            end
         end
         k1=find(max(Rxy)==Rxy);
         Rxymax(ii)=max(Rxy);
```

```
      pmax(ii)=min(k1);
      Mmax=datacnt/(20*pmax(ii));
   end
end
k1=find(max(Rxymax)==Rxymax);
M=MM(min(k1));
for ii=1:LTN0
   clear Rxy xx yy
   N=floor(datacnt/M);
   for j1=p1:p2
      if direct>0
         xx=datax(N0(ii)+1:N0(ii)+N);
         yy=datay(j1+N0(ii)+1:j1+N0(ii)+N);
      else
         xx=datax(j1+N0(ii)+1:j1+N0(ii)+N);
         yy=datay(N0(ii)+1:N0(ii)+N);
      end
      xave=mean(xx);
      yave=mean(yy);
      stdx=std(xx,1);
      stdy=std(yy,1);
      if stdx*stdy==0
         Rxy(j1)=0;
      else
         Rxy(j1)=mean((xx-xave).*(yy-yave))/(stdx*stdy);
      end
   end
   k1=find(max(Rxy)==Rxy);
   coef(ii)=max(Rxy);
   dt(ii)=min(k1)*ddtt;
end

% Plot original signals

% plotout2(datacnt,datagap,datax,datay,tt,dt,LTN0,coef)

% Preview of time delay and correlation coefficient
[tmp_coef sequ]=sort(coef);
tmp_dt=dt(sequ(floor(0.8*LTN0):LTN0))*1000;
dt_ave_part=direct*mean(tmp_dt);
dt_ave_all=direct*mean(dt)*1000;
figure
SUBPLOT(1,2,1)
plot(dt*1000,coef,'ms')
hold on
if 0.8*min(dt*1000)>1
   xlow1=floor(0.8*min(dt*1000)/1)*1;
   xhi1=floor(1.2*max(dt*1000)/1)*1;
else
   xlow1=0.8*min(dt*1000);
   xhi1=1.2*max(dt*1000);
end
if xhi1-xlow1<1e-3
   axis_tmp=axis;
   xlow1=axis_tmp(1);
   xhi1=axis_tmp(2);
end
```

```
%set(gca,'XLim',[xlow1,xhi1]);
set(gca,'YLim',[0,1]);
plot(abs(dt_ave_all)*ones(20,1),(0:1/19:1),'r-')
plot((xlow1:(xhi1-xlow1)/(LTN0-1):xhi1),0.6*ones(LTN0,1),'b--')
xlabel('Time (ms)');
ylabel('Correlation Coefficient');

dt_a=sort(dt)*1000;
m_a=1;
jj=1;
while jj<=LTN0
   Y_a(m_a)=1;
   X_a(m_a)=dt_a(jj);
   if jj<LTN0
      for kk=jj+1:LTN0
         if dt_a(kk)-dt_a(jj)<1e-3
            Y_a(m_a)=Y_a(m_a)+1;
            if kk==LTN0
               jj=kk+1;
            end
         else
            jj=kk;
            break
         end
      end
   else
      jj=jj+1;
   end
   m_a=m_a+1;
end

% Statistical analysis----Distribution of time delay
SUBPLOT(1,2,2)
bar(X_a,Y_a)
hold on
if 0.8*min(X_a)>1
   xlow2=floor(0.8*min(X_a)/1)*1;
   xhi2=floor(1.2*max(X_a)/1)*1;
else
   xlow2=0.8*min(X_a);
   xhi2=1.2*max(X_a);
end
if xhi2-xlow2<1e-3
   axis_tmp1=axis;
   xlow2=axis_tmp1(1);
   xhi2=axis_tmp1(2);
end
if max(Y_a)>=10
   yhi=floor(1.2*max(Y_a)/10)*10;
else
   yhi=10;
end
plot(abs(dt_ave_all)*ones(20,1),(0:yhi/19:yhi),'r-')
%set(gca,'XLim',[xlow2,xhi2]);
set(gca,'YLim',[0,yhi]);
xlabel('Time (ms)');
ylabel('Distribution Number');
```

```
      title(Namestr);
      text(0.8*xhi2,0.95*yhi,['LL=',num2str(LL,3)],'FontSize',14);

      max_index=find(max(coef)==coef);
      dt_max_coef=mean(direct*dt(max_index)*1000);
      max_index1=find(max(Y_a)==Y_a);
      dt_max_freq=mean(direct*X_a(max_index1));
      %*******************************************************%
      Namestr1((12-length(Namestr)+1):12)=Namestr;
      for jj=1:(12-length(Namestr))
         Namestr1(jj)=' ';
      end
      sum_Y_a=sum(Y_a);
      fprintf(fid2,'%s %14.6f %17.6f %21.6f %24.6f %17i\n',Namestr1
,dt_ave_part,dt_ave_all,dt_max_coef,dt_max_freq,sum_Y_a);

      Namestr2(1:9)=Namestr1(1:9);
      Namestr2(10)='d';
      Namestr2(11)='a';
      Namestr2(12)='t';
      fid3=fopen(Namestr2,'w');
      fprintf(fid3,'%s\n','    dt(ms)     Correlation Coefficient');
      for jj1=1:LTN0
         fprintf(fid3,'%11.6f %18.6f\n',direct*dt(jj1)*1000,coef(jj1));
      end
      fprintf(fid3,'%s\n','*********************************');
      fprintf(fid3,'%s\n','    dt(ms)     Frequency');
      for jj2=1:length(X_a)
         fprintf(fid3,'%11.6f %9i\n',direct*X_a(jj2),Y_a(jj2));
      end
      fprintf(fid3,'%s\n','*********************************');
      fprintf(fid3,'%s %11.6f\n','dt_ave_part  =',dt_ave_part);
      fprintf(fid3,'%s %11.6f\n','dt_ave_all   =',dt_ave_all);
      fprintf(fid3,'%s %11.6f\n','dt_max_coef  =',dt_max_coef);
      fprintf(fid3,'%s %11.6f\n','max_coef     =',max(coef));
      fprintf(fid3,'%s %11.6f\n','dt_max_freq  =',dt_max_freq);
      fclose(fid3);

      clear X_a Y_a dt m_a dt_a sum_Y_a coef tmp_dt;
   end
end
fclose(fid1);
fclose(fid2);
%*******************************************************%
toc
```

find_direct.m

```
function [direct,Rxymax,pmax]=find_direct(MM,Mmax,datacnt,datax,datay,N0);
% Find upwind or downwind
M=MM(1);
N=floor(datacnt/M);
p1=10;
p2=500;
% Upwind( X ------> Y )
```

```
for j1=p1:1:p2
   clear xx yy
   xx=datax(N0(1)+1:N0(1)+N);
   yy=datay(j1+N0(1)+1:j1+N0(1)+N);
   xave=mean(xx);
   yave=mean(yy);
   stdx=std(xx,1);
   stdy=std(yy,1);
   if stdx*stdy==0
      Rxy(j1)=0;
   else
      Rxy(j1)=mean((xx-xave).*(yy-yave))/(stdx*stdy);
   end
end
k1=find(max(Rxy)==Rxy);
Rxymax_up=max(Rxy);
pmax_up=min(k1);

clear Rxy

% Downwind( Y ------> X )
for j1=p1:1:p2
   clear xx yy
   xx=datax(j1+N0(1)+1:j1+N0(1)+N);
   yy=datay(N0(1)+1:N0(1)+N);
   xave=mean(xx);
   yave=mean(yy);
   stdx=std(xx,1);
   stdy=std(yy,1);
   if stdx*stdy==0
      Rxy(j1)=0;
   else
      Rxy(j1)=mean((xx-xave).*(yy-yave))/(stdx*stdy);
   end
end
k2=find(max(Rxy)==Rxy);
Rxymax_dn=max(Rxy);
pmax_dn=min(k2);

if Rxymax_up>0
   if Rxymax_up>Rxymax_dn
      direct=1.;
      Rxymax=Rxymax_up;
      pmax=pmax_up;
   else
      direct=-1.;
      Rxymax=Rxymax_dn;
      pmax=pmax_dn;
   end
else
   if Rxymax_dn>0
      direct=-1;
      Rxymax=Rxymax_dn;
      pmax=pmax_dn;
   else
      direct=0;
      Rxymax=0;
```

```
      pmax=0;
   end
end
```

plotout2.m

```
function plotout=plotout2(datacnt,datagap,datax,datay,tt,dt)
% Plot original signals
figure;
plot([1:datacnt]*0.001*datagap,datax/255.*5.,[1:datacnt]*0.001*datagap,datay/
255.*5.+5.);
hold on;
xmax=datacnt*0.001*datagap;
xlimit1=floor(xmax);
xlimit2=floor(xmax+0.5);
if xlimit2-xlimit1>0.5
   xlimit=xlimit2;
else
   xlimit=xlimit1+0.5;
end
plot([0,xlimit],[5,5]);
set(gca,'XLim',[0,xlimit]);
set(gca,'YLim',[0,10]);
set(gca,'yticklabel',{'0';'1';'2';'3';'4';'0';'1';'2';'3';'4';'5'});
xlabel('Time (s)');
ylabel('Voltage Signal (v)');

% Plot original binary signals with time delay considered
figure;
plot(tt(1:datacnt),datax,'r-')
hold on
plot(tt(1:datacnt)+mean(dt),datay,'b--')
xlabel('Time (s)');
ylabel('Binary Signal');


fprintf('%s\n','    Time Delay     Coefficient')
for i4=1:LTN0
   fprintf('%12.4f %15.4f\n',dt(i4)*1000,coef(i4))
end
```

ave_PVA.m (Main program for calculating average values of sampled signals)

```
%path(path,'G:\2005solidvelocity\vsvd_bed')
%%%%%%%%%%%%%%%%%%%%%%%%%%%%%%%%%%%%%%%%%%%%%%%%%%%%%%%%%%%%%%%%%%
%%                                                              %
%% Read the data from .pct and .pva files, which is the processed %
%% data of optical probe.                                       %
%%                                                              %
%% Namestr: Data file name                                      %
%% M      : Number of groups                                    %
%% datax  : Data series of CH1                                  %
%% datay  : Data series of CH2                                  %
%% datacnt: Data counts                                         %
```

```
%% datagap: 1/Frenquency                                          %
%%                                                                %
%%%%%%%%%%%%%%%%%%%%%%%%%%%%%%%%%%%%%%%%%%%%%%%%%%%%%%%%%%%%%%%%%%%

tic
clear
clc
Firp=1;
Nexp=136;
skip=0;
%******************************************************%
fid1=fopen('namelist136_z5vs.txt','r');
fid2=fopen('ave_results_z5vs.dat','w');
fprintf(fid2,'%s\n',' File Name     CH1(Part Average)     CH2(Part Average)
CH1(All Average)     CH2(All Average)');
for LL2=1:skip
   skip_line=fgetl(fid1);
end
for ll=Firp:Nexp
   Namestr=fgetl(fid1);
%******************************************************%

fid=fopen(Namestr,'r');
tmp0=fscanf(fid,'%d,%f',2);
dxtoy=tmp0(2);
tt1=fgets(fid);
tmp1=fscanf(fid,'%d,%f',2);
datacnt=tmp1(1);
tmp2=fscanf(fid,'%f,%f',2);
ave_part_x=tmp2(1);
ave_part_y=tmp2(2);
for n=1:4
   tt2=fgets(fid);
end
datax=fscanf(fid,'%d',datacnt);
tt3=fgets(fid);
tt4=fgets(fid);
datay=fscanf(fid,'%d',datacnt);
fclose(fid);
ave_all_x=mean(datax)/255.*5.;
ave_all_y=mean(datay)/255.*5.;

%******************************************************%
Namestr1((12-length(Namestr)+1):12)=Namestr;
for jj=1:(12-length(Namestr))
   Namestr1(jj)=' ';
end
fprintf(fid2,'%s %13.4f %21.4f %20.4f
%21.4f\n',Namestr1,ave_part_x,ave_part_y,ave_all_x,ave_all_y);

end
fclose(fid1);
fclose(fid2);
%******************************************************%
toc
```

APPENDIX J

PROGRAMS FOR ESTIMATING MEAN RESIDENCE TIME AND VARIANCE

Processing of experimental data

n13Ffitmain.m (Main program)

```
tic
path(path,'G:\2005gasmixing')
path(path,'G:\2005gasmixing\4q')
%path(path,'E:\wzg\Gasmixing\Sept1')

clear
clc
global tnn1 FF_tmp

Firp=10;    % Adjustable parameter used to select data files to be treated
Nexp=10;    % Adjustable parameter used to select data files to be treated
skip=9;     % Adjustable parameter used to select data files to be treated
%*****************************************************%
fid1=fopen('namelist10_4q.txt','r');
for LL2=1:skip
   skip_line=fgetl(fid1);
end
for LL1=Firp:Nexp
   clear CH1 CH2 CH1_ori CH2_ori CH1_final CH2_final tt CH3_final tnn FFc1
FFc2 FFc FFc5 FFc6 FFc7
   clear FF FF1 FF2 FF3 E1 E2 E3 EEc1 EEc2 EEc3 tmp1 tmp xx yy zz CH3 EE
EE_tmp tnn1 EE1 EE2 EE3 EE11 EE22

   namestr=fgetl(fid1);

AA=0;
BB=2.5;

%namestr='2Probes-RTD4.dat';

kn01=0;     % Adjustable parameter used to obtain best fitted curve
kn02=0;     % Adjustable parameter used to obtain best fitted curve
peak1=0.2;  % Adjustable parameter used to reasonably eliminate sharp peaks
peak2=0.2;  % Adjustable parameter used to reasonably eliminate sharp peaks
step_CH1=50;
step_CH2=20;

fid=fopen(namestr,'r');
for i1=1:6
   fgetl(fid);
end
```

```
fseek(fid,31,0);
NN0=fscanf(fid,'%i',1);
n_start=600;
n_end=1800;
if NN0/1000-floor(NN0/1000)>1e-6
   namestr
   fprintf('%s','Please check the offset.')
%   stop
end
tt2=fgets(fid);
fseek(fid,30,0);
ttotal=fscanf(fid,'%f',1);
for ii=1:3
   tt3=fgets(fid);
end
for ii=1:NN0
   tmp1=fscanf(fid,'%f,%f',2);
   tmp(ii,:)=tmp1';
end
fclose(fid);
dt=ttotal/(NN0-1);

CH1_ori=tmp(n_start:1:n_end,1);
CH2_ori=tmp(n_start:1:n_end,2);
LL=length(CH1_ori);
tt=(0:1*dt:(LL-1)*dt);
%%%%%%%%%%%%%%%%%%%%%%%%%%%%%%%%%%%%%%%%%%%%%%%%%%%%%%%%%%%%%%%%%%%%%%%%
% Eliminate all sharp peaks
CH1_final=CH1_ori;
CH2_final=CH2_ori;

first1=1;
first2=1;
kdn1=1;
kdn2=1;
kup1=1;
kup2=1;
flag1='ud';
for i2=1:LL-1
   if CH1_final(i2)>CH1_final(i2+1)+peak1
      if first1==1 & kdn2==1
         kdn1=i2;
         first1=2;
      end
   end
   if CH1_final(i2)+peak1<CH1_final(i2+1) & kdn1>1
      kdn2=i2+1;
      flag1='dn';
   end
   if CH1_final(i2)+peak1<CH1_final(i2+1)
      if first2==1 & kup2==1
         kup1=i2;
         first2=2;
      end
   end
   if CH1_final(i2)>CH1_final(i2+1)+peak1 & kup1>1
      kup2=i2+1;
```

```
      flag1='up';
   end
   if flag1=='dn'
      if (CH1_final(kdn1)-CH1_final(kdn2))<peak1 & kdn2>1 & kdn1>1 & kdn2-
kdn1<100
         if CH1_final(kdn1)==CH1_final(kdn2)
            CH1_final(kdn1:kdn2)=CH1_final(kdn2);
         else
            CH1_final(kdn1:kdn2)=CH1_final(kdn1):(CH1_final(kdn1)-
CH1_final(kdn2))/(kdn1-kdn2):CH1_final(kdn2);
         end
         first1=1;
         first2=1;
         kdn1=1;
         kdn2=1;
         kup1=1;
         kup2=1;
         flag1='ud';
      end
   elseif flag1=='up'
      if (CH1_final(kup2)-CH1_final(kup1))<peak1 & kup2>1 & kup1>1 & kup2-
kup1<100
         if CH1_final(kup1)==CH1_final(kup2)
            CH1_final(kup1:kup2)=CH1_final(kup2);
         else
            CH1_final(kup1:kup2)=CH1_final(kup1):(CH1_final(kup1)-
CH1_final(kup2))/(kup1-kup2):CH1_final(kup2);
         end
         first1=1;
         first2=1;
         kdn1=1;
         kdn2=1;
         kup1=1;
         kup2=1;
         flag1='ud';
      end
   end
end

first1=1;
first2=1;
kdn1=1;
kdn2=1;
kup1=1;
kup2=1;
flag1='ud';
for i3=1:LL-1
   if CH2_final(i3)>CH2_final(i3+1)+peak2
      if first1==1 & kdn2==1
         kdn1=i3;
         first1=2;
      end
   end
   if CH2_final(i3)+peak2<CH2_final(i3+1) & kdn1>1
      kdn2=i3+1;
      flag1='dn';
   end
```

```
   if CH2_final(i3)+peak2<CH2_final(i3+1)
      if first2==1 & kup2==1
         kup1=i3;
         first2=2;
      end
   end
   if CH2_final(i3)>CH2_final(i3+1)+peak2 & kup1>1
      kup2=i3+1;
      flag1='up';
   end
   if flag1=='dn'
      if (CH2_final(kdn1)-CH2_final(kdn2))<1.2*peak2 & kdn2>1 & kdn1>1 &
kdn2-kdn1<100
         if CH2_final(kdn1)==CH2_final(kdn2)
            CH2_final(kdn1:kdn2)=CH2_final(kdn2);
         else
            CH2_final(kdn1:kdn2)=CH2_final(kdn1):(CH2_final(kdn1)-
CH2_final(kdn2))/(kdn1-kdn2):CH2_final(kdn2);
         end
         first1=1;
         first2=1;
         kdn1=1;
         kdn2=1;
         kup1=1;
         kup2=1;
         flag1='ud';
      end
   elseif flag1=='up'
      if (CH2_final(kup2)-CH2_final(kup1))<peak2 & kup2>1 & kup1>1 & kup2-
kup1<100
         if CH2_final(kup1)==CH2_final(kup2)
            CH2_final(kup1:kup2)=CH2_final(kup2);
         else
            CH2_final(kup1:kup2)=CH2_final(kup1):(CH2_final(kup1)-
CH2_final(kup2))/(kup1-kup2):CH2_final(kup2);
         end
         first1=1;
         first2=1;
         kdn1=1;
         kdn2=1;
         kup1=1;
         kup2=1;
         flag1='ud';
      end
   else
      if kdn1>1 & i3-kdn1>100
         for i5=kdn1:-1:kdn1-50
            if CH2_final(i5)>0.1*peak2+CH2_final(kdn1)
               kud1=i5;
               kud2=kdn1+1;
               CH2_final(kud1:kud2)=CH2_final(kud1):(CH2_final(kud1)-
CH2_final(kud2))/(kud1-kud2):CH2_final(kud2);
               first1=1;
               first2=1;
               kdn1=1;
               kdn2=1;
               kup1=1;
```

```
            kup2=1;
            flag1='ud';
            break
         end
      end
   end
   if kup1>1 & i3-kup1>100
      first1=1;
      first2=1;
      kdn1=1;
      kdn2=1;
      kup1=1;
      kup2=1;
      flag1='ud';
   end
 end
end
%%%%%%%%%%%%%%%%%%%%%%%%%%%%%%%%%%%%%%%%%%%%%%%%%%%%%%%%%%%%%%%%%%%%%%%%%%

figure
SUBPLOT(2,1,1)
hold on
plot(tt,CH1_ori,'ro-')
plot(tt,CH2_ori,'bd-')
xlabel('t (s)','FontSize',18)
ylabel('V(V)','FontSize',18)
legend('Channel 1','Channel 2');

NL=floor(LL/10);
for i6=1:LL
   if CH1_final(i6)>mean(CH1_final(1:NL))-(mean(CH1_final(1:NL))-
mean(CH1_final(LL-NL:LL)))/50
      k1=i6-10;
   end
   if CH1_final(i6)>mean(CH1_final(LL-NL:LL))+(mean(CH1_final(1:NL))-
mean(CH1_final(LL-NL:LL)))/50
      k2=i6+10;
   else
      break
   end
end
k3=k1-200;
k4=k2+200;
if k3<1
   k3=1;
end
if k4>LL
   k4=LL;
end
%CH1_0=mean(CH1_final(1:k1));
%CH1_inf=mean(CH1_final(k2:LL));
CH1_0=mean(CH1_ori(1:k1));
CH1_inf=mean(CH1_ori(k2:LL));

for jjw=1:length(CH1_final)
   if (CH1_final(jjw)<CH1_inf)
      CH1_final(jjw)=CH1_inf;
```

```
   end
end


for jj1=1:k1-step_CH1
   CH1_final(jj1)=mean(CH1_final(jj1:jj1+step_CH1));
end
for jj1=k1-step_CH1+1:k1
   CH1_final(jj1)=mean(CH1_final(jj1-step_CH1:jj1));
end

for jj1=k2:LL-step_CH1
   CH1_final(jj1)=mean(CH1_final(jj1:jj1+step_CH1));
end
for jj1=LL-step_CH1+1:LL
   CH1_final(jj1)=mean(CH1_final(jj1-step_CH1:jj1));
end


for i7=1:LL
   if CH2_final(i7)>mean(CH2_final(1:NL))-(mean(CH2_final(1:NL))-
mean(CH2_final(LL-NL:LL)))/50
      kk1=i7-10;
   end
   if CH2_final(i7)>mean(CH2_final(LL-NL:LL))+(mean(CH2_final(1:NL))-
mean(CH2_final(LL-NL:LL)))/50
      kk2=i7+10;
   else
      break
   end
end
kk3=kk1-200;
kk4=kk2+200;
if kk3<1
   kk3=1;
end
if kk4>LL
   kk4=LL;
end
CH2_0=mean(CH2_final(1:kk1));
CH2_inf=mean(CH2_final(kk2:LL));

for jj1=1:kk1-step_CH2
   CH2_final(jj1)=mean(CH2_final(jj1:jj1+step_CH2));
end
for jj1=kk1-step_CH2+1:kk1
   CH2_final(jj1)=mean(CH2_final(jj1-step_CH2:jj1));
end

for jj1=kk2:LL-step_CH2
   CH2_final(jj1)=mean(CH2_final(jj1:jj1+step_CH2));
end
for jj1=LL-step_CH2+1:LL
   CH2_final(jj1)=mean(CH2_final(jj1-step_CH2:jj1));
end

plot(tt,CH1_final,'g--')
```

```
plot(tt,CH2_final,'m-')

kk3=min(k3,kk3);
kk4=max(k4,kk4);
%CH1=CH1_ori;
%CH2=CH2_ori;
CH1=CH1_final;
CH2=CH2_final;

%%%%%%%%%%%
for i8=kk1+15:LL
   if CH2(i8+1)<CH2(i8)
   else
      kk5=i8;
      kk6=kk5+300;
      break
   end
end

Lname=length(namestr)-4;
kx=4;                                  % Number of unknowns
lam(1:kx)=[0.47 1.51e11 -4.15 0.1];
lam=lam';
tol=1e-6;
trace=0;
options(14)=50000;
CH3=CH2;
%%%%%%%%%%%
FF1=1-(CH1-CH1_inf)./(CH1_0-CH1_inf);
FF2=1-(CH2-CH2_inf)./(CH2_0-CH2_inf);
FF3=1-(CH3-CH2_inf)./(CH2_0-CH2_inf);
%%%%%%%%%%%%%%
dt=(max(tt)-min(tt))/(length(tt)-1);
tnn=0:dt:max(tt);
mm1=10;
Ltnn=length(tnn);
E1=solveE(FF1,tnn,dt,mm1);
E2=solveE(FF2,tnn,dt,mm1);
E3=solveE(FF3,tnn,dt,mm1);

CH3_final=CH2;
indexE1=find(E1==max(E1));
tE1max=tnn(indexE1);
while E1(indexE1-10)<0.2*max(E1) & E1(indexE1+10)<0.2*max(E1)
   E1(indexE1-10:indexE1+10)=0.5*(E1(indexE1-11)+E1(indexE1+11));
   FF1(indexE1-10:indexE1+10)=0.5*(FF1(indexE1-11)+FF1(indexE1+11));
   CH1_final(indexE1-10:indexE1+10)=0.5*(CH1_final(indexE1-
11)+CH1_final(indexE1+11));
   indexE1=find(E1==max(E1));
   tE1max=tnn(indexE1);
end
indexE2=find(E2==max(E2));
tE2max=tnn(indexE2);
while E2(indexE2-10)<0.2*max(E2) & E2(indexE2+10)<0.2*max(E2)
   E2(indexE2-10:indexE2+10)=0.5*(E2(indexE2-11)+E2(indexE2+11));
   E3(indexE2-10:indexE2+10)=0.5*(E3(indexE2-11)+E3(indexE2+11));
   FF2(indexE1-10:indexE1+10)=0.5*(FF2(indexE1-11)+FF2(indexE1+11));
```

```
   FF3(indexE1-10:indexE1+10)=0.5*(FF3(indexE1-11)+FF3(indexE1+11));
   CH2_final(indexE1-10:indexE1+10)=0.5*(CH2_final(indexE1-
11)+CH2_final(indexE1+11));
   CH3_final(indexE1-10:indexE1+10)=0.5*(CH3_final(indexE1-
11)+CH3_final(indexE1+11));
   indexE2=find(E2==max(E2));
   tE2max=tnn(indexE2);
end


SUBPLOT(2,1,2)
hold on
plot(tt(kk3:kk4),CH1_final(kk3:kk4),'r--')
plot(tt(kk3:kk4),CH2_final(kk3:kk4),'b-')
plot(tt(kk3:kk4),CH3_final(kk3:kk4),'m-.')
xlabel('t (s)','FontSize',18)
ylabel('V(V)','FontSize',18)
legend('Channel 1','Channel 2','Fitted results');
axis([tt(kk3) tt(kk4) -1 5])
text(1.05*tnn(kk3),4.5,namestr(1:Lname),'FontSize',14)


yy=CH1_final;
zz=CH2_final;
xx=tt;
namestr1=namestr(1:Lname);
namestr1(Lname+1:Lname+9)='_XYZ1.dat';
fid2=fopen(namestr1,'wt');
fprintf(fid2,'%s\n','           tt            CH1(cal)        CH2(cal)
CH1(exp)        CH2(exp)');
for jj=kk3:kk4
   fprintf(fid2,'%15.5f %15.5f %15.5f %15.5f %15.5f\n',xx(jj),yy(jj)-
CH1_inf,zz(jj)-CH2_inf,CH1_ori(jj)-CH1_inf,CH2_ori(jj)-CH2_inf);
end
fclose(fid2);

figure
SUBPLOT(2,1,1)
plot(tnn(kk3:kk4),FF1(kk3:kk4),'r--',tnn(kk3:kk4),FF2(kk3:kk4),'b-
',tnn(kk3:kk4),FF3(kk3:kk4),'m-.')
xlabel('t (s)','FontSize',18)
ylabel('F(t)','FontSize',18)
legend('Channel 1','Channel 2','Fitted results');
text(1.05*tnn(kk3),1.1,namestr(1:Lname),'FontSize',14)
%%%%%%
%1111111111
%%%%%%
SUBPLOT(2,1,2)
plot(tnn(kk3:kk4),E1(kk3:kk4),'r--',tnn(kk3:kk4),E2(kk3:kk4),'b-
',tnn(kk3:kk4),E3(kk3:kk4),'m-.')
xlabel('t (s)','FontSize',18)
ylabel('E(t)','FontSize',18)
legend('Channel 1','Channel 2','Fitted results');
ymax=1.2*max(max(E1),max(E2));
text(1.05*tnn(kk3),0.8*ymax,namestr(1:Lname),'FontSize',14)

for jj=1:3
```

```
    clear FF_tmp FFz EE tnn1
    if jj==1
       indexE=indexE1;
       FFz=FF1;
       for i9=indexE-1:-1:1
          if E1(i9)>1e-3
          else
             kn=i9;
             break
          end
       end
       indexepun=kn-kn01;
       tnn1=tnn(indexepun:indexepun+500)-tnn(indexepun);
       t001=tnn(indexepun);
       FF_tmp=FFz(indexepun:indexepun+500);
       Eo1=E1(indexepun:indexepun+500);
       FFo1=FF_tmp;
       tnn2=tnn1;
    elseif jj==2
       indexE=indexE2;
       FFz=FF2;
       for i9=indexE-1:-1:1
          if E2(i9)>1e-3
          else
             kn=i9;
             break
          end
       end
       indexepun=kn-kn02;
       tnn1=tnn(indexepun:indexepun+500)-tnn(indexepun);
       t002=tnn(indexepun);
       FF_tmp=FFz(indexepun:indexepun+500);
       Eo2=E2(indexepun:indexepun+500);
       FFo2=FF_tmp;
       tnn3=tnn1;
    else
       indexE=indexE2;
       FFz=FF3;
       for i9=indexE-1:-1:1
          if E3(i9)>1e-3
          else
             kn=i9;
             break
          end
       end
       indexepun=kn-kn02;
       tnn1=tnn(indexepun:indexepun+500)-tnn(indexepun);
       t003=tnn(indexepun);
       FF_tmp=FFz(indexepun:indexepun+500);
       Eo3=E3(indexepun:indexepun+500);
       FFo3=FF_tmp;
       tnn4=tnn1;
    end


 kk=4;
 AK0=[-0.01 0.035 0.995 3.36]';
```

```
eps=5e-4;
Lambda1=1e-3;
AK=h4_LMarq('FT_model',FF_tmp,tnn1,AK0,eps,Lambda1);
lambd=h4_LMarq('FT_model',FF_tmp,tnn1,AK,eps,0);
%%%%%%%%%%%%%%%%%%%%%%%%%%%%%%%%%%%%%%%%%%%%%%%%%%%%%%%%%%%%%%%%%%%%%%%%
% Comparison between experimental data and calculated results
figure
Ft_tmp=(lambd(1)*lambd(2)+lambd(3).*(tnn1).^lambd(4))./(lambd(2)+(tnn1).^lamb
d(4));
plot(Ft_tmp,FF_tmp,'ms')
hold on
fplot('fy',[0,1.1*max(FF_tmp)],'b-')
hold off
xlabel('{F}_{cal}','FontSize',14)
ylabel('{F}_{exp}','FontSize',14)
text(0.8*max(FF_tmp),0.5*max(FF_tmp),['A=',num2str(lambd(1),5)],'FontSize',14
)
text(0.8*max(FF_tmp),0.4*max(FF_tmp),['B=',num2str(lambd(2),5)],'FontSize',14
)
text(0.8*max(FF_tmp),0.3*max(FF_tmp),['C=',num2str(lambd(3),5)],'FontSize',14
)
text(0.8*max(FF_tmp),0.2*max(FF_tmp),['D=',num2str(lambd(4),5)],'FontSize',14
)
text(0.6*max(FF_tmp),0.1*max(FF_tmp),'{F=(A*B+C*t^D)/(B+t^D)}','FontSize',14)
axis([0 1.20 0 1.20])
title('Comparison of experimental data and calculated results','FontSize',14)

%%%%%%%%%%%%%%%%%%%%%
Fpres=sym('(lambd(1)*lambd(2)+lambd(3)*tval^lambd(4))/(lambd(2)+tval^lambd(4)
)');
Epres=diff(Fpres,'tval');
ttt=(0:0.001:5);
for ii1=1:length(ttt)
   tval=ttt(ii1);
   FFnn(ii1)=eval(Fpres);
   if ii1==1
      EEnn(ii1)=0;
   else
      EEnn(ii1)=eval(Epres);
   end
end
%%%%%%%%%%%%%%%%%%%%%

mm2=3;
   clear EE tnn1
   if jj==1
      FFn1=FFnn;
      tnn2n=ttt;
      EE1=EEnn;
      EE=EE1;
      tnn1=tnn2n;
   elseif jj==2
      tnn3=tnn3+(t002-t001-0.000);
      FFn2=FFnn;
      tnn3n=ttt+(t002-t001-0.000);
      EE2=EEnn;
      EE=EE2;
```

```
        tnn1=tnn3n;
    else
        tnn4=tnn4+(t003-t001-0.000);
        FFn3=FFnn;
        tnn4n=ttt+(t003-t001-0.000);
        EE3=EEnn;
        EE=EE3;
        tnn1=tnn4n;
    end

    tmp111=0;
    tmp222=0;
    tmp333=0;

    for i4=1:length(EE)
        tmp111=tmp111+EE(i4);
        tmp222=tmp222+(tnn1(i4))*EE(i4);
        tmp333=tmp333+(tnn1(i4))^2*EE(i4);
    end
    t_ave=tmp222/tmp111;
    t_std=tmp333/tmp111-t_ave^2;
    std_ch=t_std/t_ave^2;
    if jj==1
        Tao_ch1=t_ave;
        t_std_ch1=t_std;
        std_ch1=std_ch;
    elseif jj==2
        Tao_ch2=t_ave;
        t_std_ch2=t_std;
        std_ch2=std_ch;
    else
        Tao_ch3=t_ave;
        t_std_ch3=t_std;
        std_ch3=std_ch;
    end
end

NN1=length(tnn1);
figure
SUBPLOT(2,1,1)
hold on
plot(t001+tnn2,FFo1,'ro')
plot(t001+tnn3,FFo2,'bd')
%%%%%%%%%%%%%%%%%%%%%%%%%%%%%%%%%%%%%%%%%%%%%%%%%%%%
plot(t001+tnn2n,FFn1,'r-')
plot(t001+tnn3n,FFn2,'b-')
legend('CH1---Exp','CH2---Exp','CH1---Cal','CH2---Cal');
xlabel('t (s)','FontSize',18)
ylabel('F(t)','FontSize',18)
text(t001+0.9*AA,1.1,namestr(1:Lname),'FontSize',14)
axis([t001+AA t001+BB 0 1.2])

SUBPLOT(2,1,2)
hold on
plot(t001+tnn2,Eo1,'ro',t001+tnn3,Eo2,'bd')
plot(t001+tnn2n,EE1,'r-')
plot(t001+tnn3n,EE2,'b-')
```

```
axis([t001+AA t001+BB 0 1.2*max(max(EE1),max(EE2))])
xlabel('t (s)','FontSize',18)
ylabel('E(t)','FontSize',18)
legend('CH1---Exp','CH2---Exp','CH1---Cal','CH2---Cal');
text(t001+0.9*AA,1.1*max(max(EE1),max(EE3)),namestr(1:Lname),'FontSize',14)
namestr2=namestr(1:Lname);
namestr2(Lname+1:Lname+9)='_exp1.dat';
fid2=fopen(namestr2,'wt');
fprintf(fid2,'%s\n','           tt1           E1(exp)         F1(exp)
tt2           E2(exp)         F2(exp)');
for jj=1:length(tnn2)
   fprintf(fid2,'%15.5f %15.5f %15.5f %15.5f %15.5f
%15.5f\n',tnn2(jj),Eo1(jj),FFo1(jj),tnn3(jj),Eo2(jj),FFo2(jj));
end
fprintf(fid2,'%s %13.10f\n','Tao_ch1=',Tao_ch1);
fprintf(fid2,'%s %13.10f\n','t_std_ch1=',t_std_ch1);
fprintf(fid2,'%s %13.10f\n','std_ch1=',std_ch1);
fprintf(fid2,'%s %13.10f\n','t001=',t001);
fprintf(fid2,'%s \n','------------------------------');
fprintf(fid2,'%s %13.10f\n','Tao_ch2=',Tao_ch2);
fprintf(fid2,'%s %13.10f\n','t_std_ch2=',t_std_ch2);
fprintf(fid2,'%s %13.10f\n','std_ch2=',std_ch2);
fprintf(fid2,'%s %13.10f\n','t002=',t002);
fprintf(fid2,'%s \n','------------------------------');
fprintf(fid2,'%s %8.5f\n','kn01=',kn01);
fprintf(fid2,'%s %8.5f\n','kn02=',kn02);
fprintf(fid2,'%s %8.5f\n','peak1=',peak1);
fprintf(fid2,'%s %8.5f\n','peak2=',peak2);
fprintf(fid2,'%s %8.5f\n','step_CH1=',step_CH1);
fprintf(fid2,'%s %8.5f\n','step_CH2=',step_CH2);
fclose(fid2);

namestr3=namestr(1:Lname);
namestr3(Lname+1:Lname+9)='_cal1.dat';
fid3=fopen(namestr3,'wt');
fprintf(fid3,'%s\n','           tt1           E1(cal)         F1(cal)
tt2           E2(cal)         F2(cal)');
for jj=1:10:length(tnn2n)
   fprintf(fid3,'%15.5f %15.5f %15.5f %15.5f %15.5f
%15.5f\n',tnn2n(jj),EE1(jj),FFn1(jj),tnn3n(jj),EE2(jj),FFn2(jj));
end
fprintf(fid3,'%s %13.10f\n','Tao_ch1=',Tao_ch1);
fprintf(fid3,'%s %13.10f\n','t_std_ch1=',t_std_ch1);
fprintf(fid3,'%s %13.10f\n','std_ch1=',std_ch1);
fprintf(fid3,'%s %13.10f\n','t001=',t001);
fprintf(fid3,'%s \n','------------------------------');
fprintf(fid3,'%s %13.10f\n','Tao_ch2=',Tao_ch2);
fprintf(fid3,'%s %13.10f\n','t_std_ch2=',t_std_ch2);
fprintf(fid3,'%s %13.10f\n','std_ch2=',std_ch2);
fprintf(fid3,'%s %13.10f\n','t002=',t002);
fprintf(fid3,'%s \n','------------------------------');
fprintf(fid3,'%s %8.5f\n','kn01=',kn01);
fprintf(fid3,'%s %8.5f\n','kn02=',kn02);
fprintf(fid2,'%s %8.5f\n','peak1=',peak1);
fprintf(fid2,'%s %8.5f\n','peak2=',peak2);
fprintf(fid3,'%s %8.5f\n','step_CH1=',step_CH1);
fprintf(fid3,'%s %8.5f\n','step_CH2=',step_CH2);
```

```
fclose(fid3);
end
fclose(fid1);
toc
```

solveE.m

```
%path(path,'G:\2005gasmixing')
%path(path,'G:\2005gasmixing\4q')
function EE=solveE(FF,tt,dt,mm)
hh=mm*dt;
Ltt=length(tt);
for jj=1:Ltt
   if abs(tt(jj)-min(tt))<hh
      % Direct differentiation of the data using forward differencing---
Second order
      EE(jj)=(-FF(jj+2*mm)+4*FF(jj+1*mm)-3*FF(jj))/(2*hh);
   elseif abs(tt(jj)-max(tt))<hh
      % Direct differentiation of the data using backward differencing---
Second order
      EE(jj)=(FF(jj-2*mm)-4*FF(jj-1*mm)+3*FF(jj))/(2*hh);
   else
      %1 Direct differentiation of the data using central differencing---
Second order
      EE(jj)=(FF(jj+1*mm)-FF(jj-1*mm))/(2*hh);
   end
end
```

h4_LMarq.m

```
%path(path,'E:\homework\Project')
% Subroutine for curve fitting by using Levenberg-Marquardt method
%function [f,CC,Chi2]=h4_LMarq(MODEL,tt1,tt2,DD,AK0,eps,Lambda1)
function [f,CC,Chi2]=h4_LMarq(MODEL,DD,tnn1,AK0,eps,Lambda1)
dAK=1E-4;                              % Input
NN=length(DD);
MM=length(AK0);
ratio=10;
crit=1;
while crit>=eps
   for i0=1:MM
      AK(:,i0)=AK0;
      AK(i0,i0)=AK0(i0)+dAK;
   end
   for j1=1:MM
      sum1=0;
      Chi2=0;
      for i1=1:NN
%        AK0(MM+1)=tt1(i1);
%        AK(MM+1,j1)=tt1(i1);
%        AK0(MM+2)=tt2(i1);
%        AK(MM+2,j1)=tt2(i1);
         AK0(MM+1)=i1;
         AK(MM+1,j1)=i1;
```

```
         DF(j1,i1)=(feval(MODEL,AK(:,j1),tnn1(i1))-
feval(MODEL,AK0,tnn1(i1)))/dAK;
         VF=feval(MODEL,AK0,tnn1(i1));
         sum1=sum1+(DD(i1)-VF)*DF(j1,i1);
         Chi2=Chi2+(DD(i1)-VF)^2;
      end
      BETA1(j1)=sum1;
   end
   %BETA1=BETA1';
   ALPHA1=DF*DF';
   for i2=1:MM
      ALPHA1(i2,i2)=ALPHA1(i2,i2)*(1+Lambda1);
   end
   %dA1=(ALPHA1\BETA1')';
   dA1=h2GaussE(ALPHA1,BETA1');
   %dA1=h2fLU(ALPHA1,BETA1');
   AK01=AK0(1:MM)+dA1';
   crit=norm(dA1'./AK01);
   Chi2_1=0;
   for i3=1:NN
%     AK01(MM+1)=tt1(i3);
%     AK01(MM+2)=tt2(i3);
      AK01(MM+1)=i3;
      VF=feval(MODEL,AK01,tnn1(i3));
      Chi2_1=Chi2_1+(DD(i3)-VF)^2;
   end
   if Chi2_1<Chi2
      AK0=AK01;
      Lambda1=Lambda1/ratio;
   else
      Lambda1=Lambda1*ratio;
   end
end
f=AK01(1:MM);

CC=inv(ALPHA1);
AK2=f;
Chi2=0;
for i3=1:NN
%  AK2(MM+1)=tt1(i3);
%  AK2(MM+2)=tt2(i3);
   AK2(MM+1)=i3;
   VF=feval(MODEL,AK2,tnn1(i3));
   Chi2=Chi2+(DD(i3)-VF)^2;
end
```

h2GaussE.m

```
% Gauss Elimination with Column Pivoting
function f=h2GaussE(A,B)
N=length(B);
A1=A;
A1(:,length(B)+1)=B;
for k=1:N-1
   amax=0;
```

```
   for i=k:N
      if amax<abs(A1(i,k))
         amax=abs(A1(i,k));
         ik=i;
      end
   end
   if amax==0
      result='No result!'
      return
   elseif abs(ik-k)>0
      for j=k:N+1
         tmp=A1(k,j);
         A1(k,j)=A1(ik,j);
         A1(ik,j)=tmp;
      end
   end
   for i=k+1:N
      lik=A1(i,k)/A1(k,k);
      for j=k+1:N+1
         A1(i,j)=A1(i,j)-lik*A1(k,j);
      end
   end
end
if A1(N,N)==0
   result='No result!'
else
   Xgauss(N)=A1(N,N+1)/A1(N,N);
   for i=N-1:-1:1
      sum1=0;
      for j=i+1:N
         sum1=sum1+A1(i,j)*Xgauss(j);
      end
      Xgauss(i)=(A1(i,N+1)-sum1)/A1(i,i);
   end
end
f=Xgauss;
```

FT_model.m

```
%path(path,'G:\2005gasmixing')
%path(path,'G:\2005gasmixing\4q')
function f=FT_model(AK,tt)
NN=length(AK);
ii=AK(NN);
f=(AK(1)*AK(2)+AK(3)*tt^AK(4))/(AK(2)+tt^AK(4));
```

fy.m

```
%path(path,'E:\homework\Project')
function y=fy(xxxx)
y=xxxx;
```

Processing of CFD simulation data

nnFfitmain.m (Main program)

```
tic
clear
clc
path(path,'G:\RTD\gasmixing_Mar')

%path(path,'G:\RTD\gasmixing_Mar\D0po_ave')%1111111111%
%path(path,'G:\RTD\gasmixing_Mar\D0po_ori')%2222222222%
%path(path,'G:\RTD\gasmixing_Mar\D0s001apo')%3333333333%
%path(path,'G:\RTD\gasmixing_Mar\D001po')%4444444444%
%path(path,'G:\RTD\gasmixing_Mar\D001s0apo')%5555555555%
%path(path,'G:\RTD\gasmixing_Mar\D0002po')%6666666666%
%path(path,'G:\RTD\gasmixing_Mar\D005po')%7777777777%
%path(path,'G:\RTD\gasmixing_Mar\kku1_vg0')%8888888888%
%path(path,'G:\RTD\gasmixing_Mar\kku2_vg0')%9999999999%
%path(path,'G:\RTD\gasmixing_Mar\kku2n')%0000000000%
%path(path,'G:\RTD\gasmixing_Mar\kku4_vg0')%aaaaaaaaaa%
%path(path,'G:\RTD\gasmixing_Mar\kku8_vg0')%bbbbbbbbbb%
%path(path,'G:\RTD\gasmixing_Mar\kku16_vg0')%cccccccccc%
%path(path,'G:\RTD\gasmixing_Mar\kkv2')%dddddddddd%
%path(path,'G:\RTD\gasmixing_Mar\nkkv')%eeeeeeeeee%
%path(path,'G:\RTD\gasmixing_Mar\nkkv1')%ffffffffff%
%path(path,'G:\RTD\gasmixing_Mar\zkkv1')%gggggggggg%
%path(path,'G:\RTD\gasmixing_Mar\zkkv2')%hhhhhhhhhh%
%path(path,'G:\RTD\gasmixing_Mar\zkkv3')%iiiiiiiii%

%    nnFfitmain.m    %
name3='L';
Firp=1;
Nexp=18;
skip=0;
%*******************************************************%
fid1=fopen('namelist18_CFD.txt','r');
for LL2=1:skip
   skip_line=fgetl(fid1);
end
for LL1=Firp:Nexp
   clear tt FF EE t_ave t_std std_ch tmp1 tmp2 tmp
   namestr=fgetl(fid1);
   Lname=length(namestr)-4;
   AA=0;
   BB=8;
   fid=fopen(namestr,'r');
   for i1=1:3
      fgetl(fid);
   end
   NN0=400;
   dt=0.01;
   for ii=1:NN0
      tmp1=fscanf(fid,'%f',1);
      tmp2=fscanf(fid,'%f',1);
      tmp(ii,1)=tmp1;
      tmp(ii,2)=tmp2;
```

```
   end
   fclose(fid);
   namestr(3)=name3;

   tt=tmp(:,1)-(0.000);
   FF=tmp(:,2);
   LL=length(FF);

%%%%%%%%%%%%%
   mm1=1;
   EE=nsolveE(FF,tt,dt,mm1);

   tmp111=0;
   tmp222=0;
   tmp333=0;

   for i4=1:length(EE)
      tmp111=tmp111+EE(i4);
      tmp222=tmp222+(tt(i4))*EE(i4);
      tmp333=tmp333+(tt(i4))^2*EE(i4);
   end
   t_ave=tmp222/tmp111;
   t_std=tmp333/tmp111-t_ave^2;
   std_ch=t_std/t_ave^2;

   figure
   SUBPLOT(2,1,1)
   hold on
   plot(tt,FF,'bd-')
%%%%%%%%%%%%%%%%%%%%%%%%%%%%%%%%%%%%%%%%%%%%%%%
   legend('F(t)---Exp');
   xlabel('t (s)','FontSize',18)
   ylabel('F(t)','FontSize',18)
   text(0.9*AA,1.1,namestr(1:Lname),'FontSize',14)
   axis([AA BB 0 1.2])

   SUBPLOT(2,1,2)
   hold on
   plot(tt,EE,'ro-')
   axis([AA BB 0 1.2*max(EE)])
   xlabel('t (s)','FontSize',18)
   ylabel('E(t)','FontSize',18)
   legend('E(t)---Exp');
   text(0.9*AA,1.1*max(EE),namestr(1:Lname),'FontSize',14)

   namestr2=namestr(1:Lname);
   namestr2(Lname+1:Lname+9)='_exp1.dat';
   fid2=fopen(namestr2,'wt');
   fprintf(fid2,'%s\n','           tt           EE(exp)         FF(exp)');
   for jj=1:length(tt)
      fprintf(fid2,'%15.5f %15.5f %15.5f\n',tt(jj),EE(jj),FF(jj));
   end
   fprintf(fid2,'%s \n','------------------------------');
   fprintf(fid2,'%s %13.10f\n','Tao_ch2=',t_ave);
   fprintf(fid2,'%s %13.10f\n','t_std_ch2=',t_std);
   fprintf(fid2,'%s %13.10f\n','std_ch2=',std_ch);
   fprintf(fid2,'%s \n','------------------------------');
```

```
   fclose(fid2);
   t_ave1(LL1)=t_ave;
   t_std1(LL1)=t_std;
end
fclose(fid1);
t_ave2=t_ave1(1);
t_std2=t_std1(1);
r=[0 0 0.015 0.03 0.045 0.06 0.075 0.09 0.105 0.12 0.125 0.13 0.135 0.14
0.145 0.15 0.165 0.18];
for LL1=Firp+1:Nexp
   dt_ave(LL1)=t_ave1(LL1)-t_ave1(1);
   dt_std(LL1)=t_std1(LL1)-t_std1(1);
   dt_std_ch(LL1)=dt_std(LL1)/dt_ave(LL1)^2.0;
   Pe(LL1)=6.0/(-2.0+(4.0+12.0*dt_std_ch(LL1))^0.5);
end

namestr3=namestr(1:Lname);
namestr3(Lname+1:Lname+9)='_cal1.dat';
fid2=fopen(namestr3,'wt');
fprintf(fid2,'%s\n',' t_ave(In) t_ave(Out)  std(In)  std(Out)   dt_ave
dt_std     std_ch    r     Pe');
for jj=Firp+1:Nexp
   fprintf(fid2,'%9.4f %9.4f %9.4f %9.4f %9.4f %10.2e %9.4f %6.3f
%6.2f\n',t_ave1(1),t_ave1(jj),t_std1(1),t_std1(jj),dt_ave(jj),dt_std(jj),dt_s
td_ch(jj),r(jj),Pe(jj));
end
fclose(fid2);
toc
```

nsolveE.m

```
function EE=nsolveE(FF,tt,dt,mm)
hh=mm*dt;
Ltt=length(tt);
for jj=1:Ltt
   if abs(tt(jj)-min(tt))<hh
      % Direct differentiation of the data using forward differencing---
Second order
      EE(jj)=(-FF(jj+2*mm)+4*FF(jj+1*mm)-3*FF(jj))/(2*hh);
   elseif abs(tt(jj)-max(tt))<hh
      % Direct differentiation of the data using backward differencing---
Second order
      EE(jj)=(FF(jj-2*mm)-4*FF(jj-1*mm)+3*FF(jj))/(2*hh);
   else
      %1 Direct differentiation of the data using central differencing---
Second order
      EE(jj)=(FF(jj+1*mm)-FF(jj-1*mm))/(2*hh);
   end
end
```

APPENDIX K

USER DEFINED FUNCTIONS USED IN CFD SIMULATIONS

```
#include "udf.h"

#define pi 4.*atan(1.)        /*     (-)     */
#define g -9.81               /*  (m/s2) */
#define nn 7.0                /*     (-)    */

/* Operating conditions */
#define dp 1.16e-3            /*     (m)   */
#define void0 0.39            /*     (-)     */
#define Di 0.0381             /*     (m)   */
#define D0 0.01905            /*     (m)   */
#define Dc 0.45               /*     (m)   */
#define Ro 1.225              /*(kg/m3) */
#define Mu 1.7894e-5          /*  (Pa.s)  */
#define gamma 45.             /*     (o)   */
#define H0 0.396              /*     (m)  */
#define Ugb 23.5              /*  (m/s)  */
#define kks 1.0               /*     (-)   */

/* Gasmixing conditions */
#define D  0.0002             /* (m2/s)*/
#define tt0 1.75000           /*   (s)   *//* Read the exact value from FLUENT.*/


/* Inlet velocity profile */
DEFINE_PROFILE(inlet_x_velocity, thread, index)
{
    real x[ND_ND];
    real y, temp, Vave;
    real Re;
    face_t f;
    temp = (nn + 1.) * (2. * nn + 1.) / (2. * pow(nn, 2.));
    Vave = Ugb * pow((Di / D0),2.);
    Re = Ro * Vave * D0 / Mu;
    begin_f_loop(f, thread)
    {
        F_CENTROID(x,f,thread);
        y = x[1];
        if ( Re >= 4000.)
        {
```

```
            F_PROFILE(f, thread, index) = (temp * Vave) * pow((1.- y / (D0 / 2.)),(1. / nn));
        }
        else
        {
            F_PROFILE(f, thread, index) = (2. * Vave) * (1. - pow((y / (D0 / 2.)),2.));
        }
    }
    end_f_loop(f, thread)
}


/* Outlet velocity profile */
DEFINE_PROFILE(outlet_x_velocity, thread, index)
{
    real x[ND_ND];
    real Vave;
    face_t f;
    Vave = Ugb * pow((Di / Dc),2.);
    begin_f_loop(f, thread)
    {
        F_PROFILE(f, thread, index) = - Vave;
    }
    end_f_loop(f, thread)
}


/* Axial solid phase source term */
DEFINE_SOURCE(axial_solid_source, cell, ct5, dS, eqn)
{
    /* X direction */
    real source;
    int air_index = 0; /* primary phase index is 0 */
    int solids_index = 1; /* secondary phase index is 1 */
    double DPfb, AA, BB, DPfb0, DPt, kka;
    double rho_g, rho_s, mu_g, void_g, x_vel_g, x_vel_s, slip_x;
    double URx, Rex, cd0, kgs_x;
    double xc[ND_ND];

    /* find the threads for the gas (primary) */
    /* and solids (secondary phases) */
    Thread *mixture_thread = THREAD_SUPER_THREAD(ct5); /* mixture-level thread pointer */
    Thread *thread_g, *thread_s;
    thread_g = THREAD_SUB_THREAD(mixture_thread, air_index); /* gas phase */
    thread_s = THREAD_SUB_THREAD(mixture_thread, solids_index); /* solid phase*/
    /* find phase velocities and properties*/
```

```
    void_g = C_VOF(cell, thread_g);/* gas volume fraction*/
    x_vel_s = C_U(cell, thread_s);
x_vel_g = C_U(cell, thread_g);
slip_x = x_vel_g - x_vel_s;

rho_g = C_R(cell, thread_g);
rho_s = C_R(cell, thread_s);
mu_g = C_MU_L(cell, thread_g);

DPfb0 = -(1.-void0)*rho_s*g*H0;
/* Stable Spouting (29.8898------18.8941m/s) */
DPt = -0.0530902*Ugb+3.69937;
kka = DPt * 1000. / DPfb0;
/* printf("kka = %f\n",kka);*/

    DPfb = (1.-void_g)*rho_s*g;
    C_CENTROID(xc,cell,ct5);
    if ((xc[0] <= H0) && (void_g <= 0.8))
    {
        /* source term */
        source = (-DPfb + kka * DPfb);
        /* derivative of source term w.r.t. x-velocity. */
        dS[eqn] = 0;
    }
    else
    {
        /* source term */
        source = (-DPfb + kks * DPfb);
        /* derivative of source term w.r.t. x-velocity. */
        dS[eqn] = 0;
    }
    return source;
}


/* Define which user-defined scalars to use. */
enum
{
    C_RTD_UDS
};


/* Diffusivity */
DEFINE_DIFFUSIVITY(UDS1_diff, c, t, i)
{
    int air_index = 0; /* primary phase index is 0 */
```

```
    int solids_index = 1; /* secondary phase index is 1 */
    double rho_g, void_g, D1;

    /* find the threads for the gas (primary) */
    /* and solids (secondary phases) */
    Thread *mixture_thread = THREAD_SUPER_THREAD(t); /* mixture-level thread pointer
*/
    Thread *thread_g, *thread_s;
    thread_g = THREAD_SUB_THREAD(mixture_thread, air_index); /* gas phase */
    /* find phase velocities and properties*/
void_g = C_VOF(c, thread_g);/* gas volume fraction*/
rho_g = C_R(c, thread_g);
    if (void_g <= 0.8)
    {
        D1 = 0.0; /* in the annulus */
    }
    else
    {
        D1 = 0.001; /* in the spout */
    }
    return D * rho_g;/* by changing D to D1 to obtain different setting*/
}


/* Outlet boundary condition for UDS */
DEFINE_PROFILE(outlet_bc, thread, position)
{
    face_t f;
    begin_f_loop (f,thread)
    {
            cell_t cf = F_C0(f,thread);
            Thread *tf = THREAD_T0(thread);
            F_PROFILE(f,thread,position) = C_UDSI(cf,tf,0);
    }
    end_f_loop (f,thread)
}


/* Inlet boundary condition for UDS ----Negative step tracer */
DEFINE_PROFILE(ngF_inlet_tracer, thread, index)
{
    real flow_time = CURRENT_TIME;
    real tmp;
    real dt = flow_time - tt0;
    face_t f;
    begin_f_loop(f, thread)
```

```
    {
        if ( dt < 0.52 )
        {
            tmp = 0;
        }
        else if ( dt < 0.617 )
        {
            tmp = 11.3373*pow(dt,3) -14.6376*pow(dt,2)+ 6.19851*dt-0.858493;
        }
        else if ( dt < 1.54 )
        {
            tmp = -0.202443*pow(dt,4.)+ 1.79258*pow(dt,3.)- 5.78275*pow(dt,2.)+ 8.05988*dt-
3.10627;
        }
        else
        {
            tmp = 1.;
        }
        F_PROFILE(f, thread, index) = 1. - tmp;
    }
    end_f_loop(f, thread)
}


/* Inlet boundary condition for UDS ----Pulse tracer */
DEFINE_PROFILE(E_inlet_tracer, thread, index)
{
    real flow_time = CURRENT_TIME;
    real dt = flow_time - tt0;
    face_t f;
    begin_f_loop(f, thread)
    {
        if ( dt < 0.11 )
        {
            F_PROFILE(f, thread, index) = 0;
        }
        else if ( dt < 0.185 )
        {
            F_PROFILE(f, thread, index) = 0.00425345+0.0378165*dt-3.7252*pow(dt,2.)-
15.2474*pow(dt,3.)+394.917*pow(dt,4.);
        }
        else if ( dt < 0.9 )
        {
            F_PROFILE(f, thread, index) = 10.455-165.279*dt+952.681*pow(dt,2.)-
2449.1*pow(dt,3.)+3152.28*pow(dt,4.)-2002.95*pow(dt,5.)+502.123*pow(dt,6.);
        }
```

```
        else if ( dt <= 1.69 )
        {
            F_PROFILE(f, thread, index) = 2.2287-3.53085*dt+1.85693*pow(dt,2.)-
0.324204*pow(dt,3.);
        }
        else
        {
            F_PROFILE(f, thread, index) = 0;
        }
    }
    end_f_loop(f, thread)
}


/* Inlet boundary condition for UDS ----Positive step tracer */
DEFINE_PROFILE(F_inlet_tracer, thread, index)
{
    real flow_time = CURRENT_TIME;
    real dt = flow_time - tt0;
    face_t f;
    begin_f_loop(f, thread)
    {
        if ( dt < 0.52 )
        {
            F_PROFILE(f, thread, index) = 0;
        }
        else if ( dt < 0.617 )
        {
            F_PROFILE(f, thread, index) = 11.3373*pow(dt,3) -14.6376*pow(dt,2)+ 6.19851*dt-
0.858493;
        }
        else if ( dt < 1.54 )
        {
            F_PROFILE(f, thread, index) = -0.202443*pow(dt,4.)+ 1.79258*pow(dt,3.)-
5.78275*pow(dt,2.)+ 8.05988*dt-3.10627;
        }
        else
        {
            F_PROFILE(f, thread, index) = 1;
        }
    }
    end_f_loop(f, thread)
}
```

```
/* Save average velocity field and gas volume fraction to UDMs */
DEFINE_ON_DEMAND(average_field)
{
    Thread *t;
    cell_t c;
    Domain *d = Get_Domain(2);
    real delta_time_sampled = RP_Get_Real("delta-time-sampled");
    real flow_time = CURRENT_TIME;
    printf("time_sampled = %f\n",delta_time_sampled);
    thread_loop_c (t,d)
    {
        begin_c_loop (c,t)
        {
            C_UDMI(c,t,0) = C_STORAGE_R(c,t, SV_VOF_MEAN)/delta_time_sampled;
            C_UDMI(c,t,1) = C_STORAGE_R(c,t, SV_U_MEAN)/delta_time_sampled;
            C_UDMI(c,t,2) = C_STORAGE_R(c,t, SV_V_MEAN)/delta_time_sampled;
        }
        end_c_loop (c,t)
    }
    printf("current_time = %f\n",flow_time);
}


/* Save adjusted velocity field to UDMs */
DEFINE_ON_DEMAND(Varied_field_Ug)
{
    Thread *t;
    cell_t c;
    Domain *d = Get_Domain(2);
    double Db, zkkv, roR, tmp1;
    double x[ND_ND];
    thread_loop_c (t,d)
    {
        begin_c_loop (c,t)
        {
            C_CENTROID(x,c,t);
            Db = Di + 2. * x[0] * tan(gamma / 2. * pi / 180.);
            if (x[0] <= H0)
            {
                roR = x[1] / (Db / 2.);
                if (roR <= 0.5)
                {
                    zkkv = 0.5;
                }
                else
                {
```

```
                zkkv = (-3.5897555 + 7.600385 * roR);
            }

            tmp1 = 2.2323612 + 29.601017 * x[0] - 2545.8697 * pow(x[0],2.) + 78050.446 *
pow(x[0],3.);
            tmp1 = tmp1 - 1312673.5 * pow(x[0],4.) + 12862832. * pow(x[0],5.) - 76390063.
* pow(x[0],6.);
            tmp1 = tmp1 + 279236060. * pow(x[0],7.) - 614885800. * pow(x[0],8.) +
748780690. * pow(x[0],9.);
            tmp1 = tmp1-387529290. * pow(x[0],10.);
            zkkv = zkkv * tmp1;
        }
        else
        {
            zkkv=1.;
        }
        C_UDMI(c,t,3) = C_U(c,t) * zkkv;
    }
    end_c_loop (c,t)
  }
}
```